The structural selectivity and various ligands of PPAR gamma

by

Benjamin Soon Kai Chua

Department of Molecular Life Sciences

School of Biological Sciences

Thesis submitted for fulfilment of the requirements for the degree of

Doctor of Philosophy

July 2023

THE UNIVERSITY of ADELAIDE

HDR declaration

I certify that this work contains no material which has been accepted for the award of any other degree or diploma in my name, in any university or other tertiary institution and, to the best of my knowledge and belief, contains no material previously published or written by another person, except where due reference has been made in the text. In addition, I certify that no part of this work will, in the future, be used in a submission in my name, for any other degree or diploma in any university or other tertiary institution without the prior approval of the University of Adelaide and where applicable, any partner institution responsible for the joint award of this degree. The author acknowledges that copyright of published works contained within the thesis resides with the copyright holder(s) of those works. I give permission for the digital version of my thesis to be made available on the web, via the University's digital research repository, the Library Search and also through web search engines, unless permission has been granted by the University to restrict access for a period of time.

Acknowledgements

Finishing this thesis has not been easy. I want to thank my supervisors and teachers for their expertise and patience, and for their kind words of advice right before I left. I want to thank my fellow students, some of whom are now already Doctors. You are a special bunch, I could not have asked for better people to be with, especially in a foreign country. To the two who spoke to me when the deadline was nearing, I honestly think that your words pushed me past the finish line and I can never thank you both enough. I also want to thank my family, these two years have not been easy, but I am glad to have all of your support. To my partner, thank you for coming along on this journey. I have spoken to every one of you and thanked you in person, but this is just a little paragraph for everyone else to know that all of you have, in your own ways, changed my life, and I am better for it.

Abstract

The peroxisomal proliferator activated receptor (PPAR) is a nuclear receptor that regulates a range of genes, involved in processes related to energy metabolism, energy storage, inflammation and cell differentiation. These processes are dysregulated in diseases such as metabolic syndrome (MS), diabetes, cardiovascular disease and non-alcoholic fatty liver disease. In addition, due to its involvement in processes that generate energy in cells, PPARs are thought to play roles in diseases that affect the central nervous system, including dementias such as Alzheimer's disease and mental illnesses such as depression. PPARs could even play a role in cancer progression and treatment through cancer immunotherapy. However, despite its involvement in various pathologies, there are currently only a few clinically approved PPAR activating drugs in use for management of dyslipidemia and type 2 diabetes. Currently there is difficulty in designing drugs that target PPARγ. It was noticed that the PPARγ ligands that resulted in less off-target side effects, in many cases did not differ greatly in structure than those with off-target side effects (eg. Glitazones). PPARα/γ ligands that were thought to be potentially unsafe, did not display side effects and had good efficacy for various metabolic diseases (eg. Saroglitazar). A new PPARα ligand that was shown to be safe and efficacious, did not meet primary endpoints in clinical trials (eg. Pemafibrate). Studies suggested that full agonism of PPARγ may cause side effects and partial agonism of PPARγ could potentially provide the same benefits as full agonism of PPAR. Individuals also seem to respond differently to PPAR agonists.

In this thesis, we characterised various ligands in hopes of creating a PPAR targeting molecule with reduced side effects. We started by understanding the differences between the amino acid residues that make up the ligand binding pocket of the three PPAR subtypes α, δ and γ. Through this thesis, we characterised various ligands that target PPARγ with activation profiles based on the current trends in PPAR ligand design. A PPARγ partial agonist was explored, followed by a structural study of a series of ligands resulting in a compound that was a partial agonist for PPARγ but inhibited LOX and COX enzymes which are involved in inflammation. Then we characterised ligands with various activation profiles that were screened using a machine learning algorithm from a wide chemical space, distinct from traditional PPAR ligands to avoid ligand specific side effects. Finally, we demonstrated that clinically observed mutations typically resulted in a diminished response to PPAR ligands, but in some cases could increase an individual's response to the same ligand. Mutations also differentially affect responses to ligands of different activity profiles. This thesis characterised various ligands with favourable PPAR activation profiles for further investigation and suggests a possible explanation for side effects with PPAR activation.

Content page

Chapter 1

Introduction

1.1 Nuclear receptors and PPARs

Nuclear receptors (NRs) are a family of transcription factors, which are proteins that control the transcription of genes. NRs are involved in a range of biological processes, including metabolism, development, reproduction and cognition, and disrupting the function of these NRs may lead to various diseases and cancer (Nuclear Receptors Nomenclature Committee, 1999, Germain et al. 2006, Weikrum, et al., 2018). Briefly, NRs contain 5 domains named A-E: Domains A/B, which is typically disordered and contains an activation function 1 (AF1) region which interacts with coregulator proteins; Domain C which contains a DNA binding domain; Domain D, a short linker region; Domain E which contains a ligand binding domain (LBD) that binds an intra or extracellular lipophilic biological signal and an activation function 2 (AF2) region which interacts with coregulator proteins (discussed in detail below, sections 1.3 and 1.4). On binding of the ligand and recruitment of coregulator proteins (DNA modifying proteins or DNA transcription machinery), NRs regulate expression of sets of genes. There are 48 human NRs, which are organized into subfamilies and groups based on a phylogenetic tree constructed from amino acid sequence similarity (Nuclear Receptors Nomenclature Committee, 1999, Germain et al. 2006). Each NR can have subtypes and isotypes, subtypes refer to proteins expressed from different genes, while isotypes refer to proteins expressed from the same gene but differ in sequence due to alternate promotor usage or splicing of introns and exons (Mangelsdorf et al., 1995).

The peroxisome proliferator-activated receptor (PPAR) is one of these NRs, and it controls various aspects of energy metabolism, storage and usage in the body through gene regulation. Three subtypes of PPARs are known to exist in the human body, α, β/δ and γ, and these subtypes play complementary and non-redundant functions in the human body (Dubois et al., 2017). The PPARδ and γ subtypes display different isoforms (Table 1.) which are produced by differential splicing of introns/exons of the PPAR genes, producing different mRNA transcripts. These isoforms might be involved in regulating the transactivation of genes as well as translation efficiency of the PPAR protein, for example, by generating truncated PPAR proteins that bind ligands but are unable to transactivate genes (Lundell et al., 2007, Aprile et al. 2018).

Subtypes	Isoforms	Other names	Uniprot identifier	References
PPARα		NR1C1	Q07869-1	Sher et al., 1993
PPARδ	δ1, δ2	PPARβ, NUC1, NUCII, NR1C2, FAAR	Q03181-1	Schmidt et al., 1992, Kliewer et al., 1994, Amri et al., 1995, Lundell et al., 2007
PPARγ	γ1, γ2, γ3	NR1C3, ARF6	P37231-1	Greene et al., 1995, Zhou et al., 2002, Farmer 2006

Table 1. The PPAR subtypes, isoforms, other aliases and Uniprot identifiers. Acronyms: NR1C1, refers to Nuclear Receptor Subfamily 1 Group C Member 1. FAAR, refers to Fatty Acid activated Receptor.

Official nomenclature (NR1C_) follows recommendations of reference: Nuclear Receptors Nomenclature Committee, 1999.

1.2 Discovery of PPAR

In 1990, the PPARα encoding gene was first described in mice through low stringency hybridization of DNA probes to cDNA libraries, designed based on a conserved region in the DNA binding domain (DBD) of several known NRs (Issemann and Green, 1990). The first human PPAR (hPPAR) to be isolated was the subtype hPPARδ in 1992, using primers corresponding to conserved regions in both the DBD and LBD (Schmidt et al., 1992). At that time, it was classified as a separate receptor (named NUCI) and not a direct human homolog to mouse PPARδ (mPPARδ) due to its low sequence similarity (Schmidt et al., 1992, Sher et al., 1993, Greene et al., 1995). Sequencing results prompted the renaming of NUCI to PPARβ/δ (Michalik et al., 2006). This was followed by the discovery hPPARα in 1993 and then finally hPPARγ in 1995, using variations of the same method mentioned above (Sher et al., 1993, Greene et al., 1995).

The PPARs were known as an 'orphan receptor' – which referred to NRs discovered without their corresponding endogenous ligands (Chawla et al., 2001, Benoit et al., 2006). However, due to the prior development of the co-transfection assay (transfecting two plasmids into a cell simultaneously, one expressing the protein of interest and one expressing the reporter gene) as well as the discovery that the DBD and LBD of NRs were able to function independently of one another, it was possible to screen for potential ligands that targeted these orphan receptors, including PPAR. This was done by fusing the LBD of an orphan receptor to the DBD of a known NR, which has a known DNA binding site (also known as a response element), and cloning this same DNA sequence upstream of the reporter gene. On binding of a ligand to the LBD, conformational change occurs and the DBD binds to the DNA binding site and activates transcription of the reporter gene, resulting in a quantifiable output. This discovery process was termed as 'reverse endocrinology', which differed from the 'traditional' process where the high affinity ligands of NRs (eg. Glucocorticoid Receptor, Estrogen Receptor, Vitamin D Receptor) were first isolated and characterised before the description of their corresponding NRs (Blumberg and Evans 1998, Evans and Mangelsdorf 2014). The co-transfection assay allowed for greater versatility in the cell models used, and more importantly, the inducibility and sensitivity of the transfected system allowed screening of possible lower affinity endogenous ligands (Evans and Mangelsdorf 2014).

Using the co-transfection assay, Fibrates, a group of chemicals derived from fibric acid, were identified as synthetic ligands selective for hPPARα based on the observations from mPPARα (Sher et al., 1993, Issemann and Green 1990). This was quickly followed by studies using various techniques to prove direct binding of the Fibrates to hPPARα, as opposed to metabolic intermediates of or upregulated endogenous ligands due to the Fibrates (Forman et al., 1997). Using a ligand binding assay along with a co-transfection assay, the Thiazolidoine (TZDs) compound class, which were synthesized from

Fibrates, was found to bind the PPARγ subtype selectively (Lehmann et al., 1995). The selectivity of a ligand here refers to the ability of a ligand to discriminate between related protein subtypes. The TZD chemical class then paved the way for the synthesis of the first hPPARδ selective compounds, which till that point, did not have a chemical compound that activated it in the nanomolar concentration range in co-transfection assays (Oliver et al., 2001).

The identification of endogenous ligands for PPARs were also of great interest as it would shed light on PPAR function, which could potentially lead to new therapeutic avenues (Schupp and Lazar 2010, Evans and Mangelsdorf 2014). Using co-transfection assays, researchers demonstrated binding of various fatty acids and eicosanoids to PPARs (Keller et al., 1993, Bocos et al., 1995, Yu et al., 1995, Kliewer et al., 1995, Forman et al., 1997, Kliewer et al., 1997, Krey et al., 1997). However, transfection assays do not demonstrate direct ligand binding (Varanasi et al., 1996). This was a key issue since most fatty acids and derivatives activated PPAR at relatively higher concentrations (micromolar concentrations) compared to classic NRs like vitamin D receptor (VDR) and estrogen receptor (ER) and their respective endogenous ligands (Göttlicher et al., 1992, Forman et al., 1995, Nagy et al., 1998, Chawla et al., 2001). This observation casted doubt on fatty acids and metabolites as PPAR ligands, as they may not be present at high enough concentrations physiologically to definitively demonstrate binding (Lehrke and Lazar, 2005). From this point, researchers used other *in vitro* methods to not only demonstrate direct binding of fatty acids to PPAR but also at physiologically relevant concentrations, like radioligand or fluorescence-based competition binding assays, scintillation proximity assays, Förster resonance energy transfer (FRET) assays (Kliewer et al., 1995, Nagy et al., 1998, Xu et al., 1999, Hostetler et al., 2005). Researchers also used mass spectrometry to analyse the concentrations of the various fatty acids available in human serum that bind PPAR (Jüngling and Kammermeier, 1988, Banner et al., 1993, Kopf and Schmitz, 2013). Eventually, crystal structures of PPAR bound to various fatty acids and its metabolites and were published (Xu et al. 1999, Fyffe et al., 2006, Itoh et al., 2008, Jin et al., 2011, Egawa et al., 2016, Shang et al., 2018, Kamata et al., 2020). Currently, there are only endogenous ligands identified for PPARγ and α but not PPARδ, and not all of these endogenous ligands have an identified physiological role (Chakravarthy et al., 2009, Takada and Makishima 2020).

1.3 Structure of the PPAR protein

The PPARs share a conserved structure with most NRs. It is about 441-505 amino acids long and is organized into 5 domains, labelled A to E from N to C terminus (Figure 1, Germain et al., 2006, Weikrum et al., 2018, Uniprot identifiers PPARα, γ, δ: Q07869-1, P37231-1, Q03181-1).

Domains A/B contain an AF1 region, which allows for transcriptional activation that is ligand independent (Brunmeir and Xu 2018). This region is usually unstructured and is poorly conserved between the PPAR subtypes, as well as between all NRs (Germain et al., 2006, Chandra et al., 2008,

Rochel et al., 2011, Garza et al., 2011, Weikrum et al., 2018). The A/B domains are involved in the recruitment of coregulators and contain sites for post-translational modifications (PTMs) such as phosphorylation, acetylation, ubiquitination and small-ubiquitin-like-modifier-ylation (SUMOylation). These PTMs may affect gene transcription by altering recruitment of coregulators, interfering with ligand binding, or affecting degradation (Viswakarma et al., 2010, Brunmeir and Xu 2018). It is also hypothesized that this region stabilizes and organizes upon the binding of ligands to the LBD, which modulates recruitment of other coregulators or components of the DNA transcription complex (Germain et al., 2006, Brunmeir and Xu 2018, Weikrum et al., 2018, Yu et al., 2020, Mosure et al., 2022). This region contains a nuclear localization signal (NLS), NLS 2 (Umemoto and Fujiki 2012).

Domain C contains a DBD which is highly conserved between NRs. The DBD comprises two zinc finger motifs that bind to stretches of DNA sequences referred to as NR Response Elements (REs) or in the case of PPAR, PPAR response elements (PPREs, Chandra et al., 2008). Domain D is a flexible 'hinge region' that bridges domains C and E, which allows the NR to position itself to interact with DNA as well as its dimer partner, the Retinoid X Receptor (RXR, Chandra et al., 2008, Rochel et al., 2011). These regions contain a nuclear localization signal, NLS 1, spanning the end of Domain C to Domain D, and a nuclear export signal (NES), NES1 in Domain C (Umemoto and Fujiki 2012).

Domain E contains the LBD and is responsible for ligand dependent transactivation activity seen with PPAR. It is the largest domain of the PPAR protein and is arranged into a three layered alpha helical sandwich that forms a cavity of about 1300Å, which functions as a ligand binding pocket (Figure 2b). PPARs contains one of the largest ligand binding pockets seen in NRs, and the increased area has been attributed to the additional amino acids making up an extra helix (Helix will be abbreviated to H) that are unique to PPARs, H2', situated between H2 and H3 (Xu et al., 1999, Figure 2a). This domain contains an activation function 2 (AF2) region near the carboxyl terminal end of the protein spanning from the end of H11 through to H12. The AF2 refers to the region in the protein that is necessary for transcriptional activation, determined through mutational analysis (Glass et al. 1997). The 'AF2 coactivator surface', sometimes mentioned in the literature, refers to the solvent exposed face of the protein of the protein formed by H3, 4 and 12 in the agonist-bound LBD conformation (Figure 3a, Kroker and Bruning 2015). Coactivators bind to the hydrophobic pocket delineated by the helices that make up the AF2 coactivator surface (Figure 3a, Xu et al., 1999). Domain F is not seen in PPARs.

1.4 Ligand delivery, recruitment of cofactors and gene transcription

All NR ligands, endogenous and synthetic, augment NR gene transcription to different degrees. The impact that various ligands have on gene transcription can be grouped into the following categories: agonists, partial agonists, antagonists, and inverse agonists (Figure 4). Agonists typically fully activate gene transcriptional activity, partial agonists to 50% or less of the activity of full agonists, antagonists

interfere with gene transcription, reducing it to 0% or control experiment (basal) levels, and inverse agonists brings activity below 0%, or promotes gene modulating activity of the corepressor bound NR complex (Cohen 2006, Tan et al., 2016, Irwin et al., 2022). PPARs are known to have basal activity, even when no ligands are introduced (Frkic et al., 2021). Percentage activity is typically defined relative to activity of the model ligand used in the individual study, for example, studies involving PPARγ typically use Rosiglitazone as a full agonist for comparison, for PPARδ, GW501516 and for PPARα, Fenofibrate. The exact distinction between full and partial agonist also varies between studies.

Regardless of ligand binding, PPAR and RXR form heterodimers (Feige et al., 2005). After heterodimerizing, the PPAR-RXR complex is then able to bind to DNA sequences upstream of PPAR controlled genes, referred to as PPAR Response Elements (PPREs), via the zinc fingers in the DBD/ domain C (Juge-Aubry et al., 1997, Giguere, 1999, Bernardes et al., 2012, Tan et al. 2016). PPREs are composed of two imperfect, hexameric direct repeats of the nucleotide sequence AGGTCA, referred to as half sites. These half sites are spaced by a single adenine residue (Juge-Aubry et al., 1997). Direct repeats with a single nucleotide spacing are grouped under direct repeat 1 (DR1), other response elements contain nucleotide spacings ranging from 1-5 (DR1-5). These spacer residues between the half sites were thought to be a key determinant for NR DNA binding specificity (Mangelsdorf and Evans, 1995, Germain, et al., 2006). However, it seems that many NR dimer pairs including PPAR-RXR, were able to bind to half-sites with different lengths of nucleotide spacings with high affinity (Penvose et al., 2019). It is now understood that the DNA sequence in the 5' and 3' region of PPREs, also called extended sites, contribute significantly to the specificity of NR dimer pair to DNA binding (Tzeng et al., 2015, Penvose et al., 2019). For example, PPARγ preferentially binds to PPREs with AT rich extended half-sites (Penvose et al., 2019).

The PPARs, like most NRs, demonstrate both ligand dependent and independent gene activation (Tan et al., 2016, Hernandez-Quiles et al., 2021). To date, the generally accepted model of PPAR ligand dependent gene activation is as follows: In the cytoplasm, PPAR ligands bind to Fatty Acid Binding Proteins (FABP, Figure 5). On binding, a conformational change in the FABP occurs, resulting in increased localization to the nucleus, either by exposing a NLS which allows translocation of the FABP-ligand complex into the nucleus, or by increasing its association with PPAR and hence its retention within the nucleus (Gillilan et al., 2007, Armstrong et al., 2014, Hughes et al., 2015, Patil et al., 2019). five of nine FABP subtypes have been shown to interact with and potentiate the gene transcription activity of the PPAR subtypes, and each FABP subtype is thought to only localize in the nucleus upon binding to endogenous and synthetic ligands that are selective for a single PPAR subtype (Tan et al., 2002, Gillilan et al., 2007, Armstrong et al., 2014, Hughes et al., 2015). Once in the nucleus, the FABP-ligand complex forms protein-protein interactions with the PPAR, conformational change occurs and the ligand passes into the PPAR ligand binding pocket (Tan et al., 2002, Gillilan 2007, Armstrong et al. 2014, Tan et al., 2016, Patil et al., 2019).

Subtypes	Corresponding FABP
PPARα	FABP 1 (L-FABP), FABP2, FABP 3 (H-FABP)
PPARδ	FABP 5 (E/K-FABP)
PPARγ	FABP 4 (A-FABP)

Table 2. PPARs and their corresponding FABP subtypes. FABP – Fatty Acid Binding Protein. FABP abbreviations: L – Liver, H – Heart, E/K – Epidermal/Keratinocyte, A – Adipose.

On binding to the PPAR ligand binding pocket, agonistic ligands elicit a conformational change that results in the stabilization of H12 in a position pointing from H3, across H4 and towards H10 (Figure 3a, Gampe et al., 2000, Michalik et al., 2006, Bruning et al., 2007, Chandra et al., 2008, Viswakarma et al., 2010). In this ligand-bound state, the PPAR-RXR complex recruits proteins referred to as coactivators to the PPREs, such as the steroid receptor complex (SRC) proteins or the PPARγ coactivator 1α (PGC1α) proteins (Viswakarma et al., 2010, Tan et al., 2016). These coactivators proteins contain the amino acid sequence motif, LXXLL, that binds to a specific region on the AF2 surface between helices H3, H4 and H12 (Gampe et al., 2000, Figure 3a). These coactivator proteins then promote the recruitment of proteins such as histone acetyltransferases (HATs) or methyl transferases which results in unwinding of DNA, as well as other proteins such as the Mediator complex which enables recruitment of the other parts of the general gene transcription complex resulting in the transcription of target genes (Viswakarma et al., 2010). Interestingly, the PPAR-RXR heterodimer is permissive, as in, either the binding of an RXR-targeting or PPAR-targeting ligand to their respective NR LBDs would lead to induction of transcription of gene sets under PPAR-RXR control, and binding of both ligands would have a synergistic effect on transcription of PPAR controlled genes (Kilu et al., 2021). Additionally, in an agonist bound state, PPARs can also repress genes by binding to or releasing other transcription factors, or by sequestering transcription factors from their respective REs through protein-protein interactions (Tan et al., 2016, Sasaki et al., 2019, Francque et al., 2021, Yagai and Nakamura 2022).

On the other hand, on binding to the PPAR ligand binding pocket antagonistic ligands disrupt the AF2 region by interfering with H12 sterically. This alternate H12 conformation promotes the recruitment of corepressors such as the nuclear corepressor (NCoR), silencing mediator for retinoid and thyroid hormone receptor (SMRT, Viswakarma 2010, Legrand et al., 2019). These corepressors have an LXXLXXXL amino acid sequence motif that binds to the same region on the AF2 that is bound by coactivators, between H3, H4 and a displaced H12 (Xu et al., 2002). This longer motif covers a larger area spanning across H4/5 and towards H10/11, which would be partially blocked off if H12 was stabilized in the 'active conformation' seen with agonist binding and coactivator interaction (Figure 3b, Gampe et al., 2000, Xu et al., 2002). Corepressors then recruit histone deacetylases (HDACs) that deacetylate histone tails, resulting in tighter association of DNA and histones, leading to decreased transcription (Germain et al., 2006, Viswakarma 2010, Legrand et al., 2019).

1.5 Biochemistry of PPAR activation

On ligand activation, binding of the ligand-PPAR-RXR complex to the PPREs, followed by the recruitment of various coregulators and components of the general transcriptional complex to the ligand-PPAR-RXR complex results in the transcription of PPAR controlled genes (Viswakarma et al., 2010). These genes code for proteins and enzymes involved in processes such as the transport and uptake of its ligands, metabolism of glucose, fatty acids and its metabolites, and also coordinate gene programs resulting in the differentiation of cells, or larger physiological responses such as inflammation. For simplicity, this section will discuss genes controlled by all PPAR subtypes as a whole – from the literature, PPAR subtype specific genes seem to differ across cell types, and even between different individuals and animal species. References are provided for further reading.

Activation of PPARs results in the regulation of the expression of a number of genes that are involved in the movement of its own ligands between tissues, into cells, as well as between the various cell components. Examples include proteins such as: the CD36 and long chain fatty acid transport protein 4 (FATP4, coded by SLC27A4), which imports free fatty acids from the bloodstream into cells (Rogue et al., 2011, Anderson and Stahl, 2013, Cifarelli and Abumrad et al., 2018); Aquaporin 3 imports glycerol that was released via lipolysis from adipose tissue in response to fasting (Kersten 2014); The monocarboxylate transporter 1 (MCT1, coded by SLC16A1) protein imports ketone bodies from the blood into the cell for β-oxidation (Grabacka et al., 2016); FABPs as mentioned above, bind and transport PPAR-targeting ligands from the cytoplasm into the nucleus (Smathers and Petersen 2011); Proteins such as the carnitine palmitoyltransferases (CPTs) and carnitine-acylcarnitine translocase (CACT, encoded by SLC25A20) move fatty acids from the cytoplasm into the mitochondria for β-oxidation (Rakhshandehroo et al., 2010, Grabacka et al., 2016, Tonazzi et al., 2021). PPARs also regulate transcription of genes involved in cholesterol absorption as well as reverse cholesterol transport, such as Niemann-Pick C1-like 1 (NPC1L1), Apolipoproteins (APO), Adenosine triphosphate – binding cassette transporters (ABC), and VLDR proteins (Rakhshandehroo et al., 2010, Iwayanagi et al., 2011, Kersten 2014, Fang et al., 2016, Hennuyer et al., 2016).

PPAR activation results in the modulation of enzymes involved in the processes of the fatty Acid oxidation (FAO), glycogen synthesis, gluconeogenesis, lipogenesis, ketone body synthesis and ketolysis and lipoprotein and cholesterol metabolism in various tissues (Rakhshandehroo et al., 2010, Kersten 2014, Fang et al., 2016, Dubois et al., 2017, Hong et al., 2019). Examples include: long chain Acetyl-Coa Synthetases (ACSL), which converts fatty acids into their acetyl-CoA derivatives and feeds into the TCA cycle, Acyl-CoA dehydrogenases, which catalyses the first step of Fatty acid β-oxidation (Rakhshandehroo et al., 2010, Kersten 2014, Fang et al., 2016, Dubois et al., 2017); Pyruvate dehydrogenase kinase (PDK), which inhibits the pyruvate dehydrogenase complex (PDC), the enzyme linking glycolysis and oxidative phosphorylation) through phosphorylation, which causes a cell to switch from utilizing glucose to fatty acids as fuel to meet cellular energy requirements (Rakhshandehroo et al., 2010, Zhang et al., 2014); Glycerol kinase (GYK), Phosphoenol pyruvate

carboxykinase 1 (Pck1) and fructose biphosphatase 1 (FBP1), enzymes in the gluconeogenesis pathway (Rakhshandehroo et al., 2010, Kersten 2014); Lipogenesis, through stimulation of genes such as sterol regulatory element-binding protein (SREBP-1) and stearoyl-CoA 9-desaturase (SCD-1, Xu et al., 2018); Mitochondrial proteins acyl-CoA dehydrogenase and HMG-CoA synthetase (HMGCS2), key enzymes in ketogenesis and ketolysis (Rakhshandehroo et al., 2010, Grabacka et al., 2016). PPAR also controls the process of thermogenesis, which is viewed as a mechanism for venting of excess energy, through the transcriptional control of uncoupling protein 1 (UCP1) and transcription factor PPARγ coactivator 1α (PGC1α, Dubois et al., 2017, Lamichanae et al., 2018). UCPs promote the dissipation of energy via heat by allowing 'leaking' of protons across the inner mitochondrial membrane that would otherwise be used for ATP generation, while PGC1α is a crucial cofactor that coordinates transcription of gene programs that not only result in thermogenesis, but also the upregulation of mitochondrial oxidative phosphorylation, biogenesis and mitophagy (Crichton et al., 2017, Chen et al., 2022).

PPARs also modulate inflammation through their interaction with various proteins. PPAR's anti-inflammatory effects generally involves the disruption of NF-κB activity, an essential regulator of inflammation and the immune response, but can also involve other pathways such as the activator protein 1 (AP-1) and signal transducer and activator of transcription (STAT) pathways (Adhikary et al., 2015, Liu et al., 2017, Christofides et al., 2021, Korbecki et al., 2019). Mechanisms include: Interference with NF-κB activity by direct PPAR- NF-κB interaction; Interference with NF-κB activity through modulation of other targets that can influence NF-κB activity, such as via increasing expression of IκBα or B cell lymphoma-6 (BCL-6) which inhibits NF-κB gene expression; altering degradation rate and post translational modifications of NF-κB (Rakhshandehroo et al., 2010, Yang et al., 2008, Tan et al., 2016, Korbecki et al., 2019, Christofides et al., 2021). Other links to inflammation include: PPARs suppress release of inflammatory cytokines – PPAR directly increases expression of interleukin-1 receptor antagonist (IL1-ra), which inhibits the action of the pro-inflammatory cytokine interleukin-1 (IL-1, Chong et al., 2009); PPARs upregulate release of anti-inflammatory cytokines – PPARs directly upregulate the production of IL-10 (Thompson et al., 2007, Muzio et al., 2021); PPARs enhance the innate immune response – PPARs affect expression of mannose binding lectin 2 (MBL2), which serves as an activator of the complement activation pathway in the innate immune response, as well as acute phase proteins complement component 3 (C3, Jack et al., 2001, Mogilenko et al., 2013, Kersten 2014, Dubois et al., 2017, Christofides et al., 2021); PPARs control the expression of antioxidant genes – PPARs modulate expression of catalase and gluthathione peroxidase 3 (Muzio et al., 2021); PPARs interfere with the formation of the inflammasome complex, particularly NLR family pyrin domain containing 3 (NLRP3, Muzio et al., 2021). PPAR activation also suppresses macrophage cell death under hypoxic conditions through upregulation of genes, as well as modulates the function of T cells (Adhikary et al., 2015, Toobian et al., 2021).

Other than specific enzymes and signalling molecules, PPARs are also involved in larger physiological responses through the control of secreted factors such as adiponectin, fibroblast growth factor 21 (FGF21), lipoprotein lipase (LPL), angiopoietin like protein (ANGPTL) and adipsin/complement factor d (Choi et al., 2010, Laganà et al., 2016, Tan et al., 2016, Fang and Judd (2018), Kersten, 2021, Sun et al., 2021, Milek et al., 2022). The ANGPTLs modulate the activity of LPL, an enzyme which metabolizes lipoproteins that contain triglycerides and cholesterol – This promotes lipid repartitioning into storage tissues, prevents lipotoxicity and foam cell formation, and possibly regulates blood vessel permeability (Fernández-Hernando and Suárez, 2020, Kersten, 2021). FGF21 has positive effects on insulin sensitivity and dyslipidemic conditions, through upregulation of adiponectin (Geng et al., 2020). Adiponectin is an adipokine, or adipose-derived hormone, under the control of PPARγ that participates in various metabolic processes (Fang and Judd, 2018). Of interest: Adiponectin is involved in insulin sensitization through the AMPK signalling pathway, the Insulin receptor substrate (IRS)/PI3K/AKt signalling pathway as well as PPARα controlled FAO; Adiponectin promotes anti-inflammatory activity in macrophages and certain cell types – in macrophages, through promoting differentiation and polarization to a less atherogenic phenotype and switching to secretion of anti-inflammatory cytokines, and in certain cell types, through inhibiting inflammatory cytokines (IL-6), and cell adhesion molecules such as vascular cell adhesion molecule – 1 (VCAM1) and intercellular cell adhesion molecule – 1 (ICAM-1, Fang and Judd 2018). Adipsin, another adipokine also known as complement factor D, was found to be related to obesity and has been demonstrated as a target gene correlated with PPARγ phosphorylation S243 in animal models (Choi et al., 2010, Milek et al., 2022).

PPARs are also involved in cell differentiation. PPARs are shown to be involved in chondrocyte, keratinocyte, fibroblast to myofibroblast differentiation (Tan et al., 2002, Ham et al., 2015). PPARs also promote differentiation of monocytes into macrophages, polarization of macrophages, maturation of dendritic cells, which are regulators of T cell function, as well as T cell differentiation (Adhikary et al., 2015, Fang and Judd et al., 2018, Christofides et al., 2021, Toobian et al., 2021). The most well-known example involves PPARγ: PPARγ is both crucial and sufficient for adipocyte differentiation, and is involved in maintaining the status and function of mature adipocytes and its adipocyte class, and plays a role in the eventual apoptosis of adipocytes (Choi et al., 2010, Lefterova et al., 2014, Ambele et al., 2016, Ma et al., 2018).

The activity of PPARs can also be regulated by PTMs. Small molecule modifications, like phosphorylation and acetylation events, are mediated by proteins such as the mitogen-activated protein kinases (MAPKs), cyclin-dependent kinases (CDKs), extracellular signal-regulated kinases (ERKs) and the p38/ c-Jun N-terminal kinases (JNKs). Large molecule modifications such as SUMOylation and ubiquitination are possibly mediated by SUMO, muscle specific RING finger (MuRF)/ tripartite motif containing (TRIM), SUMO-specific protease 2 (SENP2). These PTMs can alter the transactivation potential of PPAR through modulating coregulator interactions, changing rates of

nuclear export as well as affecting rates of PPAR protein degradation (Brunmeir and Xu, 2018). An example involves the phosphorylation of PPARδ by epidermal growth factor receptor (EGFR), resulting in increased interaction with the microtubule-associated proteins 1A/1B light chain 3B (LC3) protein, sequestering LC3 from the autophagosome complex and inhibiting autophagy (Lee and Lee, 2016, Gou et al., 2020). Another notable PTM is the phosphorylation of PPARγ residue S245 (PPARγ1), which is induced by a high-fat diet and results in the dysregulation of a subset of PPARγ controlled genes that is independent of PPAR agonism (Choi et al., 2010). This generated considerable interest in developing non-activating PPARγ agonists for clinical therapy, which refers to PPARγ agonists that do not activate transcription of reporter genes in a reporter gene assay compared to controls (Choi et al., 2010, Frkic et al., 2021).

PPARs also regulate the transcriptional activity of other PPARs. PPARδ was demonstrated to repress PPARα and γ mediated gene transcription by competing for PPREs (Tan et al., 2016). Kilu and colleagues (2021) also demonstrated that PPAR subtypes have different affinities for heterodimerization with RXR, suggesting that the PPARs may be able to indirectly affect the DNA transcription of the other PPAR subtypes by competition limited amounts of RXR protein. Similarly, the PPARs are also involved in crosstalk with other NR-RXR pairs through competition with other RXR partners for heterodimerization (Chan and wells 2009). PPARs also regulate the activity of other NRs. In the case of LXR, PPAR directly regulates its transcription through the binding of a PPRE upstream of the LXR promotor (Xu et al., 2018). The progesterone receptor (PR) regulates the activity of PPAR in the same way – PR binds a Progesterone Receptor Element (PRE) in the promotor region for the PPARγ gene (Yang et al., 2016).

Although PPAR subtypes overlap in control of specific genes and (more generally) pathways, they do so in different tissues due to the different tissue distributions of the PPAR subtypes – PPARα predominantly in liver, kidney, heart and skeletal muscles, γ predominantly in adipose tissue and δ in most tissues (Figure 6, Karlsson et al., 2021). In addition, each subtype also responds to different ligands, giving each PPAR a distinct physiological role (Dubois et al., 2017).

1.6 Significance of PPARs in disease

Due to its role in various pathways, developing ligands targeting PPARs have great utility for treatment of a range of diseases, particularly metabolic diseases (Cheng et al., 2019). Metabolic syndrome (MetS), a disease involving the dysregulation of energy metabolism and homeostasis, is the diagnosis for patients who present three or more of the following metabolism-related disruptions: hyperglycemia, hypertriglyceridemia, high blood pressure, lowered high density lipoprotein (HDL) cholesterol levels or obesity (Belete et al., 2021). Unfortunately, MetS affects a significant proportion of major countries – For example, In the US, about 30% of all adults aged eighteen and above suffer

from MetS (Moore et al., 2017, Hirode and Wong 2020, Virani et al., 2021); In Xinjiang, China, 20.85% of a survey of 9.7 million multi-ethnic Chinese were affected by MetS (Su et al., 2020). This translates to a major source of healthcare burden, since 3/5 of the components of MetS have been consistently identified as part of the top 10 risk factors contributing to global disease burden, with the other components at least related to other factors in this list. For example, low HDL cholesterol levels are typically linked with high LDL cholesterol levels (Stanaway et al., 2018, Murray et al., 2020b). These metabolic disruptions in patients significantly increase the chance of developing related cardiometabolic diseases, such as Type 2 Diabetes (T2D) and cardiovascular diseases (CVD) and non-alcoholic fatty liver disease (NAFLD, Gross et al., 2017, Fougerat et al., 2020, Virani et al., 2021). In addition, patients diagnosed with one of the above metabolic diseases are at increased risk of developing other mentioned diseases, and even cancers (Mendrick et a., 2018, Francque et la., 2021, Virani et al., 2021). On top of that, each of these MetS-associated diseases are by themselves a significant health threat.

The first related disease, diabetes, is estimated to affect 536.6 million people worldwide, or 10.5% of the world population (Sun et al., 2022). In the US, diabetes affects 14% of United States (US) adults, with another 37.9% of adults diagnosed with prediabetes, which translates to an estimated health spending of $327 billion in the US alone (2017, 25% of healthcare spending), with $90 billion spent simply due to a loss in productivity (Mendola et al., 2018, Virani et al., 2021). Globally, expenditure on Diabetes makes up 11.5% of total global health spending and is estimated to increase to $2.1 to $2.5 Trillion dollars by 2030, accounting for 1.8-2% of the world's projected GDP (Bommer et al., 2018, Virani et al., 2021, OECD 2021, Sun et al., 2022). The second related disease, CVD is estimated to take 17.9 million lives each year, accounting for 32% of annual global deaths (World Health Organization, 2021a, Zhao 2021). According to the Global Health Estimates 2019, CVDs also take up the top two positions of causes of total mortality in the world (World Health Organization 2020). Alarmingly, the trend of decrease in CVD seen in developed countries has recently slowed or even reversed, likely due to an aging population arising from socioeconomic development and reduction in communicable diseases (Murray et al., 2020a, Zhao, 2021). The last related disease, NAFLD is estimated to affect two billion people worldwide, or around 25% of the global population (Lazarus et al., 2020). In the US alone, costs for NAFLD are estimated at $292 billion in 2016, and despite being a significant risk factor for the other related cardiometabolic diseases and vice versa, most countries do not have a response to NAFLD (Younossi et al., 2016, Francque et la., 2021, Huang et al., 2022, Lazarus et al., 2022).

MetS and its related diseases share similar characteristics – first and foremost, the overwhelming of typical storage depots resulting in an excess of glucose and lipids in the bloodstream leading to the accumulation of ectopic fat, as well as other characteristics such as insulin resistance, chronic low-grade systemic inflammation, endothelial cell dysfunction and gut dysbiosis (Palomer et al., 2016, Dubois et al., 2017, Gross et al., 2017, Mendrick et al., 2018, Cheng et al., 2019, Yamshita et al., 2019,

Fougerat et al., 2020, Huang et al., 2022 Francque et la., 2021). PPAR controlled genes, highlighted in the previous section, provide multiple mechanisms by which PPAR ligands can directly ameliorate the abnormalities seen with these diseases.

For example, through activation of upregulation of proteins involved in nutrient uptake and utilization in various tissues, PPARs manage excess glucose and lipids in the bloodstream (Dubois et al., 2017, Ma et al., 2018). Extracellular and intracellular fatty acid transporters, genes involved in FAO (as well as switching from glucose to FAO) and thermogenesis are upregulated, increasing use of excess nutrients and insulin sensitivity (include PPARδ glycogen synthesis). Systemic inflammation is also addressed by inhibition of NF-κβ, and other mechanisms, potentially addressing adipose tissue dysfunction, accumulation of atherogenic epicardial fat, foam cell formation and gut dysbiosis (Grabacka et al., 2016, Tan et al., 2016, Sun et al., 2021, Francque et al., 2021, Huang et al., 2022). ANGPTL4 prevents toxic overload in epicardial adipose and macrophages, preventing foam cell formation in atherogenic conditions (Kersten 2021). Adipose storage capacity is also increased through adipocyte differentiation, resulting in a switch from more to less atherogenic adipocyte phenotype – allowing accommodation of excess nutrients, decreasing lipotoxicity and increasing insulin sensitivity (Dubois et al., 2017). PPARγ activated upregulation of Adiponectin, as mentioned previously, also increases FAO, glucose utilization and insulin sensitivity (Fang and Judd 2018). It also prevents foam cell formation through inhibiting macrophage polarization, vascular permeability and cholesterol accumulation (Fang and Judd 2018).

In fact, the therapeutic effects of PPAR ligands have already been demonstrated in clinical trials (Cheng et al., 2019). Classical PPARα targeting ligands, Fibrates, have been used for the treatment of dyslipidemia in patients and have shown to reduce risk of CVD (Cheng et al., 2019). PPARδ-targeting ligands have shown good efficacy in early phases of clinical trials for dyslipidemia, NAFLD and T2D, but have been discontinued due to concerns of carcinogenicity, as well as for lack of efficacy (RESOLVE-IT: NCT02704403, Tan et al., 2016, Cheng et al., 2019). PPARγ targeting ligands, specifically TZDs, have been used for treatment of T2D and have positive effects on whole body insulin sensitivity, glycemic and lipid parameters, CVD events in diabetic patients and progression from prediabetes to diabetes (Cariou et al., 2012, Cheng et al., 2019, Lebovitz 2019). TZDs currently outperforms other available treatments in glycemic durability after treatment, and till recently, have been the only ligands (specifically Pioglitazone) found to be effective in NAFLD, the other currently being another PPAR ligand (Saroglitazar discussed below, Cariou et al., 2012, Cheng et al., 2019, Lebovitz 2019).

The PPARs are a very attractive target to ease a very significant proportion of the global disease burden and healthcare spending. Clinical trial evidence currently supports the therapeutic efficacy of PPAR activation in treatment of MetS, but further work is required to develop new ligands with reduced side effects and increased efficacy for specific conditions (Cheng et al., 2019).

Due to its role in energy homeostasis as well as inflammation, PPARs may also play a central role in the central nervous system (CNS, Zolezzi et al., 2017). Mental and neurological and substance abuse (MNS) disorders make up a significant share of the healthcare burden (World Health Organization 2022). Under the broad group of MNS disorders, particular interest, are dementias and mental disorders (Patel et al., 2016). In the 'Global status report on the public health response to dementia' published by the WHO, it is estimated that dementia affects a total of 55.2 million people in 2019, accruing about $1.3 trillion in economic costs (World Health Organization 2021b). In addition, dementia is one of the leading causes for burden of disease as estimated by disability-adjusted life years (DALYs), which doubled over the past 20 years (World Health Organization 2021b). WHO also ranks Alzheimer's disease (AD) and other dementias 7th in the top 10 leading causes of death (World Health Organization 2020). As the global population ages, Dementia represents a significant health and economic threat. Since age is the strongest risk factor and because almost half of the economic costs are due to the need for informal care (care that is rendered by unpaid individuals i.e. family members or other caretakers), there is a need for better treatment strategies (World Health Organization 2021b). In 2019, mental disorders are estimated to affect 970 million people, ranking 7th in the top 10 global causes of disease burden (GBD 2019 Mental Disorders Collaborators, 2022). Worryingly, majority of the burden of mental disorders arises from the population of working age, suggesting a significant loss of productivity, likely due to inability to show up to or perform well at work (World Health Organization 2020, Arias et al., 2022, GBD 2019 Mental Disorders Collaborators, 2022). Of the global health burden (measured by DALYs) due to mental disorders, 37.4% could be attributed to depression, 22.9% to anxiety and 12.1% to schizophrenia (GBD 2019 Mental Disorders Collaborators, 2022).

Mental disorders and neurological degenerative disorders, such as depression, AD, Parkinson's disease (PD) and multiple sclerosis (MS), all share common characteristics, such as an increase in sterile inflammation, mitochondrial dysfunction, impaired energy metabolism and, interestingly, and insulin resistance (Dickey et al., 2016, Tong et al., 2016, Zolezzi et al., 2017, Ferret-Sena et al., 2018, Rudko et al., 2020, Gold 2021, Sagheddu et al., 2021, Pérez-Segura et al., 2023). Interestingly, depression is also associated with onset of various diseases such as CVD and diabetes, reminiscent of MetS and its related conditions (Gold 2021). PPAR modulation directly addresses two common characteristics of these disorders, insulin resistance and inflammation, through mechanisms similar to those that addresses MetS as previously discussed (Zolezzi et al., 2017). Regarding impaired energy metabolism, ketone bodies have also been shown to have positive effects on diseases involving the CNS (such as AD, PD and Epilepsy) through the restoration of energy supply to the cells, as well as through its inherent anti-inflammatory properties – Ketogenesis is under the control of PPARα (Grabacka et al., 2016, Gough et al., 2021). PPARs could also potentially address the pathogenic mechanisms of Huntington's disease (HTT), PD and AD. Part of the pathogenesis of HTT and PD

involves mitochondrial dysfunction and failure in energy generation, while AD has been associated with reductions in brain glucose metabolism – PPARδ could restore mitochondrial function via PGC-1α, as well as increase energy generation via FAO and glucose utilization (Dickey et al., 2016, Tong et al., 2016, Zolezzi et al., 2017, Chamberlain et al., 2020).

PPARγ agonists (Rosiglitazone and Pioglitazone) have been in clinical trials for AD due to promising results in phase 2 trials, but displayed a lack of efficacy in later phases of clinical trials (Cheng et al., 2019). This does not exclude possibility of PPARγ-targeted treatment for AD or other mental and neurological disorders – PPARγ agonist treatment has shown efficacy for treatment of depression, schizophrenia and MS (Cheng et al., 2019). Other PPAR-targeting agonists may potentially be more effective, as PPARα and δ subtypes are more abundant in different cell types in the brain, cell types which are also relevant to AD (Figure 6, Karlsson et al., 2021, Dickey et al., 2016). In fact, fibrates such as Fenofibrate (PPARα-targeting) demonstrated effectiveness for treatment of epilepsy, and Gemfibrozil (PPARα/γ dual agonist) is currently in Phase 1 trials for AD (Cheng et al., 2019). T3D-959 is currently in Phase 2 trials for Alzheimer's disease – it is a PPARδ/γ dual agonist, capitalizing on the abundance of PPARδ in the brain (ClinicalTrials.gov Identifier: NCT04251182, Chamberlain et al., 2020).

The links between metabolic disruptions and neurological disorders and diseases point to the PPARs as an obvious target for novel therapeutic solutions. There is a pressing need, seeing as many current treatments target only part of the pathology of these diseases (Pérez-Segura et al., 2023). Further investigation into the pathological mechanisms of these conditions is required to fully appreciate the actual utility of PPAR agonist treatment.

PPARs are also particularly relevant in cancers since they play roles in modulating inflammation, immune response, angiogenesis and reactive oxygen species (ROS). Cancers, according to the WHO, ranks at or near the top cause of death before the age of 70 in more than two-thirds of all countries in the world (World Health Organization 2020). Cancers account for a total of almost 10 million deaths in 2020 and seems to be increasing in prevalence in developed countries and disproportionately affects older populations (Sung et al., 2021). Current cancer therapies typically include surgical removal of malignant tissue, radiotherapy and administration of often toxic and ineffective chemotherapeutic drugs (Cheng et al., 2019).

Cancer cells complete for nutrients in the tumour microenvironment (TME) to survive and proliferate, and the mechanisms by which these cancer cells do so is highly context dependent – For example, the tissue of origin determines the limiting nutrients that cells have to compete for (Gillies and Gatenby, 2015, Koundouros and Poulogiannis 2020). In general, all tumour proliferation requires substrate production, energy generation, blood supply, management of inflammation and ROS as well as

evasion from the immune system (Hanahan and Weinberg 2011, Zugazagoitia et al., 2016, Hanahan 2022).

PPARs play a role in many of these processes required for cancer cell survival (Wagner and Wagner 2020b). For example, cancer cells typically require access to the blood circulation to fulfil its metabolic needs – PPARs play a role in angiogenesis. Specifically, PPARα and γ were shown to posses anti-angiogenic effects while PPARδ was demonstrated to be proangiogenic (Wagner and Wagner 2020a). PPARs also play a role in vascular integrity, which is important in metastasis (Tan et al., 2016, Muzio et al., 2021, Tan et al., 2021, Tomita et al., 2021). Vascular integrity is closely linked with inflammation (Tan et al., 2021, Tomita et al., 2021). Increased inflammation and oxidative stress is another key characteristic of the TME and PPARs play significant roles in both processes, through modulation of targets such as NF-κB and catalase (Hanahan and Weinberg 2011, Greten and Grivennikov 2019, Christofides et al., 2021, Muzio et al., 2021). In addition, cancer cells commonly display dysregulated lipid transport and metabolic processes, for energy generation as well as substrate synthesis (Koundouros and Poulogiannis 2020, Hartley and Ahmad 2023). As discussed above, PPARs, play an integral role in regulating lipid metabolism, providing various mechanisms to tackle exploit the metabolic dependencies of tumours, for example by redirecting lipids away from cancers to adipose tissues (Dubois et al., 2017, Koundouros and Poulogiannis 2020).

Many studies have highlighted the relationship of PPAR function to various cancers, such as bladder, pancreatic, prostate and oral cancers (Schumann et al., 2015, Goldstein et al., 2017, Hall et al., 2020, Parejo-Alonso et al., 2021, Hartley and Ahmad 2023). PPAR agonists have in fact, been in clinical trials for treatment of a range of cancers (Cheng et al., 2019). PPARs could also aid cancer immunotherapy - it was demonstrated in a mice model for melanoma, that PPARα agonist fenofibrate increased the efficacy of cancer vaccines to boost CD8 T cell function against solid tumours, presumably through prevention of T cell exhaustion by metabolic switch to lipids for energy generation (Chekaoui and Ertl 2021).

The function of PPARs are dysregulated in many cancers, and pathways under the control of PPARs address abnormalities seen in cancer. However, to appropriately utilize PPAR ligand therapy, more studies need to be done exploring the mechanisms behind the effects of PPAR modulation in a variety of cancer models and determine if PPAR ligands are suitable in treating the specific cancer context of the patients (Cheng et al., 2021).

To summarize, the PPARs play a central role in metabolism as well as other processes across multiple tissues, which addresses disruptions seen across wide range of diseases, each contributing significantly to the health burden on countries worldwide. These diseases often stem from and affect multiple tissues. They may also be interconnected, increasing the risk of developing further disease and comorbidities. Designing a safe and effective PPAR ligand could potentially provide a single solution

that addresses the multifactorial nature of these diseases without the issue of polypharmacy, which would relieve significant portion of the global health burden.

1.7 Problems with existing ligands

Despite having utility and potential to address multiple diseases, each with a significant impact on global health burden, PPAR targeting ligands have only been licensed for the treatment of conditions such as T2D and lipid associated disruptions (Hong et al., 2018, Cheng et al., 2019). There are only currently 6 PPAR targeting drugs with nanomolar affinities for any PPAR subtype and four other fibrates approved for use in various countries (Cheng et al., 2019). The PPARγ targeting drugs Rosiglitazone and Pioglitazone are well known examples, although Rosiglitazone has not been frequently used in clinical therapy since initial concerns regarding their side effects (on and off-target), even after the FDA retracted the ban on its use in the US (Lebovitz 2019). Lobeglitazone (PPAR α/γ agonist dual agonist) has been licensed for use in Korea, and Saroglitazar (PPAR α/γ agonist dual agonist) in India, Chiglitazar (PPAR α/γ agonist dual agonist) in China and Pemafibrate (PPAR α agonist) for clinical therapy in Japan, and the other fibrates are still used for dyslipidemia (Cheng et al., 2019, Table 3). Many prospective PPAR targeting ligands for treatment of various diseases have fell out of clinical trials due to efficacy and safety concerns, despite encouraging results in preclinical studies (Hong et al., 2018, Cheng et al., 2019).

PPAR ligands with nanomolar affinity					
Ligands	**Subtype**	**Affinity, α/δ/γ (μM)**			**Treatment of diseases**
Rosiglitazone[3]	PPAR γ	>10	>10	0.018	T2D
Pioglitazone[2]	PPAR γ	~1-10	>10	0.490	T2D
Lobeglitazone*	PPAR α/γ	546	?	0.1374	T2D
Saroglitazar[7]	PPAR α/γ	0.00065	?	0.003	Lipid associated conditions in T2D
Chiglitazar[8]	PPAR α/δ/γ	1.10	1.70	0.080	T2D
Pemafibrate[5]	PPAR α	0.001	1.58	1.10	Lipid associated conditions
Fibrates and lower affinity drugs					
Ligands	**Subtype**	**Affinity, α/δ/γ (μM)**			**Treatment of diseases**
Cipofibrate[6]	PPAR α/δ/γ	0.9	?	?	Lipid associated conditions
Fenofibrate[1]	PPAR α/γ	30	Ia	300	Lipid associated conditions
Bezafibrate[1]	PPAR α/δ/γ	50	20	60	Lipid associated conditions
Gemfibrozil[4]	PPAR α/γ	193.3	147.8	-	Lipid associated conditions

Table 3. **PPAR ligands currently approved for clinical therapy.** *Lobeglitazone EC50 values were reported using a Time Resolved FRET (TR-FRET) assay (Bae et al., 2021). Symbols: ~ – approximately. Ia – inactive, as defined by Willson et al., 2000. ? – not tested by the quoted reference. References: [1]

Willson et al., 2000, [2] Sakamoto et al., 2000, [3] Xu et al., 2001, [4] Kim et al., 2007, [5] Yamazaki et al., 2007, [6] Quang et al., 2012, [7] Jain et al., 2015, Hong et al., 2018, Cheng et al., 2019, [8] Ji et al., 2021, Deeks 2022.

Generally, a well-designed ligand will be able to reach the intended tissues and cells and activate the targeted PPAR subtype(s), i.e having subtype selectivity. The choice of the appropriate PPAR subtype(s) to target depends on the intended physiological outcome. As touched on in chapter 1.6, according to the current available evidence, PPARγ ligand treatment results in insulin sensitizing effects, while PPARα ligand treatment has lipid modulating effects. The concentration of the ligand should be high enough to achieve activation of transcription of only the genes under the control of the PPAR subtype but not other subtypes or targets, but not be too high that adverse effects occur. Due to the nature of the large ligand binding pocket of PPARs as well as similarity of the residues that line the ligand binding pocket in different PPAR subtypes, ligands that target one PPAR subtype might also bind other subtypes at higher ligand concentrations (Table 3). Well-designed ligands must also have appropriate potency and efficacy – typically high potency is desired as lower therapeutic concentrations of a ligand would be required, reducing chance of off-target side effects. Deciding on the level of desired efficacy (i.e ligands with different activation profiles, figure 4), however, requires the understanding of the regulation of and interplay between the various receptor-controlled gene pathways as well as the pathology of the treated disease (Dubois et al., 2017).

The currently licensed PPAR ligands can be classified into their respective drug classes. Each class usually contains a certain defining chemical motif – TZDs contain the thiazolidinedione chemical group; Fibrates, which are derivatives of fibric acids, contain structural features of fibric acid; Glitazars are a more diverse class of chemicals usually containing an acidic head group that activate both PPARα and γ.

TZDs as alluded to above, are a class of insulin sensitizing drugs. This class of ligands contain a Thiazolidinedione chemical group that was thought to bind selectively to the PPARγ subtype, which includes compounds such as Troglitazone, Rosiglitazone, Pioglitazone and Lobeglitazone (Lehmann et al., 1995, Jang et al., 2018, Lebovitz 2019). Despite their benefits on insulin sensitivity, older TZDs were also reported to have side effects such as weight gain, edema and bone fractures, and some TZDs were removed from clinical use due to increased incidences of hepatitis, CVD events and bladder cancer (Jang et al., 2018, Tang et al., 2018, Cheng et al., 2019, Lebovitz 2019). There were also instances of both Rosiglitazone and Pioglitazone reported as having PPARα activating properties in transactivation assays in the 1-10μM range, with Pioglitazone exhibiting maximum transactivation activity resembling PPARα fibrate WY14643 (Sakamoto et al., 2000, Sauerberg et al., 2003, He et al., 2012). This PPAR transactivation profile suggests that Pioglitazone acts similarly to other dual and pan agonists, at least at the clinically administered doses (Eckland and Danhof 2000). These reasons prompted the discovery of newer, more subtype selective ligands (Lee et al., 2017, Jang et al., 2018).

Lobeglitazone is a recently approved, PPARγ selective TZD with a 3000-fold selectivity for PPARγ vs α (Jin et al., 2015, Bae et al., 2021). Long term studies show comparable or better reduction in glycated hemoglobin (HbA1C) at much lower doses (0.4mg) as well as reduced CVD events and bone fractures compared to those seen with Rosiglitazone and Pioglitazone therapy (Lebovitz 2019, Kim et al., 2022). Structurally, Troglitazone and Pioglitazone differs very slightly from Rosiglitazone and Lobeglitazone – 1-2 carbon atoms from the 5-(4-Hydroxybenzyl)-2,4-thiazolidinedione moiety to the tail region (Chua and Bruning, 2021, Figure 7). Pioglitazone and Lobeglitazone are also notably longer than Troglitazone and Rosiglitazone. Such differences resulted in an order of magnitude difference in affinities for the PPARγ (Troglitazone and Pioglitazone lower affinity than Rosiglitazone and Lobeglitazone), as well as increased transactivation activity at PPARα (Pioglitazone, Willson et al., 2000, He at al., 2012, Lee et al., 2017).

Most dual PPARα/γ agonists belonged to the drug class 'Glitazars'. Glitazars were intended to combine the cardioprotective effects of PPARα activation as well as the insulin sensitizing effects of PPARγ activation, to prevent CVD events arising from PPARγ therapy (Cheng et al., 2019). Many earlier Glitazars (eg. Tesaglitazar, Farglitazar and Aleglitazar) were discontinued from clinical trials due to a range of side effects such as bleeding in the gastrointestinal tract, carcinogenicity, renal dysfunction, hepatotoxicity, cardiovascular impairment and edema, with the exception of Cevoglitazar which failed to show efficacy in phase 2 clinical trials (Hong et al., 2018, Tassopoulou et al., 2022). Despite a rocky start with the Glitazar drug class, Saroglitazar received approval for treatment of T2D as well as lipid associated conditions in patients with T2D (Krishnappa et al., 2020). Even though Saroglitazar has very high affinity (in the low nM range) for both the PPAR α and γ subtypes, it has been reported to have a more favourable safety profile compared to TZDs (Krishnappa et al., 2020, Gawrieh et al., 2021, Rajesh et al., 2022). Saroglitazar has even been approved for treatment of NAFLD (first in the world) and gained FDA approval to proceed with clinical trials for treatment of primary biliary cholangitis (PBC, Jaiswal et al., 2021, Vuppalanchi et al., 2022). Structurally, Saroglitazar is similar to Aleglitazar, Tesaglitazar and Naveglitazar and has a similar binding mode to Aleglitazar and Tesaglitazar, but is the only Glitazar-class ligand that did not display serious side effects (Kalliora and Drosatos 2020, Tassopoulou et al., 2022).

Pemafibrate (described as a selective PPARα modulator) matches Saroglitazar's affinity for PPARα (low nM range) but displays a much lower activity for the PPARγ receptor and also increased activity for PPARδ as well (1µM range, Yamazaki et al., 2007). Pemafibrate was meant to be an improvement over the previous generations of fibrates, which are a drug class known for their lipid modulating properties, showing much higher affinity for PPARα and selectivity over the other PPAR subtypes Pemafibrate (Yamashita et al., 2020). The older fibrates, which were thought to be selective for PPARα, in fact activated the other PPAR subtypes at higher concentrations (Willson et al., 2000). The first fibrate, Clofibrate was associated with increased mortality and quickly discontinued (Oliver et al.,

2012). Later-generation fibrates were safer (Fenofibrate and Bezafibrate) even though they activated the PPAR subtypes at similar affinities, but also displayed different side effects (Willson et al., 2000, Jakob et al., 2016). The newest fibrate, Pemafibrate displays the same efficacy in lipid modulation (compared to Fenofibrate) with a smaller prescribed dose and increased safety profiles (Arai et al., 2018, Yamashita et al., 2020). Additionally, in contrast to most fibrates, Pemafibrate was safe for concurrent use with statins, and performed significantly better on kidney and liver function tests (Yamashita et al., 2019a, Yamashita et al., 2020, Ginsberg et al., 2022). Structurally, Pemafibrate differs from the older fibrates, taking a much larger Y-shaped structure rather than the smaller L-shaped structure seen with other fibrates (Figure 8).

Chiglitazar, a pan agonist that displays high selectivity for PPARγ, was considered safe, efficacious and non-inferior compared to Pioglitazone and Sitagliptin in clinical trials, and was subsequently approved for therapeutic use (He et al., 2012, Deeks 2022). Chiglitazar had higher maximal activity than Rosiglitazone at every subtype and Pioglitazone at PPARγ and δ, but similar maximal activities with Pioglitazone at PPARα, relative to reference compounds WY14643 for PPARα and 2-bromohexadecanoic acid for PPARδ. It should be noted that WY14643 roughly matches the maximal activity of PPARα full agonist Pemafibrate and 2-Bromohexadecanoic acid is not typically used as a reference agonist for PPARδ activity (Amri et al., 1995, He et al., 2012, Takei et al., 2017). Structurally, Chiglitazar is unique, containing different chemical motifs to typical Glitazars as well as the only other approved pan agonist, Bezafibrate (Figure 9).

Despite having significant positive effects on lipid and glucose parameters, the improved PPARα agonist Pemafibrate was still unable to meet primary endpoints in phase 3 clinical trials for prevention of CVD events, despite the higher PPARα affinity as well as selectivity (Yamashita et al., 2020, Yokote et al., 2021, Das Pradhan et al., 2022). Large clinical trials of older generation fibrates have mostly showed neutral results except in subgroups of patients, however retrospective meta-analyses showed beneficial effects on prevention of CVD events (Jakob et al., 2016, Kim and Kim, 2020, Zhu et al., 2020). This contradiction in results suggests that there might be aspects of CVD development and/or prevention that are not addressed solely by increasing selectivity for PPARα activation and modulating lipid and lipoprotein parameters (Das Pradhan et al., 2022). Since it has been demonstrated that different ligands could induce different sets of genes, likely through differential recruitment of coregulators, novel ligands might prove to be more effective in treating the same disease (Rogue et al., 2011, Dietz et al., 2012, Yamashita 2019b).

Full agonism of PPARγ has also been hypothesized to cause side effects seen with TZDs (Dubois et al., 2017). Very interestingly, side effects differ between ligands, for example between Rosiglitazone and Pioglitazone (Lebovitz 2019). As mentioned previously, it is currently accepted in the literature that the insulin sensitizing effects of PPARγ agonists are correlated with the inhibition of phosphorylation

of residue S245 (PPARγ1) rather than the full activation of PPARγ through H12 (Choi et al., 2010, Frkic et al., 2018). This inhibition can be achieved by the stabilization of the residues on the H2-H2' loop, H2' and H2'-H3 loop (Bruning et al., 2007, Filho et al., 2019). Ligands that interact with the β-sheet region can stabilize these areas (eg. H2-H2' loop) without full activation of PPARγ through interaction with H12. Ligands that do not interact with H12 but stabilize the β-sheet areas are typically partial agonists, antagonists or inverse agonists (Frkic et al., 2018). However, despite numerous attempts, there are currently no PPARγ ligands with such activation profiles approved for T2D therapy (Cheng et al., 2019, Ribeiro Filho et al., 2019).

As mentioned, the newer PPARγ selective Lobeglitazone was efficacious at a much smaller dose and showed improvements in terms of observed side effects over previous TZDs (specifically bone fractures and CVD events). The PPARγ targeting Chiglitazar (48mg dose, peak serum concentration or Cmax: 1-2 micromolar range) was also non-inferior compared to TZDs and safe when used concurrently with other T2D drugs. However, both PPARγ acting agonists still presented with comparable weight gain and edema incidence (Kim et al., 2011, Jani et al., 2013, Lebovitz 2019, Deeks 2022, Kim et al., 2022). In contrast, Saroglitazar (4mg dose, Cmax 1-10 nanomolar range) treatment actually resulted in a reduction in weight compared to Pioglitazone, while maintaining positive effects on glycemic and lipid parameters (Krishnappa et al., 2020). Despite its full PPARγ agonism, Saroglitazar seems to have less side effects compared to TZDs, possibly through concurrent activation of PPARα. However, since there are safety concerns with concurrent PPARα and γ agonism, it might be beneficial to explore agonists with other activation profiles (Kalliora and Drosatos 2020). Even now, patents are being filled for PPAR ligands for treatment of various diseases, reflecting the pharmacological interest in PPAR modulation (Takada and Makishima 2020).

In a study by Raza-Iqbal et al. (2015), micro-array analysis was conducted on primary human hepatocytes from three different donors, which were cultured and treated with Pemafibrate or Fenofibrate. The donors each showed different gene regulation patterns in response to the PPAR ligands, for example donor JGM showed smallest change in up and down regulated gene sets across all the treatments. Additionally, JGM also displayed the lowest upregulation of CD36, but highest upregulation of FGF21 across all ligand treatments. In another study, TZDs and glitazars were also found to induce differential responses in Human hepatocytes (Rogue et al., 2011). This raised an interesting observation – that individuals could have differential responses to PPAR modulation. In addition, in an early proof of concept experiment, Takada and colleagues (2000) demonstrated that the mutation of a single amino acid could cause a switch in drug binding preferences of a PPAR LBD. Majithia et al. (2016) went on to demonstrate that mutations in the human PPARγ protein negatively impacted agonist stimulated gene transcription of CD36 to different degrees – theoretically, different mutations in PPARγ gene, while benign, could impact response to PPAR agonists and thus susceptibility to metabolic disease and treatment. Gene association studies have been conducted

linking certain PPAR genetic polymorphisms to various diseases and even cancer (Burch et al., 2010, Maciejewska-Skrendo et al. 2019, Ding et al., 2020, Maculewicz et al., 2021, Maciejewska-Skrendo et al., 2022, Song et al., 2022). These observations suggest that individual differences can affect PPAR activity.

1.8 Approach and aims

Despite the licensing of new PPAR ligands, there is still much room for development of PPAR based therapeutics for various diseases. Although increasing affinity for the PPAR subtypes seems to have positive clinical effects across most ligands, it does not completely remove side effects seen with PPAR agonism (Hong et al., 2018, Kalliora and Drosatos 2020). Slight differences in chemical structure can result in vast differences in affinity as well as clinical utility, likely due to different recruitment of coregulators – for example Rosiglitazone versus Pioglitazone (Pan et al., 2017, Lebovitz 2019).

To improve on the current repertoire of PPAR ligands, it would be beneficial to understand the underlying structural determinants for ligand binding to the PPARs. This can be done by analysing crystal structures of ligand bound PPAR and comparing binding modes. Next, novel PPARγ ligands synthesized with varying affinities and design philosophies would be characterised, since PPARγ is currently the most studied PPAR subtype with the greatest therapeutic utility. Then to understand the impact of mutations on PPAR function, clinically characterised mutations would be analysed, using cell-based assays and structural studies.

Aims:

1. To determine structural determinants for selective binding to each PPAR subtype based on analysis of previous structures, addressed in chapter 2.
2. To further clarify the structural determinants of partial agonism of PPARγ by investigating other novel partial agonists of PPARγ, addressed in chapters 3 and 4.
3. To determine if machine learning could be used to discover novel agonists of different chemical spaces that target PPARγ, addressed in chapter 5.
4. To understand how mutations in the PPARγ LBD affect ligand binding and transactivation activity, addressed in chapter 6.

1.9 Figures

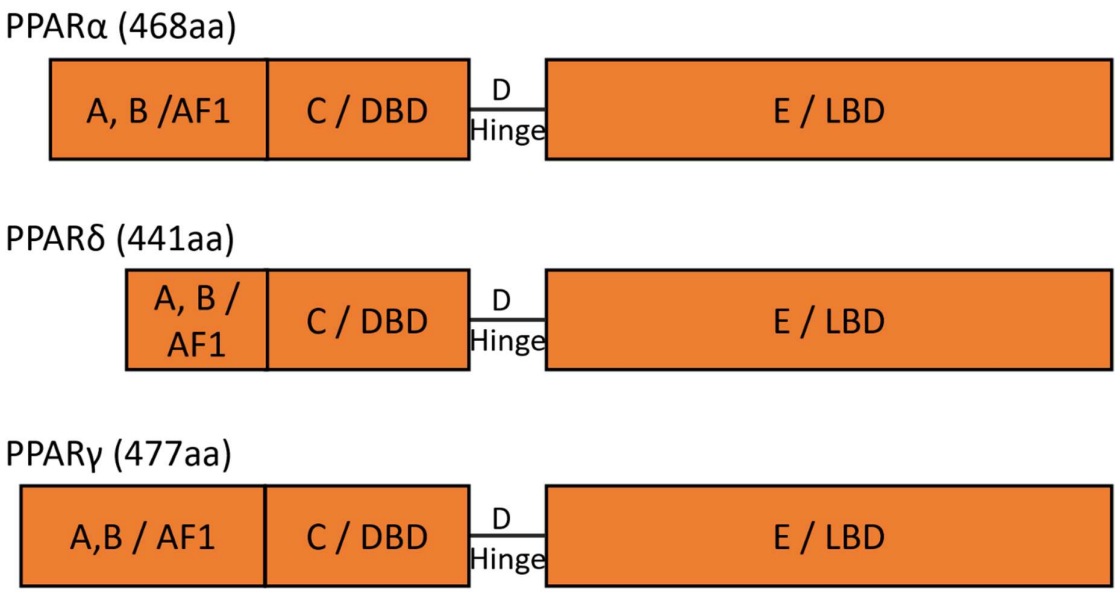

Figure 1. **PPAR protein architecture.** The PPAR protein subtypes contain 5 domains A-E. The A/B domains contain the activation function 1 (AF1) sequence. Domain C contains the DNA binding domain (DBD). Domain D contains a hinge region connecting domain C and E. Domain E contains the ligand binding domain (LBD). The PPARα, δ and γ proteins are 468, 441 and 477 amino acids long respectively. Figure is taken from Chapter 2, Figure 6.1a.

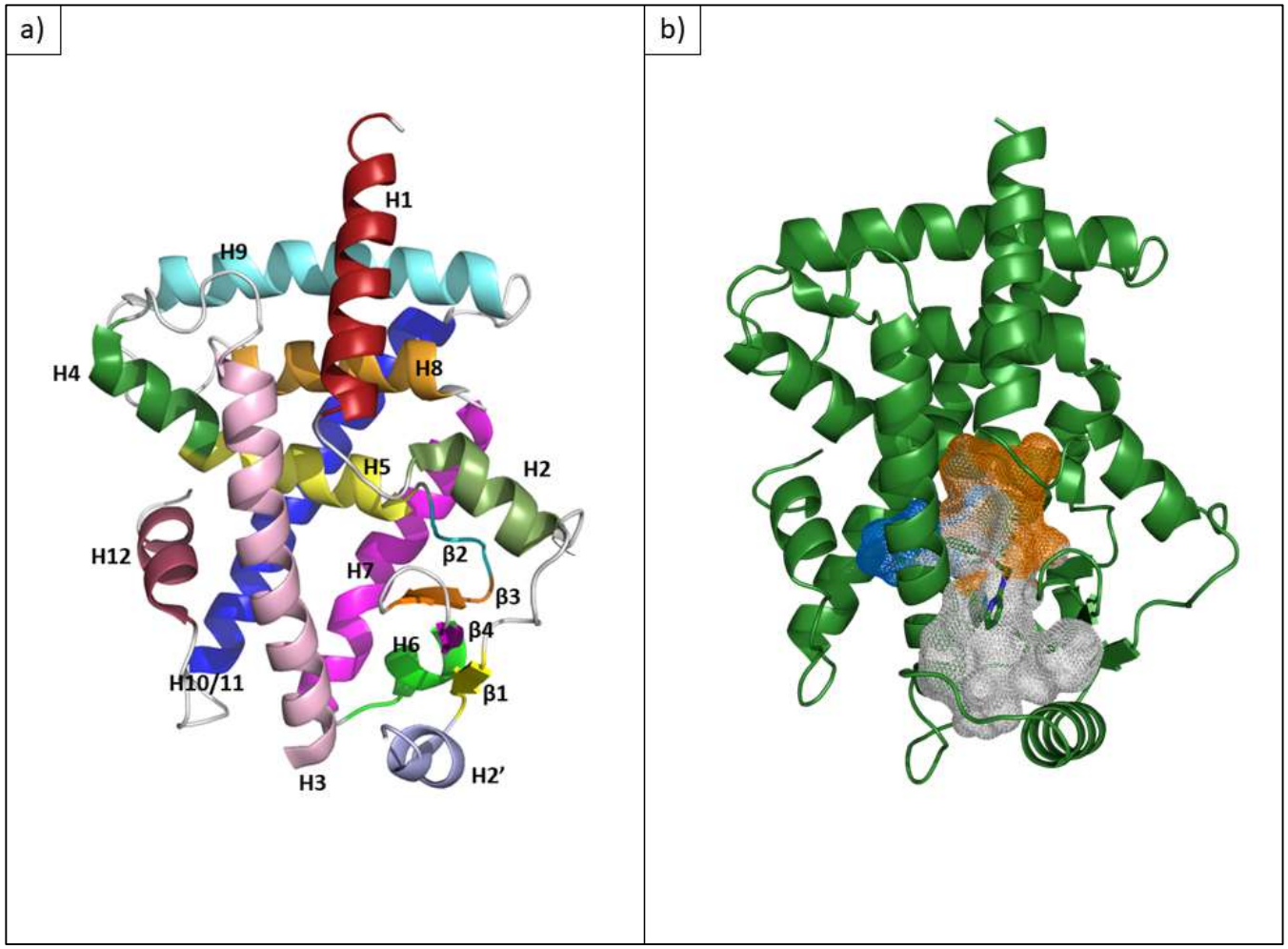

Figure 2. **The PPAR ligand binding domain (LBD).** a) The LBD as represented by the PPARγ subunit of PDB ID: 3DZY. Each helix is labelled and assigned a colour, H1 (Firebrick) H2 (Smudge) H2' (light blue) B1 (yellow) H3 (light pink) H4 (Forest) H5 (Pale Yellow) B2 (Cyan) B3 (Orange) B4 (Magenta) H6 (Green) H7 (Magenta) H8 (Bright orange) H9 (Aquamarine) H10/11 (Blue) H12 (Raspberry). Helices are labelled according to nomenclature established by Uppenberg et al. (1998). b) The PPAR ligand binding pocket represented by PPARγ structure PDB ID: 2PRG (in forest). The cavity is visualized as a mesh, with each section of the ligand binding pocket labelled in a different colour, arm 1 (in marine), arm 2 (in white) and arm 3 (in orange). Coactivator peptide was hidden for visual clarity. Colour names used in Pymol are given in parentheses.

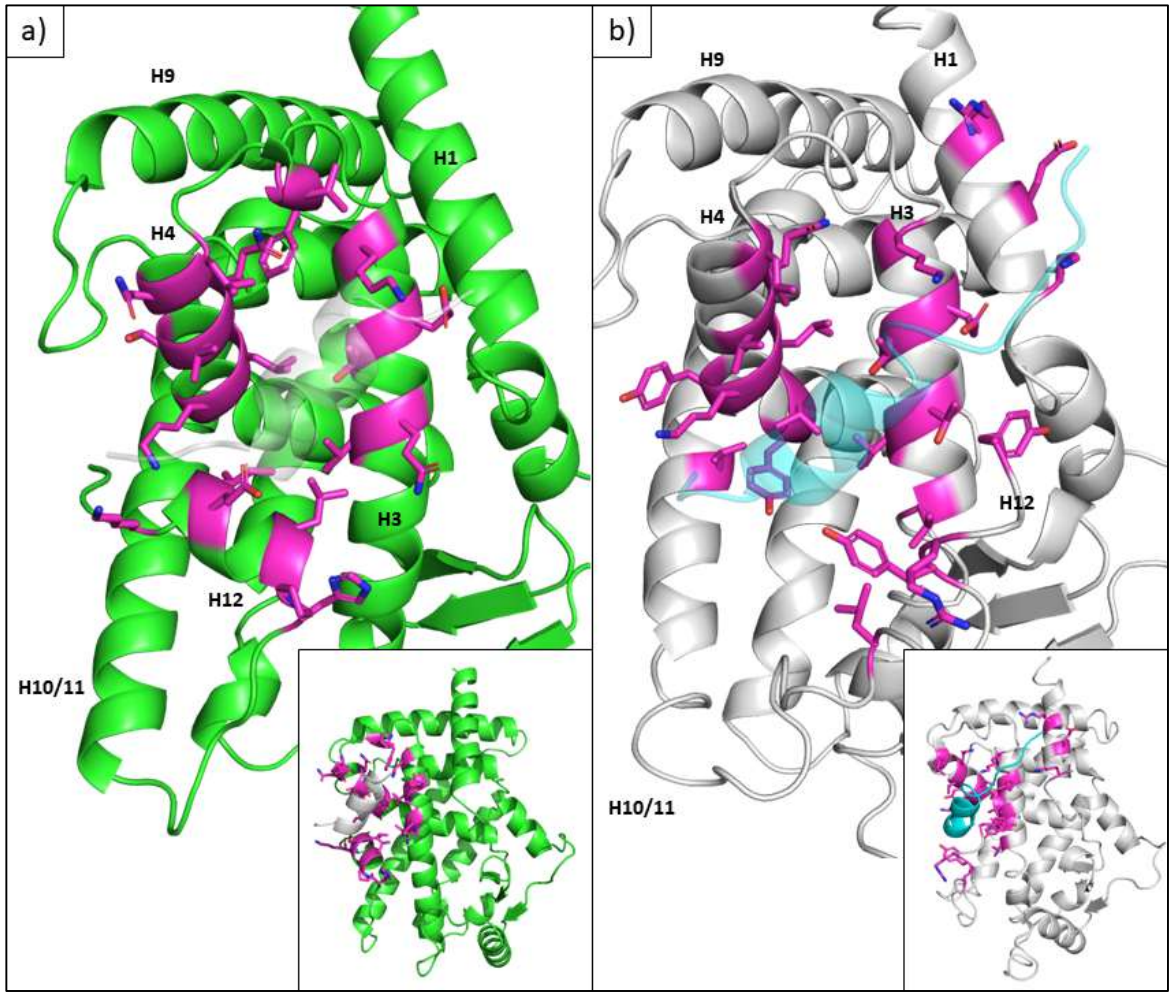

Figure 3. **The coregulator interaction surface of PPAR.** a) The activation function 2 (AF2) surface (in magenta) on the PPAR protein, which was represented by PPARγ structure PDB ID: 2PRG (in green). Coactivator peptide SRC1 (in grey 90) was made translucent to aid visualization. b) The corepressor binding surface (in magenta) on the PPAR protein, which was represented by PPARα structure PDB ID: 1KKQ (in grey 90). Corepressor peptide nuclear receptor corepressor 2 (in teal) was made translucent to aid visualization. Incut boxes within the panels represent the same protein zoomed out with H3 facing the viewer. Colour names used in Pymol are given in parentheses.

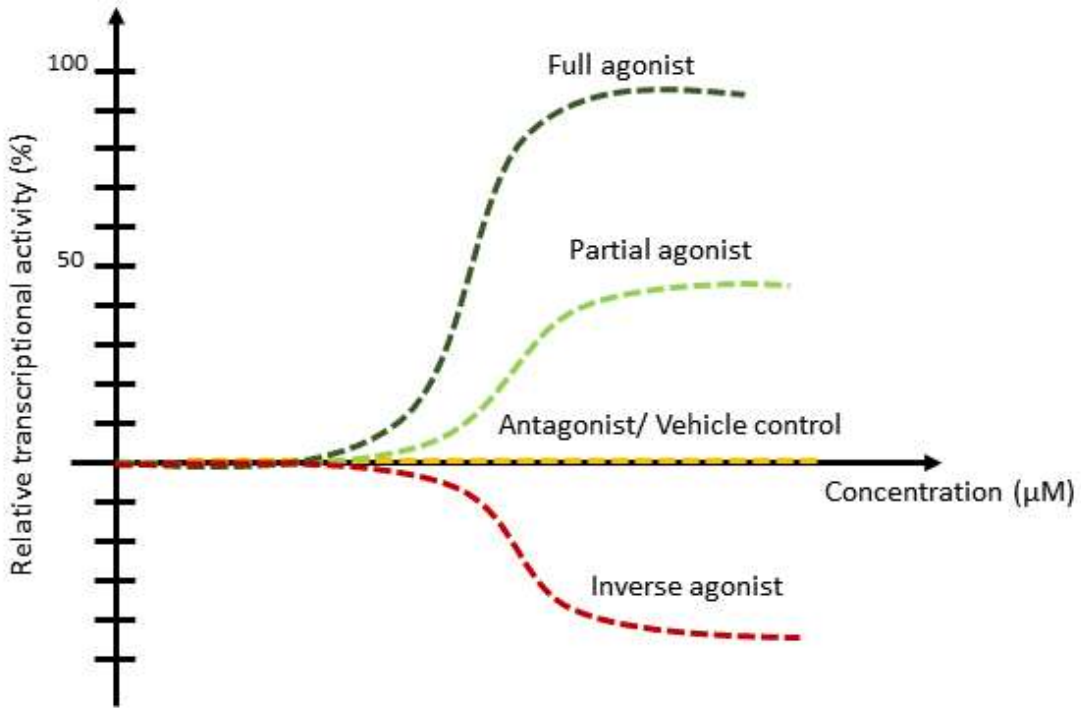

Figure 4. **Ligand activity profiles.** The activity profiles of full and partial agonists (dark green and light green respectively), antagonists (yellow) and inverse agonists (red) in dashed lines. 100% activity is defined by the full agonist used as reference, while 0% is defined by the activity of the vehicle control.

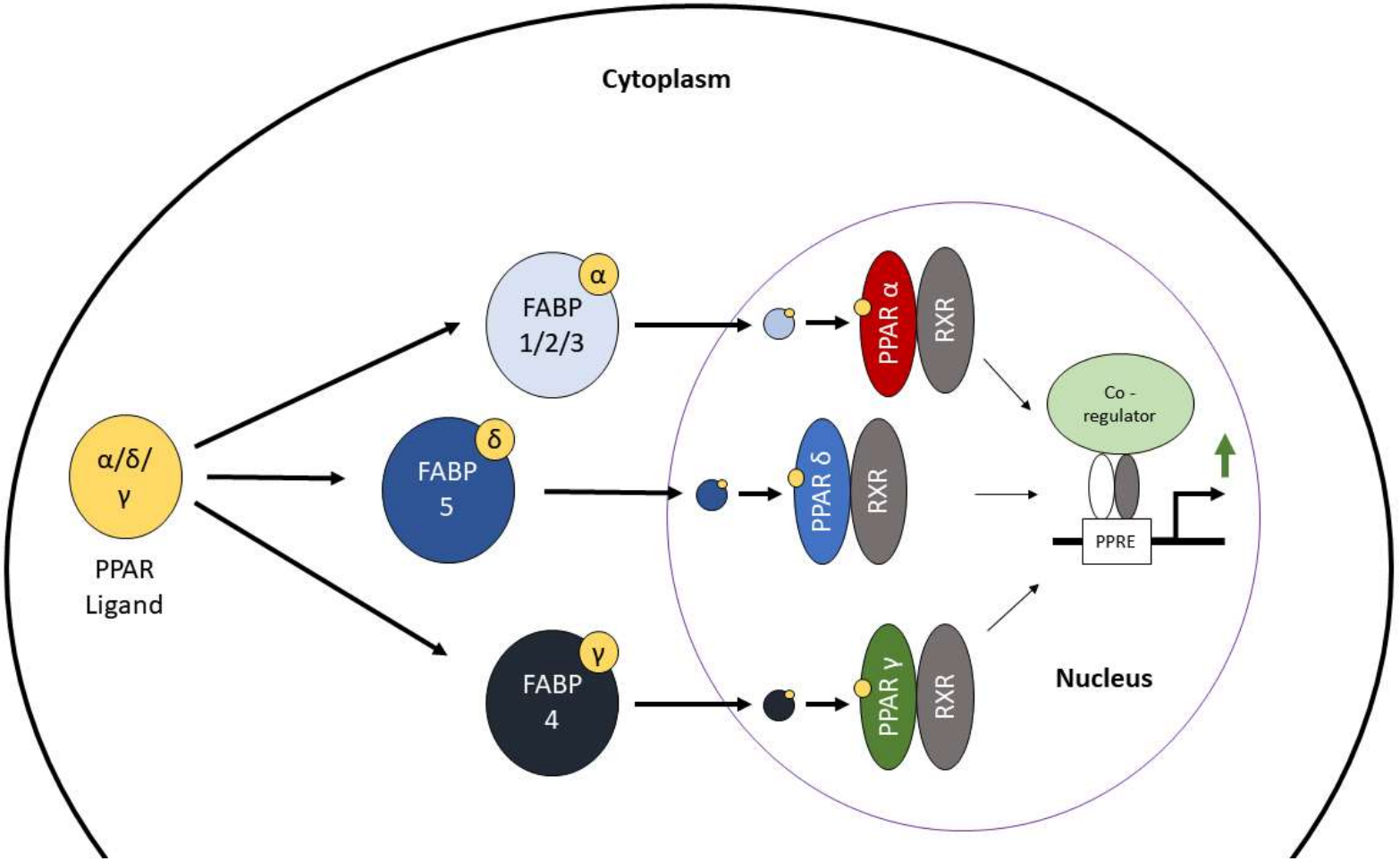

Figure 5. **Fatty acid binding proteins (FABPs), their ligands and PPAR subtype selectivity.** PPAR ligands selective for a certain PPAR subtype bind to specific FABPs, which shuttle ligands from the cytoplasm into the nucleus. There it interacts with the PPAR-RXR dimer and transfers the ligands, activating the PPAR -RXR dimer. This activated dimer binds to PPAR response elements (PPREs), recruit coactivators and increase transcription of genes.

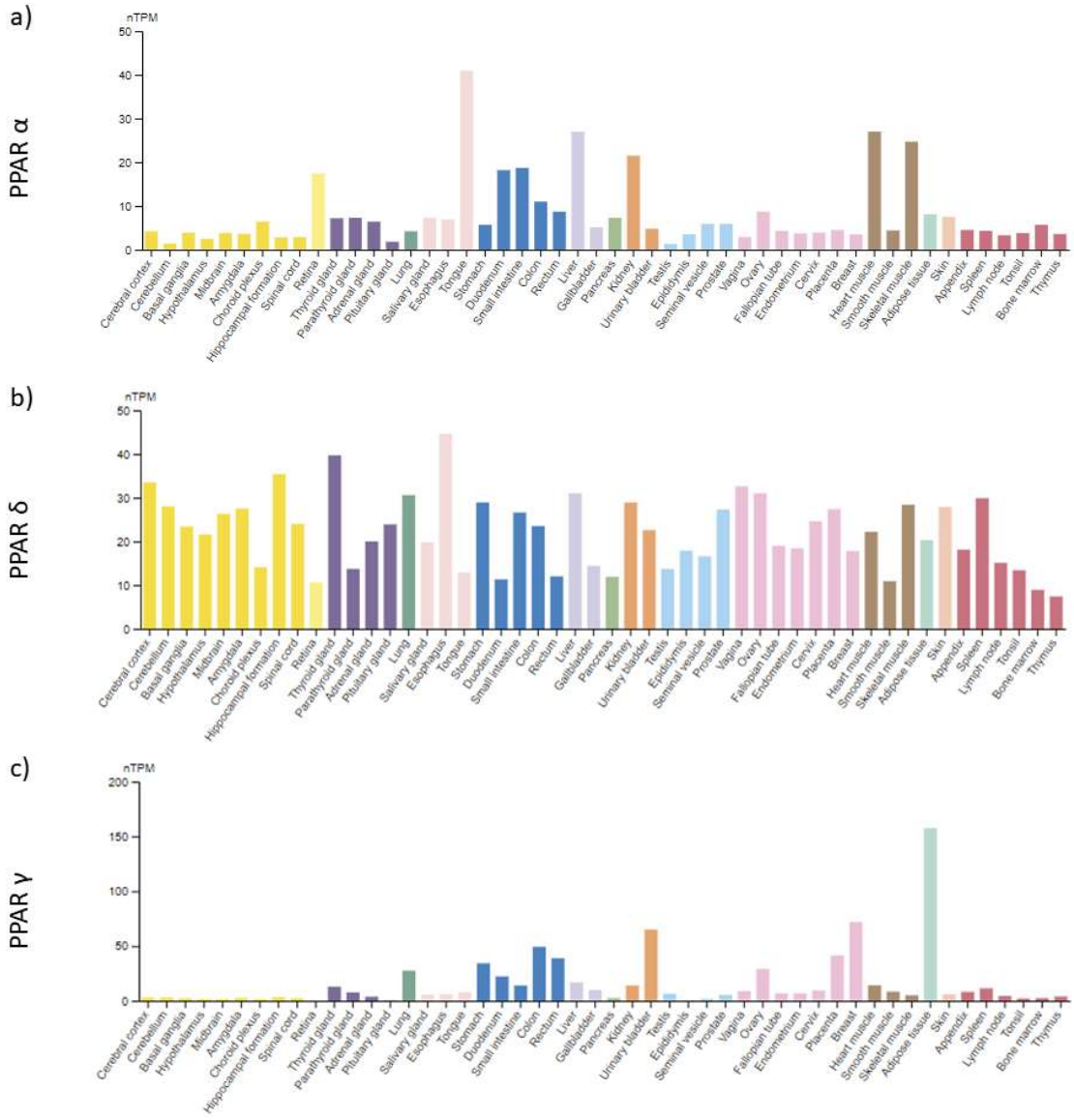

Figure 6. **mRNA expression of PPAR in the various tissues, by the Human Protein Atlas**. The mRNA expression of PPAR in various tissues was determined by a consensus of the RNA sequencing data from the Human Protein Atlas project and the Genotype tissue expression project (Karlsson et al., 2021). a) to c) represents the mRNA expression of PPARα, δ and γ respectively in the various tissues, normalized to allow for between sample comparisons. From left to right, colours represent the brain (yellow), endocrine tissues (purple), respiratory system (forest green), proximal digestive tract (light pink), gastrointestinal tract (blue), liver and gallbladder (light purple), pancreas (green), kidney and urinary bladder (orange), male tissues (light blue), female tissues (pink), muscle tissues (brown), connective and soft tissue (light green), skin (beige), bone marrow and lymphoid tissues (red). For more information, visit Human Protein Atlas at https://www.proteinatlas.org/about/assays. The specific links for PPARs are: PPARα, at https://www.proteinatlas.org/ENSG00000186951-PPARA, PPARδ, at https://www.proteinatlas.org/ENSG00000112033-PPARD and PPAR γ, at https://www.proteinatlas.org/ENSG00000132170-PPARG/tissue

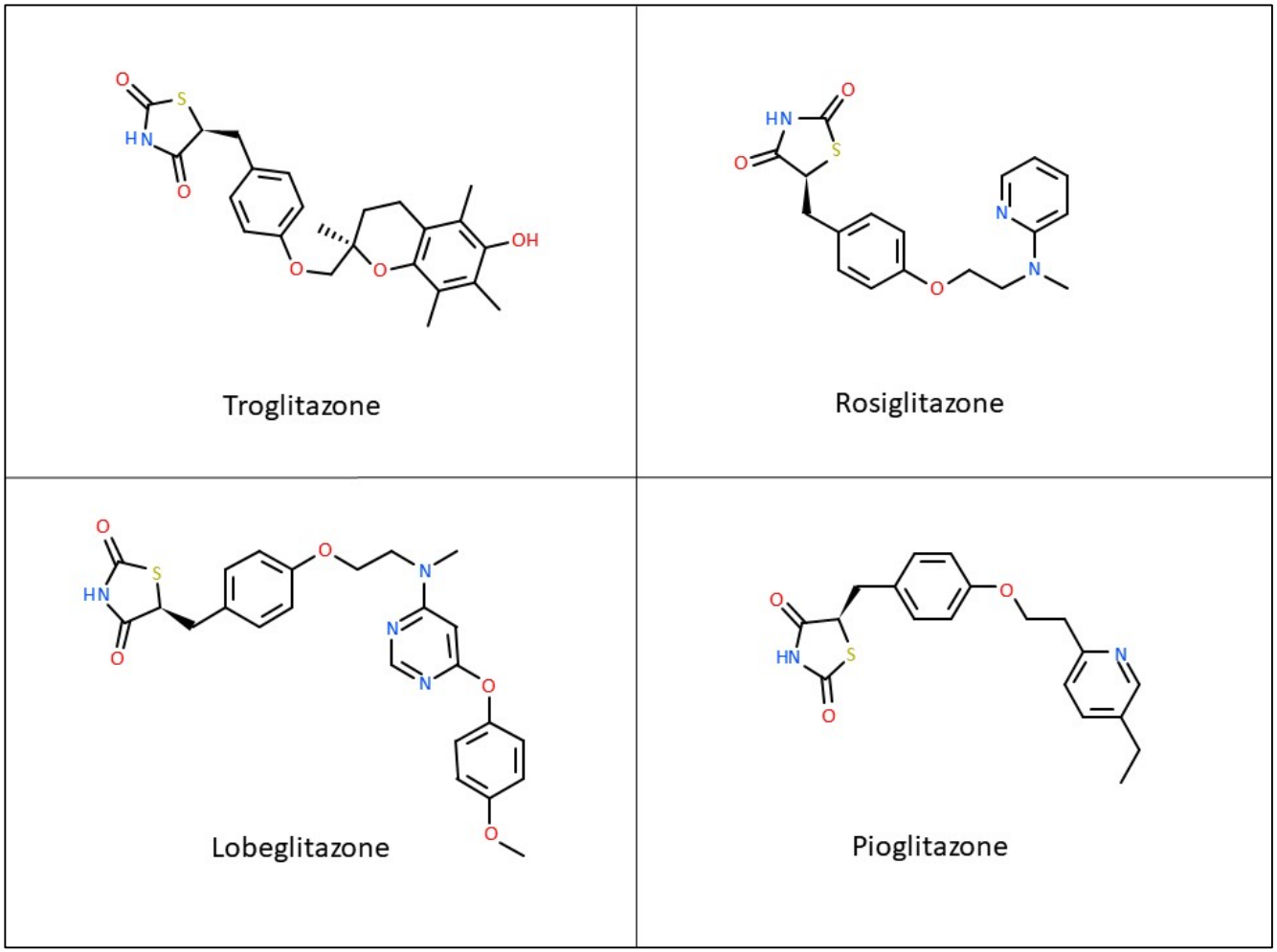

Figure 7. **2d Chemical structures of PPARγ selective drugs.** In clockwise order, Troglitazone, Rosiglitazone, Lobeglitazone and Pioglitazone.

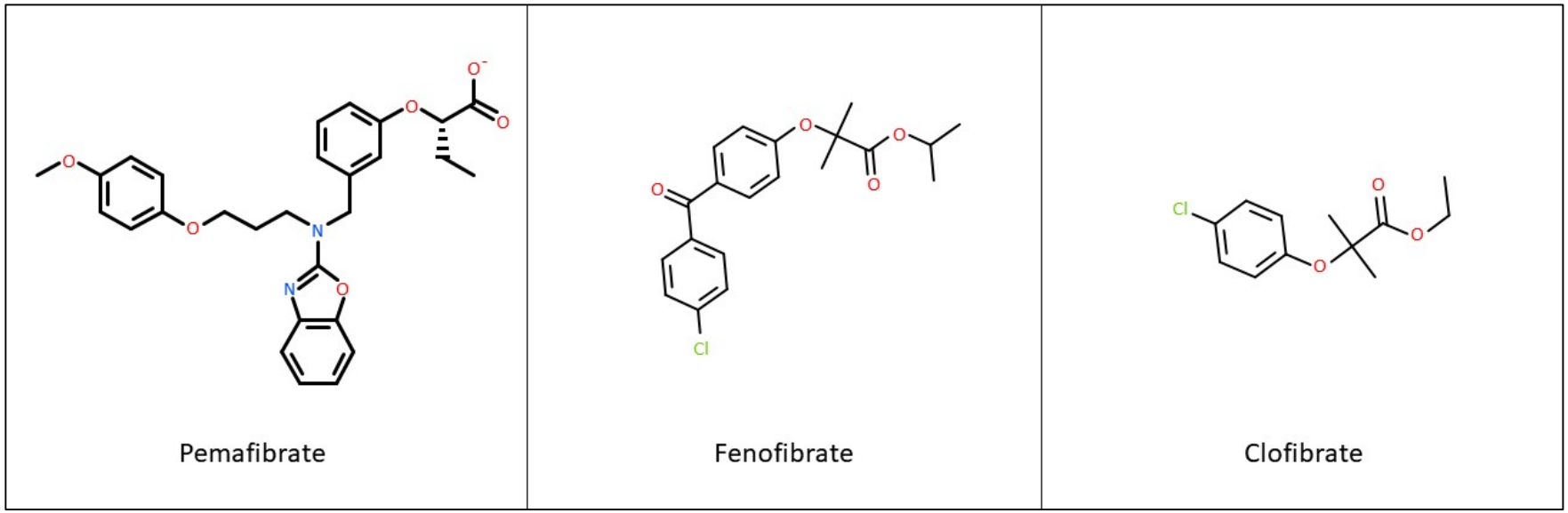

Figure 8. **2d Chemical structures of PPARα selective drugs.** From left to right, Pemafibrate, Fenofibrate and Clofibrate.

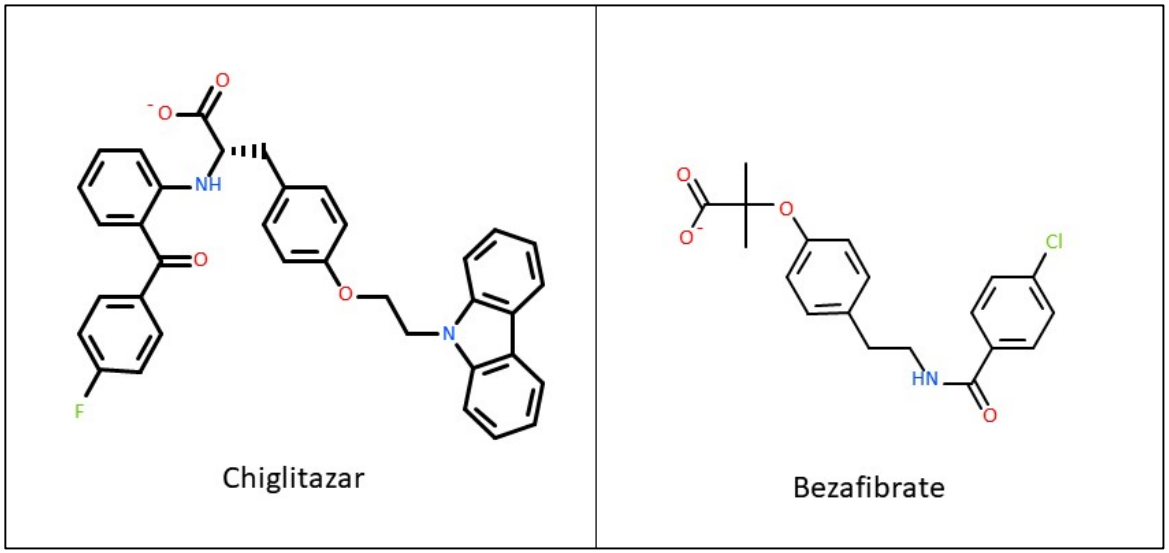

Figure 9. **2d Chemical structures of pan-activating PPAR drugs.** Left, Chiglitazar. Right, Bezafibrate.

1.10 References

Adhikary, T., Wortmann, A., Schumann, T., Finkernagel, F., Lieber, S., Roth, K., Toth, P. M., Diederich, W. E., Nist, A., Stiewe, T., Kleinesudeik, L., Reinartz, S., Müller-Brüsselbach, S. & Müller, R. (2015) The transcriptional PPARβ/δ network in human macrophages defines a unique agonist-induced activation state. *Nucleic Acids Research.* 43 (10), 5033-5051. doi: 10.1093/nar/gkv331.

Ambele, M. A., Dessels, C., Durandt, C. & Pepper, M. S. (2016) Genome-wide analysis of gene expression during adipogenesis in human adipose-derived stromal cells reveals novel patterns of gene expression during adipocyte differentiation. *Stem Cell Research.* 16 (3), 725-734. doi: 10.1016/j.scr.2016.04.011.

Amri, E.-Z., Bonino, F., Ailhaud, G., Abumrad, N. A. & Grimaldi, P. A. (1995) Cloning of a Protein That Mediates Transcriptional Effects of Fatty Acids in Preadipocytes. *Journal of Biological Chemistry.* 270 (5), 2367-2371. doi: 10.1074/jbc.270.5.2367.

Anderson, C. M. & Stahl, A. (2013) SLC27 fatty acid transport proteins. *Molecular Aspects of Medicine.* 34 (2-3), 516-528. doi: 10.1016/j.mam.2012.07.010.

Aprile, M., Cataldi, S., Ambrosio, M. R., D'Esposito, V., Lim, K., Dietrich, A., Blüher, M., Savage, D. B., Formisano, P., Ciccodicola, A. & Costa, V. (2018) PPARγΔ5, a Naturally Occurring Dominant-Negative Splice Isoform, Impairs PPARγ Function and Adipocyte Differentiation. *Cell Reports.* 25 (6), 1577-1592.e6. doi: 10.1016/j.celrep.2018.10.035.

Arai, H., Yamashita, S., Yokote, K., Araki, E., Suganami, H., Ishibashi, S. & Group, o. b. o. t. K.-S. (2018) Efficacy and Safety of Pemafibrate Versus Fenofibrate in Patients with High Triglyceride and Low HDL Cholesterol Levels: A Multicenter, Placebo-Controlled, Double-Blind, Randomized Trial. *Journal of Atherosclerosis and Thrombosis.* 25 (6), 521-538. doi: 10.5551/jat.44412.

Arias, D., Saxena, S. & Verguet, S. (2022) Quantifying the global burden of mental disorders and their economic value. *eClinicalMedicine.* 54, 101675. doi: 10.1016/j.eclinm.2022.101675.

Armstrong, E. H., Goswami, D., Griffin, P. R., Noy, N. & Ortlund, E. A. (2014) Structural Basis for Ligand Regulation of the Fatty Acid-binding Protein 5, Peroxisome Proliferator-activated Receptor β/δ (FABP5-PPARβ/δ) Signaling Pathway. *Journal of Biological Chemistry.* 289 (21), 14941-14954. doi: 10.1074/jbc.M113.514646.

Bae, J., Park, T., Kim, H., Lee, M. & Cha, B.-S. (2021) Lobeglitazone: A Novel Thiazolidinedione for the Management of Type 2 Diabetes Mellitus. *Diabetes & Metabolism Journal.* 45 (3), 326-336. doi: 10.4093/dmj.2020.0272.

Banner, C., Göttlicher, M., Widmark, E., Sjövall, J., Rafter, J. & Gustafsson, J. (1993) A systematic analytical chemistry/cell assay approach to isolate activators of orphan nuclear receptors from biological extracts: characterization of peroxisome proliferator-activated receptor activators in plasma. *Journal of Lipid Research.* 34 (9), 1583-1591. doi: 10.1016/S0022-2275(20)36951-0.

Belete, R., Ataro, Z., Abdu, A. & Sheleme, M. (2021) Global prevalence of metabolic syndrome among patients with type I diabetes mellitus: a systematic review and meta-analysis. *Diabetology & Metabolic Syndrome.* 13 (1), 25. doi: 10.1186/s13098-021-00641-8.

Benoit, G., Cooney, A., Giguere, V., Ingraham, H., Lazar, M., Muscat, G., Perlmann, T., Renaud, J.-P., Schwabe, J., Sladek, F., Tsai, M.-J. & Laudet, V. (2006) International Union of Pharmacology. LXVI. Orphan Nuclear Receptors. *Pharmacological Reviews.* 58 (4), 798-836. doi: 10.1124/pr.58.4.10.

Bernardes, A., Batista, F. A. H., de Oliveira Neto, M., Figueira, A. C. M., Webb, P., Saidemberg, D., Palma, M. S. & Polikarpov, I. (2012) Low-Resolution Molecular Models Reveal the Oligomeric State of the PPAR and the Conformational Organization of Its Domains in Solution. *PLoS ONE.* 7 (2), e31852. doi: 10.1371/journal.pone.0031852.

Blumberg, B. & Evans, R. M. (1998) Orphan nuclear receptors—new ligands and new possibilities: Figure 1. *Genes & Development.* 12 (20), 3149-3155. doi: 10.1101/gad.12.20.3149.

Bocos, C., Göttlicher, M., Gearing, K., Banner, C., Enmark, E., Teboul, M., Crickmore, A. & Gustaffson, J.-Å. (1995) Fatty acid activation of peroxisome proliferator-activated receptor (PPAR). *The Journal of Steroid Biochemistry and Molecular Biology.* 53 (1-6), 467-473. doi: 10.1016/0960-0760(95)00093-F.

Bommer, C., Sagalova, V., Heesemann, E., Manne-Goehler, J., Atun, R., Bärnighausen, T., Davies, J. & Vollmer, S. (2018) Global Economic Burden of Diabetes in Adults: Projections From 2015 to 2030. *Diabetes Care.* 41 (5), 963-970. doi: 10.2337/dc17-1962.

Bruning, J. B., Chalmers, M. J., Prasad, S., Busby, S. A., Kamenecka, T. M., He, Y., Nettles, K. W. & Griffin, P. R. (2007) Partial Agonists Activate PPARγ Using a Helix 12 Independent Mechanism. *Structure.* 15 (10), 1258-1271. doi: 10.1016/j.str.2007.07.014.

Brunmeir, R. & Xu, F. (2018) Functional Regulation of PPARs through Post-Translational Modifications. *International Journal of Molecular Sciences.* 19 (6), 1738. doi: 10.3390/ijms19061738.

Burch, L. R., Donnelly, L. A., Doney, A. S. F., Brady, J., Tommasi, A. M., Whitley, A. L., Goddard, C., Morris, A. D., Hansen, M. K. & Palmer, C. N. A. (2010) Peroxisome Proliferator-Activated Receptor-δ Genotype Influences Metabolic Phenotype and May Influence Lipid Response to Statin Therapy in Humans: A Genetics of Diabetes Audit and Research Tayside Study. *The Journal of Clinical Endocrinology & Metabolism.* 95 (4), 1830-1837. doi: 10.1210/jc.2009-1201.

Cariou, B., Charbonnel, B. & Staels, B. (2012) Thiazolidinediones and PPARγ agonists: time for a reassessment. *Trends in Endocrinology & Metabolism.* 23 (5), 205-215. doi: 10.1016/j.tem.2012.03.001.

Chakravarthy, M. V., Lodhi, I. J., Yin, L., Malapaka, R. R. V., Xu, H. E., Turk, J. & Semenkovich, C. F. (2009) Identification of a Physiologically Relevant Endogenous Ligand for PPARα in Liver. *Cell.* 138 (3), 476-488. doi: 10.1016/j.cell.2009.05.036.

Chamberlain, S., Gabriel, H., Strittmatter, W. & Didsbury, J. (2020) An Exploratory Phase IIa Study of the PPAR delta/gamma Agonist T3D-959 Assessing Metabolic and Cognitive Function in Subjects with Mild to Moderate Alzheimer's Disease. *Journal of Alzheimer's Disease.* 73 (3), 1085-1103. doi: 10.3233/JAD-190864.

Chan, L. S. A. & Wells, R. A. (2009) Cross-Talk between PPARs and the Partners of RXR: A Molecular Perspective. *PPAR Research.* 2009, 1-9. doi: 10.1155/2009/925309.

Chandra, V., Huang, P., Hamuro, Y., Raghuram, S., Wang, Y., Burris, T. P. & Rastinejad, F. (2008) Structure of the intact PPAR-γ–RXR-α nuclear receptor complex on DNA. *Nature.* 456 (7220), 350-356. doi: 10.1038/nature07413.

Chawla, A., Repa, J. J., Evans, R. M. & Mangelsdorf, D. J. (2001) Nuclear Receptors and Lipid Physiology: Opening the X-Files. *Science.* 294 (5548), 1866-1870. doi: 10.1126/science.294.5548.1866.

Chekaoui, A. & Ertl, H. C. J. (2021) PPARα Agonist Fenofibrate Enhances Cancer Vaccine Efficacy. *Cancer Research.* 81 (17), 4431-4440. doi: 10.1158/0008-5472.CAN-21-0052.

Chen, L., Qin, Y., Liu, B., Gao, M., Li, A., Li, X. & Gong, G. (2022) PGC-1α-Mediated Mitochondrial Quality Control: Molecular Mechanisms and Implications for Heart Failure. *Frontiers in Cell and Developmental Biology.* 10, 871357. doi: 10.3389/fcell.2022.871357.

Cheng, H. S., Tan, W. R., Low, Z. S., Marvalim, C., Lee, J. Y. H. & Tan, N. S. (2019) Exploration and Development of PPAR Modulators in Health and Disease: An Update of Clinical Evidence. *International Journal of Molecular Sciences.* 20 (20), 5055. doi: 10.3390/ijms20205055.

Choi, J. H., Banks, A. S., Estall, J. L., Kajimura, S., Boström, P., Laznik, D., Ruas, J. L., Chalmers, M. J., Kamenecka, T. M., Blüher, M., Griffin, P. R. & Spiegelman, B. M. (2010) Anti-diabetic drugs inhibit obesity-linked phosphorylation of PPARγ by Cdk5. *Nature.* 466 (7305), 451-456. doi: 10.1038/nature09291.

Chong, H. C., Tan, M. J., Philippe, V., Tan, S. H., Tan, C. K., Ku, C. W., Goh, Y. Y., Wahli, W., Michalik, L. & Tan, N. S. (2009) Regulation of epithelial–mesenchymal IL-1 signaling by PPARβ/δ is essential for

skin homeostasis and wound healing. *Journal of Cell Biology.* 184 (6), 817-831. doi: 10.1083/jcb.200809028.

Christofides, A., Konstantinidou, E., Jani, C. & Boussiotis, V. A. (2021) The role of peroxisome proliferator-activated receptors (PPAR) in immune responses. *Metabolism.* 114, 154338. doi: 10.1016/j.metabol.2020.154338.

Chua, B. S. K. & Bruning, J. B. (2021) PPARα and δ Ligand Design: Honing the Traditional Empirical Method with a More Holistic Overview. In: Badr, M.Z. (ed.) *Nuclear Receptors.* Cham, Springer International Publishing, pp. 111-178.

Cifarelli, V. & Abumrad, N. A. (2018) Intestinal CD36 and Other Key Proteins of Lipid Utilization: Role in Absorption and Gut Homeostasis. In: Terjung, R. (ed.) *Comprehensive Physiology.* 1 ed., Wiley, pp. 493-507.

Cohen, R. N. (2006) Nuclear Receptor Corepressors and PPARγ. *Nuclear Receptor Signaling.* 4 (1), nrs.04003. doi: 10.1621/nrs.04003.

Collaborators, G. M. D. (2022) Global, regional, and national burden of 12 mental disorders in 204 countries and territories, 1990–2019: a systematic analysis for the Global Burden of Disease Study 2019. *The Lancet Psychiatry.* 9 (2), 137-150. doi: 10.1016/S2215-0366(21)00395-3.

Committee, N. R. N. (1999) A Unified Nomenclature System for the Nuclear Receptor Superfamily. *Cell.* 97 (2), 161-163. doi: 10.1016/S0092-8674(00)80726-6.

Crichton, P. G., Lee, Y. & Kunji, E. R. S. (2017) The molecular features of uncoupling protein 1 support a conventional mitochondrial carrier-like mechanism. *Biochimie.* 134, 35-50. doi: 10.1016/j.biochi.2016.12.016.

Das Pradhan, A., Glynn, R. J., Fruchart, J.-C., MacFadyen, J. G., Zaharris, E. S., Everett, B. M., Campbell, S. E., Oshima, R., Amarenco, P., Blom, D. J., Brinton, E. A., Eckel, R. H., Elam, M. B., Felicio, J. S., Ginsberg, H. N., Goudev, A., Ishibashi, S., Joseph, J., Kodama, T., Koenig, W., Leiter, L. A., Lorenzatti, A. J., Mankovsky, B., Marx, N., Nordestgaard, B. G., Páll, D., Ray, K. K., Santos, R. D., Soran, H., Susekov, A., Tendera, M., Yokote, K., Paynter, N. P., Buring, J. E., Libby, P. & Ridker, P. M. (2022) Triglyceride Lowering with Pemafibrate to Reduce Cardiovascular Risk. *New England Journal of Medicine.* 387 (21), 1923-1934. doi: 10.1056/NEJMoa2210645.

Deeks, E. D. (2022) Chiglitazar: First Approval. *Drugs.* 82 (1), 87-92. doi: 10.1007/s40265-021-01648-1.

Dickey, A. S., Pineda, V. V., Tsunemi, T., Liu, P. P., Miranda, H. C., Gilmore-Hall, S. K., Lomas, N., Sampat, K. R., Buttgereit, A., Torres, M.-J. M., Flores, A. L., Arreola, M., Arbez, N., Akimov, S. S.,

Gaasterland, T., Lazarowski, E. R., Ross, C. A., Yeo, G. W., Sopher, B. L., Magnuson, G. K., Pinkerton, A. B., Masliah, E. & La Spada, A. R. (2016) PPAR-δ is repressed in Huntington's disease, is required for normal neuronal function and can be targeted therapeutically. *Nature Medicine.* 22 (1), 37-45. doi: 10.1038/nm.4003.

Dietz, M., Mohr, P., Kuhn, B., Maerki, H. P., Hartman, P., Ruf, A., Benz, J., Grether, U. & Wright, M. B. (2012) Comparative Molecular Profiling of the PPARα/γ Activator Aleglitazar: PPAR Selectivity, Activity and Interaction with Cofactors. *ChemMedChem.* 7 (6), 1101-1111. doi: 10.1002/cmdc.201100598.

Ding, X., Han, X., Yuan, H., Zhang, Y. & Gao, Y. (2020) The Impact of PPARD and PPARG Polymorphisms on Glioma Risk and Prognosis. *Scientific Reports.* 10 (1), 5140. doi: 10.1038/s41598-020-60996-2.

Dubois, V., Eeckhoute, J., Lefebvre, P. & Staels, B. (2017) Distinct but complementary contributions of PPAR isotypes to energy homeostasis. *Journal of Clinical Investigation.* 127 (4), 1202-1214. doi: 10.1172/JCI88894.

Eckland, D. A. & Danhof, M. (2000) Clinical pharmacokinetics of Pioglitazone. *Exp Clin Endocrinol Diabetes.* 108 (Suppl 2), S234-S242.

Egawa, D., Itoh, T., Akiyama, Y., Saito, T. & Yamamoto, K. (2016) 17-OxoDHA Is a PPARα/γ Dual Covalent Modifier and Agonist. *ACS Chemical Biology.* 11 (9), 2447-2455. doi: 10.1021/acschembio.6b00338.

Evans, Ronald M. & Mangelsdorf, David J. (2014) Nuclear Receptors, RXR, and the Big Bang. *Cell.* 157 (1), 255-266. doi: 10.1016/j.cell.2014.03.012.

Fang, H. & Judd, R. L. (2018) Adiponectin Regulation and Function. In: Terjung, R. (ed.) *Comprehensive Physiology.* 1 ed., Wiley, pp. 1031-1063.

Fang, L., Zhang, M., Li, Y., Liu, Y., Cui, Q. & Wang, N. (2016) PPARgene: A Database of Experimentally Verified and Computationally Predicted PPAR Target Genes. *PPAR Research.* 2016, 1-6. doi: 10.1155/2016/6042162.

Farmer, S. R. (2006) Transcriptional control of adipocyte formation. *Cell Metabolism.* 4 (4), 263-273. doi: 10.1016/j.cmet.2006.07.001.

Feige, J. N., Gelman, L., Tudor, C., Engelborghs, Y., Wahli, W. & Desvergne, B. (2005) Fluorescence Imaging Reveals the Nuclear Behavior of Peroxisome Proliferator-activated Receptor/Retinoid X Receptor Heterodimers in the Absence and Presence of Ligand*♦. *Journal of Biological Chemistry.* 280 (18), 17880-17890. doi: 10.1074/jbc.M500786200.

Fernández-Hernando, C. & Suárez, Y. (2020) ANGPTL4: a multifunctional protein involved in metabolism and vascular homeostasis. *Current Opinion in Hematology.* 27 (3), 206-213. doi: 10.1097/MOH.0000000000000580.

Ferret-Sena, V., Capela, C. & Sena, A. (2018) Metabolic Dysfunction and Peroxisome Proliferator-Activated Receptors (PPAR) in Multiple Sclerosis. *International Journal of Molecular Sciences.* 19 (6), 1639. doi: 10.3390/ijms19061639.

Forman, B. M., Chen, J. & Evans, R. M. (1997) Hypolipidemic drugs, polyunsaturated fatty acids, and eicosanoids are ligands for peroxisome proliferator-activated receptors α and δ. *Proceedings of the National Academy of Sciences.* 94 (9), 4312-4317. doi: 10.1073/pnas.94.9.4312.

Forman, B. M., Tontonoz, P., Chen, J., Brun, R. P., Spiegelman, B. M. & Evans, R. M. (1995) 15-Deoxy-Δ12,14-Prostaglandin J2 is a ligand for the adipocyte determination factor PPARγ. *Cell.* 83 (5), 803-812. doi: 10.1016/0092-8674(95)90193-0.

Fougerat, A., Montagner, A., Loiseau, N., Guillou, H. & Wahli, W. (2020) Peroxisome Proliferator-Activated Receptors and Their Novel Ligands as Candidates for the Treatment of Non-Alcoholic Fatty Liver Disease. *Cells.* 9 (7), 1638. doi: 10.3390/cells9071638.

Francque, S., Szabo, G., Abdelmalek, M. F., Byrne, C. D., Cusi, K., Dufour, J.-F., Roden, M., Sacks, F. & Tacke, F. (2021) Nonalcoholic steatohepatitis: the role of peroxisome proliferator-activated receptors. *Nature Reviews Gastroenterology & Hepatology.* 18 (1), 24-39. doi: 10.1038/s41575-020-00366-5.

Frkic, R. L., Marshall, A. C., Blayo, A.-L., Pukala, T. L., Kamenecka, T. M., Griffin, P. R. & Bruning, J. B. (2018) PPARγ in Complex with an Antagonist and Inverse Agonist: a Tumble and Trap Mechanism of the Activation Helix. *iScience.* 5, 69-79. doi: 10.1016/j.isci.2018.06.012.

Frkic, R. L., Richter, K. & Bruning, J. B. (2021) The therapeutic potential of inhibiting PPARγ phosphorylation to treat type 2 diabetes. *Journal of Biological Chemistry.* 297 (3), 101030. doi: 10.1016/j.jbc.2021.101030.

Fyffe, S. A., Alphey, M. S., Buetow, L., Smith, T. K., Ferguson, M. A. J., Sørensen, M. D., Björkling, F. & Hunter, W. N. (2006) Recombinant Human PPAR-β/δ Ligand-binding Domain is Locked in an Activated Conformation by Endogenous Fatty Acids. *Journal of Molecular Biology.* 356 (4), 1005-1013. doi: 10.1016/j.jmb.2005.12.047.

Gampe, R. T., Montana, V. G., Lambert, M. H., Miller, A. B., Bledsoe, R. K., Milburn, M. V., Kliewer, S. A., Willson, T. M. & Xu, H. E. (2000) Asymmetry in the PPARγ/RXRα Crystal Structure Reveals the Molecular Basis of Heterodimerization among Nuclear Receptors. *Molecular Cell.* 5 (3), 545-555. doi: 10.1016/S1097-2765(00)80448-7.

Garza, A. S., Khan, S. H., Moure, C. M., Edwards, D. P. & Kumar, R. (2011) Binding-Folding Induced Regulation of AF1 Transactivation Domain of the Glucocorticoid Receptor by a Cofactor That Binds to Its DNA Binding Domain. *PLoS ONE.* 6 (10), e25875. doi: 10.1371/journal.pone.0025875.

Gawrieh, S., Noureddin, M., Loo, N., Mohseni, R., Awasty, V., Cusi, K., Kowdley, K. V., Lai, M., Schiff, E., Parmar, D., Patel, P. & Chalasani, N. (2021) Saroglitazar, a PPAR-α/γ Agonist, for Treatment of NAFLD: A Randomized Controlled Double-Blind Phase 2 Trial. *Hepatology.* 74 (4), 1809-1824. doi: 10.1002/hep.31843.

Geng, L., Lam, K. S. L. & Xu, A. (2020) The therapeutic potential of FGF21 in metabolic diseases: from bench to clinic. *Nature Reviews Endocrinology.* 16 (11), 654-667. doi: 10.1038/s41574-020-0386-0.

Germain, P., Staels, B., Dacquet, C., Spedding, M. & Laudet, V. (2006) Overview of Nomenclature of Nuclear Receptors. *Pharmacological Reviews.* 58 (4), 685-704. doi: 10.1124/pr.58.4.2.

Giguère, V. (1999) Orphan Nuclear Receptors: From Gene to Function*. *Endocrine Reviews.* 20 (5), 689-725. doi: 10.1210/edrv.20.5.0378.

Gillies, R. J. & Gatenby, R. A. (2015) Metabolism and Its Sequelae in Cancer Evolution and Therapy. *The Cancer Journal.* 21 (2), 88-96. doi: 10.1097/PPO.0000000000000102.

Gillilan, R. E., Ayers, S. D. & Noy, N. (2007) Structural Basis for Activation of Fatty Acid-binding Protein 4. *Journal of Molecular Biology.* 372 (5), 1246-1260. doi: 10.1016/j.jmb.2007.07.040.

Ginsberg, H. N., Hounslow, N. J., Senko, Y., Suganami, H., Bogdanski, P., Ceska, R., Kalina, A., Libis, R. A., Supryadkina, T. V. & Hovingh, G. K. (2022) Efficacy and Safety of K-877 (Pemafibrate), a Selective PPARα Modulator, in European Patients on Statin Therapy. *Diabetes Care.* 45 (4), 898-908. doi: 10.2337/dc21-1288.

Glass, C. K., Rose, D. W. & Rosenfeld, M. G. (1997) Nuclear receptor coactivators. *Current Opinion in Cell Biology.* 9 (2), 222-232. doi: 10.1016/S0955-0674(97)80066-X.

Gold, P. W. (2021) The PPARg System in Major Depression: Pathophysiologic and Therapeutic Implications. *International Journal of Molecular Sciences.* 22 (17), 9248. doi: 10.3390/ijms22179248.

Goldstein, J. T., Berger, A. C., Shih, J., Duke, F. F., Furst, L., Kwiatkowski, D. J., Cherniack, A. D., Meyerson, M. & Strathdee, C. A. (2017) Genomic Activation of *PPARG* Reveals a Candidate Therapeutic Axis in Bladder Cancer. *Cancer Research.* 77 (24), 6987-6998. doi: 10.1158/0008-5472.CAN-17-1701.

Göttlicher, M., Widmark, E., Li, Q. & Gustafsson, J. A. (1992) Fatty acids activate a chimera of the clofibric acid-activated receptor and the glucocorticoid receptor. *Proceedings of the National Academy of Sciences.* 89 (10), 4653-4657. doi: 10.1073/pnas.89.10.4653.

Gou, Q., Jiang, Y., Zhang, R., Xu, Y., Xu, H., Zhang, W., Shi, J. & Hou, Y. (2020) PPARδ is a regulator of autophagy by its phosphorylation. *Oncogene.* 39 (25), 4844-4853. doi: 10.1038/s41388-020-1329-x.

Gough, S. M., Casella, A., Ortega, K. J. & Hackam, A. S. (2021) Neuroprotection by the Ketogenic Diet: Evidence and Controversies. *Frontiers in Nutrition.* 8, 782657. doi: 10.3389/fnut.2021.782657.

Grabacka, M., Pierzchalska, M., Dean, M. & Reiss, K. (2016) Regulation of Ketone Body Metabolism and the Role of PPARα. *International Journal of Molecular Sciences.* 17 (12), 2093. doi: 10.3390/ijms17122093.

Greene, M. E., Blumberg, B., McBride, O. W., Yi, H. F., Kronquist, K., Kwan, K., Hsieh, L., Greene, G. & Nimer, S. D. (1995) Isolation of the human peroxisome proliferator activated receptor gamma cDNA: expression in hematopoietic cells and chromosomal mapping. *Gene Expression.* 4 (4-5), 281-299.

Greten, F. R. & Grivennikov, S. I. (2019) Inflammation and Cancer: Triggers, Mechanisms, and Consequences. *Immunity.* 51 (1), 27-41. doi: 10.1016/j.immuni.2019.06.025.

Gross, B., Pawlak, M., Lefebvre, P. & Staels, B. (2017) PPARs in obesity-induced T2DM, dyslipidaemia and NAFLD. *Nature Reviews Endocrinology.* 13 (1), 36-49. doi: 10.1038/nrendo.2016.135.

Hall, J. A., Rusten, M., Abughazaleh, R. D., Wuertz, B., Souksavong, V., Escher, P. & Ondrey, F. (2020) Effects of PPAR-γ agonists on oral cancer cell lines: Potential horizons for chemopreventives and adjunctive therapies. *Head & Neck.* 42 (9), 2542-2554. doi: 10.1002/hed.26286.

Ham, S. A., Hwang, J. S., Yoo, T., Lee, W. J., Paek, K. S., Oh, J.-W., Park, C.-K., Kim, J.-H., Do, J. T., Kim, J.-H. & Seo, H. G. (2015) Ligand-activated PPARδ upregulates α-smooth muscle actin expression in human dermal fibroblasts: A potential role for PPARδ in wound healing. *Journal of Dermatological Science.* 80 (3), 186-195. doi: 10.1016/j.jdermsci.2015.10.005.

Hanahan, D. (2022) Hallmarks of Cancer: New Dimensions. *Cancer Discovery.* 12 (1), 31-46. doi: 10.1158/2159-8290.CD-21-1059.

Hanahan, D. & Weinberg, Robert A. (2011) Hallmarks of Cancer: The Next Generation. *Cell.* 144 (5), 646-674. doi: 10.1016/j.cell.2011.02.013.

Hartley, A. & Ahmad, I. (2023) The role of PPARγ in prostate cancer development and progression. *British Journal of Cancer.* 128 (6), 940-945. doi: 10.1038/s41416-022-02096-8.

He, B. K., Ning, Z. Q., Li, Z. B., Shan, S., Pan, D. S., Ko, B. C. B., Li, P. P., Shen, Z. F., Dou, G. F., Zhang, B. L., Lu, X. P. & Gao, Y. (2012) *In Vitro* and *In Vivo* Characterizations of Chiglitazar, a Newly Identified PPAR Pan-Agonist. *PPAR Research.* 2012, 1-13. doi: 10.1155/2012/546548.

Hennuyer, N., Duplan, I., Paquet, C., Vanhoutte, J., Woitrain, E., Touche, V., Colin, S., Vallez, E., Lestavel, S., Lefebvre, P. & Staels, B. (2016) The novel selective PPARα modulator (SPPARMα)

pemafibrate improves dyslipidemia, enhances reverse cholesterol transport and decreases inflammation and atherosclerosis. *Atherosclerosis.* 249, 200-208. doi: 10.1016/j.atherosclerosis.2016.03.003.

Hernandez-Quiles, M., Broekema, M. F. & Kalkhoven, E. (2021) PPARgamma in Metabolism, Immunity, and Cancer: Unified and Diverse Mechanisms of Action. *Frontiers in Endocrinology.* 12, 624112. doi: 10.3389/fendo.2021.624112.

Hirode, G. & Wong, R. J. (2020) Trends in the Prevalence of Metabolic Syndrome in the United States, 2011-2016. *JAMA.* 323 (24), 2526. doi: 10.1001/jama.2020.4501.

Hong, F., Pan, S., Guo, Y., Xu, P. & Zhai, Y. (2019) PPARs as Nuclear Receptors for Nutrient and Energy Metabolism. *Molecules.* 24 (14), 2545. doi: 10.3390/molecules24142545.

Hong, F., Xu, P. & Zhai, Y. (2018) The Opportunities and Challenges of Peroxisome Proliferator-Activated Receptors Ligands in Clinical Drug Discovery and Development. *International Journal of Molecular Sciences.* 19 (8), 2189. doi: 10.3390/ijms19082189.

Hostetler, H. A., Petrescu, A. D., Kier, A. B. & Schroeder, F. (2005) Peroxisome Proliferator-activated Receptor α Interacts with High Affinity and Is Conformationally Responsive to Endogenous Ligands. *Journal of Biological Chemistry.* 280 (19), 18667-18682. doi: 10.1074/jbc.M412062200.

Huang, D. Q., Downes, M., Evans, R. M., Witztum, J. L., Glass, C. K. & Loomba, R. (2022) Shared Mechanisms between Cardiovascular Disease and NAFLD. *Seminars in Liver Disease.* 42 (04), 455-464. doi: 10.1055/a-1930-6658.

Hughes, M. L. R., Liu, B., Halls, M. L., Wagstaff, K. M., Patil, R., Velkov, T., Jans, D. A., Bunnett, N. W., Scanlon, M. J. & Porter, C. J. H. (2015) Fatty Acid-binding Proteins 1 and 2 Differentially Modulate the Activation of Peroxisome Proliferator-activated Receptor α in a Ligand-selective Manner. *Journal of Biological Chemistry.* 290 (22), 13895-13906. doi: 10.1074/jbc.M114.605998.

Irwin, S., Karr, C., Furman, C., Tsai, J., Gee, P., Banka, D., Wibowo, A. S., Dementiev, A. A., O'Shea, M., Yang, J., Lowe, J., Mitchell, L., Ruppel, S., Fekkes, P., Zhu, P., Korpal, M. & Larsen, N. A. (2022) Biochemical and structural basis for the pharmacological inhibition of nuclear hormone receptor PPARγ by inverse agonists. *Journal of Biological Chemistry.* 298 (11), 102539. doi: 10.1016/j.jbc.2022.102539.

Issemann, I. & Green, S. (1990) Activation of a member of the steroid hormone receptor superfamily by peroxisome proliferators. *Nature.* 347 (6294), 645-650. doi: 10.1038/347645a0.

Itoh, T., Fairall, L., Amin, K., Inaba, Y., Szanto, A., Balint, B. L., Nagy, L., Yamamoto, K. & Schwabe, J. W. R. (2008) Structural basis for the activation of PPARγ by oxidized fatty acids. *Nature Structural & Molecular Biology.* 15 (9), 924-931. doi: 10.1038/nsmb.1474.

Iwayanagi, Y., Takada, T., Tomura, F., Yamanashi, Y., Terada, T., Inui, K.-i. & Suzuki, H. (2011) Human NPC1L1 Expression is Positively Regulated by PPARα. *Pharmaceutical Research.* 28 (2), 405-412. doi: 10.1007/s11095-010-0294-4.

Jack, D. L., Klein, N. J. & Turner, M. W. (2001) Mannose-binding lectin: targeting the microbial world for complement attack and opsonophagocytosis: MBL and antimicrobial defence. *Immunological Reviews.* 180 (1), 86-99. doi: 10.1034/j.1600-065X.2001.1800108.x.

Jain, M. R., Giri, S. R., Trivedi, C., Bhoi, B., Rath, A., Vanage, G., Vyas, P., Ranvir, R. & Patel, P. R. (2015) Saroglitazar, a novel PPAR *α* / *γ* agonist with predominant PPAR *α* activity, shows lipid-lowering and insulin-sensitizing effects in preclinical models. *Pharmacology Research & Perspectives.* 3 (3). doi: 10.1002/prp2.136.

Jaiswal, A., Jain, K. & Singh, A. K. (2021) Role of Saroglitazar in Non Diabetic Non Alcoholic Fatty Liver Disease Patients: A Retrospective Observational Study. *JOURNAL OF CLINICAL AND DIAGNOSTIC RESEARCH.* doi: 10.7860/JCDR/2021/52065.15738.

Jakob, T., Nordmann, A. J., Schandelmaier, S., Ferreira-González, I. & Briel, M. (2016) Fibrates for primary prevention of cardiovascular disease events. *The Cochrane Database of Systematic Reviews.* 11 (11), CD009753. doi: 10.1002/14651858.CD009753.pub2.

Jang, J. Y., Bae, H., Lee, Y. J., Choi, Y. I., Kim, H.-J., Park, S. B., Suh, S. W., Kim, S. W. & Han, B. W. (2018) Structural Basis for the Enhanced Anti-Diabetic Efficacy of Lobeglitazone on PPARγ. *Scientific Reports.* 8 (1), 31. doi: 10.1038/s41598-017-18274-1.

Jani, R. H., Kansagra, K., Jain, M. R. & Patel, H. (2013) Pharmacokinetics, Safety, and Tolerability of Saroglitazar (ZYH1), a Predominantly PPARα Agonist with Moderate PPARγ Agonist Activity in Healthy Human Subjects. *Clinical Drug Investigation.* 33 (11), 809-816. doi: 10.1007/s40261-013-0128-3.

Ji, L., Song, W., Fang, H., Li, W., Geng, J., Wang, Y., Guo, L., Cai, H., Yang, T., Li, H., Yang, G., Li, Q., Liu, K., Li, S., Liu, Y., Shi, F., Li, X., Gao, X., Tian, H., Ji, Q., Su, Q., Zhou, Z., Wang, W., Zhou, Z., Li, X., Xu, Y., Ning, Z., Cao, H., Pan, D., Yao, H., Lu, X. & Jia, W. (2021) Efficacy and safety of chiglitazar, a novel peroxisome proliferator-activated receptor pan-agonist, in patients with type 2 diabetes: a randomized, double-blind, placebo-controlled, phase 3 trial (CMAP). *Science Bulletin.* 66 (15), 1571-1580. doi: 10.1016/j.scib.2021.03.019.

Jin, L., Lin, S., Rong, H., Zheng, S., Jin, S., Wang, R. & Li, Y. (2011) Structural Basis for Iloprost as a Dual Peroxisome Proliferator-activated Receptor α/δ Agonist. *Journal of Biological Chemistry.* 286 (36), 31473-31479. doi: 10.1074/jbc.M111.266023.

Jin, S. M., Park, C. Y., Cho, Y. M., Ku, B. J., Ahn, C. W., Cha, B. S., Min, K. W., Sung, Y. A., Baik, S. H., Lee, K. W., Yoon, K. H., Lee, M. K. & Park, S. W. (2015) Lobeglitazone and pioglitazone as add-ons to metformin for patients with type 2 diabetes: a 24-week, multicentre, randomized, double-blind, parallel-group, active-controlled, phase III clinical trial with a 28-week extension. *Diabetes, Obesity and Metabolism.* 17 (6), 599-602. doi: 10.1111/dom.12435.

Juge-Aubry, C., Pernin, A., Favez, T., Burger, A. G., Wahli, W., Meier, C. A. & Desvergne, B. (1997) DNA Binding Properties of Peroxisome Proliferator-activated Receptor Subtypes on Various Natural Peroxisome Proliferator Response Elements. *Journal of Biological Chemistry.* 272 (40), 25252-25259. doi: 10.1074/jbc.272.40.25252.

Jüngling, E. & Kammermeier, H. (1988) A one-vial method for routine extraction and quantification of free fatty acids in blood and tissue by HPLC. *Analytical Biochemistry.* 171 (1), 150-157. doi: 10.1016/0003-2697(88)90136-4.

Kalliora, C. & Drosatos, K. (2020) The Glitazars Paradox: Cardiotoxicity of the Metabolically Beneficial Dual PPARα and PPARγ Activation. *Journal of Cardiovascular Pharmacology.* 76 (5), 514-526. doi: 10.1097/FJC.0000000000000891.

Kamata, S., Oyama, T., Saito, K., Honda, A., Yamamoto, Y., Suda, K., Ishikawa, R., Itoh, T., Watanabe, Y., Shibata, T., Uchida, K., Suematsu, M. & Ishii, I. (2020) PPARα Ligand-Binding Domain Structures with Endogenous Fatty Acids and Fibrates. *iScience.* 23 (11), 101727. doi: 10.1016/j.isci.2020.101727.

Karlsson, M., Zhang, C., Méar, L., Zhong, W., Digre, A., Katona, B., Sjöstedt, E., Butler, L., Odeberg, J., Dusart, P., Edfors, F., Oksvold, P., Von Feilitzen, K., Zwahlen, M., Arif, M., Altay, O., Li, X., Ozcan, M., Mardinoglu, A., Fagerberg, L., Mulder, J., Luo, Y., Ponten, F., Uhlén, M. & Lindskog, C. (2021) A single–cell type transcriptomics map of human tissues. *Science Advances.* 7 (31), eabh2169. doi: 10.1126/sciadv.abh2169.

Keller, H., Dreyer, C., Medin, J., Mahfoudi, A., Ozato, K. & Wahli, W. (1993) Fatty acids and retinoids control lipid metabolism through activation of peroxisome proliferator-activated receptor-retinoid X receptor heterodimers. *Proceedings of the National Academy of Sciences.* 90 (6), 2160-2164. doi: 10.1073/pnas.90.6.2160.

Kersten, S. (2014) Integrated physiology and systems biology of PPARα. *Molecular Metabolism.* 3 (4), 354-371. doi: 10.1016/j.molmet.2014.02.002.

Kersten, S. (2021) Role and mechanism of the action of angiopoietin-like protein ANGPTL4 in plasma lipid metabolism. *Journal of Lipid Research.* 62, 100150. doi: 10.1016/j.jlr.2021.100150.

Kilu, W., Merk, D., Steinhilber, D., Proschak, E. & Heering, J. (2021) Heterodimer formation with retinoic acid receptor RXRα modulates coactivator recruitment by peroxisome proliferator-activated receptor PPARγ. *Journal of Biological Chemistry.* 297 (1), 100814. doi: 10.1016/j.jbc.2021.100814.

Kim, B.-Y., Kwon, H.-S., Kim, S. K., Noh, J.-H., Park, C.-Y., Park, H.-K., Song, K.-H., Won, J. C., Yu, J. M., Lee, M. Y., Lee, J. H., Lim, S., Chun, S. W., Jeong, I.-K., Chung, C. H., Han, S. J., Kim, H.-S., Min, J.-Y. & Kim, S. (2022) A Real-World Study of Long-Term Safety and Efficacy of Lobeglitazone in Korean Patients with Type 2 Diabetes Mellitus. *Diabetes & Metabolism Journal.* 46 (6), 855-865. doi: 10.4093/dmj.2021.0264.

Kim, J. W., Kim, J.-R., Yi, S., Shin, K.-H., Shin, H.-S., Yoon, S. H., Cho, J.-Y., Kim, D.-H., Shin, S.-G., Jang, I.-J. & Yu, K.-S. (2011) Tolerability and Pharmacokinetics of Lobeglitazone (CKD-501), a Peroxisome Proliferator-Activated Receptor-γ Agonist: A Single- and Multiple-Dose, Double-Blind, Randomized Control Study in Healthy Male Korean Subjects. *Clinical Therapeutics.* 33 (11), 1819-1830. doi: 10.1016/j.clinthera.2011.09.023.

Kim, N. H., Han, K. H., Choi, J., Lee, J. & Kim, S. G. (2019) Use of fenofibrate on cardiovascular outcomes in statin users with metabolic syndrome: propensity matched cohort study. *BMJ.* l5125. doi: 10.1136/bmj.l5125.

Kim, N. H. & Kim, S. G. (2020) Fibrates Revisited: Potential Role in Cardiovascular Risk Reduction. *Diabetes & Metabolism Journal.* 44 (2), 213. doi: 10.4093/dmj.2020.0001.

Kim, N.-J., Lee, K.-O., Koo, B.-W., Li, F., Yoo, J.-K., Park, H.-J., Min, K.-H., Lim, J. I., Kim, M. K., Kim, J.-K. & Suh, Y.-G. (2007) Design, synthesis, and structure–activity relationship of carbamate-tethered aryl propanoic acids as novel PPARα/γ dual agonists. *Bioorganic & Medicinal Chemistry Letters.* 17 (13), 3595-3598. doi: 10.1016/j.bmcl.2007.04.057.

Kliewer, S. A., Forman, B. M., Blumberg, B., Ong, E. S., Borgmeyer, U., Mangelsdorf, D. J., Umesono, K. & Evans, R. M. (1994) Differential expression and activation of a family of murine peroxisome proliferator-activated receptors. *Proceedings of the National Academy of Sciences.* 91 (15), 7355-7359. doi: 10.1073/pnas.91.15.7355.

Kliewer, S. A., Lenhard, J. M., Willson, T. M., Patel, I., Morris, D. C. & Lehmann, J. M. (1995) A prostaglandin J2 metabolite binds peroxisome proliferator-activated receptor γ and promotes adipocyte differentiation. *Cell.* 83 (5), 813-819. doi: 10.1016/0092-8674(95)90194-9.

Kliewer, S. A., Sundseth, S. S., Jones, S. A., Brown, P. J., Wisely, G. B., Koble, C. S., Devchand, P., Wahli, W., Willson, T. M., Lenhard, J. M. & Lehmann, J. M. (1997) Fatty acids and eicosanoids

regulate gene expression through direct interactions with peroxisome proliferator-activated receptors α and γ. *Proceedings of the National Academy of Sciences.* 94 (9), 4318-4323. doi: 10.1073/pnas.94.9.4318.

Kopf, T. & Schmitz, G. (2013) Analysis of non-esterified fatty acids in human samples by solid-phase-extraction and gas chromatography/mass spectrometry. *Journal of Chromatography B.* 938, 22-26. doi: 10.1016/j.jchromb.2013.08.016.

Korbecki, J., Bobiński, R. & Dutka, M. (2019) Self-regulation of the inflammatory response by peroxisome proliferator-activated receptors. *Inflammation Research.* 68 (6), 443-458. doi: 10.1007/s00011-019-01231-1.

Koundouros, N. & Poulogiannis, G. (2020) Reprogramming of fatty acid metabolism in cancer. *British Journal of Cancer.* 122 (1), 4-22. doi: 10.1038/s41416-019-0650-z.

Krey, G., Braissant, O., L'Horset, F., Kalkhoven, E., Perroud, M., Parker, M. G. & Wahli, W. (1997) Fatty Acids, Eicosanoids, and Hypolipidemic Agents Identified as Ligands of Peroxisome Proliferator-Activated Receptors by Coactivator-Dependent Receptor Ligand Assay. *Molecular Endocrinology.* 11 (6), 779-791. doi: 10.1210/mend.11.6.0007.

Krishnappa, M., Patil, K., Parmar, K., Trivedi, P., Mody, N., Shah, C., Faldu, K., Maroo, S., group, f. t. P. X. s., Desai, P., Fatania, K., Murthy, S., Balamurugan, R., Agarwal, M., Singh, K. P., Kalra, G. S., Khandelwal, V., Singwala, A., Thacker, H., Tulle, R., Rao, H., Kumbla, M., Singh, P., Khatri, A., Agrawal, S., Sarkar, R. N., Agarwal, D., Bhatia, G., Agarwal, R. P., Kumar, S., Vamsi Krishna, P. R., Ajmani, A. K., Asalkar, A., Basu, I., Chatterjee, S., Pavithran, V. K., Das, R., Dharmadhikari, A., Vardhan, V., Madusudhan Babu, M., Sengupta, N., Abkari, S., Harikrishna, R., Chovatia, R. & Parmar, D. (2020) Effect of saroglitazar 2 mg and 4 mg on glycemic control, lipid profile and cardiovascular disease risk in patients with type 2 diabetes mellitus: a 56-week, randomized, double blind, phase 3 study (PRESS XII study). *Cardiovascular Diabetology.* 19 (1), 93. doi: 10.1186/s12933-020-01073-w.

Kroker, A. J. & Bruning, J. B. (2015) Review of the Structural and Dynamic Mechanisms of PPAR *γ* Partial Agonism. *PPAR Research.* 2015, 1-15. doi: 10.1155/2015/816856.

Laganà, A., Vitale, S., Nigro, A., Sofo, V., Salmeri, F., Rossetti, P., Rapisarda, A., La Vignera, S., Condorelli, R., Rizzo, G. & Buscema, M. (2016) Pleiotropic Actions of Peroxisome Proliferator-Activated Receptors (PPARs) in Dysregulated Metabolic Homeostasis, Inflammation and Cancer: Current Evidence and Future Perspectives. *International Journal of Molecular Sciences.* 17 (7), 999. doi: 10.3390/ijms17070999.

Lamichane, S., Dahal Lamichane, B. & Kwon, S.-M. (2018) Pivotal Roles of Peroxisome Proliferator-Activated Receptors (PPARs) and Their Signal Cascade for Cellular and Whole-Body Energy Homeostasis. *International Journal of Molecular Sciences.* 19 (4), 949. doi: 10.3390/ijms19040949.

Lazarus, J. V., Colombo, M., Cortez-Pinto, H., Huang, T. T.-K., Miller, V., Ninburg, M., Schattenberg, J. M., Seim, L., Wong, V. W. S. & Zelber-Sagi, S. (2020) NAFLD — sounding the alarm on a silent epidemic. *Nature Reviews Gastroenterology & Hepatology.* 17 (7), 377-379. doi: 10.1038/s41575-020-0315-7.

Lazarus, J. V. & Mark, H. E. & Anstee, Q. M. & Arab, J. P. & Batterham, R. L. & Castera, L. & Cortez-Pinto, H. & Crespo, J. & Cusi, K. & Dirac, M. A. & Francque, S. & George, J. & Hagström, H. & Huang, T. T.-K. & Ismail, M. H. & Kautz, A. & Sarin, S. K. & Loomba, R. & Miller, V. & Newsome, P. N. & Ninburg, M. & Ocama, P. & Ratziu, V. & Rinella, M. & Romero, D. & Romero-Gómez, M. & Schattenberg, J. M. & Tsochatzis, E. A. & Valenti, L. & Wong, V. W.-S. & Yilmaz, Y. & Younossi, Z. M. & Zelber-Sagi, S. & Consortium, t. N. C. & Åberg, F. & Adams, L. & Khatry, M. S. A. & Naamani, K. A. & Murillo, O. A. & Allen, A. M. & Alnaser, F. & Alqahtani, S. A. & Alswat, K. & Alvaro, D. & Andrade, R. J. & Arrese, M. & Awuku, Y. A. & Ayesha, M. & Baatarkhuu, O. & Bakieva, S. & Basu, R. & Bataller, R. & Bedri, S. & Bosi, E. & Bourliere, M. & Bruha, R. & Bugianesi, E. & Burra, P. & Buti, M. & Byrne, C. D. & Calleja, J. L. & Carrieri, P. & Carter, F. & Fernandez, M. I. C. & Castillo-Lopez, G. & Castro-Narro, G. E. & Chan, H. L. Y. & Chan, W.-K. & Chang, Y. & Colombo, M. & Coppell, K. J. & Corey, K. & Craxi, A. & Cryer, D. & Dassanayake, A. & Martins, A. d. A. S. & de Ledinghen, V. & DelPrato, S. & Demaio, A. & Desalegn, H. & Dillon, J. & Duseja, A. & Dorairaj, P. & Ekstedt, M. & El Kassas, M. & Elsanousi, O. M. & Esmat, G. & Fan, J.-G. & Farpour-Lambert, N. & Flisiak, R. & Fouad, Y. & Fuchs, M. & Gani, R. A. & Gerber, L. & Ghazinyan, H. & Gheorghe, L. & Goh, G. B.-B. & Grønbæk, H. & Gulnara, A. & Hamid, S. & Hebditch, V. & Hickman, I. J. & Hocking, S. L. & Hunyady, B. & Idilman, R. & Isakov, V. A. & Jamal, M. H. & Jepsen, P. & Iskandar, N. J. & Song, M. J. & Sudhamshu, K. C. & Kakizaki, S. & Kalamitsis, G. & Kanwal, F. & Kao, J.-H. & Kaplan, L. & Kawaguchi, T. & Khader, Y. & Kim, S. U. & Kodjoh, N. & Koek, G. & Koike, K. & Komas, N. P. & Korenjak, M. & Kugelmas, M. & Labidi, A. & Lange, N. F. & Lavine, J. E. & Lazo, M. & Lee, N. & Lesmana, C. R. A. & Liu, C.-J. & Long, M. T. & Lopez-Jaramillo, P. & Malekzadeh, R. & Mahtab, M. A. & Marchesini, G. & Marinho, R. & Vázquez, S. E. M. & Mateva, L. & Nlombi, C. M. & Melin, P. & Mikolasevic, I. & Milovanovic, T. & Musso, C. & Nakajima, A. & Nava, E. & Nersesov, A. V. & Nikolova, D. & Norris, S. & Novak, K. & Oben, J. & Ong, J. P. & Onyekwere, C. & Papatheodoridis, G. & Paruk, I. & Patel, K. & Macedo, M. P. & Penha-Gonçalves, C. & Figueroa, M. P. & Hofmann, W. P. & Petta, S. & de Oliveira, C. P. M. S. & Puri, P. & Pan, C. Q. & Rac, M. & Ralston, J. & Ramji, A. & Razavi, H. & Alvares-da-Silva, M. R. & Roberts, S. & Roden, M. & Rose, T. & Rouabhia, S. & Rovere-Querini, P. & Rowe, I. A. & Sadirova, S. & Salupere, R. & Saparbu, T. & Sayegh, R. & Sebastiani, G. & Seki, Y. & Selmo, J. & Serme, A. K. & Shaw, J. E. & Shenoy, T. & Sheron, N. & Shibolet, O. & Silva, M. & Skrypnyk, I. & Socha, P. & Soriano, J. & Spearman, C. W. & Sridharan, K. & Suárez, J. J. & Sheriff, D.

S. & Sung, K.-C. & Swain, M. & Tacke, F. & Taheri, S. & Tan, S.-S. & Tapper, E. B. & Yki-Järvinen, H. & Thiele, M. & Shawa, I. T. & Tolmane, I. & Torres, E. A. & Trauner, M. & Treeprasertsuk, S. & Turcanu, A. & Valantinas, J. & Vesterhus, M. & Waked, I. & Wild, S. H. & Willemse, J. & Wong, R. J. & Xanthakos, S. & Young, D. Y. & Yu, M.-L. & Zheng, K. I. & Zeybel, M. & Zheng, M.-H. (2022) Advancing the global public health agenda for NAFLD: a consensus statement. *Nature Reviews Gastroenterology & Hepatology.* 19 (1), 60-78. doi: 10.1038/s41575-021-00523-4.

Lebovitz, H. E. (2019) Thiazolidinediones: the Forgotten Diabetes Medications. *Current Diabetes Reports.* 19 (12), 151. doi: 10.1007/s11892-019-1270-y.

Lee, M. A., Tan, L., Yang, H., Im, Y.-G. & Im, Y. J. (2017) Structures of PPARγ complexed with lobeglitazone and pioglitazone reveal key determinants for the recognition of antidiabetic drugs. *Scientific Reports.* 7 (1), 16837. doi: 10.1038/s41598-017-17082-x.

Lee, Y.-K. & Lee, J.-A. (2016) Role of the mammalian ATG8/LC3 family in autophagy: differential and compensatory roles in the spatiotemporal regulation of autophagy. *BMB Reports.* 49 (8), 424-430. doi: 10.5483/BMBRep.2016.49.8.081.

Lefterova, M. I., Haakonsson, A. K., Lazar, M. A. & Mandrup, S. (2014) PPARγ and the global map of adipogenesis and beyond. *Trends in Endocrinology & Metabolism.* 25 (6), 293-302. doi: 10.1016/j.tem.2014.04.001.

Legrand, N., Bretscher, C. L., Zielke, S., Wilke, B., Daude, M., Fritz, B., Diederich, W. E. & Adhikary, T. (2019) PPARβ/δ recruits NCOR and regulates transcription reinitiation of ANGPTL4. *Nucleic Acids Research.* 47 (18), 9573-9591. doi: 10.1093/nar/gkz685.

Lehmann, J. M., Moore, L. B., Smith-Oliver, T. A., Wilkison, W. O., Willson, T. M. & Kliewer, S. A. (1995) An Antidiabetic Thiazolidinedione Is a High Affinity Ligand for Peroxisome Proliferator-activated Receptor γ (PPARγ). *Journal of Biological Chemistry.* 270 (22), 12953-12956. doi: 10.1074/jbc.270.22.12953.

Lehrke, M. & Lazar, M. A. (2005) The Many Faces of PPARγ. *Cell.* 123 (6), 993-999. doi: 10.1016/j.cell.2005.11.026.

Liu, T., Zhang, L., Joo, D. & Sun, S.-C. (2017) NF-κB signaling in inflammation. *Signal Transduction and Targeted Therapy.* 2 (1), 17023. doi: 10.1038/sigtrans.2017.23.

Lundell, K., Thulin, P., Hamsten, A. & Ehrenborg, E. (2007) Alternative splicing of human peroxisome proliferator-activated receptor delta (PPARdelta):effects on translation efficiency and trans-activation ability. *BMC Molecular Biology.* 8 (1), 70. doi: 10.1186/1471-2199-8-70.

Ma, X., Wang, D., Zhao, W. & Xu, L. (2018) Deciphering the Roles of PPARγ in Adipocytes via Dynamic Change of Transcription Complex. *Frontiers in Endocrinology.* 9, 473. doi: 10.3389/fendo.2018.00473.

Maciejewska-Skrendo, A., Massidda, M., Tocco, F. & Leźnicka, K. (2022) The Influence of the Differentiation of Genes Encoding Peroxisome Proliferator-Activated Receptors and Their Coactivators on Nutrient and Energy Metabolism. *Nutrients.* 14 (24), 5378. doi: 10.3390/nu14245378.

Maciejewska-Skrendo, A., Pawlik, A., Sawczuk, M., Rać, M., Kusak, A., Safranow, K. & Dziedziejko, V. (2019) PPARA, PPARD and PPARG gene polymorphisms in patients with unstable angina. *Gene.* 711, 143947. doi: 10.1016/j.gene.2019.143947.

Maculewicz, E., Mastalerz, A., Maciejewska-Skrendo, A., Cięszczyk, P., Cywińska, A., Borecka, A., Garbacz, A., Szarska, E., Dziuda, Ł., Lorenz, K., Łakomy, R., Lepionka, T., Anyżewska, A., Białek, A. & Bertrandt, J. (2021) Association between peroxisome proliferator-activated receptor-alpha, -delta and -gamma gene (PPARA, PPARD, PPARG) polymorphisms and overweight parameters in physically active men. *Biology of Sport.* 38 (4), 767-776. doi: 10.5114/biolsport.2022.109957.

Majithia, A. R., Tsuda, B., Agostini, M., Gnanapradeepan, K., Rice, R., Peloso, G., Patel, K. A., Zhang, X., Broekema, M. F., Patterson, N., Duby, M., Sharpe, T., Kalkhoven, E., Rosen, E. D., Barroso, I., Ellard, S., Kathiresan, S., O'Rahilly, S., Chatterjee, K., Florez, J. C., Mikkelsen, T., Savage, D. B. & Altshuler, D. (2016) Prospective functional classification of all possible missense variants in PPARG. *Nature Genetics.* 48 (12), 1570-1575. doi: 10.1038/ng.3700.

Mangelsdorf, D. J. & Evans, R. M. (1995) The RXR heterodimers and orphan receptors. *Cell.* 83 (6), 841-850. doi: 10.1016/0092-8674(95)90200-7.

Mangelsdorf, D. J., Thummel, C., Beato, M., Herrlich, P., Schütz, G., Umesono, K., Blumberg, B., Kastner, P., Mark, M., Chambon, P. & Evans, R. M. (1995) The nuclear receptor superfamily: the second decade. *Cell.* 83 (6), 835-839. doi: 10.1016/0092-8674(95)90199-x.

Mendola, N. D., Chen, T.-C., Gu, Q., Eberhardt, M. S. & Saydah, S. (2018) Prevalence of Total, Diagnosed, and Undiagnosed Diabetes Among Adults: United States, 2013-2016. *NCHS data brief.* (319), 1-8.

Mendrick, D. L., Diehl, A. M., Topor, L. S., Dietert, R. R., Will, Y., La Merrill, M. A., Bouret, S., Varma, V., Hastings, K. L., Schug, T. T., Emeigh Hart, S. G. & Burleson, F. G. (2018) Metabolic Syndrome and Associated Diseases: From the Bench to the Clinic. *Toxicological Sciences.* 162 (1), 36-42. doi: 10.1093/toxsci/kfx233.

Michalik, L., Auwerx, J., Berger, J. P., Chatterjee, V. K., Glass, C. K., Gonzalez, F. J., Grimaldi, P. A., Kadowaki, T., Lazar, M. A., O'Rahilly, S., Palmer, C. N. A., Plutzky, J., Reddy, J. K., Spiegelman, B. M., Staels, B. & Wahli, W. (2006) International Union of Pharmacology. LXI. Peroxisome Proliferator-Activated Receptors. *Pharmacological Reviews.* 58 (4), 726-741. doi: 10.1124/pr.58.4.5.

Milek, M., Moulla, Y., Kern, M., Stroh, C., Dietrich, A., Schön, M. R., Gärtner, D., Lohmann, T., Dressler, M., Kovacs, P., Stumvoll, M., Blüher, M. & Guiu-Jurado, E. (2022) Adipsin Serum Concentrations and Adipose Tissue Expression in People with Obesity and Type 2 Diabetes. *International Journal of Molecular Sciences.* 23 (4), 2222. doi: 10.3390/ijms23042222.

Mogilenko, D. A., Kudriavtsev, I. V., Shavva, V. S., Dizhe, E. B., Vilenskaya, E. G., Efremov, A. M., Perevozchikov, A. P. & Orlov, S. V. (2013) Peroxisome Proliferator-activated Receptor α Positively Regulates Complement C3 Expression but Inhibits Tumor Necrosis Factor α-mediated Activation of C3 Gene in Mammalian Hepatic-derived Cells. *Journal of Biological Chemistry.* 288 (3), 1726-1738. doi: 10.1074/jbc.M112.437525.

Moore, J. X., Chaudhary, N. & Akinyemiju, T. (2017) Metabolic Syndrome Prevalence by Race/Ethnicity and Sex in the United States, National Health and Nutrition Examination Survey, 1988–2012. *Preventing Chronic Disease.* 14, 160287. doi: 10.5888/pcd14.160287.

Mosure, S. A., Munoz-Tello, P., Kuo, K.-T., MacTavish, B., Yu, X., Scholl, D., Williams, C. C., Strutzenberg, T. S., Bass, J., Brust, R., Deniz, A. A., Griffin, P. R. & Kojetin, D. J. (2022) *Structural basis of interdomain communication in PPARγ*. Biochemistry. [Accessed 2023-06-17 13:58:56]

Murray, C. J. L. & Abbafati, C. & Abbas, K. M. & Abbasi, M. & Abbasi-Kangevari, M. & Abd-Allah, F. & Abdollahi, M. & Abedi, P. & Abedi, A. & Abolhassani, H. & Aboyans, V. & Abreu, L. G. & Abrigo, M. R. M. & Abu-Gharbieh, E. & Abu Haimed, A. K. & Abushouk, A. I. & Acebedo, A. & Ackerman, I. N. & Adabi, M. & Adamu, A. A. & Adebayo, O. M. & Adelson, J. D. & Adetokunboh, O. O. & Afarideh, M. & Afshin, A. & Agarwal, G. & Agrawal, A. & Ahmad, T. & Ahmadi, K. & Ahmadi, M. & Ahmed, M. B. & Aji, B. & Akinyemiju, T. & Akombi, B. & Alahdab, F. & Alam, K. & Alanezi, F. M. & Alanzi, T. M. & Albertson, S. B. & Alemu, B. W. & Alemu, Y. M. & Alhabib, K. F. & Ali, M. & Ali, S. & Alicandro, G. & Alipour, V. & Alizade, H. & Aljunid, S. M. & Alla, F. & Allebeck, P. & Almadi, M. A. H. & Almasi-Hashiani, A. & Al-Mekhlafi, H. M. & Almulhim, A. M. & Alonso, J. & Al-Raddadi, R. M. & Altirkawi, K. A. & Alvis-Guzman, N. & Amare, B. & Amare, A. T. & Amini, S. & Amit, A. M. L. & Amugsi, D. A. & Anbesu, E. W. & Ancuceanu, R. & Anderlini, D. & Anderson, J. A. & Andrei, T. & Andrei, C. L. & Anjomshoa, M. & Ansari, F. & Ansari-Moghaddam, A. & Antonio, C. A. T. & Antony, C. M. & Anvari, D. & Appiah, S. C. Y. & Arabloo, J. & Arab-Zozani, M. & Aravkin, A. Y. & Arba, A. A. K. & Aripov, T. & Ärnlöv, J. & Arowosegbe, O. O. & Asaad, M. & Asadi-Aliabadi, M. & Asadi-Pooya, A. A. & Ashbaugh, C. & Assmus, M. & Atout, M. M. d. W. & Ausloos, M. & Ausloos, F. & Ayala Quintanilla, B. P. & Ayano,

G. & Ayanore, M. A. & Azari, S. & Azene, Z. N. & B, D. B. & Babaee, E. & Badawi, A. & Badiye, A. D. & Bagherzadeh, M. & Bairwa, M. & Bakhtiari, A. & Bakkannavar, S. M. & Balachandran, A. & Banach, M. & Banerjee, S. K. & Banik, P. C. & Baraki, A. G. & Barker-Collo, S. L. & Basaleem, H. & Basu, S. & Baune, B. T. & Bayati, M. & Baye, B. A. & Bedi, N. & Beghi, E. & Bell, M. L. & Bensenor, I. M. & Berhe, K. & Berman, A. E. & Bhagavathula, A. S. & Bhala, N. & Bhardwaj, P. & Bhattacharyya, K. & Bhattarai, S. & Bhutta, Z. A. & Bijani, A. & Bikbov, B. & Biondi, A. & Bisignano, C. & Biswas, R. K. & Bjørge, T. & Bohlouli, S. & Bohluli, M. & Bolla, S. R. R. & Boloor, A. & Bose, D. & Boufous, S. & Brady, O. J. & Braithwaite, D. & Brauer, M. & Breitborde, N. J. K. & Brenner, H. & Breusov, A. V. & Briant, P. S. & Briggs, A. M. & Britton, G. B. & Brugha, T. & Burugina Nagaraja, S. & Busse, R. & Butt, Z. A. & Caetano Dos Santos, F. L. & Cámera, L. L. A. & Campos-Nonato, I. R. & Campuzano Rincon, J. C. & Car, J. & Cárdenas, R. & Carreras, G. & Carrero, J. J. & Carvalho, F. & Castaldelli-Maia, J. M. & Castelpietra, G. & Castro, F. & Catalá-López, F. & Causey, K. & Cederroth, C. R. & Cercy, K. M. & Cerin, E. & Chandan, J. S. & Chang, J.-C. & Charan, J. & Charlson, F. J. & Chattu, V. K. & Chaturvedi, S. & Cherbuin, N. & Chin, K. L. & Chirinos-Caceres, J. L. & Cho, D. Y. & Choi, J.-Y. J. & Chu, D.-T. & Chung, S.-C. & Chung, M. T. & Cicuttini, F. M. & Cirillo, M. & Cislaghi, B. & Cohen, A. J. & Compton, K. & Corso, B. & Cortesi, P. A. & Costa, V. M. & Cousin, E. & Cowden, R. G. & Cross, M. & Crowe, C. S. & Cummins, S. & Dai, H. & Dai, H. & Damiani, G. & Dandona, L. & Dandona, R. & Daneshpajouhnejad, P. & Darwesh, A. M. & Das, J. K. & Das Gupta, R. & Das Neves, J. & Davey, G. & Dávila-Cervantes, C. A. & Davis, A. C. & De Leo, D. & Denova-Gutiérrez, E. & Deribe, K. & Dervenis, N. & Desai, R. & Deuba, K. & Dhungana, G. P. & Dianatinasab, M. & Diaz, D. & Dichgans, M. & Didarloo, A. & Dippenaar, I. N. & Dokova, K. & Dolecek, C. & Dorostkar, F. & Doshi, P. P. & Doshi, C. P. & Doshmangir, L. & Doxey, M. C. & Driscoll, T. R. & Duncan, B. B. & Eagan, A. W. & Ebrahimi, H. & Ebrahimi Kalan, M. & Edvardsson, D. & Ehrlich, J. R. & Elbarazi, I. & Elgendy, I. Y. & El-Jaafary, S. I. & El Sayed Zaki, M. & Elsharkawy, A. & El Tantawi, M. & Elyazar, I. R. & Emamian, M. H. & Eshrati, B. & Eskandarieh, S. & Esteghamati, A. & Esteghamati, S. & Fanzo, J. & Faro, A. & Farzadfar, F. & Fattahi, N. & Feigin, V. L. & Fereshtehnejad, S.-M. & Fernandes, E. & Ferrara, P. & Ferrari, A. J. & Filip, I. & Fischer, F. & Fisher, J. L. & Fitzgerald, R. & Foigt, N. A. & Folayan, M. O. & Fomenkov, A. A. & Foroutan, M. & Franklin, R. C. & Freitas, M. & Fukumoto, T. & Furtado, J. M. & Gad, M. M. & Gaidhane, A. M. & Gakidou, E. & Gallus, S. & Gardner, W. M. & Geberemariyam, B. S. & Gebremedhin, K. B. & Gebremeskel, L. G. & Gebresillassie, B. M. & Geramo, Y. C. D. & Gesesew, H. A. & Gething, P. W. & Gezae, K. E. & Ghadiri, K. & Ghaffarifar, F. & Ghafourifard, M. & Ghamari, F. & Ghashghaee, A. & Gholamian, A. & Giampaoli, S. & Gill, P. S. & Gillum, R. F. & Ginawi, I. A. & Giussani, G. & Gnedovskaya, E. V. & Godinho, M. A. & Golechha, M. & Gona, P. N. & Gopalani, S. V. & Gorini, G. & Goulart, B. N. G. & Goulart, A. C. & Grada, A. & Greaves, F. & Gudi, N. & Guimarães, R. A. & Guo, Y. & Gupta, S. S. & Gupta, R. & Gupta, R. & Haagsma, J. A. & Hachinski, V. & Hafezi-Nejad, N. & Haile, L. M. & Haj-Mirzaian, A. & Hall, B. J. & Hamadeh, R. R. & Hamidi, S. & Han, C. & Hankey, G. J. & Haro, J. M. & Hasaballah, A. I. & Hashi, A. & Hassan, A. &

Hassanipour, S. & Hassankhani, H. & Havmoeller, R. J. & Hay, S. I. & Hayat, K. & Henok, A. & Henry, N. J. & Herteliu, C. & Heydarpour, F. & Ho, H. C. & Hole, M. K. & Holla, R. & Hoogar, P. & Hopf, K. P. & Hosgood, H. D. & Hossain, N. & Hosseinzadeh, M. & Hostiuc, M. & Hostiuc, S. & Househ, M. & Hoy, D. G. & Hu, G. & Huda, T. M. & Hugo, F. N. & Humayun, A. & Hussain, R. & Hwang, B.-F. & Iavicoli, I. & Ibeneme, C. U. & Ibitoye, S. E. & Ikuta, K. S. & Ilesanmi, O. S. & Ilic, I. M. & Ilic, M. D. & Inbaraj, L. R. & Iqbal, U. & Irvani, S. S. N. & Islam, M. M. & Islam, S. M. S. & Iso, H. & Iwu, C. C. D. & Jaafari, J. & Jahagirdar, D. & Jahani, M. A. & Jakovljevic, M. & Jalali, A. & Jalilian, F. & Janodia, M. D. & Javaheri, T. & Jenabi, E. & Jha, R. P. & Jha, V. & Ji, J. S. & Johnson, C. O. & Jonas, J. B. & Jürisson, M. & Kabir, A. & Kabir, Z. & Kalani, R. & Kalankesh, L. R. & Kalhor, R. & Kanchan, T. & Kapoor, N. & Karami Matin, B. & Karch, A. & Karim, M. A. & Karimi, S. E. & Kasa, A. S. & Kassebaum, N. J. & Kayode, G. A. & Kazemi Karyani, A. & Keiyoro, P. & Khalid, N. & Khammarnia, M. & Khan, M. & Khan, E. A. & Khan, G. & Khatab, K. & Khater, M. M. & Khatib, M. N. & Khazaie, H. & Khoja, A. T. & Khubchandani, J. & Kianipour, N. & Kieling, C. & Kim, Y.-E. & Kim, Y. J. & Kimokoti, R. W. & Kinfu, Y. & Kisa, S. & Kisa, A. & Kissoon, N. & Kivimäki, M. & Kneib, C. J. & Knight, M. & Koh, D. S. Q. & Komaki, H. & Kopec, J. A. & Kosen, S. & Kotlo, A. & Koul, P. A. & Koyanagi, A. & Krishan, K. & Krohn, K. J. & Ks, S. & Kumar, G. A. & Kumar, N. & Kumar, M. & Kurmi, O. P. & Kusuma, D. & Kyu, H. H. & Lacey, B. & Lal, D. K. & Lalloo, R. & Lallukka, T. & Lan, Q. & Landires, I. & Larson, H. J. & Lasrado, S. & Lau, K. M.-M. & Lauriola, P. & La Vecchia, C. & Leal, L. F. & Leasher, J. L. & Ledesma, J. R. & Lee, P. H. & Lee, S. W. H. & Leonardi, M. & Leung, J. & Li, B. & Li, S. & Lim, L.-L. & Lin, R.-T. & Listl, S. & Liu, X. & Liu, Y. & Logroscino, G. & Lopez, J. C. F. & Lorkowski, S. & Lozano, R. & Lu, A. & Lugo, A. & Lunevicius, R. & Lyons, R. A. & Ma, J. & Machado, D. B. & Maddison, E. R. & Mahasha, P. W. & Mahmoudi, M. & Majeed, A. & Maled, V. & Maleki, S. & Maleki, A. & Malekzadeh, R. & Malta, D. C. & Mamun, A. A. & Manguerra, H. & Mansouri, B. & Mansournia, M. A. & Mantilla Herrera, A. M. & Martini, S. & Martins-Melo, F. R. & Martopullo, I. & Masoumi, S. Z. & Massenburg, B. B. & Mathur, M. R. & Maulik, P. K. & Mazidi, M. & McAlinden, C. & McGrath, J. J. & McKee, M. & Mehndiratta, M. M. & Mehri, F. & Mehta, K. M. & Melese, A. & Memish, Z. A. & Mendoza, W. & Menezes, R. G. & Mengesha, E. W. & Meretoja, T. J. & Meretoja, A. & Mestrovic, T. & Miazgowski, B. & Michalek, I. M. & Milne, G. J. & Miri, M. & Mirica, A. & Mirrakhimov, E. M. & Mirzaei, H. & Mirzaei, M. & Mirzaei-Alavijeh, M. & Misganaw, A. T. & Moazen, B. & Moghadaszadeh, M. & Mohajer, B. & Mohamad, O. & Mohammad, Y. & Mohammad, D. K. & Mohammad Gholi Mezerji, N. & Mohammadian-Hafshejani, A. & Mohammed, S. & Mohebi, F. & Mokdad, A. H. & Molokhia, M. & Monasta, L. & Mooney, M. D. & Moradi, M. & Moradi, G. & Moradi-Lakeh, M. & Moradzadeh, R. & Moraga, P. & Morawska, L. & Morgado-da-Costa, J. & Morrison, S. D. & Mosapour, A. & Mosser, J. F. & Mousavi, S. M. & Mousavi Khaneghah, A. & Mueller, U. O. & Mullany, E. C. & Musa, K. I. & Naderi, M. & Nagarajan, A. J. & Naghavi, M. & Naghshtabrizi, B. & Naimzada, M. D. & Najafi, F. & Naldi, L. & Nayak, V. C. & Nazari, J. & Ndejjo, R. & Negoi, I. & Negoi, R. I. & Netsere, H. B. N. & Nguefack-Tsague, G. & Ngunjiri, J. W. & Nguyen, D. N. &

Nguyen, H. L. T. & Nichols, E. & Nigatu, Y. T. & Nikbakhsh, R. & Nixon, M. R. & Nnaji, C. A. & Nomura, S. & Noubiap, J. J. & Nowak, C. & Nsoesie, E. O. & Nunez-Samudio, V. & Ogbo, F. A. & Oghenetega, O. B. & Okunga, E. W. & Oladnabi, M. & Olagunju, A. T. & Olusanya, J. O. & Olusanya, B. O. & Omar Bali, A. & Omer, M. O. & Ong, S. & Ong, K. L. & Onwujekwe, O. E. & Oren, E. & Ortiz, A. & Ostroff, S. M. & Oţoiu, A. & Otstavnov, N. & Otstavnov, S. S. & Øverland, S. & Owolabi, M. O. & P A, M. & Padubidri, J. R. & Pakhale, S. & Pakshir, K. & Palladino, R. & Pana, A. & Panda-Jonas, S. & Parmar, P. G. K. & Pathak, M. & Patton, G. C. & Pazoki Toroudi, H. & Peden, A. E. & Pepito, V. C. F. & Peprah, E. K. & Pereira, D. M. & Pereira, A. & Pereira, J. & Perico, N. & Pescarini, J. M. & Pham, H. Q. & Phillips, M. R. & Piccinelli, C. & Pilz, T. M. & Pinheiro, M. & Piradov, M. A. & Pirsaheb, M. & Pishgar, F. & Pond, C. D. & Postma, M. J. & Pottoo, F. H. & Pourjafar, H. & Pourmalek, F. & Prada, S. I. & Prasad, N. & Pribadi, D. R. A. & Pupillo, E. & Quazi Syed, Z. & Rabiee, N. & Rabiee, M. & Radfar, A. & Rafiee, A. & Raggi, A. & Rahman, M. H. U. & Rahman, M. A. & Ramezanzadeh, K. & Ranabhat, C. L. & Ranta, A. & Rao, S. J. & Rao, P. C. & Rasella, D. & Rashedi, V. & Rastogi, P. & Rawaf, S. & Rawaf, D. L. & Rawal, L. & Rawassizadeh, R. & Rawat, R. & Razo, C. & Regassa, L. D. & Reitsma, M. B. & Remuzzi, G. & Renjith, V. & Renzaho, A. M. N. & Resnikoff, S. & Rezaei, N. & Rezaei, N. & Rezai, M. S. & Rezapour, A. & Rhinehart, P.-A. & Riahi, S. M. & Ribeiro, A. L. P. & Ribeiro, D. C. & Rickard, J. & Roever, L. & Romoli, M. & Ronfani, L. & Roshandel, G. & Rubagotti, E. & Rumisha, S. F. & Rwegerera, G. M. & Saadatagah, S. & Sabour, S. & Sachdev, P. S. & Saddik, B. & Sadeghi, M. & Sadeghi, E. & Saeedi Moghaddam, S. & Sahebkar, A. & Sahraian, M. A. & Sajadi, S. M. & Salem, M. R. R. & Salem, H. & Salimzadeh, H. & Salomon, J. A. & Salz, I. & Samad, Z. & Samadi Kafil, H. & Samy, A. M. & Sanabria, J. & Santomauro, D. F. & Santric-Milicevic, M. M. & Saraswathy, S. Y. I. & Sarrafzadegan, N. & Sartorius, B. & Sarveazad, A. & Sathian, B. & Sathish, T. & Sattin, D. & Schaeffer, L. E. & Schiavolin, S. & Schmidt, M. I. & Schutte, A. E. & Schwebel, D. C. & Schwendicke, F. & Sepanlou, S. G. & Sha, F. & Shafaat, O. & Shahabi, S. & Shaheen, A. A. & Shaikh, M. A. & Shams-Beyranvand, M. & Shamsizadeh, M. & Sharafi, K. & Sharara, F. & Sheikh, A. & Shetty, B. S. K. & Shibuya, K. & Shigematsu, M. & Shin, M.-J. & Shin, J. I. & Shiri, R. & Shivakumar, K. M. & Shrime, M. G. & Shuval, K. & Sigfusdottir, I. D. & Sigurvinsdottir, R. & Silva, D. A. S. & Silva, J. P. & Simonetti, B. & Singh, J. A. & Singh, P. & Singh, A. & Sinha, D. N. & Skryabin, V. Y. & Sliwa, K. & Smith, E. U. R. & Soheili, A. & Soltani, S. & Somefun, O. D. & Sorensen, R. J. D. & Soriano, J. B. & Sorrie, M. B. & Soyiri, I. N. & Sreeramareddy, C. T. & Sripada, K. & Stanaway, J. D. & Ştefan, S. C. & Stein, D. J. & Steiner, C. & Stokes, M. A. & Stranges, S. & Suchdev, P. S. & Sudaryanto, A. & Sufiyan, M. a. B. & Suliankatchi Abdulkader, R. & Sulo, G. & Swope, C. B. & Sylte, D. O. & Tabarés-Seisdedos, R. & Tabuchi, T. & Tadakamadla, S. K. & Taddele, B. W. & Taherkhani, A. & Tahir, Z. & Tamiru, A. T. & Tang, M. & Tareque, M. I. & Tefera, Y. G. G. & Tela, F. G. G. & Temsah, M.-H. & Terrason, S. & Thakur, B. & Thankappan, K. R. & Thapar, R. & Thomas, N. & Titova, M. V. & Tlou, B. & Tonelli, M. & Topor-Madry, R. & Torre, A. E. & Touvier, M. & Tovani-Palone, M. R. R. & Tran, B. X. & Travillian, R. & Uddin, R. & Ullah, I. & Unnikrishnan, B. & Upadhyay, E. & Vacante, M. &

Vaicekonyte, R. & Valdez, P. R. & Valli, A. & Vasankari, T. J. & Vasseghian, Y. & Venketasubramanian, N. & Vidale, S. & Violante, F. S. & Vlassov, V. & Vollset, S. E. & Vongpradith, A. & Vu, G. T. & W/hawariat, F. G. & Waheed, Y. & Wamai, R. G. & Wang, F. & Wang, H. & Wang, J. & Wang, Y. & Wang, Y.-P. & Watson, A. & Wei, J. & Weintraub, R. G. & Weiss, J. & Welay, F. T. & Werdecker, A. & Westerman, R. & Whiteford, H. A. & Wiangkham, T. & Wickramasinghe, N. D. & Wilner, L. B. & Wojtyniak, B. & Wolfe, C. D. A. & Wondmeneh, T. G. & Wu, A.-M. & Wu, C. & Wulf Hanson, S. & Wunrow, H. Y. & Xie, Y. & Yahyazadeh Jabbari, S. H. & Yamagishi, K. & Yaya, S. & Yazdi-Feyzabadi, V. & Yearwood, J. A. & Yeheyis, T. Y. & Yeshitila, Y. G. & Yip, P. & Yonemoto, N. & Yoon, S.-J. & Younis, M. Z. & Younker, T. P. & Yousefinezhadi, T. & Yu, C. & Yu, Y. & Yuce, D. & Yusefzadeh, H. & Zaidi, S. S. & Zaman, S. B. & Zamanian, M. & Zangeneh, A. & Zarafshan, H. & Zastrozhin, M. S. & Zewdie, K. A. & Zhang, Z.-J. & Zhang, J. & Zhang, Y. & Zhao, X.-J. G. & Zhao, Y. & Zheleva, B. & Zheng, P. & Zhu, C. & Ziapour, A. & Zimsen, S. R. M. & Lopez, A. D. & Vos, T. & Lim, S. S. (2020) Five insights from the Global Burden of Disease Study 2019. *The Lancet.* 396 (10258), 1135-1159. doi: 10.1016/S0140-6736(20)31404-5.

Murray, C. J. L. & Aravkin, A. Y. & Zheng, P. & Abbafati, C. & Abbas, K. M. & Abbasi-Kangevari, M. & Abd-Allah, F. & Abdelalim, A. & Abdollahi, M. & Abdollahpour, I. & Abegaz, K. H. & Abolhassani, H. & Aboyans, V. & Abreu, L. G. & Abrigo, M. R. M. & Abualhasan, A. & Abu-Raddad, L. J. & Abushouk, A. I. & Adabi, M. & Adekanmbi, V. & Adeoye, A. M. & Adetokunboh, O. O. & Adham, D. & Advani, S. M. & Agarwal, G. & Aghamir, S. M. K. & Agrawal, A. & Ahmad, T. & Ahmadi, K. & Ahmadi, M. & Ahmadieh, H. & Ahmed, M. B. & Akalu, T. Y. & Akinyemi, R. O. & Akinyemiju, T. & Akombi, B. & Akunna, C. J. & Alahdab, F. & Al-Aly, Z. & Alam, K. & Alam, S. & Alam, T. & Alanezi, F. M. & Alanzi, T. M. & Alemu, B. w. & Alhabib, K. F. & Ali, M. & Ali, S. & Alicandro, G. & Alinia, C. & Alipour, V. & Alizade, H. & Aljunid, S. M. & Alla, F. & Allebeck, P. & Almasi-Hashiani, A. & Al-Mekhlafi, H. M. & Alonso, J. & Altirkawi, K. A. & Amini-Rarani, M. & Amiri, F. & Amugsi, D. A. & Ancuceanu, R. & Anderlini, D. & Anderson, J. A. & Andrei, C. L. & Andrei, T. & Angus, C. & Anjomshoa, M. & Ansari, F. & Ansari-Moghaddam, A. & Antonazzo, I. C. & Antonio, C. A. T. & Antony, C. M. & Antriyandarti, E. & Anvari, D. & Anwer, R. & Appiah, S. C. Y. & Arabloo, J. & Arab-Zozani, M. & Ariani, F. & Armoon, B. & Ärnlöv, J. & Arzani, A. & Asadi-Aliabadi, M. & Asadi-Pooya, A. A. & Ashbaugh, C. & Assmus, M. & Atafar, Z. & Atnafu, D. D. & Atout, M. M. d. W. & Ausloos, F. & Ausloos, M. & Ayala Quintanilla, B. P. & Ayano, G. & Ayanore, M. A. & Azari, S. & Azarian, G. & Azene, Z. N. & Badawi, A. & Badiye, A. D. & Bahrami, M. A. & Bakhshaei, M. H. & Bakhtiari, A. & Bakkannavar, S. M. & Baldasseroni, A. & Ball, K. & Ballew, S. H. & Balzi, D. & Banach, M. & Banerjee, S. K. & Bante, A. B. & Baraki, A. G. & Barker-Collo, S. L. & Bärnighausen, T. W. & Barrero, L. H. & Barthelemy, C. M. & Barua, L. & Basu, S. & Baune, B. T. & Bayati, M. & Becker, J. S. & Bedi, N. & Beghi, E. & Béjot, Y. & Bell, M. L. & Bennitt, F. B. & Bensenor, I. M. & Berhe, K. & Berman, A. E. & Bhagavathula, A. S. & Bhageerathy, R. & Bhala, N. & Bhandari, D. & Bhattacharyya, K. & Bhutta, Z. A. & Bijani, A. & Bikbov, B. & Bin Sayeed, M. S. & Biondi, A. & Birihane,

B. M. & Bisignano, C. & Biswas, R. K. & Bitew, H. & Bohlouli, S. & Bohluli, M. & Boon-Dooley, A. S. & Borges, G. & Borzì, A. M. & Borzouei, S. & Bosetti, C. & Boufous, S. & Braithwaite, D. & Breitborde, N. J. K. & Breitner, S. & Brenner, H. & Briant, P. S. & Briko, A. N. & Briko, N. I. & Britton, G. B. & Bryazka, D. & Bumgarner, B. R. & Burkart, K. & Burnett, R. T. & Burugina Nagaraja, S. & Butt, Z. A. & Caetano dos Santos, F. L. & Cahill, L. E. & Cámera, L. L. A. & Campos-Nonato, I. R. & Cárdenas, R. & Carreras, G. & Carrero, J. J. & Carvalho, F. & Castaldelli-Maia, J. M. & Castañeda-Orjuela, C. A. & Castelpietra, G. & Castro, F. & Causey, K. & Cederroth, C. R. & Cercy, K. M. & Cerin, E. & Chandan, J. S. & Chang, K.-L. & Charlson, F. J. & Chattu, V. K. & Chaturvedi, S. & Cherbuin, N. & Chimed-Ochir, O. & Cho, D. Y. & Choi, J.-Y. J. & Christensen, H. & Chu, D.-T. & Chung, M. T. & Chung, S.-C. & Cicuttini, F. M. & Ciobanu, L. G. & Cirillo, M. & Classen, T. K. D. & Cohen, A. J. & Compton, K. & Cooper, O. R. & Costa, V. M. & Cousin, E. & Cowden, R. G. & Cross, D. H. & Cruz, J. A. & Dahlawi, S. M. A. & Damasceno, A. A. M. & Damiani, G. & Dandona, L. & Dandona, R. & Dangel, W. J. & Danielsson, A.-K. & Dargan, P. I. & Darwesh, A. M. & Daryani, A. & Das, J. K. & Das Gupta, R. & das Neves, J. & Dávila-Cervantes, C. A. & Davitoiu, D. V. & De Leo, D. & Degenhardt, L. & DeLang, M. & Dellavalle, R. P. & Demeke, F. M. & Demoz, G. T. & Demsie, D. G. & Denova-Gutiérrez, E. & Dervenis, N. & Dhungana, G. P. & Dianatinasab, M. & Dias da Silva, D. & Diaz, D. & Dibaji Forooshani, Z. S. & Djalalinia, S. & Do, H. T. & Dokova, K. & Dorostkar, F. & Doshmangir, L. & Driscoll, T. R. & Duncan, B. B. & Duraes, A. R. & Eagan, A. W. & Edvardsson, D. & El Nahas, N. & El Sayed, I. & El Tantawi, M. & Elbarazi, I. & Elgendy, I. Y. & El-Jaafary, S. I. & Elyazar, I. R. & Emmons-Bell, S. & Erskine, H. E. & Eskandarieh, S. & Esmaeilnejad, S. & Esteghamati, A. & Estep, K. & Etemadi, A. & Etisso, A. E. & Fanzo, J. & Farahmand, M. & Fareed, M. & Faridnia, R. & Farioli, A. & Faro, A. & Faruque, M. & Farzadfar, F. & Fattahi, N. & Fazlzadeh, M. & Feigin, V. L. & Feldman, R. & Fereshtehnejad, S.-M. & Fernandes, E. & Ferrara, G. & Ferrari, A. J. & Ferreira, M. L. & Filip, I. & Fischer, F. & Fisher, J. L. & Flor, L. S. & Foigt, N. A. & Folayan, M. O. & Fomenkov, A. A. & Force, L. M. & Foroutan, M. & Franklin, R. C. & Freitas, M. & Fu, W. & Fukumoto, T. & Furtado, J. M. & Gad, M. M. & Gakidou, E. & Gallus, S. & Garcia-Basteiro, A. L. & Gardner, W. M. & Geberemariyam, B. S. & Gebreslassie, A. A. A. A. & Geremew, A. & Gershberg Hayoon, A. & Gething, P. W. & Ghadimi, M. & Ghadiri, K. & Ghaffarifar, F. & Ghafourifard, M. & Ghamari, F. & Ghashghaee, A. & Ghiasvand, H. & Ghith, N. & Gholamian, A. & Ghosh, R. & Gill, P. S. & Ginindza, T. G. G. & Giussani, G. & Gnedovskaya, E. V. & Goharinezhad, S. & Gopalani, S. V. & Gorini, G. & Goudarzi, H. & Goulart, A. C. & Greaves, F. & Grivna, M. & Grosso, G. & Gubari, M. I. M. & Gugnani, H. C. & Guimarães, R. A. & Guled, R. A. & Guo, G. & Guo, Y. & Gupta, R. & Gupta, T. & Haddock, B. & Hafezi-Nejad, N. & Hafiz, A. & Haj-Mirzaian, A. & Haj-Mirzaian, A. & Hall, B. J. & Halvaei, I. & Hamadeh, R. R. & Hamidi, S. & Hammer, M. S. & Hankey, G. J. & Haririan, H. & Haro, J. M. & Hasaballah, A. I. & Hasan, M. M. & Hasanpoor, E. & Hashi, A. & Hassanipour, S. & Hassankhani, H. & Havmoeller, R. J. & Hay, S. I. & Hayat, K. & Heidari, G. & Heidari-Soureshjani, R. & Henrikson, H. J. & Herbert, M. E. & Herteliu, C. & Heydarpour, F. & Hird, T. R. & Hoek, H. W. & Holla, R. & Hoogar, P. &

Hosgood, H. D. & Hossain, N. & Hosseini, M. & Hosseinzadeh, M. & Hostiuc, M. & Hostiuc, S. & Househ, M. & Hsairi, M. & Hsieh, V. C.-r. & Hu, G. & Hu, K. & Huda, T. M. & Humayun, A. & Huynh, C. K. & Hwang, B.-F. & Iannucci, V. C. & Ibitoye, S. E. & Ikeda, N. & Ikuta, K. S. & Ilesanmi, O. S. & Ilic, I. M. & Ilic, M. D. & Inbaraj, L. R. & Ippolito, H. & Iqbal, U. & Irvani, S. S. N. & Irvine, C. M. S. & Islam, M. M. & Islam, S. M. S. & Iso, H. & Ivers, R. Q. & Iwu, C. C. D. & Iwu, C. J. & Iyamu, I. O. & Jaafari, J. & Jacobsen, K. H. & Jafari, H. & Jafarinia, M. & Jahani, M. A. & Jakovljevic, M. & Jalilian, F. & James, S. L. & Janjani, H. & Javaheri, T. & Javidnia, J. & Jeemon, P. & Jenabi, E. & Jha, R. P. & Jha, V. & Ji, J. S. & Johansson, L. & John, O. & John-Akinola, Y. O. & Johnson, C. O. & Jonas, J. B. & Joukar, F. & Jozwiak, J. J. & Jürisson, M. & Kabir, A. & Kabir, Z. & Kalani, H. & Kalani, R. & Kalankesh, L. R. & Kalhor, R. & Kanchan, T. & Kapoor, N. & Karami Matin, B. & Karch, A. & Karim, M. A. & Kassa, G. M. & Katikireddi, S. V. & Kayode, G. A. & Kazemi Karyani, A. & Keiyoro, P. N. & Keller, C. & Kemmer, L. & Kendrick, P. J. & Khalid, N. & Khammarnia, M. & Khan, E. A. & Khan, M. & Khatab, K. & Khater, M. M. & Khatib, M. N. & Khayamzadeh, M. & Khazaei, S. & Kieling, C. & Kim, Y. J. & Kimokoti, R. W. & Kisa, A. & Kisa, S. & Kivimäki, M. & Knibbs, L. D. & Knudsen, A. K. S. & Kocarnik, J. M. & Kochhar, S. & Kopec, J. A. & Korshunov, V. A. & Koul, P. A. & Koyanagi, A. & Kraemer, M. U. G. & Krishan, K. & Krohn, K. J. & Kromhout, H. & Kuate Defo, B. & Kumar, G. A. & Kumar, V. & Kurmi, O. P. & Kusuma, D. & La Vecchia, C. & Lacey, B. & Lal, D. K. & Lalloo, R. & Lallukka, T. & Lami, F. H. & Landires, I. & Lang, J. J. & Langan, S. M. & Larsson, A. O. & Lasrado, S. & Lauriola, P. & Lazarus, J. V. & Lee, P. H. & Lee, S. W. H. & LeGrand, K. E. & Leigh, J. & Leonardi, M. & Lescinsky, H. & Leung, J. & Levi, M. & Li, S. & Lim, L.-L. & Linn, S. & Liu, S. & Liu, S. & Liu, Y. & Lo, J. & Lopez, A. D. & Lopez, J. C. F. & Lopukhov, P. D. & Lorkowski, S. & Lotufo, P. A. & Lu, A. & Lugo, A. & Maddison, E. R. & Mahasha, P. W. & Mahdavi, M. M. & Mahmoudi, M. & Majeed, A. & Maleki, A. & Maleki, S. & Malekzadeh, R. & Malta, D. C. & Mamun, A. A. & Manda, A. L. & Manguerra, H. & Mansour-Ghanaei, F. & Mansouri, B. & Mansournia, M. A. & Mantilla Herrera, A. M. & Maravilla, J. C. & Marks, A. & Martin, R. V. & Martini, S. & Martins-Melo, F. R. & Masaka, A. & Masoumi, S. Z. & Mathur, M. R. & Matsushita, K. & Maulik, P. K. & McAlinden, C. & McGrath, J. J. & McKee, M. & Mehndiratta, M. M. & Mehri, F. & Mehta, K. M. & Memish, Z. A. & Mendoza, W. & Menezes, R. G. & Mengesha, E. W. & Mereke, A. & Mereta, S. T. & Meretoja, A. & Meretoja, T. J. & Mestrovic, T. & Miazgowski, B. & Miazgowski, T. & Michalek, I. M. & Miller, T. R. & Mills, E. J. & Mini, G. & Miri, M. & Mirica, A. & Mirrakhimov, E. M. & Mirzaei, H. & Mirzaei, M. & Mirzaei, R. & Mirzaei-Alavijeh, M. & Misganaw, A. T. & Mithra, P. & Moazen, B. & Mohammad, D. K. & Mohammad, Y. & Mohammad Gholi Mezerji, N. & Mohammadian-Hafshejani, A. & Mohammadifard, N. & Mohammadpourhodki, R. & Mohammed, A. S. & Mohammed, H. & Mohammed, J. A. & Mohammed, S. & Mokdad, A. H. & Molokhia, M. & Monasta, L. & Mooney, M. D. & Moradi, G. & Moradi, M. & Moradi-Lakeh, M. & Moradzadeh, R. & Moraga, P. & Morawska, L. & Morgado-da-Costa, J. & Morrison, S. D. & Mosapour, A. & Mosser, J. F. & Mouodi, S. & Mousavi, S. M. & Mousavi Khaneghah, A. & Mueller, U. O. & Mukhopadhyay, S. & Mullany, E. C. & Musa, K. I. &

Muthupandian, S. & Nabhan, A. F. & Naderi, M. & Nagarajan, A. J. & Nagel, G. & Naghavi, M. & Naghshtabrizi, B. & Naimzada, M. D. & Najafi, F. & Nangia, V. & Nansseu, J. R. & Naserbakht, M. & Nayak, V. C. & Negoi, I. & Ngunjiri, J. W. & Nguyen, C. T. & Nguyen, H. L. T. & Nguyen, M. & Nigatu, Y. T. & Nikbakhsh, R. & Nixon, M. R. & Nnaji, C. A. & Nomura, S. & Norrving, B. & Noubiap, J. J. & Nowak, C. & Nunez-Samudio, V. & Oţoiu, A. & Oancea, B. & Odell, C. M. & Ogbo, F. A. & Oh, I.-H. & Okunga, E. W. & Oladnabi, M. & Olagunju, A. T. & Olusanya, B. O. & Olusanya, J. O. & Omer, M. O. & Ong, K. L. & Onwujekwe, O. E. & Orpana, H. M. & Ortiz, A. & Osarenotor, O. & Osei, F. B. & Ostroff, S. M. & Otstavnov, N. & Otstavnov, S. S. & Øverland, S. & Owolabi, M. O. & P A, M. & Padubidri, J. R. & Palladino, R. & Panda-Jonas, S. & Pandey, A. & Parry, C. D. H. & Pasovic, M. & Pasupula, D. K. & Patel, S. K. & Pathak, M. & Patten, S. B. & Patton, G. C. & Pazoki Toroudi, H. & Peden, A. E. & Pennini, A. & Pepito, V. C. F. & Peprah, E. K. & Pereira, D. M. & Pesudovs, K. & Pham, H. Q. & Phillips, M. R. & Piccinelli, C. & Pilz, T. M. & Piradov, M. A. & Pirsaheb, M. & Plass, D. & Polinder, S. & Polkinghorne, K. R. & Pond, C. D. & Postma, M. J. & Pourjafar, H. & Pourmalek, F. & Poznańska, A. & Prada, S. I. & Prakash, V. & Pribadi, D. R. A. & Pupillo, E. & Quazi Syed, Z. & Rabiee, M. & Rabiee, N. & Radfar, A. & Rafiee, A. & Raggi, A. & Rahman, M. A. & Rajabpour-Sanati, A. & Rajati, F. & Rakovac, I. & Ram, P. & Ramezanzadeh, K. & Ranabhat, C. L. & Rao, P. C. & Rao, S. J. & Rashedi, V. & Rathi, P. & Rawaf, D. L. & Rawaf, S. & Rawal, L. & Rawassizadeh, R. & Rawat, R. & Razo, C. & Redford, S. B. & Reiner, R. C. & Reitsma, M. B. & Remuzzi, G. & Renjith, V. & Renzaho, A. M. N. & Resnikoff, S. & Rezaei, N. & Rezaei, N. & Rezapour, A. & Rhinehart, P.-A. & Riahi, S. M. & Ribeiro, D. C. & Ribeiro, D. & Rickard, J. & Rivera, J. A. & Roberts, N. L. S. & Rodríguez-Ramírez, S. & Roever, L. & Ronfani, L. & Room, R. & Roshandel, G. & Roth, G. A. & Rothenbacher, D. & Rubagotti, E. & Rwegerera, G. M. & Sabour, S. & Sachdev, P. S. & Saddik, B. & Sadeghi, E. & Sadeghi, M. & Saeedi, R. & Saeedi Moghaddam, S. & Safari, Y. & Safi, S. & Safiri, S. & Sagar, R. & Sahebkar, A. & Sajadi, S. M. & Salam, N. & Salamati, P. & Salem, H. & Salem, M. R. R. & Salimzadeh, H. & Salman, O. M. & Salomon, J. A. & Samad, Z. & Samadi Kafil, H. & Sambala, E. Z. & Samy, A. M. & Sanabria, J. & Sánchez-Pimienta, T. G. & Santomauro, D. F. & Santos, I. S. & Santos, J. V. & Santric-Milicevic, M. M. & Saraswathy, S. Y. I. & Sarmiento-Suárez, R. & Sarrafzadegan, N. & Sartorius, B. & Sarveazad, A. & Sathian, B. & Sathish, T. & Sattin, D. & Saxena, S. & Schaeffer, L. E. & Schiavolin, S. & Schlaich, M. P. & Schmidt, M. I. & Schutte, A. E. & Schwebel, D. C. & Schwendicke, F. & Senbeta, A. M. & Senthilkumaran, S. & Sepanlou, S. G. & Serdar, B. & Serre, M. L. & Shadid, J. & Shafaat, O. & Shahabi, S. & Shaheen, A. A. & Shaikh, M. A. & Shalash, A. S. & Shams-Beyranvand, M. & Shamsizadeh, M. & Sharafi, K. & Sheikh, A. & Sheikhtaheri, A. & Shibuya, K. & Shield, K. D. & Shigematsu, M. & Shin, J. I. & Shin, M.-J. & Shiri, R. & Shirkoohi, R. & Shuval, K. & Siabani, S. & Sierpinski, R. & Sigfusdottir, I. D. & Sigurvinsdottir, R. & Silva, J. P. & Simpson, K. E. & Singh, J. A. & Singh, P. & Skiadaresi, E. & Skou, S. T. S. & Skryabin, V. Y. & Smith, E. U. R. & Soheili, A. & Soltani, S. & Soofi, M. & Sorensen, R. J. D. & Soriano, J. B. & Sorrie, M. B. & Soshnikov, S. & Soyiri, I. N. & Spencer, C. N. & Spotin, A. & Sreeramareddy, C. T. & Srinivasan, V. & Stanaway, J. D. & Stein, C.

& Stein, D. J. & Steiner, C. & Stockfelt, L. & Stokes, M. A. & Straif, K. & Stubbs, J. L. & Sufiyan, M. a. B. & Suleria, H. A. R. & Suliankatchi Abdulkader, R. & Sulo, G. & Sultan, I. & Szumowski, Ł. & Tabarés-Seisdedos, R. & Tabb, K. M. & Tabuchi, T. & Taherkhani, A. & Tajdini, M. & Takahashi, K. & Takala, J. S. & Tamiru, A. T. & Taveira, N. & Tehrani-Banihashemi, A. & Temsah, M.-H. & Tesema, G. A. & Tessema, Z. T. & Thurston, G. D. & Titova, M. V. & Tohidinik, H. R. & Tonelli, M. & Topor-Madry, R. & Topouzis, F. & Torre, A. E. & Touvier, M. & Tovani-Palone, M. R. R. & Tran, B. X. & Travillian, R. & Tsatsakis, A. & Tudor Car, L. & Tyrovolas, S. & Uddin, R. & Umeokonkwo, C. D. & Unnikrishnan, B. & Upadhyay, E. & Vacante, M. & Valdez, P. R. & van Donkelaar, A. & Vasankari, T. J. & Vasseghian, Y. & Veisani, Y. & Venketasubramanian, N. & Violante, F. S. & Vlassov, V. & Vollset, S. E. & Vos, T. & Vukovic, R. & Waheed, Y. & Wallin, M. T. & Wang, Y. & Wang, Y.-P. & Watson, A. & Wei, J. & Wei, M. Y. W. & Weintraub, R. G. & Weiss, J. & Werdecker, A. & West, J. J. & Westerman, R. & Whisnant, J. L. & Whiteford, H. A. & Wiens, K. E. & Wolfe, C. D. A. & Wozniak, S. S. & Wu, A.-M. & Wu, J. & Wulf Hanson, S. & Xu, G. & Xu, R. & Yadgir, S. & Yahyazadeh Jabbari, S. H. & Yamagishi, K. & Yaminfirooz, M. & Yano, Y. & Yaya, S. & Yazdi-Feyzabadi, V. & Yeheyis, T. Y. & Yilgwan, C. S. & Yilma, M. T. & Yip, P. & Yonemoto, N. & Younis, M. Z. & Younker, T. P. & Yousefi, B. & Yousefi, Z. & Yousefinezhadi, T. & Yousuf, A. Y. & Yu, C. & Yusefzadeh, H. & Zahirian Moghadam, T. & Zamani, M. & Zamanian, M. & Zandian, H. & Zastrozhin, M. S. & Zhang, Y. & Zhang, Z.-J. & Zhao, J. T. & Zhao, X.-J. G. & Zhao, Y. & Zhou, M. & Ziapour, A. & Zimsen, S. R. M. & Brauer, M. & Afshin, A. & Lim, S. S. (2020) Global burden of 87 risk factors in 204 countries and territories, 1990–2019: a systematic analysis for the Global Burden of Disease Study 2019. *The Lancet.* 396 (10258), 1223-1249. doi: 10.1016/S0140-6736(20)30752-2.

Muzio, G., Barrera, G. & Pizzimenti, S. (2021) Peroxisome Proliferator-Activated Receptors (PPARs) and Oxidative Stress in Physiological Conditions and in Cancer. *Antioxidants.* 10 (11), 1734. doi: 10.3390/antiox10111734.

Nagy, L., Tontonoz, P., Alvarez, J. G. A., Chen, H. & Evans, R. M. (1998) Oxidized LDL Regulates Macrophage Gene Expression through Ligand Activation of PPARγ. *Cell.* 93 (2), 229-240. doi: 10.1016/S0092-8674(00)81574-3.

OECD (2021) *OECD Economic Outlook, Volume 2021 Issue 2: Preliminary version. OECD Economic Outlook.* OECD.

Oliver, M. (2012) The clofibrate saga: a retrospective commentary: Commentary. *British Journal of Clinical Pharmacology.* 74 (6), 907-910. doi: 10.1111/j.1365-2125.2012.04282.x.

Oliver, W. R., Shenk, J. L., Snaith, M. R., Russell, C. S., Plunket, K. D., Bodkin, N. L., Lewis, M. C., Winegar, D. A., Sznaidman, M. L., Lambert, M. H., Xu, H. E., Sternbach, D. D., Kliewer, S. A., Hansen, B. C. & Willson, T. M. (2001) A selective peroxisome proliferator-activated receptor delta agonist

promotes reverse cholesterol transport. *Proceedings of the National Academy of Sciences of the United States of America.* 98 (9), 5306-5311. doi: 10.1073/pnas.091021198.

Palomer, X., Barroso, E., Zarei, M., Botteri, G. & Vázquez-Carrera, M. (2016) PPARβ/δ and lipid metabolism in the heart. *Biochimica et Biophysica Acta (BBA) - Molecular and Cell Biology of Lipids.* 1861 (10), 1569-1578. doi: 10.1016/j.bbalip.2016.01.019.

Pan, D.-S., Wang, W., Liu, N.-S., Yang, Q.-J., Zhang, K., Zhu, J.-Z., Shan, S., Li, Z.-B., Ning, Z.-Q., Huang, L. & Lu, X.-P. (2017) Chiglitazar Preferentially Regulates Gene Expression via Configuration-Restricted Binding and Phosphorylation Inhibition of PPAR *γ*. *PPAR Research.* 2017, 1-16. doi: 10.1155/2017/4313561.

Parejo-Alonso, B., Barneda, D., Trabulo, S., Courtois, S., Compte-Sancerni, S., Ruiz-Cañas, L., Zheng, Q., Tang, J., Chen, M., Guo, Z., Schmitz, U., Irún, P., Penin-Peyta, L., Crusz, S. M., Cano-Galiano, A., Lopez-Escalona, S., Jagust, P., Espiau-Romera, P., Yuneva, M., Lin, M.-L., Lanas, A., Sainz, B., Heeschen, C. & Sancho, P. (2021) *PPAR-delta acts as a metabolic master checkpoint for metastasis in pancreatic cancer*. Cancer Biology. [Accessed 2023-06-29 20:25:05]

Patel, V., Chisholm, D., Parikh, R., Charlson, F. J., Degenhardt, L., Dua, T., Ferrari, A. J., Hyman, S., Laxminarayan, R., Levin, C., Lund, C., Medina Mora, M. E., Petersen, I., Scott, J., Shidhaye, R., Vijayakumar, L., Thornicroft, G. & Whiteford, H. (2016) Addressing the burden of mental, neurological, and substance use disorders: key messages from Disease Control Priorities, 3rd edition. *The Lancet.* 387 (10028), 1672-1685. doi: 10.1016/S0140-6736(15)00390-6.

Patil, R., Mohanty, B., Liu, B., Chandrashekaran, I. R., Headey, S. J., Williams, M. L., Clements, C. S., Ilyichova, O., Doak, B. C., Genissel, P., Weaver, R. J., Vuillard, L., Halls, M. L., Porter, C. J. H. & Scanlon, M. J. (2019) A ligand-induced structural change in fatty acid–binding protein 1 is associated with potentiation of peroxisome proliferator–activated receptor α agonists. *Journal of Biological Chemistry.* 294 (10), 3720-3734. doi: 10.1074/jbc.RA118.006848.

Penvose, A., Keenan, J. L., Bray, D., Ramlall, V. & Siggers, T. (2019) Comprehensive study of nuclear receptor DNA binding provides a revised framework for understanding receptor specificity. *Nature Communications.* 10 (1), 2514. doi: 10.1038/s41467-019-10264-3.

Pérez-Segura, I., Santiago-Balmaseda, A., Rodríguez-Hernández, L. D., Morales-Martínez, A., Martínez-Becerril, H. A., Martínez-Gómez, P. A., Delgado-Minjares, K. M., Salinas-Lara, C., Martínez-Dávila, I. A., Guerra-Crespo, M., Pérez-Severiano, F. & Soto-Rojas, L. O. (2023) PPARs and Their Neuroprotective Effects in Parkinson's Disease: A Novel Therapeutic Approach in α-Synucleinopathy? *International Journal of Molecular Sciences.* 24 (4), 3264. doi: 10.3390/ijms24043264.

Quang, T. H., Ngan, N. T. T., Minh, C. V., Kiem, P. V., Tai, B. H., Thao, N. P., Song, S. B. & Kim, Y. H. (2012) Anti-inflammatory and PPAR transactivational effects of secondary metabolites from the roots of Asarum sieboldii. *Bioorganic & Medicinal Chemistry Letters.* 22 (7), 2527-2533. doi: 10.1016/j.bmcl.2012.01.136.

Rajesh, N. A., Drishya, L., Ambati, M. M. R., Narayanan, A. L., Alex, M., R, K. K., Abraham, J. J. & Vijayakumar, T. M. (2022) Safety and Efficacy of Saroglitazar in Nonalcoholic Fatty Liver Patients With Diabetic Dyslipidemia—A Prospective, Interventional, Pilot Study. *Journal of Clinical and Experimental Hepatology.* 12 (1), 61-67. doi: 10.1016/j.jceh.2021.03.012.

Rakhshandehroo, M., Knoch, B., Müller, M. & Kersten, S. (2010) Peroxisome Proliferator-Activated Receptor Alpha Target Genes. *PPAR Research.* 2010, 1-20. doi: 10.1155/2010/612089.

Raza-Iqbal, S., Tanaka, T., Anai, M., Inagaki, T., Matsumura, Y., Ikeda, K., Taguchi, A., Gonzalez, F. J., Sakai, J. & Kodama, T. (2015) Transcriptome Analysis of K-877 (a Novel Selective PPARα Modulator (SPPARMα))-Regulated Genes in Primary Human Hepatocytes and the Mouse Liver. *Journal of Atherosclerosis and Thrombosis.* 22 (8), 754-772. doi: 10.5551/jat.28720.

Ribeiro Filho, H. V., Guerra, J. V., Cagliari, R., Batista, F. A. H., Le Maire, A., Oliveira, P. S. L. & Figueira, A. C. M. (2019) Exploring the mechanism of PPARγ phosphorylation mediated by CDK5. *Journal of Structural Biology.* 207 (3), 317-326. doi: 10.1016/j.jsb.2019.07.007.

Rochel, N., Ciesielski, F., Godet, J., Moman, E., Roessle, M., Peluso-Iltis, C., Moulin, M., Haertlein, M., Callow, P., Mély, Y., Svergun, D. I. & Moras, D. (2011) Common architecture of nuclear receptor heterodimers on DNA direct repeat elements with different spacings. *Nature Structural & Molecular Biology.* 18 (5), 564-570. doi: 10.1038/nsmb.2054.

Rogue, A., Lambert, C., Jossé, R., Antherieu, S., Spire, C., Claude, N. & Guillouzo, A. (2011) Comparative Gene Expression Profiles Induced by PPARγ and PPARα/γ Agonists in Human Hepatocytes. *PLoS ONE.* 6 (4), e18816. doi: 10.1371/journal.pone.0018816.

Rudko, O. I., Tretiakov, A. V., Naumova, E. A. & Klimov, E. A. (2020) Role of PPARs in Progression of Anxiety: Literature Analysis and Signaling Pathways Reconstruction. *PPAR Research.* 2020, 1-15. doi: 10.1155/2020/8859017.

Sagheddu, C., Melis, M., Muntoni, A. L. & Pistis, M. (2021) Repurposing Peroxisome Proliferator-Activated Receptor Agonists in Neurological and Psychiatric Disorders. *Pharmaceuticals.* 14 (10), 1025. doi: 10.3390/ph14101025.

Sakamoto, J., Kimura, H., Moriyama, S., Odaka, H., Momose, Y., Sugiyama, Y. & Sawada, H. (2000) Activation of Human Peroxisome Proliferator-Activated Receptor (PPAR) Subtypes by Pioglitazone.

Biochemical and Biophysical Research Communications. 278 (3), 704-711. doi: 10.1006/bbrc.2000.3868.

Sasaki, Y., Raza-Iqbal, S., Tanaka, T., Murakami, K., Anai, M., Osawa, T., Matsumura, Y., Sakai, J. & Kodama, T. (2019) Gene Expression Profiles Induced by a Novel Selective Peroxisome Proliferator-Activated Receptor α Modulator (SPPARMα) Pemafibrate. *International Journal of Molecular Sciences.* 20 (22), 5682. doi: 10.3390/ijms20225682.

Sauerberg, P., Bury, P. S., Mogensen, J. P., Deussen, H.-J., Pettersson, I., Fleckner, J., Nehlin, J., Frederiksen, K. S., Albrektsen, T., Din, N., Svensson, L. A., Ynddal, L., Wulff, E. M. & Jeppesen, L. (2003) Large Dimeric Ligands with Favorable Pharmacokinetic Properties and Peroxisome Proliferator-Activated Receptor Agonist Activity in Vitro and in Vivo. *Journal of Medicinal Chemistry.* 46 (23), 4883-4894. doi: 10.1021/jm0309046.

Schmidt, A., Endo, N., Rutledge, S. J., Vogel, R., Shinar, D. & Rodan, G. A. (1992) Identification of a new member of the steroid hormone receptor superfamily that is activated by a peroxisome proliferator and fatty acids. *Molecular Endocrinology.* 6 (10), 1634-1641. doi: 10.1210/mend.6.10.1333051.

Schumann, T., Adhikary, T., Wortmann, A., Finkernagel, F., Lieber, S., Schnitzer, E., Legrand, N., Schober, Y., Nockher, W. A., Toth, P. M., Diederich, W. E., Nist, A., Stiewe, T., Wagner, U., Reinartz, S., Müller-Brüsselbach, S. & Müller, R. (2015) Deregulation of PPARβ/δ target genes in tumor-associated macrophages by fatty acid ligands in the ovarian cancer microenvironment. *Oncotarget.* 6 (15), 13416-13433. doi: 10.18632/oncotarget.3826.

Schupp, M. & Lazar, M. A. (2010) Endogenous Ligands for Nuclear Receptors: Digging Deeper. *Journal of Biological Chemistry.* 285 (52), 40409-40415. doi: 10.1074/jbc.R110.182451.

Shang, J., Brust, R., Mosure, S. A., Bass, J., Munoz-Tello, P., Lin, H., Hughes, T. S., Tang, M., Ge, Q., Kamenekca, T. M. & Kojetin, D. J. (2018) Cooperative cobinding of synthetic and natural ligands to the nuclear receptor PPARγ. *eLife.* 7, e43320. doi: 10.7554/eLife.43320.

Sher, T., Yi, H. F., McBride, O. W. & Gonzalez, F. J. (1993) cDNA cloning, chromosomal mapping, and functional characterization of the human peroxisome proliferator activated receptor. *Biochemistry.* 32 (21), 5598-5604. doi: 10.1021/bi00072a015.

Smathers, R. L. & Petersen, D. R. (2011) The human fatty acid-binding protein family: Evolutionary divergences and functions. *Human Genomics.* 5 (3), 170. doi: 10.1186/1479-7364-5-3-170.

Song, Y., Li, S. & He, C. (2022) PPARγ Gene Polymorphisms, Metabolic Disorders, and Coronary Artery Disease. *Frontiers in Cardiovascular Medicine.* 9, 808929. doi: 10.3389/fcvm.2022.808929.

Stanaway, J. D. & Afshin, A. & Gakidou, E. & Lim, S. S. & Abate, D. & Abate, K. H. & Abbafati, C. & Abbasi, N. & Abbastabar, H. & Abd-Allah, F. & Abdela, J. & Abdelalim, A. & Abdollahpour, I. & Abdulkader, R. S. & Abebe, M. & Abebe, Z. & Abera, S. F. & Abil, O. Z. & Abraha, H. N. & Abrham, A. R. & Abu-Raddad, L. J. & Abu-Rmeileh, N. M. & Accrombessi, M. M. K. & Acharya, D. & Acharya, P. & Adamu, A. A. & Adane, A. A. & Adebayo, O. M. & Adedoyin, R. A. & Adekanmbi, V. & Ademi, Z. & Adetokunboh, O. O. & Adib, M. G. & Admasie, A. & Adsuar, J. C. & Afanvi, K. A. & Afarideh, M. & Agarwal, G. & Aggarwal, A. & Aghayan, S. A. & Agrawal, A. & Agrawal, S. & Ahmadi, A. & Ahmadi, M. & Ahmadieh, H. & Ahmed, M. B. & Aichour, A. N. & Aichour, I. & Aichour, M. T. E. & Akbari, M. E. & Akinyemiju, T. & Akseer, N. & Al-Aly, Z. & Al-Eyadhy, A. & Al-Mekhlafi, H. M. & Alahdab, F. & Alam, K. & Alam, S. & Alam, T. & Alashi, A. & Alavian, S. M. & Alene, K. A. & Ali, K. & Ali, S. M. & Alijanzadeh, M. & Alizadeh-Navaei, R. & Aljunid, S. M. & Alkerwi, A. a. & Alla, F. & Alsharif, U. & Altirkawi, K. & Alvis-Guzman, N. & Amare, A. T. & Ammar, W. & Anber, N. H. & Anderson, J. A. & Andrei, C. L. & Androudi, S. & Animut, M. D. & Anjomshoa, M. & Ansha, M. G. & Antó, J. M. & Antonio, C. A. T. & Anwari, P. & Appiah, L. T. & Appiah, S. C. Y. & Arabloo, J. & Aremu, O. & Ärnlöv, J. & Artaman, A. & Aryal, K. K. & Asayesh, H. & Ataro, Z. & Ausloos, M. & Avokpaho, E. F. G. A. & Awasthi, A. & Ayala Quintanilla, B. P. & Ayer, R. & Ayuk, T. B. & Azzopardi, P. S. & Babazadeh, A. & Badali, H. & Badawi, A. & Balakrishnan, K. & Bali, A. G. & Ball, K. & Ballew, S. H. & Banach, M. & Banoub, J. A. M. & Barac, A. & Barker-Collo, S. L. & Bärnighausen, T. W. & Barrero, L. H. & Basu, S. & Baune, B. T. & Bazargan-Hejazi, S. & Bedi, N. & Beghi, E. & Behzadifar, M. & Behzadifar, M. & Béjot, Y. & Bekele, B. B. & Bekru, E. T. & Belay, E. & Belay, Y. A. & Bell, M. L. & Bello, A. K. & Bennett, D. A. & Bensenor, I. M. & Bergeron, G. & Berhane, A. & Bernabe, E. & Bernstein, R. S. & Beuran, M. & Beyranvand, T. & Bhala, N. & Bhalla, A. & Bhattarai, S. & Bhutta, Z. A. & Biadgo, B. & Bijani, A. & Bikbov, B. & Bilano, V. & Bililign, N. & Bin Sayeed, M. S. & Bisanzio, D. & Biswas, T. & Bjørge, T. & Blacker, B. F. & Bleyer, A. & Borschmann, R. & Bou-Orm, I. R. & Boufous, S. & Bourne, R. & Brady, O. J. & Brauer, M. & Brazinova, A. & Breitborde, N. J. K. & Brenner, H. & Briko, A. N. & Britton, G. & Brugha, T. & Buchbinder, R. & Burnett, R. T. & Busse, R. & Butt, Z. A. & Cahill, L. E. & Cahuana-Hurtado, L. & Campos-Nonato, I. R. & Cárdenas, R. & Carreras, G. & Carrero, J. J. & Carvalho, F. & Castañeda-Orjuela, C. A. & Castillo Rivas, J. & Castro, F. & Catalá-López, F. & Causey, K. & Cercy, K. M. & Cerin, E. & Chaiah, Y. & Chang, H.-Y. & Chang, J.-C. & Chang, K.-L. & Charlson, F. J. & Chattopadhyay, A. & Chattu, V. K. & Chee, M. L. & Cheng, C.-Y. & Chew, A. & Chiang, P. P.-C. & Chimed-Ochir, O. & Chin, K. L. & Chitheer, A. & Choi, J.-Y. J. & Chowdhury, R. & Christensen, H. & Christopher, D. J. & Chung, S.-C. & Cicuttini, F. M. & Cirillo, M. & Cohen, A. J. & Collado-Mateo, D. & Cooper, C. & Cooper, O. R. & Coresh, J. & Cornaby, L. & Cortesi, P. A. & Cortinovis, M. & Costa, M. & Cousin, E. & Criqui, M. H. & Cromwell, E. A. & Cundiff, D. K. & Daba, A. K. & Dachew, B. A. & Dadi, A. F. & Damasceno, A. A. M. & Dandona, L. & Dandona, R. & Darby, S. C. & Dargan, P. I. & Daryani, A. & Das Gupta, R. & Das Neves, J. & Dasa, T. T. & Dash, A. P. & Davitoiu, D. V. & Davletov, K. & De La Cruz-Góngora, V. & De La Hoz, F. P. & De Leo, D. & De Neve, J.-

W. & Degenhardt, L. & Deiparine, S. & Dellavalle, R. P. & Demoz, G. T. & Denova-Gutiérrez, E. & Deribe, K. & Dervenis, N. & Deshpande, A. & Des Jarlais, D. C. & Dessie, G. A. & Deveber, G. A. & Dey, S. & Dharmaratne, S. D. & Dhimal, M. & Dinberu, M. T. & Ding, E. L. & Diro, H. D. & Djalalinia, S. & Do, H. P. & Dokova, K. & Doku, D. T. & Doyle, K. E. & Driscoll, T. R. & Dubey, M. & Dubljanin, E. & Duken, E. E. & Duncan, B. B. & Duraes, A. R. & Ebert, N. & Ebrahimi, H. & Ebrahimpour, S. & Edvardsson, D. & Effiong, A. & Eggen, A. E. & El Bcheraoui, C. & El-Khatib, Z. & Elyazar, I. R. & Enayati, A. & Endries, A. Y. & Er, B. & Erskine, H. E. & Eskandarieh, S. & Esteghamati, A. & Estep, K. & Fakhim, H. & Faramarzi, M. & Fareed, M. & Farid, T. A. & Farinha, C. S. E. S. & Farioli, A. & Faro, A. & Farvid, M. S. & Farzaei, M. H. & Fatima, B. & Fay, K. A. & Fazaeli, A. A. & Feigin, V. L. & Feigl, A. B. & Fereshtehnejad, S.-M. & Fernandes, E. & Fernandes, J. C. & Ferrara, G. & Ferrari, A. J. & Ferreira, M. L. & Filip, I. & Finger, J. D. & Fischer, F. & Foigt, N. A. & Foreman, K. J. & Fukumoto, T. & Fullman, N. & Fürst, T. & Furtado, J. M. & Futran, N. D. & Gall, S. & Gallus, S. & Gamkrelidze, A. & Ganji, M. & Garcia-Basteiro, A. L. & Gardner, W. M. & Gebre, A. K. & Gebremedhin, A. T. & Gebremichael, T. G. & Gelano, T. F. & Geleijnse, J. M. & Geramo, Y. C. D. & Gething, P. W. & Gezae, K. E. & Ghadimi, R. & Ghadiri, K. & Ghasemi Falavarjani, K. & Ghasemi-Kasman, M. & Ghimire, M. & Ghosh, R. & Ghoshal, A. G. & Giampaoli, S. & Gill, P. S. & Gill, T. K. & Gillum, R. F. & Ginawi, I. A. & Giussani, G. & Gnedovskaya, E. V. & Godwin, W. W. & Goli, S. & Gómez-Dantés, H. & Gona, P. N. & Gopalani, S. V. & Goulart, A. C. & Grada, A. & Grams, M. E. & Grosso, G. & Gugnani, H. C. & Guo, Y. & Gupta, R. & Gupta, R. & Gupta, T. & Gutiérrez, R. A. & Gutiérrez-Torres, D. S. & Haagsma, J. A. & Habtewold, T. D. & Hachinski, V. & Hafezi-Nejad, N. & Hagos, T. B. & Hailegiyorgis, T. T. & Hailu, G. B. & Haj-Mirzaian, A. & Haj-Mirzaian, A. & Hamadeh, R. R. & Hamidi, S. & Handal, A. J. & Hankey, G. J. & Hao, Y. & Harb, H. L. & Harikrishnan, S. & Haro, J. M. & Hassankhani, H. & Hassen, H. Y. & Havmoeller, R. & Hawley, C. N. & Hay, S. I. & Hedayatizadeh-Omran, A. & Heibati, B. & Heidari, B. & Heidari, M. & Hendrie, D. & Henok, A. & Heredia-Pi, I. & Herteliu, C. & Heydarpour, F. & Heydarpour, S. & Hibstu, D. T. & Higazi, T. B. & Hilawe, E. H. & Hoek, H. W. & Hoffman, H. J. & Hole, M. K. & Homaie Rad, E. & Hoogar, P. & Hosgood, H. D. & Hosseini, S. M. & Hosseinzadeh, M. & Hostiuc, M. & Hostiuc, S. & Hoy, D. G. & Hsairi, M. & Hsiao, T. & Hu, G. & Hu, H. & Huang, J. J. & Hussen, M. A. & Huynh, C. K. & Iburg, K. M. & Ikeda, N. & Ilesanmi, O. S. & Iqbal, U. & Irvani, S. S. N. & Irvine, C. M. S. & Islam, S. M. S. & Islami, F. & Jackson, M. D. & Jacobsen, K. H. & Jahangiry, L. & Jahanmehr, N. & Jain, S. K. & Jakovljevic, M. & James, S. L. & Jassal, S. K. & Jayatilleke, A. U. & Jeemon, P. & Jha, R. P. & Jha, V. & Ji, J. S. & Jonas, J. B. & Jonnagaddala, J. & Jorjoran Shushtari, Z. & Joshi, A. & Jozwiak, J. J. & Jürisson, M. & Kabir, Z. & Kahsay, A. & Kalani, R. & Kanchan, T. & Kant, S. & Kar, C. & Karami, M. & Karami Matin, B. & Karch, A. & Karema, C. & Karimi, N. & Karimi, S. M. & Kasaeian, A. & Kassa, D. H. & Kassa, G. M. & Kassa, T. D. & Kassebaum, N. J. & Katikireddi, S. V. & Kaul, A. & Kawakami, N. & Kazemi, Z. & Karyani, A. K. & Kefale, A. T. & Keiyoro, P. N. & Kemp, G. R. & Kengne, A. P. & Keren, A. & Kesavachandran, C. N. & Khader, Y. S. & Khafaei, B. & Khafaie, M. A. & Khajavi, A. & Khalid, N. & Khalil, I. A. & Khan, G. &

Khan, M. S. & Khan, M. A. & Khang, Y.-H. & Khater, M. M. & Khazaei, M. & Khazaie, H. & Khoja, A. T. & Khosravi, A. & Khosravi, M. H. & Kiadaliri, A. A. & Kiirithio, D. N. & Kim, C.-I. & Kim, D. & Kim, Y.-E. & Kim, Y. J. & Kimokoti, R. W. & Kinfu, Y. & Kisa, A. & Kissimova-Skarbek, K. & Kivimäki, M. & Knibbs, L. D. & Knudsen, A. K. S. & Kochhar, S. & Kokubo, Y. & Kolola, T. & Kopec, J. A. & Kosen, S. & Koul, P. A. & Koyanagi, A. & Kravchenko, M. A. & Krishan, K. & Krohn, K. J. & Kromhout, H. & Kuate Defo, B. & Kucuk Bicer, B. & Kumar, G. A. & Kumar, M. & Kuzin, I. & Kyu, H. H. & Lachat, C. & Lad, D. P. & Lad, S. D. & Lafranconi, A. & Lalloo, R. & Lallukka, T. & Lami, F. H. & Lang, J. J. & Lansingh, V. C. & Larson, S. L. & Latifi, A. & Lazarus, J. V. & Lee, P. H. & Leigh, J. & Leili, M. & Leshargie, C. T. & Leung, J. & Levi, M. & Lewycka, S. & Li, S. & Li, Y. & Liang, J. & Liang, X. & Liao, Y. & Liben, M. L. & Lim, L.-L. & Linn, S. & Liu, S. & Lodha, R. & Logroscino, G. & Lopez, A. D. & Lorkowski, S. & Lotufo, P. A. & Lozano, R. & Lucas, T. C. D. & Lunevicius, R. & Ma, S. & Macarayan, E. R. K. & Machado, Í. E. & Madotto, F. & Mai, H. T. & Majdan, M. & Majdzadeh, R. & Majeed, A. & Malekzadeh, R. & Malta, D. C. & Mamun, A. A. & Manda, A.-L. & Manguerra, H. & Mansournia, M. A. & Mantovani, L. G. & Maravilla, J. C. & Marcenes, W. & Marks, A. & Martin, R. V. & Martins, S. C. O. & Martins-Melo, F. R. & März, W. & Marzan, M. B. & Massenburg, B. B. & Mathur, M. R. & Mathur, P. & Matsushita, K. & Maulik, P. K. & Mazidi, M. & McAlinden, C. & McGrath, J. J. & McKee, M. & Mehrotra, R. & Mehta, K. M. & Mehta, V. & Meier, T. & Mekonnen, F. A. & Melaku, Y. A. & Melese, A. & Melku, M. & Memiah, P. T. N. & Memish, Z. A. & Mendoza, W. & Mengistu, D. T. & Mensah, G. A. & Mensink, G. B. M. & Mereta, S. T. & Meretoja, A. & Meretoja, T. J. & Mestrovic, T. & Mezgebe, H. B. & Miazgowski, B. & Miazgowski, T. & Millear, A. I. & Miller, T. R. & Miller-Petrie, M. K. & Mini, G. K. & Mirarefin, M. & Mirica, A. & Mirrakhimov, E. M. & Misganaw, A. T. & Mitiku, H. & Moazen, B. & Mohajer, B. & Mohammad, K. A. & Mohammadi, M. & Mohammadifard, N. & Mohammadnia-Afrouzi, M. & Mohammed, S. & Mohebi, F. & Mokdad, A. H. & Molokhia, M. & Momeniha, F. & Monasta, L. & Moodley, Y. & Moradi, G. & Moradi-Lakeh, M. & Moradinazar, M. & Moraga, P. & Morawska, L. & Morgado-Da-Costa, J. & Morrison, S. D. & Moschos, M. M. & Mouodi, S. & Mousavi, S. M. & Mozaffarian, D. & Mruts, K. B. & Muche, A. A. & Muchie, K. F. & Mueller, U. O. & Muhammed, O. S. & Mukhopadhyay, S. & Muller, K. & Musa, K. I. & Mustafa, G. & Nabhan, A. F. & Naghavi, M. & Naheed, A. & Nahvijou, A. & Naik, G. & Naik, N. & Najafi, F. & Nangia, V. & Nansseu, J. R. & Nascimento, B. R. & Neal, B. & Neamati, N. & Negoi, I. & Negoi, R. I. & Neupane, S. & Newton, C. R. J. & Ngunjiri, J. W. & Nguyen, A. Q. & Nguyen, G. & Nguyen, H. T. & Nguyen, H. L. T. & Nguyen, H. T. & Nguyen, M. & Nguyen, N. B. & Nichols, E. & Nie, J. & Ningrum, D. N. A. & Nirayo, Y. L. & Nishi, N. & Nixon, M. R. & Nojomi, M. & Nomura, S. & Norheim, O. F. & Noroozi, M. & Norrving, B. & Noubiap, J. J. & Nouri, H. R. & Nourollahpour Shiadeh, M. & Nowroozi, M. R. & Nsoesie, E. O. & Nyasulu, P. S. & Obermeyer, C. M. & Odell, C. M. & Ofori-Asenso, R. & Ogbo, F. A. & Oh, I.-H. & Oladimeji, O. & Olagunju, A. T. & Olagunju, T. O. & Olivares, P. R. & Olsen, H. E. & Olusanya, B. O. & Olusanya, J. O. & Ong, K. L. & Ong, S. K. & Oren, E. & Orpana, H. M. & Ortiz, A. & Ota, E. & Otstavnov, S. S. & Øverland, S. & Owolabi, M. O. & P A, M. & Pacella, R. &

Pakhare, A. P. & Pakpour, A. H. & Pana, A. & Panda-Jonas, S. & Park, E.-K. & Parry, C. D. H. & Parsian, H. & Patel, S. & Pati, S. & Patil, S. T. & Patle, A. & Patton, G. C. & Paudel, D. & Paulson, K. R. & Paz Ballesteros, W. C. & Pearce, N. & Pereira, A. & Pereira, D. M. & Perico, N. & Pesudovs, K. & Petzold, M. & Pham, H. Q. & Phillips, M. R. & Pillay, J. D. & Piradov, M. A. & Pirsaheb, M. & Pischon, T. & Pishgar, F. & Plana-Ripoll, O. & Plass, D. & Polinder, S. & Polkinghorne, K. R. & Postma, M. J. & Poulton, R. & Pourshams, A. & Poustchi, H. & Prabhakaran, D. & Prakash, S. & Prasad, N. & Purcell, C. A. & Purwar, M. B. & Qorbani, M. & Radfar, A. & Rafay, A. & Rafiei, A. & Rahim, F. & Rahimi, Z. & Rahimi-Movaghar, A. & Rahimi-Movaghar, V. & Rahman, M. & Rahman, M. H. U. & Rahman, M. A. & Rai, R. K. & Rajati, F. & Rajsic, S. & Raju, S. B. & Ram, U. & Ranabhat, C. L. & Ranjan, P. & Rath, G. K. & Rawaf, D. L. & Rawaf, S. & Reddy, K. S. & Rehm, C. D. & Rehm, J. & Reiner, R. C. & Reitsma, M. B. & Remuzzi, G. & Renzaho, A. M. N. & Resnikoff, S. & Reynales-Shigematsu, L. M. & Rezaei, S. & Ribeiro, A. L. P. & Rivera, J. A. & Roba, K. T. & Rodríguez-Ramírez, S. & Roever, L. & Román, Y. & Ronfani, L. & Roshandel, G. & Rostami, A. & Roth, G. A. & Rothenbacher, D. & Roy, A. & Rubagotti, E. & Rushton, L. & Sabanayagam, C. & Sachdev, P. S. & Saddik, B. & Sadeghi, E. & Saeedi Moghaddam, S. & Safari, H. & Safari, Y. & Safari-Faramani, R. & Safdarian, M. & Safi, S. & Safiri, S. & Sagar, R. & Sahebkar, A. & Sahraian, M. A. & Sajadi, H. S. & Salam, N. & Salamati, P. & Saleem, Z. & Salimi, Y. & Salimzadeh, H. & Salomon, J. A. & Salvi, D. D. & Salz, I. & Samy, A. M. & Sanabria, J. & Sanchez-Niño, M. D. & Sánchez-Pimienta, T. G. & Sanders, T. & Sang, Y. & Santomauro, D. F. & Santos, I. S. & Santos, J. V. & Santric Milicevic, M. M. & Sao Jose, B. P. & Sardana, M. & Sarker, A. R. & Sarmiento-Suárez, R. & Sarrafzadegan, N. & Sartorius, B. & Sarvi, S. & Sathian, B. & Satpathy, M. & Sawant, A. R. & Sawhney, M. & Saylan, M. & Sayyah, M. & Schaeffner, E. & Schmidt, M. I. & Schneider, I. J. C. & Schöttker, B. & Schutte, A. E. & Schwebel, D. C. & Schwendicke, F. & Scott, J. G. & Seedat, S. & Sekerija, M. & Sepanlou, S. G. & Serre, M. L. & Serván-Mori, E. & Seyedmousavi, S. & Shabaninejad, H. & Shaddick, G. & Shafieesabet, A. & Shahbazi, M. & Shaheen, A. A. & Shaikh, M. A. & Shamah Levy, T. & Shams-Beyranvand, M. & Shamsi, M. & Sharafi, H. & Sharafi, K. & Sharif, M. & Sharif-Alhoseini, M. & Sharifi, H. & Sharma, J. & Sharma, M. & Sharma, R. & She, J. & Sheikh, A. & Shi, P. & Shibuya, K. & Shiferaw, M. S. & Shigematsu, M. & Shin, M.-J. & Shiri, R. & Shirkoohi, R. & Shiue, I. & Shokraneh, F. & Shoman, H. & Shrime, M. G. & Shupler, M. S. & Si, S. & Siabani, S. & Sibai, A. M. & Siddiqi, T. J. & Sigfusdottir, I. D. & Sigurvinsdottir, R. & Silva, D. A. S. & Silva, J. P. & Silveira, D. G. A. & Singh, J. A. & Singh, N. P. & Singh, V. & Sinha, D. N. & Skiadaresi, E. & Skirbekk, V. & Smith, D. L. & Smith, M. & Sobaih, B. H. & Sobhani, S. & Somayaji, R. & Soofi, M. & Sorensen, R. J. D. & Soriano, J. B. & Soyiri, I. N. & Spinelli, A. & Sposato, L. A. & Sreeramareddy, C. T. & Srinivasan, V. & Starodubov, V. I. & Steckling, N. & Stein, D. J. & Stein, M. B. & Stevanovic, G. & Stockfelt, L. & Stokes, M. A. & Sturua, L. & Subart, M. L. & Sudaryanto, A. & Sufiyan, M. a. B. & Sulo, G. & Sunguya, B. F. & Sur, P. J. & Sykes, B. L. & Szoeke, C. E. I. & Tabarés-Seisdedos, R. & Tabuchi, T. & Tadakamadla, S. K. & Takahashi, K. & Tandon, N. & Tassew, S. G. & Tavakkoli, M. & Taveira, N. & Tehrani-Banihashemi, A. & Tekalign, T. G. &

Tekelemedhin, S. W. & Tekle, M. G. & Temesgen, H. & Temsah, M.-H. & Temsah, O. & Terkawi, A. S. & Tessema, B. & Teweldemedhin, M. & Thankappan, K. R. & Theis, A. & Thirunavukkarasu, S. & Thomas, H. J. & Thomas, M. L. & Thomas, N. & Thurston, G. D. & Tilahun, B. & Tillmann, T. & To, Q. G. & Tobollik, M. & Tonelli, M. & Topor-Madry, R. & Torre, A. E. & Tortajada-Girbés, M. & Touvier, M. & Tovani-Palone, M. R. & Towbin, J. A. & Tran, B. X. & Tran, K. B. & Truelsen, T. C. & Truong, N. T. & Tsadik, A. G. & Tudor Car, L. & Tuzcu, E. M. & Tymeson, H. D. & Tyrovolas, S. & Ukwaja, K. N. & Ullah, I. & Updike, R. L. & Usman, M. S. & Uthman, O. A. & Vaduganathan, M. & Vaezi, A. & Valdez, P. R. & Van Donkelaar, A. & Varavikova, E. & Varughese, S. & Vasankari, T. J. & Venkateswaran, V. & Venketasubramanian, N. & Villafaina, S. & Violante, F. S. & Vladimirov, S. K. & Vlassov, V. & Vollset, S. E. & Vos, T. & Vosoughi, K. & Vu, G. T. & Vujcic, I. S. & Wagnew, F. S. & Waheed, Y. & Waller, S. G. & Walson, J. L. & Wang, Y. & Wang, Y. & Wang, Y.-P. & Weiderpass, E. & Weintraub, R. G. & Weldegebreal, F. & Werdecker, A. & Werkneh, A. A. & West, J. J. & Westerman, R. & Whiteford, H. A. & Widecka, J. & Wijeratne, T. & Winkler, A. S. & Wiyeh, A. B. & Wiysonge, C. S. & Wolfe, C. D. A. & Wong, T. Y. & Wu, S. & Xavier, D. & Xu, G. & Yadgir, S. & Yadollahpour, A. & Yahyazadeh Jabbari, S. H. & Yamada, T. & Yan, L. L. & Yano, Y. & Yaseri, M. & Yasin, Y. J. & Yeshaneh, A. & Yimer, E. M. & Yip, P. & Yisma, E. & Yonemoto, N. & Yoon, S.-J. & Yotebieng, M. & Younis, M. Z. & Yousefifard, M. & Yu, C. & Zaidi, Z. & Zaman, S. B. & Zamani, M. & Zavala-Arciniega, L. & Zhang, A. L. & Zhang, H. & Zhang, K. & Zhou, M. & Zimsen, S. R. M. & Zodpey, S. & Murray, C. J. L. (2018) Global, regional, and national comparative risk assessment of 84 behavioural, environmental and occupational, and metabolic risks or clusters of risks for 195 countries and territories, 1990–2017: a systematic analysis for the Global Burden of Disease Study 2017. *The Lancet.* 392 (10159), 1923-1994. doi: 10.1016/S0140-6736(18)32225-6.

Su, Y., Lu, Y., Li, W., Xue, M., Chen, C., Haireti, M., Li, Y., Liu, Z., Liu, Y., Wang, S. & Yao, H. (2020) Prevalence and Correlation of Metabolic Syndrome: A Cross-Sectional Study of Nearly 10 Million Multi-Ethnic Chinese Adults. *Diabetes, Metabolic Syndrome and Obesity: Targets and Therapy.* Volume 13, 4869-4883. doi: 10.2147/DMSO.S278346.

Sun, C., Mao, S., Chen, S., Zhang, W. & Liu, C. (2021) PPARs-Orchestrated Metabolic Homeostasis in the Adipose Tissue. *International Journal of Molecular Sciences.* 22 (16), 8974. doi: 10.3390/ijms22168974.

Sun, H., Saeedi, P., Karuranga, S., Pinkepank, M., Ogurtsova, K., Duncan, B. B., Stein, C., Basit, A., Chan, J. C. N., Mbanya, J. C., Pavkov, M. E., Ramachandaran, A., Wild, S. H., James, S., Herman, W. H., Zhang, P., Bommer, C., Kuo, S., Boyko, E. J. & Magliano, D. J. (2022) IDF Diabetes Atlas: Global, regional and country-level diabetes prevalence estimates for 2021 and projections for 2045. *Diabetes Research and Clinical Practice.* 183, 109119. doi: 10.1016/j.diabres.2021.109119.

Sung, H., Ferlay, J., Siegel, R. L., Laversanne, M., Soerjomataram, I., Jemal, A. & Bray, F. (2021) Global Cancer Statistics 2020: GLOBOCAN Estimates of Incidence and Mortality Worldwide for 36 Cancers in 185 Countries. *CA: A Cancer Journal for Clinicians.* 71 (3), 209-249. doi: 10.3322/caac.21660.

Takada, I. & Makishima, M. (2020) Peroxisome proliferator-activated receptor agonists and antagonists: a patent review (2014-present). *Expert Opinion on Therapeutic Patents.* 30 (1), 1-13. doi: 10.1080/13543776.2020.1703952.

Takada, I., Yu, R. T., Xu, H. E., Lambert, M. H., Montana, V. G., Kliewer, S. A., Evans, R. M. & Umesono, K. (2000) Alteration of a Single Amino Acid in Peroxisome Proliferator-Activated Receptor-α (PPARα) Generates a PPARδ Phenotype. *Molecular Endocrinology.* 14 (5), 733-740. doi: 10.1210/mend.14.5.0456.

Takei, K., Han, S.-i., Murayama, Y., Satoh, A., Oikawa, F., Ohno, H., Osaki, Y., Matsuzaka, T., Sekiya, M., Iwasaki, H., Yatoh, S., Yahagi, N., Suzuki, H., Yamada, N., Nakagawa, Y. & Shimano, H. (2017) Selective peroxisome proliferator-activated receptor-α modulator K-877 efficiently activates the peroxisome proliferator-activated receptor-α pathway and improves lipid metabolism in mice. *Journal of Diabetes Investigation.* 8 (4), 446-452. doi: 10.1111/jdi.12621.

Tan, N. S., Vázquez-Carrera, M., Montagner, A., Sng, M. K., Guillou, H. & Wahli, W. (2016) Transcriptional control of physiological and pathological processes by the nuclear receptor PPARβ/δ. *Progress in Lipid Research.* 64, 98-122. doi: 10.1016/j.plipres.2016.09.001.

Tan, N.-S., Shaw, N. S., Vinckenbosch, N., Liu, P., Yasmin, R., Desvergne, B., Wahli, W. & Noy, N. (2002) Selective Cooperation between Fatty Acid Binding Proteins and Peroxisome Proliferator-Activated Receptors in Regulating Transcription. *Molecular and Cellular Biology.* 22 (14), 5114-5127. doi: 10.1128/MCB.22.14.5114-5127.2002.

Tan, Y., Wang, M., Yang, K., Chi, T., Liao, Z. & Wei, P. (2021) PPAR-α Modulators as Current and Potential Cancer Treatments. *Frontiers in Oncology.* 11, 599995. doi: 10.3389/fonc.2021.599995.

Tang, H., Shi, W., Fu, S., Wang, T., Zhai, S., Song, Y. & Han, J. (2018) Pioglitazone and bladder cancer risk: a systematic review and meta-analysis. *Cancer Medicine.* 7 (4), 1070-1080. doi: 10.1002/cam4.1354.

Tassopoulou, V. P., Tzara, A. & Kourounakis, A. P. (2022) Design of Improved Antidiabetic Drugs: A Journey from Single to Multitarget Agents. *ChemMedChem.* 17 (23). doi: 10.1002/cmdc.202200320.

Thompson, P. W., Bayliffe, A. I., Warren, A. P. & Lamb, J. R. (2007) Interleukin-10 is upregulated by nanomolar rosiglitazone treatment of mature dendritic cells and human CD4+ T cells. *Cytokine.* 39 (3), 184-191. doi: 10.1016/j.cyto.2007.07.191.

Tomita, T., Kato, M. & Hiratsuka, S. (2021) Regulation of vascular permeability in cancer metastasis. *Cancer Science.* 112 (8), 2966-2974. doi: 10.1111/cas.14942.

Tonazzi, A., Giangregorio, N., Console, L., Palmieri, F. & Indiveri, C. (2021) The Mitochondrial Carnitine Acyl-carnitine Carrier (SLC25A20): Molecular Mechanisms of Transport, Role in Redox Sensing and Interaction with Drugs. *Biomolecules.* 11 (4), 521. doi: 10.3390/biom11040521.

Tong, M., Deochand, C., Didsbury, J. & de la Monte, S. M. (2016) T3D-959: A Multi-Faceted Disease Remedial Drug Candidate for the Treatment of Alzheimer's Disease. *Journal of Alzheimer's Disease.* 51 (1), 123-138. doi: 10.3233/JAD-151013.

Toobian, D., Ghosh, P. & Katkar, G. D. (2021) Parsing the Role of PPARs in Macrophage Processes. *Frontiers in Immunology.* 12, 783780. doi: 10.3389/fimmu.2021.783780.

Tzeng, J., Byun, J., Park, J. Y., Yamamoto, T., Schesing, K., Tian, B., Sadoshima, J. & Oka, S.-i. (2015) An Ideal PPAR Response Element Bound to and Activated by PPARα. *PLoS ONE.* 10 (8), e0134996. doi: 10.1371/journal.pone.0134996.

Umemoto, T. & Fujiki, Y. (2012) Ligand-dependent nucleo-cytoplasmic shuttling of peroxisome proliferator-activated receptors, PPARα and PPARγ. *Genes to Cells.* 17 (7), 576-596. doi: 10.1111/j.1365-2443.2012.01607.x.

Uppenberg, J., Svensson, C., Jaki, M., Bertilsson, G., Jendeberg, L. & Berkenstam, A. (1998) Crystal Structure of the Ligand Binding Domain of the Human Nuclear Receptor PPARγ. *Journal of Biological Chemistry.* 273 (47), 31108-31112. doi: 10.1074/jbc.273.47.31108.

Varanasi, U., Chu, R., Huang, Q., Castellon, R., Yeldandi, A. V. & Reddy, J. K. (1996) Identification of a Peroxisome Proliferator-responsive Element Upstream of the Human Peroxisomal Fatty Acyl Coenzyme A Oxidase Gene. *Journal of Biological Chemistry.* 271 (4), 2147-2155. doi: 10.1074/jbc.271.4.2147.

Virani, S. S., Alonso, A., Aparicio, H. J., Benjamin, E. J., Bittencourt, M. S., Callaway, C. W., Carson, A. P., Chamberlain, A. M., Cheng, S., Delling, F. N., Elkind, M. S. V., Evenson, K. R., Ferguson, J. F., Gupta, D. K., Khan, S. S., Kissela, B. M., Knutson, K. L., Lee, C. D., Lewis, T. T., Liu, J., Loop, M. S., Lutsey, P. L., Ma, J., Mackey, J., Martin, S. S., Matchar, D. B., Mussolino, M. E., Navaneethan, S. D., Perak, A. M., Roth, G. A., Samad, Z., Satou, G. M., Schroeder, E. B., Shah, S. H., Shay, C. M., Stokes, A., VanWagner, L. B., Wang, N.-Y., Tsao, C. W. & Subcommittee, O. b. o. t. A. H. A. C. o. E. a. P. S. C. a. S. S. (2021) Heart Disease and Stroke Statistics—2021 Update: A Report From the American Heart Association. *Circulation.* 143 (8). doi: 10.1161/CIR.0000000000000950.

Viswakarma, N., Jia, Y., Bai, L., Vluggens, A., Borensztajn, J., Xu, J. & Reddy, J. K. (2010) Coactivators in PPAR-Regulated Gene Expression. *PPAR Research.* 2010, 1-21. doi: 10.1155/2010/250126.

Vuppalanchi, R., Caldwell, S. H., Pyrsopoulos, N., deLemos, A. S., Rossi, S., Levy, C., Goldberg, D. S., Mena, E. A., Sheikh, A., Ravinuthala, R., Shaikh, F., Bainbridge, J. D., Parmar, D. V. & Chalasani, N. P. (2022) Proof-of-concept study to evaluate the safety and efficacy of saroglitazar in patients with primary biliary cholangitis. *Journal of Hepatology.* 76 (1), 75-85. doi: 10.1016/j.jhep.2021.08.025.

Wagner, N. & Wagner, K.-D. (2020) PPARs and Angiogenesis—Implications in Pathology. *International Journal of Molecular Sciences.* 21 (16), 5723. doi: 10.3390/ijms21165723.

Wagner, N. & Wagner, K.-D. (2020) PPAR Beta/Delta and the Hallmarks of Cancer. *Cells.* 9 (5), 1133. doi: 10.3390/cells9051133.

Weikum, E. R., Liu, X. & Ortlund, E. A. (2018) The nuclear receptor superfamily: A structural perspective: The Nuclear Receptor Superfamily. *Protein Science.* 27 (11), 1876-1892. doi: 10.1002/pro.3496.

Willson, T. M., Brown, P. J., Sternbach, D. D. & Henke, B. R. (2000) The PPARs: From Orphan Receptors to Drug Discovery. *Journal of Medicinal Chemistry.* 43 (4), 527-550. doi: 10.1021/jm990554g.

World Health Organization (2020) *Global Health Estimates 2019: Deaths by Cause, Age, Sex, by Country and by Region, 2000-2019.* World Health Organization.

World Health Organization (2021) *Cardiovascular diseases (CVDs)* Available at: https://www.who.int/en/news-room/fact-sheets/detail/cardiovascular-diseases-(cvds) (Accessed: 26 June 2023).

World Health Organization (2021) *Global status report on the public health response to dementia.* Geneva, World Health Organization.

World Health Organization (2022) *World health statistics 2022: monitoring health for the SDGs, sustainable development goals. Geneva: World Health Organization.* ISBN: 978-92-4-005114-0. Licence: CC BY-NC-SA 3.0 IGO.

Xu, H. E., Lambert, M. H., Montana, V. G., Parks, D. J., Blanchard, S. G., Brown, P. J., Sternbach, D. D., Lehmann, J. M., Wisely, G. B., Willson, T. M., Kliewer, S. A. & Milburn, M. V. (1999) Molecular Recognition of Fatty Acids by Peroxisome Proliferator–Activated Receptors. *Molecular Cell.* 3 (3), 397-403. doi: 10.1016/S1097-2765(00)80467-0.

Xu, H. E., Lambert, M. H., Montana, V. G., Plunket, K. D., Moore, L. B., Collins, J. L., Oplinger, J. A., Kliewer, S. A., Gampe, R. T., McKee, D. D., Moore, J. T. & Willson, T. M. (2001) Structural determinants of ligand binding selectivity between the peroxisome proliferator-activated receptors.

Proceedings of the National Academy of Sciences. 98 (24), 13919-13924. doi: 10.1073/pnas.241410198.

Xu, H. E., Stanley, T. B., Montana, V. G., Lambert, M. H., Shearer, B. G., Cobb, J. E., McKee, D. D., Galardi, C. M., Plunket, K. D., Nolte, R. T., Parks, D. J., Moore, J. T., Kliewer, S. A., Willson, T. M. & Stimmel, J. B. (2002) Structural basis for antagonist-mediated recruitment of nuclear co-repressors by PPARα. *Nature.* 415 (6873), 813-817. doi: 10.1038/415813a.

Xu, P., Zhai, Y. & Wang, J. (2018) The Role of PPAR and Its Cross-Talk with CAR and LXR in Obesity and Atherosclerosis. *International Journal of Molecular Sciences.* 19 (4), 1260. doi: 10.3390/ijms19041260.

Yagai, T. & Nakamura, T. (2022) Mechanistic insights into the peroxisome proliferator-activated receptor alpha as a transcriptional suppressor. *Frontiers in Medicine.* 9, 1060244. doi: 10.3389/fmed.2022.1060244.

Yamashita, Arai, Yokote, Araki, Matsushita, Nojima, Suganami & Ishibashi (2019) Efficacy and Safety of Pemafibrate, a Novel Selective Peroxisome Proliferator-Activated Receptor α Modulator (SPPARMα): Pooled Analysis of Phase 2 and 3 Studies in Dyslipidemic Patients with or without Statin Combination. *International Journal of Molecular Sciences.* 20 (22), 5537. doi: 10.3390/ijms20225537.

Yamashita, S., Masuda, D. & Matsuzawa, Y. (2019) Clinical Applications of a Novel Selective PPARα Modulator, Pemafibrate, in Dyslipidemia and Metabolic Diseases. *Journal of Atherosclerosis and Thrombosis.* 26 (5), 389-402. doi: 10.5551/jat.48918.

Yamashita, S., Masuda, D. & Matsuzawa, Y. (2020) Pemafibrate, a New Selective PPARα Modulator: Drug Concept and Its Clinical Applications for Dyslipidemia and Metabolic Diseases. *Current Atherosclerosis Reports.* 22 (1), 5. doi: 10.1007/s11883-020-0823-5.

Yamazaki, Y., Abe, K., Toma, T., Nishikawa, M., Ozawa, H., Okuda, A., Araki, T., Oda, S., Inoue, K., Shibuya, K., Staels, B. & Fruchart, J.-C. (2007) Design and synthesis of highly potent and selective human peroxisome proliferator-activated receptor α agonists. *Bioorganic & Medicinal Chemistry Letters.* 17 (16), 4689-4693. doi: 10.1016/j.bmcl.2007.05.066.

Yang, X., Zhang, W., Chen, Y., Li, Y., Sun, L., Liu, Y., Liu, M., Yu, M., Li, X., Han, J. & Duan, Y. (2016) Activation of Peroxisome Proliferator-activated Receptor γ (PPARγ) and CD36 Protein Expression. *Journal of Biological Chemistry.* 291 (29), 15108-15118. doi: 10.1074/jbc.M116.726737.

Yang, Y., Gocke, A. R., Lovett-Racke, A., Drew, P. D. & Racke, M. K. (2008) PPAR Alpha Regulation of the Immune Response and Autoimmune Encephalomyelitis. *PPAR Research.* 2008, 1-6. doi: 10.1155/2008/546753.

Yokote, K., Yamashita, S., Arai, H., Araki, E., Matsushita, M., Nojima, T., Suganami, H. & Ishibashi, S. (2021) Effects of pemafibrate on glucose metabolism markers and liver function tests in patients with hypertriglyceridemia: a pooled analysis of six phase 2 and phase 3 randomized double-blind placebo-controlled clinical trials. *Cardiovascular Diabetology.* 20 (1), 96. doi: 10.1186/s12933-021-01291-w.

Younossi, Z. M., Blissett, D., Blissett, R., Henry, L., Stepanova, M., Younossi, Y., Racila, A., Hunt, S. & Beckerman, R. (2016) The economic and clinical burden of nonalcoholic fatty liver disease in the United States and Europe. *Hepatology.* 64 (5), 1577-1586. doi: 10.1002/hep.28785.

Yu, K., Bayona, W., Kallen, C. B., Harding, H. P., Ravera, C. P., McMahon, G., Brown, M. & Lazar, M. A. (1995) Differential Activation of Peroxisome Proliferator-activated Receptors by Eicosanoids. *Journal of Biological Chemistry.* 270 (41), 23975-23983. doi: 10.1074/jbc.270.41.23975.

Yu, X., Yi, P., Hamilton, R. A., Shen, H., Chen, M., Foulds, C. E., Mancini, M. A., Ludtke, S. J., Wang, Z. & O'Malley, B. W. (2020) Structural Insights of Transcriptionally Active, Full-Length Androgen Receptor Coactivator Complexes. *Molecular Cell.* 79 (5), 812-823.e4. doi: 10.1016/j.molcel.2020.06.031.

Zhang, S., Hulver, M. W., McMillan, R. P., Cline, M. A. & Gilbert, E. R. (2014) The pivotal role of pyruvate dehydrogenase kinases in metabolic flexibility. *Nutrition & Metabolism.* 11 (1), 10. doi: 10.1186/1743-7075-11-10.

Zhao, D. (2021) Epidemiological Features of Cardiovascular Disease in Asia. *JACC: Asia.* 1 (1), 1-13. doi: 10.1016/j.jacasi.2021.04.007.

Zhou, J., Wilson, K. M. & Medh, J. D. (2002) Genetic analysis of four novel peroxisome proliferator activated receptor-γ splice variants in monkey macrophages. *Biochemical and Biophysical Research Communications.* 293 (1), 274-283. doi: 10.1016/S0006-291X(02)00138-9.

Zhu, L., Hayen, A. & Bell, K. J. L. (2020) Legacy effect of fibrate add-on therapy in diabetic patients with dyslipidemia: a secondary analysis of the ACCORDION study. *Cardiovascular Diabetology.* 19 (1), 28. doi: 10.1186/s12933-020-01002-x.

Zolezzi, J. M., Santos, M. J., Bastías-Candia, S., Pinto, C., Godoy, J. A. & Inestrosa, N. C. (2017) PPARs in the central nervous system: roles in neurodegeneration and neuroinflammation: PPARs in the CNS and neurodegenerative diseases. *Biological Reviews.* 92 (4), 2046-2069. doi: 10.1111/brv.12320.

Zugazagoitia, J., Guedes, C., Ponce, S., Ferrer, I., Molina-Pinelo, S. & Paz-Ares, L. (2016) Current Challenges in Cancer Treatment. *Clinical Therapeutics.* 38 (7), 1551-1566. doi: 10.1016/j.clinthera.2016.03.026.

Chapter 2

PPARα and δ Ligand Design: Honing the Traditional Empirical Method with a More Holistic Overview.

Benjamin S.K. Chua [a], John B. Bruning [b]

[a] School of Biological Sciences, The University of Adelaide, Adelaide, South Australia, 5005, Australia

[b] Institute for Photonics and Advanced Sensing, The School of Biological Sciences, The University of Adelaide, North Tce, Adelaide, South Australia, 5005, Australia

Published, DOI: 10.1007/978-3-030-78315-0_6

Statement of Authorship

Title of Paper	PPARα and δ Ligand Design: Honing the Traditional Empirical Method with a More Holistic Overview.
Publication Status	☑ Published ☐ Accepted for Publication ☐ Submitted for Publication ☐ Unpublished and Unsubmitted w ork w ritten in manuscript style
Publication Details	This paper summarizes the PPARα and δ structures deposited in the PDB, analyses the protein ligand interactions, and gives recommendations for synthesizing ligands specific to each PPAR subtype. The paper also reviews other methods, tools and perspectives for successful PPAR ligand design.

Principal Author

Name of Principal Author (Candidate)	Benjamin Soon Kai Chua		
Contribution to the Paper	Conducted the literature review, synthesis of information, generation of figures and tables, and writing.		
Overall percentage (%)	90		
Certification:	This paper reports on original research I conducted during the period of my Higher Degree by Research candidature and is not subject to any obligations or contractual agreements with a third party that would constrain its inclusion in this thesis. I am the primary author of this paper.		
Signature		Date	16/06/2023

Co-Author Contributions

By signing the Statement of Authorship, each author certifies that:

i. the candidate's stated contribution to the publication is accurate (as detailed above);

ii. permission is granted for the candidate in include the publication in the thesis; and

iii. the sum of all co-author contributions is equal to 100% less the candidate's stated contribution.

Name of Co-Author	John B Bruning		
Contribution to the Paper	Supervised the research and writing of the paper		
Overall percentage (%)	10		
Signature		Date	16/06/2023

Chapter 6
PPARα and δ Ligand Design: Honing the Traditional Empirical Method with a More Holistic Overview

Benjamin S. K. Chua and John B. Bruning

Abstract Peroxisome proliferator-activated receptor (PPAR) ligands have been used in clinical therapy to treat metabolic disease since the 1960s. However, these ligands have side effects that restrict their use, thought to be caused, in part, by their broad specificity. Efforts have been made to synthesize new ligands; however, most have failed to pass clinical trials. Here we examine the available crystal structures of PPAR in complex with ligands to identify common ligand design factors for selectivity towards a PPAR subtype. Methods to improve drug-lead identification and optimization and other factors that may contribute to design of a successful PPAR ligand are discussed.

Keywords PPAR · Metabolism · Specificity · Structure guided drug design

6.1 Introduction to the PPAR Protein

The peroxisome proliferator-activated receptors (PPARs) are a group of ligand-activated nuclear receptors that control various cellular pathways, most notably involved in energy metabolism and homeostasis [23, 61]. These receptors belong to the nuclear receptor type II (NR2) subgroup, which dimerizes with the retinoid X receptor Retinoid X Receptor (RXR). There are three subtypes of PPAR in humans, each with a distinct tissue distribution and function [23, 62]. PPARα coordinates the regulation fatty acid metabolism and is predominantly expressed in the liver, heart and intestines [23, 85]. Activation of PPARα improves serum lipid and cholesterol profiles as well as glucose tolerance in type 2 diabetes mellitus (T2D) patients [23,

B. S. K. Chua · J. B. Bruning (✉)
The University of Adelaide, Adelaide, SA, Australia
e-mail: john.bruning@adelaide.edu.au

M. Z. Badr (ed.), *Nuclear Receptors*, https://doi.org/10.1007/978-3-030-78315-0_6

116]. PPARγ controls adipogenesis and is expressed mainly in adipose tissue and macrophages [18, 51]. Activation of this receptor induces adipocyte differentiation and improves insulin sensitivity and glucose tolerance [23]. PPARδ is expressed ubiquitously, at lower levels throughout the body [7, 19, 102]. Its exact function has not been determined to date, but PPARδ has been shown to play a role in lipid, glucose, lipoprotein and cholesterol metabolism, cancer, muscular fiber switching and endurance and cell differentiation in the CNS [7, 81, 102, 109, 113, 115]. The PPARs coordinate a wide array of genes that, when disrupted, lead to diseases such as metabolic syndrome, heart and neurological diseases and even cancer [23]. Thus, the PPARs represent a prime target for drug development [23, 82].

In fact, synthetic ligands for the PPARs have already been in development for a few decades. It was observed early on that PPARs were able to bind a wide variety of naturally occurring and synthetic ligands [31, 106]. Fibrates have been in clinical use for dyslipidemia since the 1960s but were only found to act through PPARα later on [80]. The discovery of the PPAR NR subfamily sparked a wave of development of synthetic PPAR ligands, of which two classes are currently licensed for clinical use: Fibrates, which bind PPARα preferentially, are used as hypolipidemic agents and Thiazolidines (TZDs) that bind PPARγ preferentially and are used as hypoglycemic agents and insulin sensitizers [23, 91]. However, these drugs have either limited efficacy or presented side effects that limit their therapeutic utility; these include edema, obesity, osteoporosis, hepatotoxicity, bladder cancer, increased atherogenic risk, and mortality rate [16, 19, 23, 111]. Currently, there are no clinically approved drug classes for PPARδ. In the early 2000s, PPARδ agonist GW501516 was synthesized by GlaxoSmithKline (GSK) and displayed excellent cholesterol-modulating properties. However clinical trials of GW501516 were halted when it was found to be carcinogenic in mice models [28, 64, 65]. Initially, to alleviate the side effects seen from single PPAR subtype activation, the idea of dual or even pan subtype acting agonists was conceived. The Glitazar drug class was aimed at reducing the weight gain from PPARγ activation with the fat-oxidizing or energy-modulating properties of PPARα and δ activation, respectively. However, most have been dropped from clinical trials due to various safety concerns [23, 71, 72]. Later, research moved towards improving subtype selectivity [28, 58, 63–65].

The fear of side effects, widely thought to be caused by the lack of subtype selectivity, limits the exploitation of the enormous therapeutic utility of PPAR activation [16, 23]. Despite this, attempts to identify ligands of PPAR and new therapeutic uses for existing drugs are still underway [23, 28]. To facilitate this effort, this review attempts to provide tools to design a subtype specific ligand. First, we present an introduction to the PPAR protein structure, focusing on its ligand binding domain (LBD), and we review different ligands and examine the structural basis for their selectivity and potency, to provide possible explanations for variations of potency between ligands. We also present common ligand design factors, followed by novel methods and other insights that could streamline the reader's efforts in designing a clinically effective and, more importantly, safe PPAR ligand.

6.1.1 *Overall PPAR LBD Protein Structure*

Like most nuclear receptors, the PPAR protein consists of five domains A–E (Fig. 6.1a). The highly mobile domains A and B contain the activation function 1 (AF1) sequence which is involved in ligand-independent transcriptional activation and nuclear localization and also contain sites of phosphorylation [21, 62, 105]. This is followed by domains C, the DNA binding domain (DBD); D, the hinge region; and E, which contains the LBD and Activation Function 2 (AF2) surface (Fig. 6.1a). Amino acid sequence numbers for the PPAR LBD referred to here were taken from the following UniProt entries: Identifier Q07869-1 for PPARα, P37231-2 for PPARγ and Q03181-1 for PPARδ. The secondary structure elements in the LBD were first numbered based on the RXR crystal, a convention that has been used by most crystallographers since (Fig. 6.1b) [106, 113, 114].

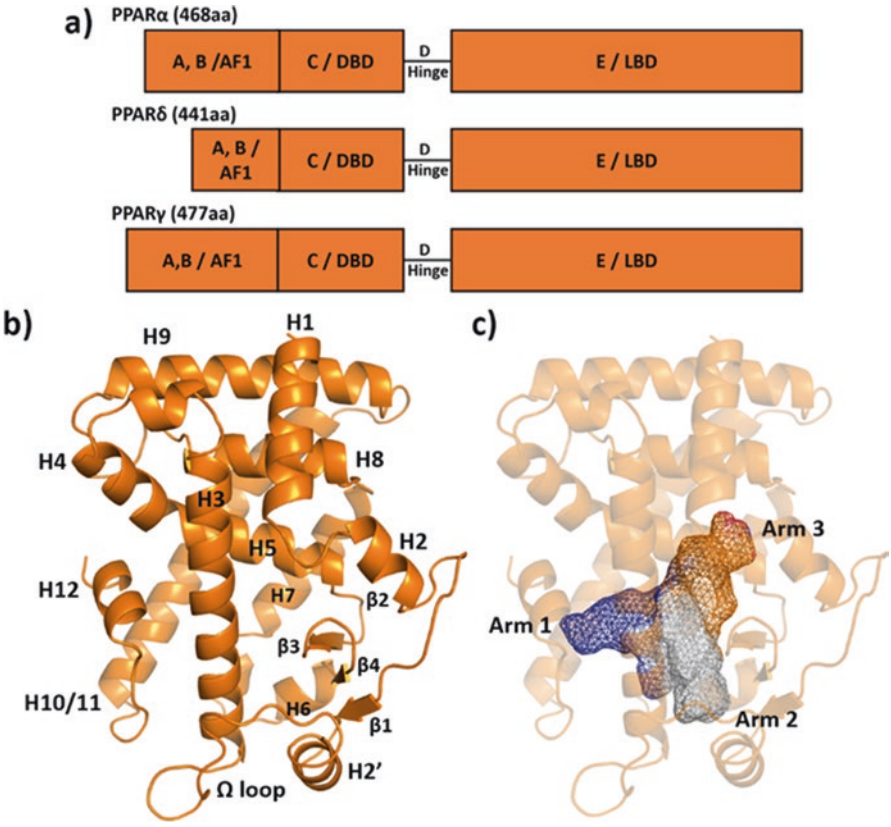

Fig. 6.1 (**a**) The domain architecture of the PPAR protein subtypes. (Adapted from Uppenberg et al. [106]). (**b**) The canonical PPAR LBD with helices labelled according to convention established by Uppenberg et al. [106] (PDB ID: 2GWX). (**c**) The PPARδ Y-shaped LBD cavity highlighted (PDB ID: 2GWX Arms 1: dark blue, 2: light grey, 3: orange)

The LBD (domain E, Fig. 6.1b) consists of 13 α helices and 4 β-stranded sheets. The LBD contains a Y shaped cavity of approximately 1300 Å, bordered by helices H4 and 5 superiorly, H2′ and H6 inferiorly, H3 and Ω loop anteriorly, H7 and H10/11 posteriorly and H12 and β stranded sheets laterally (Fig. 6.1b) [114]. Most ligands of PPAR bind in this cavity, referred to as the ligand binding pocket (LBP). The LBD contains the AF2 surface, which sits in a cleft above H12, formed by H3, H4, H5 and H12. This surface contains the four polar residues that typically form hydrogen bonds with ligands binding in the LBP (Table 6.1). The LBD also contains a dimerization surface made up of H8, H9 and H10 (Fig. 6.2) [42, 115].

The PPAR LBD, compared to other nuclear receptors, contains two unique structural characteristics. Firstly, PPAR contains an extra helix, designated as helix H2′ between the first β sheet strand and helix 3. The extra helix H2′ increases the space in the PPAR LBD (the largest of the NRs) which allows accommodation of a wide variety of ligands [113]. Due to the position of H2′, H2 is arranged differently in the tertiary structure and is hypothesized to allow easier access for ligands [33, 79]. Secondly, the H2′–H3 loop or the 'ω loop' is thermally mobile and typically left unmodelled in most PPAR structures [79, 113]. This loop is the proposed entry site for PPAR ligands and is restricted by a hydrogen bond 'latch', formed by residues α: Y334 and E282, γ: E343 and E291 and δ: N307 and E255 [11, 27, 33]. This flexible H2′–H3 loop is thought to allow PPAR to adapt to chemically diverse ligands [113].

6.1.2 Mechanism of PPAR Gene Transcription

PPAR forms an obligate dimer with RXR, regardless of ligand binding status, via helices 8, 9, 10 and 12 (Fig. 6.2) [7, 21, 42, 121]. The PPARs can dimerize with all three subtypes of RXR, forming different PPAR-RXR subtype complex combinations [108]. These PPAR-RXR complexes then bind to PPAR response elements (PPREs), which are comprised of direct repeat elements of hexanucleotide sequences separated by a single nucleotide spacer (DR1), recruit various cofactors and assemble the gene transcriptional complex to regulate gene transcription [17, 121].

In the apo or antagonist bound state, H12 of PPAR remains flexible and assumes a range of conformations [14, 21, 40, 95, 115, 116, 123]. When H12 is flexible, the larger 3 turn α-helical LXXXIXXXL corepressor motif preferentially occupies the space parallel to H3, bordered by H3, H4, H5 and H12 [52, 116]. This corepressor motif is positioned by interactions between the conserved clamp and motif residues α: K310 and E+2, the carbonyl backbone of α: Y464 and K+7 and α: K292 and carbonyl backbone of L+9 (Fig. 6.2b.). This positions the L+1, I+5 and L+9 residues optimally to interact with the cleft between H3 and H4. The PPAR-corepressor complex then binds to PPREs and causes repression of downstream target genes [88, 102, 121].

Table 6.1 Corresponding residues of the PPAR LBD subtypes
Conserved residues are highlighted in grey, the four polar residues of the AF2 surface that form hydrogen bonds are highlighted in green. Residue numbers used are taken from UniProt ID: P37231-2, Q03181-1, Q07869-1 and aligned using Jalview

Region	PPAR±	PPAR´	PPAR³	Secondary structure
Arm 1	E269	S242	A278	H3
	F273	F246	F282	
	Q277	Q250	Q286	
	S280	T253	S289	
	Y314	H287	H323	H5
	I317	I290	I326	
	F318	F291	Y327	
	F351	F324	F360	H7
	I354	I327	F363	
	H440	H413	H449	H10/11
	V444	M417	L453	
	I447	I420	I456	
	K448	K421	K457	H11-12 loop
	A454	T427	M463	
	A455	S428	S464	
	L456	L429	L465	
	L460	L433	L469	H12
	Y464	Y437	Y473	
Arm 2	I241	I213	I249	β-sheet 4
	M244	I216	M252	H2'
	L247	L219	L255	
	A250	A222	G258	
	E251	E223	E259	
	A268	I241	V277	H3
	R271	H244	R280	
	I272	V245	I281	
	C275	R248	G284	
	C276	C249	C285	
	T279	T252	R288	
	V332	V305	I341	β-sheet 2
	I339	V312	M348	β-sheet 3
	F343	F316	F352	H6
	L344	L317	L353	
	L347	L320	L356	
	M355	I328	M364	H7

Arm 3	N219	N191	P227	H1-2 loop
	M220	M192	L228	
	E282	E255	E291	H3
	T283	T256	A292	
	E286	E259	E295	
	M320	M293	M329	H5
	L321	L294	L330	
	V324	I297	L333	
	M325	V298	M334	β-sheet 1
	M330	L303	V339	β-sheet 2
	L331	L304	L340	
	Y334	N307	E343	β-sheet 2-3 loop
	K358	K331	K367	H7
	F359	F332	F368	

Tab. 6.1 (continued)

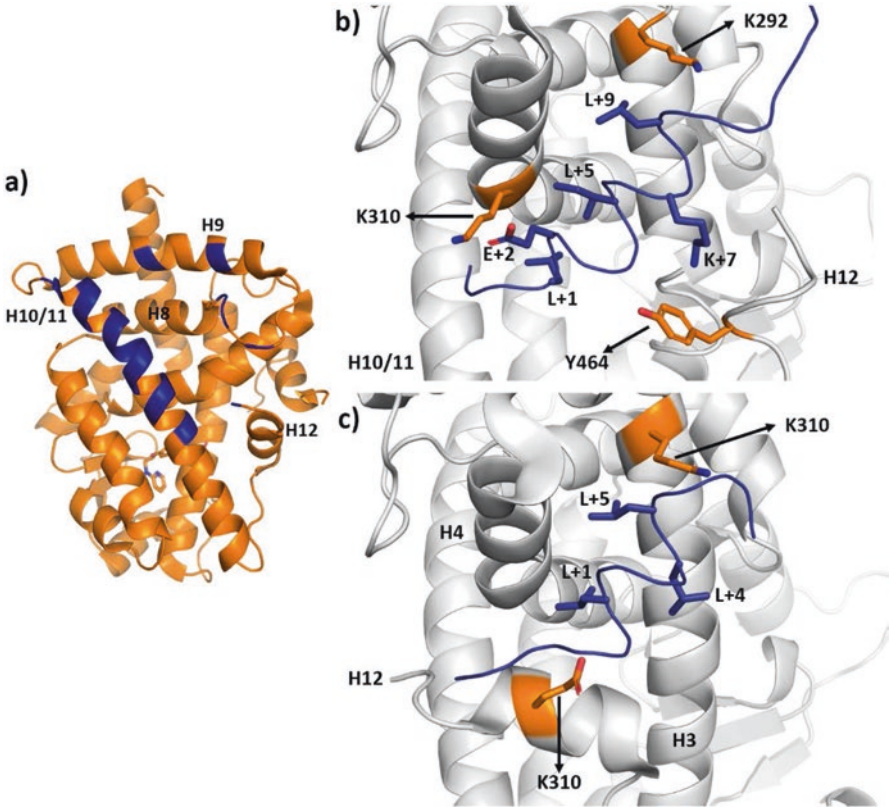

Fig. 6.2 (**a**) PPARδ LBD dimerization surface highlighted (PDB ID: 2GWX), (**b**) PPARα LBD complexed with the corepressor motif (PDB ID: 1KKQ) and (**c**) the coactivator motif (PDB ID: 1K7L)

On agonist binding, H12 is stabilized in the active position through direct or indirect interactions with the ligand [11, 106, 113]. H12 interaction is crucial, but not sufficient for full activation of PPAR [6]. In this active position, the AF2 surface is stabilized – the 'charge clamp' residues α: E462 δ: E436 γ: E472 and α: K292 δ: K265 γ: K301 are optimally positioned to interact with the coactivator motif LXXLL. The charge clamp positions the leucine residues to interact with the hydrophobic pockets created by H3, H4 and H12 and stabilizes the complex. The charge clamp is essential for interaction with the smaller LXXLL motif [116]. The PPAR-RXR-coactivator complex then binds to PPREs, recruits the gene transcriptional machinery and transcribes PPAR controlled genes.

The PPAR complex can also exert functions through non-genomic means, for example, by sequestering coregulators from other metabolic pathways in an apo state or binding to kinases and phosphotases [43, 66, 102].

6.1.3 Differences in LBD Between PPAR Subtypes

Although the overall fold of the three receptors is very similar and about 80% of the LBD residues are conserved, each subtype has a distinct pharmacological or ligand binding profile [41, 101]. The differences in the sequence of the PPAR subtypes lie in regions that are likely to affect ligand binding, such as the Ω loop and, more importantly, the ligand binding pocket [27, 113]. Of note, the Ω loop and H9 regions contain the highest sequence deviation between the PPAR subtypes, which could have implications in interactions with other components of the gene transcriptional complex [21].

Generally, differences in amino acid sequence change the possible interactions that each PPAR subtype can form with the chemical motifs of a ligand; mutation of a single residue was sufficient to change the ligand binding phenotype of one subtype to another [101]. These differences in the ligand binding pocket confer the affinity of each subtype for certain ligands and can be exploited to create subtype specific ligands. In Table 6.1, we list the residues of the ligand binding pocket of the PPAR subtypes [41].

6.2 Catalogue of Known Ligands

Numerous attempts have been made by research groups to exploit the therapeutic effects of PPAR activation. Counting structural-based investigations alone, there are 288 unique entries in the Protein Data Bank (PDB) for PPAR-ligand complexes as of 2020 (rcsb.org) [10]. However, there are currently only 9 PPAR-activating ligands that are approved for clinical use [23]. To attempt to bridge this disparity between effort and successes, we examine the previous attempts at synthesizing PPAR ligands, focusing on ligand design and PPAR-ligand interactions.

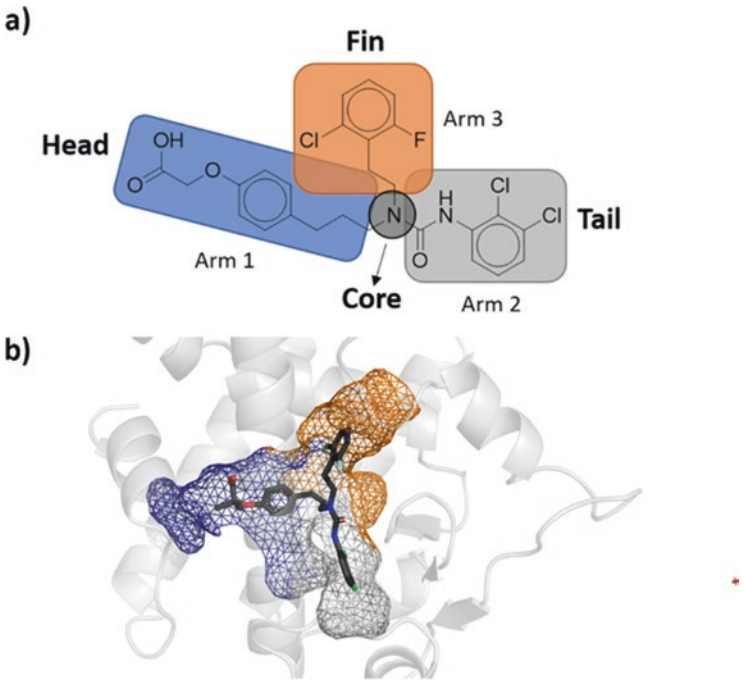

Fig. 6.3 (**a**) The regions of the archetypal Y-shaped PPAR ligand. Arms 1, 2 and 3 are highlighted in blue, orange and grey, respectively (GW2433, PDB ID: 1GWX). (**b**) The PPAR ligand bound to the PPAR LBP. The parts of the ligand are highlighted

Ligands generally consist of a few regions, a 'head' that interacts with residues in Arm 1, a 'tail' that forms hydrophobic interactions with residues in Arm 2 and a 'fin' region that interacts with residues in Arm 3. These three Arms are connected to the ligand 'core, marked by the amino acid residue α: T279, δ: T252, γ: R288' (Fig. 6.3) [113]. PPARγ ligand design has already been discussed in a previous publication [62]. Here we focus on examining attempts at synthesizing chemical tools and therapeutic drugs for PPARα and δ, although we will include PPARγ – activating dual or pan agonist examples. PPAR-ligand interactions were determined using Discovery Studio Visualizer© with the default search parameters [29]. We define the total number of interactions as all unique interactions between receptor and ligand.

6.2.1 PPARα Ligands

In the early 1950s, an analogue of an insecticide was found to have plasma cholesterol-lowering effects [16, 80]. This class of drugs, called fibrates, were later found to mediate their effects through the PPARα receptors [80]. Thus, PPARα

became the first PPAR subtype with a clinically available, subtype specific drug class. Fibrates contain the fibrate head group, a phenoxyisobutyric acid motif in the ligand head region which makes hydrogen bond contacts with the AF2 surface, and are typically full agonists for PPARα [13, 16].

Fenofibrates are one such example in clinical use – they have considerably milder side effects compared to the PPARγ-specific TZDs and have been beneficial in treating cholesterol- or lipid-related conditions [16, 23]. However, PPARα-specific fibrates have low affinity and poor subtype selectivity and may as a result have lower efficacy than statins [16, 23, 76]. As such, research groups have focused on designing more potent full agonists of PPARα, hypothesizing that increasing affinity will increase therapeutic effects [58, 76, 97].

6.2.1.1 PPARα Full Agonists

WY14643 or Pirinixic Acid

WY14643, a potent PPARα agonist, has been used in therapy as an anticholestoremic agent. It was initially used for its peroxisome-proliferating properties in the discovery of PPAR [49, 93] and has since been used as a control for PPARα drug discovery [11]. The WY14643-PPARα complex was first crystallized by Bernardes and group, in their study to understand its binding mode and the role of PPARα in ocular inflammation (Fig. 6.4, Table 6.2) [11]. This is the first crystal structure of a single PPARα LBD monomer binding to two ligand molecules.

WY14643 is smaller than the typical ligand, only containing the head and core regions. Like other PPAR agonists, WY14643 forms hydrogen bonds with 4/4 of the polar residues in Arm 1 and hydrophobic contacts with seven residues from Arm 1, 2 and 3. Selectivity is likely imparted by interactions with the larger side chains of residues α: Y314 and M330 that are unique to PPARα. Surprisingly, it was found that WY14643 also bound to a secondary binding site, around the solvent exposed surface of H3, sandwiched between H2′, H2′–H3 loop and H3. The charge cluster formed between α: D453-H274-K266-WY14643 in the second binding pocket anchors H12 to H3 via the Ω loop, resulting in stabilization of the AF2 surface. The stabilization imparted by the binding of two ligand molecules in the LBD was sufficient to induce gene transactivation despite making substantially fewer contacts in the LBP.

GW590735/Compound 25a

GSK developed the high affinity PPARα agonist GW590735 to treat dyslipidemia and tackle the risk factors of coronary artery disease. GW590735 lowered serum triglycerides (TG), very low density cholesterol (VLDLc) and low density cholesterol (LDLc) and raised high density cholesterol (HDLc) in animal models. It had improved potency and selectivity for PPARα compared to previous Fibrates, which

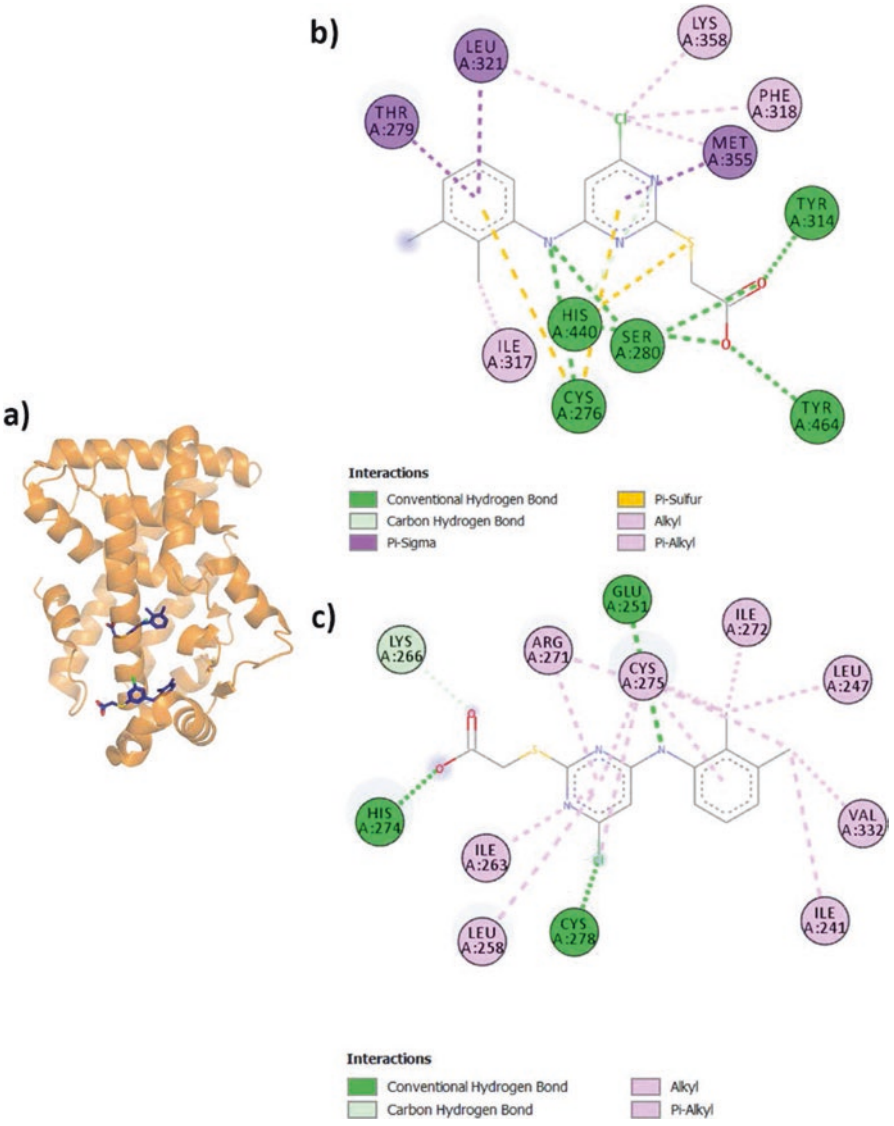

Fig. 6.4 (**a**) PPARα LBD in orange complexed with WY14643 in dark purple (PDB ID: 4BCR). (**b**) Interaction map of WY14643 in the LBP with PPARα. (**c**) Interaction map of WY14643 in the secondary binding site with PPARα

was proposed to increase therapeutic benefits and reduce side effects [58, 97]. The PPARα-GW590735 complex was crystallized by Sierra et al. [97] as part of their SAR study to synthesize a high affinity, PPARα-specific agonist using GW501516 as the lead compound (Fig. 6.5, Table 6.3).

Table 6.2 The activity of WY14643 at each PPAR subtype

	EC_{50} (μM)		
Ligand	PPARα	PPARδ	PPARγ
WY14643	5.38	>100	>100

EC_{50} values were determined by dual luciferase assay in HepG2 cells, values were normalized to *Renilla* activity

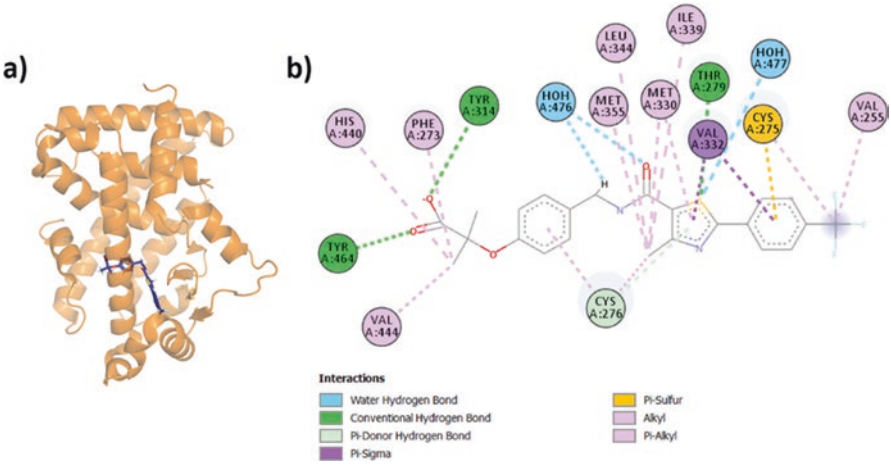

Fig. 6.5 (**a**) PPARα LBD in orange complexed with GW590735 in dark purple (PDB ID: 2P54). (**b**) Interaction map of GW590735 with PPARα

By swapping the oxy-propanoic head with an isobutyric acid head, the L-shaped GW590735 makes hydrogen bond contacts with 4/4 of the polar residues of Arm 1 in PPARα. The gem-dimethyl groups make additional hydrophobic interactions with α: V444 (γ: L453, δ: M417) and F273. The bulkier corresponding residues of α: V444 in the other subtypes may sterically interfere with ligand, accounting for the affinity of the gem-methyl motif for PPARα.

The amide group in the core region confers rigidity to the ligand, which tends to increase the stability of interactions with and affinity for the LBP [113]. The phenoxy motif in the head region as well as the thiazole motif in the tail region interacts with α: C276. The 4-methyl substitution on the thiazole motif makes multiple alkyl interactions with α: M330 and M355 in Arm 3 and I339 on the β3. Corresponding residues of PPARδ and γ in Arm 3 are not bulky enough to form favorable interactions with the 4-methyl group. In addition, corresponding residue of α: I339 in PPARγ (γ: M348) might sterically interfere with this group. The tail region makes hydrophobic and π-donor hydrogen bond interactions with residues in Arm 2 as well as α: V255 in the Ω loop. Only the corresponding residues in PPARδ can make similar interactions with the ligand, which explains why this scaffold was successful in both PPARα and δ but not γ.

Table 6.3 The activity of GW590735 at each PPAR subtype

	EC_{50} (μM)		
Ligand	PPARα	PPARδ	PPARγ
GW590735/25a	0.004 ± 0.002 (95%)	2.83 ± 1.18 (82%)	>10

EC_{50} values were determined by dual luminescence assay in CV-1 cells, measuring alkaline phosphatase activity normalized to β-galactosidase activity. Maximal activity (%) was defined as the activity of Compound 25a, Compound 1 and Rosiglitazone for PPARα, δ and γ, respectively [97]

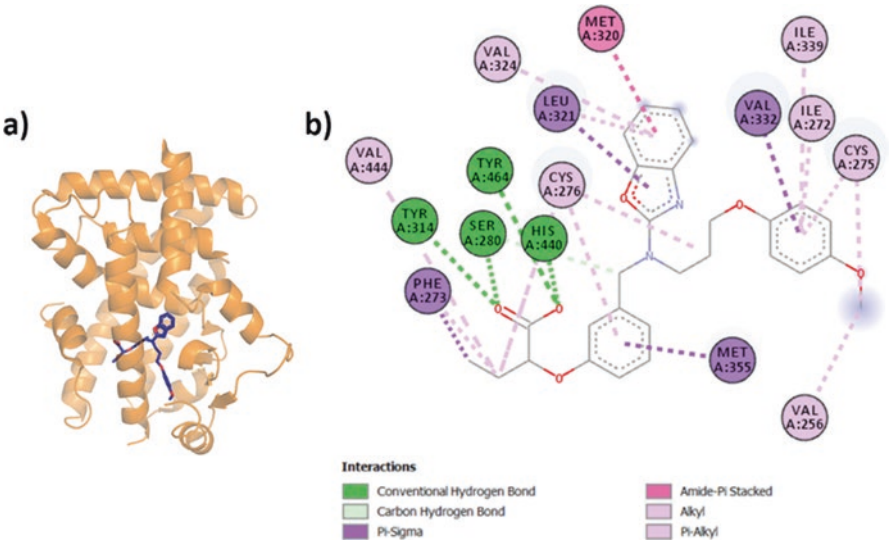

Fig. 6.6 (**a**) PPARα LBD in orange complexed with pemafibrate in dark purple (PDB ID: 6L96). (**b**) Interaction map of pemafibrate with PPARα

Table 6.4 The activity of Permafibrate at each PPAR subtype

Ligand	PPARα	PPARδ	PPARγ
Pemafibrate	IC_{50} (μM)		
	0.13 ± 0.04	–	9.58 ± 1.85
	EC_{50} (μM)		
	0.001	1.58	1.10

IC_{50} values were determined by isothermal titration calorimetry (ITC). EC_{50} values were taken from Yamazaki et al. [119], determined by dual luciferase assay in HepG2 cells, values were normalized to *Renilla* activity

Pemafibrate

Pemafibrate is a selective, high affinity PPARα agonist synthesized by Kowa Pharmaceuticals [119]. Pemafibrate has been in clinical trials for treatment of multiple ailments and is set to replace previous PPARα agonists [23]. The

PPARα-Pemafibrate-SRC1 complex was crystallized by Kawasaki and colleagues (Fig. 6.6, Table 6.4) [58].

Pemafibrate has a Y-shaped design that contains a 2-phenoxybutanoic acid head, instead of a isobutyric acid head as seen in GW590735. This fibrate head forms hydrogen bonds with 4/4 of the polar residues in Arm 1, but sits slightly lower to accommodate the shorter distance to the core, as well as the fin substituent in Arm 3 [119]. The unique α: Y314 residue in PPARα allows the formation of favourable hydrogen bonds with the acid head compared to the histidine residues in PPARδ/γ. The ethyl substituent (versus gem-dimethyl) interacts more closely with α: F273 than V444. α: M355 'stretches out' (compared to GW590735 structure PDB ID: 2P54) to interact with the phenoxy motif in the head region. The head is connected to the fin and tail regions via a nitrogen core.

Pemafibrate is one of the only fibrates that contains a benzoxazole fin substituent that interacts with three residues in Arm 3. The area of the tail region adjacent to the core does not contain substituents. The tail 1-butoxy-4-methoxybenzene motif interacts with residues in Arm 2. The methyl group at the tip of the tail region rotates and interacts with α: V256 or V247. The lack of posterior facing substituents in the core and tail regions might contribute to the decrease of affinity for PPARδ, due to its smaller residues in Arm 2 compared to other subtypes (δ: V245, I328, V312).

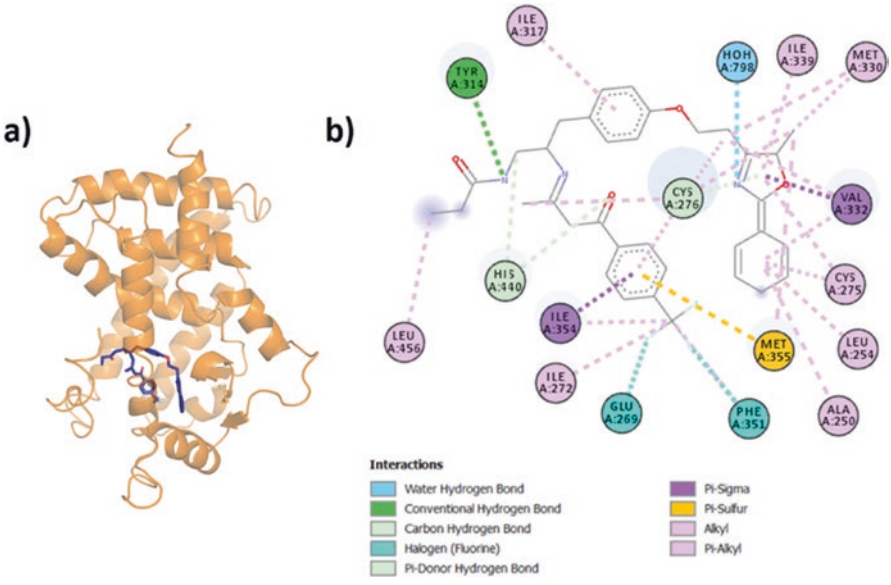

Fig. 6.7 (**a**) PPARα LBD in orange complexed with GW6471 in dark purple (PDB ID: 1KKQ). (**b**) Interaction map of GW6471 with PPARα

Table 6.5 The activity of GW6471 at each PPAR subtype

	IC_{50} (μM)		
Ligand	PPARα	PPARδ	PPARγ
GW6471	0.24	–	–

IC_{50} values were determined by dual luminescence assay in CV-1 cells, measuring alkaline phosphatase activity normalized to β-galactosidase activity, in the presence of 10 nM GW409544

6.2.1.2 PPARα Antagonist

GW6471

GW6471 is an antagonist developed by GSK using the PPARα and γ dual agonist GW409544 as a chemical scaffold. The PPARα-GW6471-SMRT complex was crystallized by Xu and colleagues in 2002 to explore the structural basis for PPAR antagonist binding (Fig. 6.7, Table 6.5) [116]. This was the first PPAR structure crystallized with an antagonist.

The N-shaped GW6471 contains a non-acidic N-phenylpropyl-propanamide head motif. The propylamide group occupies the typical position of H12 residue α: L460, destabilizing H12 and disrupting the AF2 surface. This group also forms interactions with the corepressor. This group sits 5.2 Å further laterally towards H12 than typically seen with the carboxylic acid groups in full PPARα agonists.

GW6471 contains a unique amino-phenylbutanone substituent at the head region that is not normally seen in ligands. This motif occupies the inferior part of Arm 1 and extends into the posterior area of Arm 2, forcing H3 and H7 outward, compared to full agonists. The tail substituent utilizes a similar design to GW590735, having a methyl substituent that projects into the back of the junction/Arm 2 area. This tail substituent makes interactions with Arm 2 and Ω loop residues α: L254 and A250.

6.2.2 PPARδ Ligands

As of 2020, PPARδ remains as the only PPAR subtype without a clinically approved drug. Unlike PPARα and γ, there were no preexisting drug classes that were found to mediate their effects through PPARδ, and early efforts to create such a drug class were plagued by discouraging results [23, 64, 65]. Nevertheless, the clinical success of Bezafibrate shows that PPARδ activation is not inherently toxic [16]. Due to its role in energy and lipid metabolism, and the side effects seen with long term use of PPARα/γ-based therapies, PPARδ makes for a particularly attractive therapeutic target [16, 28, 113]. Most of the work on PPARδ ligands have been directed towards creating full agonists.

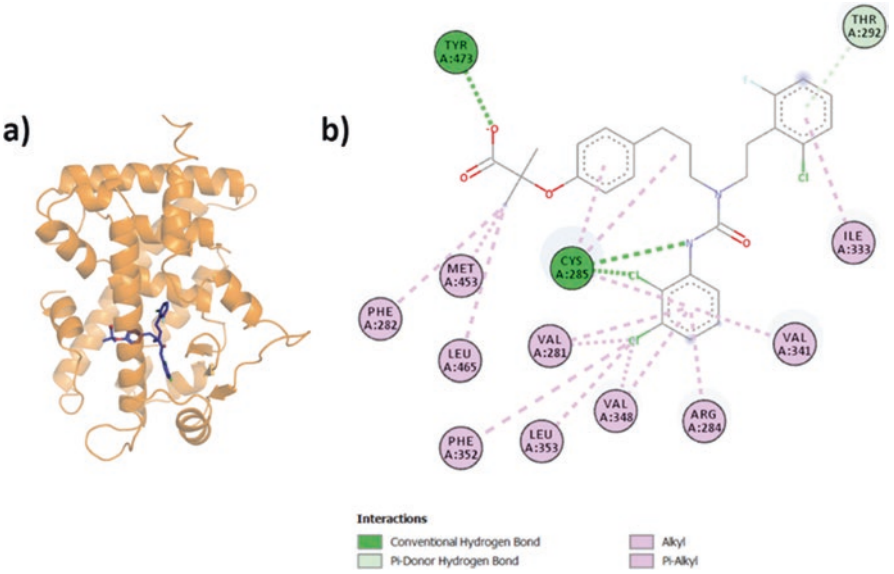

Fig. 6.8 (**a**) PPARδ LBD in orange complexed with GW2433 in dark purple (PDB ID: 1GWX). (**b**) Interaction map of GW2433 with PPARδ

Table 6.6 The activity of GW2433 at each PPAR subtype

	EC_{50} (μM)		
Ligand	PPARα	PPARδ	PPARγ
GW2433	0.17	0.19	2.5

EC_{50} values were taken from [112], determined by dual luminescence assay in CV-1 cells, measuring alkaline phosphatase activity normalized to β-galactosidase activity

6.2.2.1 PPARδ Full Agonists

GW2433

GW2433 was the first high affinity PPARδ ligand developed by GSK [13]. GW2433 was developed from a 'biased library' comprised of motifs taken from other successful ligands. The PPARδ-GW2433 complex was crystallized by Xu and colleagues in their study (Fig. 6.8, Table 6.6) [114]. This was the first crystal structure of the human PPARδ LBD. Despite containing a fibrate head, this ligand shows affinity for PPARδ, showing that the fibrate motif is insufficient for PPARα specificity.

GW2433 is a Y-shaped ligand that contains the typical phenoxyisobutyric acid head that forms hydrogen bonds with 3/4 of the polar residues in Arm 1. The gem-dimethyl substituents form hydrophobic interactions with five residues in the inferior region of Arm 1. GW2433 wraps around δ: C249, which interacts with the different regions of the GW2433. The tail phenyl also makes interactions with six

residues in Arm 2. GW2433 contains a chloro-ethylbenzene fin substituent, that interacts with four residues along the Arm 1/Arm 3 region. In PPARγ, residues γ: M348 and R288 likely interferes sterically with the halogen substituents on the ligand in Arms 2 and 3, respectively, selecting against PPARγ affinity. The three ligand regions are connected to a nitrogen core.

GW2331

GW2331 is a fibrate that was developed as a high affinity ligand, to be used as a control for PPAR α and γ in ligand binding assays. In 1997, Kliewer and colleagues designed and used GW2331 in an inhibitory assay to prove that several fatty acids and eicosanoids bind to PPARα directly. GW2331 was shown to activate PPARδ at concentrations of >1 μM). Interestingly, despite being a PPARα/γ dual agonist, GW2331 was only ever crystallized with PPARδ. The PPARδ – GW2331 complex was obtained by Takada and colleagues as part of their study into PPAR subtype selectivity and PPAR phylogenetics (Fig. 6.9, Table 6.7) [101]. Strangely, this compound was successfully crystallized with PPARδ despite having no detectable IC_{50} values.

GW2331 is a Y-shaped ligand that contains a 2-methyl-2-phenoxybutanoic acid head, which makes hydrogen bond interactions with 3/4 of the polar residues in Arm 1. The methyl and ethyl groups in the head region form hydrophobic

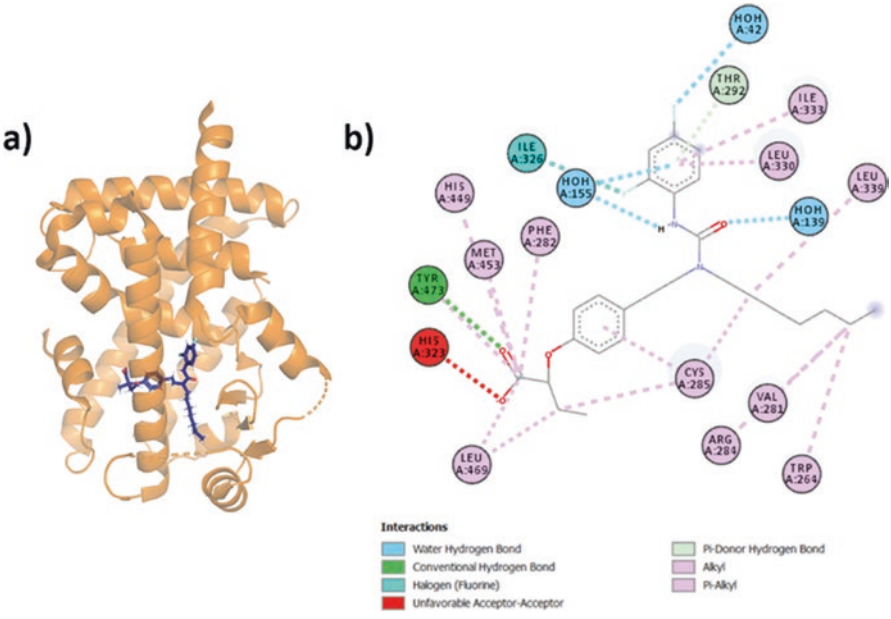

Fig. 6.9 (**a**) PPARδ LBD in orange complexed with GW2331 in dark purple (PDB ID: 1Y0S). (**b**) Interaction map of GW2331 with PPARδ

Table 6.7 The activity of GW2331 at each PPAR subtype

Ligand	PPARα	PPARδ	PPARγ
GW2331	IC_{50} (μM)		
	0.348	ND	0.670
	EC_{50} (μM)		
	0.071 ± 0.035 (79%)	ND	0.249 ± 0.238 (90%)

IC_{50} and EC_{50} values were taken from [32]. IC_{50} values were determined by fluorescence polarization assay. EC_{50} values were determined by luciferase assay in HEK293 cells. Maximal activity (%) was defined as the activity of 1 μM of ligand relative to 1 μM of GW2331 and Rosiglitazone for PPARα and γ, respectively. ND – not determined; compounds had no activity against PPARδ

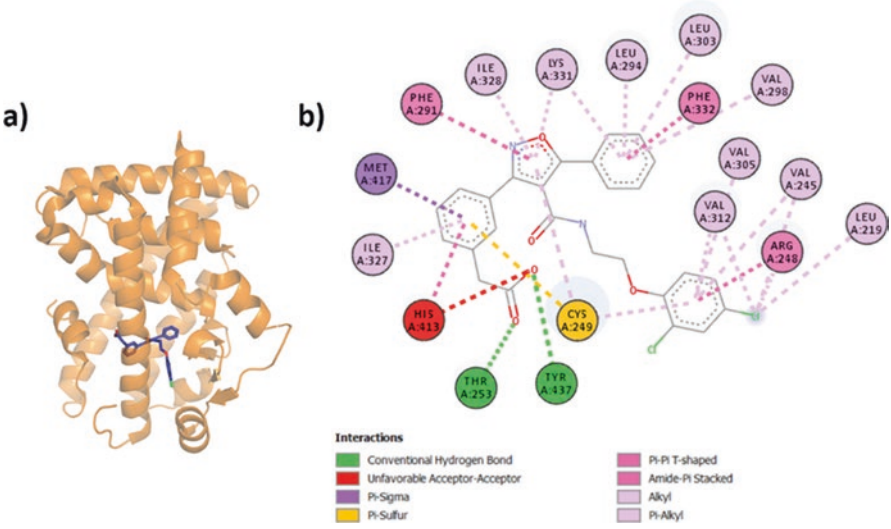

Fig. 6.10 (**a**) PPARδ LBD in orange complexed with LC1765 in dark purple (PDB ID: 2J14). (**b**) Interaction map of LC1765 with PPARδ

interactions with Arms 1 and 2.The larger ethyl group was observed to sit very near to H3 (3.3 Å) possibly causing repulsion. The larger δ: M417 also likely interferes with the accommodation of these alkyl substituents in Arm 1. The heptane chain in the tail region makes interactions with only three residues in Arm 2, 1 in Arm 3 and δ: W228 on the Ω loop. GW2331 contains a N-(1,4-difluorophenyl)amide fin substituent, which makes interactions with four residues in Arms 1 and 3 as well as a bridging interaction to δ: T252 in Arm 2. The three ligand regions are connected to a nitrogen core. The repulsion caused by the ethyl substituent in the head coupled, with the lack of interactions in Arm 2 possibly explains the selectivity of GW2331 against PPARδ.

Table 6.8 The activity of LC1765 at each PPAR subtype

	EC_{50} (μM)		
Ligand	PPARα	PPARδ	PPARγ
LC1765	>10	0.07 (83%)	>10

EC_{50} values were determined by cell-based transactivation assay. Maximal activity (%) was defined as relative to GW501516 for PPARδ

LC1765

Epple and colleagues derived PPARδ selective full agonist LC1765, to be used as a tool for investigation of the pharmaceutical benefits of activating PPARδ. The PPARδ-LC1765 complex was crystallized by Epple and colleagues, in their study to improve the pharmacokinetic properties of their 3,4,5-trisubstituted isoxazoles (Fig. 6.10, Table 6.8) [38].

LC1765 had a Y-shaped design, with a phenylacetic acid head region, forming hydrogen bond interactions with 4/4 of the polar residues in Arm 1 and hydrophobic interactions with two and one residues in Arms 1 and 2, respectively. This phenyl ring in the head region is 1,3 substituted as opposed to 1,4 substituted and thus sits lower than other PPARδ ligands to accommodate the core and fin substituents in Arm 3.

The isoxazole core of LC1765 sits further posteriorly than where the typical ligand core sits and interacts with residues in the interface of Arms 1, 2 and 3. Corresponding methionine residues of δ: I328 in PPARα and γ (α: M355 γ: M364) likely clash sterically with the core, selecting for affinity towards PPARδ. The phenyl fin substituent projects backward into H7, making hydrophobic contacts with four residues in the inferior area of Arm 3. The tail region contains a 1-ethoxy-2,4-dichlorobenzene, N-linked via an amide to the isoxazole core. This amide lies in the same plane as the core, pushing the 1-ethoxy-2,4-dichlorobenzene substituent forward anteriorly. The 2,4 substituted chloride groups on the tail substituent points down and backwards, making hydrophobic interactions with six residues in Arm 2.

Compound 48

This PPARδ selective full agonist was developed by GSK, continuing their work on partial agonists [39, 96]. Optimization of a lead from a search of their internal database resulted in Compounds 46 and 47. The Compound 48–PPARδ complex was crystallized to understand the structural basis for the activity of the partial agonist Compounds 46 and 47 in the series (Fig. 6.11, Table 6.9).

This Y-shaped Compound 48 contains a naphthoxyacetic acid head region. It forms the hydrogen bond interactions with 4/4 of the polar residues in Arm 1. The naphthalene interacts with three residues in Arms 1 and 2. The sulfonamide core interacts with δ: F291 and forces a cis conformation between the head and tail regions. The butane fin substituent interacts with five residues in the inferior part of

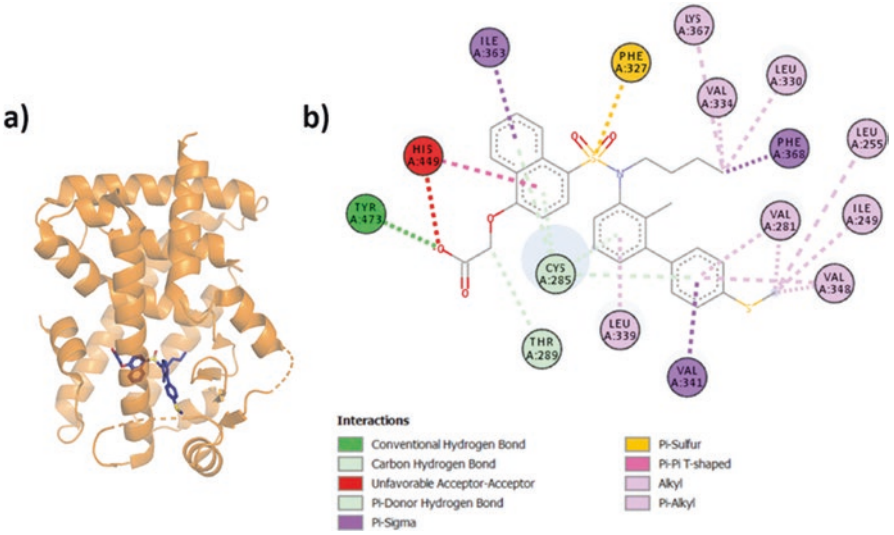

Fig. 6.11 (**a**) PPARδ LBD in orange complexed with Compound 48 in dark purple (PDB ID: 3PEQ). (**b**) Interaction map of Compound 48 with PPARδ

Table 6.9 The activity of Compound 48 at each PPAR subtype

Ligand	PPARα	PPARδ	PPARγ
Compound 48	IC_{50} (μM)		
	–	0.0316	–
	EC_{50} (μM)		
	–	0.0079 (90%)	–

IC_{50} values were determined by scintillation proximity assay (SPA), using [H^3]GW2331, [H^3]GW2433 and [H^3]BRL49653 as radioligands for PPARα, δ and γ, respectively. EC_{50} values were determined by dual luminescence assay in CV-1 cells, measuring alkaline phosphatase activity normalized to β-galactosidase activity. Maximal activity (%) was defined as relative to GW501516 for PPARδ.

Arm 3. The tail biphenyl interacts with four residues in Arms 1 and 2. The methanethiol *para* substituent interacts with five residues in Arm 2 and δ: W228 on the Ω loop, spanning the whole of Arm 2.

Affinity to PPARδ is likely imparted by the close proximity of the core and tail to δ: I328 and V312, respectively, and by the fin interactions with δ: L303 and V298 in Arm 3. The corresponding bulkier methionine residues in PPARα and γ likely clash sterically with compound 48, presumably having a negative impact on PPARα/γ binding.

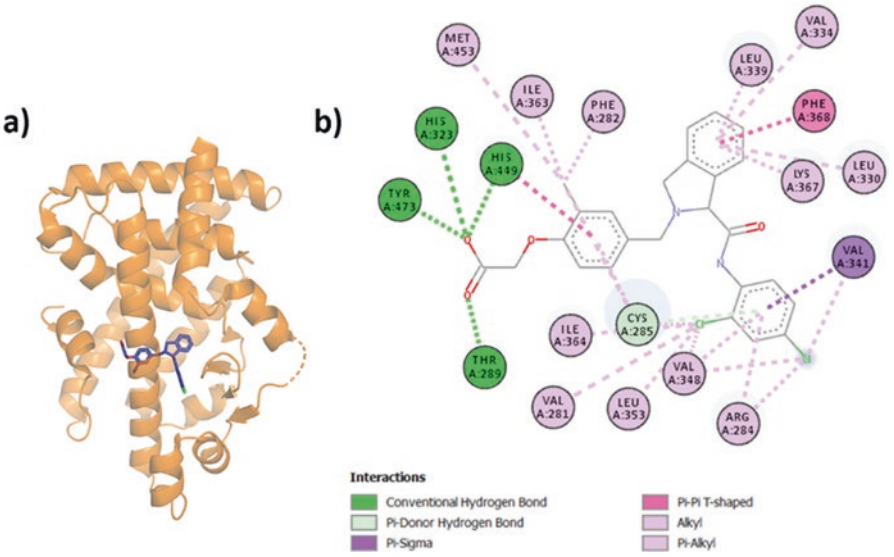

Fig. 6.12 (**a**) PPARδ LBD in orange complexed with Compound 5 in dark purple (PDB ID: 3OZ0). (**b**) Interaction map of Compound 5 with PPARδ

Table 6.10 The activity of isoquinoline compound 5 at each PPAR subtype

	EC_{50} (μM)		
Ligand	PPARα	PPARδ	PPARγ
Compound 5	>30	0.025 (110%)	>30

EC_{50} values were determined by luciferase assay in HEK-293 cells. Maximal activity (%) was defined as relative to GW501516

Isoquinoline Compound 5

Compound 5 was part of the optimization process that led to identification of tetrahydroisoquinoline compound 18 by Luckhurst and colleagues using leads from AstraZeneca's hit identification program. The PPARδ-Compound 5 complex was crystallized by Luckhurst and colleagues (Fig. 6.12, Table 6.10) [72] in their study to identify a less lipophilic drug for PPARδ.

In the Y-shaped Compound 5, the (2-methylphenoxy)acetic acid motif makes hydrogen bonds with 4/4 of the polar residues and hydrophobic contacts with five other residues in Arm 1. The tail 2,4-dichlorophenylamide motif also interacts with seven residues in the superior part of Arm 2. The phenyl portion in the core isoquinoline act as a fin substituent, interacting with five residues in Arm 3. However, it does not make any interactions with residues at the bottom of Arm 2 or the Ω loop due to the shorter ligand tail. This double ring core sits further back into H7. Corresponding methionine residues in PPARα and γ (α: M355 γ: M364) likely clash with the core motif, selecting for affinity towards PPARδ. This compound is the

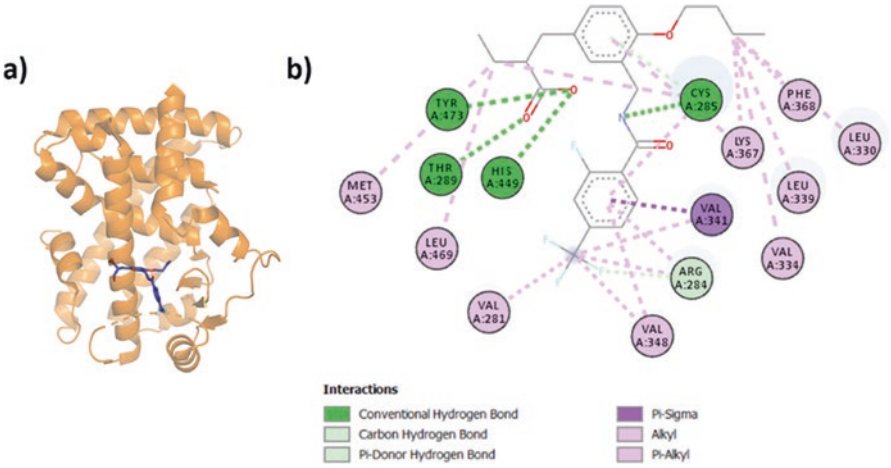

Fig. 6.13 (**a**) PPARδ LBD in orange complexed with TIPP-204 in dark purple (PDB ID: 2ZNP). (**b**) Interaction map of TIPP-204 with PPARδ

Table 6.11 The activity of TIPP-204 at each PPAR subtype

	EC_{50} (μM)		
Ligand	PPARα	PPARδ	PPARγ
TIPP-204	0.250	0.00091	1.100

EC_{50} values were determined by GAL4 transactivation activity in HEK-293 cells, relative to GW501516 for PPARδ and rosiglitazone for PPARγ [54]

only reported crystal structure of a full agonist with 110% activity compared to GW501516 in a cell-based assay.

TIPP-204

Kasuga and group synthesized the PPARδ-specific agonist TIPP-204 from the PPARα/γ agonist TIPP-401, which was in turn synthesized from PPARα agonist KCL [54]. The PPARδ-TIPP-204 complex was crystallized by Oyama and colleagues to understand the different binding modes in their series of compounds that includes PPARα and PPARδ-specific agonists and a PPARα/γ dual agonist (Fig. 6.13, Table 6.11) [82]. The TIPP ligands have a reversed amide compared to KCL and differ from each other by an extended fin substituent in TIPP-204 compared to TIPP-401.

TIPP-204 is a Y-shaped ligand. The isobutyric acid head interacts with 3/4 polar of the residues and three other residues (including δ: M417) in Arm 1. The 1,3,4-substituted phenoxy core interacts with two residues in Arm 2 and 3. Its tail substituent, an amino linked 2-fluoro-4-(trifluoromethyl)benzene interacts with

V312, four other residues and δ: W228 on the Ω loop. Its fin butanol substituent interacts with δ: I328 in Arm 2, and four other residues in Arms 3.

Affinity for PPARδ is likely mediated by δ: L303 and V298 in Arm 3. The larger corresponding residues in PPARα/γ (α: M330 and α: M325 γ: M334) sterically clash with the fin. The tail substituent interacts with δ: V312 and potentially clashes with PPARγ (γ: M348). The relatively high affinity for PPARα might be due to the reversed amide, which makes contacts with α: T279 (δ: T252, γ: R288) and the flexibility of α: M355, to accommodate the fin substituent. This might also be the case for the other methionine residues in PPARα (α: M330 and M325). Strangely, increasing the length of the fin also increased the potency towards PPARγ, compared to TIPP-401. This may suggest the ligand adopts an alternative top-down conformation in PPARγ as seen for compounds GL479 and compound 21 and that the fin substituent may be able to make additional contacts in Arm 1 (PDB ID: 4CI5 and 3H0A).

GW0742

PPARδ full agonist GW0742 was synthesized by GSK along with GW501516 and showed superior selectivity against PPARγ compared to GW501516 [100]. Batista and colleagues crystallized the PPARδ-GW0742 complex in their study (Fig. 6.14, Table 6.12) [9]. This compound is still in the preclinical stages as of 2020, although it was found to be associated with side effects [23, 28].

The L-shaped ligand contains a (2-methylphenoxy)acetic acid motif in the head region that interacts with 3/4 of the polar residues and hydrophobic contacts with

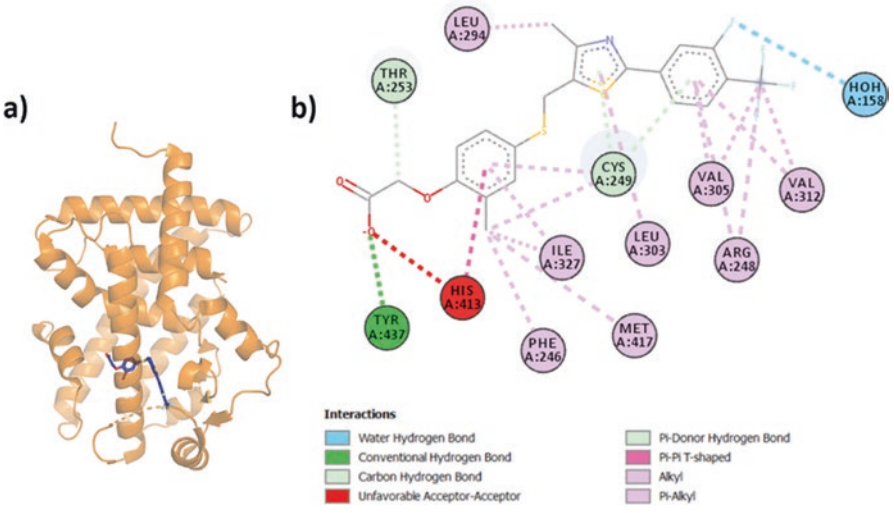

Fig. 6.14 (**a**) PPARδ LBD in orange complexed with GW0742 in dark purple (PDB ID: 3TKM). (**b**) Interaction map of GW0742 with PPARδ

Table 6.12 The activity of GW0742 at each PPAR subtype

	EC_{50} (μM)		
Ligand	PPARα	PPARδ	PPARγ
GW0742	ND	0.00325	ND

EC_{50} values were determined by dual luciferase assay in HepG2 cells, values were normalized to *Renilla* activity. ND – not determined; EC_{50} values could not be calculated up to 10 μM of ligand

five residues in Arm 1. The thiazole core interacts with two residues in Arm 3 and one in Arm 2. The 3-fluoro,4-(trifluormethyl)benzene motif in the tail region interacts with three residues in Arm 2. The compound GW0742 does not contain a fin substituent.

The structural selectivity was likely imparted by three residues: δ: I328 α: M355 γ: M364, δ: V312 α: I339 γ: M348 and δ: M417 α: V444 γ: L453. The corresponding methionine residues at position δ: I328 and V312 will clash with PPARα and PPARγ, respectively, increasing selectivity for the PPARδ. This was confirmed by the binding assays of δ: I328M and V312M mutants [9]. δ: M417 in Arm 1 makes closer contacts with the carboxylate head than the corresponding PPARα and γ residues, which might contribute to GW0742's strong selectivity towards PPARδ. The interactions with other residues in Arm 1 likely contribute to the high potency of GW0742.

GW501516, Compounds 1–16

GW501516 was the first highly selective and potent PPARδ to make it to clinical trials when, unfortunately, it was found to be carcinogenic in mice models [64, 65, 81, 100]. Wu and colleagues synthesized Compounds 1–16 to mimic fatty acids and to occupy Arm 3 of the PPARδ LBD, using GW501516 as a benchmark in their SAR study. The PPARδ-GW501516/Compounds 1–16 complexes were crystallized by Wu and colleagues as part of their SAR study to identify new selective and potent compounds for PPARδ (Fig. 6.15, Table 6.13) [113]. Here we discuss GW501516 as well as their representative lead compounds 2 and 4.

The L-shaped GW501516 contains a (2-methylphenoxy)acetic acid head motif. The acetic acid motif forms hydrogen bonds with 4/4 of the polar residues in Arm 1. The 2-meythlphenoxy motif in the head region makes hydrophobic contacts with five other residues in Arms 1 and 2. It is connected to the core tail motif via a methanethiol linker. The tail motif consists of a 3-thiazolidine, which makes contacts with δ: C249 and two other residues, and a (trifluoromethyl)benzene, which makes interactions with five other residues in Arm 2.

In the Y-shaped Compound 2, the phenoxyhexanoic acid head region forms hydrogen bonds with 1/4 polar residues in Arm 1 and forms hydrophobic interactions with five other residues in Arms 1, 2 and 3. The head region is linked via a methyl chain to an amide core. This amide core forms hydrogen bonds with one water molecule and is N-linked to an isopropyl fin substituent. The fin substituent

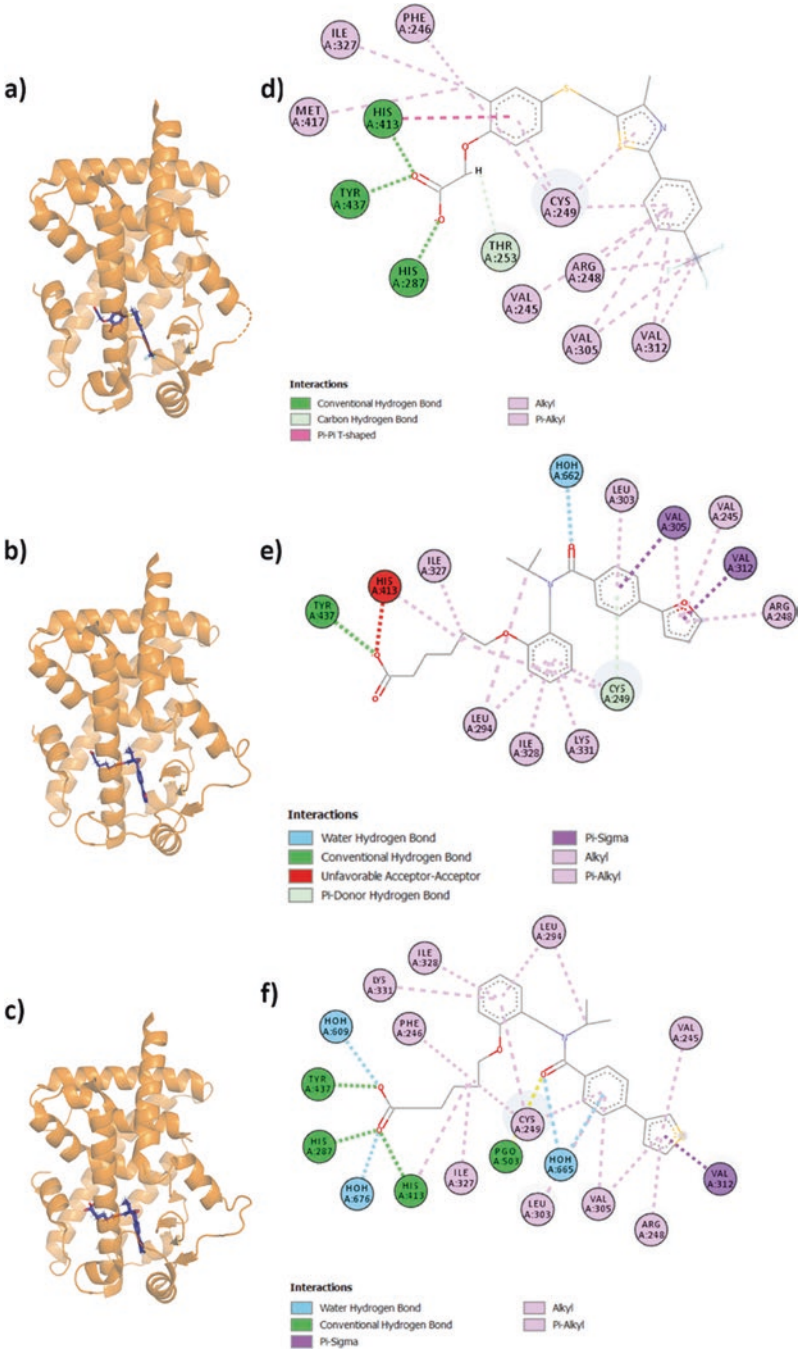

Fig. 6.15 (**a**) PPARδ LBD in orange complexed with GW501516 in dark purple (PDB ID: 5U46). (**b**) PPARδ LBD in orange complexed with Compound 2 in dark purple (PDB ID: 5U3R). (**c**) PPARδ LBD in orange complexed with Compound 4 in dark purple (PDB ID: 5U3T). (**d**) Interaction map of GW501516 with PPARδ. (**e**) Interaction map of Compound 2 with PPARδ. (**f**) Interaction map of Compound 4 with PPARδ

Table 6.13 The activity of lead compounds at each PPAR subtype

	EC_{50} (μM)		
Ligand	PPARα[a]	PPARδ	PPARγ[a]
GW501516	2.591 ± 0.0012	0.0012 ± 0.0003	2.591 ± 0.0012
Compound 2	>10	0.0090 ± 0.0003	>10
Compound 4	>10	0.0172 ± 0.0007	>10

EC_{50} values were determined by luciferase assay
[a]EC_{50} for PPARα and γ was given as a single value in the study. Luciferase assay methods were not given

forms hydrophobic contacts with one residue in Arm 3. The core is C-linked to the biaryl tail substituent. The biaryl tail substituent consists of a phenyl ring and 2-furyl group, which forms hydrophobic contacts with five residues in Arm 2.

In Compound 4, the phenoxyhexanoic acid head region forms hydrogen bonds with 3/4 polar residues in Arm 1 and forms hydrophobic interactions with six other residues in Arms 1, 2 and 3. The head region is also linked via a methyl chain to an amide core and contains the same N-linked isopropyl fin substituent. The core makes hydrogen bonds with one water molecule and S-1,2-propanediol, an additive used in crystallization. The fin makes hydrophobic interactions with one residue in Arm 3. The core is also C-linked to a biaryl tail substituent, which consists of a phenyl ring and 3-thienyl group, which makes hydrophobic contacts with five residues in Arm 2 and 3.

Affinity of GW501516, Compounds 2 and 4 against PPARα and PPARγ is likely imparted by residue δ: V312. The larger corresponding methionine residues (α: M330 γ: M348) interfere with the tail region of GW501516. Compared to Compounds 2 and 4, GW501516 has lower absolute affinity towards PPARα and γ [100] (EC_{50} α: 1.1 μM and γ: 0.85 μM). This might be due to the lack of posterior facing substituents in the core or tail region of GW501516. Even though Compounds 2 and 4 do not contain such substituents, the core region is positioned slightly lower compared to GW501516 and closer toward H7, causing interference with corresponding residues of δ: I328 and V298 in PPARα and γ (α: M355, M325 γ: M364, M334). In PPARα, interference between the larger α: Y314 (δ: H287 γ: H323) residue on the AF2 surface and the longer hexanoic acid head would possibly force the core and tail substituent of the ligand into an unfavourable position, clashing with corresponding residue of δ: L303 (α: M330). These observations were confirmed by mutagenesis [113].

Compound 18 and Compound 13

Compounds 18 and 13 were synthesized by Astellas pharma in SAR studies which eventually led to MA-0204, a potential therapeutic for Duchenne Muscular Dystrophy (DMD). These compounds were optimized to have better pharmacokinetics and an improved safety profile over GW501516 [63–65]. The

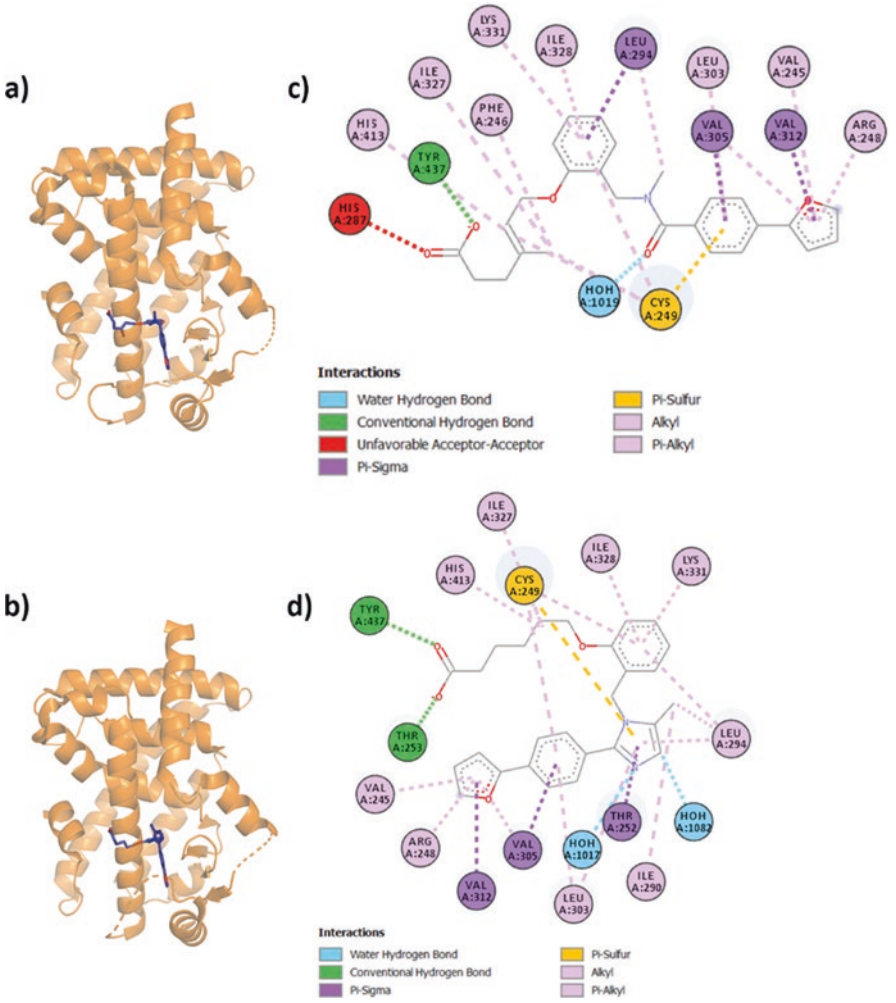

Fig. 6.16 (**a**) PPARδ LBD in orange complexed with Compound 18 in purple (PDB ID: 5XMX). (**b**) PPARδ LBD in orange complexed with Compound 13 in purple (PDB ID: 5ZXI). (**c**) Interaction map of Compound 18 with PPARδ. (**d**) Interaction map of Compound 13 with PPARδ

PPARδ – Compound 18/13 complexes was crystallized by Lagu and colleagues (Fig. 6.16, Table 6.14) [63–65] in their search for a potent, selective and safer PPARδ agonist.

These L-shaped compounds differ slightly in the arrangement of the acidic head and tail region. Compound 18 contains a 4-methyl,4-hexenoic acid head and an amide motif in the tail, and Compound 13 contains a hexanoic acid head and an imidazole motif in the tail. The head region of compounds 18 and 13 makes similar hydrogen-bonding interactions with 4/4 of the polar residues and hydrophobic contacts with two residues in Arm 1 and 2. The extra 4-methyl substituent in compound

Table 6.14 The activity of lead compounds at each PPAR subtype

Ligand	PPARα	PPARδ	PPARγ
	IC_{50} (μM)		
Compound 18	–	0.057 ± 0.001	–
	EC_{50} (μM)		
Compound 18	6.100	0.0370 ± 0.0050	>10.000
Compound 13	6.970	0.0007 ± 0.0002	>10.000

IC_{50} values were determined by surface plasmon resonance (SPR) [63]. EC_{50} values were determined by luciferase assay in CV-1 cells [63]

18 makes an additional contact in Arm 1. The core phenoxy motif in both compounds interacts with four residues in Arms 2 and 3. The 2-phenylfuran tail motif of Compound 18 interacts with 5 residues in Arm 2 and 1 in Arm 3. The larger imidazole motif of Compound 13 makes additional contacts with 3 residues in Arms 1 and 2.

The compound has increased affinity for PPARδ due to having the head and tail connected to the phenyl core at the *ortho* position, pushing the core closer to H7. Corresponding methionine residues of δ: I328 in PPARα and γ (α: M355 γ: M364) would clash sterically with the core. The corresponding residue of δ: V312 in PPARγ (γ: M348) would also interfere with the 2-furyl group in the tail end, selecting for affinity towards PPARδ.

6.2.2.2 PPARδ Partial Agonists

Partial agonism of PPARδ has been studied by several groups, motivated by the increased safety profile seen from partial agonism of PPARγ [14]. Having a suite of chemical tools is beneficial for exploration of PPAR function, but whether partial agonism of PPARδ has any therapeutic benefits over full agonism remains to be seen.

Compound 2

Novo Nordisk synthesized the partial PPARδ agonist Compound 2. The goal of lowered efficacy came from the observations of the reduced side effects seen in partial agonists for PPARγ [14, 84]. This compound was derived from GW501516, to design a rigid PPARδ selective full agonist that could fill the PPAR LBP. The PPARδ-Compound 2 complex was crystallized by Pettersson and colleagues to investigate the structural basis for partial agonism induced by Compound 2 (Fig. 6.17, Table 6.15) [84]. This was the first crystal structure of a partial agonist of PPARδ.

Compound 2 utilizes a Y-shaped design, swapping the methyl substituent in the (2-methylphenoxy)acetic acid in the head region to a cyclopentyl. The head region

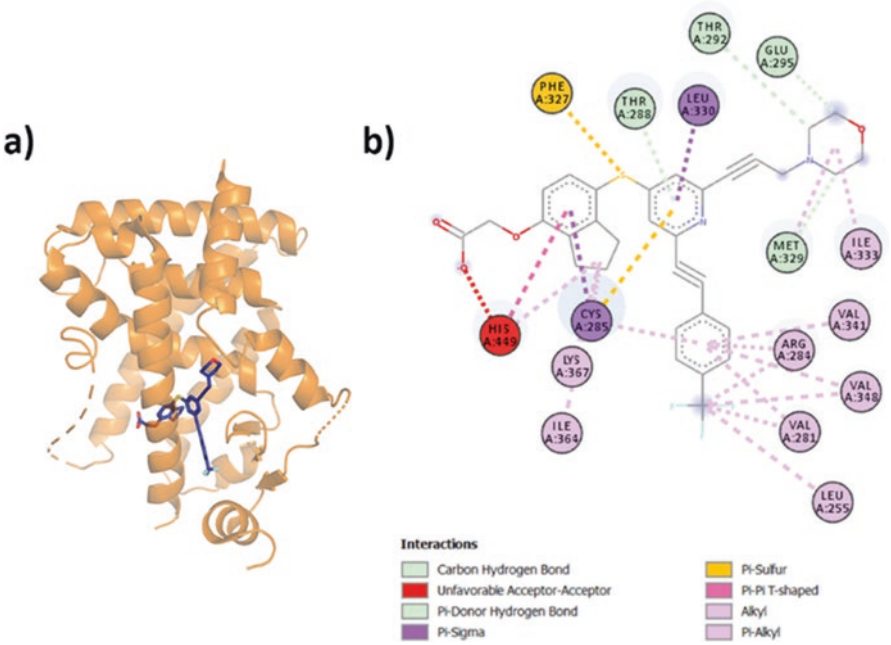

Fig. 6.17 (**a**) PPARδ LBD in orange complexed with Compound 2 in dark purple (PDB ID: 2Q5G). (**b**) Interaction map of Compound 2 with PPARδ

Table 6.15 The activity of Compound 2 at each PPAR subtype

	EC_{50} (μM)		
Ligand	PPARα	PPARδ	PPARγ
Compound 2	ND	0.13 (39%)	ND

EC_{50} values were determined by dual luminescence assay in CV-1 cells, measuring alkaline phosphatase activity normalized to β-galactosidase activity. Maximal activity (%) was defined as relative to NNC 61-4655, GW501516 and rosiglitazone for PPARα, PPARδ and PPARγ, respectively. ND – not determined; EC_{50}.was not calculated if activity was lower than 10% at ligand concentration of 30 μM

adopts a lower position compared to full agonists and forms hydrogen bonds with 1/4 of the polar residues in Arm 1 and interacts with five other residues in Arms 1, 2 and 3. The lack of interactions with residues on H12 might have destabilized H12 (unmodelled in structure) and the AF2 surface, contributing to its partial agonistic activity. The core interacts with two residues from Arms 2 and 3. The trifluoromethylbenzene motif in the tail interacts with five residues in Arm 2. The morpholine motif in the fin interacts with four residues in Arm 3, reaching up to H5. The fin is connected to the core via a rigid alkyne carbon linker.

To accommodate the fin, the core sits further anteriorly than usually seen for PPARδ ligands. The cyclopentyl motif in the head is too close to the core due to the short core-head sulphur linker and points posteriorly into δ: I328, selecting against

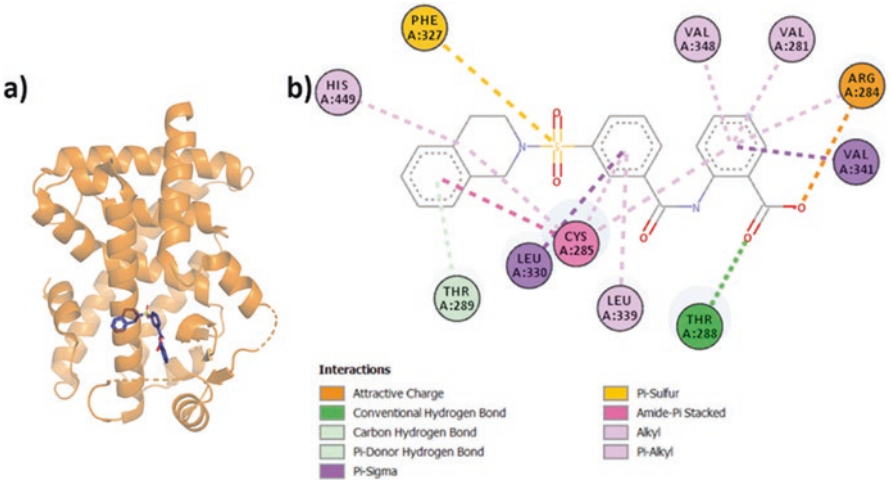

Fig. 6.18 (**a**) PPARδ LBD in orange complexed with GW9371 in dark purple (PDB ID: 3DY6). (**b**) Interaction map of GW9371 with PPARδ

PPARα/γ affinity as previously mentioned and pushing H7 out posteriorly. This causes the carboxylic acid head to sit lower than other PPARδ agonists, preventing interaction with H12. The trifluoromethyl substituent in the tail also interacts with δ: V312, selecting against PPARγ affinity.

GW9371

The PPARδ partial agonist GW9371 was identified by GSK through a high throughput screening (HTPS) of their in-house compound collection. This was part of their efforts to identify a range of chemical tools to investigate biological role of PPARδ. The PPARδ-GW9371 complex was crystallized by Shearer and colleagues in their SAR study that yielded partial agonist compounds GSK1115 and GSK7227 (Fig. 6.18, Table 6.16) [96].

The L-shaped GW9371 contains a tetrahydroisoquinoline interacts with 1/4 of the polar residues in Arm 1 and 2 residues in Arms 2 and 3. This motif does not form hydrogen bonds with H12, likely resulting in its partial agonistic activity. It contains a sulfonyl core which makes a total of four interactions with residues in Arms 1, 2 and 3. A formylanthranilic acid motif comprises the tail region of the ligand and makes polar interactions with δ: T252 and R248 and hydrophobic interactions with four other residues in Arm 2.

Ortho-substituted acids are generally not tolerated in Arm 1 of PPARδ, and thus the compound binds to Arm 2 as predicted by Shearer and colleagues [96]. The proximity of the carboxylic acid and amide substituents likely causes intra-ligand interactions, further reducing the likelihood of accommodation of this motif in Arm 1, which then places the tetrahydroisoquinoline motif in Arm 1. Affinity to PPARδ

Table 6.16 The activity of GW9371 at each PPAR subtype

Ligand	PPARα	PPARδ	PPARγ
GW9371	IC_{50} (μM)		
	>10	0.1258	7.9432
	EC_{50} (μM)		
	–	1.2589 (61%)	–

IC_{50} values were determined by scintillation proximity assay (SPA), using [H^3]GW2331, [H^3]GW2433 and [H^3]BRL49653 as radioligands for PPARα, PPARδ and PPARγ respectively. EC_{50} values were determined by dual luminescence assay in CV-1 cells, measuring alkaline phosphatase activity normalized to β-galactosidase activity. Maximal activity (%) was defined as relative to GW501516 for PPARδ.

is likely due to the proximity of the sulfonyl core to δ: I328 (α: M355 γ: M364), clashing with methionine residues in and selecting against PPARα and γ.

6.2.3 Dual or Pan Agonist Ligands

Dual or pan agonists refer to agonists that bind specifically to at least two or all three of the PPAR subtypes, respectively, and result in transactivation of PPAR genes. Groups that synthesize these agonists attempt to combine the unique pharmacological benefits of activating each PPAR subtype [23]. This was initially done to alleviate the side effects seen in activation of a single subtype, such as weight gain with PPARγ-activating TZDs. Another motive for such therapeutics is that ligands combining the effects of multiple receptors may reduce risks associated with using multiple drugs in combination to treat complex ailments [6]. Some dual agonists combine the effects of different nuclear receptor families or enzymes, opening the possibility of an even wider range of pharmacological outcomes [37, 68]. Examining the structural basis of dual and pan agonists often reveal important insights into selectivity and unexpected binding modes.

6.2.3.1 PPARα/γ Dual Agonists

TZD-based therapies were efficacious in lowering blood glucose levels, decreasing insulin levels and increasing sensitivity to insulin. However, they did not modulate serum lipid levels and often resulted in weight gain. Since fibrates modulate serum lipid levels, the prominent idea during this period was to create ligands with PPAR α and γ affinity. In theory this would combine the insulin sensitization effects of TZDs and the lipid modifying effects of fibrates to reduce the weight gain seen with TZD treatment [34]. Based on this hypothesis, many groups have attempted to synthesize dual α/γ agonists, however many of these drugs have been dropped during various stages of clinical trials due to side effects [23, 110, 123]. Since then, several PPARα/γ dual agonists have been approved for clinical use, such as lobeglitazone.

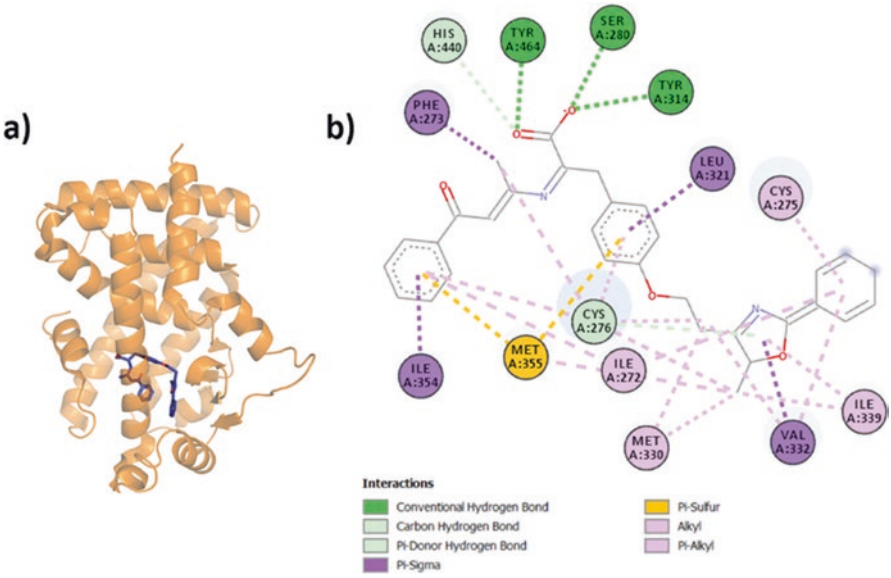

Fig. 6.19 (**a**) PPARα LBD in orange complexed with GW409544 in dark purple (PDB ID: 1K7L). (**b**) Interaction map of GW409544 with PPARα

Table 6.17 The activity of GW409544 at each PPAR subtype

	EC_{50} (μM)		
Ligand	PPARα	PPARδ	PPARγ
GW409544	0.0023 ± 0.0005	>10	0.00028 ± 0.00006

EC_{50} values were determined by dual luminescence assay in CV1 cells, measuring luciferase activity normalized to β-galactosidase activity

This suggests that PPARα/γ dual agonism may not be inherently toxic, but further investigation is required to synthesize and determine the safety of new compounds [45, 123].

GW409544

GW409544 is a L-tyrosine analogue, modified from Farglitazar [115]. It was developed to improve on Farglitazar's affinity for PPARα and to balance its affinity for PPARα and γ [115]. The GW409544-PPARα-SRC1 complex was crystallized by Xu and colleagues (Fig. 6.19, Table 6.17) [115], continuing their study into the structural determinants of selectivity between the PPAR subtypes [114, 115]. This is the first PPARα crystal structure published, as well as the first PPARα structure crystallized with a coactivator motif.

The N-shaped GW409544 forms H bonds with 4/4 of the polar residues in Arm 1. It contains an atypical a phenyl-butanone substituent near the acidic head group.

This group points downwards from Arm 1 diagonally towards H7, pushing against F273 and interacting with four other residues in Arms 1 and 2. The phenoxy core wraps around H3 and makes interactions with three different residues in Arms 2 and 3. The tail substituent makes interactions with six residues in Arms 2 and 3.

Selectivity to PPARα and γ is likely imparted by a few features. Firstly, residues α: F273 γ: F282 is flexible and can accommodate the head phenyl-butanone substituent, but in PPARδ, δ: M417 likely prevents flexing of corresponding δ: F246. This substituent is able to occupy the posterior part of Arm 2, a characteristic not normally seen in PPARα agonists due to methionine residues α: M355 and M330. The phenyl ring at the tip of the tail does not contain bulky, polar substituents that interfere with γ: M348. Finally, the tail is connected to the phenoxy core via a flexible alkyl chain linker. The skinny alkyl chain does not interfere with methionine residues in PPARα/γ (α: M355 γ: M364 and α: M330) and allows optimal positioning of the tail substituent to accommodate PPAR γ: M348 in Arm 2. The smaller corresponding residues in PPARδ are unable to form favourable interactions with GW409544.

Azetidinone Compounds 17 and 35

Wang and colleagues from Bristol-Myers Squibb developed the dual α/γ agonist Azetidinone Compounds 17 and 35. These compounds were developed to be structurally distinct from Muraglitazar to avoid the associated side effects seen with the ligand [110]. Only the PPARα-Compound 17 complex was crystallized to confirm the stereochemistry of Compound 17, as part of their SAR study (Fig. 6.20, Table 6.18) [110].

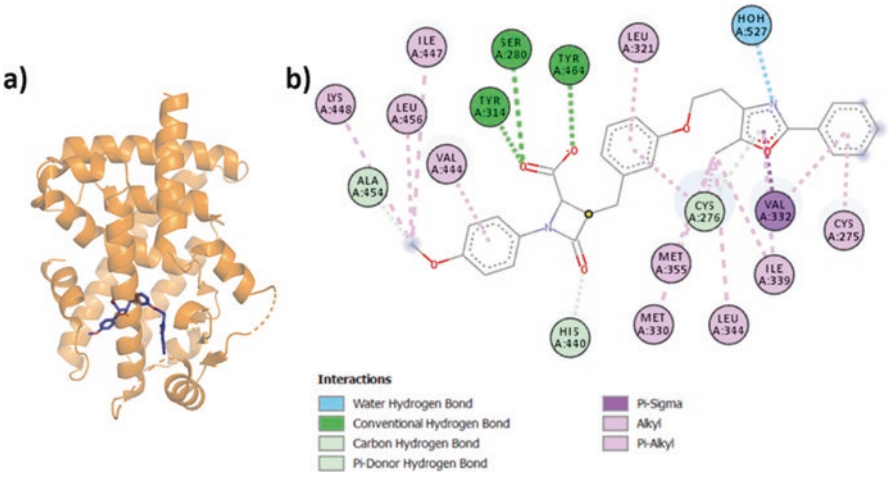

Fig. 6.20 (**a**) PPARα LBD in orange complexed with Compound 17 in dark purple (PDB ID: 2REW). (**b**) Interaction map of Compound 17 with PPARα

Table 6.18 The activity of Azetidinone compound 17 at each PPAR subtype

Ligand	PPARα	PPARδ	PPARγ
Compound 17	IC_{50} (μM) Ki		
	0.360 ± 0.005	–	0.100 ± 0.003
	EC_{50} (μM)		
	0.070 ± 0.005 (>90%)	–	0.090 ± 0.021 (>90%)

IC_{50} values were determined by fluorescence polarization assay (FPA), against probes 7-benzyloxy-4-trifluoromethyl coumarin and 7-benzyloxyresorufin for PPARα and PPARγ, respectively. EC_{50} values were determined by luciferase assay in HEK293 cells. Maximal activity (%) was defined as activity of 1 μM of ligand relative to 1 μM of GW-2331 and rosiglitazone for PPARα and γ, respectively.

Compound 17 is an N-shaped, full PPARα/γ agonist. In the head region, the 2-substituted formic acid group on the azetidinone motif forms hydrogen bonds with 4/4 of the polar residues in Arm 1. It contains an atypical 1-substituted methoxbenzene motif which makes interactions with five residues in the 'Benzophenone pocket', bordered by H3, H11 and the H11–H12 loop. The *para*-substituted phenoxy core interacts with two residues in Arms 2 and 3. This optimally positions the tail substituent, to interact with the bulky methionine residues in the Arm 3 region of PPARα. In the tail region, the aryl rings interact with eight residues in Arm 2 and 3.

Compound 17 selects against PPARδ, similar to GW409544 described above. The core and tail motifs are identical, making contacts with the methionine residues in PPARα and PPARγ. However, α: F273 flexes and points towards H7 allowing the head methoxybenzene substituent to occupy the benzophenone pocket, a conformation previously seen for PPARγ in Montanari et al. [77]. PPARδ cannot accommodate this substituent due to the presence of a bulkier δ: M417 residue in this pocket. This conformation of α: F273 might also push H3 anteriorly (compared to all other PPARαs structures examined) and induce instability to H3, accounting for the variation in affinity between Compound 17 and GW409544.

GL479

In 2012, Giampietro and colleagues synthesized compound GL479, a dual α/γ agonist that had full agonistic activity toward PPARα and partial agonistic activity toward PPARγ. This specific activation profile was selected based on the hypothesis that side effects seen in previous dual α/γ agonists were caused by full agonist activity toward PPARγ [45]. The PPARα/γ – GL479 complexes were crystallized by dos Santos and colleagues in their study (Fig. 6.21, Table 6.19) [33].

The L-shaped GL479 contains a fibrate head which forms hydrogen bonds with ¾ of the polar residues in Arm 1. The gem-dimethyl motif here interacts with four other residues in Arm 1. An ethanol core links the head to the tail region. The tail azobenzene motif interacts with six residues in Arms 2 and 3. Interestingly, in

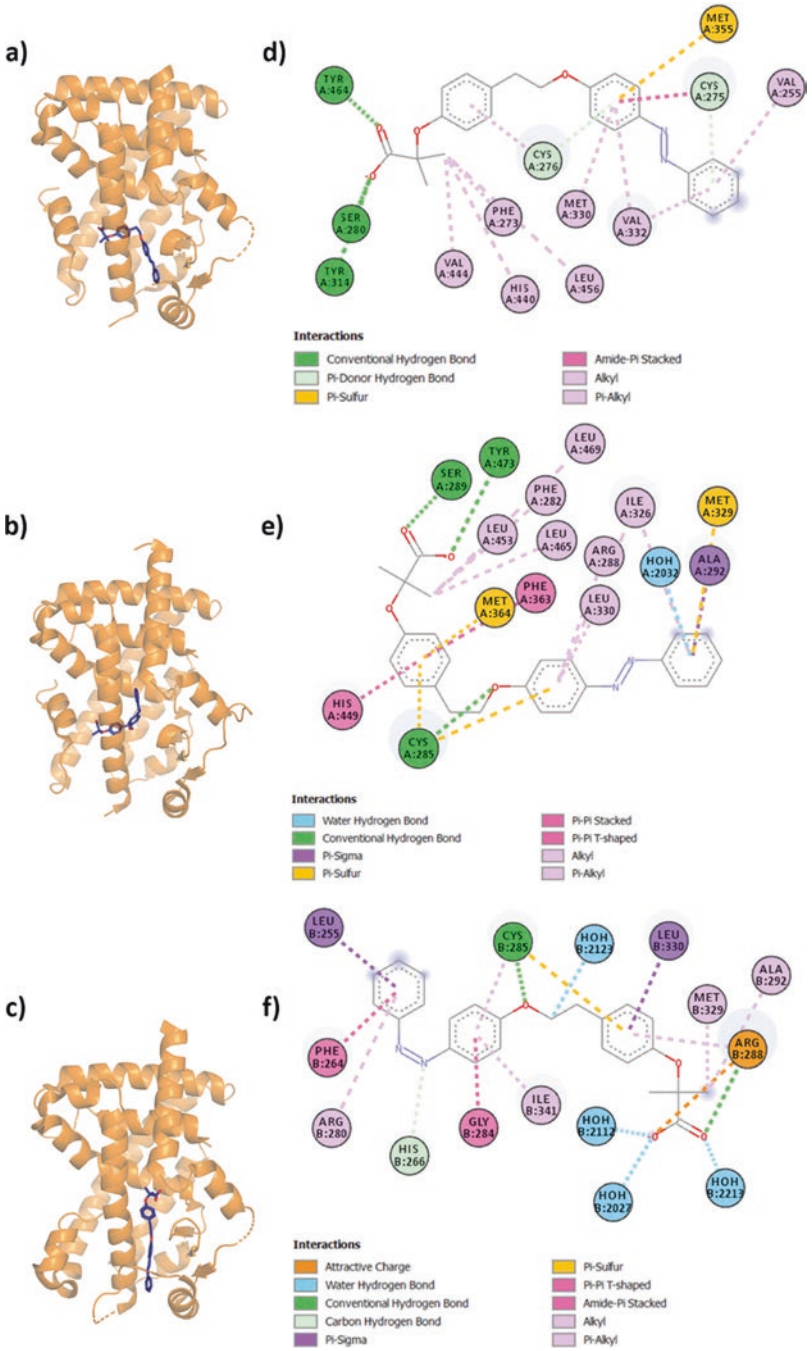

Fig. 6.21 (**a**) PPARα LBD in orange complexed with GL479 in dark purple (PDB ID: 4CI4). (**b**) PPARγ LBD in orange complexed with GL479 in the 'tail-up' conformation in dark purple (PDB ID: 4CI5). (**c**) PPARγ LBD in orange complexed with GL479 in the 'top-down' conformation in dark purple (PDB ID: 4CI5). (**d**) Interaction map of compound GL479 with PPARα. (**e**) Interaction map of GL479 in the 'tail-up' conformation with PPARγ. (**f**) Interaction map of GL479 in the top-down conformation with PPARγ

Table 6.19 The activity of GL479 at each PPAR subtype

	EC_{50} (μM)		
Ligand	PPARα	PPARδ	PPARγ
GL479	0.6 ± 0.01 (158%)	–	1.4 ± 0.02 (21%)

EC_{50} values were determined by dual luciferase assay in HEK293 cells, values were normalized to *Renilla* activity. Maximal activity (%) was defined as relative to Clofibric acid Rosiglitazone for PPARα and γ respectively [45].

PPARγ GL479 adopts two distinct conformations. In the first conformation, it adopts a tail-up conformation and interacts with Arm 3 [114]. This can be due to: (1) The smaller γ: H323 (α: Y314) residue forces the ligand to bind closer to H12 in PPARγ. The ligand would be unable to effectively span across H3 into Arm 2, possibly explaining its partial agonism for PPARγ. (2) The tail region likely makes more contacts in the tail up conformation for PPARγ, due to the smaller corresponding residues of α: C275 and M330 in Arms 2 and 3 (γ: G284, V339). It forms interactions with five residues in Arm 3. In the second conformation of PPARγ-GL479 complex, GL479 adopted a top-down conformation spanning Arms 3 and 2. Partial agonists for PPARγ often adopt this top-down conformation [14, 25]. It makes interactions with three residues in Arm 1, six residues in Arm 2 and γ: H266 and F264 on the Ω loop.

The affinity towards PPARα and γ, like GW409544 and Azetidinone compounds 17 comes from the slim core and tail design, allowing accommodation by the methionine residues in PPARα and γ Arms 2 and 3. However, it is the lack of substituents in the tail region that likely accounts for its low potency. GL479 makes 16 interactions with PPARα, which is comparable to other ligands with low affinity like WY14643 or 17-oxoDHA. Although GL479 makes more interactions (20 in both conformations) with PPARγ, it is more potent at PPARα (16 interactions). The top down conformation is possible in PPARγ due to residues γ: G284 and R280.

6.2.3.2 PPARα/δ Dual Agonists

Targeting PPARα and γ has been the focus drug discovery due to availability of selective ligands and thus a better understanding of its biochemistry and therapeutic utility. Tools for PPARδ arrived much later, and consequently the therapeutic benefits of PPARδ were discovered later compared to PPARα and γ [53]. As such, PPARα/δ and δ/γ dual agonists are very rare [23]. A recent example was PPARα/δ Elafibranor which displayed a desirable safety profile but did not perform significantly better than placebo against non-alcoholic steatohepatitis [44, 86]. Whether this problem was specific to elafibranor or due to the inherent biochemistry of PPARα/δ activation remains to be seen.

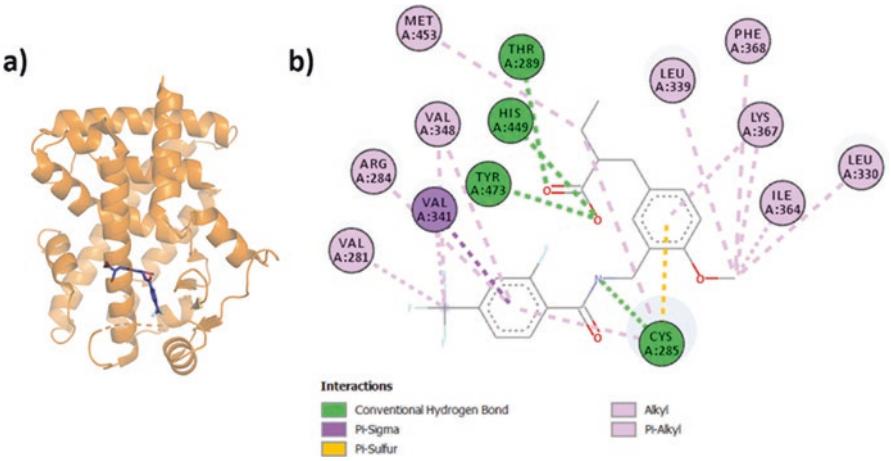

Fig. 6.22 (**a**) PPARδ LBD in orange complexed with TIPP-401 in dark purple (PDB ID: 2ZNQ). (**b**) Interaction map of TIPP-401 with PPARδ

Table 6.20 The activity of TIPP-401 at each PPAR subtype

	EC_{50} (μM)		
Ligand	PPARα	PPARδ	PPARγ
TIPP-401	0.010	0.012	4.900

EC_{50} values were determined by luciferase activity in HEK-293 cells. Maximal activity (%) was defined as relative to GW501516 for PPARδ and Rosiglitazone for PPARγ [53]

TIPP-401

Kasuga and colleagues first synthesized TIPP-401 by optimizing the ligand tail and core regions, using their previous PPARα specific compound KCL as a lead [53]. The PPARδ-TIPP-401complex was later crystallized by Oyama and colleagues to explore the structural selectivity between the PPAR subtypes (Fig. 6.22, Table 6.20) [82]. The only difference between the PPARα selective KCL and PPARα/δ dual agonist TIPP-401 is a 2-substituted fluorine atom on the phenyl in the tail motif and a reversed carbon amide core-tail linker.

TIPP-401 is a Y-shaped ligand that interacts with 3/4 of the polar residues and two other residues (including δ: M417) via the isobutyric acid head motif in Arm 1. It contains a 1,3,4-substituted phenyl core that interacts with two residues in Arm 2. The tail amino linker interacts with δ: T288. Its tail substituent, an amino linked 2-fluoro-4-(trifluoromethyl)benzene interacts with δ: V312, five other residues and W228 on the Ω loop, similar to TIPP-204. Its fin methanol substituent interacts with δ: I328 in Arm 2 and four other residues in Arms 3.

Like TIPP-204, affinity for PPARδ of TIPP-401 was likely increased by reversing the amide linker, compared to the PPARα specific KCL, creating interactions

between the carbonyl and residue δ: T288 [54]. Affinity against PPARγ is likely mediated by the close proximity of the tail to δ: V312, corresponding residues in PPARγ would clash sterically (γ: M348). As seen in the PPARα-TIPP-703 complex (PDB ID: 2ZNN), α: M355 flexes to avoid clashing with the fin substituent, explaining the high affinity of TIPP-401 for PPARα.

6.2.3.3 PPARδ/γ Dual Agonists

Phenoxyacetic Acid Compounds 10 and 21

Connors and colleagues identified Compounds 10 and 21 from a SAR study [25]. They attempted to combine the fatty acid-oxidizing properties of PPARδ activation,and the safer, antiadipogenic character of partial agonists of PPARγ. The PPARδ-Compound 10 and PPARγ-Compound 21 complexes were crystallized by Connors and colleagues to understand the structural basis for the binding profile of the compounds (Fig. 6.23, Table 6.21) [25].

Compounds 10 and 21 both uses a Y-shaped design. In the PPARδ – Compound 10 complex, we see that the (2,3-dimethylphenoxy)acetic acid head motif in compound 10 makes hydrogen bonds with 4/4 polar residues in Arm 1 and hydrophobic interactions with five residues in Arms 2 and 3. It contains a phenyl core which interacts with δ: L294 in Arm 3. This core is 1,2,4-substituted with the head, fin and tail regions, respectively. The ethanol fin interacts with four residues in Arm 3. The 4-trifluoromethylphenol interacts with seven residues in Arm 2. In the PPARγ-Compound 21 complex, the ligand adopts a top-down conformation. The head interacts with γ: R288 and three other residues in Arm 3. The core and tail regions interact with five residues in Arm 2 and γ: I262 on the Ω loop. The 2-pentyn-1-ol fin sits between H3 and H7 below Arm 1.

Affinity for PPARδ is likely imparted by the oxygen and sulphur linkers from the head, tail and fin to the core. This 1,2,4-substituted core optimally positions it to interact with δ: I328 and V334. Corresponding methionine residues in PPARα and γ would likely clash with the ligand. This clash likely forces Compound 21 to assume an atypical top-down conformation in PPARγ but not α, which was possible due to residue γ: G284 (α: C275 δ: R248) and R280 (α: R271 δ: H244). These residues create space for the tail substituent to be accommodated in Arm 2, away from γ: M348.

Sulfonylthiadiazole Compounds 6, 11t and 20a

Compounds 6, 11t and 20a are sulfonylthiadiazole analogues synthesized by Sanofi-Aventis from a SAR study of PPAR. The rationale for this series of compounds was similar to the study by Connors et al. [25]. The PPARδ-compound 6, 11t and 20a complexes were crystallized by Keil and colleagues to understand the binding mode of and optimize their compounds (Fig. 6.24, Table 6.22) [59]. The lead compound,

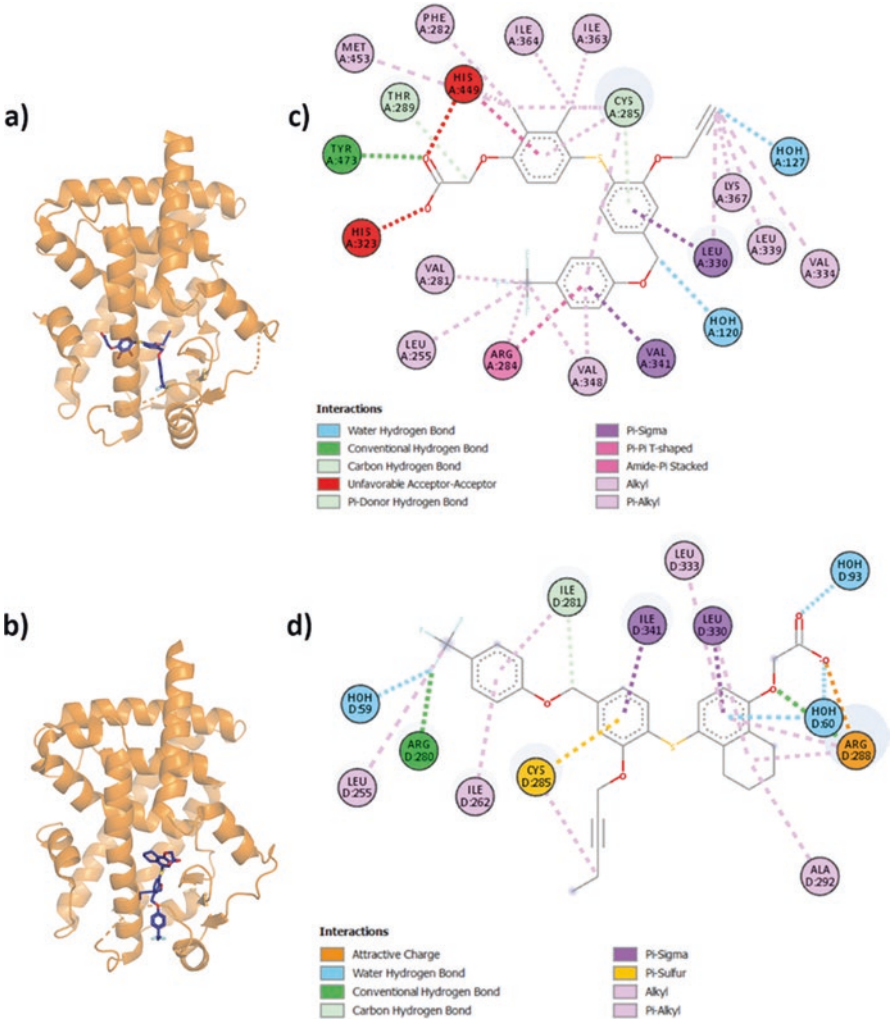

Fig. 6.23 (**a**) PPARδ LBD in orange complexed with Compound 10 in dark purple (PDB ID: 3GZ9). (**b**) PPARγ LBD in orange complexed with Compound 21 in dark purple (PDB ID: 3H0A). (**c**) Interaction map of Compound 10 with PPARδ. (**d**) Interaction map of Compound 21 with PPARγ

Table 6.21 The activity of phenoxyacetic acid compounds at each PPAR subtype

Ligand	PPARα	PPARδ	PPARγ
	IC_{50} (μM)		
Compound 10	0.21	0.004	0.30
Compound 21	0.88	0.005	0.033
	EC_{50} (μM)		
Compound 10	6.1 (48%)	0.054 (86%)	3.0 (40%)
Compound 21	>10	0.044 (94%)	0.16 (34%)

IC_{50} values for PPARα and δ were determined by scintillation proximity assay (SPA), using [^{3}H] GW2433 as a radioligand for PPARα and δ. IC_{50} values for PPARγ were determined by a filtration assay (FA), using [^{3}H] rosiglitazone. EC_{50} values were determined by luciferase assay in CV-1 cells. Maximal activity (%) was defined as relative to GW501516 and rosiglitazone for PPARδ and PPARγ, respectively

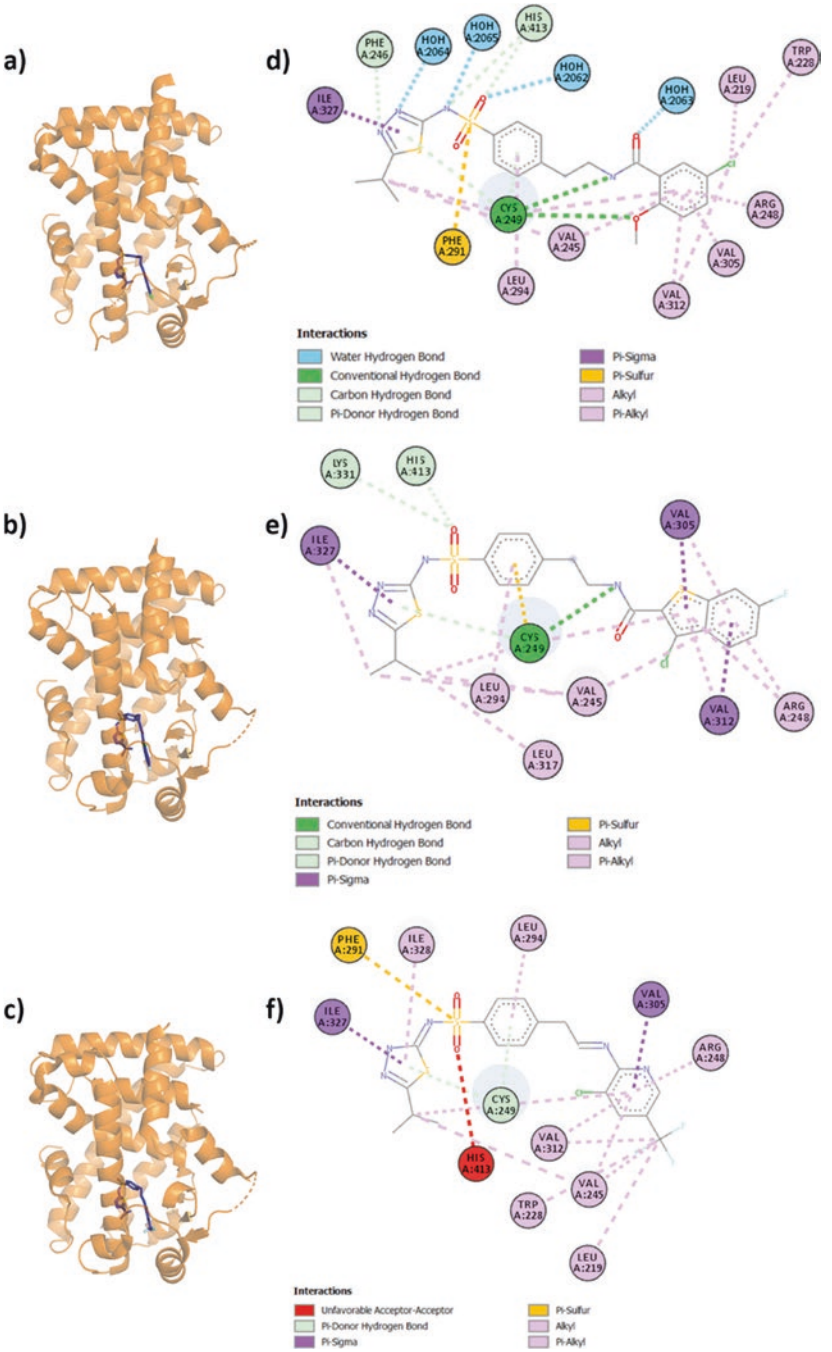

Fig. 6.24 (**a**) PPARδ LBD in orange complexed with Compound 6 in dark purple (PDB ID: 2XYJ). (**b**) PPARδ LBD in orange complexed with Compound 11t in dark purple (PDB ID: 2XYW). (**c**) PPARδ LBD in orange complexed with Compound 20a in dark purple (PDB ID: 2XYX). (**d**) Interaction map of Compound 6 with PPARδ. (**e**) Interaction map of Compound 11t with PPARδ. (**f**) Interaction map of Compound 20a with PPARδ

Table 6.22 The activity of lead sulfonylthiadiazole analogues at each PPAR subtype

	EC_{50} (μM)		
Ligand	PPARα	PPARδ	PPARγ
Compound 6	1.6900 (13%)	0.7380 (30%)	3.2300 (13%)
Compound 11t	ND	0.3180 (40%)	1.1990 (33%)
Compound 20a	ND	0.0016 (26%)	0.3360 (26%)

For PPARα and δ, EC_{50} values were determined by luciferase activity in stably transfected HEK cells. For PPARγ, EC_{50} values were determined by dual luciferase assay in HEK cells, and values were normalized to *Renilla* activity. Maximal activity (%) was defined as relative to fenofibric acid, GW501516 and rosiglitazone for PPARα, PPARδ and PPARγ, respectively. Compounds were tested up to 30 μM. ND – not determined; if compounds exhibited <10% activity, the EC_{50} values would not be calculated

Compound 6, was a low affinity, low efficacy pan agonist compound. The tail region of Compound 6 was optimized to give Compound 11t and Compound 20a with vastly improved affinity, potency and efficacy.

These N-shaped compounds bind to the bottom of Arm 1, between H3 and H7 in the inferior region of LBD and Arm 2. All three compounds occupy similar position and binding mode in PPARδ. These compounds contain a sulfonyl head region with a 2-isopropyl-1, 3, 4-thiadiazole substituent and wrap around H3 at δ: C249.

The sulfonyl head region in Compound 6 forms hydrogen bonds with three water molecules. It makes π-donor hydrogen bonds with two residues in Arm 1 and 2 and interactions with two other residues in the inferior region of Arm 1. The phenyl core interacts with two residues in Arm 1 and 2. The core is linked to the tail substituent via an N-ethylformamide linker, which forms hydrogen bonds with δ: C249 and one water molecule. The 2-methoxy-5-chlorobenzene tail substituent makes hydrophobic interactions with five residues in Arm 2 and δ: W228, and one hydrogen bond with δ: C249 via the methoxy group.

The sulfonyl head region in Compound 11t forms weak hydrogen bonds with three residues in Arms 1, 2 and 3. It makes hydrophobic interactions with four other residues in Arms 1, 2 and 3. The phenyl core makes interactions with two residues in Arm 2. The core is linked to the tail substituent with the same N-ethylformamide linker, which forms hydrogen bonds with δ: C249. The benzothiophene tail substituent makes hydrophobic interactions with five residues in Arm 2.

In Compound 20a, the sulfonyl head region forms a π-donor hydrogen bond with δ: C249 and interacts with four other residues in Arms 1 and 2. The phenyl core interacts with two residues in Arms 2 and 3. The core is connected to the tail substituent via a propanimine linker. The 3-chloro-5-trifluoromethylpyridine tail substituent forms interactions with six residues in Arm 2.

The high potency of this series of compounds can be attributed to the strong interactions between the linker and δ: C249. The rigidity of Compound 20a compared to Compounds 6 and 11t might account for its increased potency. Compared

to GW501516 [97, 113], the trifluouromethyl motif in the tail substituent sits lower, reducing interference with corresponding methionine residue of δ: V312 in PPARγ (γ: M348).

6.2.3.4 Pan Agonists

The rationale behind synthesizing pan agonists follows that for dual agonists – to combine the therapeutic benefits of each PPAR subtype and to reduce the risk of multiple pharmacology [6, 55, 56, 82]. These efforts are spurred on by the clinical success of bezafibrate [16, 55, 56]. Pan agonism presents a challenging design problem, as pan agonists need to interact with areas conserved among all three subtypes – this is difficult as these regions of dissimilarity are spread throughout the LBP (Table 6.1). Here we see two different design approaches: (1) by decreasing the size of the ligand [6, 19] and (2) by using a Y-shaped ligand [82].

Indeglitazar

Artis and group synthesized the pan agonist indeglitazar. The group took an unorthodox approach in the drug screening phase where they selected ligands with weak activity across all three receptors and then optimized for affinity towards all PPAR subtypes, as opposed to selecting ligands with stronger affinity for a specific subtype and then optimizing for selectivity. The rationale was that the side effects of PPAR activation were not only caused by non-specific binding but also by the supraphysiological activation of the PPAR receptor [118]. The PPARδ, PPARα and PPARγ-indeglitazar complexes were crystallized by Artis and colleagues to understand the binding mode of their pan agonist (Fig. 6.25, Table 6.23) [6].

The Y-shaped indeglitazar assumes a nearly identical conformation in all three PPAR subtypes. It binds to the inferior area of Arm 1, in the space between H3 and H7. It has a propionic acid head that interacts with 3/4 of the polar residues in PPARα, δ and γ. In PPARα, α: Y314 pushes this acid motif slightly towards H3 to interact with S280 instead of H440. In PPARγ, the acid motif rotates slightly in comparison, interacting with γ: S289 instead of H449. This acid group is connected to the 5-methoxy-1H-indene group, which makes interactions with six residues in PPARα/γ and seven residues with PPARδ in Arms 1 and 2. The short tail substituent, a 4-methoxy1-sulfonylbenzene, wraps around H3 at the interface of Arms 2 and 3. It makes interactions with five residues in PPARα, with seven residues in PPARδ and γ, in Arms 1, 2 and 3.

The atypical architecture of indeglitazar avoids the methionine residues in Arms 2 and 3 and makes contacts in the inferior region of Arm 1 and posterior region of Arm 2. Although indeglitazar interacts with most polar residues in PPAR, it does not have full agonistic activity, showing that interaction with H12 is not sufficient for full agonism.

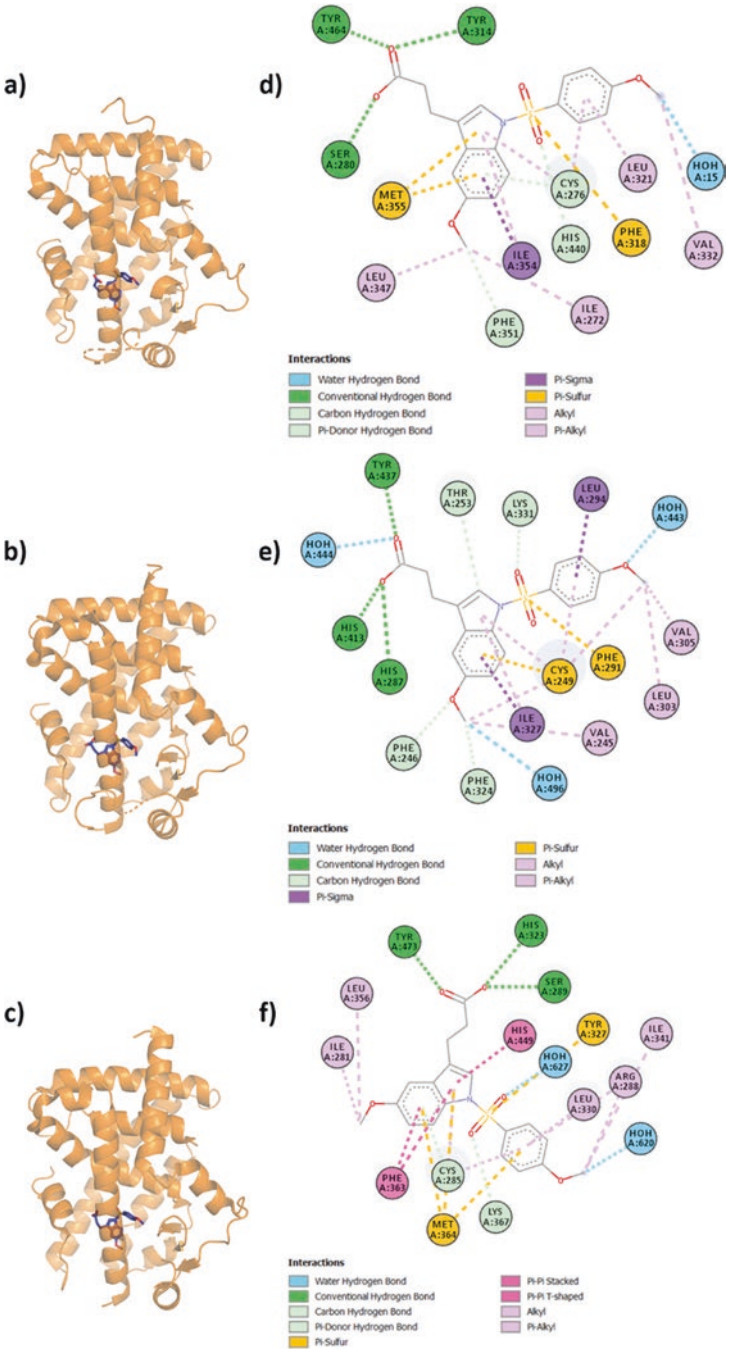

Fig. 6.25 (**a**) PPARα LBD in orange complexed with Indeglitazar in dark purple (PDB ID: 3ET1). (**b**) PPARδ LBD in orange complexed with Indeglitazar in dark purple (PDB ID: 3ET2). (**c**) PPARγ LBD in orange complexed with Indeglitazar in dark purple (PDB ID: 3ET3). (**d**) Interaction map of Indeglitazar with PPARα. (**e**) Interaction map of Indeglitazar with PPARδ. (**f**) Interaction map of Indeglitazar with PPARγ

Table 6.23 The activity of Indeglitazar at each PPAR subtype

	EC_{50} (μM)		
Ligand	PPARα	PPARδ	PPARγ
Compound 1	≈100	>200	≈150
Indeglitazar	0.99	1.3 (67 ± 18%)	0.85 (45 ± 10%)

EC_{50} values were determined by luciferase assay in HEK293T cells. Maximal activity (%) was defined as relative to WY-14643, L-165041 and rosiglitazone for PPARα, PPARδ and PPARγ, respectively

TIPP-703

Kasuga and group synthesized the pan agonist TIPP-703 during their exploration of the effects of the trifluoromethyl tail substituent on structural selectivity [55, 56]. The PPARα/γ-TIPP-703 complexes were later crystallized by Oyama and colleagues to explore the structural selectivity of PPAR (Fig. 6.26, Table 6.24) [82].

TIPP-703 is an L-shaped ligand. In PPARα, the isobutyric acid head motif interacts with 3/4 of the polar residues and three other residues in Arm 1. The 1,3,4-substituted phenyl core interacts with α: C276. The core-tail amide linker interacts with T279. The tail substituent interacts with six residues in Arm 2 and α: L254 V255 on the Ω loop. The fin propanol substituent interacts with four residues in Arms 2 and 3 including α: M330 and M355. In PPARγ, the isobutyric acid head motif forms hydrogen bonds with 2/4 of the polar residues and hydrophobic interactions with four other residues in Arm 1. The 1,3,4-substituted phenyl core interacts with four different residues. The tail phenyl interacts with three residues including γ: G284, while the adamantyl group interacts with γ: R280 and two other residues. In the PPARγ crystal structure the fin propanol substituent is disordered and left unmodelled.

The affinity for all three PPARs is likely explained by the slim core area with the longer tail motif with the bulky adamantyl group. The core avoids the methionine residues in PPAR α and γ. The architecture of the tail substituent avoids clashing with γ: M348 in PPARγ. Additionally the flexible γ: R288 (α: T279, δ: T252) allows the tail motif to move closer to H3 and for the adamantyl group to occupy the space between γ: G284 and R280 in Arm 2 of PPARγ. This adamantyl group is still able to make favourable interactions with Arm 2 of PPARα/δ. The propanol fin substituent makes sufficient contacts with the Arm 3 area which likely increases affinity for PPARδ without interfering with PPARα α: M330 [55, 56].

AL29-26

Capelli et al. [19] synthesized compound AL29-26, selected through a structure-based virtual screening process that considers experimentally determined PPAR-ligand interactions. The PPARα/γ-AL29-26 complexes were crystallized by Capelli

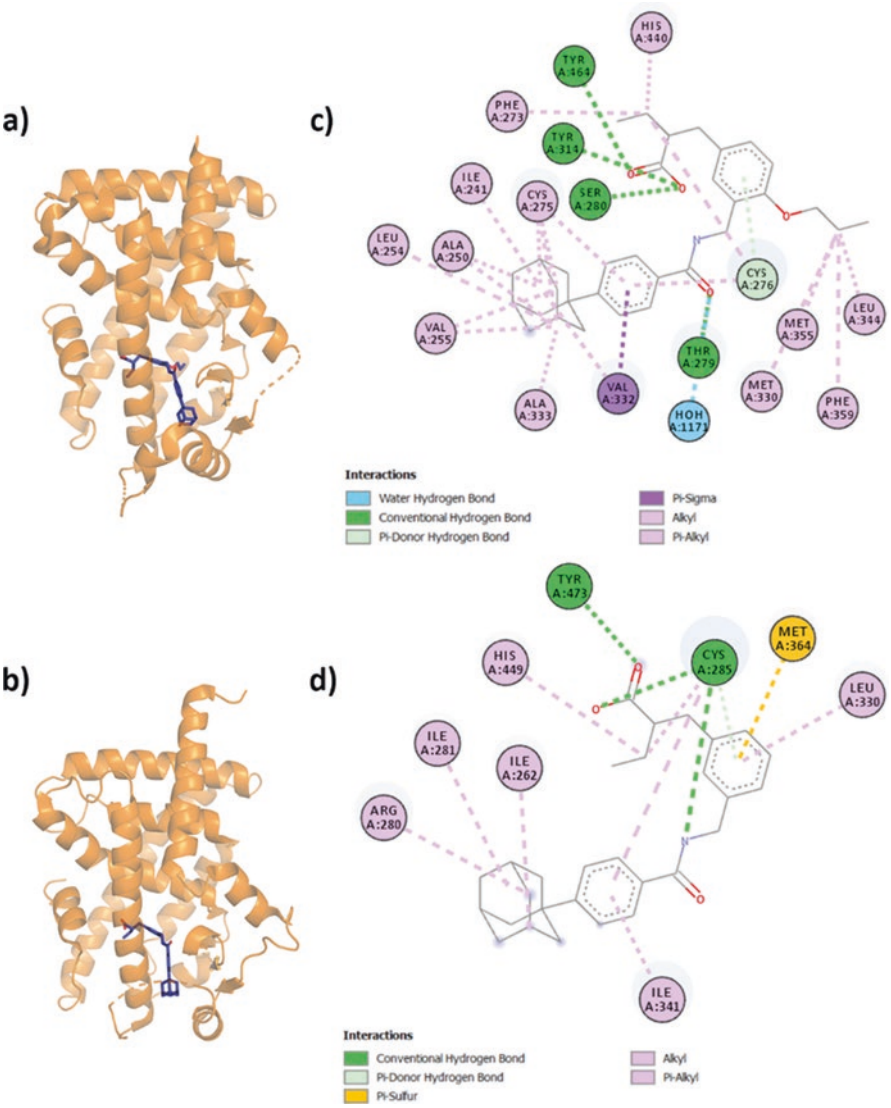

Fig. 6.26 (**a**) PPARα LBD in orange complexed with TIPP-703 in dark purple (PDB ID: 2ZNN). (**b**) PPARγ LBD in orange complexed with TIPP-703 in white (PDB ID: 2ZNO). (**c**) Interaction map of TIPP-703 with PPARα. (**d**) Interaction map of TIPP-703 with PPARγ

and colleagues (Fig. 6.27, Table 6.25) [19] to identify the structural basis for the difference in AL29-26 activity at the three PPAR subtypes.

AL29-26 adopts a similar, L-shaped conformation in both PPARα and γ. In PPARα, the isobutyric acid head forms hydrogen bonds with 4/4 of the polar residues in Arm 1 and hydrophobic interactions with three other residues. The

Table 6.24 The activity of TIPP-703 at each PPAR subtype

	EC_{50} (μM)		
Ligand	PPARα	PPARδ	PPARγ
TIPP-703	0.061	0.120	0.043

EC_{50} values were determined by Dual luminescence assay in HEK293 cells, measuring luciferase activity normalized to β-galactosidase activity [53]

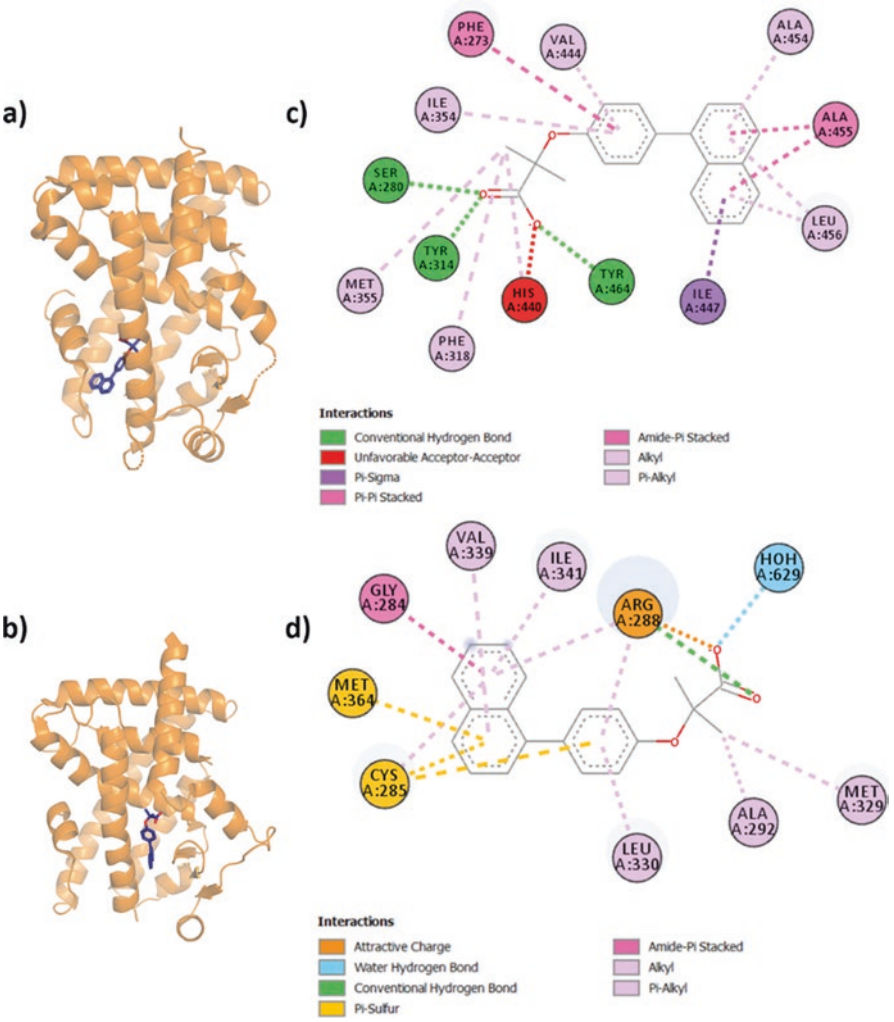

Fig. 6.27 (**a**) PPARα LBD in orange complexed with AL29-26 in dark purple (PDB ID: 5HYK). (**b**) PPARγ LBD in orange complexed with AL29-26 in dark purple (PDB ID: 5HZC). (**c**) Interaction map of AL29-26 with PPARα. (**d**) Interaction map of AL29-26 with PPARγ

Table 6.25 The activity of AL29-26 at each PPAR subtype

	EC_{50} (μM)		
Ligand	PPARα	PPARδ	PPARγ
AL29-26	0.31 ± 0.13 (87 ± 8%)	11.0 ± 2 (54 ± 6%)	5.3 ± 1.6 (27 ± 3%)

EC_{50} values were determined by dual luminescence assay in HepG2 cells, measuring luciferase activity normalized to β-galactosidase activity

phenoxy core interacts with three residues in Arm 1. The diphenyl tail makes interactions with four residues in the 'benzophenone pocket' in Arm 1 [77]. This is made possible by the flexing of α: F273 to accommodate the diphenyl. In PPARγ, the isobutyric acid head forms interactions with γ: R288 and two other residues in Arm 3. The phenoxy core and diphenyl tail interacts with seven residues in Arms 2 and 3.

This ligand possesses a much lower transactivation activity for PPARδ and PPARγ than seen for other ligands. This is likely due to the relatively smaller number of residues it interacts with in the PPAR LBD. Selectivity of this ligand for all subtypes likely arises from the fact that the ligand is small and does not interfere with residues of the different subtypes in PPAR. The fibrate motif in the acidic head may increase affinity towards PPARα, due to the larger α: Y314 residue, positioning it to interact with S280 [19]. AL29-26 resembles another known peroxisome proliferator nafenopin.

6.2.3.5 Endogenous Agonists

The PPAR subtypes have unique and overlapping affinities for different endogenous ligands, usually fatty acids or related metabolites [31, 61]. These fatty acids are usually present at micromolar concentrations in blood in the human body [114]. Various techniques have been used in the discovery of these ligands, but it was Xu and colleagues that first confirmed fatty acids as bona fide endogenous PPAR ligands through protein crystallography [31, 114]. Analysis of the binding mode of endogenous ligands often reveals important insights that can be applied to the design of better or safer synthetic ligands [82, 113].

Eicosapentaenoic Acid (20:5 EPA)

Eicosapentaenoic acid (C20:5) is a polyunsaturated fatty acid (PUFA). These PUFAs are thought to act through the PPAR receptor and has lipid lowering and insulin sensitization effects [114]. The PPARδ-EPA complex was crystallized by Xu and colleagues as part of their study into structural selectivity of PPARδ (Fig. 6.28, Table 6.26) [114]. In this study, EPA was found to bind in two distinct conformations, the 'tail-up' and 'tail-down' modes.

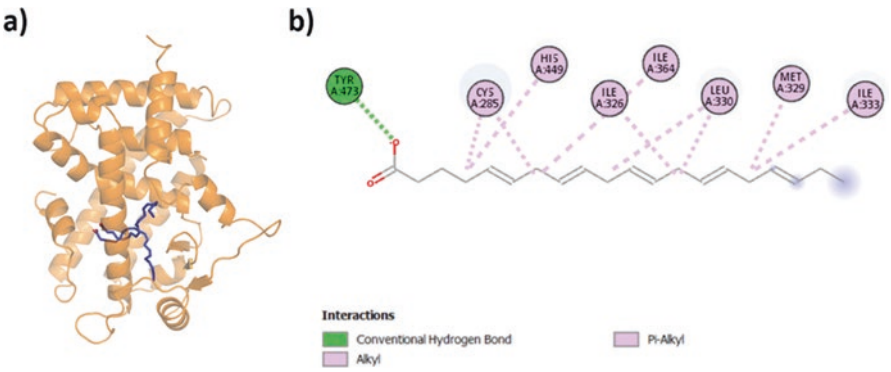

Fig. 6.28 (**a**) PPARδ LBD in orange complexed with EPA in both conformations in dark purple (PDB ID: 3GWX). (**b**) Interaction map of EPA in the tail-down conformation with PPARδ. Interaction map of the tail-up conformation is not available

Table 6.26 The activity of Eicosapentaenoic acid at each PPAR subtype

	IC_{50} (μM)			
Ligand	PPARα	PPARδ	PPARγ	Assay
Eicosapentaenoic acid (C20:5)	1.1 ± 0.23	4.0 ± 0.90	1.6 ± 0.20	SPA

IC_{50} values were determined by scintillation proximity assay (SPA), using [^{3}H] GW2331, [^{3}H] GW2433 and [^{3}H] BRL49653 as radioligands for PPARα, PPARδ and PPARγ respectively [114]

The EPA molecule assumes an L-shaped conformation. The carboxylic acid head forms hydrogen bonds with δ: Y473. Its lipophilic alkyl tail interacts with residues in Arm 2 or Arm 3 of PPARδ in the tail down or tail up conformation respectively. In the tail-up conformation, the lipophilic tail interacts with three residues in Arm 1, two residues in Arm 2, three residues in Arm 3. In the tail-down conformation, the lipophilic tail interacts with δ: H449, Q286 in Arm 1 and I363, I364, L339, C285, V281 and L255 in Arm 2.

In both conformations, all the unsaturated bonds adopt a cis configuration. In the tail-up conformation, the tail curves upwards to δ: M329 in H5 and then back down and out anteriorly towards the plane of H3. In the tail down confirmation, the tail it extends along the lateral edges of Arm 2 interacting with δ: I328, V312, L303, H7 and the β-sheet.

Vaccenic Acid (18:1)

Fyffe and colleagues found that a previously published 'apo' PPARδ protein structure contained significant electron density in the LBP. They found that bacterial fatty acid vaccenic acid binds to PPARδ during the protein purification process,

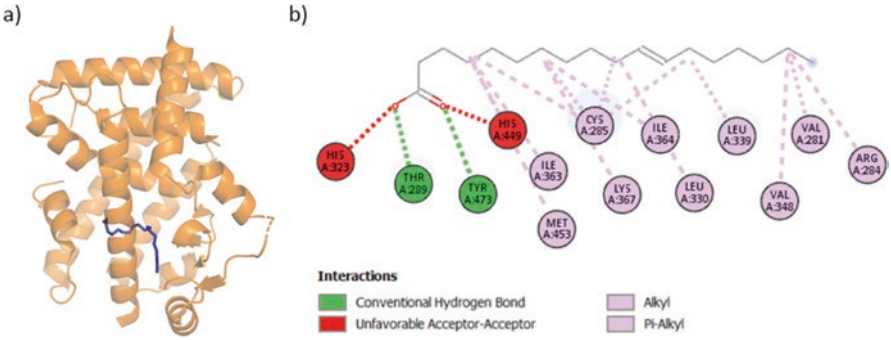

Fig. 6.29 (**a**) PPARδ LBD in orange complexed with vaccenic acid in dark purple (PDB ID: 2AWH). (**b**) Interaction map of Vaccenic acid with PPARδ

causing H12 of PPARδ to be locked in an active conformation. The PPARδ-vaccenic acid complex was crystallized by Fyffe and colleagues to prove that vaccenic acid binds to PPARδ during protein purification (Fig. 6.29) [41].

Vaccenic acid assumes an L-shaped conformation. The acidic head interacts with Arm 1 residues via δ: Y473, H449, H323 and T289. The lipophilic tail interacts with δ: M453, K367, I364, I363, V348, L339, L330, C285, R284 and V281, wrapping around H3 and interacting with Arm 2.

Iloprost

Iloprost is a prostaglandin I_2 (PGI_2) synthetic analogue, developed to study the role of a related but metabolically unstable eicosanoid PGI_3 in cardiovascular homeostasis. It was previously demonstrated that PPAR subtypes are differentially regulated by prostaglandins [122]. Here, the PPARα/δ-Iloprost-coactivator complexes were crystallized by Jin and colleagues to uncover the molecular mechanisms for selectivity of Iloprost towards PPARα and δ (Fig. 6.30 Table 6.27) [52].

The Iloprost assumes an L-shaped conformation. In PPARα, the 5-hexenoic acid head interacts with 3/4 of the polar residues in Arm 1. It forms hydrophobic interactions with five other residues in Arms 1 and 2. The 2-oxy-octahydropentalene core interacts with four residues in Arms 1, 2 and 3. The tail region forms a hydrogen bond with α: T279 in Arm 2 and hydrophobic interactions with two other residues in Arm 2.In PPARδ, the acidic head motif interacts with 2/4 polar residues in Arm 1. It also forms hydrophobic interactions with three other residues in Arm 1 and 2. The 2-oxy-octahydropentalene core interacts with four residues in Arms 2 and 3. The tail region forms a hydrogen bond with δ: T252 in Arm 2 as well as six other residues in Arm 2.

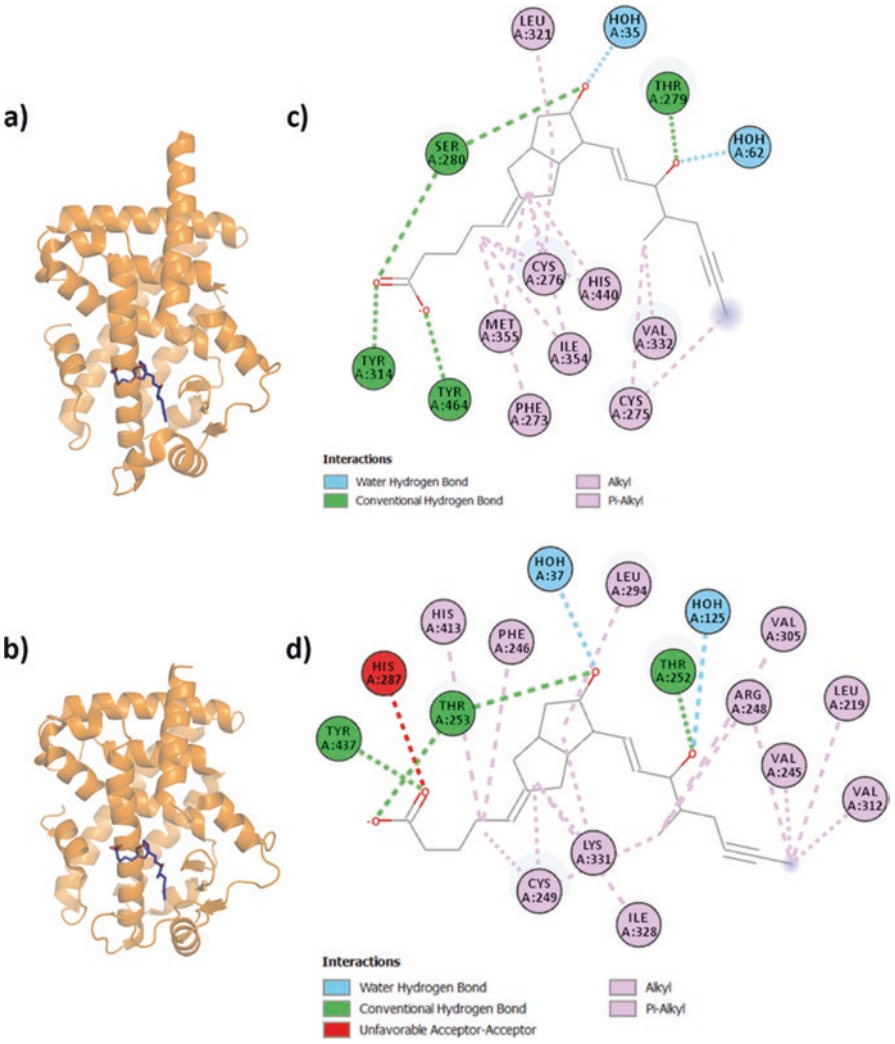

Fig. 6.30 (**a**) PPARα LBD in orange complexed with Iloprost in dark blue (PDB ID: 3SP6). (**b**) PPARδ LBD in orange complexed with Iloprost in dark blue (PDB ID: 3SP9). (**c**) Interaction map of Iloprost with PPARα. (**d**) Interaction map of Iloprost with PPARδ

Table 6.27 The activity of Iloprost at each PPAR subtype

	EC_{50} (μM)		
Ligand	PPARα	PPARδ	PPARγ
Iloprost	≈0.200	≈0.200	>20

The EC_{50} values were determined by dual luciferase assay in Cos-7 cells, and values were normalized to *Renilla* activity

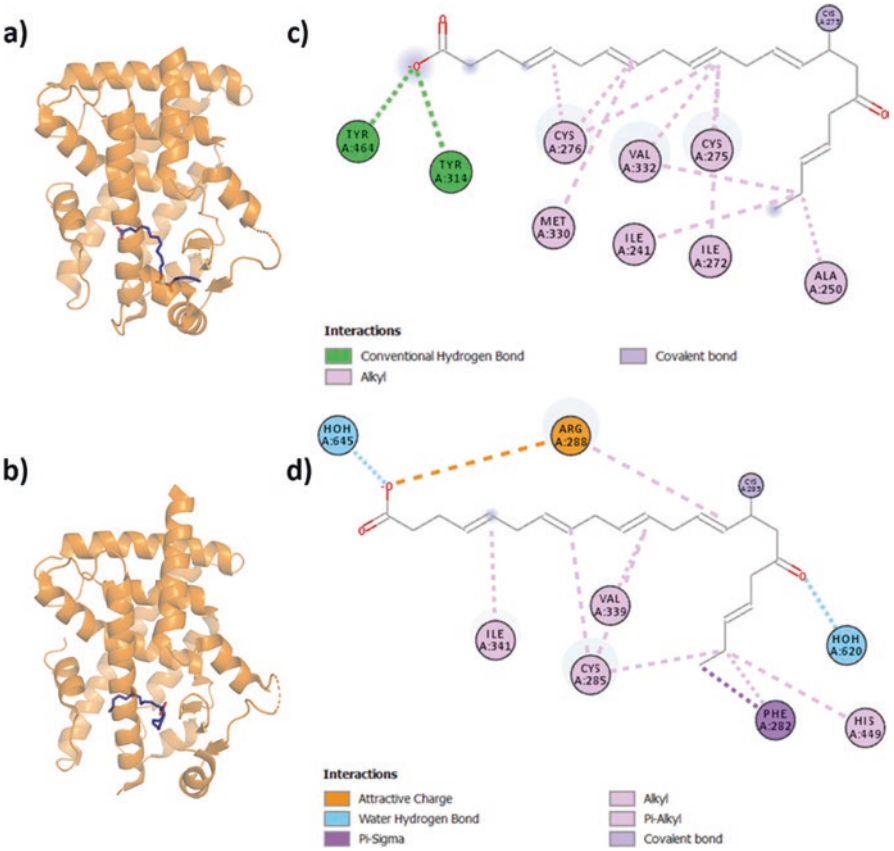

Fig. 6.31 (**a**) PPARα LBD in orange complexed with 17(S)-oxoDHA in dark purple (PDB ID: 5AZT). (**b**) PPARγ LBD in orange complexed with 17(S)-oxoDHA in dark purple (PDB ID: 5AZV). (**c**) Interaction map of 17(S)-oxoDHA with PPARα. (**d**) Interaction map of 17(S)-oxoDHA with PPARγ

Selectivity against PPARγ may be caused by interference with the corresponding residue γ: R288 (α: T279, δ: T252). γ: R288 would also be unable to form hydrogen bonds with the oxygen group in the tail substituent.

17(S)-oxoDHA (22:6)

17(S)-oxodocosahexaenoic acid (17(S)-oxoDHA) is an endogenous ligand of PPAR. The PPARα/γ – 17(S)-oxoDHA complexes have been crystallized by Egawa and colleagues, continuing their previous research into binding mode of endogenous ligands (Fig. 6.31) [35]. This represents the first crystallized example of an endogenous fatty acid bound to PPARα.

17(S)-oxoDHA assumes an L-shaped conformation in PPARα. Here, the acidic head of 17(S)-oxoDHA interacts α: Y464, Y314 and S280. The lipophilic tail interacts with Arm 1, 2 and the Ω loop. It makes a covalent bond with α: C275 and interacts with α: V332, M330, C276, C275, I272, A250, L247 and I241.

In PPARγ 17(S)-oxoDHA adopts a slightly different, folded L-shaped conformation and occupies the Arm 1, 2 area near the β1 sheet. The lipophilic tail interacts with γ: H449, M348, I341, V339, L330, Y327, R288, C285, F282, I281 and forms a covalent bond with γ: C285. The acidic head interacts with R288. This covalent bond is also seen in other PPARγ-endogenous ligand complexes [50; 107].

6.3 Ligand Design Factors

The PPAR ligand binding pocket contains areas of similarity and dissimilarity between the subtypes (Table 6.1). From SAR studies, especially studies regarding dual and pan agonists, interesting trends can be observed – different substituents on the same general ligand scaffold changes affinity of the ligand towards each PPAR subtype [13, 82, 113]. The structural basis for the variations in affinity can be elucidated when structural information is present, and for this reason, drug-discovery studies now typically include some form of structure-related information, protein docking or simulation, NMR, MS or crystallography. Our analysis of the PPAR-ligand interactions in Sect. 6.2 revealed common observations of the binding patterns of ligands, which we describe below.

1. PPARδ has the ‘narrowest’ Arm 1 and does not appear to accommodate residues in the ‘Benzophenone pocket’ observed in α or γ [77].

   The size of Arm 1 was noted in [115]. PPARα-specific agonist GW590735 was optimized based on this difference, between PPARδ vs α in Arm 1 by replacing the acid head motif with the ‘Fibrate head’ motif that tends to be specific to PPARα [97]. Some groups achieve different subtype selectivity by swapping the head region of the ligands. GSK has made multiple ligands with this method: GW590735 from GW501516, GW6471 from GW409544 and compound 48 from GW501516.
2. PPARα contains a unique AF2 hydrogen bonding network α: Y464, H440, Y314 instead of δ: Y437, H413, H287 γ: Y473, H449, H323.

   This difference has been used to optimize for and against PPARα selectivity [115, 119]. α: Y314 in PPARα allows binding of ligands with a shorter head region. This was seen in the optimization of pemafibrate, where it was found that increasing the distance between the core and acid motif decreases specificity for PPARα [119]. A counter example is seen in Sierra et al. [97], where the longer head-core distance allows for better interaction between PPARδ/γ (δ: H287/γ: H323) and the fibrate head.

3. PPARδ has the widest Arm 2, followed by α and γ.

   Ligands selecting against PPARδ tend to contain smaller tail motifs that do not contain substituents that project posteriorly into Arm 2, for example, TIPP-204 and TIPP-401 vs KCL and GW590735 and pemafibrate compared to LC1765 [82]. Kasuga and colleagues also observed that a longer core-tail linker increased affinity for PPARδ [53]. Trifluoride tail designs in this area have been very successful for high affinity activation of PPARs (GW409544, GW0742, TIPP-204, TIPP-401, GW501516, Compound 20a). Adding fluoride atoms to the tail has been used to achieve more favourable pharmacokinetic properties [55, 56]. Wu et al. [113] made a similar observation in their study and confirmed this using mutagenesis of PPARδ residues δ: V298, L303 and V312.
4. Each PPAR has a unique Ω loop forming the anterior wall of Arm 2. PPARδ has the bulkiest Ω loop residues, followed by α and then γ.

   Studies showed that showed that substituents at the tail can interact favourably with the Ω loop. LC1765 and pemafibrate demonstrated the use of halogen substituents in its ligand tail region to make interactions with Arm 2 [58, 97]. In their study, Wu and colleagues demonstrated that their compounds caused a conformational switch in residue δ: W228 [113].
5. PPARδ has the widest Arm 3, followed by γ and then α.

   Kasuga and colleagues observed that a longer fin substituent that extended into the inferior area of Arm 3 increased selectivity for PPARδ [54].
6. PPARα and PPARγ contain a series of methionine residues in Arms 2 and 3 (α: 355 γ: 364, α: 325 γ: 334, α: M330, γ: M348), differing at residue α: M330 and γ: M348. PPARδ contains none of these residues.

   These methionine residues serve as an important selection criteria between the PPARs. The methionine residues in LBD for PPARα and γ seem to have an 'induced fit' effect, stretching or compressing to accommodate chemical groups when needed (PDB ID: 6L69/2ZNN vs 2P54). Many PPARδ specific agonists adopt an ortho substituted cyclic core design which tends to fully occupy the extra space in this region α: M355 δ: I328 γ: M364 [38, 113]. Decreasing the size of the core or ligand substitutions in the tail region just adjacent to the core selects against PPARδ, as less interactions with the PPARδ LBP are formed [53]. These methionine residues are very sensitive to proximity, the same trifluoromethyl substitution affects affinity differently due to slight shifts in position in the LBD (PDB ID: 2XYX vs 5U46)
7. Forming multiple interactions with residue α: C276 δ: C249 γ: C285 on H3 seems to be correlated to high affinity.

   Ligands that form multiple interactions with this cysteine residue on H3 tend to show high affinity [28]. The sulfonylthiadiazole compound series by Keil and colleagues made significant interactions with δ: C249 and displayed high affinity despite having low efficacy [59]. Partial agonists of PPARγ also interact with this residue [14]. In PPARγ, this cysteine residue is able to form a covalent bond with endogenous ligands [35].

6.4 Tools and New Information

In this section, we mention some of the novel methods used by groups in conjunction with protein crystallography during their drug discovery process.

6.4.1 Examples of Computer-Aided Drug Design

Traditionally, new ligands for PPAR were identified and/or optimized from previously synthesized compounds and validated through binding or cell-based assays. These methods are still frequently used [13, 45, 54, 63, 84, 97, 115]. In many SAR studies, researchers identified lead compounds from their own internal databases [13, 39, 59, 72, 96]. As an example, the scaffold for GW501516 was identified from a screen of libraries for compounds with characteristics of lipophilic carboxylic acids, prepared using combinatorial chemistry and structure-based design [100].

These methods have been quickly surpassed by virtual screening methods that are able to sift through massive, open access chemical databases for novel chemical scaffolds [6, 19, 28]. Chemical ligand databases include ENAMINE, CHEMBL, and WOMBAT [28, 104]. Typically, virtual screening methods can be grouped into ligand-based or structure-based [104]. Lu and colleagues adopted a ligand shape-based search method, for ligands that are likely to adopt a specific conformation that would fit the LBP [71]. On top of a multi-step structure-based virtual screening process, Capelli and colleagues utilized a 'structure interaction fingerprints' approach which considers important interactions with the PPAR subtypes, as opposed to the shape of the LBP [19]. Da'adoosh et al. [28] recently identified 13 chemically diverse, novel compounds with nanomolar affinity at the PPARδ receptor by screening a database of 1.56 million molecules, a feat that trumped all previous lead-based compound optimization in terms of number of novel compounds identified in a single study and the affinity of the compounds identified. They made use of a machine learning algorithm to screen for potential PPAR agonists from the ENAMINE database [28]. Ehrt et al. [36] provide an overview on some computer-based methods in rational ligand design, specifically for to distinguishing between different protein subtypes.

Virtual screening methods frequently use docking programs to validate hits in silico or to understand the structural basis for ligand affinity, especially when biophysical or biochemical techniques are inaccessible, impractical or unsuccessful [24]. Research groups have utilized many different programs such as Glide, GOLD, AutoDock Vina, MOE and OEdocking, typically validating docking results with cell-based assays [28, 37, 69, 91, 104]. However, the transferability of in silico docking results to in vitro/in vivo experiments depends greatly on the appropriate validation of the docking program used and scoring criteria. In addition, accurate selection of the ligand binding site, as well as appropriate preparation of both the molecular target and the chemical ligand, such as assigning adding hydrogens,

replacing unmodelled residues and hydrogen atoms and selection of force fields, is also required [28, 99, 104]. Docking tools have been discussed in recent reviews [99, 104].

Currently, it is still a requirement that in silico docking programs and its results are validated by experimental structural information [104]. This is due to inherent limitations in simulation algorithms, computing power or simply due to wrongly processed input data or faulty parameterization [99, 104]. These limitations are exemplified by the fact that crystallization can often reveal unexpected and novel binding modes – although crystallization comes with its own caveats as discussed by Davis and colleagues [30]. In the case of pemafibrate, the docking result predicted a conformation different from that of the crystal structure PDB ID: 6L69 [58, 117]. Uncommon binding modes were also seen in crystal structures of PPARγ antagonist SR10171 and PPARα agonist WY14643, with ligands binding outside of the typically defined ligand binding pocket [11, 40].

6.4.2 Pharmacokinetics and Pharmacodynamics

Early drug discovery is a multistep process that involves the interrogation of the pharmacokinetic and pharmacodynamic properties of a lead compound [48]. These properties can cause discrepancies between their apparent binding affinity in vitro and their potency or efficacy in vivo [74]. Commonly, researchers measure pharmacokinetic properties, such as maximum drug plasma levels (Cmax), ligand half-life and clearance rate and oral bioavailability in mice or rat models [25, 38, 39, 63–65].

One aspect of the pharmacokinetics of a ligand is its absorption, which can be affected by its lipophilicity [48, 74]. Some examples of researchers that optimize against hydrophobicity include Luckhurst et al. [72], who optimized their compounds based on favourable cLogP value, a measure of hydrophobicity, and Evans et al. [39] and Lagu et al. [63] who used various measures to gauge the solubility of their compounds. Other researchers employ cell permeability tests for their compounds. Evans et al. [39] tested permeability of their compounds 46 and 47 through an artificial membrane. Lagu et al. [63] used Caco-2 permeability assays as a measure of cell permeability.

Another aspect is the metabolism of the ligand [48, 74]. The inclusion of certain chemical motifs in the ligand could slow its metabolism, therefore increasing the bioavailability of the ligand [74]. For example, some researchers intentionally adopt fluorine atoms into their ligands, which block metabolically labile sites [55, 56, 74]. Unfavourable rates of metabolism of ligands could also be predicted by its reactivity against cytochromes P450s. Bristol-Myers Squibb, GSK and Astellas Pharma implemented inhibition tests against cytochrome P450 isoforms 3A4, 2C9, 2C19, 2D6 and 1A2 [39, 63, 110]. In their study, AstraZeneca employed a more direct measure of metabolism by checking their compounds for clearance, via incubation

with rat hepatocytes [72]. Other researchers utilized a similar strategy with liver microsomes to check the metabolic stability of their compounds [38, 39]. Astellas Pharma used liquid chromatography–mass spectrometry (LC-MS) to analyse the metabolites formed from incubation with liver microsomes, revealing 'metabolic fault lines' in their compounds [63]. This allowed for optimization of the chemical motifs in the compounds to reduce liver clearance, increasing exposure. However, one should exercise caution when optimizing solely for low clearance. Lagu et al. [64, 65] hypothesize that, at least for PPARδ ligands, maximum exposure achieved with a relatively low dosage and any more might have toxic effects.

Acknowledging the inherent differences between models, some researchers incorporate simultaneous in vitro and in vivo tests with their structural studies [38]. Research groups from GSK, Takara bio, Plexxikon and Astellas Pharma conducted receptor cross-reactivity tests to ensure ligand specificity towards PPAR only [6, 64, 65, 81, 82]. Other cross-reactivity targets include human Ether-a-go-go-Related Gene (hERG). Wang et al. [110] performed a hERG assay to ensure their compounds do not interfere with cardiac repolarization. hERG testing has since become regulation for any compounds to be approved by the FDA and has been performed by other studies [64, 65, 103]. Inherent genetic differences between animal models and humans can also result in discrepancies. One such difference is the absence of a PPRE in the Apo-A1 gene in mice. Some researchers used human Apo-A1 transgenic mice for their in vivo tests to account for this difference [92, 97].

Such in vitro/in vivo tests can be costly and time consuming for smaller research groups or simply impractical during the identification process of new drug leads. Fortunately, there are a range of in silico web tools that can be used to predict pharmacokinetic and even pharmacodynamic properties such as hydrophobicity, CP450 inhibition and hERG inhibition. Online tools such as preADMET can be used to predict pharmacokinetic parameters of any compound. In addition, preADMET can predict the 'drug-likeness' of a compound based on Lipinski's Rule of 5 and other defined drug-like rules [67]. A similar tool, FAF-Drugs3 (now FAF-Drugs4), was used by Capelli et al. [19] as a final screening step in their initial virtual screening process. Ehrt et al. [36] lists binding site comparison tools, which can be invaluable in identifying off-target effects. It is important to note, however, that as of now these web tools are still unable to completely substitute in vitro/in vivo tests [2].

6.4.3 Wider Considerations for PPAR

In this section we examine other factors that might affect the translation of in vitro/in vivo successes into a clinical setting. This could also provide possible explanations as to why some patients respond to currently available drugs, while others do not.

Table 6.28 Non-exhaustive list of PPAR LBD mutations and its associated diseases

PPAR	Mutation	Disease	Reference
α	V227A	Non-alcoholic fatty liver disease	Chen et al. [22]
γ	V290M, P467L	Familial partial lipodystrophy type 3	Barroso et al. [8]
	Q286P, R288H	Colon cancer	Sarraf et al. [90]
	F360L	Familial partial lipodystrophy type 3	Hegele et al. [47]
	R397C	Familial partial lipodystrophy type 3	Agarwal and Garg [1]
	D396N	Familial partial lipodystrophy type 3	Ludtke et al. [73]
	R280P, A233E	Familial partial lipodystrophy type 3	Agostini et al. [3]
	K422Q, L423P	Colon cancer, familial partial lipodystrophy type 3	Broekema et al. [12]
	S221L, M252I, I262M, T447M	Luminal bladder tumor	Rochel et al. [89]

6.4.3.1 LBD Mutations

Mutations in the PPAR protein can result in aberrant gene activation or repression [3, 89]. In fact, these mutations are relatively common – it is estimated that 1 in 500 people have mutations in their PPARγ genes [75]. As previously mentioned in Sect. 6.1.3, in their study, Takada and colleagues demonstrated that even the mutation of one amino acid residue could change the ligand binding phenotype from one subtype to another [101]. The first documented mutation for PPARγ was a dominant-negative mutation of γ: V290M and P467L in the PPARγ LBD [8]. This and other characterized PPARγ mutations have been correlated with familial partial lipodystrophy type 3 and also with various cancers (Table 6.28).

Majithia and colleagues observed that single mutations in the protein sequence altered protein function to a variable degree, resulting in a gradient of phenotypes instead of the traditionally conceptualized 'on/off' effects of mutations [75]. These mutations can have varying effects on the stability and thus on the activity of the LBD, perturbations that can be rescued by synthetic ligands as demonstrated by Agostini and colleagues [3]. These mutations can also potentially alter ligand binding and subtype affinity, causing aberrant cross activation [3, 101]. A patient could even have mutations in other related genes and/or proteins that alter their downstream responses or cross-reactivity to a PPAR ligand [89]. Thus, it is important that mutations in PPAR and other related genes are considered during treatment of patients with drugs [3].

6.4.3.2 PPAR Intact Structure and Implications

While the focus of this review was on the interactions in the LBD, PPAR works in concert with multiple components to exert its gene transcriptional activity [121]. Hence, models of ligand binding and stabilization of the LBD should always be considered in the context of the full intact structure.

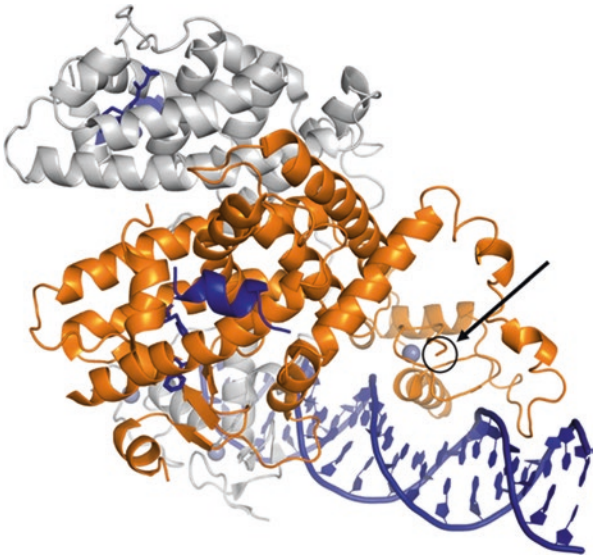

Fig. 6.32 Intact structure of PPARγ LBD-DBD region (orange) complexed with RXRα (light grey) and bound by their respective ligands rosiglitazone and 9-*cis*-retinoic acid (dark blue), coactivator peptides (dark blue) and DNA sequence 5′-GCAAACTAGGTCAAAGGTCAG-3′ and 5′-CTGACCTTTGACCTAGTTTGC-3′ (dark blue). The N terminal end of the modelled protein is circled in black (PDB ID: 3DZY)

Chandra et al. [21] crystallized the ligand-PPAR-RXR-coactivator-DNA complex, providing the first look at a ligand bound DNA/NR complex (Fig. 6.32). Each component of complex assumed conformations similar to previously, individually determined structures [21] (PDB ID: 2ENV). In this complex, the RXRα DBD and PPARγ DBD interact with the β-sheet and H2 region and H7–8 loop and H9–10/11 of the PPARγ LBD, respectively [21, 120] (Fig. 6.32). This suggests that partial agonists, that only stabilize the β-sheet region and/or inhibit phosphorylation of S245 (on H2–H2′ loop), may be able to induce gene transcription through stabilization of the DBD [14, 87].

As mentioned previously in Sect. 6.1.3, the poorly conserved regions Ω loop and H9 in the LBD and the hinge region (domain C) are exposed to the bulk solvent [21, 113]. These regions could possibly form interactions with other components of the gene transcriptional complex [21, 120]. Mutations in H9 and the hinge region could affect assembly of the PPAR gene transcriptional complex. Ligands that aim to bind and stabilize the Ω loop can also have similar effects [57].

The poorly conserved and highly mobile A/B domains were left unmodelled in this structure, and its exact position is still currently unknown even though experiments have been conducted to uncover details of these domains [17, 94]. A recent electron cryo-microscopy (cryoEM) structure of ER suggests that its A/B domains sits lateral to the ER/RXR dimer core, exposed to the solvent [120]. In this PPAR-RXR structure, N terminal end of the modelled PPARγ protein leading to the A/B

domain seems to point towards the anterior face of the PPARγ LBD, suggesting that the PPARγ A/B domains occupy a similar position to that for ER (Fig. 6.32) [21, 120]. If so, mutations or post translational modifications (PTMs) in A/B domains could have a structural effect on the LBD and vice versa [15, 46, 78, 120]. This scenario is likely, as mutations in A/B domains have also been correlated with diseases, and PTMs have been shown to affect receptor activity [4, 7, 17, 89]. It has even been shown that domains A/B are involved in binding of cofactors and increase selectivity of each PPAR subtype [17]. More work needs to be done to understand the structure and implications of domains A and B in PPAR.

Adding on to the puzzle, it was noted that all the intact NR/DNA complexes published so far adopt different quaternary conformations [60]. In the case of PPAR, its length was laterally aligned with the DNA [21]. This observation could possibly challenge the paradigm that ligands in general should aim to stabilize H12 in the active conformation, as this could potentially have varying effects in different NR, assembly of the gene transcriptional complex and transcription of downstream genes.

6.4.3.3 Coregulators and FABPs

Just from the studies examined in Sect. 6.2, we see a wide variety of cell types, assay formats and animal models used. The variety of experimental methods used generally depends on availability or ease of access. However, using different models can become an issue when comparing results between studies, due to inherent differences between models, such as differences in the levels of proteins that could affect potentiation of a ligand's effects [26, 121].

Fatty acid binding proteins (FABPs) bind to and shuttle endogenous and synthetic ligands into the nucleus for interaction with PPARs. Each FABP subtype interact specifically with one PPAR subtype and typically only bind ligands that are specific for its own PPAR subtype (α: FABP1, δ: FABP5 γ: FABP4) [5, 83]. The transactivation assays that are commonly used to test ligand-LBD EC_{50} values should also, in theory, test for ligand-FABP binding. While FABPs can bind ligands specific for another PPAR subtype, it does not potentiate its transcriptional activity. This has potential implications on research conducted with different cellular models as different cells contain different subtypes and levels of FABP [83].

Coregulators play a crucial part in gene regulation. Each coregulator seems to be able to coordinate different and distinct genetic pathways [88, 121]. PPARs are able to bind to a range of coregulators, including NCoR1, SMRT, PGC-1α, CBP and SRC1 [18, 52, 70, 88, 116, 121]. Coregulators play a huge part in potentiation of NR-activated gene transcription [26]. Interestingly, PPAR ligands were able to differentially recruit coregulators. Specifically, this was observed for PPARγ partial agonist PA-082, where PGC-1α seems to be preferentially recruited as opposed to SRC1 when compared to rosiglitazone [18, 70]. In PPARδ, Lagu and colleagues demonstrated that two compounds can activate different subsets of genes, despite having similar affinities and plasma exposure [64, 65]. This difference could possibly be mediated by differential recruitment of cofactors. Considering that different

cells models have different levels of coregulators, the implications on cell-based assays or data could be significant [7].

6.5 Conclusion

The biology of PPARs presents a valuable therapeutic target for the treatment of metabolic diseases, heart and neurological conditions and cancers [23, 82]. However, there are many structural, pharmacological and biochemical challenges to designing a safe but efficacious PPAR drug [6, 64, 65]. There seems to be an interesting irony with PPAR ligand discovery. On one hand, a potential PPAR drug candidate must perform significantly better than currently available drugs on a given set of parameters. However, in the case of PPAR, it seems that most drug candidates that improve on affinity, potency and efficacy often fall short due to unforeseen side effects. A widely held hypothesis suggests that a lack of selectivity for one specific subtype causes side effects [58, 72, 113]. Interestingly, this issue of selectivity is not unique to the PPAR subtypes; two proteins with different sequences and even folds can have similar binding pocket environments, and ligands can adapt to multiple binding pockets [36, 98]. Another recent hypothesis states that PPAR might also have a therapeutic index; if a specific range of ligand concentration in the blood or if a hypothetical 'threshold of activation' is exceeded, side effects will occur [64, 65]. These side effects of PPAR activation may also be due to aspects of cross talk with other nuclear receptors that are still currently unknown [20, 64, 65].

For now, the complexity of the PPAR regulation network will remain an obstacle when scaling from cell and animal-based models to a clinical setting [26]. The differences in cell and animal models used between studies also add to the complexity [7, 102, 109]. An important point not discussed in this review is that different species have different PPAR ligand binding selectivity; the implications of species selectivity becomes significant, considering preclinical safety trials are conducted in animal models [31, 61]. However, advances in global screening methods and single cell quantitative polymerase chain reaction (qPCR) analysis of human tissues may play a key role in unravelling this problem [7, 26]. The research into PPAR ligand discovery thus far has revealed many insights into the activation and function of the PPARs. In this review, we have attempted to tackle the issue of absolute selectivity of PPAR ligands, by examining the available structural information of the PPAR ligand binding domain. From this, we have identified a few observations that can be used to create a subtype-specific PPAR agonist. There still remain a few issues in the field of PPAR structural selectivity: The identification of the full-length structure, including the A/B domains for all the PPAR subtypes, its implications on ligand function and selectivity between subtypes, the elucidation of PPAR gene activation networks and the regulation of those networks in different contexts, such as cell and animal models.

References

1. Agarwal AK, Garg A. A novel heterozygous mutation in peroxisome proliferator-activated receptor-γ gene in a patient with familial partial lipodystrophy. J Clin Endocrinol Metabol. 2002;87:408. https://doi.org/10.1210/jcem.87.1.8290.
2. Agoni C, Olotu FA, Ramharack P, Soliman ME. Druggability and drug-likeness concepts in drug design: are biomodelling and predictive tools having their say? J Mol Model. 2020;26:120. https://doi.org/10.1007/s00894-020-04385-6.
3. Agostini M, Schoenmakers E, Beig J, Fairall L, Szatmari I, Rajanayagam O, Muskett FW, Adams C, Marais AD, O'Rahilly S, Semple RK, Nagy L, Majithia AR, Schwabe JWR, Blom DJ, Murphy R, Chatterjee K, Savage DB. A pharmacogenetic approach to the treatment of patients with PPARG mutations. Diabetes. 2018;67:1086–92. https://doi.org/10.2337/db17-1236.
4. Al-Shali K, Cao H, Knoers N, Hermus AR, Tack CJ, Hegele RA. A single-base mutation in the peroxisome proliferator-activated receptor γ4 promoter associated with altered in vitro expression and partial lipodystrophy. J Clin Endocrinol Metabol. 2004;89:5655–60. https://doi.org/10.1210/jc.2004-0280.
5. Armstrong EH, Goswami D, Griffin PR, Noy N, Ortlund EA. Structural basis for ligand regulation of the fatty acid-binding protein 5, peroxisome proliferator-activated receptor β/δ (FABP5-PPARβ/δ) signaling pathway. J Biol Chem. 2014;289:14941–54. https://doi.org/10.1074/jbc.M113.514646.
6. Artis DR, Lin JJ, Zhang C, Wang W, Mehra U, Perreault M, Erbe D, Krupka HI, England BP, Arnold J, Plotnikov AN, Marimuthu A, Nguyen H, Will S, Signaevsky M, Kral J, Cantwell J, Settachatgull C, Yan DS, Fong D, Oh A, Shi S, Womack P, Powell B, Habets G, West BL, Zhang KYJ, Milburn MV, Vlasuk GP, Hirth KP, Nolop K, Bollag G, Ibrahim PN, Tobin JF. Scaffold-based discovery of indeglitazar, a PPAR pan-active anti-diabetic agent. Proc Natl Acad Sci. 2009;106:262–7. https://doi.org/10.1073/pnas.0811325106.
7. Attianese GMG, Desvergne B. Integrative and systemic approaches for evaluating PPARβ/δ (PPARD) function. Nucl Recept Signal. 2015;13:e001. https://doi.org/10.1621/nrs.13001.
8. Barroso I, Gurnell M, Crowley VEF, Agostini M, Schwabe JW, Soos MA, Maslen GL, Williams TDM, Lewis H, Schafer AJ, Chatterjee VKK, O'Rahilly S. Dominant negative mutations in human PPARγ associated with severe insulin resistance, diabetes mellitus and hypertension. Nature. 1999;402:880–3. https://doi.org/10.1038/47254.
9. Batista FAH, Trivella DBB, Bernardes A, Gratieri J, Oliveira PSL, Figueira ACM, Webb P, Polikarpov I. Structural insights into human peroxisome proliferator activated receptor delta (PPAR-delta) selective ligand binding. PLoS One. 2012;7:e33643. https://doi.org/10.1371/journal.pone.0033643.
10. Berman HM. The Protein Data Bank. Nucleic Acids Res. 2000;28:235–42. https://doi.org/10.1093/nar/28.1.235.
11. Bernardes A, Souza PCT, Muniz JRC, Ricci CG, Ayers SD, Parekh NM, Godoy AS, Trivella DBB, Reinach P, Webb P, Skaf MS, Polikarpov I. Molecular mechanism of peroxisome proliferator-activated receptor α activation by WY14643: a new mode of ligand recognition and receptor stabilization. J Mol Biol. 2013;425:2878–93. https://doi.org/10.1016/j.jmb.2013.05.010.
12. Broekema MF, Massink MPG, Donato C, de Ligt J, Schaarschmidt J, Borgman A, Schooneman MG, Melchers D, Gerding MN, Houtman R, Bonvin AMJJ, Majithia AR, Monajemi H, van Haaften GW, Soeters MR, Kalkhoven E. Natural helix 9 mutants of PPARγ differently affect its transcriptional activity. Mol Metab. 2019;20:115–27. https://doi.org/10.1016/j.molmet.2018.12.005.
13. Brown PJ, Smith-Oliver TA, Charifson PS, Tomkinson NCO, Fivush AM, Sternbach DD, Wade LE, Orband-Miller L, Parks DJ, Blanchard SG, Kliewer SA, Lehmann JM, Willson TM. Identification of peroxisome proliferator-activated receptor ligands from a biased chemical library. Chem Biol. 1997;4:909–18. https://doi.org/10.1016/S1074-5521(97)90299-4.

14. Bruning JB, Chalmers MJ, Prasad S, Busby SA, Kamenecka TM, He Y, Nettles KW, Griffin PR. Partial agonists activate PPARγ using a helix 12 independent mechanism. Structure. 2007;15:1258–71. https://doi.org/10.1016/j.str.2007.07.014.
15. Brunmeir R, Xu F. Functional regulation of PPARs through post-translational modifications. IJMS. 2018;19:1738. https://doi.org/10.3390/ijms19061738.
16. Bugge A, Holst D. PPAR agonists, – could tissue targeting pave the way? Biochimie. 2017;136:100–4. https://doi.org/10.1016/j.biochi.2016.10.017.
17. Bugge A, Mandrup S. Molecular mechanisms and genome-wide aspects of PPAR subtype specific transactivation. PPAR Res. 2010;2010:1–12. https://doi.org/10.1155/2010/169506.
18. Burgermeister E, Schnoebelen A, Flament A, Benz J, Stihle M, Gsell B, Rufer A, Ruf A, Kuhn B, Märki HP, Mizrahi J, Sebokova E, Niesor E, Meyer M. A novel partial agonist of peroxisome proliferator-activated receptor-γ (PPARγ) recruits PPARγ-coactivator-1α, prevents triglyceride accumulation, and potentiates insulin signaling in vitro. Mol Endocrinol. 2006;20:809–30. https://doi.org/10.1210/me.2005-0171.
19. Capelli D, Cerchia C, Montanari R, Loiodice F, Tortorella P, Laghezza A, Cervoni L, Pochetti G, Lavecchia A. Structural basis for PPAR partial or full activation revealed by a novel ligand binding mode. Sci Rep. 2016;6:34792. https://doi.org/10.1038/srep34792.
20. Chan LSA, Wells RA. Cross-talk between PPARs and the partners of RXR: a molecular perspective. PPAR Res. 2009;2009:1–9. https://doi.org/10.1155/2009/925309.
21. Chandra V, Huang P, Hamuro Y, Raghuram S, Wang Y, Burris TP, Rastinejad F. Structure of the intact PPAR-γ–RXR-α nuclear receptor complex on DNA. Nature. 2008;456:350–6. https://doi.org/10.1038/nature07413.
22. Chen S, Li Y, Li S, Yu C. A Val227Ala substitution in the peroxisome proliferator activated receptor alpha (PPAR alpha) gene associated with non-alcoholic fatty liver disease and decreased waist circumference and waist-to-hip ratio. J Gastroenterol Hepatol. 2008;23:1415–8. https://doi.org/10.1111/j.1440-1746.2008.05523.x.
23. Cheng T, Low M, Lee T. Exploration and development of PPAR modulators in health and disease: an update of clinical evidence. IJMS. 2019;20:5055. https://doi.org/10.3390/ijms20205055.
24. Congreve M, Chessari G, Tisi D, Woodhead AJ. Recent developments in fragment-based drug discovery. J Med Chem. 2008;51:3661–80. https://doi.org/10.1021/jm8000373.
25. Connors RV, Wang Z, Harrison M, Zhang A, Wanska M, Hiscock S, Fox B, Dore M, Labelle M, Sudom A, Johnstone S, Liu J, Walker NPC, Chai A, Siegler K, Li Y, Coward P. Identification of a PPARδ agonist with partial agonistic activity on PPARγ. Bioorg Med Chem Lett. 2009;19:3550–4. https://doi.org/10.1016/j.bmcl.2009.04.151.
26. Costa V, Gallo MA, Letizia F, Aprile M, Casamassimi A, Ciccodicola A. PPARG: gene expression regulation and next-generation sequencing for unsolved issues. PPAR Res. 2010;2010:1–17. https://doi.org/10.1155/2010/409168.
27. Cronet P, Petersen JFW, Folmer R, Blomberg N, Sjöblom K, Karlsson U, Lindstedt E-L, Bamberg K. Structure of the PPARα and -γ ligand binding domain in complex with AZ 242; ligand selectivity and agonist activation in the PPAR family. Structure. 2001;9:699–706. https://doi.org/10.1016/S0969-2126(01)00634-7.
28. Da'adoosh B, Marcus D, Rayan A, King F, Che J, Goldblum A. Discovering highly selective and diverse PPAR-delta agonists by ligand based machine learning and structural modeling. Sci Rep. 2019;9:1106. https://doi.org/10.1038/s41598-019-38508-8.
29. Dassault Systèmes BIOVIA. Discovery Studio Visualizer, v20.1.0.19295. San Diego: Dassault Systèmes; 2019.
30. Davis A, Stgallay S, Kleywegt G. Limitations and lessons in the use of X-ray structural information in drug design. Drug Discov Today. 2008;13:831–41. https://doi.org/10.1016/j.drudis.2008.06.006.
31. Desvergne B, Wahli W. Peroxisome proliferator-activated receptors: nuclear control of metabolism*. Endocr Rev. 1999;20:649–88. https://doi.org/10.1210/edrv.20.5.0380.

32. Devasthale P, Chen S, Jeon Y, Qu F, Ryono D, Wang W, Zhang H, Cheng L, Farrelly D, Golla R, Grover G, Ma Z, Moore L, Seethala R, Sun W, Doweyko A, Chandrasena G, Sleph P, Hariharan N, Cheng P. Discovery of tertiary aminoacids as dual PPARα/γ agonists-I. Bioorg. Med. Chem. Lett. 2007;17(8):2312–2316.
33. dos Santos JC, Bernardes A, Giampietro L, Ammazzalorso A, De Filippis B, Amoroso R, Polikarpov I. Different binding and recognition modes of GL479, a dual agonist of peroxisome proliferator-activated receptor α/γ. J Struct Biol. 2015;191:332–40. https://doi.org/10.1016/j.jsb.2015.07.006.
34. Ebdrup S, Pettersson I, Rasmussen HB, Deussen H-J, Frost Jensen A, Mortensen SB, Fleckner J, Pridal L, Nygaard L, Sauerberg P. Synthesis and biological and structural characterization of the dual-acting peroxisome proliferator-activated receptor α/γ agonist ragaglitazar. J Med Chem. 2003;46:1306–17. https://doi.org/10.1021/jm021027r.
35. Egawa D, Itoh T, Akiyama Y, Saito T, Yamamoto K. 17-OxoDHA is a PPARα/γ dual covalent modifier and agonist. ACS Chem Biol. 2016;11:2447–55. https://doi.org/10.1021/acschembio.6b00338.
36. Ehrt C, Brinkjost T, Koch O. Impact of binding site comparisons on medicinal chemistry and rational molecular design. J Med Chem. 2016;59:4121–51. https://doi.org/10.1021/acs.jmedchem.6b00078.
37. Elzahhar PA, Alaaeddine R, Ibrahim TM, Nassra R, Ismail A, Chua BSK, Frkic RL, Bruning JB, Wallner N, Knape T, von Knethen A, Labib H, El-Yazbi AF, Belal ASF. Shooting three inflammatory targets with a single bullet: novel multi-targeting anti-inflammatory glitazones. Eur J Med Chem. 2019;167:562–82. https://doi.org/10.1016/j.ejmech.2019.02.034.
38. Epple R, Azimioara M, Russo R, Xie Y, Wang X, Cow C, Wityak J, Karanewsky D, Bursulaya B, Kreusch A, Tuntland T, Gerken A, Iskandar M, Saez E, Martin Seidel H, Tian S-S. 3,4,5-Trisubstituted isoxazoles as novel PPARδ agonists. Part 2. Bioorg Med Chem Lett. 2006;16:5488–92. https://doi.org/10.1016/j.bmcl.2006.08.052.
39. Evans KA, Shearer BG, Wisnoski DD, Shi D, Sparks SM, Sternbach DD, Winegar DA, Billin AN, Britt C, Way JM, Epperly AH, Leesnitzer LM, Merrihew RV, Xu RX, Lambert MH, Jin J. Phenoxyacetic acids as PPARδ partial agonists: synthesis, optimization, and in vivo efficacy. Bioorg Med Chem Lett. 2011;21:2345–50. https://doi.org/10.1016/j.bmcl.2011.02.077.
40. Frkic RL, Marshall AC, Blayo A-L, Pukala TL, Kamenecka TM, Griffin PR, Bruning JB. PPARγ in complex with an antagonist and inverse agonist: a tumble and trap mechanism of the activation helix. iScience. 2018;5:69–79. https://doi.org/10.1016/j.isci.2018.06.012.
41. Fyffe SA, Alphey MS, Buetow L, Smith TK, Ferguson MAJ, Sørensen MD, Björkling F, Hunter WN. Recombinant human PPAR-β/δ ligand-binding domain is locked in an activated conformation by endogenous fatty acids. J Mol Biol. 2006;356:1005–13. https://doi.org/10.1016/j.jmb.2005.12.047.
42. Gampe RT, Montana VG, Lambert MH, Miller AB, Bledsoe RK, Milburn MV, Kliewer SA, Willson TM, Xu HE. Asymmetry in the PPARγ/RXRα crystal structure reveals the molecular basis of heterodimerization among nuclear receptors. Mol Cell. 2000;5:545–55. https://doi.org/10.1016/S1097-2765(00)80448-7.
43. Gavzan H, Hashemi F, Babaei J, Sayyah M. A role for peroxisome proliferator-activated receptor α in anticonvulsant activity of docosahexaenoic acid against seizures induced by pentylenetetrazole. Neurosci Lett. 2018;681:83–6. https://doi.org/10.1016/j.neulet.2018.05.042.
44. GENFIT. GENFIT: announces results from interim analysis of RESOLVE-IT phase 3 trial of elafibranor in adults with NASH and fibrosis. https://ir.genfit.com/news-releases/news-release-details/genfit-announces-results-interim-analysis-resolve-it-phase-3/. Accessed 1 Sept 2020.
45. Giampietro L, D'Angelo A, Giancristofaro A, Ammazzalorso A, De Filippis B, Fantacuzzi M, Linciano P, Maccallini C, Amoroso R. Synthesis and structure–activity relationships of fibrate-based analogues inside PPARs. Bioorg Med Chem Lett. 2012;22:7662–6. https://doi.org/10.1016/j.bmcl.2012.09.111.

46. Gou Q, Jiang Y, Zhang R, Xu Y, Xu H, Zhang W, Shi J, Hou Y. PPARδ is a regulator of autophagy by its phosphorylation. Oncogene. 2020;39:4844–53. https://doi.org/10.1038/s41388-020-1329-x.
47. Hegele RA, Cao H, Frankowski C, Mathews ST, Leff T. PPARG F388L, a transactivation-deficient mutant, in familial partial lipodystrophy. Diabetes. 2002;51:3586–90. https://doi.org/10.2337/diabetes.51.12.3586.
48. Hughes J, Rees S, Kalindjian S, Philpott K. Principles of early drug discovery: principles of early drug discovery. Br J Pharmacol. 2011;162:1239–49. https://doi.org/10.1111/j.1476-5381.2010.01127.x.
49. Issemann I, Green S. Activation of a member of the steroid hormone receptor superfamily by peroxisome proliferators. Nature. 1990;347:645–50. https://doi.org/10.1038/347645a0.
50. Itoh T, Fairall L, Amin K, Inaba Y, Szanto A, Balint B, Nagy L, Yamamoto K, Schwabe J. Structural basis for the activation of PPARγ by oxidized fatty acids. Nat. Str. Mol. Biol. 2008;15(9):924–931.
51. Janani C, Ranjitha Kumari BD. PPAR gamma gene – a review. Diabetes Metab Syndr Clin Res Rev. 2015;9:46–50. https://doi.org/10.1016/j.dsx.2014.09.015.
52. Jin L, Lin S, Rong H, Zheng S, Jin S, Wang R, Li Y. Structural basis for iloprost as a dual peroxisome proliferator-activated receptor α/δ agonist. J Biol Chem. 2011;286:31473–9. https://doi.org/10.1074/jbc.M111.266023.
53. Kasuga J, Yamasaki D, Araya Y, Nakagawa A, Makishima M, Doi T, Hashimoto Y, Miyachi H. Design, synthesis, and evaluation of a novel series of α-substituted phenylpropanoic acid derivatives as human peroxisome proliferator-activated receptor (PPAR) α/δ dual agonists for the treatment of metabolic syndrome. Bioorg Med Chem. 2006;14:8405–14. https://doi.org/10.1016/j.bmc.2006.09.001.
54. Kasuga J, Nakagome I, Aoyama A, Sako K, Ishizawa M, Ogura M, Makishima M, Hirono S, Hashimoto Y, Miyachi H. Design, synthesis, and evaluation of potent, structurally novel peroxisome proliferator-activated receptor (PPAR) δ-selective agonists. Bioorg Med Chem. 2007;15:5177–90. https://doi.org/10.1016/j.bmc.2007.05.023.
55. Kasuga J, Oyama T, Hirakawa Y, Makishima M, Morikawa K, Hashimoto Y, Miyachi H. Improvement of the transactivation activity of phenylpropanoic acid-type peroxisome proliferator-activated receptor pan agonists: effect of introduction of fluorine at the linker part. Bioorg Med Chem Lett. 2008a;18:4525–8. https://doi.org/10.1016/j.bmcl.2008.07.046.
56. Kasuga J, Yamasaki D, Ogura K, Shimizu M, Sato M, Makishima M, Doi T, Hashimoto Y, Miyachi H. SAR-oriented discovery of peroxisome proliferator-activated receptor pan agonist with a 4-adamantylphenyl group as a hydrophobic tail. Bioorg Med Chem Lett. 2008b;18:1110–5. https://doi.org/10.1016/j.bmcl.2007.12.001.
57. Kaupang Å, Hansen TV. The PPAR Ω pocket: renewed opportunities for drug development. PPAR Res. 2020;2020:1–21. https://doi.org/10.1155/2020/9657380.
58. Kawasaki M, Kambe A, Yamamoto Y, Arulmozhiraja S, Ito S, Nakagawa Y, Tokiwa H, Nakano S, Shimano H. Elucidation of molecular mechanism of a selective PPARα modulator, pemafibrate, through combinational approaches of X-ray crystallography, thermodynamic analysis, and first-principle calculations. IJMS. 2020;21:361. https://doi.org/10.3390/ijms21010361.
59. Keil S, Matter H, Schönafinger K, Glien M, Mathieu M, Marquette J-P, Michot N, Haag-Diergarten S, Urmann M, Wendler W. Sulfonylthiadiazoles with an unusual binding mode as partial dual peroxisome proliferator-activated receptor (PPAR) γ/δ agonists with high potency and in vivo efficacy. ChemMedChem. 2011;6:633–53. https://doi.org/10.1002/cmdc.201100047.
60. Khorasanizadeh S, Rastinejad F. Visualizing the architectures and interactions of nuclear receptors. Endocrinology. 2016;157:4212–21. https://doi.org/10.1210/en.2016-1559.
61. Kliewer SA, Sundseth SS, Jones SA, Brown PJ, Wisely GB, Koble CS, Devchand P, Wahli W, Willson TM, Lenhard JM, Lehmann JM. Fatty acids and eicosanoids regulate gene expres-

sion through direct interactions with peroxisome proliferator-activated receptors and. Proc Natl Acad Sci. 1997;94:4318–23. https://doi.org/10.1073/pnas.94.9.4318.
62. Kroker AJ, Bruning JB. Review of the structural and dynamic mechanisms of PPAR γ partial agonism. PPAR Res. 2015;2015:1–15. https://doi.org/10.1155/2015/816856.
63. Lagu B, Kluge AF, Fredenburg RA, Tozzo E, Senaiar RS, Jaleel M, Panigrahi SK, Tiwari NK, Krishnamurthy NR, Takahashi T, Patane MA. Novel highly selective peroxisome proliferator-activated receptor δ (PPARδ) modulators with pharmacokinetic properties suitable for once-daily oral dosing. Bioorg Med Chem Lett. 2017;27:5230–4. https://doi.org/10.1016/j.bmcl.2017.10.037.
64. Lagu B, Kluge AF, Goddeeris MM, Tozzo E, Fredenburg RA, Chellur S, Senaiar RS, Jaleel M, Babu DRK, Tiwari NK, Takahashi T, Patane MA. Highly selective peroxisome proliferator-activated receptor δ (PPARδ) modulator demonstrates improved safety profile compared to GW501516. Bioorg Med Chem Lett. 2018a;28:533–6. https://doi.org/10.1016/j.bmcl.2017.11.006.
65. Lagu B, Kluge AF, Tozzo E, Fredenburg R, Bell EL, Goddeeris MM, Dwyer P, Basinski A, Senaiar RS, Jaleel M, Tiwari NK, Panigrahi SK, Krishnamurthy NR, Takahashi T, Patane MA. Selective PPARδ modulators improve mitochondrial function: potential treatment for Duchenne muscular dystrophy (DMD). ACS Med Chem Lett. 2018b;9:935–40. https://doi.org/10.1021/acsmedchemlett.8b00287.
66. Lazou A, Barlaka E. Peroxisome proliferator-activated receptor (PPAR). In: Choi S, editor. Encyclopedia of signaling molecules. New York: Springer; 2016. p. 1–7.
67. Lee SK, Chang GS, Lee IH, Chung JE, Sung KY, No KT. The PreADME: PC-BASED PROGRAM FOR BATCH PREDICTION OF ADME PROPERTIES. EuroQSAR 2004, Istanbul, Turkey. September 5–10, 2004.
68. Li Z, Chen Y, Zhou Z, Deng L, Xu Y, Hu L, Liu B, Zhang L. Discovery of first-in-class thiazole-based dual FFA1/PPARδ agonists as potential anti-diabetic agents. Eur J Med Chem. 2019;164:352–65. https://doi.org/10.1016/j.ejmech.2018.12.069.
69. Li Z, Xu Y, Cai Z, Wang X, Ren Q, Zhou Z, Xie R. Discovery of novel dual PPARα/δ agonists based on benzimidazole scaffold for the treatment of non-alcoholic fatty liver disease. Bioorg Chem. 2020;99:103803. https://doi.org/10.1016/j.bioorg.2020.103803.
70. Liu C, Feng T, Zhu N, Liu P, Han X, Chen M, Wang X, Li N, Li Y, Xu Y, Si S. Identification of a novel selective agonist of PPARγ with no promotion of adipogenesis and less inhibition of osteoblastogenesis. Sci Rep. 2015;5:9530. https://doi.org/10.1038/srep09530.
71. Lu I-L, Huang C-F, Peng Y-H, Lin Y-T, Hsieh H-P, Chen C-T, Lien T-W, Lee H-J, Mahindroo N, Prakash E, Yueh A, Chen H-Y, Goparaju CMV, Chen X, Liao C-C, Chao Y-S, Hsu JT-A, Wu S-Y. Structure-based drug design of a novel family of PPARγ partial agonists: virtual screening, X-ray crystallography, and in vitro/in vivo biological activities. J Med Chem. 2006;49:2703–12. https://doi.org/10.1021/jm051129s.
72. Luckhurst CA, Stein LA, Furber M, Webb N, Ratcliffe MJ, Allenby G, Botterell S, Tomlinson W, Martin B, Walding A. Discovery of isoindoline and tetrahydroisoquinoline derivatives as potent, selective PPARδ agonists. Bioorg Med Chem Lett. 2011;21:492–6. https://doi.org/10.1016/j.bmcl.2010.10.117.
73. Ludtke A, Buettner J, Schmidt HH-J, Worman HJ. New PPARG mutation leads to lipodystrophy and loss of protein function that is partially restored by a synthetic ligand. J Med Genet. 2007;44:e88. https://doi.org/10.1136/jmg.2007.050567.
74. Maddaford SP. A medicinal chemistry perspective on structure-based drug design and development. In: Tari LW, editor. Structure-based drug discovery. Totowa: Humana Press; 2012. p. 351–81.
75. Majithia AR, Tsuda B, Agostini M, Gnanapradeepan K, Rice R, Peloso G, Patel KA, Zhang X, Broekema MF, Patterson N, Duby M, Sharpe T, Kalkhoven E, Rosen ED, Barroso I, Ellard S, Kathiresan S, O'Rahilly S, Chatterjee K, Florez JC, Mikkelsen T, Savage DB, Altshuler D, UK Monogenic Diabetes Consortium, Myocardial Infarction Genetics Consortium, UK

Congenital Lipodystrophy Consortium. Prospective functional classification of all possible missense variants in PPARG. Nat Genet. 2016;48:1570–5. https://doi.org/10.1038/ng.3700.
76. Miyachi H, Nomura M, Tanase T, Takahashi Y, Ide T, Tsunoda M, Murakami K, Awano K. Design, synthesis and evaluation of substituted phenylpropanoic acid derivatives as peroxisome proliferator-activated receptor (PPAR) activators: novel human PPARα-selective activators. Bioorg Med Chem Lett. 2002;12:77–80. https://doi.org/10.1016/S0960-894X(01)00672-2.
77. Montanari R, Saccoccia F, Scotti E, Crestani M, Godio C, Gilardi F, Loiodice F, Fracchiolla G, Laghezza A, Tortorella P, Lavecchia A, Novellino E, Mazza F, Aschi M, Pochetti G. Crystal structure of the peroxisome proliferator-activated receptor γ (PPARγ) ligand binding domain complexed with a novel partial agonist: a new region of the hydrophobic pocket could be exploited for drug design. J Med Chem. 2008;51:7768–76. https://doi.org/10.1021/jm800733h.
78. Nakamura M, Liu T, Husain S, Zhai P, Warren JS, Hsu C-P, Matsuda T, Phiel CJ, Cox JE, Tian B, Li H, Sadoshima J. Glycogen synthase kinase-3α promotes fatty acid uptake and lipotoxic cardiomyopathy. Cell Metab. 2019;29:1119–1134.e12. https://doi.org/10.1016/j.cmet.2019.01.005.
79. Nolte RT, Wisely GB, Westin S, Cobb JE, Lambert MH, Kurokawa R, Rosenfeld MG, Willson TM, Glass CK, Milburn MV. Ligand binding and co-activator assembly of the peroxisome proliferator-activated receptor-γ. Nature. 1998;395:137–43. https://doi.org/10.1038/25931.
80. Oliver M. The clofibrate saga: a retrospective commentary: commentary. Br J Clin Pharmacol. 2012;74:907–10. https://doi.org/10.1111/j.1365-2125.2012.04282.x.
81. Oliver WR, Shenk JL, Snaith MR, Russell CS, Plunket KD, Bodkin NL, Lewis MC, Winegar DA, Sznaidman ML, Lambert MH, Xu HE, Sternbach DD, Kliewer SA, Hansen BC, Willson TM. A selective peroxisome proliferator-activated receptor agonist promotes reverse cholesterol transport. Proc Natl Acad Sci. 2001;98:5306–11. https://doi.org/10.1073/pnas.091021198.
82. Oyama T, Toyota K, Waku T, Hirakawa Y, Nagasawa N, Kasuga J, Hashimoto Y, Miyachi H, Morikawa K. Adaptability and selectivity of human peroxisome proliferator-activated receptor (PPAR) pan agonists revealed from crystal structures. Acta Crystallogr D Biol Crystallogr. 2009;65:786–95. https://doi.org/10.1107/S0907444909015935.
83. Patil R, Mohanty B, Liu B, Chandrashekaran IR, Headey SJ, Williams ML, Clements CS, Ilyichova O, Doak BC, Genissel P, Weaver RJ, Vuillard L, Halls ML, Porter CJH, Scanlon MJ. A ligand-induced structural change in fatty acid–binding protein 1 is associated with potentiation of peroxisome proliferator–activated receptor α agonists. J Biol Chem. 2019;294:3720–34. https://doi.org/10.1074/jbc.RA118.006848.
84. Pettersson I, Ebdrup S, Havranek M, Pihera P, Kořínek M, Mogensen JP, Jeppesen CB, Johansson E, Sauerberg P. Design of a partial PPARδ agonist. Bioorg Med Chem Lett. 2007;17:4625–9. https://doi.org/10.1016/j.bmcl.2007.05.079.
85. Rakhshandehroo M, Knoch B, Müller M, Kersten S. Peroxisome proliferator-activated receptor alpha target genes. PPAR Res. 2010;2010:1–20. https://doi.org/10.1155/2010/612089.
86. Ratziu V, Harrison SA, Francque S, Bedossa P, Lehert P, Serfaty L, Romero-Gomez M, Boursier J, Abdelmalek M, Caldwell S, Drenth J, Anstee QM, Hum D, Hanf R, Roudot A, Megnien S, Staels B, Sanyal A, Mathurin P, Gournay J, Nguyen-Khac E, De Ledinghen V, Larrey D, Tran A, Bourliere M, Maynard-Muet M, Asselah T, Henrion J, Nevens F, Cassiman D, Geerts A, Moreno C, Beuers UH, Galle PR, Spengler U, Bugianesi E, Craxi A, Angelico M, Fargion S, Voiculescu M, Gheorghe L, Preotescu L, Caballeria J, Andrade RJ, Crespo J, Callera JL, Ala A, Aithal G, Abouda G, Luketic V, Huang MA, Gordon S, Pockros P, Poordad F, Shores N, Moehlen MW, Bambha K, Clark V, Satapathy S, Parekh S, Reddy RK, Sheikh MY, Szabo G, Vierling J, Foster T, Umpierrez G, Chang C, Box T, Gallegos-Orozco J. Elafibranor, an agonist of the peroxisome proliferator−activated receptor−α and −δ, induces resolution of nonalcoholic steatohepatitis without fibrosis worsening. Gastroenterology. 2016;150:1147–1159.e5. https://doi.org/10.1053/j.gastro.2016.01.038.

87. Ribeiro Filho HV, Guerra JV, Cagliari R, Batista FAH, Le Maire A, Oliveira PSL, Figueira ACM. Exploring the mechanism of PPARγ phosphorylation mediated by CDK5. J Struct Biol. 2019;207:317–26. https://doi.org/10.1016/j.jsb.2019.07.007.
88. Ricote M, Glass C. PPARs and molecular mechanisms of transrepression. Biochim Biophys Acta. 2007;1771:926–35. https://doi.org/10.1016/j.bbalip.2007.02.013.
89. Rochel N, Krucker C, Coutos-Thévenot L, Osz J, Zhang R, Guyon E, Zita W, Vanthong S, Hernandez OA, Bourguet M, Badawy KA, Dufour F, Peluso-Iltis C, Heckler-Beji S, Dejaegere A, Kamoun A, de Reyniès A, Neuzillet Y, Rebouissou S, Béraud C, Lang H, Massfelder T, Allory Y, Cianférani S, Stote RH, Radvanyi F, Bernard-Pierrot I. Recurrent activating mutations of PPARγ associated with luminal bladder tumors. Nat Commun. 2019;10:253. https://doi.org/10.1038/s41467-018-08157-y.
90. Sarraf P, Mueller E, Smith WM, Wright HM, Kum JB, Aaltonen LA, de la Chapelle A, Spiegelman BM, Eng C. Loss-of-function mutations in PPARγ associated with human colon cancer. Mol Cell. 1999;3:799–804. https://doi.org/10.1016/S1097-2765(01)80012-5.
91. Sauerberg P, Olsen GS, Jeppesen L, Mogensen JP, Pettersson I, Jeppesen CB, Daugaard JR, Galsgaard ED, Ynddal L, Fleckner J, Panajotova V, Polivka Z, Pihera P, Havranek M, Wulff EM. Identification and synthesis of a novel selective partial PPARδ agonist with full efficacy on lipid metabolism in vitro and in vivo. J Med Chem. 2007;50:1495–503. https://doi.org/10.1021/jm061202u.
92. Schäfer HL, Linz W, Falk E, Glien M, Glombik H, Korn M, Wendler W, Herling AW, Rütten H. AVE8134, a novel potent PPARα agonist, improves lipid profile and glucose metabolism in dyslipidemic mice and type 2 diabetic rats. Acta Pharmacol Sin. 2012;33:82–90. https://doi.org/10.1038/aps.2011.165.
93. Schmidt A, Endo N, Rutledge SJ, Vogel R, Shinar D, Rodan GA. Identification of a new member of the steroid hormone receptor superfamily that is activated by a peroxisome proliferator and fatty acids. Mol Endocrinol. 1992;6:1634–41. https://doi.org/10.1210/mend.6.10.1333051.
94. Schwarz R, Tänzler D, Ihling CH, Sinz A. Monitoring solution structures of peroxisome proliferator-activated receptor β/δ upon ligand binding. PLoS One. 2016;11:e0151412. https://doi.org/10.1371/journal.pone.0151412.
95. Shang J, Mosure SA, Zheng J, Brust R, Bass J, Nichols A, Solt LA, Griffin PR, Kojetin DJ. A molecular switch regulating transcriptional repression and activation of PPARγ. Nat Commun. 2020;11:956. https://doi.org/10.1038/s41467-020-14750-x.
96. Shearer BG, Patel HS, Billin AN, Way JM, Winegar DA, Lambert MH, Xu RX, Leesnitzer LM, Merrihew RV, Huet S, Willson TM. Discovery of a novel class of PPARδ partial agonists. Bioorg Med Chem Lett. 2008;18:5018–22. https://doi.org/10.1016/j.bmcl.2008.08.011.
97. Sierra ML, Beneton V, Boullay A-B, Boyer T, Brewster AG, Donche F, Forest M-C, Fouchet M-H, Gellibert FJ, Grillot DA, Lambert MH, Laroze A, Le Grumelec C, Linget JM, Montana VG, Nguyen V-L, Nicodème E, Patel V, Penfornis A, Pineau O, Pohin D, Potvain F, Poulain G, Ruault CB, Saunders M, Toum J, Xu HE, Xu RX, Pianetti PM. Substituted 2-[(4-aminomethyl)phenoxy]-2-methylpropionic acid PPARα agonists. 1. Discovery of a novel series of potent HDLc raising agents. J Med Chem. 2007;50:685–95. https://doi.org/10.1021/jm058056x.
98. Sturm N, Desaphy J, Quinn RJ, Rognan D, Kellenberger E. Structural insights into the molecular basis of the ligand promiscuity. J Chem Inf Model. 2012;52:2410–21. https://doi.org/10.1021/ci300196g.
99. Sulimov VB, Kutov DC, Sulimov AV. Advances in docking. CMC. 2020;26:7555–80. https://doi.org/10.2174/0929867325666180904115000.
100. Sznaidman ML, Haffner CD, Maloney PR, Fivush A, Chao E, Goreham D, Sierra ML, LeGrumelec C, Xu HE, Montana VG, Lambert MH, Willson TM, Oliver WR, Sternbach DD. Novel selective small molecule agonists for peroxisome proliferator-activated receptor δ (PPARδ)—synthesis and biological activity. Bioorg Med Chem Lett. 2003;13:1517–21. https://doi.org/10.1016/S0960-894X(03)00207-5.
101. Takada I, Yu RT, Xu HE, Lambert MH, Montana VG, Kliewer SA, Evans RM, Umesono K. Alteration of a single amino acid in peroxisome proliferator-activated receptor-α (PPARα)

generates a PPARδ phenotype. Mol Endocrinol. 2000;14:733–40. https://doi.org/10.1210/mend.14.5.0456.
102. Tan NS, Vázquez-Carrera M, Montagner A, Sng MK, Guillou H, Wahli W. Transcriptional control of physiological and pathological processes by the nuclear receptor PPARβ/δ. Prog Lipid Res. 2016;64:98–122. https://doi.org/10.1016/j.plipres.2016.09.001.
103. Titus SA, Beacham D, Shahane SA, Southall N, Xia M, Huang R, Hooten E, Zhao Y, Shou L, Austin CP, Zheng W. A new homogeneous high-throughput screening assay for profiling compound activity on the human ether-a-go-go-related gene channel. Anal Biochem. 2009;394:30–8. https://doi.org/10.1016/j.ab.2009.07.003.
104. Torres PHM, Sodero ACR, Jofily P, Silva-Jr FP. Key topics in molecular docking for drug design. IJMS. 2019;20:4574. https://doi.org/10.3390/ijms20184574.
105. Umemoto T, Fujiki Y. Ligand-dependent nucleo-cytoplasmic shuttling of peroxisome proliferator-activated receptors, PPARα and PPARγ. Genes Cells. 2012;17:576–96. https://doi.org/10.1111/j.1365-2443.2012.01607.x.
106. Uppenberg J, Svensson C, Jaki M, Bertilsson G, Jendeberg L, Berkenstam A. Crystal structure of the ligand binding domain of the human nuclear receptor PPARγ. J Biol Chem. 1998;273:31108–12. https://doi.org/10.1074/jbc.273.47.31108.
107. Waku T, Shiraki T, Oyama T, Fujimoto Y, Maebara K, Kamiya N, Jingami H, Morikawa, K. Structural Insight into PPARγ Activation Through Covalent Modification with Endogenous Fatty Acids. J. Mol. Biol. 2009;385(1):188–199.
108. Wagner K-D, Wagner N. Peroxisome proliferator-activated receptor beta/delta (PPARβ/δ) acts as regulator of metabolism linked to multiple cellular functions. Pharmacol Ther. 2010;125:423–35. https://doi.org/10.1016/j.pharmthera.2009.12.001.
109. Wagner N, Wagner K-D. PPAR beta/delta and the hallmarks of cancer. Cell. 2020;9:1133. https://doi.org/10.3390/cells9051133.
110. Wang W, Devasthale P, Farrelly D, Gu L, Harrity T, Cap M, Chu C, Kunselman L, Morgan N, Ponticiello R, Zebo R, Zhang L, Locke K, Lippy J, O'Malley K, Hosagrahara V, Zhang L, Kadiyala P, Chang C, Muckelbauer J, Doweyko AM, Zahler R, Ryono D, Hariharan N, Cheng PTW. Discovery of azetidinone acids as conformationally-constrained dual PPARα/γ agonists. Bioorg Med Chem Lett. 2008;18:1939–44. https://doi.org/10.1016/j.bmcl.2008.01.126.
111. Wang W, Zhang L, Wang X, Lin D, Pan Q, Guo L. Functional network analysis of gene phenotype connectivity based on pioglitazone. Exp Ther Med. 2019;18(6):4790–8. https://doi.org/10.3892/etm.2019.8162.
112. Willson T, Brown P, Sternbach D, Henke, B. The PPARs: From Orphan Receptors to Drug Discovery. J. Med. Chem. 2000;43(4):527–550.
113. Wu C-C, Baiga TJ, Downes M, La Clair JJ, Atkins AR, Richard SB, Fan W, Stockley-Noel TA, Bowman ME, Noel JP, Evans RM. Structural basis for specific ligation of the peroxisome proliferator-activated receptor δ. Proc Natl Acad Sci U S A. 2017;114:E2563–70. https://doi.org/10.1073/pnas.1621513114.
114. Xu HE, Lambert MH, Montana VG, Parks DJ, Blanchard SG, Brown PJ, Sternbach DD, Lehmann JM, Wisely GB, Willson TM, Kliewer SA, Milburn MV. Molecular recognition of fatty acids by peroxisome proliferator–activated receptors. Mol Cell. 1999;3:397–403. https://doi.org/10.1016/S1097-2765(00)80467-0.
115. Xu HE, Lambert MH, Montana VG, Plunket KD, Moore LB, Collins JL, Oplinger JA, Kliewer SA, Gampe RT, McKee DD, Moore JT, Willson TM. Structural determinants of ligand binding selectivity between the peroxisome proliferator-activated receptors. Proc Natl Acad Sci. 2001;98:13919–24. https://doi.org/10.1073/pnas.241410198.
116. Xu HE, Stanley TB, Montana VG, Lambert MH, Shearer BG, Cobb JE, McKee DD, Galardi CM, Plunket KD, Nolte RT, Parks DJ, Moore JT, Kliewer SA, Willson TM, Stimmel JB. Structural basis for antagonist-mediated recruitment of nuclear co-repressors by PPARα. Nature. 2002;415:813–7. https://doi.org/10.1038/415813a.
117. Yamamoto Y, Takei K, Arulmozhiraja S, Sladek V, Matsuo N, Han S, Matsuzaka T, Sekiya M, Tokiwa T, Shoji M, Shigeta Y, Nakagawa Y, Tokiwa H, Shimano H. Molecular association model of PPARα and its new specific and efficient ligand, pemafibrate: structural basis for SPPARMα. Biochem Biophys Res Commun. 2018;499:239–45. https://doi.org/10.1016/j.bbrc.2018.03.135.

118. Yamauchi T, Kamon J, Waki H, Murakami K, Motojima K, Komeda K, Ide T, Kubota N, Terauchi Y, Tobe K, Miki H, Tsuchida A, Akanuma Y, Nagai R, Kimura S, Kadowaki T. The mechanisms by which both heterozygous peroxisome proliferator-activated receptor γ (PPARγ) deficiency and PPARγ agonist improve insulin resistance. J Biol Chem. 2001;276:41245–54. https://doi.org/10.1074/jbc.M103241200.
119. Yamazaki Y, Abe K, Toma T, Nishikawa M, Ozawa H, Okuda A, Araki T, Oda S, Inoue K, Shibuya K, Staels B, Fruchart J-C. Design and synthesis of highly potent and selective human peroxisome proliferator-activated receptor α agonists. Bioorg Med Chem Lett. 2007;17:4689–93. https://doi.org/10.1016/j.bmcl.2007.05.066.
120. Yi P, Wang Z, Feng Q, Pintilie GD, Foulds CE, Lanz RB, Ludtke SJ, Schmid MF, Chiu W, O'Malley BW. Structure of a biologically active Estrogen receptor-coactivator complex on DNA. Mol Cell. 2015;57:1047–58. https://doi.org/10.1016/j.molcel.2015.01.025.
121. Yu S, Reddy J. Transcription coactivators for peroxisome proliferator-activated receptors. Biochim Biophys Acta. 2007;1771:936–51. https://doi.org/10.1016/j.bbalip.2007.01.008.
122. Yu K, Bayona W, Kallen CB, Harding HP, Ravera CP, McMahon G, Brown M, Lazar MA. Differential activation of peroxisome proliferator-activated receptors by eicosanoids. J Biol Chem. 1995;270:23975–83. https://doi.org/10.1074/jbc.270.41.23975.
123. Zheng J, Corzo C, Chang MR, Shang J, Lam VQ, Brust R, Blayo A-L, Bruning JB, Kamenecka TM, Kojetin DJ, Griffin PR. Chemical crosslinking mass spectrometry reveals the conformational landscape of the activation helix of PPARγ; a model for ligand-dependent antagonism. Structure. 2018;26:1431–1439.e6. https://doi.org/10.1016/j.str.2018.07.007.

Chapter 3

Structural and Dynamic Elucidation of a Non-acid PPARγ Partial Agonist: SR1988.

Rebecca L. Frkic[1], **Benjamin S. Chua**[1], Youseung Shin[2], Bruce D. Pascal[2,3], Scott J. Novick[2], Theodore M. Kamenecka[2], Patrick R. Griffin[2], and John B. Bruning[1]

[1]Institute for Photonics and Advanced Sensing (IPAS), School of Biological Sciences, The University of Adelaide, Adelaide, South Australia 5005, Australia

[2]Department of Molecular Medicine, The Scripps Research Institute, Jupiter, Florida 33458, United States

[3]Omics Informatics LLC, 1050 Bishop Street #517, Honolulu, HI, 96813, Hawaii

Published, DOI: 10.11131/2018/101350

Statement of Authorship

Title of Paper	Structural and Dynamic Elucidation of a Non-acid PPARγ Partial Agonist: SR1988.
Publication Status	☑ Published ☐ Accepted for Publication ☐ Submitted for Publication ☐ Unpublished and Unsubmitted work written in manuscript style
Publication Details	This paper characterizes a partial agonist synthesized by the Scripps' institute, using cell-based assays, protein crystallization and in vitro techniques.

Principal Author

Name of Principal Author (Candidate)	Benjamin Soon Kai Chua		
Contribution to the Paper	Assistance with rebuilding and refinement of structure		
Overall percentage (%)	15		
Certification:	This paper reports on original research I conducted during the period of my Higher Degree by Research candidature and is not subject to any obligations or contractual agreements with a t is thesis.		
Signature		Date	16/06/2023

Co-Author Contributions

By signing the Statement of Authorship, each author certifies that:

i. the candidate's stated contribution to the publication is accurate (as detailed above);

ii. permission is granted for the candidate in include the publication in the thesis; and

iii. the sum of all co-author contributions is equal to 100% less the candidate's stated contribution.

Name of Co-Author	Rebecca Frkic		
Contribution to the Paper	Processing of crystallographic data, data interpretation, manuscript preparation		
Signature	John Bruning signing , author not available John Bruning	Date	10-07-2023

Name of Co-Author	Youseung Shin		
Contribution to the Paper	Chemical Synthesis		
Signature	John Bruning signing, author not available John Bruning	Date	10-07-2023

Name of Co-Author	Bruce Pascal

Contribution to the Paper	HDX analysis		
Signature	John Bruning signing, author not available John Bruning	Date	10-07-2023

Name of Co-Author	Scott Novick		
Contribution to the Paper	HDX processing		
Signature	John Bruning signing, author not available John Bruning	Date	10-07-2023

Name of Co-Author	Theodore Kamenecka		
Contribution to the Paper	Performed chemical synthesis, manuscript preparation		
Signature	John Bruning signing, author not available John Bruning	Date	10-07-2023

Name of Co-Author	Patrick Griffin		
Contribution to the Paper	Conception of project, editing of manuscript		
Signature	John Bruning signing, author not available John Bruning	Date	10-07-2023

Name of Co-Author	John Bruning		
Contribution to the Paper	Supervision of work development, performed crystallographic experiments, assisted with manuscript preparation, corresponding author		
Signature	John Bruning	Date	10-07-2023

HHS Public Access

Author manuscript

Nucl Receptor Res. Author manuscript; available in PMC 2019 March 21.

Published in final edited form as:

Nucl Receptor Res. 2018 ; 5: . doi:10.11131/2018/101350.

Structural and Dynamic Elucidation of a Non-acid PPARγ Partial Agonist: SR1988

Rebecca L. Frkic[1], **Benjamin S. Chua**[1], **Youseung Shin**[2], **Bruce D. Pascal**[2,3], **Scott J. Novick**[2], **Theodore M. Kamenecka**[2], **Patrick R. Griffin**[2], and **John B. Bruning**[1]

[1]Institute for Photonics and Advanced Sensing (IPAS), School of Biological Sciences, The University of Adelaide, Adelaide, South Australia 5005, Australia

[2]Department of Molecular Medicine, The Scripps Research Institute, Jupiter, Florida 33458, United States

[3]Omics Informatics LLC, 1050 Bishop Street #517, Honolulu, HI, 96813, Hawaii

Abstract

Targeting peroxisome proliferator-activated receptor γ (PPARγ) by synthetic compounds has been shown to elicit insulin sensitising properties in type 2 diabetics. Treatment with a class of these compounds, the thiazolidinediones (TZDs), has shown adverse side effects such as weight gain, fluid retention, and congestive heart failure. This is due to their full agonist properties on the receptor, where a number of genes are upregulated beyond normal physiological levels. Lessened transactivation of PPARγ by partial agonists has proved beneficial in terms of reducing side effects, while still maintaining insulin sensitising properties. However, some partial agonists have been associated with unfavourable pharmacokinetic profiles due to their acidic moieties, often causing partitioning to the liver. Here we present SR1988, a new partial agonist with favourable non-acid chemical properties. We used a combination of X-ray crystallography and hydrogen/deuterium exchange (HDX) to elucidate the structural basis for reduced activation of PPARγ by SR1988. This structural analysis reveals a mechanism that decreases stabilisation of the AF2 coactivator binding surface by the ligand.

Keywords

PPARγ; partial agonist; nuclear receptor; type 2 diabetes; HDX

1. Introduction

PPARγ is a ligand-modulated transcription factor belonging to the nuclear receptor superfamily. It forms a heterodimer with retinoid X receptor α (RXRα) to play key roles in metabolism and the maintenance of glucose homeostasis through modulating numerous

Corresponding Author: John B. Bruning, john.bruning@adelaide.edu.au.

Competing Interests

The authors declare no competing interests.

target genes [1,2]. The receptor is a well-established target for treatments of type 2 diabetes (T2DM) for its roles in modulating insulin sensitivity in peripheral tissues.

Sequence analysis and crystallographic studies reveal that PPARγ displays the conserved nuclear receptor domain architecture, comprising of the activation function 1 domain essential for ligand-independent coregulator binding, a DNA binding domain (DBD), a hinge region, and a ligand binding domain (LBD). The LBD binds a number of endogenous ligands, as well as facilitating dimerisation with RXRα, and contains a regulatory activation function 2 (AF2) region which binds coregulators in a ligand-dependant manner [3]. Crystal structures of the LBD show that the domain contains 13 α-helices (H1-12 and 2') and a small β-sheet, conforming to the canonical nuclear receptor LBD tertiary fold. The ligand binding pocket within the LBD is lined with hydrophobic residues, enabling binding of predominantly hydrophobic endogenous ligands.

The thiazolidinediones (TZDs) are a class of full agonist modulators of PPARγ, which include rosiglitazone (Avandia, GSK) and pioglitazone (Actos, Takeda). Crystal structures of rosiglitazone-bound PPARγ LBD have shown that the thiazolidinedione head group forms robust stabilising interactions with the activation helix (HI2) to enable coactivator binding and initiation of target gene expression [3–7]. Rosiglitazone and pioglitazone have previously been prescribed to treat type 2 diabetes, but their use has been hampered by harmful side effects associated with supraphysiological activation of PPARγ target genes. The upregulation of these genes leads to weight gain, loss of bone density, renal fluid retention and plasma volume expansion, oedema, and heart failure. These side effects have led to the clinical use of TZDs being restricted in most cases and highlights the necessity for improved antidiabetic agents targeting PPARγ.

In light of the issues with TZDs as antidiabetics, research has focused on developing ligands of PPARγ with reduced activation of the receptor which show a more favourable side effect profile due to a reduced expression of PPARγ target genes. Although these ligands show low activation of the receptor, they still exhibit robust antidiabetic effects comparable to TZDs. It has been established that the insulin sensitising properties of ligands of PPARγ are attributed to their ability to block phosphorylation of PPARγ at Ser273 by extracellular signal-regulated kinases (e.g., CDK5, ERK) [8,9]. The blocking of phosphorylation is independent of the level of transactivation of the receptor induced by the ligand. It is paramount that T2DM research focusses on ligands of PPARγ that have minimal activation of the receptor, such as partial agonists and antagonists, while still maintaining phosphorylation-blocking abilities.

A number of partial agonists have been investigated for their suitability as antidiabetic agents [10–15]. This approach is promising, with studies showing that the insulin-sensitising properties remain in these compounds with reduced transactivation of PPARγ. An example of a well-studied partial agonist of PPARγ is INT131, which shows effective blocking of Ser273 phosphorylation *in vitro*, indicative of its effectiveness as an antidiabetic agent, and showed lowered side effects as a result of limited transactivation of PPARγ [12].

The array of endogenous and synthetic ligands capable of binding in the ligand binding pocket of PPARγ have a diverse range of chemical properties [16]. These include sulphonamides, indoles, acids, benzimidazoles, thiazolidinediones, and cercosporamide derivatives [2]. The majority of these contain acid groups for stabilising helix 12 or the β-sheet of the LBD to mediate high affinity binding to the receptor [13]. However, acid moieties are disadvantageous in that they exhibit unfavourable pharmacokinetic profiles, with the compounds partitioning to the liver *in vivo* [14]. This could limit their effectiveness at their intended site of action; the peripheral tissues where the response to insulin occurs. Developing a non-acid ligand of PPARγ with limited transactivation of the receptor will be ideal for an effective antidiabetic agent with favourable pharmacokinetics and side effect profile.

We have previously reported our findings on a ligand of PPARγ which fits these criteria, SR2067, a highly potent non-acid partial agonist which displayed reduced transactivation of the receptor in a GAL4 transactivation assay [13]. Here we present an analogue of SR2067: SR1988, a non-acid partial agonist of PPARγ. A transactivation assay was performed to determine the transcriptional potency of SR1988, a crystal structure of the ligand in complex with the PPARγ LBD has been solved, and HDX was performed to further elucidate its mechanism of action through protein conformational dynamics.

2. Materials and Methods

2.1. Synthesis of SR1988

1-(2,4-difluorobenzyl)-2,3-dimethyl-N-(1-phenylpropyl)-1H-indole-5-carboxamide.

Step 1: NaH (1.1 equiv) was added to a solution of ethyl 2,3-dimethy 1–1 H-indole-5-carboxylate in DMF at room temperature. After 30 nnn, 2,4-difluorobenzyl bromide (1.1 equiv) was added to the reaction mixture and stirred for 1 h. After the reaction was completed, the solvent was removed in vacuo to obtain a crude residue which was purified by flash chromatography on silica gel (ethyl acetate/hexanes 10–100%) to obtain ethyl 1-(2,4-difluorobenzyl)-2,3-dimethyl-1H-indole-5-carboxylate. LC-MS 344 (M+H).

Step 2: A mixture of above compound and NaOH (10 equiv) in EtOH was refluxed at 100°C. for 2 h. The reaction mixture was cooled to room temperature, then acidified to pH-4 with saturated citric acid. The mixture was evaporated in vacuo to obtain the crude product, which was precipitated in water and Altered to obtain 1-(2,4-difluorobenzyl)-2,3-dimethyl-1H-indole-5-carboxylic acid which was used without further purification. LC-MS 316 (M+H).

Step 3: To a mixture of this acid in DMF was added DIPEA (1.3 equiv) and HATU (1.2 equiv). The mixture was stirred for 5 min, and then α-ethylbenzylamine (1.1 equiv) was added. The reaction mixture was stirred at room temperature for 1 h. After the reaction was completed, the solvent was removed in vacuo to obtain the crude which was purified by flash chromatography on silica gel (ethyl acetate/hexanes 10–100%) to obtain 1-(2,4-difluorobenzyl)-2,3-dimethyl-N-(1-phenylpropyl)-1H-indole-5-carboxamide as a colourless solid. LC-MS 433 (M+H).

2.2. Synthesis of SR2067

1-(naphthalen-1-ylsulfonyl)-N-(1-phenylpropyl)-1H-indole-5-carboxamide.

Step 1: To a mixture of 1 H-indole-5-carboxylic acid in DMF was added DIPEA (1.3 equiv) and HATU (1.2 equiv). The mixture was stirred for 5 min, and then α-ethylbenzylamine (1.1 equiv) was added. The reaction mixture was stirred at room temperature for 1 h. After the reaction was completed, the solvent was removed in vacuo to obtain the crude which was purified by flash chromatography on silica gel (ethyl acetate/hexanes 10–100%) to obtain N-(1-phenylpropyl)-1H-indole-5-carboxamide as a colourless solid.

Step 2: 1-naphthylsulfonyl chloride (1.1 equiv) and benzyltriethylammonium chloride (0.5 equiv) were added to a solution of N-(1-phenylpropyl)-1H-indole-5-carboxamide in CH_2Cl_2 and KOH (1.3 equiv) at room temperature. After the reaction was judged complete by analytical reverse-phase HPLC analysis, the solvent was evaporated and the crude residue was purified by silica gel column chromatography (ethyl acetate/hexanes 10–100%) to afford 1-(naphthalen-1-ylsulfonyl)-N-(1-phenylpropyl)-1H-indole-5-carboxamide as a colourless solid. LC-MS 469 (M+H).

2.3. Cell-based transactivation assay

HEK293T cells (ATCC; cat# CRL-3216) were cotransfected in batch by adding 4.5 μg human GAL4-PPARγ-Hinge-LBD, with 4.5 μg 5X multimerized UAS-luciferase reporter and 27 μL X-treme Gene 9 transfection reagent in serum-free Opti-mem reduced serum media (Gibco). After 18-h incubation at 37 °C in a 5% CO_2 incubator, transfected cells were plated in quadruplicate in white 384-well plates (Perkin Elmer) at a density of 10,000 cells per well. After replating, cells were treated with either DMSO only or the indicated compounds in increasing doses from 2 pM–10 μM. After 18-h incubation, treated cells were developed with Brite Lite Plus (Perkin Elmer) and read in 384-well Luminescence Perkin Elmer EnVision Multilabel plate reader. Graphs were plotted as fold change of treated cells over DMSO-treated control cells.

2.4. Protein purification, complex formation and crystallisation

6xHis-hPPARγ LBD (res 205–477) was expressed using a pET-1 la expression vector in BL21DE3 *E. coli* cells. Expression was induced at mid-log phase using 0.5mM IPTG at 16°C overnight. Cells were harvested and lysed using a cell disruptor in 20mM Tris 8.0, 0.5M NaCl, 10mM imidazole, and 2mM BME. Protein was purified using 5mL Ni^{2+} IMAC FF Crude Column (GE Healthcare), followed by size exclusion chromatography using a HiPrep 26/60 Sephacryl S 300 HR column. The protein was concentrated to 10mg/mL using a centrifugal concentrator with a 10,000 molecular weight cut-off. Crystals were formed at 16°C using the hanging drop method. The well consisted of 1.2M sodium citrate and 0.1M Tris 8.0. The hanging drop was formed by mixing 1 μL of well solution with 1 μL of apo protein solution.

2.5. Structure determination

Apo crystals of PPARγ were soaked with SR1988. SR1988 was soaked at a concentration of 2.5mM for 3 weeks at 16 °C. 15% ethylene glycol was used as a cryoprotectant. Diffraction

data were collected at the MX1 beamline at the Australian Synchrotron. 360° of diffraction data at 1 degree rotations were collected for the PPARγ + SR1988 crystal at one second exposure times with 85% attenuation of the beam. Processing of the data was performed using iMosflm (CCP4), which processed reflections from 58–2.4Å with space group C 1 2 1. Molecular replacement was performed using PhaserMR with PDB 4R06 (with water molecules and ligands removed) as the search model. Eight rounds of refinement in Phenix.refine showed that there was significant density for SR1988 in the binding pocket of chain A. Manual rebuilding in Coot followed by refinement in Phenix was carried out until R-factors converged. Molprobity was used for structure validation.

2.6. Hydrogen/deuterium exchange (HDX) detected by mass spectrometry (MS)

Differential HDX-MS experiments were conducted as previously described with some modifications [17].

2.6.1. Peptide identification—Peptides were identified using tandem MS (MS/MS) with an Orbitrap mass spectrometer (Q Exactive, Thermo Fisher). Product ion spectra were acquired in data-dependent mode with the top five most abundant ions selected for the product ion analysis per scan event. The MS/MS data files were submitted to Mascot (Matrix Science) for peptide identification. Peptides included in the HDX analysis peptide set had a MASCOT score greater than 20 and the MS/MS spectra were verified by manual inspection. The MASCOT search was repeated against a decoy (reverse) sequence and ambiguous identifications were ruled out and not included in the HDX peptide set.

2.6.2. HDX-MS analysis—Protein (10 μM) was incubated with the respective ligands at a 1:10 protein-to-ligand molar ratio for 1 h at room temperature. Next, 5 μl of sample was diluted into 20 μl D_2O buffer (20 mM Tris-HCl, pH 7.4; 150 mM NaCl; 2 mM DTT) and incubated for various time points (0, 10, 60, 300, and 900 s) at 4°C. The deuterium exchange was then slowed by mixing with 25 μl of cold (4°C) 3 M urea and 1% trifluoroacetic acid. Quenched samples were immediately injected into the HDX platform. Upon injection, samples were passed through an immobilized pepsin column (2mm × 2cm) at 200 μl min^{-1} and the digested peptides were captured on a 2mm × 1cm C_8 trap column (Agilent) and desalted. Peptides were separated across a 2.1mm × 5cm C_{18} column (1.9 μl Hypersil Gold, Thermo Fisher) with a linear gradient of 4% - 40% CH_3CN and 0.3% formic acid, over 5 min. Sample handling, protein digestion and peptide separation were conducted at 4°C. Mass spectrometric data were acquired using an Orbitrap mass spectrometer (Q Exactive, Thermo Fisher). HDX analyses were performed in triplicate, with single preparations of each protein ligand complex. The intensity weighted mean m/z centroid value of each peptide envelope was calculated and subsequently converted into a percentage of deuterium incorporation. This was accomplished by determining the observed averages of the undeuterated and fully deuterated spectra and using the conventional formula described elsewhere [18]. Statistical significance for the differential HDX data is determined by an unpaired t-test for each time point, a procedure that is integrated into the HDX Workbench software [19]. Corrections for back-exchange were made on the basis of an estimated 70% deuterium recovery, and accounting for the known 80% deuterium content of the deuterium exchange buffer.

3. Results and Discussion

3.1. Design and transcriptional activity of non-acid PPARγ ligand SR1988

The pharmacokinetic liabilities of PPARγ ligands with acid moieties has prompted the investigation of ligands designed to bind PPARγ with high affinity without acidic properties. Our previously reported non-acid partial agonist SR2067 displayed reduced transactivation of PPARγ while still maintaining high potency binding to the receptor [13]. We sought to probe the effects of modifying SR2067 from the site of the 1-(methylsulphonyl)naphthalene region of the ligand by generating SR1988, which still maintained the desired non-acid characteristics of SR2067.

SR1988 contains a central 2, 3-dimethylindole moiety flanked by a 2, 4-difluorobenzene and a hydrophobic phenylpropyl group with a terminal ethyl moiety joined by an amide linker (Figure 1A). The presence of key hydrophobic moieties within the ligand is vital for binding to the hydrophobic ligand binding pocket of PPARγ.

Non-acid agonists of PPARγ are advantageous in that they have ideal pharmacokinetic attributes in terms of preventing partitioning to the liver, and can carry out their insulin-sensitising properties in the required organs [13]. It is for this reason the non-acid properties of SR1988 makes it an improvement on previous partial agonists, while still retaining the advantages attributed to partial agonists as antidiabetic agents.

We have previously reported that SR2067 displays a maximal transactivation approximately 55-fold higher than DMSO, 60% relative to the maximal transactivation of rosiglitazone [13]. We performed a cell-based transactivation assay in order to compare the level of PPARγ activation exhibited by SR1988 (Figure 1B). This revealed a maximal transactivation by SR1988 approximately 50-fold higher than DMSO, 45% relative to the maximal transactivation exhibited by rosiglitazone. This is typical of partial agonists and is a desired characteristic in ligands of PPARγ for the treatment of type 2 diabetes. The low activation of the receptor by ligands means that PPARγ target genes will not be expressed at a supraphysiological level, indicative of reduced side effects in comparison to TZDs.

The concentration of SR1988 that gave half maximal transactivation (EC_{50}) was 123nM, a lower concentration than the EC_{50} of rosiglitazone, which gave half maximal transactivation at 494nM. This indicates that SR1988 is more potent than rosiglitazone in binding, and represents a major improvement on rosiglitazone in addition to the desired decrease in maximal PPARγ activation. SR2067 displayed an EC_{50} value of 16nM, approximately an 8-fold lower EC_{50} than SR1988, suggesting that SR2067 is somewhat a more highly potent ligand of PPARγ than SR1988. Despite this, both EC_{50} values are suitable in terms of clinical applications as they are both in the low nanomolar range. In addition, SR1988 shows an advantage over SR2067 in terms of its lower relative transactivation of PPARγ, where SR1988 exhibited a 45% transactivation of PPARγ, compared to 60% shown by SR2067. This lower activation will likely correspond to a more favourable side effect profile, inarguably a more important characteristic of a drug candidate.

3.2. X-ray crystal structure of PPARγ LBD bound to SR1988

We obtained a crystal structure of SR1988-bound PPARγ LBD and solved it to 2.4Å (Figure 2A), with data refinement statistics in Table 1. The asymmetric unit of the crystal was comprised of two LBD subunits with homodimeric architecture. The protein main chain conformed to the canonical homodimeric PPARγ LBD fold, with little variation in comparison to previously solved structures (RMSD of 0.58Å across 244 Cα atoms compared with rosiglitazone-bound PPARγ LBD, PDB:2PRG, and a 0.44Å RMSD over 251 Cα atoms compared with apo PPARγ LBD, PDB:1PRG). The SR1988 ligand was modelled into one chain of the homodimer, with a Polder omit map [20] displaying reduced model bias and exclusion of solvent molecules shown in Figure 1 in Supplementary Material available online at http://www.agialpress.com/journals/nurr/2018/101350/. SR1988 was bound in the ligand binding pocket of the LBD in a very similar way to a number of PPARγ agonists, wrapping around H3 to make contacts with residues of H12 as well as the β-sheet. The central amide of the ligand forms two hydrogen bonds with the receptor (Figure 2B); the carbonyl accepting a hydrogen from Tyr327 of helix 5 over a distance of 3.3Å, and the amine donating a hydrogen to Ser289 of helix 3 in a 2.4Å hydrogen bond. In addition, hydrophobic interactions are made between the ligand and residues lining the binding pocket. The indole moiety of the ligand makes hydrophobic interactions with Cys285 (H3), Ile326 (H5) and Leu330 (H5), and the 2, 4-difluorobenzene interacts with Cys285 (H3), Arg288 (H3), and Ile341 (β-sheet). The phenylpropyl moiety forms hydrophobic interactions with Leu453 (H11) and Leu469 (H12).

This combination of hydrogen bonds and hydrophobic interactions made between SR1988 and PPARγ are high affinity and probably entropically favourable, giving SR1988 the high potency revealed in the transactivation assay. This is key for the development of insulin-sensitising agents, as compounds that bind tightly to PPARγ but have only minor transactivation of the receptor are ideal for the treatment of T2DM.

Comparison of SR1988 and SR2067 binding modes reveal almost complete similarity in the specific interactions formed with residues of the binding pocket (Figure 2 in Supplementary Material available online at http://www.agialpress.com/journals/nurr/2018/101350/), with only minor differences in hydrophobic interacting residues. The central amide forms the same hydrogen bonds as seen for SR1988, across 2.6Å for both hydrogen bonds with Tyr327 and Ser289. The unmodified phenylpropyl moiety of the two analogues are positioned in the same space within the ligand binding pocket, forming hydrophobic interactions with Leu453 (H11) and Leu469 (H12). The differing chemical structures of the ligands resulted in slight differences in their EC_{50} values, which can be attributed to minor variances in their ligand binding modes. The sulphonyl linker of SR2067 does not appear to provide an advantage in terms of favourable ligand binding compared with the carbon linker of SR1988 in the same location, as both linkers enable the ligand to orient in a way that regions of the compounds either side of the linker can form favourable interactions with the receptor. The naphthalene moiety of SR2067 occupies the same region of space in the binding pocket of PPARγ, and interacts with the same residues as the 2, 4-difluorobenzene of SR1988. The higher binding potency of SR2067 could perhaps be accounted to the higher hydrophobicity of naphthalene compared with 2, 4-difluorobenzene, which would increase the likelihood of binding to

PPARγ and interacting with the hydrophobic pocket of the receptor. These discreet differences in the specific interactions made with the receptor by ligands of differing chemical structures highlight the importance of optimising ligands at the chemical level to enhance their potency and minimise their transactivation of PPARγ.

3.3. Conformational dynamics of the SR1988-PPARγ complex as measured by HDX

In order to determine the protein dynamic stabilisation profile of the ligand-bound receptor, we performed hydrogen/deuterium exchange (HDX) on PPARγ LBD in the presence of SR1988 as well as rosiglitazone (Figure 3), with HDX behaviour and peptide identities shown in Table I in Supplementary Material available online at http://www.agialpress.com/journals/nurr/2018/101350/. SR1988 displayed a HDX pattern characteristic of partial agonists. Moderate stabilisation of H12 was observed in comparison to rosiglitazone-bound PPARγ LBD, where "stabilisation" refers to decreased molecular motion of H12 in its orientation relative to the remainder of the LBD. H12 of nuclear receptor LBDs has been considered a "molecular switch" for graded nuclear receptor activation, where the degree of stabilisation of H12 governs the ability for coregulators to bind, and hence determines the degree of transcriptional output exhibited by the receptor [21, 22]. Previous structural studies have shown that rosiglitazone stabilises H12 through a network of hydrogen bonds mediated by the thiazolidinedione head group of rosiglitazone, which enables robust recruitment of coactivators through stabilisation of the ligand-dependant AF2 coactivator binding surface [4]. This hydrogen bond network is lacking in SR1988, as there is a phenylpropyl group occupying this space near H12 instead of a thiazolidinedione, placing hydrophobic moieties in the pocket near the AF2. The hydrophobic moieties are not as conformationally constraining as the extensive hydrogen bond network formed between rosiglitazone and H12, which leads to a reduced stabilisation of H12 by SR1988. A decreased stabilisation of H12 suggests a lessened propensity to recruit coactivators and so will exhibit a reduced transcriptional activation of PPARγ, indicating a key contributor to the mechanism of partial agonism by SR1988.

In addition, it has been shown that a graded transcriptional output of PPARγ can be determined by factors extending beyond the degree of H12 stabilisation [15]. Partial agonists generally stabilise regions of H3 and the β-sheet of the LBD to carry out their moderate transcriptional activation [9, 15]. HDX shows that SR1988 stabilised H3 to a higher degree than rosiglitazone. This can be attributed to the hydrogen bond with Ser289 of helix 3, as well as the stabilising hydrophobic interactions with Cys285 and Arg288 identified by the crystal structure. These interactions formed between SR1988 and helix 3 of PPARγ decrease the conformationally dynamic nature of the apo LBD, likely serving to allow decreased coactivator binding, giving SR1988 its partial agonist characteristics. A minor increase in β-sheet stabilisation was observed by HDX for SR1988 compared with rosiglitazone and DMSO controls, which has also been shown to contribute to partial agonist characteristics.

Differences in maximal transactivation efficacy of SR1988 (45%) and SR2067 (60%) can be attributed in part to differential stabilisation of regions of the LBD of PPARγ. SR2067 displayed stabilising interactions with the β-sheet and H3 to give partial agonist properties [13]. This is similar to SR1988, although a direct comparison of the stabilisation of PPARγ

by SR1988 or SR2067 using HDX can provide an explanation for the differences in PPARγ transactivation exhibited by SR1988 and SR2067.

4. Conclusion

In summary, we have used a combination of X-ray crystallography and HDX to dehne the mechanism of PPARγ partial agonism by SR1988. A reduced stabilisation of H12 as well as increased stabilisation of H3 and the β-sheet in comparison to rosiglitazone account for moderate, partial agonist like transactivation of PPARγ by SR1988. Our study demonstrates that non-acid ligands of PPARγ still exhibit high affinity binding to the receptor, despite their lack of acidic moieties to stabilise regions of the LBD. These hndings are applicable to the future development of insulin sensitising agents, particularly for its low transactivation as well as nonacid characteristics, giving it more ideal pharmacokinetic properties and likely a favourable side effect profile.

Acknowledgements

We acknowledge the hnancial support of the NIH National Institute of Diabetes and Digestive and Kidney Diseases (DK105825). This research was undertaken on the MX1 beamline at the Australian Synchrotron, part of ANSTO.

References

[1]. Issemann I, Prince RA, Tugwood JD, and Green S, “The retinoid X receptor enhances the function of the peroxisome proliferator activated receptor,” Biochimie, vol. 75, no. 3-4, pp. 251–256, 1993. [PubMed: 8389594]

[2]. Kroker AJ and Bruning JB, “Review of the structural and dynamic mechanisms of PPARγ partial agonism,” PPAR Research, vol. 2015, Article ID 816856, 15 pages, 2015.

[3]. Chandra V, Huang P, Hamuro Y et al., “Structure of the intact PPAR-γ-RXR-α nuclear receptor complex on DNA,” Nature, vol. 456, no. 7220, pp. 350–356, 2008. [PubMed: 19043829]

[4]. Nolte RT, Wisely GB, Westin S et al., “Ligand binding and co-activator assembly of the peroxisome proliferator-activated receptor-γ,” Nature, vol. 395, no. 6698, pp. 137–143, 1998. [PubMed: 9744270]

[5]. Gampe RT, Jr., Montana VG, Lambert MH et al., “Asymmetry in the PPARγ/RXRα crystal structure reveals the molecular basis of heterodimerization among nuclear receptors,” Molecular Cell, vol. 5, no. 3, pp. 545–555, 2000. [PubMed: 10882139]

[6]. Gelin M, Delfosse V, Allemand F et al., “Combining ‘dry’ co-crystallization and in situ diffraction to facilitate ligand screening by X-ray crystallography,” Acta Crystallographica Section D: Biological Crystallography, vol. 71, pp. 1777–1787, 2015. [PubMed: 26249358]

[7]. Liberato MV, Nascimento AS, Ayers SD et al., “Medium chain fatty acids are selective peroxisome proliferator activated receptor (PPAR) γ activators and Pan-PPAR partial agonists,” PLoS ONE, vol. 7, no. 5, Article ID e36297, 2012.

[8]. Banks AS, McAllister FE, Camporez JPG et al., “An ERK/Cdk5 axis controls the diabetogenic actions of PPARgamma,” Nature, vol. 517, no. 7534, pp. 391–395, 2015. [PubMed: 25409143]

[9]. Choi JH, Banks AS, Estall JL et al., “Anti-diabetic drugs inhibit obesity-linked phosphorylation of PPARγ3 by Cdk5,” Nature, vol. 466, no. 7305, pp. 451–456. 2010. [PubMed: 20651683]

[10]. Frkic RL, He Y, Rodriguez BB et al., “Structure-Activity Relationship of 2,4-Dichloro-N-(3,5-dichloro-4-(quinolin-3-yloxy)phenyl)benzenesulfonamide (INT131) Analogs for PPARγ-Targeted Antidiabetics,” Journal of Medicinal Chemistry, vol. 60, no. 11, pp. 4584–4593, 2017. [PubMed: 28485590]

[11]. Taygerly JP, McGee LR, Rubenstein SM et al., “Discovery of INT131: a selective PPARγ modulator that enhances insulin sensitivity,” Bioorganic & Medicinal Chemistry, vol. 21, no. 4, pp. 979–992, 2013. [PubMed: 23294830]

[12]. Motani A, Wang Z, Weiszmann J et al., "INT131: a selective modulator of PPARγ," Journal of Molecular Biology, vol. 386, no. 5, pp. 1301–1311, 2009. [PubMed: 19452630]

[13]. van Marrewijk LM, Polyak SW, Hijnen M et al., "SR2067 reveals a unique kinetic and structural signature for PPARγ partial agonism," ACS Chemical Biology, vol. 11, no. 1, pp. 273–283, 2016. [PubMed: 26579553]

[14]. Sime M, Allan AC, Chapman P et al., "Erratum: Discovery of GSK1997132B a novel centrally penetrant benzimidazole PPARγ partial agonist (Bioorganic and Medicinal Chemistry Letters (2011) 21 (5568–5572))," Bioorganic & Medicinal Chemistry Letters, vol. 23, no. 4, p. 1143, 2013.

[15]. Bruning JB, Chalmers MJ, Prasad S et al., "Partial agonists activate PPARγ using a helix 12 independent mechanism," Structure, vol. 15, no. 10, pp. 1258–1271, 2007. [PubMed: 17937915]

[16]. Sauer S, "Ligands for the nuclear peroxisome proliferator-activated receptor gamma," Trends in Pharmacological Sciences, vol. 36, no. 10, pp. 688–704, 2015. [PubMed: 26435213]

[17]. Chalmers MJ, Busby SA, Pascal BD et al., "Probing protein ligand interactions by automated hydrogen/deuterium exchange mass spectrometry," Analytical Chemistry, vol. 78, no. 4, pp. 1005–1014, 2006. [PubMed: 16478090]

[18]. Zhang Z and Smith DL, "Determination of amide hydrogen exchange by mass spectrometry: A new tool for protein structure elucidation," Protein Science, vol. 2, no. 4, pp. 522–531, 1993. [PubMed: 8390883]

[19]. Pascal BD, Willis S, Lauer JL et al., "HDX workbench: software for the analysis of H/D exchange MS data," Journal of The American Society for Mass Spectrometry, vol. 23, no. 9, pp. 1512–1521, 2012. [PubMed: 22692830]

[20]. Liebschner D, Afonine PV, Moriarty NW et al., "Polder maps: Improving OMIT maps by excluding bulk solvent", Acta Crystallographica Section D: Structural Biology, vol. 73, no. 2, pp. 148–157, 2017. [PubMed: 28177311]

[21]. Nagy L and Schwabe JWR, "Mechanism of the nuclear receptor molecular switch," Trends in Biochemical Sciences, vol. 29, no. 6, pp. 317–324, 2004. [PubMed: 15276186]

[22]. Batista MRB and Martínez L, "Dynamics of nuclear receptor Helix-12 switch of transcription activation by modeling time-resolved fluorescence anisotropy decays," Biophysical Journal, vol. 105, no. 7, pp. 1670–1680, 2013. [PubMed: 24094408]

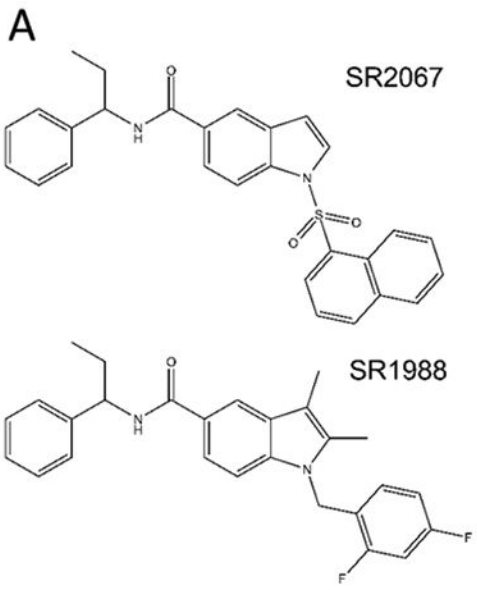

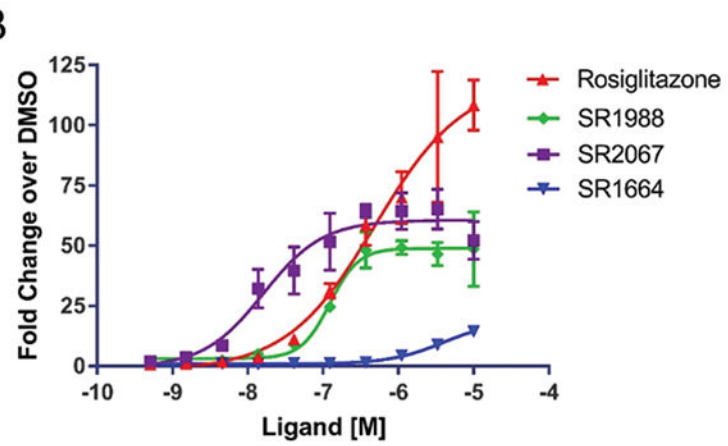

	Rosiglitazone	SR1988	SR2067	SR1664
Max Transactivation (%)	100	45	61	13
EC_{50}	494 nM	123 nM	16 nM	3965 nM

Figure 1: SR1988 is a non-acid partial agonist of PPARγ.

(A) Chemical structure of SR2067 and its analogue SR1988. (B) Transactivation data for SR1988. The transcriptional activity of SR1988 on PPARγ was determined using a GAL4 transactivation assay. Data points were repeated in triplicate. Maximum transactivation values are normalised to Rosiglitazone.

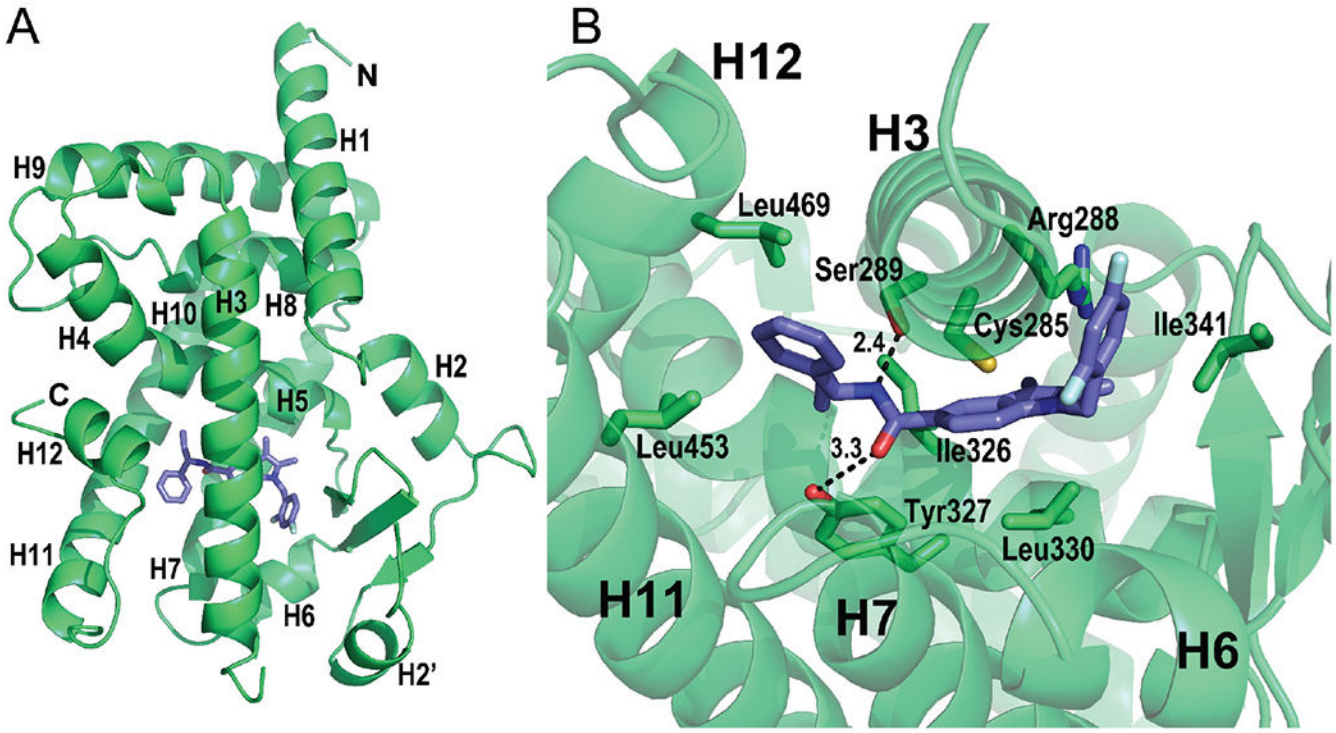

Figure 2: Crystal structure of PPARγ LBD bound to SR1988.

(A) Ribbons representation of PPARγ LBD (green) bound to SR1988 (purple sticks). Only chain A is shown of the homodimeric asymmetric unit of the crystal. (B) Interactions made between SR1988 and residues lining the ligand binding pocket. Contributing side chains are shown as green sticks, with residue identities labelled.

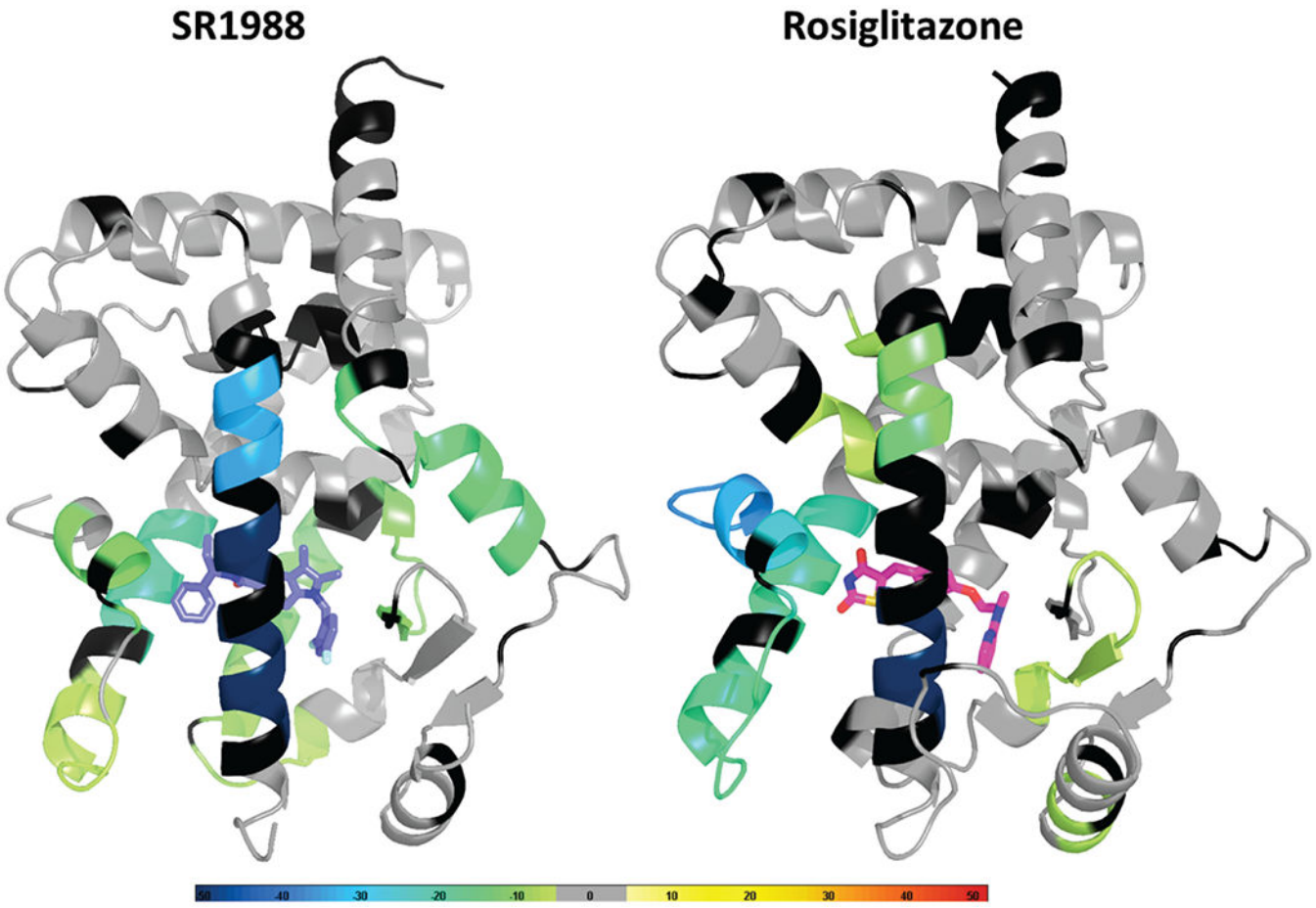

Figure 3: SR1988 displays a receptor stabilisation profile typical of PPARγ partial agonists.
HDX data for the corresponding peptides are plotted over the structures of PPARγ LBD bound to rosiglitazone (PDB 2PRG) and SR1988 (PDB: 6D3E). Percentage reduction (average of all replicates and all time points) in HDX relative to apo receptor is coloured according to the key. Residues are coloured to correspond to the average percent change in deuteration between apo and SR1988 or rosiglitazone bound PPARγ LBD.

Table 1:

Crystallographic data statistics.

PDB accession code	6D3E
Space group	C 1 2 1
Cell dimensions	
a, *b*, *c* (Å)	93.04, 62.51, 118.65
α, *β*, *γ* (°)	90, 102.32, 90
X-ray source	Australian Synchrotron MX1
Wavelength (Å)	0.9537
Resolution range (Å)	58.0-2.40 (2.49-2.40)
R_{merge} (%)[a]	0.12 (1.18)
R_{pim} (%)	0.075 (0.794)
Observations	155718 (13591)
Unique reflections	26013 (2563)
Mean (I)/σ(I)	11.8 (1.8)
Completeness	98.3 (93.0)
Multiplicity	6.0 (5.3)
CC(1/2)	0.998 (0.601)
Structure refinement	
Resolution range (Å)	39.5-2.4
R_{work}[b]	0.206 (0.283)
R_{free}[c]	0.264 (0.316)
Total number of	
Non-hydrogen atoms	4420
Protein atoms	4210
Ligand atoms	32
Water molecules	178
RMSD	
Bond length (Å)	0.002
Bond angle (deg)	0.42
B-factors (Å^2)	
Overall	63.7
Average protein atoms	63.5
Average ligand atoms	105.5
Average solvent	59.4
Ramachandran statistics	
Most favoured regions (%)	96.71
Allowed regions (%)	3.10

Disallowed regions (%)	0.19

Values in parentheses correspond to the last shell.

[a] $R_{merge} = \Sigma |I - \langle I \rangle| / \Sigma I$.

[b] $R_{work} = \Sigma |F_O - F_C| / \Sigma |F_O|$ for all data excluding data used to calculate R_{free}.

[c] $R_{free} = \Sigma |F_O - F_C| / \Sigma |F_O|$. for all data.

Chapter 4

Shooting three inflammatory targets with a single bullet: Novel multi-targeting anti-inflammatory glitazones

Perihan A. Elzahhar[a], Rana Alaaeddine[b], Tamer M. Ibrahim[c], Rasha Nassra[d], Azza Ismail[a], **Benjamin S.K. Chua**[e], Rebecca L. Frkic[f], John B. Bruning[f], Nadja Wallner[g], Tilo Knape[g], Andreas von Knethen [g, h], Hala Labib [a, i], Ahmed F. El-Yazbi [b, j,*], Ahmed S.F. Belal [a,**]

[a] Department of Pharmaceutical Chemistry, Faculty of Pharmacy, Alexandria University, Alexandria, 21521, Egypt

[b] Department of Pharmacology and Toxicology, Faculty of Medicine and Medical Centre, American University of Beirut, Beirut, Lebanon

[c] Department of Pharmaceutical Chemistry, Faculty of Pharmacy, Kafrelsheikh University, Kafr El-Sheikh, 33516, Egypt

[d] Department of Medical Biochemistry, Faculty of Medicine, Alexandria University, Egypt

[e] School of Biological Sciences, The University of Adelaide, Adelaide, South Australia, 5005, Australia

[f] Institute for Photonics and Advanced Sensing, The School of Biological Sciences, The University of Adelaide, North Tce, Adelaide, South Australia, 5005, Australia

[g] Fraunhofer Institute for Molecular Biology and Applied Ecology IME, Project Group Translational Medicine & Pharmacology TMP, Theodor-Stern-Kai 7, 60596, Frankfurt, Germany

[h] Institute of Biochemistry I, Faculty of Medicine, Goethe-University Frankfurt, Theodor-Stern-Kai 7, 60596, Frankfurt, Germany

[i] Department of Analytical & Pharmaceutical Chemistry, Faculty of Pharmacy & Drug Manufacturing, Pharos University in Alexandria, Egypt

[j] Department of Pharmacology and Toxicology, Faculty of Pharmacy, Alexandria University, Alexandria, 21521, Egypt

[*] Corresponding author. Department of Pharmacology and Toxicology, Faculty of Medicine and Medical Centre, American University of Beirut, Beirut, Lebanon.

[**] Corresponding author.

Published, DOI: 10.1016/j.ejmech.2019.02.034

Statement of Authorship

Title of Paper	Shooting three inflammatory targets with a single bullet: Novel multi-targeting anti-inflammatory glitazones
Publication Status	☑ Published ☐ Accepted for Publication ☐ Submitted for Publication ☐ Unpublished and Unsubmitted work written in manuscript style
Publication Details	This paper characterizes the hybrid partial PPARγ agonist – COX2/LOX inhibitor ligand, using

Principal Author

Name of Principal Author (Candidate)	Benjamin Soon Kai Chua		
Contribution to the Paper	Soaking of ligands, crystal data collection, structure refinement, manuscript preparation		
Overall percentage (%)	10		
Certification:	This paper reports on original research I conducted during the period of my Higher Degree by Research candidature and is not subject to any obligations or contractual agreements with a thi s thesis.		
Signature		Date	16/06/2023

Co-Author Contributions

By signing the Statement of Authorship, each author certifies that:

i. the candidate's stated contribution to the publication is accurate (as detailed above);

ii. permission is granted for the candidate in include the publication in the thesis; and

iii. the sum of all co-author contributions is equal to 100% less the candidate's stated contribution.

Name of Co-Author	Perihan A. Elzahhar		
Contribution to the Paper	Design and synthesis of the compounds, Design of the biological assays, In silico prediction of physiochemical properties, drug likeness, pharmacokinetic profile and ligand efficiency metrics and manuscript preparation		
Signature		Date	July 5th, 2023

Name of Co-Author	Rana Alaaeddine		
Contribution to the Paper	In vitro COX-1, COX-2 and 15-LOX inhibitory assays, immunohistochemical analysis of ligand-stimulated PPARg nuclear localization, inhibition of monocyte to macrophage differentiation, IL-1b and TNF-a expression and 20-HETE production assay		
Signature	author not available, John Bruning signing John Bruning	Date	10-07-2023

Name of Co-Author	Tamer M. Ibrahim		
Contribution to the Paper	Docking of the most active compounds into the active sites of the 3 biological targets		
Signature	author not available, John Bruning signing	Date	10-07-2023

Name of Co-Author	Rasha Nassra		
Contribution to the Paper	In vitro glucose uptake using rat hemi-diaphragm model and in vivo anti-inflammatory assay		
Signature	author not available, John Bruning signing	Date	10-07-2023

Name of Co-Author	Azza Ismail		
Contribution to the Paper	Synthesis of the compounds and assessment of purity via HPLC		
Signature	author not available, John Bruning signing	Date	10-07-2023

Name of Co-Author	Rebecca L. Frkic		
Contribution to the Paper	Expressed, purified, and crystallized apo protein. manuscript preparation		
Signature	author not available, John Bruning signing	Date	10-07-2023

Name of Co-Author	John B. Bruning		
Contribution to the Paper	Crystallography, manuscript preparation		
Signature	John Bruning	Date	10-07-2023

Name of Co-Author	Nadja Wallner		
Contribution to the Paper	PPARg functional reporter gene assay		
Signature	author not available, John Bruning signing	Date	10-07-2023

Name of Co-Author	Tilo Knape

Contribution to the Paper	PPARg functional reporter gene assay		
Signature	author not available, John Bruning signing	Date	10-07-2023

Name of Co-Author	Andreas von Knethen		
Contribution to the Paper	PPARg functional reporter gene assay, manuscript preparation		
Signature	author not available, John Bruning signing	Date	10-07-2023

Name of Co-Author	Hala Labib		
Contribution to the Paper	Synthesis of the compounds and assessment of purity via HPLC		
Signature	author not available, John Bruning signing	Date	10-07-2023

Name of Co-Author	Ahmed F. El-Yazbi		
Contribution to the Paper	In vitro COX-1, COX-2 and 15-LOX inhibitory assays, immunohistochemical analysis of ligand stimulated PPARg nuclear localization, inhibition of monocyte to macrophage differentiation, IL-1b and TNF-a expression and 20-HETE production assay and writing the manuscript		
Signature	author not available, John Bruning signing	Date	10-07-2023

Name of Co-Author	Ahmed S.F. Belal		
Contribution to the Paper	Design and synthesis of the compounds, design of the biological assays and writing the manuscript.		
Signature	author not available, John Bruning signing	Date	10-07-2023

European Journal of Medicinal Chemistry 167 (2019) 562–582

Contents lists available at ScienceDirect

European Journal of Medicinal Chemistry

journal homepage: http://www.elsevier.com/locate/ejmech

Research paper

Shooting three inflammatory targets with a single bullet: Novel multi-targeting anti-inflammatory glitazones

Perihan A. Elzahhar [a], Rana Alaaeddine [b], Tamer M. Ibrahim [c], Rasha Nassra [d], Azza Ismail [a], Benjamin S.K. Chua [e], Rebecca L. Frkic [f], John B. Bruning [f], Nadja Wallner [g], Tilo Knape [g], Andreas von Knethen [g, h], Hala Labib [a, i], Ahmed F. El-Yazbi [b, j, *], Ahmed S.F. Belal [a, **]

[a] Department of Pharmaceutical Chemistry, Faculty of Pharmacy, Alexandria University, Alexandria, 21521, Egypt
[b] Department of Pharmacology and Toxicology, Faculty of Medicine and Medical Centre, American University of Beirut, Beirut, Lebanon
[c] Department of Pharmaceutical Chemistry, Faculty of Pharmacy, Kafrelsheikh University, Kafr El-Sheikh, 33516, Egypt
[d] Department of Medical Biochemistry, Faculty of Medicine, Alexandria University, Egypt
[e] School of Biological Sciences, The University of Adelaide, Adelaide, South Australia, 5005, Australia
[f] Institute for Photonics and Advanced Sensing, The School of Biological Sciences, The University of Adelaide, North Tce, Adelaide, South Australia, 5005, Australia
[g] Fraunhofer Institute for Molecular Biology and Applied Ecology IME, Project Group Translational Medicine & Pharmacology TMP, Theodor-Stern-Kai 7, 60596, Frankfurt, Germany
[h] Institute of Biochemistry I, Faculty of Medicine, Goethe-University Frankfurt, Theodor-Stern-Kai 7, 60596, Frankfurt, Germany
[i] Department of Analytical & Pharmaceutical Chemistry, Faculty of Pharmacy & Drug Manufacturing, Pharos University in Alexandria, Egypt
[j] Department of Pharmacology and Toxicology, Faculty of Pharmacy, Alexandria University, Alexandria, 21521, Egypt

ARTICLE INFO

Article history:
Received 10 November 2018
Received in revised form
4 February 2019
Accepted 10 February 2019
Available online 13 February 2019

Keywords:
Inflammation
Cyclooxygenase-2
15-Lipoxygenase
Peroxisome proliferator-activated receptor-γ
Multi-targeting

ABSTRACT

In search for effective multi-targeting drug ligands (MTDLs) to address low-grade inflammatory changes of metabolic disorders, we rationally designed some novel glitazones-like compounds. This was achieved by incorporating prominent pharmacophoric motifs from previously reported COX-2, 15-LOX and PPARγ ligands. Challenging our design with pre-synthetic docking experiments on PPARγ showed encouraging results. *In vitro* tests have identified 4 compounds as simultaneous partial PPARγ agonist, potent COX-2 antagonist (nanomolar IC_{50} values) and moderate 15-LOX inhibitor (micromolar IC_{50} values). We envisioned such outcome as a prototypical balanced modulation of the 3 inflammatory targets. *In vitro* glucose uptake assay defined six compounds as insulin-sensitive and the other two as insulin-independent glucose uptake enhancers. Also, they were able to induce PPARγ nuclear translocation in immunohistochemical analysis. Their anti-inflammatory potential has been translated to effective inhibition of monocyte to macrophage differentiation, suppression of LPS-induced inflammatory cytokine production in macrophages, as well as significant *in vivo* anti-inflammatory activity. Ligand co-crystallized PPARγ X-ray of one of MTDLs has identified new clues that could serve as structural basis for its partial agonism. Docking of the most active compounds into COX-2 and 15-LOX active sites, pinpointed favorable binding patterns, similar to those of the co-crystallized ligands. Finally, *in silico* assessment of pharmacokinetics, physicochemical properties, drug-likeness and ligand efficiency indices was performed. Hence, we anticipate that the prominent biological profile of such series will rationalize relevant anti-inflammatory drug development endeavors.

1. Introduction

Inflammation is a complex and dynamic response to defend the host against potential threats such as pathogens or tissue insults [1,2]. It is associated with diverse signaling pathways involving enzymes, membrane and cellular receptors, transcription factors

* Corresponding author. Department of Pharmacology and Toxicology, Faculty of Medicine and Medical Centre, American University of Beirut, Beirut, Lebanon.
** Corresponding author.
E-mail addresses: ae88@aub.edu.lb (A.F. El-Yazbi), ahmed.belal@alexu.edu.eg (A.S.F. Belal).

https://doi.org/10.1016/j.ejmech.2019.02.034
0223-5234/

and others, operating in an orchestrated manner to counteract the imminent threat [2,3]. Neutrophils and tissue macrophages represent the first line of defense, where they stimulate the production of a plethora of inflammatory mediators as a result of sensing an initial insult [4,5]. Although inflammation is intended to be protective, exaggerated and uncontrollable neutrophil and/or macrophages activity, in addition to failure to achieve resolution often leads to persistent tissue damage, a condition underlying many chronic inflammatory disorders (such as psoriasis, multiple sclerosis, and rheumatoid arthritis) [1].

On the other hand, diabetes is perceived as a multifaceted disease implicating metabolic, cardiovascular, and immune component events; though an understanding of the underlying relating mechanisms are not clear [6,7]. Recent results from our group implicated low-grade adipose inflammation as potential underlying cause of cardiovascular and cardiac autonomic dysfunction associated with metabolic challenge [8]. Indeed, reversal of adipose inflammation was associated with an improved vascular and cardiac autonomic function [8].

Among the different pathways involved in the inflammatory response, arachidonic acid (AA) plays a major role as the biological precursor for many inflammatory mediators. Two key metabolic enzymes are involved in generating AA derivatives, namely: cyclooxygenase (COX) and lipoxygenase (LOX) [9]. COX-2 expression is induced by pro-inflammatory stimuli leading to the generation of inflammatory signaling prostaglandins (PGs) [9,10]. On the other hand, LOXs catalyze the oxygenation of polyunsaturated fatty acids (PUFAs) such as arachidonic and linoleic acids to give oxygenated lipid mediators that are involved in important cellular signaling mechanisms [11]. Based on the site of oxygenation of arachidonic acid, several mammalian LOX isoforms were discovered and denoted 5-, 12- and 15-LOX [11]. 5-LOX is famous for playing an important role in the pathology of respiratory disorders through the production of 5-hydroperoxy-eicosatetraenoic acid (5-HPETE) which is subsequently converted to leukotrienes (LTs) [11].

Contrarily, 15-LOX converts polyunsaturated fatty acids into 15-*S*-HPETE which is metabolized into either lipoxins or eoxins [11–13]. It is necessary to mention that 5-LOX also contributes to the synthesis of lipoxins [11–13]. While lipoxins are pro-resolving and anti-inflammatory [11–13], eoxins (also referred to as 14,15-LTs) have shown to be pro-inflammatory mediators specially in the context of atherosclerosis, adipocyte differentiation and development of obesity [12,14]. Also, eoxins were shown to have similar actions as leukotrienes, and hence, the probability of their implications in inflammatory and respiratory diseases could not be excluded [12,14]. Moreover, 15-LOX is hypothesized to initiate and/or promote atherosclerosis through LDL oxidation [12,14]. It is not surprising that IL-4 and/or IL-13 induce the expression of 15-LOX in cultured mast cells, monocytes, and epithelial cells [12,14].

Thus, 15-LOX can be regarded as a double-edged weapon that exert both pro- and anti-inflammatory properties and the details of the interplay between them in physiological and pathophysiological contexts are still lacking [12,14]. Up till this moment, various reports indicated that 15-LOX-inhibitors (such as PD146176 among others) could serve as effective therapeutics for a number of 15-LOX-related diseases, which include diabetes, hypertension, obesity, atherosclerosis and other disorders linked to chronic adipose tissue inflammation [14].

The notion of using selective COX-2 inhibitors as anti-inflammatories with minimal gastrointestinal (GI) side effects was very resonating in the late 1990s and early 2000s [15,16]. However, it turned out that blocking only COX-2 would shunt the inflammatory pathways towards more activity of LOX and hence blocking both COX-2 and LOX would provide safer and more effective anti-inflammatory activity [17–19].

Interestingly, *in vitro* studies demonstrated that LOX modulators can activate peroxisome proliferator-activated receptors (PPARs) [20]. Indeed, recent studies *in vivo* implicated a role for interplay between LOX-derived AA metabolites and PPARγ in mitigating post-ischemic injury in the brain [21]. PPARs are subclasses of the intracellular receptors family, that when activated act as nuclear hormones modulating the transcription of plenty of factors involved in many physiological processes [22–24]. PPARγ activity was first thought to be limited to lipid metabolism and glucose homeostasis [22–24]. However, there is ample evidence demonstrating the role of activated PPARγ in reducing the expression of pro-inflammatory mediators such as cytokines and adhesion molecules involved in neutrophils recruitment to inflammatory foci [23,25]. Moreover, PPARγ agonists were reported to be capable of inhibiting the mRNA expression of COX-2 and nitric oxide synthase (NOS), which further emphasizes the essential role that PPARγ plays in inflammation [23,25,26]. Significantly, clinical trials examining the use of pioglitazone for managing psoriasis, multiple sclerosis, and rheumatoid arthritis are currently ongoing [19].

The last decade has witnessed a paradigm shift in drug discovery programs from designing highly selective single-target ligands to modulating a multiplicity of targets within related signaling networks [27]. Hence, in seeking multi-targeting anti-inflammatory leads with potential future applications in metabolic disorders, we herein report on the development of the first-in-class MTDLs as potential simultaneous COX-2/LOX inhibitors and PPARγ agonists. As a proof of concept, the designed compounds were challenged with different biological assays and *in silico* studies. We believe that the outcomes of this study might aid in expanding the knowledge on the targeting of inflammatory reactions as a valid approach of managing metabolic disorders.

2. Results and discussion

2.1. Rationale for the design of multi-target directed ligands (MTDLs)

Thiazolidine-2,4-diones (TZDs)/rhodanines constitute diverse scaffolds that are known to exert a vast array of pleiotropic benefits, including insulin-sensitizing, anti-inflammatory and anti-proliferative activities [28–30]. They were also reported to prevent the progression of atherosclerotic lesions in patients with type 2 diabetes [31]. Over and above, telmisartan-rosiglitazone hybrid molecules were evaluated as dual PPARγ agonists/angiotensin II antagonists for management of metabolic syndrome [32]. In particular, TZDs, known as high-affinity PPARγ agonists, have been introduced into clinical practice for the treatment of type 2 diabetes [33].

Thus, in our search for multi-target anti-inflammatory leads with potential efficacy in metabolic disorders, and based on the structural features of four pleiotropic lead compounds; LYSO-7 (**A**) [34,35], pioglitazone (**B**), a reported LOX-inhibiting thiazolidinedione (**C**) [36] and a dual COX-2/15-LOX inhibitor (**D**) [37] recently reported by our lab, we adopted a pharmacophoric molecular hybridization approach to design and synthesize some novel triazolyl-thiazolidinedione/rhodanine hybrids as potential simultaneous COX-2/LOX inhibitors and PPARγ agonists. It is worth mentioning that developing a small molecule modulating these 3 targets was not encountered before.

Over and above, the designed assembly has its pharmacophoric parts rooted from pioglitazone. It comprises the essential pharmacophore TZD or its rhodanine bioisostere. This pharmacophore is decorated with a methoxybenzylidene group like compounds **A** and **C** (Fig. 1), which in turn is connected to the 1,2,3-triazole moiety. This should retain the 3-carbon atom spacer between the

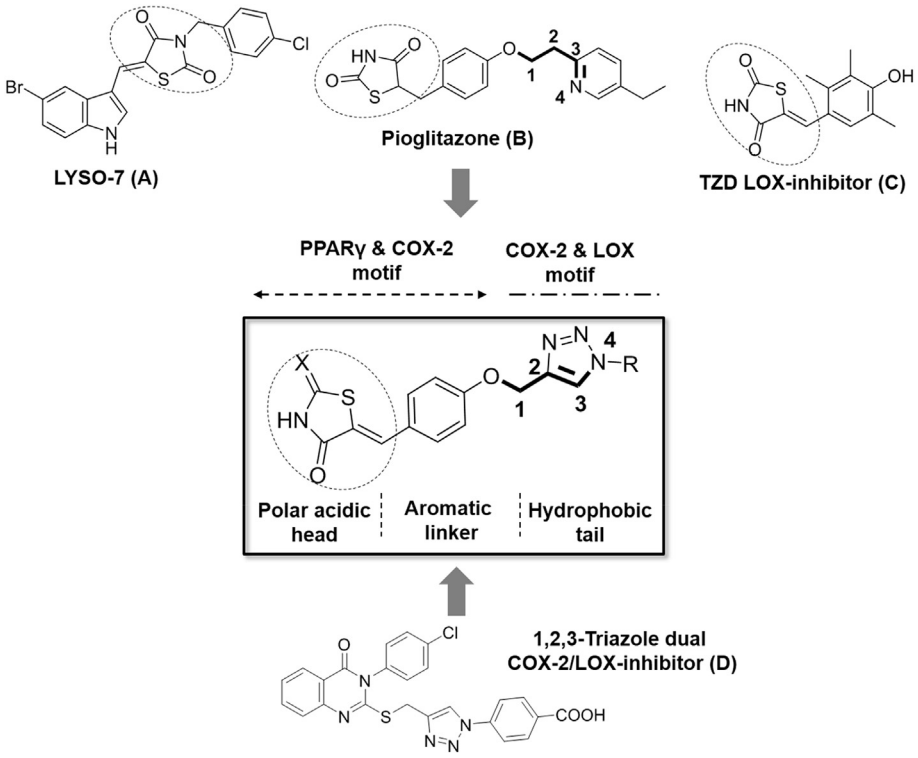

Fig. 1. Rationale for the design of the target compounds.

oxygen of the phenoxy-linker and nitrogen atom of the pyridine ring (as in pioglitazone) or N-1 of the triazole nucleus (in our designed compounds). Substitution pattern at N-1 of the triazole ring with various aryl and aralkyl groups is attempted to grant variable electronic and lipophilic environments to investigate their effect on the anticipated biological activity and with the hope of achieving better binding interactions with the potential biological targets.

In addition, our design agrees with the three-module framework proposed by Pirat et al. to represent PPARγ agonist glitazones [38]. It is composed of an acidic polar head group, TZD or rhodanine, joined to a hydrophobic tail through an aromatic linker [38]. We altered the tail group to afford chemical and biological uniqueness while conserving the polar head and the linker regions [38]. Our tail moiety was carefully chosen to be 1,4-disubstituted-1,2,3-triazole which is a pharmacophore we recently reported to show dual COX-2 and LOX inhibitory activity (Structure **D**, Fig. 1) [37]. Furthermore, target compounds were mapped out with a benzylidene attachment between the polar head and the linker instead of the usual benzyl, which is one distinct difference from pioglitazone (Fig. 1). We thought that this would be more convenient since recent reports indicated benzylidene TZD derivatives are endowed with partial PPARγ agonistic properties, which retain the desired pharmacological actions while avoiding the untoward adverse effects [39,40].

To the best of our knowledge, the click chemistry-derived 1,4-disubstituted-1,2,3-triazoles have not been explored before for their synchronous PPARγ agonistic and COX-2/LOX inhibitory activities. Together with their wide-ranging biological activities, bioorthogonal nature, being non-classical bioisosteres of the amide group and their propensity to be involved in hydrogen bond and π-π stacking interactions with potential targets [41], it would be tempting to employ this easily accessible structural motif into the aforementioned framework.

2.2. Pre-synthetic PPARγ docking study

To gain substantial theoretical evidence into the potential PPARγ agonistic activity at the molecular level, molecular docking studies were pre-synthetically applied on 18 compounds that contained our proposed design. Our selection of compounds for PPARγ crystallization and structure determination for *in silico* validation was based on its upstream occurrence in inflammatory pathways (since it is a nuclear receptor), plus its implications in lipid metabolism and glucose homeostasis.

Regarding the chemical structures of the docked compounds, the reader is advised to consult Scheme 1 using the appropriate coding. Based on literature, the screening performance of PPARγ DEKOIS 2.0 benchmark set employing various docking tools (e.g., GOLD [ChemPLP], Glide [SP] and AutoDock Vina) showed comparable and nonrandom screening performance with all three docking tools [42]. This led us to employ GOLD (ChemPLP) [43,44] as scoring function for pose prediction purposes. Additionally, we employed two additional scoring functions, AutoDock Vina [45] and AutoDock VinaXB [46], for extracting consensus ranking of our proposed compounds.

The crystal structure of PPARγ co-crystallized with rosiglitazone (PDB ID: 2PRG) was used as a model to gauge the binding affinities of the test compounds with the enzyme. The scoring function, hydrogen bonds formed with key amino acids and the relative orientation of the docked compounds with respect to the co-crystallized ligand rosiglitazone were used to estimate the binding propensities to the ligand binding domain (LBD) of PPARγ. Pose-retrieval experiment of the co-crystallized ligand reproduced the key interaction pattern in the binding site of PPARγ with acceptable RMSD values (e.g., for GOLD docking RMSD = 1.25 Å, Supplementary Information Figure SM1).

Examination of the predicted docking scores of the test compounds using GOLD, as indicated in Supplementary Information

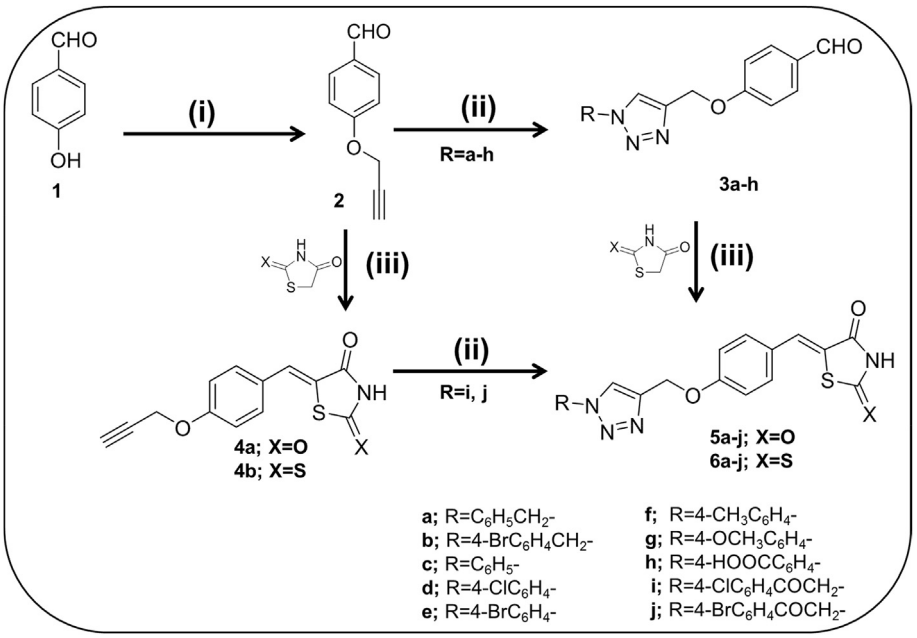

Scheme 1. Synthesis of (*Z*)-5-(4-((1-(aryl or aralkyl)-1*H*-1,2,3-triazol-4-yl)methoxy)benzylidene)thiazolidine-2,4-diones (compounds **5a-j**) or 2-thioxothiazolidin-4-one derivatives (compounds **6a-j**). Reagents and conditions: i) Propargyl bromide, K_2CO_3, Acetone, reflux for 2.5 h. ii) Appropriate azide, $CuSO_4.5H_2O$ (5 mol %), Sodium Ascorbate (20 mol %), DMF/H_2O, stirring overnight. iii) Piperidine (10 mol%), EtOH, reflux for 12 h.

Table SM1, revealed that four compounds were superior to rosiglitazone while other compounds showed slightly lower and comparable scores. According to AutoDock Vina and AutoDock VinaXB, the predicted docking scores (Table SM1) almost showed no difference, which excludes halogen-bonding as a possible type of intermolecular interaction between these poses and the backbone of the protein. In addition, all docked compounds showed higher predicted docking scores than the co-crystallized ligand.

The LBD of PPARγ consists of 13 alpha helices and a small beta sheet. Activation function 2 (AF2) is the part of the LBD that is important for ligand dependent coactivator binding and is formed by helices 3–5 and helix 12 [22]. Ser289, His323, His449 and Tyr473 are the most important conserved amino acids that are involved in target recognition of PPARγ ligands [22]. Of particular interest, the formation of a hydrogen bond between a ligand and Tyr473 triggers conformational change in the AF2 site, which enhances the recruitment of coregulatory factors to regulate gene expression [22].

Most of our compounds reproduced the key hydrogen bonding interactions of the co-crystallized ligand (rosiglitazone) via the TZD ring with the residues His449, Gln289, Tyr473, His323 and Ser289, as shown in Fig. 2A and exemplified by compounds **5e** and **5j**. Moreover, some compounds showed extra binding interactions outside AF2 site as in compound **5j** that formed a hydrogen bond with Ser342.

It is worth mentioning that compounds **5b** and **5g** displayed comparable interaction pattern to rosiglitazone in the binding site of PPARγ via their TZD rings. As well, they showed additional binding interactions with Arg288 and Met264 with the bromophenyl group of **5b** and middle phenoxy group of **5g**, respectively (Fig. 2B).

Regarding the relative orientation of the compounds in the active site of PPARγ with respect to the co-crystallized ligand, it is clearly evident that the compounds were perfectly accommodated by the LBD and occupied the same position and spatial area as rosiglitazone (as observed with **5e** and **5j**) (Fig. 2A). Guided by the above-mentioned data, it was encouraging to synthesize these proposed structures.

2.3. Chemistry

The synthetic strategies for the synthesis of intermediate and

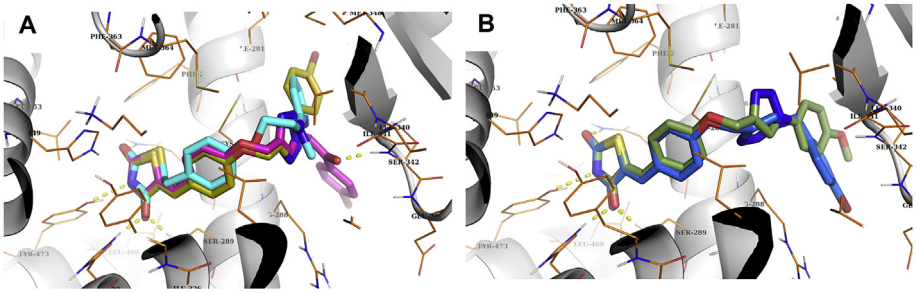

Fig. 2. (A) Overlay of the best-scored pose of **5j** (purple) and **5e** (gold) on the co-crystallized ligand (cyan) in the binding site of PPARγ crystal structure (PDB: 2PRG). **(B)** Overlay of the best-scored pose of **5b** (blue) on the pose of **5g** (olive) in the binding site of the PPARγ crystal structure. The yellow dashed-lines represent the polar contacts (H-bonding interactions). Non-polar hydrogen atoms were omitted for clarity. (For interpretation of the references to color in this figure legend, the reader is referred to the Web version of this article.)

target compounds are outlined in Scheme 1. The key intermediate 4-propargyloxybenzaldeyhde **(2)** was obtained by the alkylation of 4-hydroxy benzaldehyde with propargyl bromide in the presence of anhydrous potassium carbonate in refluxing dry acetone. Azide-alkyne cycloaddition of compound **2** and the appropriate aromatic azides in the presence of catalytic amount of copper sulphate pentahydrate and sodium ascorbate in DMF/H_2O afforded the desired regioselective 1,4-disubstituted 1,2,3-triazoles (**3a-h**) in good yields comparable to reported ones. Knoevenagel condensation of compounds (**3a-h**) with thiazolidene-2,4-dione or rhodanine in the presence of catalytic amount of piperidine generated the corresponding arylidenes **5a-h** and **6a-h**, respectively. The ^{1}H NMR of **5,6 (a–h)** showed triazole C_5–H aromatic singlet around 8.32–9.15 ppm, along with the characteristic benzylidene CH around 7.58–7.77 ppm. Furthermore, ^{13}C NMR of thiazolidene-2,4-diones (**5a-h**) displayed 2 C=O characteristic peaks at ~168.5 and 160.1 ppm, and benzylidene CH around 143–145 ppm. Additionally, ^{13}C NMR of rhodanines (**6a-h**) displayed a C=S characteristic peak at ~191.8–196.1 ppm, a C=O characteristic peak at 166.8–173.7 ppm, and benzylidene CH around 143–145 ppm.

Attempts to produce arylidene triazoles **5i-j** and **6i-j** (from phenacyl azides) using the aforementioned method were fruitless. Hence, we decided to adopt an alternative sequence; starting with Knoevenagel condensation to produce arylidenes **4a,b**, which were then subjected to CuAAC to produce the desired compounds **5i-j** and **6i-j**. It is noteworthy to indicate that the latter approach enabled us to screen for the biological activity of arylidenes **4a,b** as well. The ^{1}H NMR of **4 (a,b)** showed a propargylic characteristic triplet in the range of δ 3.61–3.63 ppm, doublet in the range of δ 4.88–4.91 ppm, that corresponds to terminal CH and CH_2, respectively. Both protons underwent a long range coupling of ~2.32 Hz. The ^{13}C NMR of **4 (a,b)** showed propargylic characteristic peaks at δ 56.2, 79.1 and 79.2 ppm corresponding to CH_2, CH and quaternary carbon, respectively. Other characteristic peaks appeared at their expected chemical shifts such as C=O and C=S. The IR spectra of **4 (a,b)** displayed characteristic sharp acetylenic-CH stretching in the range of 3275–3255 cm^{-1} and C≡C stretching in the range of 2376 cm^{-1}. The ^{1}H NMR of **5,6 (i,j)** showed triazole C_5–H aromatic singlet at 8.24 ppm, along with the disappearance of propargylic terminal CH. Furthermore, ^{13}C NMR of **5,6 (i,j)** displayed the triazole C_4 and C_5 peaks, along with the disappearance of previously mentioned propargylic CH and quaternary carbon peaks. Moreover the IR spectra of **5,6 (i,j)** were associated with the disappearance of ethynyl CH and C≡C stretching bands, clearly confirming the formation of the triazole products.

2.4. Biological evaluation

2.4.1. In vitro COX-1 and COX-2 inhibitory assay

All synthesized compounds were subjected to an *in vitro* COX-1/COX-2 inhibition assay using an ovine COX-1/human recombinant COX-2 assay kit (Catalog no. 560131; Cayman Chemicals Inc. Ann Arbor, MI, USA).

The half maximal inhibitor concentrations (IC_{50} μM) were determined and the selectivity index (SI) values were calculated as IC_{50} (COX-1)/IC_{50} (COX-2).

As summarized in Table 1; all synthesized compounds, with the exception of compound **5f**, were more potent COX-2 inhibitors than the two reference drugs diclofenac and indomethacin. They also showed higher SI than two reference drugs diclofenac and indomethacin. Although they showed lower COX-2 inhibition in comparison to celecoxib, they operated within the same range of submicromolar activity.

All compounds inhibited COX-1 in concentrations that are at least one order of magnitude higher than that experienced with COX-2, which highlights the selectivity displayed towards COX-2. Although SI values were lower than that of celecoxib, yet it could be viewed as an advantage by potentially avoiding the cardiovascular side effects of highly selective COX-2 inhibitors [47].

For triazoles prepared from benzyl azides, we observed that the addition of 4-bromo substitution enhanced both COX-2 inhibitory activity and SI values when compared to the unsubstituted analogues. The thiazolidine-2,4-dione derivative **5b** was slightly more potent than the rhodanine **5a**. It reached about 8 times the activity of diclofenac and 5 times that of indomethacin. Intriguingly, **5b** showed the highest SI value (159) out of all the synthesized compounds in the study, which accounts for almost one half that of celecoxib activity and selectivity towards COX-2.

Within the triazole series prepared from aryl azides, it was noticed that 4-substitution with lipophilic π-deficient or π-rich substituents as was seen with 4-bromo (**5e** and **6e**) and 4-methoxy (**5g** and **6g**) remarkably enhanced both COX-2 inhibitory activity and SI values over the unsubstituted congeners. 4-Bromophenyl triazolyl compounds **5e** and **6e** showed about 4–5 times the inhibitory activity of indomethacin with about 950 times its SI towards COX-2. They reached about 6–8 times the inhibitory activity of diclofenac with about 19 times its SI towards COX-2. 4-Methoxyphenyl triazolyl compounds **5g** and **6g** showed about a 3.5–6 times the inhibitory activity of indomethacin with about 700 and 1260 times its SI towards COX-2, respectively. They reached about 5–8 times the inhibitory activity of diclofenac with about 14 and 25 times its SI towards COX-2, respectively.

On the other hand, 4-substitition with methyl (**5f** and **6f**) and carboxylic functionalities significantly reduced COX-2 inhibitory activity and SI values in comparison to their unsubstituted counterparts. Surprisingly, the novel propargyl rhodanine **4b** showed higher COX-2 inhibitory activity and SI value than that of propargyl thiazolidine-2,4-dione **4a** and was among the most active compounds in the whole study.

Cycloaddition reaction of **4a** and **4b** with 4-substituted phenacyl azides generally enhanced the activity with the highest difference observed with the 4-bromo substituted derivatives **5j** and **6j**.

It is noteworthy that rhodanine derivatives demonstrated superiority in both COX-2 inhibitory activity and SI values in comparison to their thiazolidine-2,4-dione counterparts, with the exception of **5a** and **5b**. A general trend was observed that bromo-containing compounds were among the most active within the whole study.

2.4.2. In vitro 15-LOX inhibitory assay

Compounds that showed the highest *in vitro* COX-2 inhibitory activity (**4b, 5b, 5e, 5g, 5j, 6b, 6e, 6g, 6i** and **6j**) were further subjected to *in vitro* lipoxygenase inhibition assay using soybean 15-LOX assay kit (Catalog no. 760700; Cayman Chemicals Inc. Ann Arbor, MI, USA). Both soybean LOX and human 15-LOX are structurally similar in terms of the presence of both C-terminal catalytic domain and N-terminal membrane binding domain [14]. Also, their catalytic domains display a high level of conservation. More specifically, within 10 Å of the catalytic binding site they show more than 50% identity [14]. Hence, soybean LOX has been used by a lot of research groups as a valid model to gauge the ability of many novel compounds to inhibit human 15-LOX [14]. *In vitro* 15-LOX enzymatic inhibitory activities are expressed as IC_{50} values of the tested compounds and shown in Table 1. The universal LOX inhibitor, nordihydroguaiaretic acid (NDGA) [48,49] and selective 12/15-LOX inhibitor quercetin [50,51] were used as positive controls for comparison. All ten compounds showed substantial LOX inhibitory activity with IC_{50} in the range of 3.14–5.92 μM. They operated in the same order of magnitude as NDGA and quercetin. All ten compounds showed superior LOX inhibitory activity to that of

Table 1
In vitro COX-1, COX-2, 15-LOX inhibitory IC_{50} values and COX SI values of synthesized compounds.

Code	Structure	IC_{50} μM[a]			SI COX-1/COX-2[b]
		COX-1	COX-2	15-LOX	
Celecoxib		14.8	0.05	–	296
Diclofenac Na		3.9	0.8	–	4.9
Indomethacin		0.039	0.49	–	0.1
6a	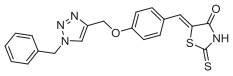	8.4	0.33	–	25.5
5a	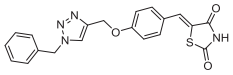	9.4	0.27	–	34.8
6b	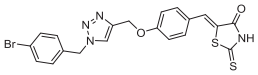	13.4	0.11	4.32	121.8
5b	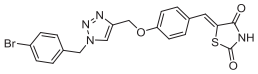	15.9	0.10	5.92	159
6c	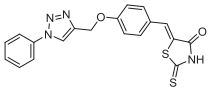	6.4	0.26	–	24.6
5c	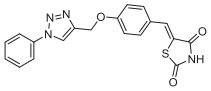	5.9	0.38	–	15.5
6d	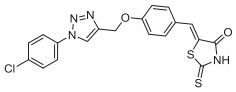	8.6	0.19	–	45.3
5d	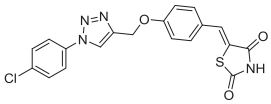	6.9	0.26	–	26.5
6e	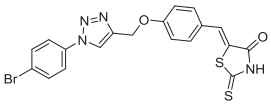	10.5	0.11	3.74	95.5
5e	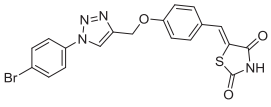	11.6	0.12	4.23	96.7
6f	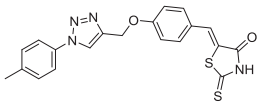	7.4	0.41	–	18.0
5f	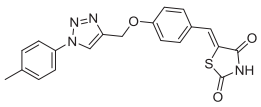	5.9	0.52	–	11.3
6g	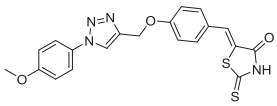	12.6	0.10	5.24	126
5g	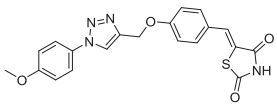	9.8	0.14	3.22	70
6h	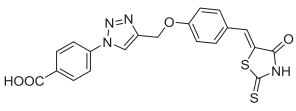	8.2	0.36	–	22.8

(*continued on next page*)

Table 1 (*continued*)

Code	Structure	IC_{50} μM[a]			SI COX-1/COX-2[b]
		COX-1	COX-2	15-LOX	
5h	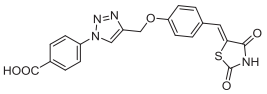	5.9	0.45	–	13.1
6i	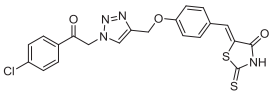	12.4	0.15	4.22	82.7
5i	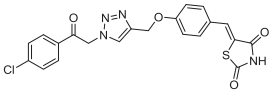	10.9	0.22	–	49.5
6j	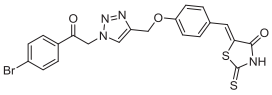	14.9	0.11	4.34	135.5
5j	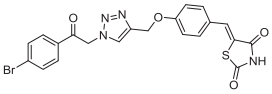	13.6	0.10	4.97	136
4b	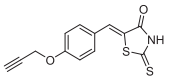	11.6	0.12	3.14	96.7
4a	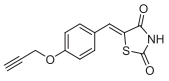	6.9	0.33	–	20.9
NDGA		–	–	10.25	–
Quercetin		–	–	3.27	–

[a] IC_{50} is the concentration (μM) needed to cause 50% inhibition of COX-1, COX-2 and 15-LOX enzymatic activity. All values are expressed as mean of three replicates with standard deviation less than 10% of the mean.
[b] Selectivity index (SI) = IC_{50} (COX-1)/IC_{50} (COX-2).

NDGA while displaying varying activity when compared to quercetin. Interestingly, the most and least potent derivatives **4b** and **5b** had almost thrice and twice the activity of NDGA, respectively. Additionally, **4b** was more potent than quercetin while **5e** and **5g** were almost equipotent to quercetin. Other compounds appeared in the following descending order of activity; **6i**, **5e**, **6b**, **6j**, **5j**, **6g** and **5b**. Consequently, the above results showed that all ten compounds have promising LOX inhibitory activity.

2.4.3. *In vitro glucose uptake using rat hemi-diaphragm model*

In order to assess the antidiabetic activity of compounds that showed the highest *in vitro* COX and LOX inhibitory activities (**4b, 5b, 5e, 5g, 5j, 6b, 6e, 6g, 6i** and **6j**), their glucose uptake potential by rat hemi-diaphragm method was measured as previously reported [31,52,53]. The glucose content of the working solution was measured, and the glucose uptake was calculated as the difference between the initial and final glucose content at 2 mg of optimized drug concentration. The glucose uptake by rat hemi-diaphragm was measured in mg/dl/45 min. Data were expressed as mean ± standard error of mean (SEM) and are shown in Fig. 3.

Data were analyzed using IBM SPSS software package version 20.0. Statistical analysis was done by ANOVA followed by Tukey *post hoc* test. Results of the *in vitro* glucose uptake assay revealed that compounds **4b, 5e, 6g** and **6j** showed equal or higher glucose uptake than pioglitazone without insulin and significantly higher uptake with insulin. Compounds **5j** and **6i** showed lower glucose uptake without insulin than pioglitazone but equal or higher uptake with insulin. Interestingly, compounds **5b** and **5g** showed equal or higher glucose uptake than pioglitazone in an insulin-independent fashion.

2.4.4. *Immunohistochemical analysis of ligand-stimulated PPARγ nuclear localization*

PPARγ agonists are known to affect the sub-cellular localization of the receptor increasing its translocation to the nucleus with subsequent regulation of gene expression [54]. The ability of the synthesized compounds to induce PPARγ nuclear translocation was studied in rat primary adipocytes as described previously [21,55]. Four compounds were selected; **4b** & **5e** shown to have an insulin-sensitive glucose uptake effect comparable to pioglitazone, and **5b** & **5g** shown to have a significant insulin-independent glucose uptake. The effect of a 3-h exposure to 10 μM concentration of each of those compounds on the nuclear localization of PPARγ in rat adipocytes was compared to that of an equivalent concentration of pioglitazone. Fig. 4 shows representative micrographs of control and treated adipocytes. Untreated controls (exposed to an equivalent volume of DMSO as the vehicle) showed diffuse cytosolic PPARγ staining. Adipocytes treated with pioglitazone or the selected test compounds showed redistribution of PPARγ staining that is superimposed with nuclear staining as depicted in the fluorescence intensity profiles along the line scans showed in Fig. 4. This is suggestive of the ability of the selected compounds to induce PPARγ nuclear translocation similar to pioglitazone. The confirmation of PPARγ nuclear translocation together with insulin-independent glucose uptake of compounds **5b** & **5g** raise the possibility of selective targeting of signaling pathways. We viewed such behavior as an analogy to the phenomenon of biased signaling that has been extensively described for GPCRs [56,57]. Theoretically speaking, the concept of signaling selective agonism can be applied to any multi-signaling receptor, yet and up to our knowledge, compounds **5b** and **5g** are the first small molecule compounds

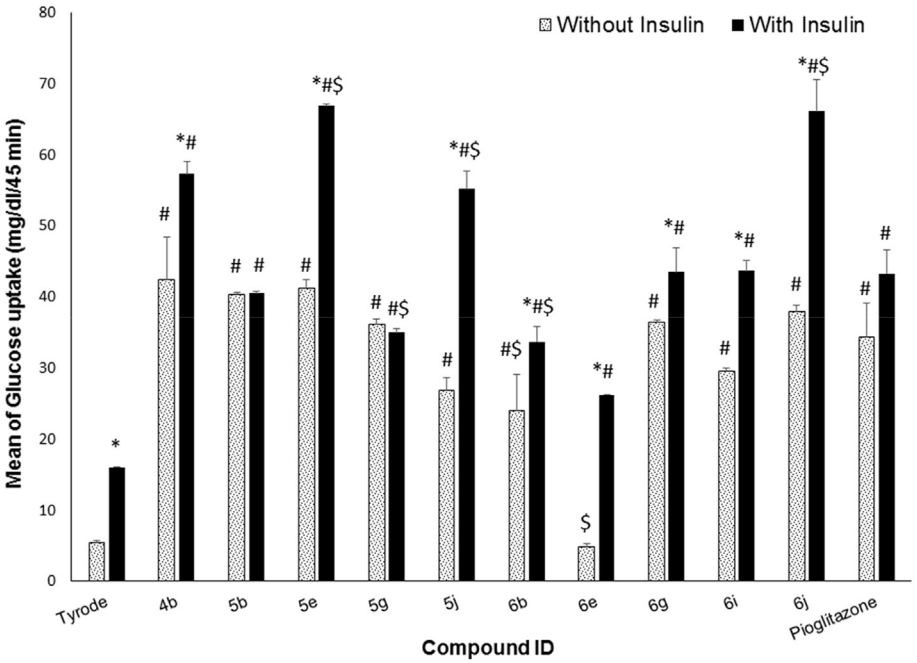

Fig. 3. *In vitro* glucose uptake activity of the most active compounds both in absence and presence of insulin using rat hemi-diaphragm model. Data represented are mean ± SD of three replicates. Statistical analysis was performed using Two-way ANOVA followed by Sidak *post hoc* test. A P-value < 0.05 was considered significant. * denotes significance vs. the corresponding effect of each compound in absence of insulin, # denotes significance vs. the corresponding arm of tyrode exposure, while $ denotes significance vs. the corresponding arm of pioglitazone treatment.

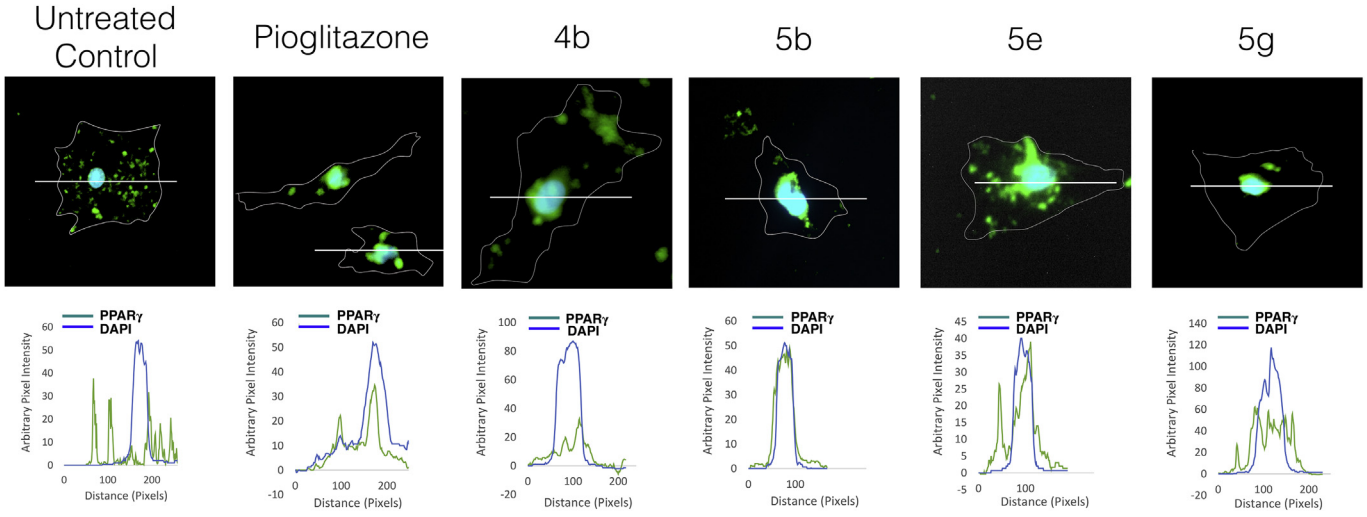

Fig. 4. Immunofluorescent staining of PPARγ in untreated rat primary adipocytes and those exposed to 10 μM of pioglitazone and different test compounds for 3 h. Phase contrast cell contours are delineated in white. Nuclei were stained with DAPI. The corresponding graphs show staining intensity for PPARγ (green) and DAPI (blue) along the scan line indicated on the corresponding micrographs. (For interpretation of the references to color in this figure legend, the reader is referred to the Web version of this article.)

reported to exhibit such behavior on PPARγ.

2.4.5. PPARγ functional reporter gene assay

The effect of the selected compounds showing PPARγ nuclear translocation on its transcriptional activity was assessed using a functional gene reporter assay [58]. Human embryonic kidney (HEK293) cells transiently transfected with two components: 1) a hybrid receptor comprising the N-terminal Gal4 DNA binding domain fused to the ligand binding domain of human PPARγ and 2) reporter Renilla luciferase gene functionally linked to the Gal4 upstream activation sequence. The transfected HEK293 cells were exposed to different concentrations of pioglitazone, **4b**, **5b**, **5e**, and **5g** for 24 h. Luciferase activity was measured and compared to basal activity in cells treated with the vehicle (DMSO). As shown in Fig. 5, at the highest concentration (10 μM), pioglitazone showed a 6-fold increase in luciferase activity compared to vehicle. At the same concentration, the tested compounds showed a 2–3 fold increase, with transcriptional activity of 25–45% that of pioglitazone. Based on the transcriptional response, a partial PPARγ agonistic activity can be assumed for the tested compounds.

2.4.6. Inhibition of monocyte to macrophage differentiation

It is widely recognized that early stages of the inflammatory response involve monocyte-to-macrophage differentiation [59].

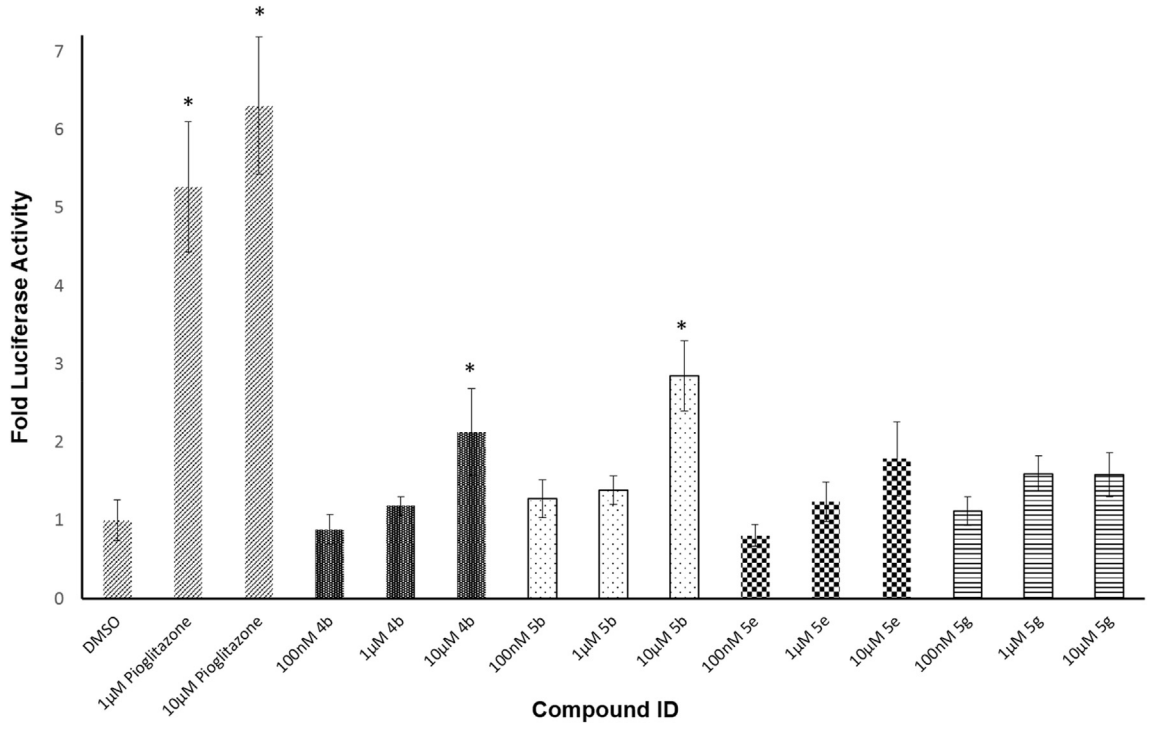

Fig. 5. Graphical representation of the increased PPARγ-mediated transcriptional activity following treatment with different concentrations of pioglitazone and selected synthetic compounds. Results are expressed as fold change compared to luciferase activity in vehicle-treated cells and represented as Mean ± Standard deviation. Luciferase activity values were compared to vehicle with One-way ANOVA followed by Dunett Multiple Comparisons test. * denotes a P-value < 0.05 vs. DMSO treated cells.

This process was shown to be particularly important in the development of atherosclerosis [60]. Interestingly, pioglitazone was shown to modulate the M1/M2 monocyte differentiation imbalance in obese diabetic patients increasing the putative anti-inflammatory M2 polarization, and this effect was postulated to underlie its glucose-independent anti-atherogenic activity [61,62]. Additionally, COX-2 expression is induced during monocytes activation into macrophages with subsequent contribution to the inflammatory response and oxidant/anti-oxidant cellular imbalance [63,64]. Of particular interest, prostaglandin E2, via its action on EP2 and EP4 receptors, was shown to stimulate the production and release of Interleukin-10 (IL-10), a cytokine with reprogramming effects on monocytes and macrophages [65]. Moreover, macrophage activation and adhesion was shown to be dependent on 15-LOX activation [66]. Our previous studies showed that compounds with dual COX-2 and LOX inhibitory activity were able to inhibit monocyte-to-macrophage differentiation [37]. As such, we anticipated that the four compounds (**4b, 5b, 5e, and 5g**) that showed dual COX-2 and LOX inhibitory activities together with PPARγ partial agonistic activities, would maintain a similar, if not enhanced, activity against THP-1 monocyte differentiation into macrophages. Towards this end, we used the PMA-induced THP-1 differentiation assay as an accepted *in vitro* model of this process [67]. The effects of these compounds in the assay were compared to diclofenac and pioglitazone as reference compounds. Results and IC_{50} values are summarized in Fig. 6. Surprisingly, pioglitazone did not produce an appreciable inhibition of PMA-induced monocyte differentiation up to 300 μM concentration. **5g** produced effects similar to pioglitazone yielding IC_{50} values in the mM range. Diclofenac produced a concentration-dependent inhibition of the differentiation process yielding an IC_{50} value close to that previously reported in a similar assay [37]. **5b** and **5e** showed IC_{50} values close to that of diclofenac, while **4b** appeared to be more potent than diclofenac in inhibiting this process. Yet, it is worth

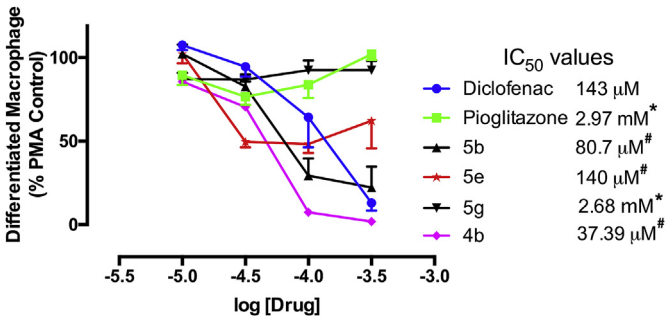

Fig. 6. Inhibition of monocyte to macrophage differentiation by diclofenac, pioglitazone, and the selected synthetic compounds. Results are represented as percentage macrophage metabolic activity of the PMA control at different exposure concentrations. IC_{50} values estimated by non-linear regression were compared using One-way ANOVA followed by Tukey Multiple Comparisons *post hoc* test. * denotes a P-value < 0.05 vs. diclofenac while # denotes a P-value < 0.05 vs. pioglitazone.

mentioning that this assay measures the differentiation of monocytes into adherent macrophages with no indication of potential differences in differential polarization, if any. Thus, a negative result might not completely rule out the beneficial effect of PPARγ agonistic activity represented by pioglitazone.

2.4.7. IL-1β and TNF-α expression and 20-HETE production assay

Previous literature consistently showed that 15-LOX activation is associated with increased cytokine production in variety of cell types [68–70]. Specifically, both the addition of 15-LOX arachidonate metabolites or their *de novo* synthesis in monocytes triggered cytokine production in macrophages, including tumor necrosis factor-α (TNF-α), interleukin-1β (IL-1β), IL-6, and monocyte chemo-attractant protein-1 [71]. Moreover, the produced IL-1β contributes to further stimulation of signaling pathways leading to

the enhancement of phospholipase A2-mediated arachidonate release and metabolism in a positive feedback loop [72]. We attempted to provide a pathophysiological context for the 15-LOX inhibitory action of our hybrid compounds. We examined the effect of the three compounds showing the highest activity against soybean LOX *in vitro* (**4b**, **5e** & **5g**) on TNF-α and IL-1β production in THP-1 monocytes differentiated into macrophages by PMA, and activated by a lipopolysaccharide (LPS) challenge. Compared to the negative control, LPS-treated macrophages showed massive increases in both TNF-α and IL-1β production Fig. 7A. The increase in both cytokines' expression was greatly attenuated in cells treated with our compounds. As well, we tested the effect of these compounds on the 20-hydroxyeicosatetraenoic acid (20-HETE) production in these cells as a general indicator of arachidonate metabolism. The concentration of 20-HETE produced in the conditioned medium of PMA-differentiated THP-1 monocytes that were challenged with LPS was measured by enzyme-linked immunosorbent assay (ELISA). 20-HETE production increased following LPS challenge compared to untreated controls. Cells treated with our compounds showed reduced 20-HETE production indicating a possible decrease in arachidonic acid release possibly as a result of the interruption of the IL-1β positive feedback loop (Fig. 7B).

2.4.8. *In vivo anti-inflammatory assay*

Formalin-induced rat paw edema protocol as an acute inflammation model was used to test the *in vivo* anti-inflammatory activity of the four most active compounds **(4b, 5b, 5e and 5g)**. Formalin was injected subcutaneously to induce inflammation and an oral dose of 5 mg/kg body weight of the test compounds was administered.

The potencies of the tested compounds relative to the negative control were identified by measuring the percentage inhibition of edema after 4 h. Celecoxib and diclofenac sodium were used as positive controls. Intriguingly, all tested compounds with the exception of **4b** showed equivalent inhibitory effect to celecoxib and diclofenac. Additionally**, 4b** demonstrated a statistically significant higher potency compared to celecoxib (Supplementary Information Table SM2 and Fig. 8).

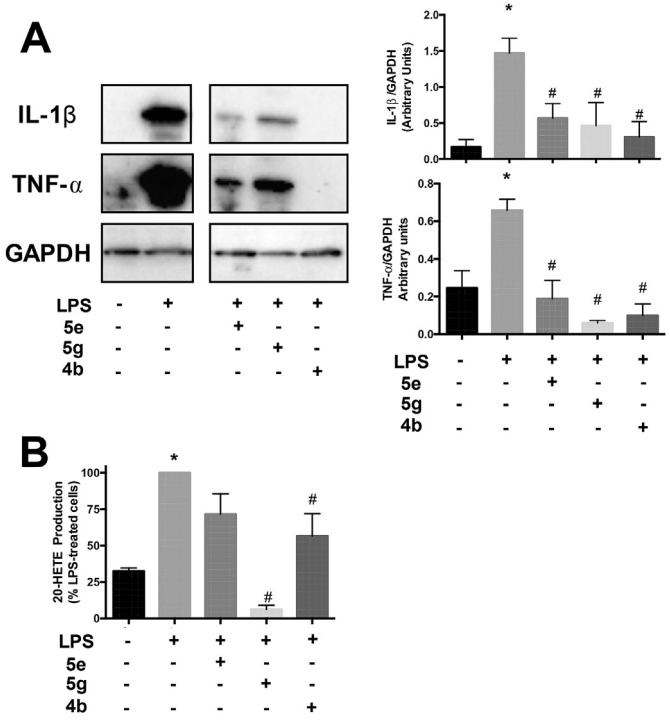

Fig. 7. The most potent 15-LOX inhibiting compounds reduce cytokine production and arachidonate metabolism in LPS-challenged PMA-differentiated THP-1 cells. A, representative western blotting of IL-1β, TNF-α, and GAPDH from THP-1 cells exposed to different treatment conditions. The bar graphs summarize the quantification of three separate experiments. B, 20-HETE concentration in the conditioned medium of THP-1 cells exposed to the indicated treatment conditions. Concentration is normalized to the values measured in untreated cells challenged with LPS. Statistical significance was measured by one-way ANOVA followed by Tukey Multiple Comparisons *post hoc* test. * denotes a P-value < 0.05 vs. untreated control while # denotes a P-value < 0.05 vs. LPS-challenged cells.

2.5. *Structure determination of compound 4b bound to PPARγ*

Recently, 5-ene rhodanine substructures have been stigmatized by some research groups and drug discovery programs as promiscuous hitters or pan assay interference (PAINS) elements [30]. However, the concept of PAINS is still controversial and, in many instances, contradicts the concept of privileged scaffolds [73,74]. Additionally, recent reports indicated that PAINS is highly structural context dependent [73]. Indeed, one of the most active compounds in this study (compound **4b**) carries the ene rhodanine substructure. Although the biological activity of **4b** was confirmed by multiple lines of evidences (molecular then cellular and finally *in vivo*), we wanted to rule out any skepticism about its proven biological activity and exclude the presence of any assay artifacts. Hence, we determined the X-ray crystal structure of compound **4b** in complex with the PPARγ ligand binding domain (LBD) which will give us the chance to probe its binding mode and detect specific binding interactions. Coordinates and structure factors were deposited in the Protein Data Bank under accession code 6E5A.

Experimental details can be found in the methods section, the crystallographic data table describing the data processing and refinement statistics can be found in the Supplementary Information Table SM3, and a stereo figure displaying the quality electron density around the ligands can be found in the Supplementary Information Figure SM2. Two subunits per asymmetric unit were found and both subunits were found bound to 4b in a similar manner. The overall fold of PPARγ was similar to most other observed structures, for example the **4b** bound structure displays an RMSD to the rivoglitazone bound structure (PDB:5U5L) of 0.48 Å (over 512 Cα atoms), signifying that the binding of compound **4b** does not induce major conformational changes as compared to other TZD based compounds. Compound **4b** is located

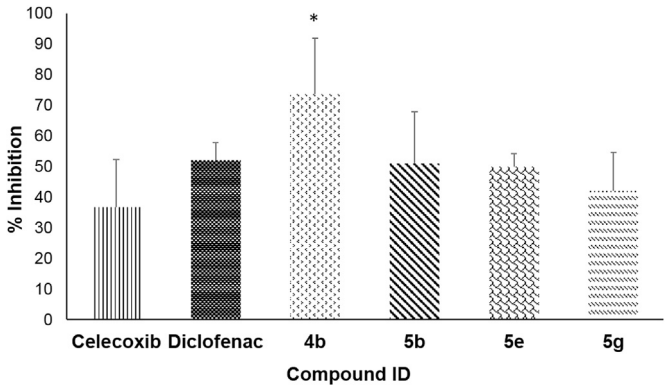

Fig. 8. Graphical representation of *in vivo* anti-inflammatory activities of selected compounds in formalin-induced rat paw edema bioassay (acute inflammation model). Results presented are Mean ± SD of four replicates. Statistical analysis was performed using One-way ANOVA followed by Tukey post hoc test. A P-value < 0.05 was considered significant. * denotes significance vs. celecoxib.

in the LBD with the ring systems of the compound located between H3 and the beta-sheet region and the carbon tail inserted into the hydrophobic patch below the AF2 region (Fig. 9A). **4b** makes only one hydrogen bond to PPARγ, via its non-protonated nitrogen atom to the protonated nitrogen backbone atom of Ser342 (3.0 Å). All other contacts are hydrophobic and Van der Waals interactions. The double ring system of compound **4b** sits between H3 and the beta sheet region making these contacts with Ile281 (H3), Ile341 side chain (beta-sheet), the non-polar portion of Ser342 side chain (beta-sheet), the non-polar portion of Arg288 side chain (H3), Leu353 side chain (H6), and the side chain of Met364 (H7). These interactions can be seen in Fig. 9B. The carbon tail of **4b** makes hydrophobic interactions with H6 and H7 which include those to the side chain of Met364, the side chain of Phe363 (H7), the side chain of Phe360 (H7), and the side chain of Leu353 (H6) as shown in Fig. 9C. Given that we also produced a docked structure of **4b** bound to PPARγ that was in excellent agreement with our X-ray crystal structure, we hypothesized that further structural analysis of the other compounds could be carried out using docking techniques.

2.6. Molecular modeling

2.6.1. Docking of compounds 4b, 5b, 5g and 5e into COX-2 active site

The screening performance of COX-2 DEKOIS 2.0 benchmark set showed a good and non-random result with three docking tools (e.g., GOLD [ChemPLP], Glide [SP] and AutoDock Vina) [42]. Hence, we employed GOLD (ChemPLP) as scoring function for pose prediction purposes using PDB code of 1CX2 crystal structure for COX-2 docking. It has been reported that variation in molecular weight can cause obvious bias in docking performance especially when employing empirical scoring functions, since heavier molecules tend to produce superior scores [75,76]. Minimizing such bias would be of benefit in the context of correlating the docking scores of compounds with their biological *in vitro* activity values.

Due to variability in molecular weights of the test compounds and in order to eliminate this bias, score normalization strategy was applied by dividing the docking score by the number of heavy atoms (N) using different arithmetic weights (e.g., square root of N ($N^{1/2}$), cube root of N ($N^{1/3}$) and cube root of the squared N ($N^{2/3}$)) [77]. To select the most suitable normalization strategy, we evaluated the docking screening performance employing such strategies using COX-2 DEKOIS 2.0 benchmark set, and visualized the results using "pROC-Chemotype" plots (Supplementary information Figures SM3-7). Besides, employing benchmarking would enable the effective detection of active ligands in a pool of their false positive decoys.

Since the screening performance results (based on pROC-AUC metric) were in the following order: $N^{1/3} > N^{1/2} > N^{2/3} >$ original score $> N$ (Supplementary information Figures SM3-7). Therefore, we employed ($N^{1/3}$) normalization scheme for our docking investigation on COX-2. We also used the same normalization scheme ($N^{1/3}$) for LOX docking experiments.

Interestingly, celecoxib and indomethacin displayed the highest and lowest docking scores with the synthesized compounds in-between, in both normalized and non-normalized panels. This correlates clearly with their *in vitro* activity against recombinant COX-2 enzyme, as seen in Supplementary information Figures SM8.

The normalized docking performance of all compounds seems to be comparable based on their mean values and standard deviation ranges, as shown in Figure SM8B. Interestingly, regarding the non-normalized docking fitness, the difference between the heaviest compound **6j** and the lightest one **4b** appeared to be significant since **4b** lies out of the standard deviation range of **6j** (Figure SM8A). However, after employing $N^{1/3}$ normalization, both **6j** and **4b** appeared comparable (Figure SM8B) which appeared to agree with their actual biological activities.

Additionally, docking of the compounds in the active sites of both COX-1 and COX-2 enzymes showed preference for COX-2 over COX-1. This was not surprising since the average molecular weights range of our compounds is 446.6 ± 64.5 which is higher than average range of the diverse and representative COX-1 and COX-2 ligands reported in DEKOIS 2.0 benchmark sets (the average molecular weight of COX-1 and COX-2 in DEKOIS 2.0 benchmark set are 333.8 [± 62.97] and 373.6 [± 50.65], respectively) [42]. As well, it is well-recognized that COX-2 binding site is topologically larger than that of COX-1 and hence accommodates heavier ligands [78].

Since compounds **4b**, **5b**, **5e** and **5g** showed the highest activities in COX-2 and LOX binding assays as well as PPARγ translocation and functional reporter gene assays, we will focus on rationalizing their pose interactions in the binding sites of these targets.

The postulated binding pose of **4b** demonstrated hydrophobic and polar contacts, comprised by its phenoxy propargyl and rhodanine moieties, respectively (Fig. 10A). The propargyl tail appeared to be packed deeply in the binding cleft formed by the side chains of Leu359, Val116, Ile345 and Arg120. Such interaction pattern resembled the favored hydrophobic contacts of the trifluoromethyl group of the co-crystallized selective COX-2 inhibitor (SC-558), albeit, with a deeper filling of the propargyl group towards the hydrophobic cleft aligned by Leu531.

The phenoxy group showed hydrophobic contacts with Tyr355 and Ala577. On the other hand, the rhodanine moiety appeared to act as a H-bonding donor to His90 via the imide group and reaches a favorable hydrophobic contact with the side chain of Ile517 via the thione group. This directed the rhodanine moiety towards the polar region of the binding site and overlaying on the sulfonamide group of SC-558.

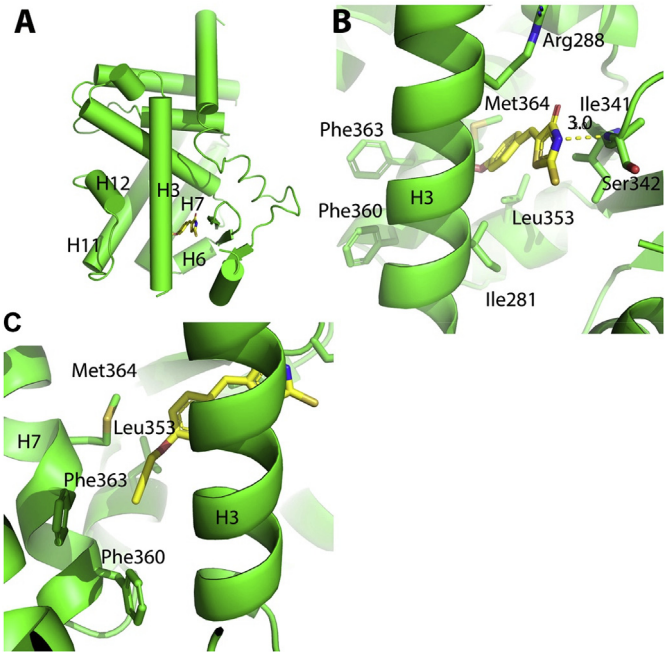

Fig. 9. Binding mode of 4b to PPARγ as determined by X-ray crystallography (PDB accession code 6E5A). PPARγ is shown in green ribbons, compound **4b** is shown in yellow sticks, and residues of PPARγ within 3.5 Å of the ligand are depicted as green sticks. **A)** Overview of the entire PPARγ LBD bound to **4b**. **B)** Interactions of **4b** with the beta-sheet and H3 region. **C)** Interactions of the carbon tail of **4b** with residues of the hydrophobic pocket formed by H7, and H3. (For interpretation of the references to color in this figure legend, the reader is referred to the Web version of this article.)

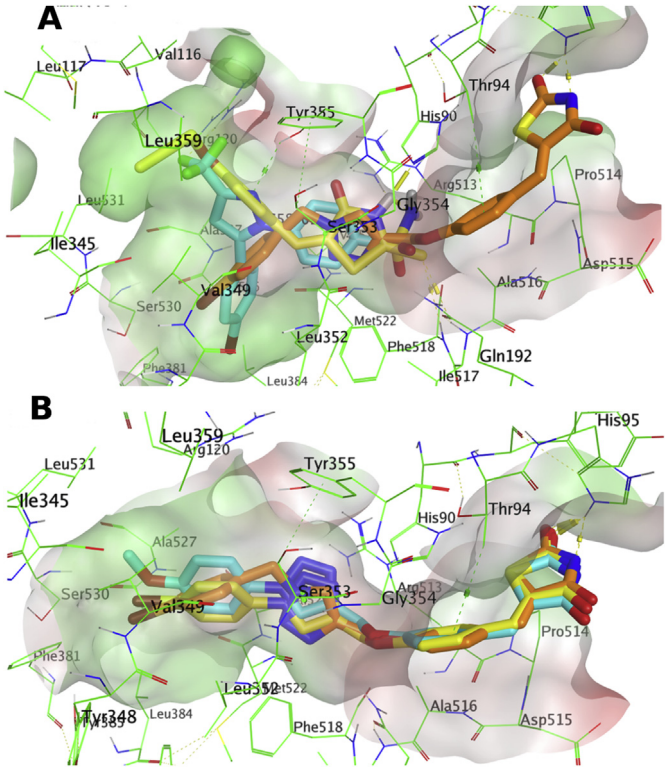

Fig. 10. **(A)** Overlay of the docking poses of **4b** (yellow sticks), the co-crystallized ligand (cyan sticks) and **5b** (orange sticks) in the binding site of COX-2 (PDB: 1cx2). **(B)** Overlay of the docking poses of **5b** (orange sticks), **5g** (cyan sticks) and **5e** (yellow sticks) in the binding site of COX-2 (PDB: 1cx2). Polar and non-polar regions of the binding site were presented by red and green colored molecular surface, respectively. Dashed lines indicate favorable interactions. Non-polar hydrogen atoms were omitted for clarity. (For interpretation of the references to color in this figure legend, the reader is referred to the Web version of this article.)

The docking poses of **5b**, **5g** and **5e** showed comparable types of interactions in the binding site of COX-2 (Fig. 10B). Their thiazolidinedionyl moieties acted as H-bonding acceptor for the side chain of His95 via the deprotonated imide and the carbonyl group at position number two in the ring.

Also, their aromatic phenoxy moieties appeared to demonstrate favorable hydrophobic interactions with the side chains of Thr94 and Ala516. Their triazolyl groups were packed between Ser353 and Val523. The lipophilic tail comprised terminal *p*-bromobenzyl, phenoxyphenyl and bromophenyl groups for **5b**, **5g** and **5e**, respectively, filled the hydrophobic region of the binding site and packed between the side chains of Val349, Leu352 and Ala527.

Generally, these postulated binding interactions of **4b** pose are obviously different than that of its congeneric analogues **5b**, **5g** and **5e**, where the latter poses showed superior scores due to more interactions and better pose accommodations. This observation is attributable to the fact that **4b** has dissimilar topological features (e.g., molecular weight and size) compared to the aforementioned 3 compounds. In addition, the large size of COX-2 binding site can accommodate different poses of a ligand.

2.6.2. Docking of compounds 4b, 5b, 5g and 5e into 15-LOX active site

Again, the original docking fitness showed obvious fluctuations especially for the reference compounds NDGA and quercetin, and **4b**. Interestingly, when employing score normalization by ($N^{1/3}$), the docking fitness distribution appeared to be more homogenous, as seen in Supplementary information Figures SM9. This correlates better with the biological activity since almost all the compounds – including the reference compounds - lay within the same activity ranges.

The postulated binding pose of **4b** demonstrated mainly hydrophobic contacts in the binding site of 15-LOX (Fig. 11A). The rhodanine moiety is packed between Gln590, Glu357, Ile418 and Ile593, Phe353. Also a postulated H-bonding interaction between the carbonyl group of the ring with Gln548 can be observed. The hydrophobic tail of **4b** comprising the phenoxy and propargyl groups packed between the backbone of Glu357, His361, His366, Asn401 and the side chain of Ile400.

Again, the postulated binding poses of **5b**, **5g** and **5e** showed comparable types of interactions in the binding site of 15-LOX mostly by hydrophobic and Van der Waal types of interactions (Fig. 11B). However, their thiazolidinedione moieties acted as H-bonding acceptor for the amidic backbone of Val594 via the carbonyl group at position two in the ring. Their aromatic phenoxy moieties packed between the hydrophobic side chains of Val409, Leu362, Leu358 and Phe415 indicating favorable hydrophobic interactions. Furthermore, their triazolyl groups filled the space formed by the side chain of Ile400, Leu408 and Leu597. The lipophilic terminals of *p*-bromobenzyl, phenoxyphenyl and bromophenyl groups for **5b**, **5g** and **5e**, respectively, packed between the side chains of Leu597, Phe175, Ileu414 and the backbone of Ala404 and Arg403; nevertheless, the bromo and methoxy groups appeared to be solvent exposed. No metal chelation was observed

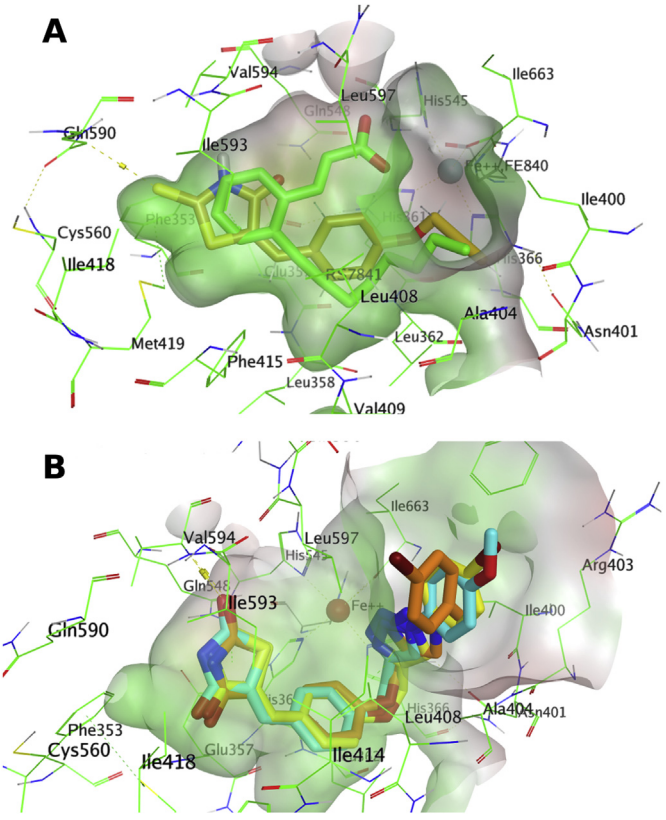

Fig. 11. (**A**) Overlay of the docking poses of 4b (gold sticks) and the co-crystallized ligand (green sticks) in the binding site of 15-LOX (PDB: 1lox). **(B)** Overlay of the docking poses of 5b (orange sticks), 5g (cyan sticks) and 5e (yellow sticks) in the binding site of 15-LOX (PDB: 1lox). Polar and non-polar regions of the binding site were presented by red and green colored molecular surface, respectively. Dashed lines indicate favorable interactions. Non-polar hydrogen atoms were omitted for clarity. (For interpretation of the references to color in this figure legend, the reader is referred to the Web version of this article.)

for postulated binding poses of **4b**, **5b**, **5g** and **5e**.

2.7. In silico prediction of physicochemical properties, drug-likeness, pharmacokinetic profile and ligand efficiency metrics

In the present work, physicochemical and pharmacokinetic parameters of the most active compounds **4b**, **5b**, **5e** and **5g** were calculated using Molinspiration [79], Molsoft [80], Pre-ADMET [81] and Data warrior [82] software.

Results presented in Supplementary Information Table SM4 showed that the four compounds obeyed Lipinski's rule, with LogP values between 2.04 and 3.69 (<5), MW ranging between 275 and 471 (<500) together with number of HBA and HBD of 3–8 (<10) and 1 (<5), respectively. Hence, these compounds should not demonstrate a problem regarding oral absorption. Moreover, the compounds showed NROTB values of 3–6 (<10) and TPSA values of 42.10–99.12 $Å^2$ (<140 $Å^2$), indicating their potential to be transported through biological membranes.

Molsoft software was used to calculate the solubility and drug-likeness model score. Although, the drug-likeness predicted values for the test compounds ranged between −0.73 and −0.1, yet they passed the solubility cut-off limit with values of 0.03–0.98 mg/L (more than 0.0001 mg/L). Since aqueous solubility is known to influence both absorption and distribution characteristics remarkably, we predict that these compounds can behave as drug-like.

Furthermore, *in silico* prediction of the pharmacokinetic parameters was carried out using Pre-ADMET software. Results of the predicted ADME parameters are recorded in Table SM4. Medium cell permeability in the Caco-2 cell model was predicted for the four compounds with values between 12.86 and 40.82 nm/s. They also can be regarded as well-absorbed molecules due to high human intestinal absorption values (around 97%). Moreover, they showed low BBB penetrability (0.03–0.1) and high binding ability to human plasma proteins (91.83–100%). As well, they were non-inhibitors of CYP2D6 enzyme and thus interactions with CYP2D6 inducers and/or inhibitors should not present a problem.

Endeavors to incorporate physicochemical properties (i.e. molecular weight, polar surface area, lipophilicity and others), together with potency into a quantitative and numerical framework have recently materialized into ligand efficiency indices. These are composite and easy-to-follow prognosticators that were formulated to help increase the robustness of the drug discovery process and provide more favorable outcomes. They blend potency, lipophilicity and heavy atom count, thus guiding the lead optimization process along the preclinical drug discovery path [83].

Hence, prospective assessment of the quality of the most active compounds as potential hits or leads was achieved by application of these metrics, namely; Ligand efficiency (LE), lipophilic ligand efficiency (LLE) and ligand efficiency-dependent lipophilicity index (LELP) using Data warrior software.

LE is a link between drug potency and its molecular size in the form of heavy (non-hydrogen) atom count. Regarding both COX-2 and 15-LOX inhibitory activities, LE values of the four compounds ranged from 0.25 to 0.53 which adhere to the accepted minimum LE for lead compounds (in the range of 0.3) or > 0.3 for drug candidates [84,85].

LLE correlates potency to lipophilicity. With the exception of **5b** and **5e** anti-LOX activity (LLE = 2.55 and 2.94, respectively), LLE values for both enzymatic inhibitory activities, shown in Table SM4, ranged from 3.86 to 5.82, which comply with the optimum cut-off values for lead compounds (≥3) or drug candidates (≥5) [85].

LELP is considered as a combined scoring function and hence with greater predictive power as it relates both molecular size and lipophilicity to potency. In addition, unlike LE and LLE, LELP has been reported to have the ability to differentiate between marketed drugs and unsuccessful leads not to mention its high correlation with pharmacokinetic profile and safety [86].

Interestingly, both COX and LOX inhibition afforded LELP values that fulfilled the accepted limits for leads (≤7.5) or marketed drugs (<10) since their values ranged from 2.09 to 9.23 [85]. This is in contrast to **5b**, which showed LELP value of 10.84 for LOX inhibition, which slightly deviated from the value reported for drug candidates.

Enlightened by the aforementioned drug-likeness, ADME and ligand efficiency predictions, these compounds demonstrated their appropriateness for further lead optimization studies.

3. Conclusion

In this study, for the first time, we have described the design of novel triazolyl-thiazolidinedione/rhodanine hybrids as potential simultaneous COX-2/LOX inhibitors and PPARγ partial agonists. We challenged our design with pre-synthetic docking experiments on PPARγ using three docking software, which showed encouraging docking scores, interactions with key amino acids and comparable orientation of the docked compounds with respect to the co-crystallized ligand rosiglitazone. Most of the synthesized hybrids showed micromolar inhibitory activities towards COX-2 and 15-LOX in *in vitro* assays. *In vitro* glucose uptake assay identified compounds **4b**, **5e** as stronger glucose uptake inducers than pioglitazone in the presence and absence of insulin, and compounds **5b**, **5g** as equal or higher glucose uptake inducers in an insulin-independent fashion, which raises the possibility of selective targeting of PPARγ signaling pathways. Immunohistochemical analysis of ligand-stimulated PPARγ nuclear localization confirmed the ability of compounds **4b**, **5b**, **5e** and **5g** to induce PPARγ nuclear translocation, similar to pioglitazone. Moreover, PPARγ functional reporter gene assay confirmed the partial agonistic activity of the latter 4 compounds towards PPARγ. The same 4 compounds were capable to inhibit monocyte to macrophage differentiation, which is a pivotal and early step in inflammatory response. As expected, the most potent 15-LOX inhibitors **4b**, **5e** & **5g** reduced inflammatory cytokine production and arachidonate metabolism in human macrophage model challenged by LPS. Over and above, compound **4b** demonstrated a statistically significant higher potency compared to celecoxib in formalin-induced rat paw edema assay. While, compounds **5b, 5e and 5g** showed equivalent inhibitory effect to the reference drugs. X-ray crystallography of compound **4b** with PPARγ showed its binding outside AF2 part of LBD, which is the part responsible for the full activation of PPARγ and hence complete recruitment of downstream signaling molecules. Instead, it managed to pursue other hydrophobic interactions with residues in H3, H6 and H7 parts of LBD via its phenyl ring and propargyl tail. Also, a key hydrogen bonding interaction with Ser342 in beta sheet was observed. We believe that the presence of only one carbonyl group in rhodanine part of **4b** probably changed its ability to bind to AF2 and hence might be partly responsible for its partial agonistic activity. Another part of the partial agonistic activity could be attributed to the hydrophobic interactions, especially those of the propargylic tail. Molecular docking experiments of compounds **4b**, **5b**, **5e** and **5g** on COX-2 and 15-LOX showed perfect fitting in the binding pocket and noticeable interactions with key amino acids. The docking scores after appropriate normalization correlated successfully with the *in vitro* biological data. Appropriate normalization was granted by using COX-2 DEKOIS 2 benchmark set. Moreover, drug-likeness assessment via Molinspiration, Molsoft, Pre-ADMET and Data warrior software elucidated their full compliance with Lipinski's rule, favorable physicochemical properties and convenient predicted pharmacokinetic parameters. Over and above, ligand efficiency metrics for

compounds **4b**, **5b** and **5e** were calculated and they indicated that these 3 compounds represent promising hits/leads to pursue as potential simultaneous COX-2/LOX inhibitors and PPARγ partial agonists for management of inflammatory disorders. We think that compounds **4b**, **5b** and **5e** will be insightful additions to the contemporary drug design programs directed towards inflammatory disorders with potential links to metabolic diseases.

4. Experimental

4.1. Chemistry

All chemicals were purchased from commercial suppliers and used without further purification. Melting points were recorded on electrotherm capillary tube Stuart melting point apparatus SMP10 and are all uncorrected. Follow up of the reactions' rates were performed by thin-layer chromatography (TLC) on silica gel-precoated aluminum sheets (Type 60 GF254; Merck; Germany) and the spots were visualized by exposure to iodine vapors or UV-lamp at λ 254 nm for few seconds. Infrared spectra (IR) were recorded using KBr discs on a Shimadzu IR 435 spectrophotometer, Faculty of Pharmacy, Cairo University. Nuclear magnetic resonance (^{1}H NMR and ^{13}C NMR) spectra were recorded on a Jeol spectrometer (500 MHz) at the Microanalytical Unit, Faculty of Science, University of Alexandria or on a Bruker (400 MHz) spectrophotometer, Faculty of Pharmacy, Cairo University using deuterated Dimethylsulfoxide (DMSO-d_6) as solvent. The data were recorded as chemical shifts expressed in δ (ppm) relative to Tetramethylsilane (TMS) as internal standard. Signal splitting are expressed by the following abbreviations: s = singlet, d = doublet, t = triplet, q = quartet and m = multiplet. The purity of the new compounds was checked by elemental analyses (C, H, N and S), conducted on FLASH 2000 CHNS/O analyzer, Thermo Scientific at the regional center for mycology and biotechnology (RCMB), Al-Azhar University. In addition, new compounds were found to be ≥ 95% pure by reversed phase HPLC analysis using Agilent 1260 infinity HPLC equipped with G1311B Quaternary pump, G1329 injector and G 1315D DAD Vl detector. A G1316A C18 column (4.6 × 150 mm) was used. An injection volume of 0.5 ml (DMF and phosphate buffer pH 5 1:1), a flow rate of 1 ml/min and an isocratic elution of acetonitrile in water (1:1) were applied. Analyses were monitored at 254 nm wavelength. The preparation of appropriate azides [87,88], propargyl derivative **2** [89] and aldehydes **3(a–h)** [90] were performed according to reported procedures.

4.1.1. Knoevenagel condensation procedure for compounds 4(a,b), 5(a-h) and 6(a-h)

A mixture of the appropriate aldehyde (**2** or **3** (**a-h**)) and thiazolidine-2,4-dione/rhodanine (1mmole) with catalytic quantity of piperidine (10 mol%) in absolute ethanol was refluxed for 12 h. After cooling to room temperature overnight, the precipitated compound was filtered, washed with ice-cooled ethanol and dried. The solid was crystallized from ethanol or ethanol/DMF to obtain the appropriate solid products.

*4.1.1.1. (Z)-5-(4-(prop-2-yn-1-yloxy)benzylidene)thiazolidine-2,4-dione **(4a)**.* Yield 74%. m.p. 216–218 °C. ^{1}H NMR (400 MHz, DMSO-d_6): δ 12.51 (s, 1H, NH, D_2O exchangeable), 7.73 (s, 1H, benzylidene-CH), 7.55 (d, J = 8.84 Hz, 2H, benzylidene- $C_{2,6}$-H), 7.13 (d, J = 8.84 Hz, 2H, benzylidene- $C_{3,5}$-H), 4.88 (d, J = 2.32 Hz, 2H, OCH_2), 3.61 (t, J = 2.32 Hz, 1H, C≡CH). ^{13}C NMR (100 MHz, DMSO-d_6): δ 168.4, 167.9, 159.3, 132.4, 132.1, 126.6, 121.3, 116.1, 79.2, 79.1, 56.2. IR (KBr): cm^{-1} 3275.13 (C≡CH), 3097.68 (NH), 2376.30-2322.29 (C≡C), 1732.08 (C=O), 1678.07 (amide C=O), 1639.49 (C=N), 1589.34 (C=C), 1257.59 and 1022.27 (C–O–C), (C–S–C). Anal. Calcd (%) for $C_{13}H_9NO_3S$ (259.28): C, 60.22; H, 3.50; N, 5.40; S, 12.37. Found C, 60.48; H, 3.64; N, 5.61; S, 12.52. HPLC/DAD: Retention time 4.93 min.

*4.1.1.2. (Z)-5-(4-(prop-2-yn-1-yloxy)benzylidene)-2-thioxothiazolidin-4-one **(4b)**.* Yield 69%. m.p. 226–228 °C. ^{1}H NMR (400 MHz, DMSO-d_6): δ 13.76 (s, 1H, NH, D_2O exchangeable), 7.60 (s, 1H, benzylidene-CH), 7.57 (d, J = 8.84 Hz, 2H, benzylidene- $C_{2,6}$-H), 7.15 (d, J = 8.84 Hz, 2H, benzylidene- $C_{3,5}$-H), 4.90 (d, J = 2.32 Hz, 2H, OCH_2), 3.63 (t, J = 2.32 Hz, 1H, C≡CH). ^{13}C NMR (100 MHz, DMSO-d_6): δ 196.1, 170.2, 159.6, 133.0, 132.0, 126.7, 123.4, 116.3, 79.2, 79.1, 56.2. IR (KBr): cm^{-1} 3255.84 (C≡CH), 3001.24 (NH), 2376.30-2322.29 (C≡C), 1685.79 (amide C=O), 1640 (C=N), 1581.63 (C=C), 1246.02 and 1068.56 (C–O–C), (C–S–C). Anal. Calcd (%) for $C_{13}H_9NO_2S_2$ (275.34): C, 56.71; H, 3.29; N, 5.09; S, 23.29. Found C, 57.04; H, 3.18; N, 5.37; S, 23.44. HPLC/DAD: Retention time 9.5 min.

*4.1.1.3. (Z)-5-(4-((1-benzyl-1H-1,2,3-triazol-4-yl)methoxy)benzylidene)thiazolidine-2,4-dione **(5a)**.* Yield 83%. m.p. 178–180 °C. ^{1}H NMR (500 MHz, DMSO-d_6): δ 12.49 (s, 1H, NH, D_2O exchangeable), 8.29 (s, 1H, triazole-C_5–H), 7.73 (s, 1H, benzylidene-CH),7.53 (d, J = 8.4 Hz, 2H, benzylidene-$C_{2,6}$-H), 7.37-7.28 (m, 5H, phenyl-$C_{1,2,3,4,5}$-H), 7.17 (d, J = 8.4 Hz, 2H, benzylidene- $C_{3,5}$-H), 5.59 (s, 2H, NCH_2), 5.20 (s, 2H, OCH_2). ^{13}C NMR (125 MHz, DMSO-d_6): δ 160.2, 143.0, 132.6, 126.4, 121.1, 116.2, 61.9, 53.4. IR (KBr): cm^{-1} 3140.11 (NH), 1743.65 (C=O), 1678.07 (amide C=O), 1635 (C=N), 1597.06 (C=C), 1249.87 and 1040 (C–O–C), (C–S–C). Anal. Calcd (%) for $C_{20}H_{16}N_4O_3S$ (392.43): C, 61.21; H, 4.11; N, 14.28; S, 8.17. Found C, 61.47; H, 4.24; N, 14.59; S, 8.24. HPLC/DAD: Retention time 4.29 min.

*4.1.1.4. (Z)-5-(4-((1-(4-bromobenzyl)-1H-1,2,3-triazol-4-yl)methoxy)benzylidene) thiazolidine-2,4-dione **(5b)**.* Yield 86%. m.p. 182–184 °C. ^{1}H NMR (500 MHz, DMSO-d_6): δ 12.45 (s, 1H, NH, D_2O exchangeable), 8.29 (s, 1H, triazole-C_5–H), 7.73 (s, 1H, benzylidene-CH), 7.37-7.28 (m, 4H, 4-bromophenyl-$C_{2,6}$-H and benzylidene-$C_{3,5}$-H), 7.24 (d, J = 8.4 Hz, 2H, benzylidene-$C_{2,6}$-H), 7.17 (d, J = 8.4 Hz, 2H, 4-bromophenyl- $C_{3,5}$-H), 5.58 (s, 2H, NCH_2), 5.20 (s, 2H, OCH_2). ^{13}C NMR (125 MHz, DMSO-d_6): δ 168.5, 168.1, 160.2, 143.1, 132.6, 126.4, 122.0, 116.2, 61.8, 52.6. IR (KBr): cm^{-1} 3136.25 (NH), 1735.93 (C=O), 1685.79 (amide C=O), 1635 (C=N), 1585.49 (C=C), 1257.59 and 1053.13 (C–O–C), (C–S–C). Anal. Calcd (%) for $C_{20}H_{15}BrN_4O_3S$ (471.33): C, 50.97; H, 3.21; N, 11.89; S, 6.80. Found C, 51.24; H, 3.39; N, 11.75; S, 6.71. HPLC/DAD: Retention time 7.83 min.

*4.1.1.5. (Z)-5-(4-((1-phenyl-1H-1,2,3-triazol-4-yl)methoxy)benzylidene)thiazolidine-2,4-dione **(5c)**.* Yield 85%. m.p. 262–264 °C. ^{1}H NMR (400 MHz, DMSO-d_6): δ 12.53 (s, 1H, NH, D_2O exchangeable), 8.99 (s, 1H, triazole-C_5–H), 7.92 (d, J = 7.8 Hz, 2H, phenyl-$C_{2,6}$-H), 7.77 (s, 1H, benzylidene-CH), 7.49–7.64 (m, 5H, benzylidene- $C_{2,6}$-H and phenyl-$C_{3,4,5}$-H), 7.26 (d, J = 8.72 Hz, 2H, benzylidene- $C_{3,5}$-H), 5.34 (s, 2H, OCH_2). ^{13}C NMR (100 MHz, DMSO-d_6): δ 168.5, 160.1, 143.9, 137.0, 132.6, 132.2, 130.4, 129.3, 126.5, 123.6, 120.7, 116.1, 61.7. IR (KBr): cm^{-1} 3151.69 (NH), 1739.79 (C=O), 1693.50 (amide C=O), 1640 (C=N), 1597.06 (C=C), 1253.73 and 1053.13 (C–O–C), (C–S–C). Anal. Calcd (%) for $C_{19}H_{14}N_4O_3S$ (378.41): C, 60.31; H, 3.73; N, 14.81; S, 8.47. Found C, 59.96; H, 3.88; N, 15.07; S, 8.65. HPLC/DAD: Retention time 5.99 min.

*4.1.1.6. (Z)-5-(4-((1-(4-chlorophenyl)-1H-1,2,3-triazol-4-yl)methoxy)benzylidene) thiazolidine-2,4-dione **(5d)**.* Yield 80%. m.p. 243–245 °C. ^{1}H NMR (400 MHz, DMSO-d_6): δ 12.54 (s, 1H, NH, D_2O exchangeable), 9.02 (s, 1H, triazole-C_5–H), 7.26–7.97 (m, 9H, 4-chlorophenyl-$C_{2,3,5,6}$-H, benzylidene- $C_{2,3,5,6}$-H and benzylidene-CH), 5.35 (s, 2H, OCH_2). ^{13}C NMR (100 MHz, DMSO-d_6): δ 168.5,

160.1, 144.0, 135.8, 133.6, 132.6, 132.2, 130.3, 126.5, 123.6, 122.3, 116.1, 61.7. IR (KBr): cm^{-1} 3159.40 (NH), 1732.08 (C=O), 1693.5 (amide C=O), 1640 (C=N), 1589.34 (C=C), 1265.30 and 1033.85 (C–O–C), (C–S–C). Anal. Calcd (%) for $C_{19}H_{13}ClN_4O_3S$ (412.85): C, 55.28; H, 3.17; N, 13.57; S, 7.77. Found C, 55.60; H, 3.08; N, 13.81; S, 7.59. HPLC/DAD: Retention time 10.51 min.

4.1.1.7. (Z)-5-(4-((1-(4-bromophenyl)-1H-1,2,3-triazol-4-yl) methoxy)benzylidene)thiazolidine-2,4-dione ***(5e)****.* Yield 88%. m.p. 143–145 °C. ^{1}H NMR (400 MHz, DMSO-d_6): δ 12.52 (s, 1H, NH, D_2O exchangeable), 8.99 (s, 1H, triazole-C_5–H), 7.88 (d, J = 8.72 Hz, 2H, 4-bromophenyl-$C_{3,5}$-H), 7.78 (d, J = 8.72 Hz, 2H, 4-bromophenyl-$C_{2,6}$-H), 7.75 (s, 1H, benzylidene-CH), 7.56 (d, J = 8.56 Hz, 2H, benzylidene- $C_{2,6}$-H), 7.23 (d, J = 8.56 Hz, 2H, benzylidene- $C_{3,5}$-H), 5.33 (s, 2H, OCH_2). ^{13}C NMR (100 MHz, DMSO-d_6): δ 168.5, 160.1, 144.1, 136.2, 133.2, 132.6, 132.2, 126.5, 123.5, 122.5, 121.9, 116.1, 61.7. IR (KBr): cm^{-1} 3143.97 (NH), 1728.22 (C=O), 1670.35 (amide C=O), 1640 (C=N), 1585.49 (C=C), 1253.73 and 1072.42 (C–O–C), (C–S–C). Anal. Calcd (%) for $C_{19}H_{13}BrN_4O_3S$ (457.30): C, 49.90; H, 2.87; N, 12.25; S, 7.01. Found C, 49.76; H, 2.91; N, 12.47; S, 7.14. HPLC/DAD: Retention time 11.90 min.

4.1.1.8. (Z)-5-(4-((1-(p-tolyl)-1H-1,2,3-triazol-4-yl)methoxy)benzylidene)thiazolidine-2,4-dione ***(5f)****.* Yield 90%. m.p. 248–250 °C. ^{1}H NMR (400 MHz, DMSO-d_6): δ 12.55 (s, 1H, NH, D_2O exchangeable), 8.92 (s, 1H, triazole-C_5–H), 7.25–7.78 (m, 9H, *p*-tolyl –$C_{2,3,5,6}$-H, benzylidene- $C_{2,3,5,6}$-H and benzylidene-CH), 5.32 (s, 2H, OCH_2), 2.38 (s, 3H, CH_3). ^{13}C NMR (100 MHz, DMSO-d_6): δ 168.5, 168.0, 160.1, 143.7, 138.9, 134.8, 132.5, 132.1, 130.7, 126.4, 123.4, 121.2, 120.5, 116.1, 61.7, 21.0. IR (KBr): cm^{-1} 3147.83 (NH), 1724.36 (C=O), 1666.50 (amide C=O), 1630 (C=N), 1589.34 (C=C), 1253.73 and 1026.13 (C–O–C), (C–S–C). Anal. Calcd (%) for $C_{20}H_{16}$ N_4O_3S (392.43): C, 61.21; H, 4.11; N, 14.28; S, 8.17. Found C, 61.48; H, 4.24; N, 14.70; S, 8.34. HPLC/DAD: Retention time 8.78 min.

4.1.1.9. (Z)-5-(4-((1-(4-methoxyphenyl)-1H-1,2,3-triazol-4-yl) methoxy)benzylidene) thiazolidine –2,4-dione ***(5g)****.* Yield 86%. m.p. 248–250 °C. ^{1}H NMR (400 MHz, DMSO-d_6): δ 12.39 (s, 1H, NH, D_2O exchangeable), 8.87 (s, 1H, triazole-C_5–H), 7.82 (d, J = 5.6, 2H, benzylidene- $C_{2,6}$-H), 7.76 (s, 1H, benzylidene-CH), 7.58 (d, J = 5.28 Hz, 2H, 4-methoxyphenyl- $C_{2,6}$-H), 7.26 (d, J = 5.28 Hz, 2H, 4-methoxyphenyl- $C_{3,5}$-H), 7.14 (d, J = 5.6 Hz, 2H, benzylidene- $C_{3,5}$-H), 5.32 (s, 2H, OCH_2), 3.84 (s, 3H, OCH_3). ^{13}C NMR (100 MHz, DMSO-d_6): δ 168.6, 168.4, 160.1, 159.8, 143.6, 132.5, 131.9, 130.4, 126.5, 123.5, 122.3, 121.4, 116.1, 115.4, 61.8, 56.0. IR (KBr): cm^{-1} 3116.97 (NH), 1739.79 (C=O), 1685.79 (amide C=O), 1635 (C=N), 1589.34 (C=C), 1249.87 and 1022 (C–O–C), (C–S–C). Anal. Calcd (%) for $C_{20}H_{16}N_4O_4S$ (408.43): C, 58.82; H, 3.95; N, 13.72; S, 7.85. Found C, 59.05; H, 4.02; N, 14.07; S, 7.59. HPLC/DAD: Retention time 6.00 min.

4.1.1.10. (Z)-4-(4-((4-((2,4-dioxothiazolidin-5-ylidene)methyl)phenoxy)methyl)-1H-1,2,3-triazol-1-yl)benzoic acid ***(5h)****.* Yield 82%. m.p. >300 °C. ^{1}H NMR (400 MHz, DMSO-d_6): δ 13.28 (s, 1H, COOH, D_2O exchangeable), 12.59 (s, 1H, NH, D_2O exchangeable), 9.15 (s, 1H, triazole-C_5–H), 8.20 (d, J = 8.6 Hz, 2H, 4-carboxyphenyl-$C_{3,5}$-H), 8.13 (d, J = 8.6 Hz, 2H, 4-carboxyphenyl- $C_{2,6}$-H), 7.82 (s, 1H, benzylidene-CH), 7.64 (d, J = 8.68 Hz, 2H, benzylidene- $C_{2,6}$-H), 7.30 (d, J = 8.68 Hz, 2H, benzylidene-$C_{3,5}$-H), 5.41 (s, 2H, OCH_2). ^{13}C NMR (100 MHz, DMSO-d_6): δ 168.4, 167.9, 166.8, 160.1, 144.2, 139.9, 132.6, 132.2, 131.6, 131.2, 126.4, 123.7, 121.1, 120.4, 116.1, 61.7. IR (KBr): cm^{-1} 3367.71-2962.66 (OH), 3143.97 (NH), 1739.79 (C=O), 1670.35 (amide C=O), 1610 (C=N), 1589.34 (C=C), 1253.73 and 1026.13 (C–O–C), (C–S–C). Anal. Calcd (%) for $C_{20}H_{14}$ N_4O_5S (422.42): C, 56.87; H, 3.34; N, 13.26; S, 7.59. Found C, 57.21; H, 3.50; N, 12.98; S, 7.81. HPLC/DAD: Retention time 2.67 min.

4.1.1.11. (Z)-5-(4-((1-benzyl-1H-1,2,3-triazol-4-yl)methoxy)benzylidene)-2-thioxothiazolidin-4-one ***(6a)****.* Yield 80%. m.p. 186–188 °C. ^{1}H NMR (400 MHz, DMSO-d_6): δ 13.75 (s, 1H, NH, D_2O exchangeable), 8.32 (s, 1H, triazole-C_5–H), 7.62 (s, 1H, benzylidene-CH), 7.58 (d, J = 8.84 Hz, 2H, benzylidene- $C_{2,6}$-H), 7.32–7.40 (m, 5H, benzyl-Hs), 7.22 (d, J = 8.84 Hz, 2H, benzylidene-$C_{3,5}$-H), 5.62 (s, 2H, benzyl-CH_2), 5.25 (s, 2H, OCH_2). ^{13}C NMR (100 MHz, DMSO-d_6): δ 196.1, 170.1, 160.5, 142.9, 136.4, 133.1, 132.2, 129.3, 128.7, 128.4, 126.3, 125.4, 123.1, 116.3, 61.8, 53.3. IR (KBr): cm^{-1} 3136.25 (NH), 1693.50 (C=O), 1640(C=N), 1585.49 (C=C), 1261.45, 1172.72, and 1053.13 (C–O–C), (C=S) and (C–S–C). Anal. Calcd (%) for $C_{20}H_{16}$ $N_4O_2S_2$ (408.49): C, 58.81; H, 3.95; N, 13.72; S, 15.70. Found C, 59.04; H, 3.88; N, 13.98; S, 15.93. HPLC/DAD: Retention time 9.44 min.

4.1.1.12. (Z)-5-(4-((1-(4-bromobenzyl)-1H-1,2,3-triazol-4-yl) methoxy)benzylidene)-2-thioxothiazolidin-4-one ***(6b)****.* Yield 81%. m.p. 138–140 °C. ^{1}H NMR (400 MHz, DMSO-d_6): δ 13.75 (s, 1H, NH, D_2O exchangeable), 8.33 (s, 1H, triazole-C_5–H), 7.62 (s, 1H, benzylidene-CH), 7.57–7.59 (m, 4H, 4-bromobenzyl-$C_{3,5}$-H and benzylidene-$C_{2,6}$-H), 7.28 (d, J = 7.88 Hz, 2H, 4-bromobenzyl-$C_{2,6}$-H), 7.21 (d, J = 8.32 Hz, 2H, benzylidene-$C_{3,5}$-H), 5.62 (s, 2H, benzyl-CH_2), 5.25 (s, 2H, OCH_2). ^{13}C NMR (100 MHz, DMSO-d_6): δ 196.1, 170.2, 160.5, 143.0, 135.8, 133.1, 132.2, 131.8, 130.7, 126.3, 125.5, 123.2, 121.9, 116.3, 61.8, 52.6. IR (KBr): cm^{-1} 3147.83 (NH), 1708.93 (C=O), 1620 (C=N), 1589.34 (C=C), 1242.16, 1172.72, and 1049.28 (C–O–C), (C=S) and (C–S–C). Anal. Calcd (%) for $C_{20}H_{15}BrN_4O_2S_2$ (487.39): C, 49.29; H, 3.10; N, 11.50; S, 13.16. Found C, 49.01; H, 3.24; N, 11.78; S, 13.49. HPLC/DAD: Retention time 15.17 min.

4.1.1.13. (Z)-5-(4-((1-phenyl-1H-1,2,3-triazol-4-yl)methoxy)benzylidene)-2-thioxothiazolidin-4-one ***(6c)****.* Yield 84%. m.p. 228–230 °C. ^{1}H NMR (400 MHz, DMSO-d_6): δ 13.70 (s, 1H, NH, D_2O exchangeable), 8.98 (s, 1H, triazole-C_5–H), 7.92 (d, J = 7.88 Hz, 2H, benzylidene- $C_{2,6}$-H), 7.48–7.63 (m, 6H, benzylidene-CH and phenyl-Hs), 7.22–7.27 (m, 2H, benzylidene- $C_{3,5}$-H), 5.34 (s, 2H, OCH_2). ^{13}C NMR (100 MHz, DMSO-d_6): δ 196.4, 173.7, 160.3, 143.8, 137.0, 133.1, 131.7, 130.4, 129.9, 129.3, 126.6, 123.5, 120.7, 116.2, 61.7. IR (KBr): cm^{-1} 3132.40 (NH), 1708.93 (C=O), 1625 (C=N), 1589.34 (C=C), 1242.16,1168.86, and 1030 (C–O–C), (C=S) and (C–S–C). Anal. Calcd (%) for $C_{19}H_{14}N_4O_2S_2$ (394.47): C, 57.85; H, 3.58; N, 14.20; S, 16.25. Found C, 58.07; H, 3.65; N, 14.53; S, 16.48. HPLC/DAD: Retention time 11.45 min.

4.1.1.14. (Z)-5-(4-((1-(4-chlorophenyl)-1H-1,2,3-triazol-4-yl) methoxy)benzylidene)-2-thioxothiazolidin-4-one ***(6d)****.* Yield 92%. m.p. 268–270 °C. ^{1}H NMR (400 MHz, DMSO-d_6): δ 13.70 (s, 1H, NH, D_2O exchangeable), 9.00 (s, 1H, triazole-C_5–H), 7.96 (d, J = 8.72 Hz, 2H, 4-chlorophenyl-$C_{2,6}$-H), 7.68 (d, J = 8.72 Hz, 2H, 4-chlorophenyl-$C_{3,5}$-H), 7.58–7.60 (m, 3H, benzylidene- $C_{2,6}$-H and benzylidene-CH), 7.26 (d, J = 8.64 Hz, 2H, benzylidene- $C_{3,5}$-H), 5.34 (s, 2H, OCH_2). ^{13}C NMR (100 MHz, DMSO-d_6): δ 196.3, 170.6, 160.3, 144.1, 135.8, 133.6, 133.1, 131.8, 130.4, 126.5, 123.6, 123.5, 122.4, 116.3, 61.7. IR (KBr): cm^{-1} 3147.83 (NH), 1708.93 (C=O), 1620 (C=N), 1589.34 (C=C), 1238.30, 1168.86 and 1025 (C–O–C), (C=S) and (C–S–C). Anal. Calcd (%) for $C_{19}H_{13}ClN_4O_2S_2$ (428.91): C, 53.21; H, 3.06; N, 13.06; S, 14.95. Found C, 53.59; H, 3.19; N, 12.89; S, 15.01. HPLC/DAD: Retention time 8.33 min.

4.1.1.15. (Z)-5-(4-((1-(4-bromophenyl)-1H-1,2,3-triazol-4-yl) methoxy)benzylidene)-2-thioxothiazolidin-4-one ***(6e)****.* Yield 89%. m.p. 271–273 °C. ^{1}H NMR (400 MHz, DMSO-d_6): δ 13.78 (s, 1H, NH, D_2O exchangeable), 9.01 (s, 1H, triazole-C_5–H), 7.90 (d, J = 11.48 Hz,

2H, 4-bromophenyl-$C_{3,5}$-H), 7.81 (d, $J = 11.48$ Hz, 2H, 4-bromophenyl-$C_{2,6}$-H), 7.62 (s, 1H, benzylidene-CH), 7.59 (d, $J = 8.84$ Hz, 2H, benzylidene- $C_{2,6}$-H), 7.26 (d, $J = 8.84$ Hz, 2H, benzylidene- $C_{3,5}$-H), 5.35 (s, 2H, OCH_2). ^{13}C NMR (100 MHz, DMSO-d_6): δ 196.1, 170.1, 160.4, 144.0, 136.2, 133.3, 133.1, 132.1, 126.4, 123.6, 123.2, 122.6, 122.0, 116.3, 61.7. IR (KBr): cm^{-1} 3143.97 (NH), 1716.65 (C=O), 1639.49 (C=N), 1589.34 (C=C), 1242.16, 1168.86 and 1056.99 (C–O–C), (C=S) and (C–S–C). Anal. Calcd (%) for $C_{19}H_{13}BrN_4O_2S_2$ (473.36): C, 48.21; H, 2.77; N, 11.84; S, 13.55. Found C, 48.50; H, 2.94; N, 11.99; S, 13.62. HPLC/DAD: Retention time 24.57 min.

4.1.1.16. (Z)-2-Thioxo-5-(4-((1-(p-tolyl)-1H-1,2,3-triazol-4-yl) methoxy)benzylidene)thiazolidin-4-one ***(6f)***. Yield 92%. m.p. 254–256 °C. ^{1}H NMR (400 MHz, DMSO-d_6): δ 13.77 (s, 1H, NH, D_2O exchangeable), 8.92 (s, 1H, triazole-C_5–H), 7.79 (d, $J = 8.32$, 2H, *p*-tolyl-$C_{2,6}$-H), 7.61 (s, 1H, benzylidene-CH), 7.59 (d, $J = 8.64$ Hz, 2H, benzylidene- $C_{2,6}$-H), 7.40 (d, $J = 8.32$ Hz, 2H, *p*-tolyl-$C_{3,5}$-H), 7.26 (d, $J = 8.64$ Hz, 2H, benzylidene- $C_{3,5}$-H), 5.34 (s, 2H, OCH_2), 2.38 (s, 3H, CH_3). ^{13}C NMR (100 MHz, DMSO-d_6): δ 196.1, 170.1, 160.4, 143.7, 138.9, 134.8, 133.1, 132.1, 131.8, 130.7, 126.4, 123.4, 120.5, 116.3, 61.8, 21.0. IR (KBr): cm^{-1} 3151.69 (NH), 1701.22 (C=O), 1630 (C=N), 1589.34 (C=C), 1261.45,1172.72 and 1053.13 (C–O–C), (C=S) and (C–S–C). Anal. Calcd (%) for $C_{20}H_{16}N_4O_2S_2$ (408.49): C, 58.81; H, 3.95; N, 13.72; S, 15.70. Found C, 59.09; H, 4.06; N, 13.96; S, 16.02. HPLC/DAD: Retention time 18.11 min.

4.1.1.17. (Z)-5-(4-((1-(4-methoxyphenyl)-1H-1,2,3-triazol-4-yl) methoxy)benzylidene)-2-thioxothiazolidin-4-one ***(6g)***. Yield 91%. m.p. 256–258 °C. ^{1}H NMR (400 MHz, DMSO-d_6): δ 13.74 (s, 1H, NH, D_2O exchangeable), 8.87 (s, 1H, triazole-C_5–H), 7.81 (d, $J = 8.64$, 2H, benzylidene- $C_{2,6}$-H), 7.62 (s, 1H, benzylidene-CH), 7.59 (d, $J = 8.4$ Hz, 2H, 4-methoxyphenyl- $C_{2,6}$-H), 7.26 (d, $J = 8.4$ Hz, 2H, 4-methoxyphenyl- $C_{3,5}$-H), 7.14 (d, $J = 8.64$ Hz, 2H, benzylidene- $C_{3,5}$-H), 5.33 (s, 2H, OCH_2), 3.84 (s, 3H, OCH_3). ^{13}C NMR (100 MHz, DMSO-d_6): δ 196.1, 170.2, 160.5, 159.8, 143.5, 133.1, 132.0, 130.4, 126.4, 123.5, 123.0, 122.3, 116.3, 115.4, 61.8, 56.0. IR (KBr): cm^{-1} 3140.11 (NH), 1685.79 (C=O), 1620 (C=N), 1589.34 (C=C), 1265.30, 1180.44 and 1041.56 (C–O–C), (C=S) and (C–S–C). Anal. Calcd (%) for $C_{20}H_{16}N_4O_3S_2$ (424.49): C, 56.59; H, 3.80; N, 13.20; S, 15.11. Found C, 56.96; H, 3.97; N, 13.01; S, 15.26. HPLC/DAD: Retention time 11.49 min.

4.1.1.18. (Z)-4-(4-((4-((4-oxo-2-thioxothiazolidin-5-ylidene)methyl) phenoxy)methyl)-1H-1,2,3-triazol-1-yl)benzoic acid ***(6h)***. Yield 75%. m.p. 278–280 °C. ^{1}H NMR (400 MHz, DMSO-d_6): δ 13.76 (s, 1H, NH, D_2O exchangeable), 13.25 (s, 1H, COOH, D_2O exchangeable), 9.10 (s, 1H, triazole-C_5–H), 8.07–8.16 (m, 4H, 4-carboxyphenyl-Hs), 7.90 (d, $J = 7.4$ Hz, 2H, benzylidene- $C_{2,6}$-H), 7.59–7.62 (m, 1H, benzylidene-CH), 7.29 (d, $J = 7.4$ Hz, 2H, benzylidene- $C_{3,5}$-H), 5.39 (s, 2H, OCH_2). ^{13}C NMR (100 MHz, DMSO-d_6): δ 191.8, 166.8, 163.3, 160.4, 144.2, 139.9, 133.1, 132.3, 131.6, 131.2, 130.5, 123.7, 120.4, 116.3, 115.7, 61.8. IR (KBr): cm^{-1} 3376.71-2792.93 (OH), 3136.25 (NH), 1685.79 (C=O), 1620 (C=N), 1577.77 (C=C), 1257.59, 1165.00 and 1041.56 (C–O–C), (C=S) and (C–S–C). Anal. Calcd (%) for $C_{20}H_{14}N_4O_4S_2$ (438.48): C, 54.79; H, 3.22; N, 12.78; S, 14.62. Found C, 54.85; H, 3.14; N, 13.01; S, 14.50. HPLC/DAD: Retention time 2.74 min.

*4.1.2. Click reaction procedure for compounds (**5i**,**5j**) and (**6i**,**6j**)*

To a mixture of 4-propargyloxy-benzylidene thiazolidene-2,4-dione/rhodanine 4 **(a,b)** (1 mmol) and appropriate phenacyl azide (1.5 mmol) in 10 mL of DMF, was added an aqueous solution (5 mL) of sodium ascorbate (0.06 g, 0.34 mmol) and $CuSO_4.5H_2O$ (0.02 g, 0.085 mmol). The mixture was stirred at room temperature for 48 h. After cooling, the mixture was poured on ice, filtered, washed with cold water, dried and recrystallized from ethanol/DMF.

4.1.2.1. (Z)-5-(4-((1-(2-(4-chlorophenyl)-2-oxoethyl)-1H-1,2,3-triazol-4-yl)methoxy)benzylidene)thiazolidine-2,4-dione ***(5i)***. Yield 90%. m.p. 265–266 °C. ^{1}H NMR (400 MHz, DMSO-d_6): δ 12.53 (s, 1H, NH, D_2O exchangeable), 8.24 (s, 1H, triazole-C_5–H), 8.09 (d, $J = 8.4$ Hz, 2H, 4-chlorophenyl-$C_{2,6}$-H), 7.96 (s, 1H, benzylidene-CH), 7.70 (d, $J = 8.4$ Hz, 2H, 4-chlorophenyl-$C_{3,5}$-H), 7.59 (d, $J = 8.6$ Hz, 2H, benzylidene-$C_{2,6}$-H), 7.24 (d, $J = 8.6$ Hz, 2H, benzylidene-$C_{3,5}$-H), 6.22 (s, 2H, OCH_2), 5.31 (s, 2H, CO=CH_2). ^{13}C NMR (100 MHz, DMSO-d_6): δ 191.8, 168.0, 162.8, 160.2, 142.7, 139.6, 133.3, 132.5, 132.1, 130.6, 129.6, 127.0, 126.4, 116.1, 61.8, 56.4. IR (KBr): cm^{-1} 3150 (NH), 1740 (C=O), 1693.50 (amide C=O), 1625 (C=N), 1590 (C=C), 1250 and 1040 (C–O–C), (C–S–C). Anal. Calcd (%) for $C_{21}H_{15}ClN_4O_4S$ (454.89): C, 55.45; H, 3.32; N, 12.32; S, 7.05. Found C, 55.81; H, 3.45; N, 12.19; S, 7.18. HPLC/DAD: Retention time 6.51 min.

4.1.2.2. (Z)-5-(4-((1-(2-(4-bromophenyl)-2-oxoethyl)-1H-1,2,3-triazol-4-yl)methoxy) benzylidene)thiazolidine-2,4-dione ***(5j)***. Yield 87%. m.p. 236–238 °C. ^{1}H NMR (400 MHz, DMSO-d_6): δ 8.24 (s, 1H, triazole-C_5–H), 8.00 (d, $J = 7.72$ Hz, 2H, 4-bromophenyl-$C_{2,6}$-H), 7.96 (s, 1H, benzylidene-CH), 7.82 (d, $J = 7.72$ Hz, 2H, 4-bromophenyl-$C_{3,5}$-H), 7.57 (d, $J = 8.44$ Hz, 2H, benzylidene-$C_{2,6}$-H), 7.24 (d, $J = 8.44$ Hz, 2H, benzylidene-$C_{3,5}$-H), 6.22 (s, 2H, OCH_2), 5.30 (s, 2H, CO=CH_2). ^{13}C NMR (100 MHz, DMSO-d_6): δ 191.9, 168.7, 162.8, 160.2, 142.7, 133.6, 132.5, 132.4, 131.9, 130.6, 128.9, 126.9, 126.4, 121.4, 116.1, 61.8, 56.4. IR (KBr): cm^{-1} 3124.68 (NH), 1735.93 (C=O),1708.93 (amide C=O), 1658.78 (C=N),1589.34 (C=C), 1240 and 1070 (C–O–C), (C–S–C). Anal. Calcd (%) for $C_{21}H_{15}BrN_4O_4S$ (499.34): C, 50.51; H, 3.03; N, 11.22; S, 6.42. Found C, 50.27; H, 3.16; N, 11.49; S, 6.38. HPLC/DAD: Retention time 7.23 min.

4.1.2.3. (Z)-5-(4-((1-(2-(4-chlorophenyl)-2-oxoethyl)-1H-1,2,3-triazol-4-yl)methoxy) benzylidene)-2-thioxothiazolidin-4-one ***(6i)***. Yield 89%. m.p. 257–259 °C. ^{1}H NMR (400 MHz, DMSO-d_6): δ 13.62 (s, 1H, NH, D_2O exchangeable), 8.24 (s, 1H, triazole-C_5–H), 8.09 (d, $J = 8.6$ Hz, 2H, 4-chlorophenyl-$C_{2,6}$-H), 7.69 (d, $J = 8.6$ Hz, 2H, 4-chlorophenyl-$C_{3,5}$-H), 7.57–7.59 (m, 3H, benzylidene-CH and benzylidene-$C_{2,6}$-H), 7.25 (d, $J = 8.84$ Hz, 2H, benzylidene-$C_{3,5}$-H), 6.22 (s, 2H, OCH_2), 5.31 (s, 2H, CO=CH_2). ^{13}C NMR (100 MHz, DMSO-d_6): δ 196.6, 191.8, 162.8, 160.4, 142.6, 139.6, 133.3, 133.0, 131.6, 130.6, 129.6, 127.0, 126.5, 123.8, 116.2, 61.8, 56.4. IR (KBr): cm^{-1} 3140.11 (NH), 1705.07 (C=O),1651.07 (C=N), 1589.34 (C=C), 1234.44, 1176.58 and 1053.13 (C–O–C), (C=S) and (C–S–C). Anal. Calcd (%) for $C_{21}H_{15}ClN_4O_3S_2$ (470.95): C, 53.56; H, 3.21; N, 11.90; S, 13.62. Found C, 53.80; H, 3.39; N, 12.18; S, 13.90. HPLC/DAD: Retention time 4.22 min.

4.1.2.4. (Z)-5-(4-((1-(2-(4-bromophenyl)-2-oxoethyl)-1H-1,2,3-triazol-4-yl)methoxy)benzylidene)-2-thioxothiazolidin-4-one ***(6j)***. Ysield 92%. m.p. 236–238 °C. ^{1}H NMR (400 MHz, DMSO-d_6): δ 8.23 (s, 1H, triazole-C_5–H), 8.01 (d, $J = 8.36$ Hz, 2H, 4-bromophenyl-$C_{2,6}$-H), 7.96 (s, 1H, benzylidene-CH), 7.84 (d, $J = 8.36$ Hz, 2H, 4-bromophenyl-$C_{3,5}$-H), 7.56 (d, $J = 8.72$ Hz, 2H, benzylidene-$C_{2,6}$-H), 7.23 (d, $J = 8.72$ Hz, 2H, benzylidene-$C_{3,5}$-H), 6.21 (s, 2H, OCH_2), 5.30 (s, 2H, CO=CH_2). ^{13}C NMR (100 MHz, DMSO-d_6): δ 196.6, 167.1, 162.8, 160.1, 142.6, 133.6, 132.7, 132.5, 131.7, 131.1, 130.6, 129.9, 128.9, 126.9, 116.2, 61.8, 56.4. IR (KBr): cm^{-1} 3136.25 (NH), 1697.36 (C=O), 1639.49 (C=N), 1589.34 (C=C), 1240, 1168.86 and 1045.42 (C–O–C), (C=S) and (C–S–C). Anal. Calcd (%) for $C_{21}H_{15}BrN_4O_3S_2$ (515.40): C, 48.94; H, 2.93; N, 10.87; S, 12.44. Found C, 49.21; H, 3.08; N, 11.12; S, 12.71. HPLC/DAD: Retention time 13.47 min.

4.2. Biological evaluation

4.2.1. In vitro COX-1 and COX-2 inhibitory assay

All the newly synthesized compounds were screened for their ability to inhibit COX-1 and COX-2 enzymes *in vitro*. This was carried out using Cayman colorimetric COX (ovine) inhibitor screening assay kit (Catalog No. 560131) supplied by Cayman chemicals, Ann Arbor, MI, USA. The preparation of reagents and testing procedures were carried out following the instructions given with the assay kit (Catalog No. 560131) and in agreement with a previously reported method.

4.2.2. In vitro 15-LOX inhibitory assay

The inhibitory activity of the test compounds listed in Table 1 against soya bean 15-LOX was assessed using Cayman lipoxygenase inhibitor screening assay kit (Catalog No. 760700). The preparation of reagents and testing procedures for determining IC_{50} values of the tested compounds were carried out following the instructions given with the assay kit (Catalog No. 760700) and in agreement with a previously reported method [37].

4.2.3. In vitro glucose uptake using rat hemi-diaphragm model

Procedures involving animals and their care were conducted in conformity with the Guide for the Care and Use of Laboratory Animals published by US National Institute of Health (NIH publication No. 83-23, revised 1996) and following the ethical guidelines of Alexandria University on laboratory animals. In all tests, adequate considerations were adopted to reduce pain or discomfort of animals. Reagent preparation and testing procedures for glucose uptake using *in vitro* rat hemi-diaphragm model of the tested compounds were carried out following the instructions in accordance with a previously reported method. In brief, Wistar rats weighing 150–250 g were used (Experimental Animal Center in Alexandria University). All animals accessed to food and water *ad libitum* and were housed in 12 h dark/light cycle in a controlled condition at 23–25 °C and fasted overnight. The animals were euthanized under ether anesthesia and diaphragms were taken out swiftly avoiding trauma and divided into two halves and weight was noted. The hemi-diaphragms were then rinsed in cold Tyrode solution (without glucose) to remove any blood clots and used accordingly. The glucose content of the working solutions was measured by GOD/POD enzymatic method using VITRO SCIENT glucose kit. The working solutions (n = 3) were categorized as follows:

- A negative control that was provided by 2 ml of Tyrode solution with 2000 mg/l glucose with and without regular insulin (Novo Nordisk, 40 IU/ml) 5 μl containing 0.2 units of insulin.
- Test solutions which contained 2 ml of Tyrode solution with 2000 mg/l glucose and 2 mg of the test compound **4b, 5b, 5e, 5g, 5j, 6b, 6e, 6g, 6j** and **6i** with and without regular insulin (Novo Nordisk, 40 IU/ml) 5 μl containing 0.2 units of insulin.
- A positive control which contained: 2 ml of Tyrode solution with 2000 mg/l glucose and 2 mg of pioglitazone (standard) with and without regular insulin (Novo Nordisk, 40 IU/ml) 5 μl containing 0.2 units of insulin.

4.2.4. Immunohistochemical analysis of ligand-stimulated PPARγ nuclear localization

Primary rat adipocytes were isolated from perivascular adipose tissue and differentially cultured as described previously [91]. Adipocytes were seeded on sterile coverslips in a 12-well plate at a density of 3000 cells/well. Cells were cultured in DMEM F-12 (Lonza, Basel, Switzerland) containing 10% fetal bovine serum (FBS, Sigma, St. Louis, MO), penicillin (100 U/mL), and streptomycin (100 μg/mL); and incubated at 37 °C in a humidified atmosphere with 5% CO2 and 95% O_2. Forty-eight hours post seeding, cells were incubated with 10 μM concentration of either pioglitazone, 4b, 5b, 5e, or 5g; or the equivalent amount of the vehicle (DMSO) in triplicates. Following a 3-h exposure interval, treatment media were discarded, cells were washed with phosphate-buffered saline (PBS) and fixed with 2% formaldehyde in PBS for 20 min at room temperature. After rinsing with PBS, cells were permeabilized by 0.1% Triton X-100 for 30 min at room temperature. Cells were then blocked with 3% normal goat serum (Abcam, Cambridge, UK) in PBS for 1 h at room temperature followed by incubation in 1:200 rabbit polyclonal anti-PPARγ (Abcam, Cambridge, UK) in PBS containing 1% normal goat serum overnight at 4 °C. Cells were rinsed three times with PBS followed by incubation with 1:100 FITC-conjugated goat anti-rabbit Ig (Abcam, Cambridge, UK) in PBS containing 1% normal goat serum in a light-proof container for 1 h at room temperature. Afterwards, cells were rinsed with PBS and mounted on microscopic slides with Fluoroshield anti-fade mounting medium containing DAPI (Abcam, Cambridge, UK). Negative control slides were prepared by omission of either the primary or the secondary antibodies. Slides were left at 4 °C overnight. FITC green fluorescence representing PPARγ staining and DAPI nuclear staining were recorded on an Axiovert Observer Z1 High Resolution Fluorescent Imaging Microscope (Zeiss, Oberkochen, Germany). Fluorescence distribution profiles along line scans in both the FITC and DAPI channels was generated using ImageJ software (National Institutes of Health, Bethesda, MD) to show cellular localization of PPARγ relative to the nucleus.

4.2.5. PPARγ functional reporter gene assay

HEK293T cells were transiently co-transfected with a hybrid receptor comprising the N-terminal Gal4 DNA binding domain fused to the ligand binding domain of Human PPARγ. The reporter vectors comprise the Renilla luciferase gene functionally linked to the Gal4 upstream activation sequence. Cells were treated with vehicle (DMSO), pioglitazone or test compounds for 24 h. Following the incubation period, treatment media were discarded and luciferase activity was measured using reporter luciferase assay kit according to the manufacturer's instructions and as reported earlier [58]. Luciferase activity was normalized to Renilla luciferase activity and reported as fold induction compared to vehicle. Each experiment was performed in triplicate and repeated at least three times.

4.2.6. Monocyte to macrophage differentiation assay

THP-1 cells (human acute monocytic leukaemia lineage, American Type Culture Collection, Manassas, VA) were cultured and differentiated as described as described previously [92]. Briefly, cells were cultured in RPMI-1640 (Lonza, Basel, Switzerland) containing 10% FBS, glucose (11 mmol/L), L-glutamine (4 mmol/L), pyruvate (1 mM), penicillin (100 U/mL), and streptomycin (100 μg/mL) and incubated at 37 °C in a humidified atmosphere of 5% CO2 and 95% air (1). THP-1 monocytes were seeded at a density of 2×10^5 cells/ml in 24-well plates. THP-1 monocytes were differentiated into macrophages by incubation with 25 ng/ml of phorbol myristate-acetate (PMA, Calbiochem, Darmstadt, Germany) for 24 h [93]. Following incubation and cell attachment, supernatants were removed and wells were washed 3x with phosphate-buffered saline. Attached cell density was estimated using a MTS colorimetric cell viability kit (Abcam, Cambridge, UK). Control treatment without PMA was used as a blank. To examine the inhibitory effect of different drugs on the differentiation process, THP-1 cells were incubated with different concentrations of each drug for 6 h prior to exposure to PMA. Cell viability readings of attached macrophages in each drug treatment was normalized to the count after PMA

exposure following a 6-h incubation with DMSO. Diclofenac was used as a reference COX1/COX2 inhibitor for comparison of the effect of the different compounds on monocyte to macrophage differentiation. All experiments were performed in triplicates. GraphPad Prism software was used to determine IC_{50} values for each compound as the best fit non-linear regression values of the log [inhibitor] vs. response curve. To confirm that the effects observed were a result of interference with the differentiation process rather than monocyte cytotoxicity, THP-1 cell viability at different drug concentrations was assessed prior to the execution of the assay. No change in cell viability was observed for different drug concentrations after 30 h incubation.

4.2.7. IL-1β and TNF-α expression and 20-HETE production assay

THP-1 cells were seeded at a density of 2.6×10^6 cells in T75 culture flasks for western blotting experiments and 3×10^5 cells in 6-well plates for the ELISA determination of 2-HETE experiments. Treatment flasks were exposed to 100 μM of the corresponding drug. THP-1 cells were activated with 25 nM PMA for 24 h followed by a 72-h challenge with 100 ng/ml LPS. At the end of the challenge period, the conditioned medium was collected from the cell cultures in the 6-well plates, extracted and 20-HETE concentration was measured using an ELISA kit from Detroit R&D Inc. (Detroit, MI, USA) according to the manufacturer instructions. For western blotting, cells in T75 flasks were extracted with a buffer composed of 100 mM dithiothreitol, 1% sodium dodecyl sulphate, 0.9% sodium chloride, and 80 mM Tris hydrochloride (pH 6.8) as described previously [8]. Sodium dodecyl sulphate polyacrylamide gel electrophoresis, blotting, and antibody labelling was done as described previously [8]. Primary rabbit polyclonal antibodies to IL-1β, TNF-α, and GAPDH were obtained from Abcam (Cambridge, UK). Bands were visualized using Clarity Western ECL substrate (BioRad, Hercules, CA, USA) and a Chemidoc imaging system (BioRad, Hercules, CA, USA). Band density was measured using ImageJ software (National Institutes of Health, Bethesda, MD) and normalized to the GAPDH band density as a loading control.

4.2.8. In vivo anti-inflammatory assay

Adult female albino rats weighing 150–250 g were used (Experimental Animal Center in Alexandria University). All animals were accessed to food and water *ad libitum* and were housed in 12 h dark/light cycle in a controlled condition at 23–25 °C. They were allowed to acclimatize for 1 week prior to experimentation. Procedures involving animals and their care were conducted in conformity with the Guide for the Care and Use of Laboratory Animals published by US National Institute of Health (NIH publication No. 83-23, revised 1996) and following the ethical guidelines of Alexandria University on laboratory animals. In all tests, adequate considerations were adopted to reduce pain or discomfort of animals.

Celecoxib and diclofenac sodium (European Egyptian Pharmaceutical industries, Alexandria, Egypt), formalin 5% made from formaldehyde 37% and saline (Merck, Germany) were used. Compounds (**4b, 5b, 5e** and **5g**) were evaluated for their *in vivo* anti-inflammatory activity applying the formalin-induced rat paw edema screening protocol as an acute inflammation model as reported previously [94].

4.3. Protein purification, crystallization, and structure determination

The PPARγ LBB was expressed in *E. coli*, purified, and concentrated as described previously [95]. Apo crystals of PPARγ were created by using the hanging drop vapour diffusion method with 500 μL well solution comprising 0.8–1.2M sodium citrate and 0.1M Tris 8.0. The hanging drop was made using 1 μL protein plus 1 μL well solution. Crystals were cubic, approximately 400 μm in each dimension, and formed within 3 days at 16 °C. Crystals were soaked with a final concentration of 2 mM **4b** in the crystallization well for 2 weeks. Crystals were harvested and transferred to well solution containing 15% ethylene glycol as a cryo-protectant. Crystals were flash cooled by direct submersion into liquid nitrogen and data collection was carried out at beamline MX2 of the Australian Synchrotron. 0.1° oscillations were collected using the Eiger 16M detector. Data was processed in XDS [96]. Molecular replacement using Phaser [97], PDB ID: 5U5L [95] as a search model, with ligands and water molecules removed), electron density for **4b** was visible initial difference density maps. Two subunits were found per asymmetric unit. Phenix.refine [98] and Coot [99] were used for refinement and multiple rounds of manual rebuilding. MolProbity was used for structure validation [100]. A Feature Enhanced Map (FEM) $2F_o - F_c$ electron density map was calculated using Phenix to help reduce model bias and improve map quality [101]; an electron density map of the ligand is shown in Supplementary Information Figure SM2. Coordinates and structure factors were deposited in the Protein Data Bank under accession code 6E5A. Data processing and refinement statistics can be found in Supplementary Information Table SM3.

4.4. Molecular modeling

4.4.1. Preparation of protein crystal structures

Coordinates for PPARγ, COX-2, COX-1 and 15-LOX crystal structures was retrieved from the Protein Data Bank (PDB codes: 2PRG, 1CX2, 1EQG and 1LOX, respectively) and handled consequently with Molecular Operating Environment program (MOE 2016.0802) [102]. Redundant chains, non-essential ions, water molecules and ligands were discarded. The default preparation scheme was conducted using “Structure Preparation” module with the default settings. Bond orders, formal charges and explicit hydrogen atoms were added to the complex structure. Subsequently, the most appropriate protonation states and optimization of the H-bond network were performed with the MOE ‘Protonate 3D’ function at standard settings (T = 300 K, pH = 7.0, ionic strength I = 0.1 mol/l). Prepared protein structures were saved as PDB files which were further used for GOLD docking. The PDB files were converted to PDBQT files by employing a python script (*prepare_receptor4.py*) provided by the MGLTools package (version 1.5.4) for AutoDock Vina (version 1.1.2) and Autodock VinaXB docking experiments. The native geometry of the binding sites was preserved without in-place ligand-protein minimization.

4.4.2. Preparation of the compounds for docking

The molecules were built and prepared by MOE 2016.0802. ‘Molecule wash’ function was used to generate meaningful protonation states by deprotonating strong acids and protonating strong bases (if required). Also generating different protomers, conformations and geometrical isomers were allowed at pH 7. Energy minimization of all molecules was performed using the MMFF94x force field at a gradient of 0.01 RMSD (i.e. if the gradient falls below RMSD, the minimization terminates). All possible chiralities were generated (if required) and partial charges were calculated according to the standard parameters of the force field. The resulting structures were saved as SD file for GOLD docking experiments. The SD files were converted and split into PDB files by open-Babel (version 2.3.1) [103], which were further converted into PDBQT files by a MGLTools (version 1.5.4) python script (*prepare_ligand4.py*) for AutoDock Vina and AutoDock VinaXB docking experiments.

4.4.3. Docking experiments

For GOLD (version 5.2) [43,44] docking, ChemPLP scoring function was used for docking experiments against all the above mentioned targets. Residues of the binding site were defined by specifying the coordinates of the co-crystallized ligands and using a cutoff radius of 10 Å, with the 'detect cavity' option enabled. The scoring function used for GOLD docking experiments was ChemPLP. The search efficiency of the genetic algorithm was at 200%. All the docking solutions were allowed and saved consequently. This docking approach was validated by successful pose-retrieval of the co-crystallized ligand when docked into its corresponding binding site of the crystal structure. All graphical representations for docking poses in the binding sites were rendered using Pymol (v1.1eval) [104] and MOE 2016.0802.

For AutoDock Vina (version 1.1.2) docking against PPARγ, we again employed default docking parameters. The size of the docking grid was generally 20 Å × 20 Å × 20 Å, with a grid spacing of 1 Å. In cases where the ligand binding site was not completely included in the grid box, the grid dimensions were expanded accordingly. By default, the docking was terminated when the maximum energy difference between the best scored pose and the worst one was 3 kcal/mol. These settings were also employed for AutoDock VinaXB docking experiments.

4.4.4. pROC-chemotype plots

pROC-Chemotype plot [105] is an automated protocol that matches and visualizes ligand chemotype information in combination with the pROC profile obtained by docking, without biasing or modifying the original pROC graph. Cluster number and rank are annotated. For each bioactive molecule, information about the type of data (TOD), the level of activity (LOA), and its bioactivity rank is provided, which also serves as a molecular identifier. The clustering method employed in this protocol is based on Maximum Common Substructures (MCS) of Small Molecule Subgraph Detector (SMSD). In this study we applied the pROC-Chemotype protocol of KNIME [106].

4.5. In silico prediction of physicochemical properties, drug-likeness, pharmacokinetic profile and ligand efficiency metrics

Compounds **4b**, **5b** and **5e** underwent molecular properties prediction by Molinspiration online property calculation toolkit, drug-likeness and solubility parameter calculation by MolSoft software, ADME profiling by PreADMET calculator and Ligand efficiency metrics calculation by Data warrior software.

Notes

The authors declare no competing financial interest. The PDB code for PPARγ in complex with **4b** is 6E5A. The authors will release the atomic coordinates and the experimental data upon article publication.

Acknowledgements

X-ray crystallography part of this research was undertaken on the MX1 beamline at the Australian Synchrotron, part of ANSTO. Also, all authors acknowledge Prof. F Boeckler, Lab for Molecular Design and Pharmaceutical Biophysics, Eberhard Karls University Tuebingen, Germany, for granting access to some computational tools. This study was partially supported by MPP grant # 320148 from the Faculty of Medicine at the American University of Beirut and was presented in preliminary form at Experimental Biology 2018.

Appendix A. Supplementary data

Supplementary data to this article can be found online at https://doi.org/10.1016/j.ejmech.2019.02.034.

References

[1] S.E. Headland, L.V. Norling, The resolution of inflammation: principles and challenges, Semin. Immunol. 27 (2015) 149–160, https://doi.org/10.1016/j.smim.2015.03.014.
[2] C.N. Serhan, Treating inflammation and infection in the 21st century: new hints from decoding resolution mediators and mechanisms, FASEB J. 31 (2017) 1273–1288, https://doi.org/10.1096/fj.201601222R.
[3] V.R. Jala, S.R. Bodduluri, S.R. Satpathy, Z. Chheda, R.K. Sharma, B. Haribabu, The yin and yang of leukotriene B 4 mediated inflammation in cancer, Semin. Immunol. 33 (2017) 58–64, https://doi.org/10.1016/j.smim.2017.09.005.
[4] C.S.N. Klose, D. Artis, Innate lymphoid cells as regulators of immunity, inflammation and tissue homeostasis, Nat. Immunol. 17 (2016) 765–774, https://doi.org/10.1038/ni.3489.
[5] C.A. Dinarello, Anti-inflammatory agents: present and future, Cell 140 (2010) 935–950, https://doi.org/10.1016/j.cell.2010.02.043.
[6] S.M. Haffner, The metabolic syndrome: inflammation, diabetes mellitus, and cardiovascular disease, Am. J. Cardiol. 97 (2006) 3–11, https://doi.org/10.1016/j.amjcard.2005.11.010.
[7] N. Esser, S. Legrand-Poels, J. Piette, A.J. Scheen, N. Paquot, Inflammation as a link between obesity, metabolic syndrome and type 2 diabetes, Diabetes Res. Clin. Pract. 105 (2014) 141–150, https://doi.org/10.1016/j.diabres.2014.04.006.
[8] O. Al-Assi, R. Ghali, A. Mroueh, A. Kaplan, N. Mougharbil, A.H. Eid, F.A. Zouein, A.F. El-Yazbi, Cardiac autonomic neuropathy as a result of mild hypercaloric challenge in absence of signs of diabetes: modulation by antidiabetic drugs, Oxid. Med. Cell. Longev. 2018 (2018) 9389784, https://doi.org/10.1155/2018/9389784.
[9] E. Schauberger, M. Peinhaupt, T. Cazares, A.W. Lindsley, Lipid mediators of allergic disease: pathways, treatments, and emerging therapeutic targets, Curr. Allergy Asthma Rep. 16 (2016) 48, https://doi.org/10.1007/s11882-016-0628-3.
[10] F.H.G. Tessaro, T.S. Ayala, J.O. Martins, Lipid mediators are critical in resolving inflammation: a review of the emerging roles of eicosanoids in diabetes mellitus, BioMed Res. Int. 2015 (2015) 1–8, https://doi.org/10.1155/2015/568408.
[11] R. Mashima, T. Okuyama, Redox Biology the role of lipoxygenases in pathophysiology ; new insights and future perspectives, Redox Biol. 6 (2015) 297–310, https://doi.org/10.1016/j.redox.2015.08.006.
[12] J.A. Ackermann, K. Hofheinz, M.M. Zaiss, G. Krönke, The double-edged role of 12/15-lipoxygenase during inflammation and immunity, Biochim. Biophys. Acta Mol. Cell Biol. Lipids 1862 (2017) 371–381, https://doi.org/10.1016/j.bbalip.2016.07.014.
[13] N. Sharma-walia, J. Chandrasekharan, Lipoxins: nature's way to resolve inflammation, J. Inflamm. Res. (2015) 181, https://doi.org/10.2147/JIR.S90380.
[14] H. Sadeghian, A. Jabbari, 15-Lipoxygenase inhibitors: a patent review, Expert Opin. Ther. Pat. 26 (2016) 65–88, https://doi.org/10.1517/13543776.2016.1113259.
[15] C.D. Funk, Prostaglandins and leukotrienes: advances in eicosanoid biology (80-.), Science 294 (2001) 1871–1875, https://doi.org/10.1126/science.294.5548.1871.
[16] C. Patrono, B. Rocca, Nonsteroidal antiinflammatory drugs: past, present and future, Pharmacol. Res. 59 (2009) 285–289, https://doi.org/10.1016/j.phrs.2009.01.011.
[17] S. Fiorucci, R. Meli, M. Bucci, G. Cirino, Dual inhibitors of cyclooxygenase and 5-lipoxygenase. A new avenue in anti-inflammatory therapy? 1 1Abbreviations: NSAIDs, nonsteroidal anti-inflammatory drugs; COX, cyclooxygenase; LT, leukotriene; 5-LOX, 5-lipoxygenase; PG, prostaglandin; DFU, 5,5-dimet, Biochem. Pharmacol. 62 (2001) 1433–1438, https://doi.org/10.1016/S0006-2952(01)00747-X.
[18] C. Charlier, C. Michaux, Dual inhibition of cyclooxygenase-2 (COX-2) and 5-lipoxygenase (5-LOX) as a new strategy to provide safer non-steroidal anti-inflammatory drugs, Eur. J. Med. Chem. 38 (2003) 645–659, https://doi.org/10.1016/S0223-5234(03)00115-6.
[19] T. Hanke, D. Merk, D. Steinhilber, G. Geisslinger, M. Schubert-Zsilavecz, Small molecules with anti-inflammatory properties in clinical development, Pharmacol. Ther. 157 (2016) 163–187, https://doi.org/10.1016/j.pharmthera.2015.11.011.
[20] Q. Li, Y.-P. Cheon, A. Kannan, S. Shanker, I.C. Bagchi, M.K. Bagchi, A novel pathway involving progesterone receptor, 12/15-lipoxygenase-derived eicosanoids, and peroxisome proliferator-activated receptor gamma regulates implantation in mice, J. Biol. Chem. 279 (2004) 11570–11581, https://doi.org/10.1074/jbc.M311773200.
[21] J. Han, L. Sun, Y. Xu, H. Liang, Y. Cheng, Activation of PPARγ by 12/15-lipoxygenase during cerebral ischemia-reperfusion injury, Int. J. Mol. Med. 35 (2015) 195–201, https://doi.org/10.3892/ijmm.2014.1998.
[22] A.J. Kroker, J.B. Bruning, Review of the structural and dynamic mechanisms

of PPAR γ partial agonism, PPAR Res. (2015) 1–15, https://doi.org/10.1155/2015/816856, 2015.
[23] M.B. Wright, M. Bortolini, M. Tadayyon, M. Bopst, Minireview: challenges and opportunities in development of PPAR agonists, Mol. Endocrinol. 28 (2014) 1756–1768, https://doi.org/10.1210/me.2013-1427.
[24] S. Yasmin, V. Jayaprakash, Thiazolidinediones and PPAR orchestra as antidiabetic agents: from past to present, Eur. J. Med. Chem. 126 (2017) 879–893, https://doi.org/10.1016/j.ejmech.2016.12.020.
[25] V. Capra, M. Bäck, S.S. Barbieri, M. Camera, E. Tremoli, G.E. Rovati, Eicosanoids and their drugs in cardiovascular diseases: focus on atherosclerosis and stroke, Med. Res. Rev. 33 (2013) 364–438, https://doi.org/10.1002/med.21251.
[26] M.T. Mansouri, B. Naghizadeh, B. Ghorbanzadeh, H. Rajabi, M. Pashmforoush, Pharmacological evidence for systemic and peripheral antinociceptive activities of pioglitazone in the rat formalin test: role of PPARγ and nitric oxide, Eur. J. Pharmacol. 805 (2017) 84–92, https://doi.org/10.1016/j.ejphar.2017.03.007.
[27] A. Bornot, U. Bauer, A. Brown, M. Firth, C. Hellawell, O. Engkvist, Systematic exploration of dual-acting modulators from a combined medicinal chemistry and biology perspective, J. Med. Chem. 56 (2013) 1197–1210, https://doi.org/10.1021/jm301653f.
[28] N. Chadha, M.S. Bahia, M. Kaur, O. Silakari, Thiazolidine-2,4-dione derivatives: programmed chemical weapons for key protein targets of various pathological conditions, Bioorg. Med. Chem. 23 (2015) 2953–2974, https://doi.org/10.1016/j.bmc.2015.03.071.
[29] M.J. Naim, M.J. Alam, S. Ahmad, F. Nawaz, N. Shrivastava, M. Sahu, O. Alam, Therapeutic journey of 2,4-thiazolidinediones as a versatile scaffold: an insight into structure activity relationship, Eur. J. Med. Chem. 129 (2017) 218–250, https://doi.org/10.1016/j.ejmech.2017.02.031.
[30] D. Kaminskyy, A. Kryshchyshyn, R. Lesyk, 5-Ene-4-thiazolidinones – an efficient tool in medicinal chemistry, Eur. J. Med. Chem. 140 (2017) 542–594, https://doi.org/10.1016/j.ejmech.2017.09.031.
[31] B.R.P. Kumar, M. Soni, S.S. Kumar, K. Singh, M. Patil, R.B.N. Baig, L. Adhikary, Synthesis, glucose uptake activity and structure-activity relationships of some novel glitazones incorporated with glycine, aromatic and alicyclic amine moieties via two carbon acyl linker, Eur. J. Med. Chem. 46 (2011) 835–844, https://doi.org/10.1016/j.ejmech.2010.12.019.
[32] A.G. Chittiboyina, C.S. Mizuno, P.V. Desai, A. Patny, T.W. Kurtz, H.A. Pershadsingh, R.C. Speth, V. Karamyan, M.A. Avery, Design, synthesis, and docking studies of novel telmisartan–glitazone hybrid analogs for the treatment of metabolic syndrome, Med. Chem. Res. 18 (2009) 589–610, https://doi.org/10.1007/s00044-008-9152-x.
[33] T. Yoshioka, T. Fujita, T. Kanai, Y. Aizawa, T. Kurumada, K. Hasegawa, H. Horikoshi, Studies on hindered phenols and analogs. 1. Hypolipidemic and hypoglycemic agents with ability to inhibit lipid peroxidation, J. Med. Chem. 32 (1989) 421–428, https://doi.org/10.1021/jm00122a022.
[34] M. Rudnicki, G.L. Tripodi, R. Ferrer, L. Boscá, M.G.R. Pitta, I.R. Pitta, D.S.P. Abdalla, New thiazolidinediones affect endothelial cell activation and angiogenesis, Eur. J. Pharmacol. 782 (2016) 98–106, https://doi.org/10.1016/j.ejphar.2016.04.038.
[35] J.R. Santin, F.D.T. Uchôa, M.D.C.A. Lima, M.M. Rabello, I.D. Machado, M.Z. Hernandes, A.A. Amato, F.A. Milton, P. Webb, F.D.A.R. Neves, S.L. Galdino, I.R. Pitta, S.H.P. Farsky, Chemical synthesis, docking studies and biological effects of a pan peroxisome proliferator-activated receptor agonist and cyclooxygenase inhibitor, Eur. J. Pharm. Sci. 48 (2013) 689–697, https://doi.org/10.1016/j.ejps.2012.12.029.
[36] J.H. Choi, J.G. Park, H.J. Jeon, M.S. Kim, M.R. Lee, M.N. Lee, S. Sonn, J.H. Kim, M.H. Lee, M.S. Choi, Y.B. Park, O.S. Kwon, T.S. Jeong, W.S. Lee, H.B. Shim, D.H. Shin, G.T. Oh, 5-(4-Hydroxy-2,3,5-trimethylbenzylidene) thiazolidine-2,4-dione attenuates atherosclerosis possibly by reducing monocyte recruitment to the lesion, Exp. Mol. Med. 43 (2011) 471–478, https://doi.org/10.3858/emm.2011.43.8.053.
[37] G. Moussa, R. Alaaeddine, L.M. Alaeddine, R. Nassra, A.S.F. Belal, A. Ismail, A.F. El-Yazbi, Y.S. Abdel-Ghany, A. Hazzaa, Novel click modifiable thioquinazolinones as anti-inflammatory agents: design, synthesis, biological evaluation and docking study, Eur. J. Med. Chem. 144 (2018) 635–650, https://doi.org/10.1016/j.ejmech.2017.12.065.
[38] C. Pirat, A. Farce, N. Lebègue, N. Renault, C. Furman, R. Millet, S. Yous, S. Speca, P. Berthelot, P. Desreumaux, P. Chavatte, Targeting peroxisome proliferator-activated receptors (PPARs): development of modulators, J. Med. Chem. 55 (2012) 4027–4061, https://doi.org/10.1021/jm101360s.
[39] S. Yasmin, F. Capone, A. Laghezza, F.D. Piaz, F. Loiodice, V. Vijayan, V. Devadasan, S.K. Mondal, Ö. Atll, M. Baysal, A.K. Pattnaik, V. Jayaprakash, A. Lavecchia, Novel benzylidene thiazolidinedione derivatives as partial PPARγ agonists and their antidiabetic effects on type 2 diabetes, Sci. Rep. 7 (2017) 1–17, https://doi.org/10.1038/s41598-017-14776-0.
[40] J.C. Silva, F.A. César, E.M. de Oliveira, W.M. Turato, G.L. Tripodi, G. Castilho, A. Machado-Lima, B. de las Heras, L. Boscá, M.M. Rabello, M.Z. Hernandes, M.G.R. Pitta, I.R. Pitta, M. Passarelli, M. Rudnicki, D.S.P. Abdalla, New PPARγ partial agonist improves obesity-induced metabolic alterations and atherosclerosis in LDLr−/− mice, Pharmacol. Res. 104 (2016) 49–60, https://doi.org/10.1016/j.phrs.2015.12.010.
[41] A. Massarotti, S. Aprile, V. Mercalli, E. Del Grosso, G. Grosa, G. Sorba, G.C. Tron, Are 1,4- and 1,5-disubstituted 1,2,3-triazoles good pharmacophoric groups? ChemMedChem 9 (2014) 2497–2508, https://doi.org/10.1002/cmdc.201402233.
[42] M.R. Bauer, T.M. Ibrahim, S.M. Vogel, F.M. Boeckler, Evaluation and optimization of virtual screening workflows with DEKOIS 2.0 – a public library of challenging docking benchmark sets, J. Chem. Inf. Model. 53 (2013) 1447–1462, https://doi.org/10.1021/ci400115b.
[43] G. Jones, P. Willett, R.C. Glen, A.R. Leach, R. Taylor, Development and validation of a genetic algorithm for flexible docking11Edited by F. E. Cohen,, J. Mol. Biol. 267 (1997) 727–748. https://doi.org/10.1006/jmbi.1996.0897.
[44] O. Korb, T. Stützle, T.E. Exner, Empirical scoring functions for advanced Protein–Ligand docking with PLANTS, J. Chem. Inf. Model. 49 (2009) 84–96, https://doi.org/10.1021/ci800298z.
[45] O. Trott, A.J. Olson, AutoDock Vina: improving the speed and accuracy of docking with a new scoring function, efficient optimization, and multithreading, J. Comput. Chem. 31 (2009) 455–461, https://doi.org/10.1002/jcc.21334.
[46] M.R. Koebel, G. Schmadeke, R.G. Posner, S. Sirimulla, AutoDock VinaXB: implementation of XBSF, new empirical halogen bond scoring function, into AutoDock Vina, J. Cheminf. 8 (2016) 27, https://doi.org/10.1186/s13321-016-0139-1.
[47] C. Patrono, Cardiovascular effects of nonsteroidal anti-inflammatory drugs, Curr. Cardiol. Rep. 18 (2016) 25, https://doi.org/10.1007/s11886-016-0702-4.
[48] Q.H. Chen, P.N. Praveen Rao, E.E. Knaus, Synthesis and biological evaluation of a novel class of rofecoxib analogues as dual inhibitors of cyclooxygenases (COXs) and lipoxygenases (LOXs), Bioorg. Med. Chem. 14 (2006) 7898–7909, https://doi.org/10.1016/j.bmc.2006.07.047.
[49] R.O. Meyers, J.D. Lambert, N. Hajicek, A. Pourpak, J.A. Kalaitzis, R.T. Dorr, Synthesis, characterization, and anti-melanoma activity of tetra-O-substituted analogs of nordihydroguaiaretic acid, Bioorg. Med. Chem. Lett 19 (2009) 4752–4755, https://doi.org/10.1016/j.bmcl.2009.06.063.
[50] I. Schneider, F. Bucar, Lipoxygenase inhibitors from natural plant sources. Part 1: medicinal plants with inhibitory activity on arachidonate 5 lipoxygenase and 5 lipoxygenase [sol] cyclooxygenase, Phyther. Res. 19 (2005) 81–102.
[51] C.D. Sadik, H. Sies, T. Schewe, Inhibition of 15-lipoxygenases by flavonoids: structure-activity relations and mode of action, Biochem. Pharmacol. 65 (2003) 773–781, https://doi.org/10.1016/S0006-2952(02)01621-0.
[52] E. Walaas, O. Walaas, EFFECT OF INSULIN ON RAT DIAPHRAGM UNDER ANAEROBIC CONDITIONS, J. Biol. Chem. 195 (1952) 367–373.
[53] K. Kar, U. Krithika, Mithuna, P. Basu, S. Santhosh Kumar, A. Reji, B.R. Prashantha Kumar, Design, synthesis and glucose uptake activity of some novel glitazones, Bioorg. Chem. 56 (2014) 27–33, https://doi.org/10.1016/j.bioorg.2014.05.006.
[54] T. Umemoto, Y. Fujiki, Ligand-dependent nucleo-cytoplasmic shuttling of peroxisome proliferator-activated receptors, PPARα and PPARγ, Genes to Cells 17 (2012) 576–596, https://doi.org/10.1111/j.1365-2443.2012.01607.x.
[55] V. Maresca, E. Flori, E. Camera, B. Bellei, N. Aspite, M. Ludovici, C. Catricalà, G. Cardinali, M. Picardo, Linking αMSH with PPARγ in B16-F10 melanoma, Pigment Cell Melanoma. Res. 26 (2013) 113–127, https://doi.org/10.1111/j.1755-148X.2012.01042.x.
[56] B. Bosier, E. Hermans, Promises of biased signaling in the development of improved therapeutics, in: Biased Signal. Physiol. Pharmacol. Ther, Elsevier, 2014, pp. 251–292, https://doi.org/10.1016/B978-0-12-411460-9.00008-2.
[57] R.M. Cooke, A.J.H. Brown, F.H. Marshall, J.S. Mason, Structures of G protein-coupled receptors reveal new opportunities for drug discovery, Drug Discov. Today 20 (2015) 1355–1364, https://doi.org/10.1016/j.drudis.2015.08.003.
[58] H. Kojo, M. Fukagawa, K. Tajima, A. Suzuki, T. Fujimura, I. Aramori, K. Hayashi, S. Nishimura, Evaluation of human peroxisome proliferator-activated receptor (PPAR) subtype selectivity of a variety of anti-inflammatory drugs based on a novel assay for PPARδ(β), J. Pharmacol. Sci. 93 (2003) 347–355, https://doi.org/10.1254/jphs.93.347.
[59] C. Auffray, D. Fogg, M. Garfa, G. Elain, O. Join-Lambert, S. Kayal, S. Sarnacki, A. Cumano, G. Lauvau, F. Geissmann, Monitoring of blood vessels and tissues by a population of monocytes with patrolling behavior, Science 317 (2007) 666–670, https://doi.org/10.1126/science.1142883.
[60] K.J. Moore, I. Tabas, Macrophages in the pathogenesis of atherosclerosis, Cell 145 (2011) 341–355, https://doi.org/10.1016/j.cell.2011.04.005.
[61] N. Satoh, A. Shimatsu, A. Himeno, Y. Sasaki, H. Yamakage, K. Yamada, T. Suganami, Y. Ogawa, Unbalanced M1/M2 phenotype of peripheral blood monocytes in obese diabetic patients: effect of pioglitazone, Diabetes Care 33 (2010), https://doi.org/10.2337/dc09-1315, 2010.
[62] M.A. Bouhlel, B. Derudas, E. Rigamonti, R. Dièvart, J. Brozek, S. Haulon, C. Zawadzki, B. Jude, G. Torpier, N. Marx, B. Staels, G. Chinetti-Gbaguidi, PPARγ activation primes human monocytes into alternative M2 macrophages with anti-inflammatory properties, Cell Metabol. 6 (2007) 137–143, https://doi.org/10.1016/j.cmet.2007.06.010.
[63] S. Wallner, M. Grandl, T. Konovalova, A. Sigrüner, T. Kopf, M. Peer, E. Orsó, G. Liebisch, G. Schmitz, Monocyte to macrophage differentiation goes along with modulation of the plasmalogen pattern through transcriptional regulation, PLoS One 9 (2014), https://doi.org/10.1371/journal.pone.0094102.
[64] F.O. Martinez, S. Gordon, M. Locati, A. Mantovani, Transcriptional profiling of the human monocyte-to-macrophage differentiation and polarization: new molecules and patterns of gene expression, J. Immunol. 177 (2006) 7303–7311, https://doi.org/10.4049/jimmunol.177.10.7303.
[65] K. Németh, A. Leelahavanichkul, P.S.T. Yuen, B. Mayer, A. Parmelee, K. Doi,

P.G. Robey, K. Leelahavanichkul, B.H. Koller, J.M. Brown, X. Hu, I. Jelinek, R.A. Star, É. Mezey, Bone marrow stromal cells attenuate sepsis via prostaglandin E2–dependent reprogramming of host macrophages to increase their interleukin-10 production, Nat. Med. 15 (2009) 42–49, https://doi.org/10.1038/nm.1905.
[66] D.M. Nikolic, M.C. Gong, J. Turk, S.R. Post, Class A scavenger receptor-mediated macrophage adhesion requires coupling of calcium-independent phospholipase A(2) and 12/15-lipoxygenase to Rac and Cdc42 activation, J. Biol. Chem. 282 (2007) 33405–33411, https://doi.org/10.1074/jbc.M704133200.
[67] H. Sakamoto, M. Aikawa, C.C. Hill, D. Weiss, W.R. Taylor, P. Libby, R.T. Lee, Biomechanical strain induces class a scavenger receptor expression in human monocyte/macrophages and THP-1 cells: a potential mechanism of increased atherosclerosis in hypertension, Circulation 104 (2001) 109–114, https://doi.org/10.1161/hc2701.091070.
[68] L. Zhang, Y. Li, M. Chen, X. Su, D. Yi, P. Lu, D. Zhu, 15-LO/15-HETE mediated vascular adventitia fibrosis via p38 MAPK-dependent TGF-β, J. Cell. Physiol. 229 (2014) 245–257, https://doi.org/10.1002/jcp.24443.
[69] C. Abrial, S. Grassin-Delyle, H. Salvator, M. Brollo, E. Naline, P. Devillier, 15-Lipoxygenases regulate the production of chemokines in human lung macrophages, Br. J. Pharmacol. 172 (2015) 4319–4330, https://doi.org/10.1111/bph.13210.
[70] C. Liu, D. Xu, L. Liu, F. Schain, A. Brunnström, M. Björkholm, H.-E. Claesson, J. Sjöberg, 15-Lipoxygenase-1 induces expression and release of chemokines in cultured human lung epithelial cells, Am. J. Physiol. Lung Cell Mol. Physiol. 297 (2009), https://doi.org/10.1152/ajplung.00036.2008. L196-203.
[71] Y. Wen, J. Gu, S.K. Chakrabarti, K. Aylor, J. Marshall, Y. Takahashi, T. Yoshimoto, J.L. Nadler, The role of 12/15-lipoxygenase in the expression of interleukin-6 and tumor necrosis factor-alpha in macrophages, Endocrinology 148 (2007) 1313–1322, https://doi.org/10.1210/en.2006-0665.
[72] J.N. Walters, J.S. Bickford, D.E. Beachy, K.J. Newsom, J.-D.H. Herlihy, M.V. Peck, X. Qiu, H.S. Nick, cPLA(2)α gene activation by IL-1β is dependent on an upstream kinase pathway, enzymatic activation and downstream 15-lipoxygenase activity: a positive feedback loop, Cell. Signal. 23 (2011), https://doi.org/10.1016/j.cellsig.2011.07.002, 1944–51.
[73] E. Gilberg, M. Gütschow, J. Bajorath, X-ray structures of target-ligand complexes containing compounds with assay interference potential, J. Med. Chem. 61 (2018) 1276–1284, https://doi.org/10.1021/acs.jmedchem.7b01780.
[74] T. Mendgen, C. Steuer, C.D. Klein, Privileged scaffolds or promiscuous binders: a comparative study on rhodanines and related heterocycles in medicinal chemistry, J. Med. Chem. 55 (2012) 743–753, https://doi.org/10.1021/jm201243p.
[75] T.M. Ibrahim, M.R. Bauer, F.M. Boeckler, Applying DEKOIS 2.0 in structure-based virtual screening to probe the impact of preparation procedures and score normalization, J. Cheminf. 7 (2015) 21, https://doi.org/10.1186/s13321-015-0074-6.
[76] G. Carta, A.J.S. Knox, D.G. Lloyd, Unbiasing scoring Functions: a new normalization and rescoring strategy, J. Chem. Inf. Model. 47 (2007) 1564–1571, https://doi.org/10.1021/ci600471m.
[77] Y. Pan, N. Huang, S. Cho, A.D. MacKerell, Consideration of molecular weight during compound selection in virtual target-based database screening, J. Chem. Inf. Comput. Sci. 43 (2003) 267–272, https://doi.org/10.1021/ci020055f.
[78] C. Charlier, C. Michaux, Dual Inhibition of Cyclooxygenase-2 (COX-2) and 5-lipoxygenase (5-LOX) as a New Strategy to Provide Safer Non-steroidal Anti-inflammatory Drugs, vol. 38, 2003, pp. 645–659, https://doi.org/10.1016/S0223-5234(03)00115-6.
[79] Molinspiration Cheminformatics, http://www.molinspiration.com/cgi-bin/properties, (n.d.).
[80] M.L.L. C., http://molsoft.com/mprop/, (n.d.).
[81] http://preadmet.bmdrc.org/adme-prediction/, (n.d.).
[82] http://www.openmolecules.org/datawarrior/, (n.d.).
[83] C. Abad-Zapatero, Ligand efficiency indices for effective drug discovery, Expert Opin. Drug Discov. 2 (2007) 469–488, https://doi.org/10.1517/17460441.2.4.469.
[84] A.L. Hopkins, C.R. Groom, A. Alex, Ligand efficiency: a useful metric for lead selection, Drug Discov, Today 9 (2004) 430–431, https://doi.org/10.1016/S1359-6446(04)03069-7.
[85] A.L. Hopkins, G.M. Keserü, P.D. Leeson, D.C. Rees, C.H. Reynolds, The role of ligand efficiency metrics in drug discovery, Nat. Rev. Drug Discov. 13 (2014) 105–121, https://doi.org/10.1038/nrd4163.
[86] M.E. Kavanagh, M.R. Doddareddy, M. Kassiou, The development of CNS-active LRRK2 inhibitors using property-directed optimisation, Bioorg. Med. Chem. Lett 23 (2013) 3690–3696, https://doi.org/10.1016/j.bmcl.2013.04.086.
[87] I. Wilkening, G. del Signore, C.P.R. Hackenberger, Synthesis of phosphonamidate peptides by Staudinger reactions of silylated phosphinic acids and esters, Chem. Commun. 47 (2011) 349–351, https://doi.org/10.1039/C0CC02472D.
[88] E.L. Myers, R.T. Raines, A phosphine-mediated conversion of azides into diazo compounds, Angew. Chem. Int. Ed. 48 (2009) 2359–2363, https://doi.org/10.1002/anie.200804689.
[89] H.H. Kinfe, Y.H. Belay, Synthesis and biological evaluation of novel thiosemicarbazone – triazole hybrid compounds antimalarial agents, S. Afr. J. Chem. 66 (2013) 130–135.
[90] K. Lal, P. Yadav, A. Kumar, Synthesis, characterization and antimicrobial activity of 4-((1-benzyl/phenyl-1H-1,2,3-triazol-4-yl)methoxy)benzaldehyde analogues, Med. Chem. Res. 25 (2016) 644–652, https://doi.org/10.1007/s00044-016-1515-0.
[91] M.E. Fernyhough, J.L. Vierck, G.J. Hausman, P.S. Mir, E.K. Okine, M.V. Dodson, Primary adipocyte culture: adipocyte purification methods may lead to a new understanding of adipose tissue growth and development, Cytotechnology 46 (2004) 163–172, https://doi.org/10.1007/s10616-005-2602-0.
[92] S.B. Vasamsetti, S. Karnewar, A.K. Kanugula, A.R. Thatipalli, J.M. Kumar, S. Kotamraju, Metformin inhibits monocyte-to-macrophage differentiation via AMPK-mediated inhibition of STAT3 activation: potential role in atherosclerosis, Diabetes 64 (2015) 2028–2041, https://doi.org/10.2337/db14-1225.
[93] E.K. Park, H.S. Jung, H.I. Yang, M.C. Yoo, C. Kim, K.S. Kim, Optimized THP-1 differentiation is required for the detection of responses to weak stimuli, Inflamm. Res. 56 (2007) 45–50, https://doi.org/10.1007/s00011-007-6115-5.
[94] M. Fereidoni, A. Ahmadiani, S. Semnanian, M. Javan, An accurate and simple method for measurement of paw edema, J. Pharmacol. Toxicol. Methods 43 (2000) 11–14, https://doi.org/10.1016/S1056-8719(00)00089-7.
[95] H. Rajapaksha, H. Bhatia, K. Wegener, N. Petrovsky, J.B. Bruning, X-ray crystal structure of rivoglitazone bound to PPARγ and PPAR subtype selectivity of TZDs, Biochim. Biophys. Acta Gen. Subj. 1861 (2017) 1981–1991, https://doi.org/10.1016/j.bbagen.2017.05.008.
[96] W. Kabsch, Xds, Acta Crystallogr. Sect. D Biol. Crystallogr. 66 (2010) 125–132, https://doi.org/10.1107/S0907444909047337.
[97] A.J. McCoy, Solving structures of protein complexes by molecular replacement with Phaser, Acta Crystallogr. Sect. D Biol. Crystallogr. 63 (2006) 32–41, https://doi.org/10.1107/S0907444906045975.
[98] P.V. Afonine, R.W. Grosse-Kunstleve, N. Echols, J.J. Headd, N.W. Moriarty, M. Mustyakimov, T.C. Terwilliger, A. Urzhumtsev, P.H. Zwart, P.D. Adams, Towards automated crystallographic structure refinement with phenix.refine, Acta Crystallogr. Sect. D Biol. Crystallogr. 68 (2012) 352–367, https://doi.org/10.1107/S0907444912001308.
[99] P. Emsley, B. Lohkamp, W.G. Scott, K. Cowtan, Features and development of Coot, Acta Crystallogr. Sect. D Biol. Crystallogr. 66 (2010) 486–501, https://doi.org/10.1107/S0907444910007493.
[100] C.J. Williams, J.J. Headd, N.W. Moriarty, M.G. Prisant, L.L. Videau, L.N. Deis, V. Verma, D.A. Keedy, B.J. Hintze, V.B. Chen, S. Jain, S.M. Lewis, W.B. Arendall, J. Snoeyink, P.D. Adams, S.C. Lovell, J.S. Richardson, D.C. Richardson, MolProbity: more and better reference data for improved all-atom structure validation, Protein Sci. 27 (2018) 293–315, https://doi.org/10.1002/pro.3330.
[101] P.V. Afonine, N.W. Moriarty, M. Mustyakimov, O.V. Sobolev, T.C. Terwilliger, D. Turk, A. Urzhumtsev, P.D. Adams, FEM: Feature-enhanced map, Acta Crystallogr. Sect. D Biol. Crystallogr. 71 (2015) 646–666, https://doi.org/10.1107/S1399004714028132.
[102] N. Demirbas, S.A. Karaoglu, A. Demirbas, K. Sancak, Synthesis and antimicrobial activities of some new 1-(5-phenylamino-[1,3,4]thiadiazol-2-yl) methyl-5-oxo-[1,2,4]triazole and 1-(4-phenyl-5-thioxo-[1,2,4]triazol-3-yl) methyl-5-oxo- [1,2,4]triazole derivatives, Eur. J. Med. Chem. 39 (2004) 793–804. https://doi.org/10.1016/j.ejmech.2004.06.007.
[103] N.M. O'Boyle, M. Banck, C.A. James, C. Morley, T. Vandermeersch, G.R. Hutchison, Open Babel: an open chemical toolbox, J. Cheminf. 3 (2011) 33, https://doi.org/10.1186/1758-2946-3-33.
[104] L. Delano, Scientific, the PyMOL Molecular Graphics System, Version 1.1eval, 2008.
[105] T.M. Ibrahim, M.R. Bauer, A. Dörr, E. Veyisoglu, F.M. Boeckler, pROC-chemotype plots enhance the interpretability of benchmarking results in structure-based virtual screening, J. Chem. Inf. Model. 55 (2015) 2297–2307, https://doi.org/10.1021/acs.jcim.5b00475.
[106] M.R. Berthold, N. Cebron, F. Dill, T.R. Gabriel, T. Kötter, T. Meinl, P. Ohl, C. Sieb, K. Thiel, B. Wiswedel, in: C. Preisach, H. Burkhardt, L. Schmidt-Thieme, R. Decker (Eds.), KNIME: the Konstanz Information Miner BT - Data Analysis, Machine Learning and Applications, Springer Berlin Heidelberg, Berlin, Heidelberg, 2008, pp. 319–326.

Supporting Information

Shooting Three Inflammatory Targets with a Single Bullet: Novel Multi-Targeting Anti-Inflammatory Glitazones

Perihan A. Elzahhar[a], Rana Alaaeddine[b], Tamer M. Ibrahim[c], Rasha Nassra[d], Azza Ismail[a], Benjamin S.K. Chua[e], Rebecca L. Frkic[f], John B. Bruning[f], Nadja Wallner[g], Tilo Knape[g], Andreas von Knethen[g,h], Hala Labib[a,i], Ahmed F . El-Yazbi[b,j*], Ahmed S. F. Belal[a*]

[a]Department of Pharmaceutical Chemistry, Faculty of Pharmacy, Alexandria University, Alexandria 21521, Egypt.
[b]Department of Pharmacology and Toxicology, Faculty of Medicine and Medical Centre, American University of Beirut, Beirut, Lebanon.
[c]Department of Pharmaceutical Chemistry, Faculty of Pharmacy, Kafr-Elsheikh University, Kafr El-Sheikh 33516, Egypt.
[d]Department of Medical Biochemistry, Faculty of Medicine, Alexandria University, Egypt.
[e]School of Biological Sciences, The University of Adelaide, Adelaide, South Australia 5005, Australia.
[f]Institute for Photonics and Advanced Sensing, The School of Biological Sciences, the University of Adelaide, North Tce, Adelaide, South Australia 5005, Australia.
[g]Fraunhofer Institute for Molecular Biology and Applied Ecology IME, Project Group Translational Medicine & Pharmacology TMP, Theodor-Stern-Kai 7, 60596 Frankfurt, Germany.
[h]Institute of Biochemistry I, Faculty of Medicine, Goethe-University Frankfurt, Theodor-Stern-Kai 7, 60590 Frankfurt, Germany.
[i]Department of Pharmaceutical Chemistry, College of Pharmacy, Arab Academy for Science, Technology and Maritime Transport, Alexandria, Egypt.
[j]Department of Pharmacology and Toxicology, Faculty of Pharmacy, Alexandria University, Alexandria 21521, Egypt.

Contents:

Table SM1. Docking scores of GOLD (ChemPLP), AutoDock Vina and Autodock VinaXB for all the proposed compounds.

Gold docking		AutoDock Vina docking		AutoDock VinaXB docking	
Cpd ID	**Fitness**	**Cpd ID**	**Score**	**Cpd ID**	**Score**
5i	100.61	6j	-10.1	6j	-10.1
5j	95.48	5j	-10.1	5j	-10.1
5b	93.83	5i	-10.1	5i	-10.1
6b	92.37	6i	-10	6i	-9.9
Co-crys Ligand	91.44	5e	-9.7	5d	-9.7
5h	89.98	6b	-9.6	5e	-9.7
6i	89.02	6d	-9.6	6d	-9.6
6j	88.99	6e	-9.6	6h	-9.6
5g	88.22	6h	-9.6	5b	-9.6
5e	87.20	5b	-9.6	5h	-9.6
5a	86.91	5d	-9.6	6a	-9.5
5d	86.44	5h	-9.6	6e	-9.5
5c	84.09	6a	-9.5	5c	-9.5
6h	83.99	6c	-9.4	5g	-9.5
6g	83.72	6g	-9.4	6c	-9.4
6e	82.99	5c	-9.4	6g	-9.4
6d	82.86	5g	-9.4	5a	-9.3
6c	78.03	5a	-9.3	6b	-9.1
6a	76.79	Co-crys Ligand	-8.3	Co-crys Ligand	-8.2

Table SM2: *In vivo* anti-inflammatory activities of selected compounds in formalin-induced rat paw edema bioassay (acute inflammation model)

Comp. Group ID		Volume of edema (ml)		Abs. diff.	% Inhibition	%Relative potency (Celecoxib)	%Relative potency (Diclofenac)
		0	4h				
Vehicle (DMSO) Control	1	4.48	6.47	1.99			
	2	4.3	6.57	2.27			
	3	3.85	6.11	2.26			
	4	4.2	6.4	2.1			
Mean ± SD		4.2 ± 0.3	6.4± 0.2	2.2 ± 0.1			
Reference1 standard (Celecoxib)	1	4.25	5.49	1.24	37.7		
	2	4.44	5.47	1.03	54.6		
	3	4.22	6.1	1.88	16.8		
	4	4.3	5.7	1.4	38.1		
Mean ± SD		4.3 ± 0.10	5.6[a] ± 0.3	1.4[a] ± 0.4	36.8 ± 15.5		
Reference2 standard (Diclofenac)	1	4.45	5.37	0.92	53.8	142.7	
	2	4.39	5.33	0.94	58.6	107.3	
	3	3.94	5.19	1.25	44.7	265.8	
	4	4.3	5.3	1.1	51.3	305.3	
Mean ± SD		4.3 ± 0.2	5.3[a] ± 0.1	1.1[a] ± 0.2	52.1 ± 5.8	**205.3 ± 95.2**	
4b	1	4.38	4.6	0.22	88.9	236.0	165.4
	2	3.38	4.34	0.96	57.7	105.6	98.5
	3	4.35	4.58	0.23	89.8	534.2	201.0
	4	3.35	4.30	0.95	58.0	344.7	129.7
Mean ± SD		3.87 ± 0.58	4.46[abc] ± 0.16	0.59[ab] ± 0.42	73.6[b] ± 18.2	**305.1 ± 181.3**	**148.7 ± 44.3**
5b	1	3.32	4.66	1.34	32.7	86.7	60.7
	2	4.26	4.96	0.7	69.2	126.6	118.0
	3	3.18	4.5	1.32	41.6	247.4	93.1
	4	4.10	4.99	0.89	60.6	360.5	135.6
Mean ± SD		3.72 ± 0.54	4.78 [ab] ± 0.24	1.06[a] ± 0.32	51.0 ± 16.8	**205.3 ± 124.0**	**101.9 ± 32.5**
5e	1	4.08	5.07	0.99	50.3	133.3	93.5
	2	3.06	4.27	1.21	46.7	85.5	79.7
	3	4.11	5.11	1.00	55.8	331.6	124.8
	4	3.10	4.3	1.20	46.9	278.9	105.0
Mean ± SD		3.59 ± 0.59	4.69 [abc] ± 0.47	1.10[a] ± 0.12	49.9 ± 4.3	**207.3 ± 116.7**	**100.8 ± 19.1**
5g	1	3	4.45	1.45	27.1	72.0	50.5
	2	3.63	4.7	1.07	52.9	96.8	90.2
	3	3.07	4.5	1.43	36.7	218.4	82.2
	4	3.58	4.67	1.09	51.8	307.9	115.8
Mean ± SD		3.32[b] ± 0.33	4.58 [abc] ± 0.12	1.26[a] ± 0.21	42.1 ± 12.4	**173.8 ± 109.9**	**84.7 ± 26.9**

a: statistically significant difference in comparison with Control group
b: statistically significant difference in comparison with Reference 1 standard group (Celecoxib)
c: statistically significant difference in comparison with Reference 2 standard group (Diclofenac Na)

Table SM3: Crystallographic data table.

Parameter	**Compound (4b)**
Space group	C2
Cell dimensions *a, b, c* (Å)	92.6, 61.2, 118.1
Monoclinic angle β (deg)	102.39
X-ray source	Synchrotron: Australian Synchrotron MX2
Wavelength (Å)	0.9537
Resolution range (Å)	45-2.5
Last shell (Å)	2.49-2.40
R_{merge} (%)*	8.0 (1.367)
R_{pim}(%)	3.4 (56.7)
CC1/2	0.99 (0.78)
Observations	170339 (17974)
Unique reflections	25380 (2647)
Mean (I)/σ(I)	11.6 (1.3)
Completeness	99.7 (99.8)
Multiplicity	6.7 (6.8)
Structure refinement	
Resolution range (Å)	45.5-2.4
R_{work} (%)	0.2209
R_{free} (%)	0.2677
Total number of	
Non-hydrogen atoms	4142
Protein atoms	4050
Ligand atoms	34
Water molecules	58
RMSD	
Bond length (Å)	0.003
Bond angle (deg)	0.631
Wilson B ($Å^2$)	61.93
Ramachandran statistics	
Most favoured regions (%)	96.2
Allowed regions (%)	2.83
Outliers (%)	1.01

*values in parenthesis represent data in the highest resolution shell

Table SM4. *In silico* physicochemical properties, ADME and ligand efficiency data of compounds **4b**, **5b**, **5e** and **5g**

	4b	**5b**	**5e**	**5g**
LogP[a]	**2.04**	**3.69**	**3.37**	**2.62**
MW[b]	**275.35**	**471.34**	**457.31**	**408.44**
HBA[c]	**3**	**7**	**7**	**8**
HBD[d]	**1**	**1**	**1**	**1**
Lipinski's violation	**0**	**0**	**0**	**0**
TPSA[e]	**42.10**	**89.89**	**89.89**	**99.12**
Volume $(A)^3$	**226.04**	**349.46**	**332.66**	**340.32**
NROTB[f]	**3**	**6**	**5**	**6**
S (mg/L)[g]	**0.98**	**0.03**	**0.03**	**0.24**
Drug likeness model score	**-0.73**	**-0.1**	**-0.44**	**-0.57**
Caco2[h]	**40.82**	**21.71**	**21.45**	**12.86**
HIA[i]	**97.08**	**97.11**	**97.21**	**98.09**
BBB[j]	**0.033**	**0.108**	**0.058**	**0.099**
PPB[k]	**96.47**	**98.80**	**100**	**91.83**
LE[l] (COX-2)	**0.53**	**0.33**	**0.34**	**0.32**
LLE[m]	**5.82**	**4.32**	**4.49**	**5.22**
LELP[n]	**2.09**	**8.10**	**7.17**	**5.04**
LE (15-LOX)	**0.42**	**0.25**	**0.26**	**0.26**
LLE	**4.40**	**2.55**	**2.94**	**3.86**
LELP	**2.63**	**10.84**	**9.23**	**6.29**

[a] **LogP:** logarithm of compound partition coefficient between n-octanol and water. [b] **MW:** molecular weight. [c] **HBA:** number of hydrogen bond acceptors. [d] **HBD:** number of hydrogen bond donors. [e] **TPSA:** topological polar surface area. [f] **NROTB:** number of rotatable bonds. [g] **S:** aqueous solubility. [h] **Caco2:** permeability through cells derived from human colon adenocarcinoma; Caco2 values < 4 nm/s (low permeability), values ranged from 4 to 70 nm/s (medium permeability) and values > 70 nm/s (high permeability). [i] **HIA:** percentage human intestinal absorption; HIA values ranged from 0 to 20% (poorly absorbed), values ranged from 20 to 70% (moderately absorbed) and ranged from 70 to 100% (well absorbed). [j] **BBB:** blood-brain barrier penetration; BBB values < 0.1 (low CNS absorption), values ranged from 0.1 to 2 (medium CNS absorption) and values > 2 (high CNS absorption). [k] **PPB:** plasma protein binding; PPB values < 90% (poorly bound) and values > 90% (strongly bound). [l] **LE:** ligand efficiency (LE = (pIC_{50} x 1.37)/non-hydrogen atoms). [m] **LLE:** lipophilic ligand efficiency *(LLE* = pIC_{50} - *LogP)*. [n] **LELP:** ligand-efficiency-dependent lipophilicity *(LELP = LogP/LE)*.

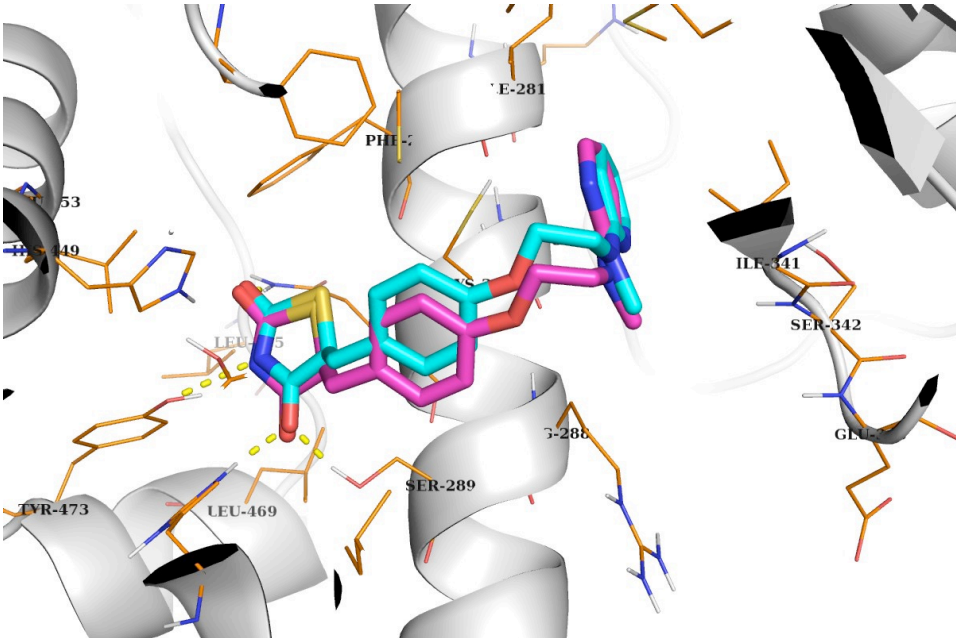

Figure SM1. Overlay of the co-crystallized ligand rosiglitazone (cyan sticks) on its GOLD docking pose (magenta sticks) in PPAR-γ LBD with RMSD= 1.25 Å. Also, the pose-retrieval runs with AutoDock Vina and AutoDock VinaXB yielded acceptable results.

Figure SM2: Electron density map of ligand **4b**. Shown is a $2F_o$-F_c FEM electron density map contoured at 1σ around compound **4b**.

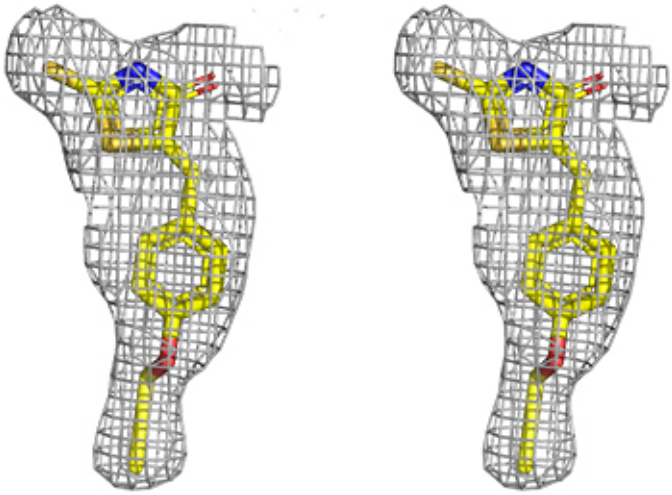

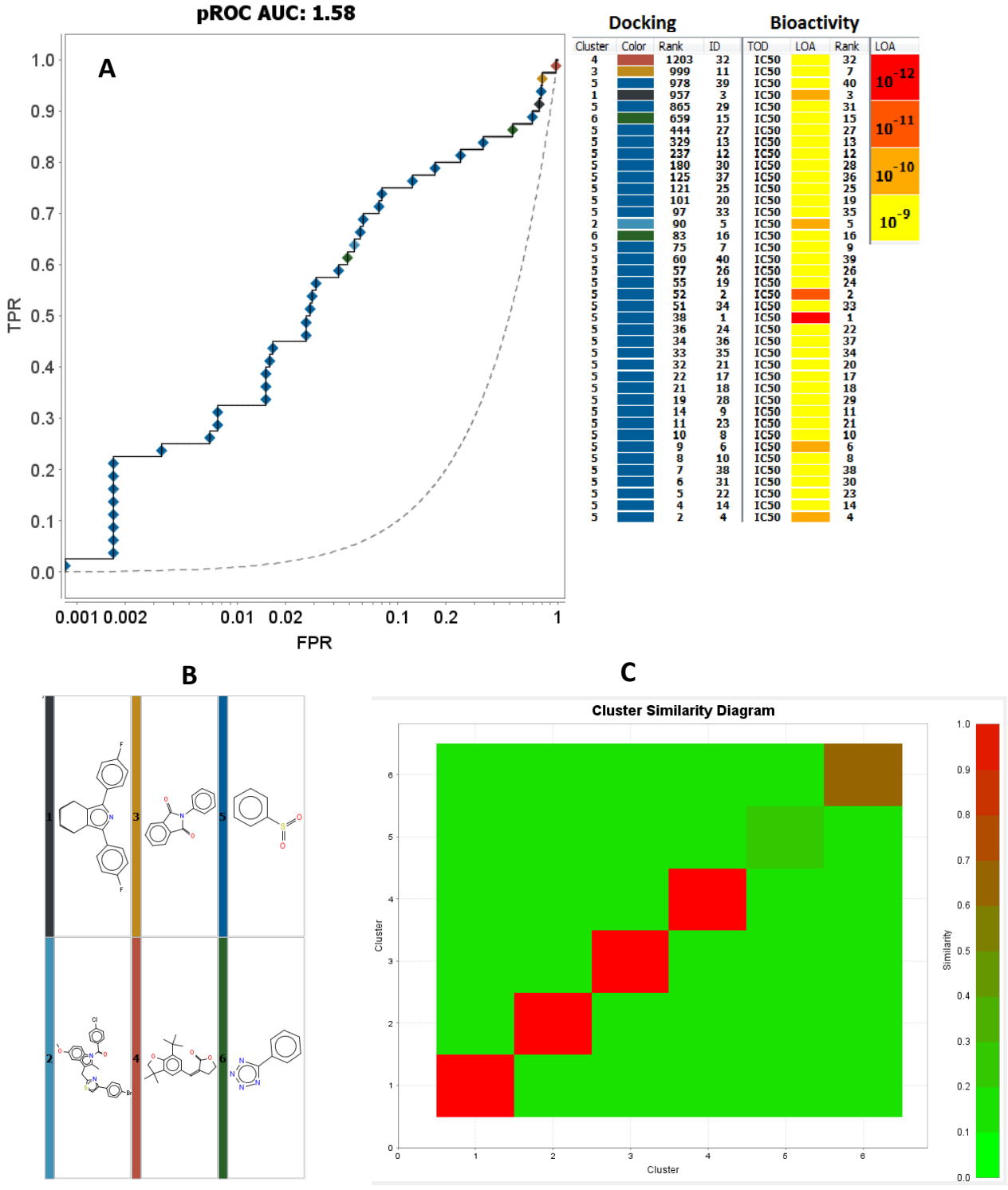

Figure SM3: pROC-Chemotype plot for the original non-normalized score for COX-2 docking by GOLD. (A) pROC Chemotype plot including color-coded pROC curve, annotated by docking (cluster, color and rank) and bioactivity (TOD, LOA and rank) bar. FPR and TPR stand for False and True Positive Rate on the X-axis and Y-axis, respectively. The chemotype legend illustrates the most common substructures of each cluster and their assignment into the color-coded annotation scheme. The docking bar is composed of a cluster number, color code, and docking rank. The bioactivity bar is composed of the type of data (TOD), the level of activity (LOA), and rank information. (B) Clusters of the bioactive ligands based on Maximum common substructure (MCS). (C) Cluster similarity diagram demonstrated as a heat map of the

six chemotype clusters of the COX-2 benchmark set based on the average Tanimoto similarity (Ts) over all cross-cluster pairs (ECFP_6 fingerprints). The color gradient represents changes in the average Ts. Green indicates maximum dissimilarity (Ts ≈ 0), and red indicates maximum similarity (Ts = 1).

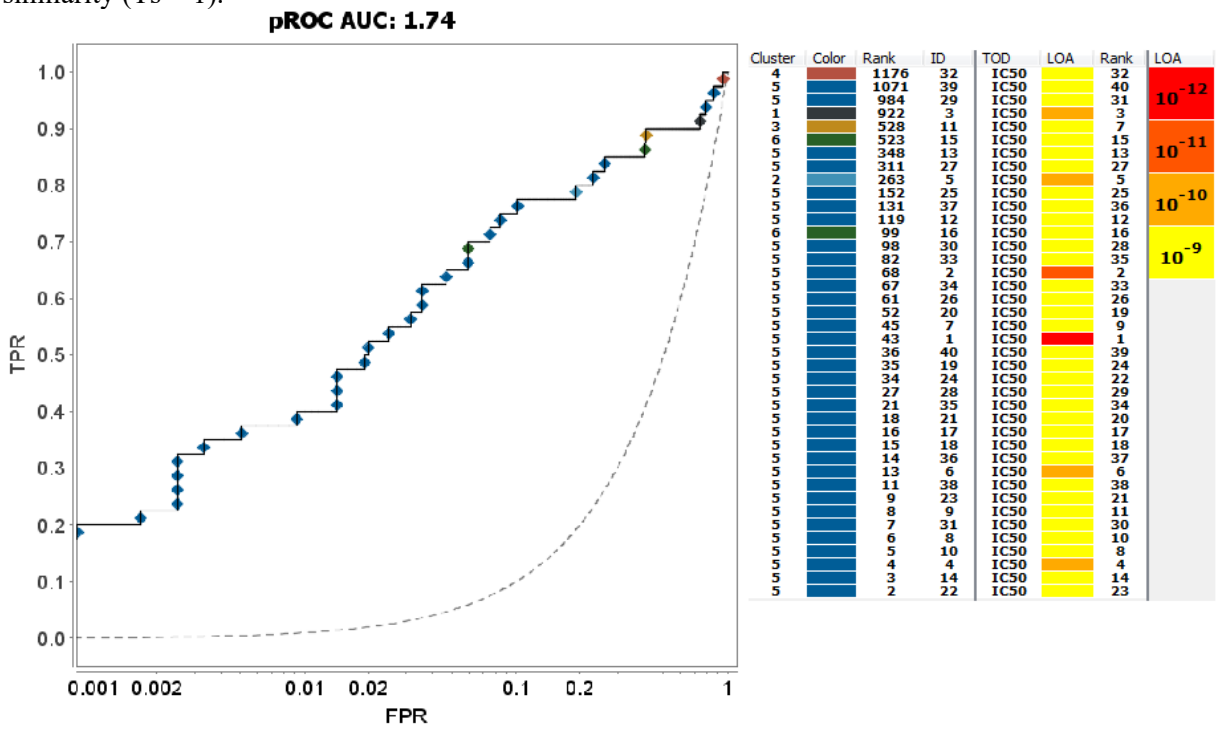

Figure SM4: pROC-Chemotype plot for the $N^{1/3}$ normalized score for COX-2 docking by GOLD.

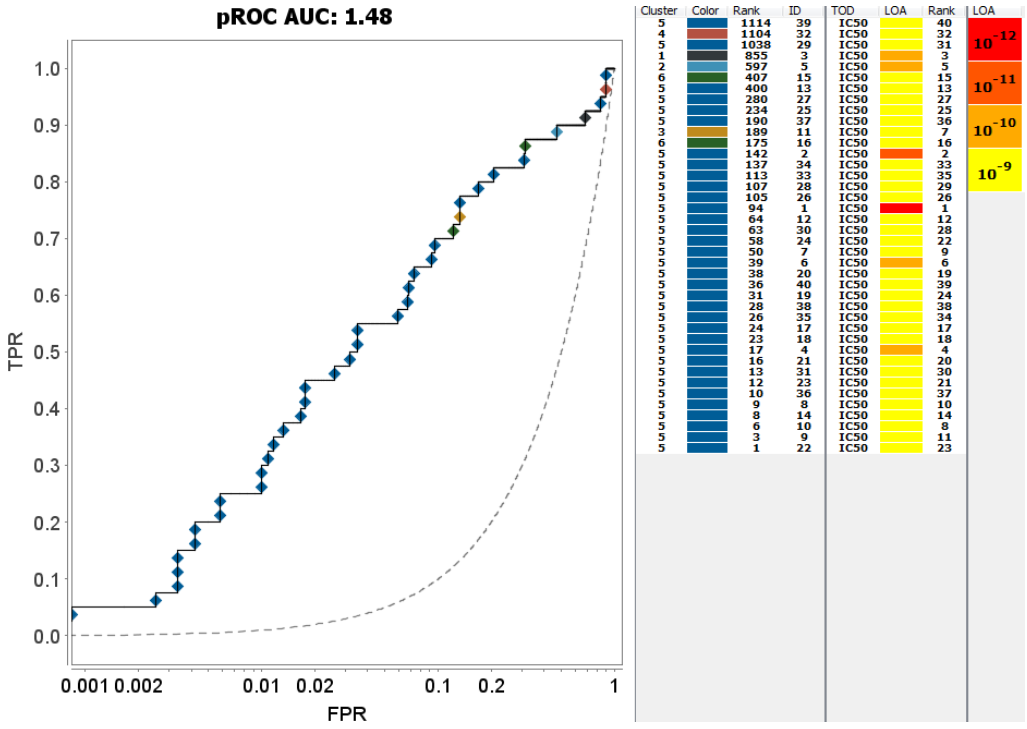

Figure SM5: pROC-Chemotype plot for the $N^{2/3}$ normalized score for COX-2 docking by GOLD.

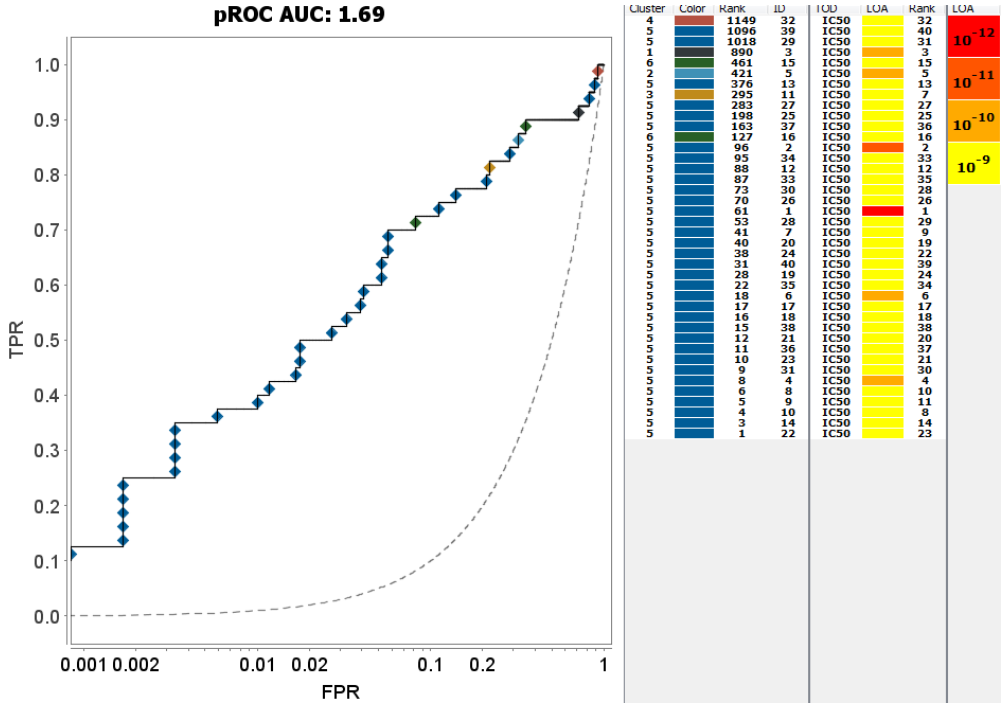

Figure SM6: pROC-Chemotype plot for the $N^{1/2}$ normalized score for COX-2 docking by GOLD.

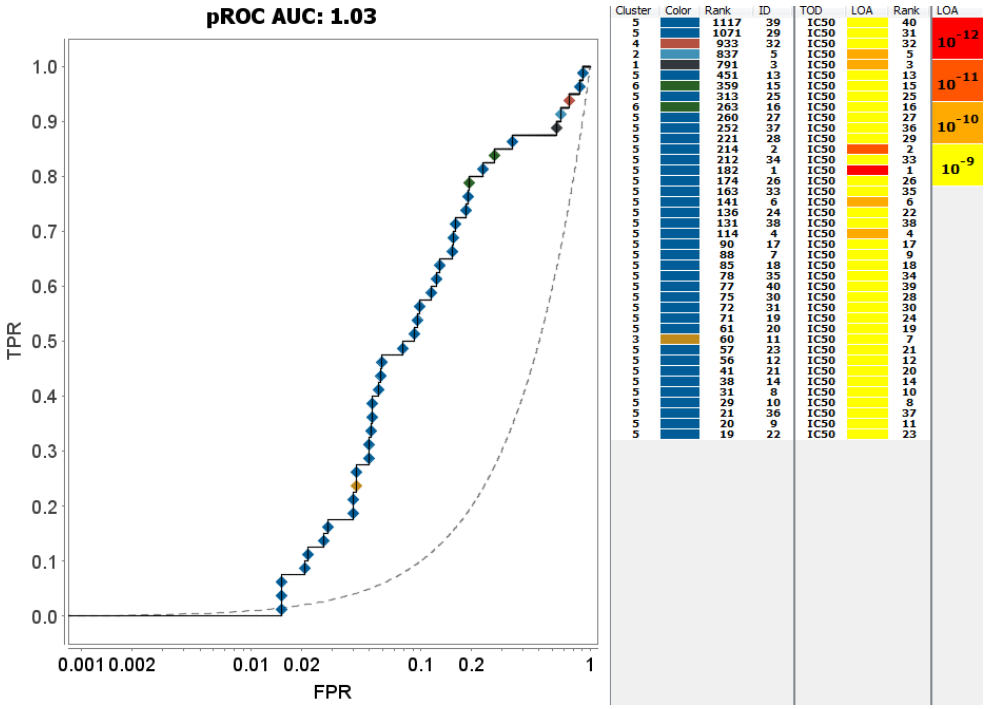

Figure SM7: pROC-Chemotype plot for the N normalized score for COX-2 docking by GOLD.

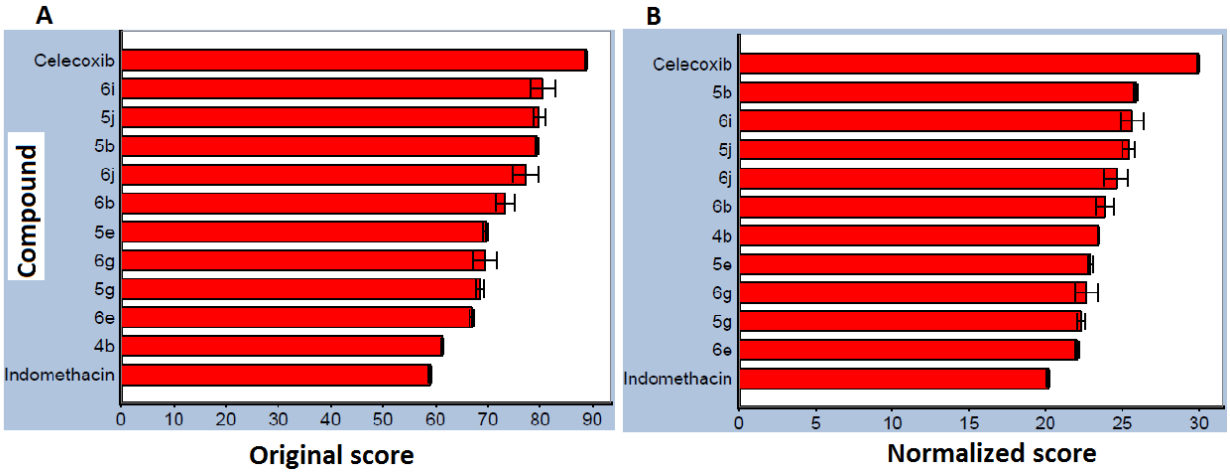

Figure SM8. Chart of the docking score of the synthesized compounds against COX-2 with original non-normalized score **(A)** and $N^{1/3}$ normalized scores **(B)**.

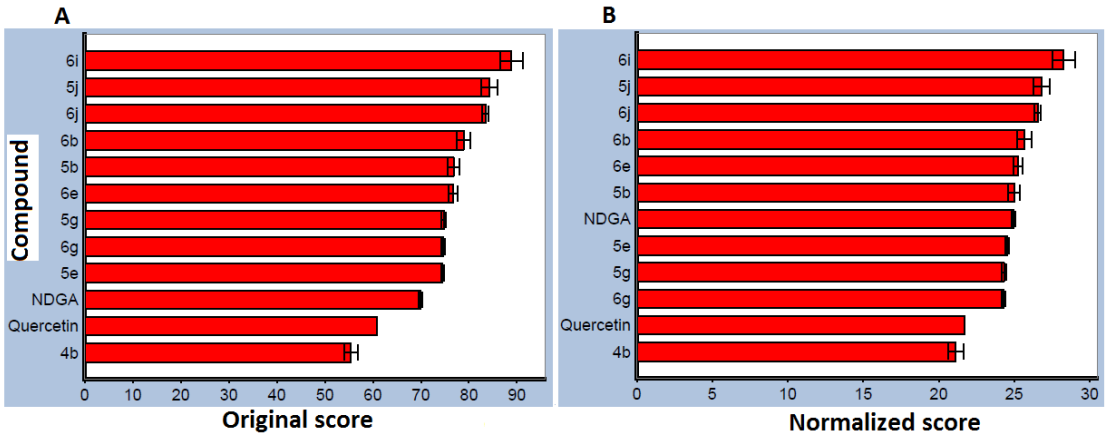

Figure SM9. Chart of the docking score of the synthesized compounds against 15-LOX with original non-normalized score **(A)** and $N^{1/3}$ normalized scores **(B)**

^{1}H-NMR and ^{13}C-NMR spectra:

(*Z*)-5-(4-(prop-2-yn-1-yloxy)benzylidene)thiazolidine-2,4-dione **(4a)**

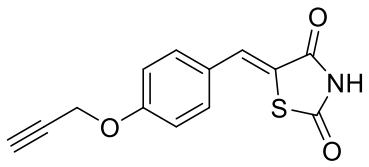

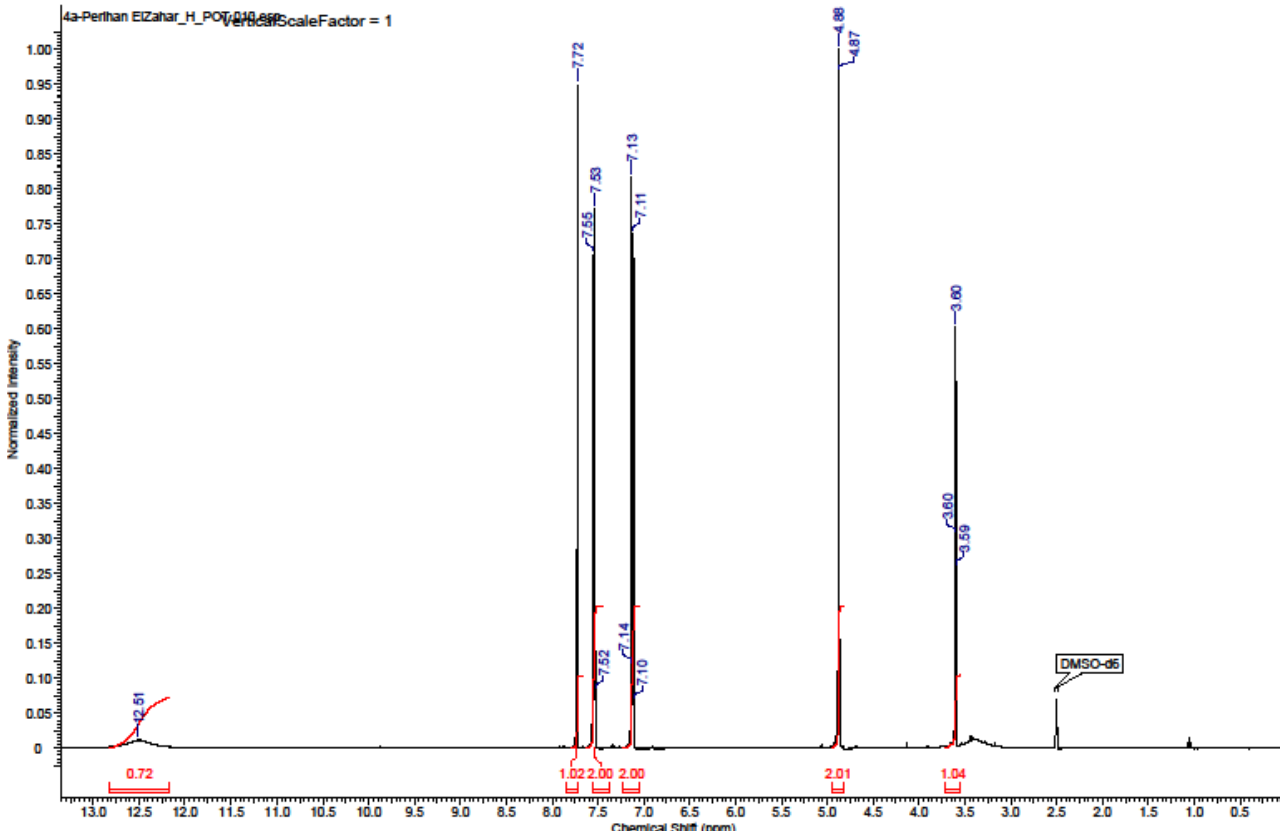

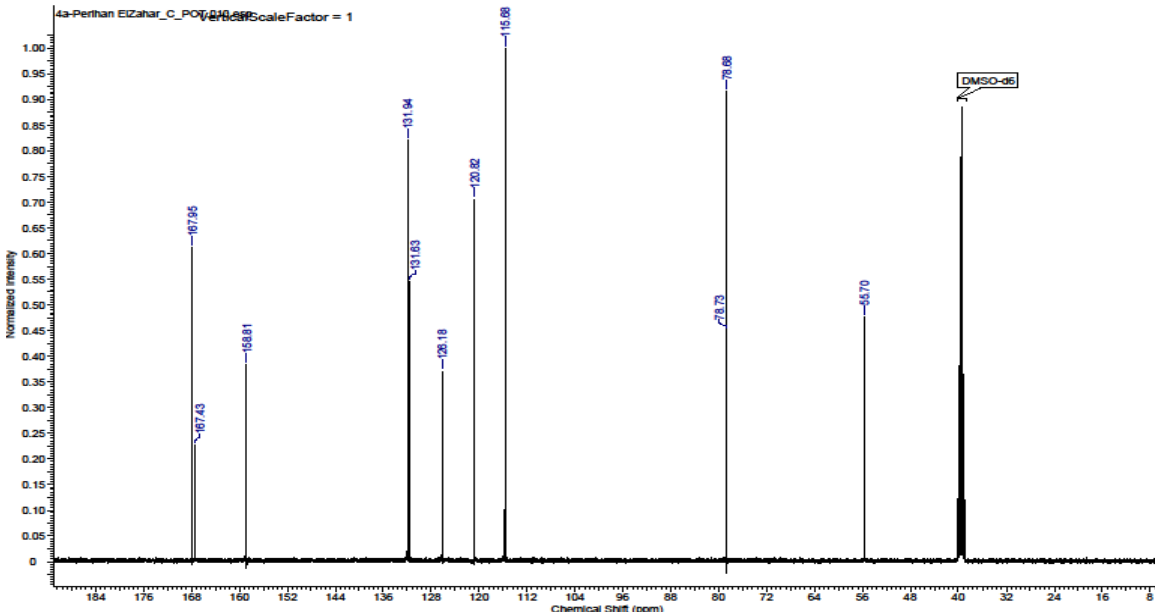

(*Z*)-5-(4-(prop-2-yn-1-yloxy)benzylidene)-2-thioxothiazolidin-4-one **(4b)**

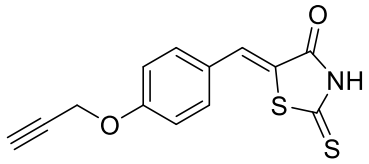

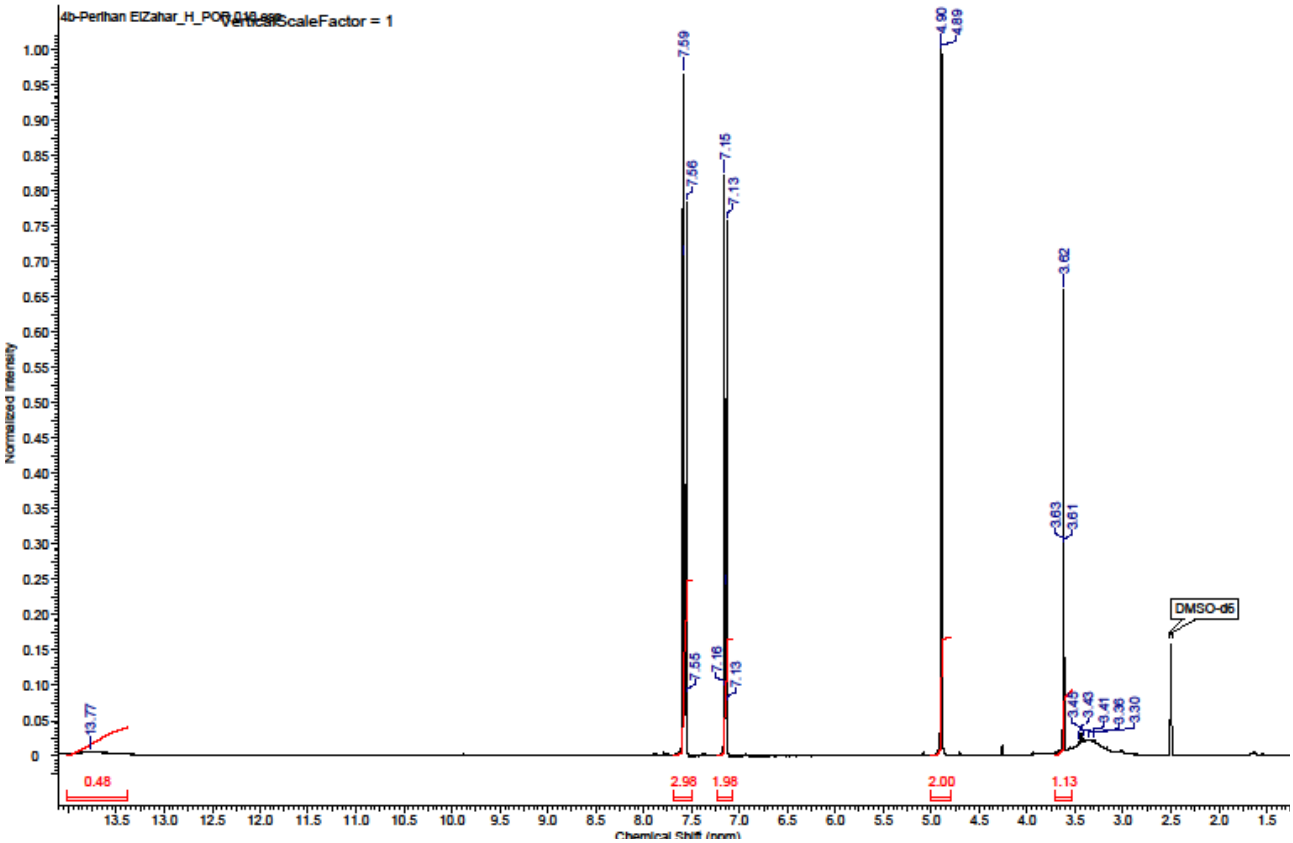

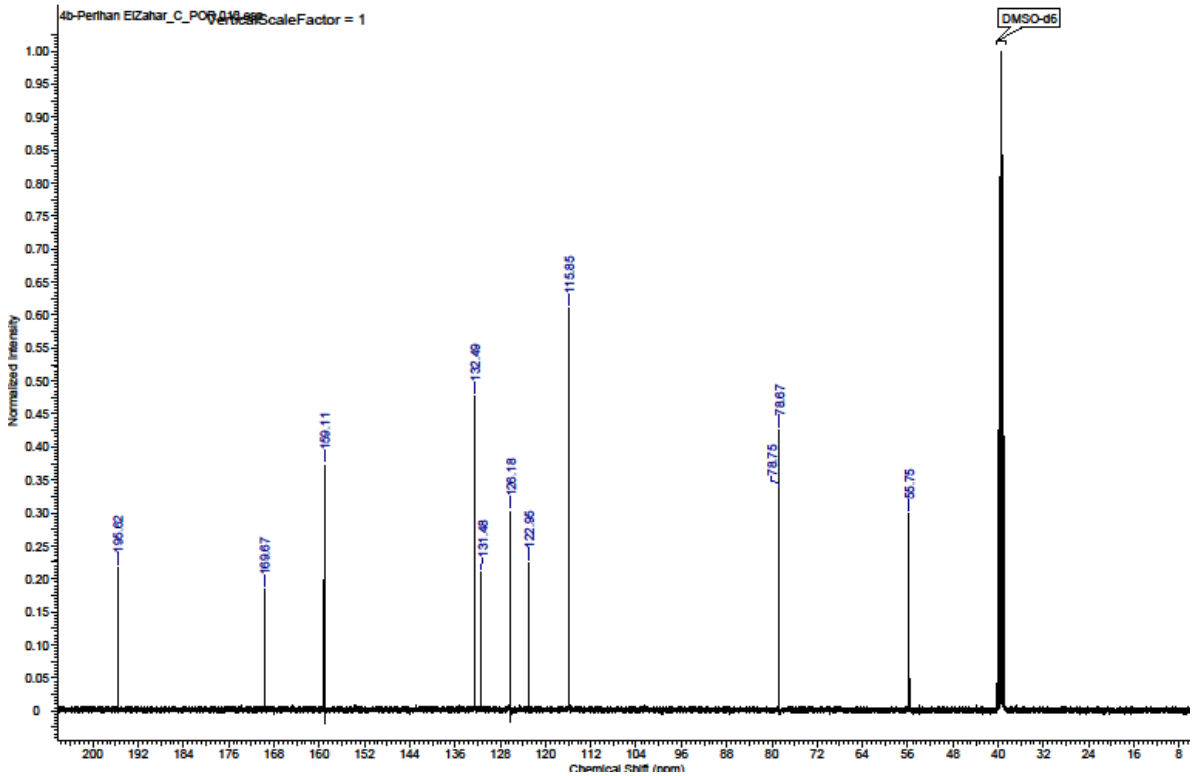

(*Z*)-5-(4-((1-benzyl-1*H*-1,2,3-triazol-4-yl)methoxy)benzylidene)thiazolidine-2,4-dione **(5a)**

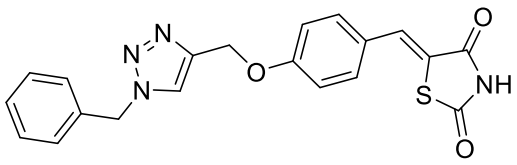

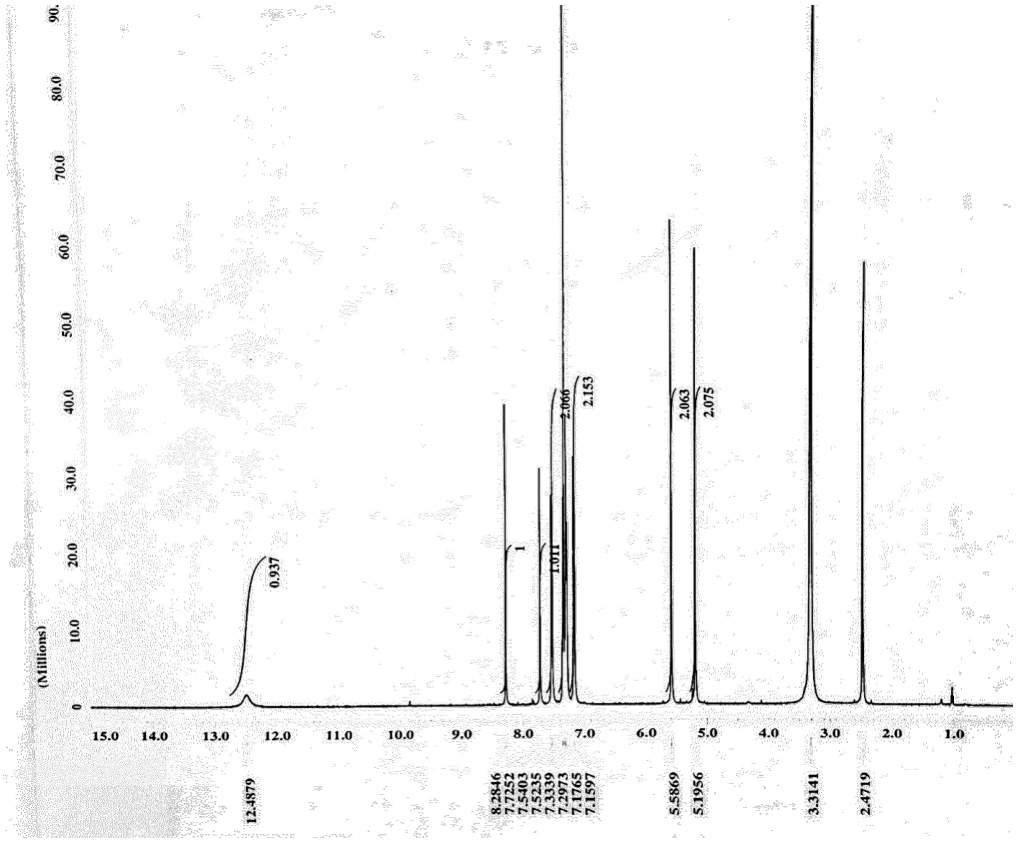

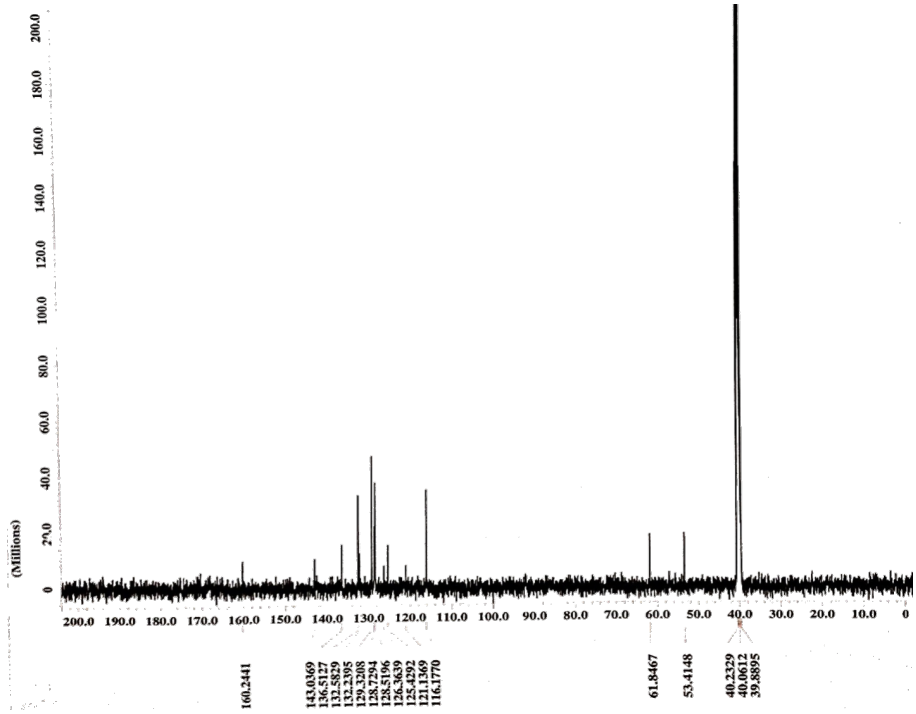

(*Z*)-5-(4-((1-(4-bromobenzyl)-1*H*-1,2,3-triazol-4-yl)methoxy)benzylidene) thiazolidine-2,4-dione **(5b)**

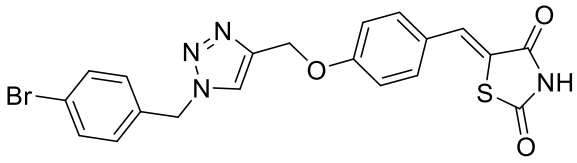

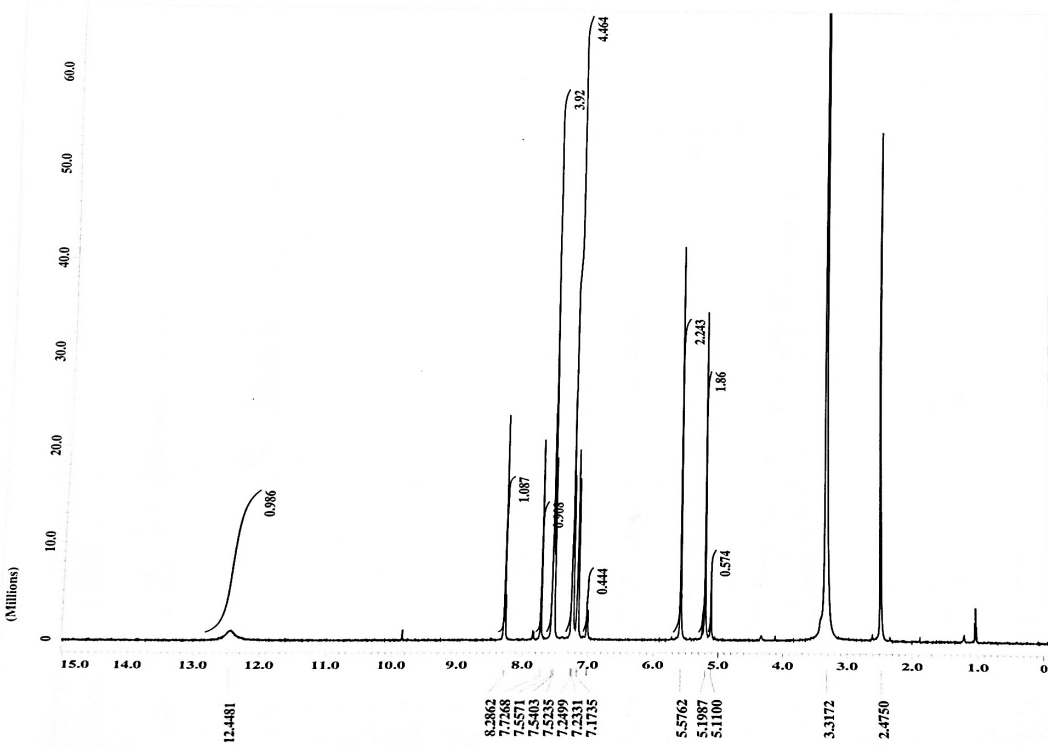

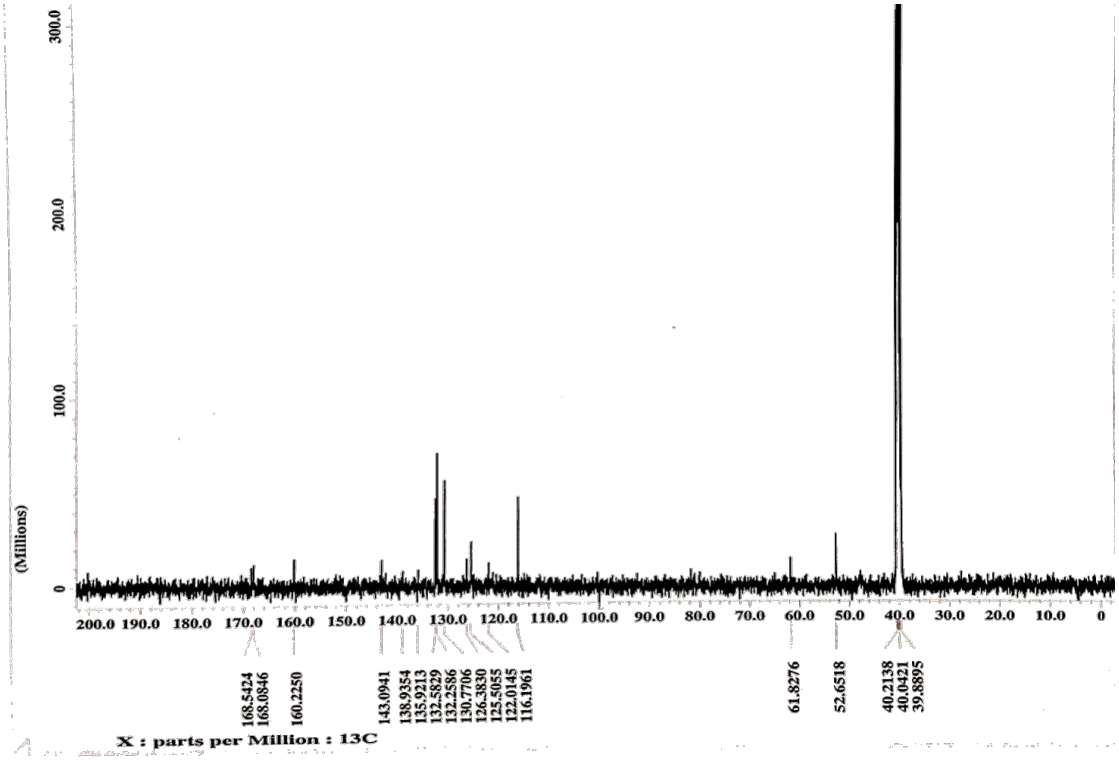

(*Z*)-5-(4-((1-phenyl-1*H*-1,2,3-triazol-4-yl)methoxy)benzylidene)thiazolidine-2,4-dione **(5c)**

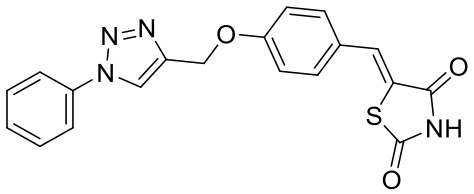

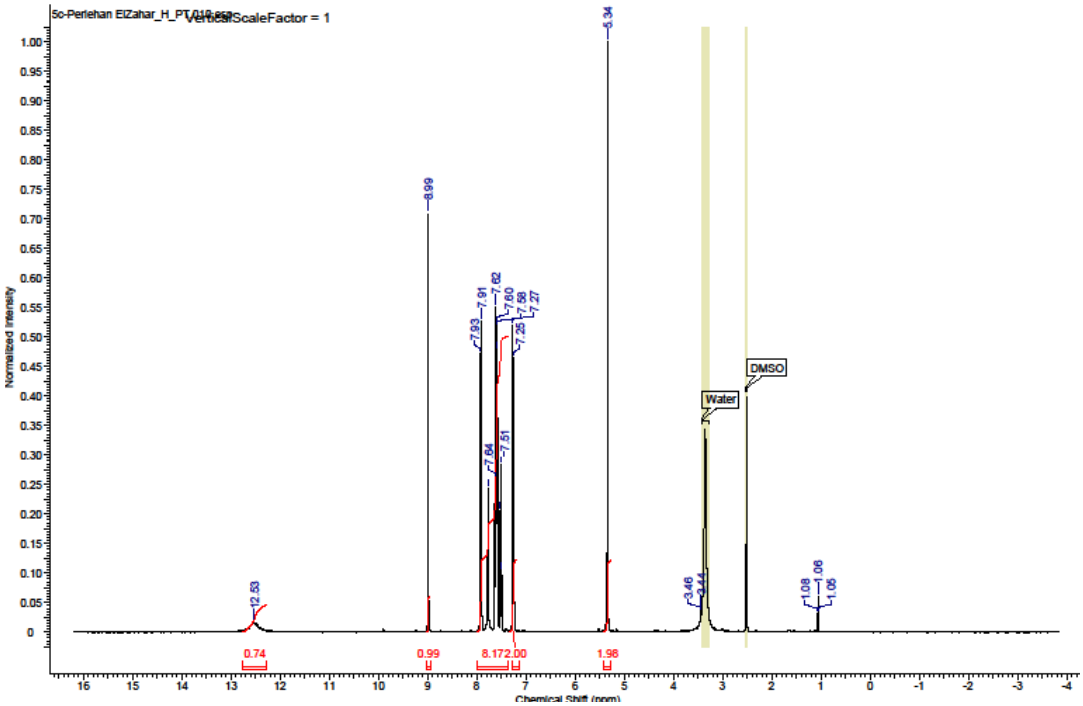

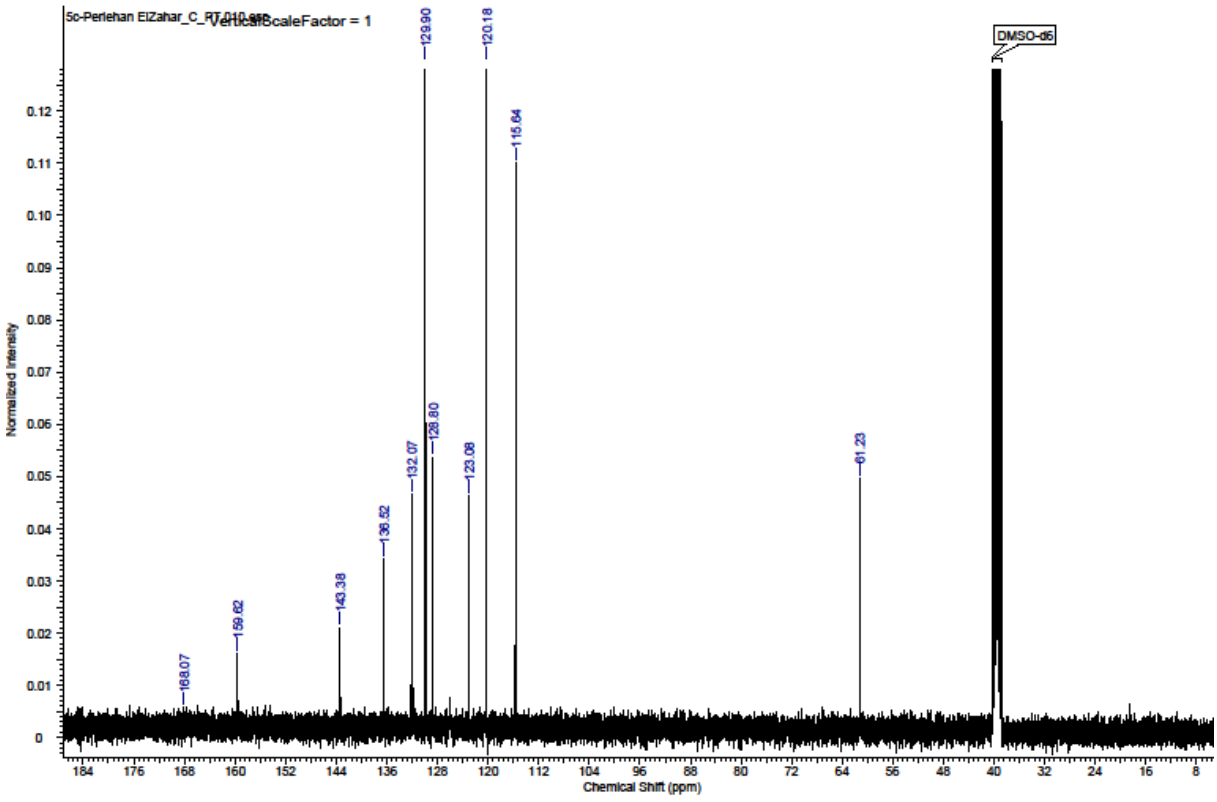

(*Z*)-5-(4-((1-(4-chlorophenyl)-1*H*-1,2,3-triazol-4-yl)methoxy)benzylidene) thiazolidine-2,4-dione **(5d)**

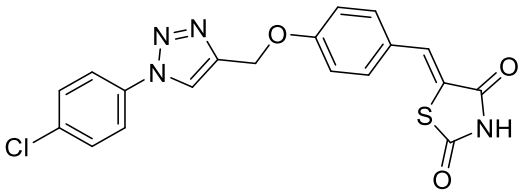

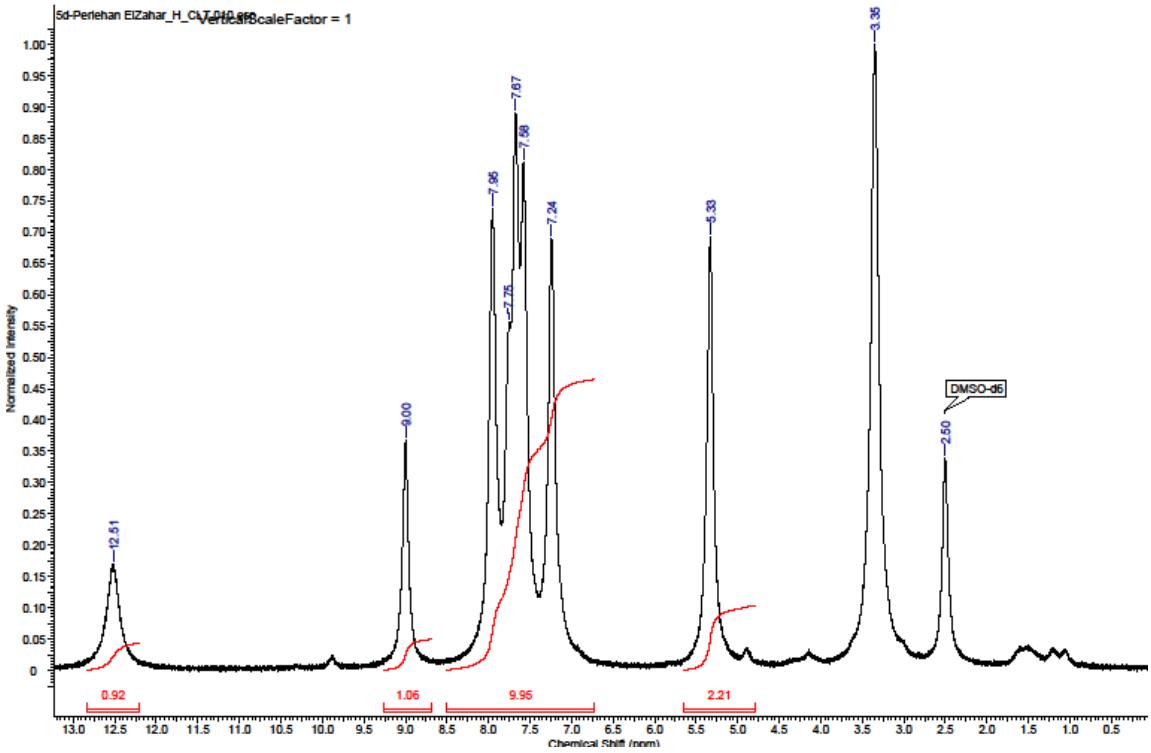

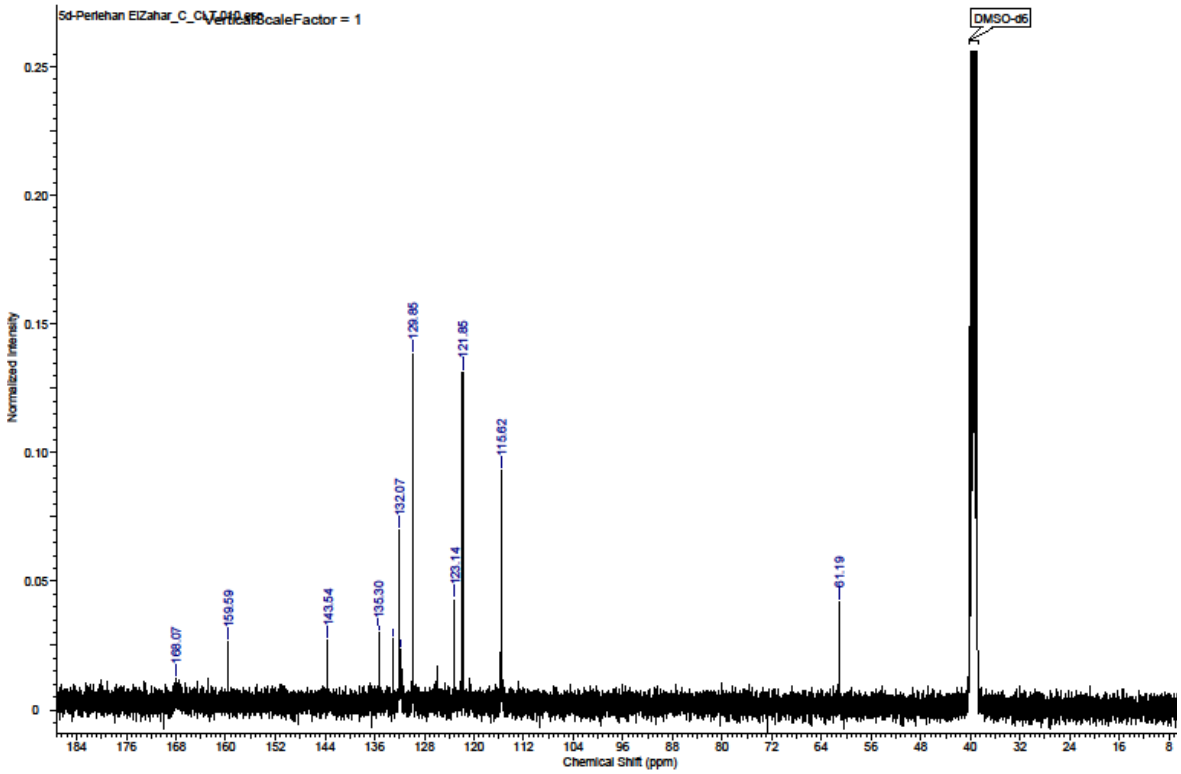

(*Z*)-5-(4-((1-(4-bromophenyl)-1*H*-1,2,3-triazol-4-yl)methoxy)benzylidene) thiazolidine-2,4-dione **(5e)**

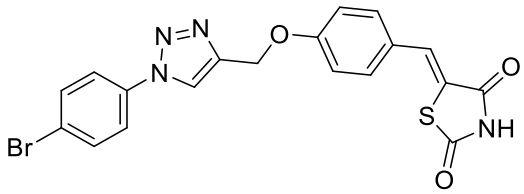

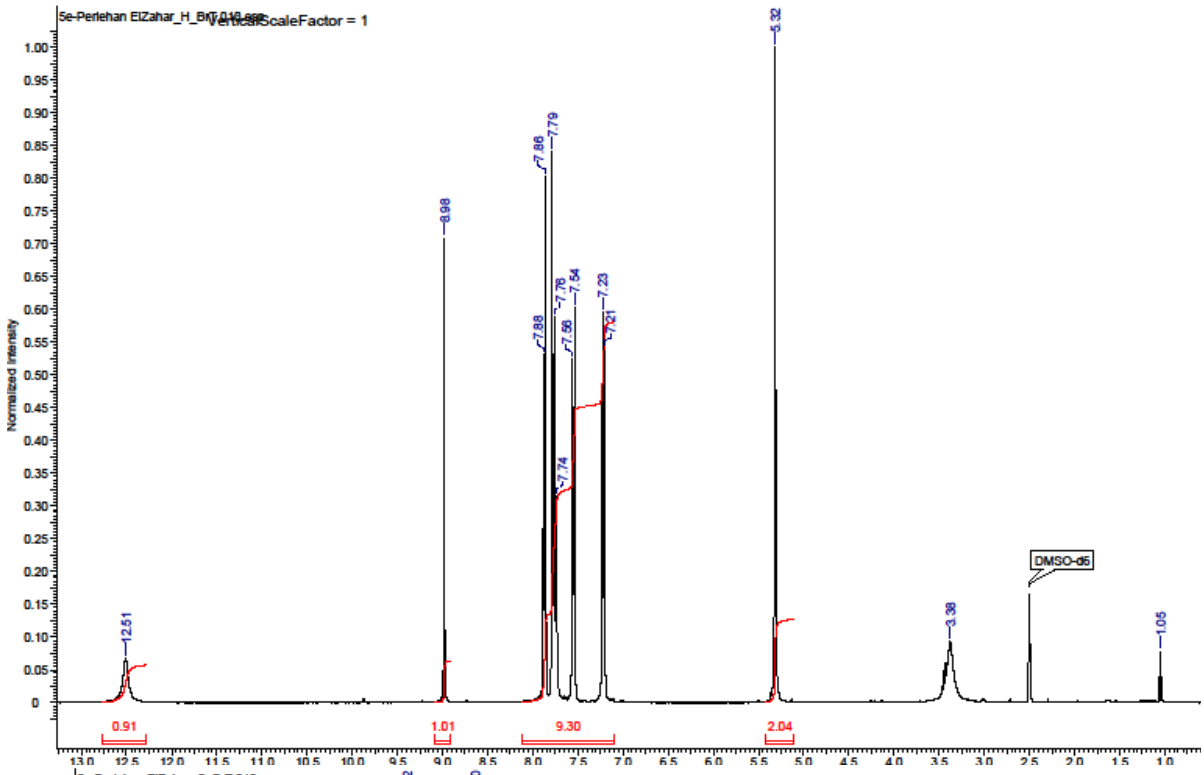

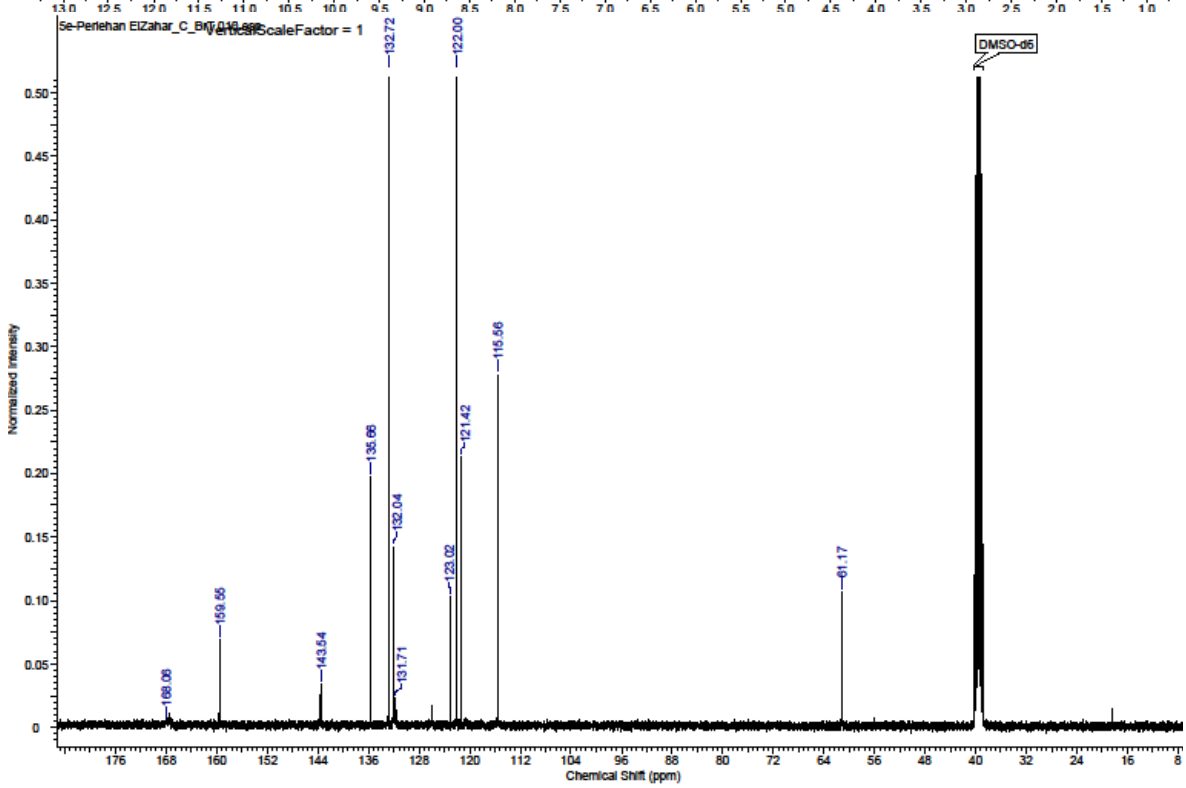

(*Z*)-5-(4-((1-(p-tolyl)-1*H*-1,2,3-triazol-4-yl)methoxy)benzylidene)thiazolidine-2,4-dione **(5f)**

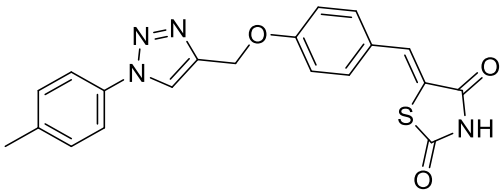

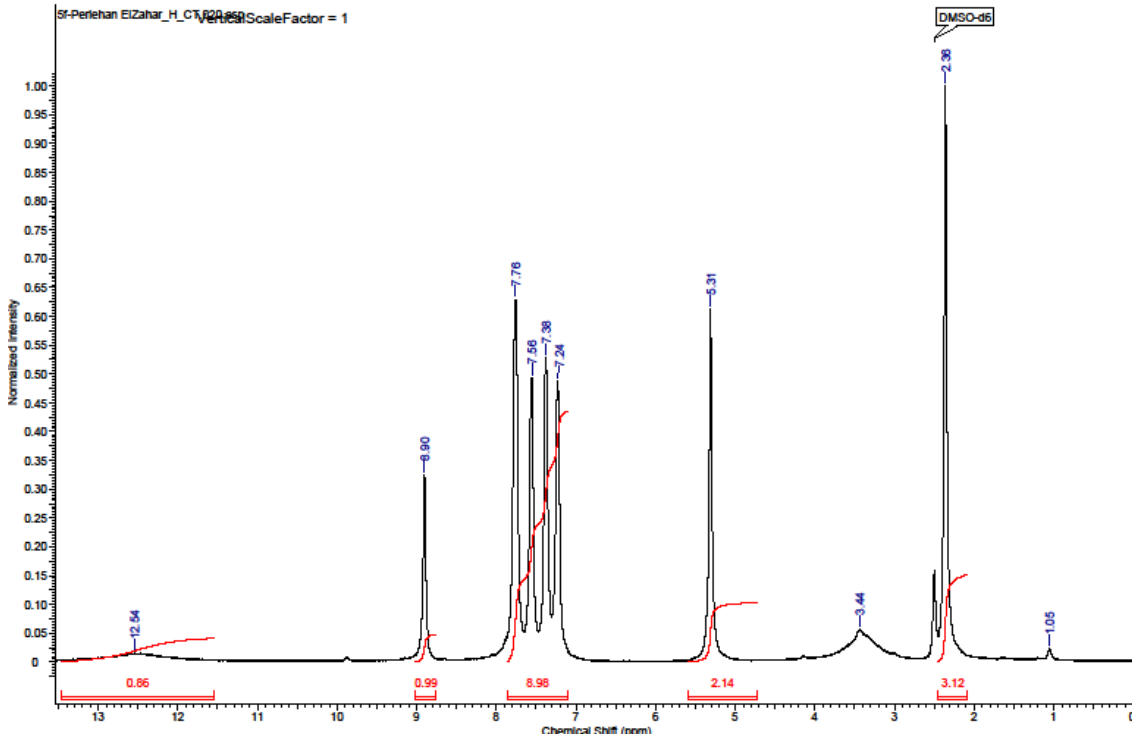

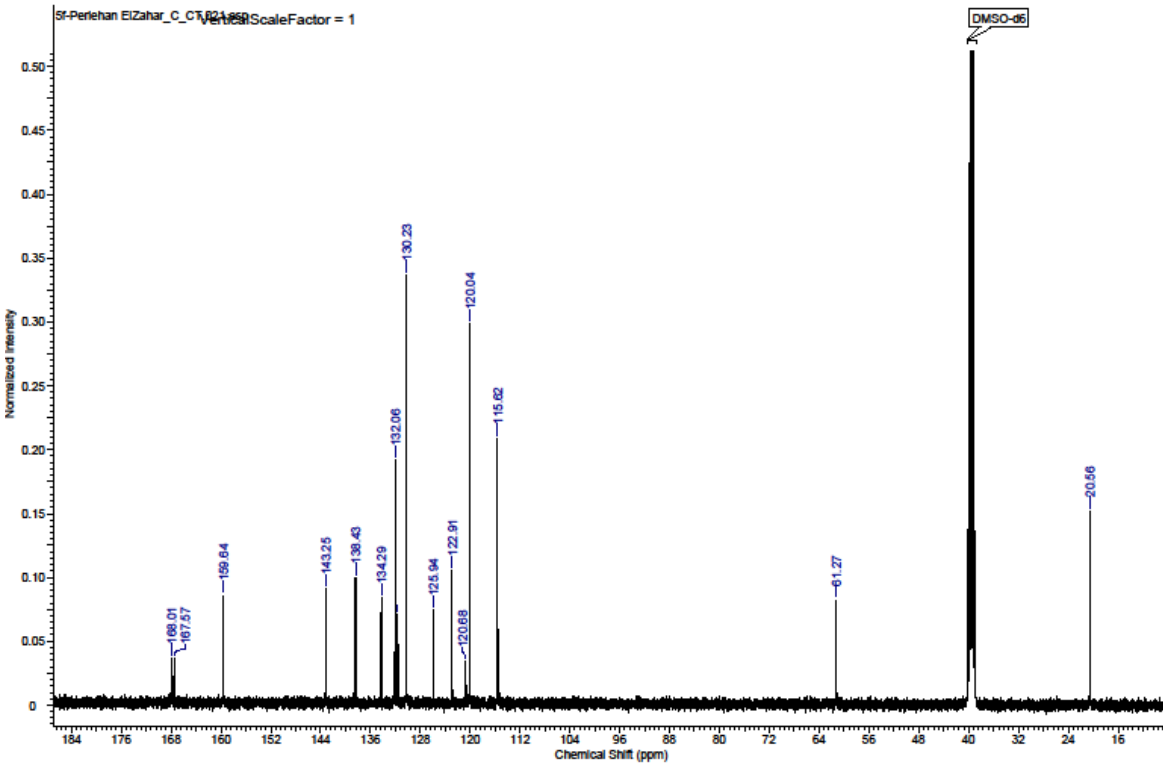

(*Z*)-5-(4-((1-(4-methoxyphenyl)-1*H*-1,2,3-triazol-4-yl)methoxy)benzylidene) thiazolidine-2,4-dione **(5g)**

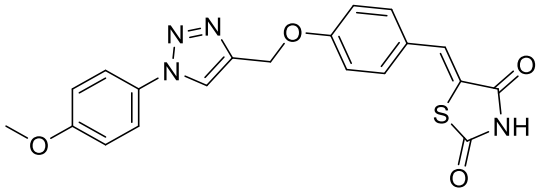

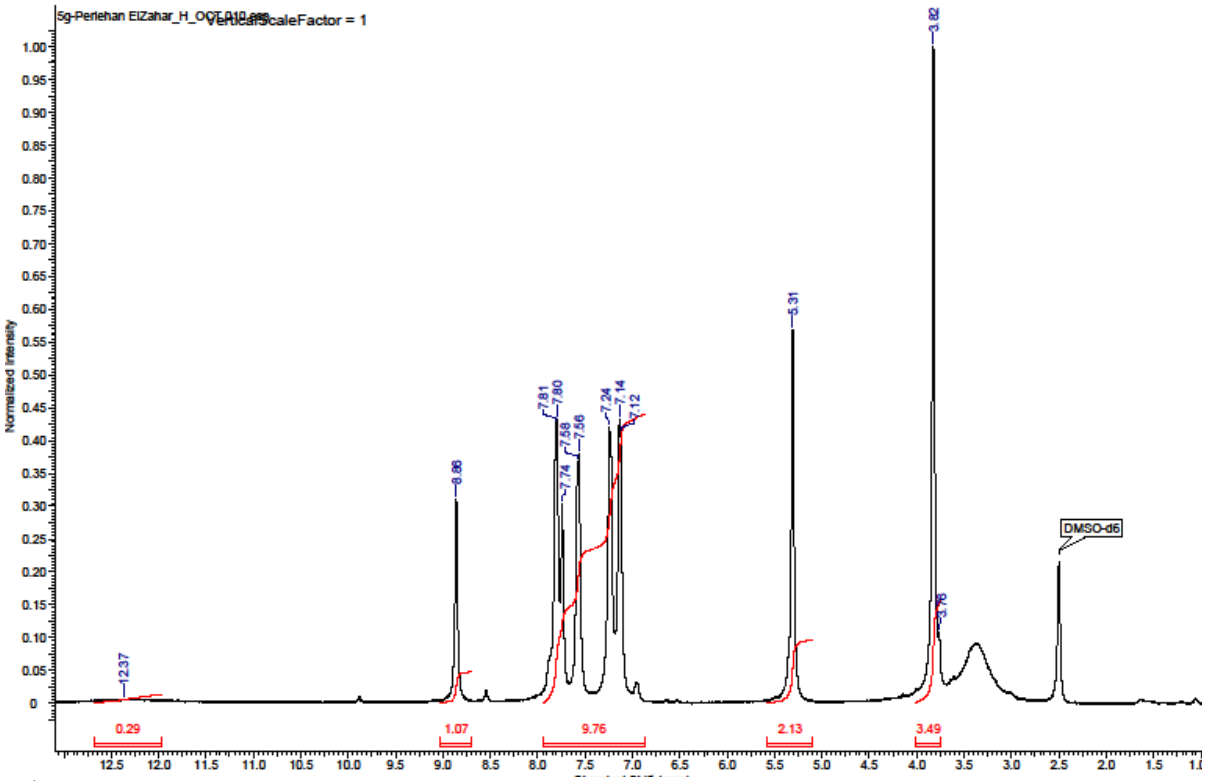

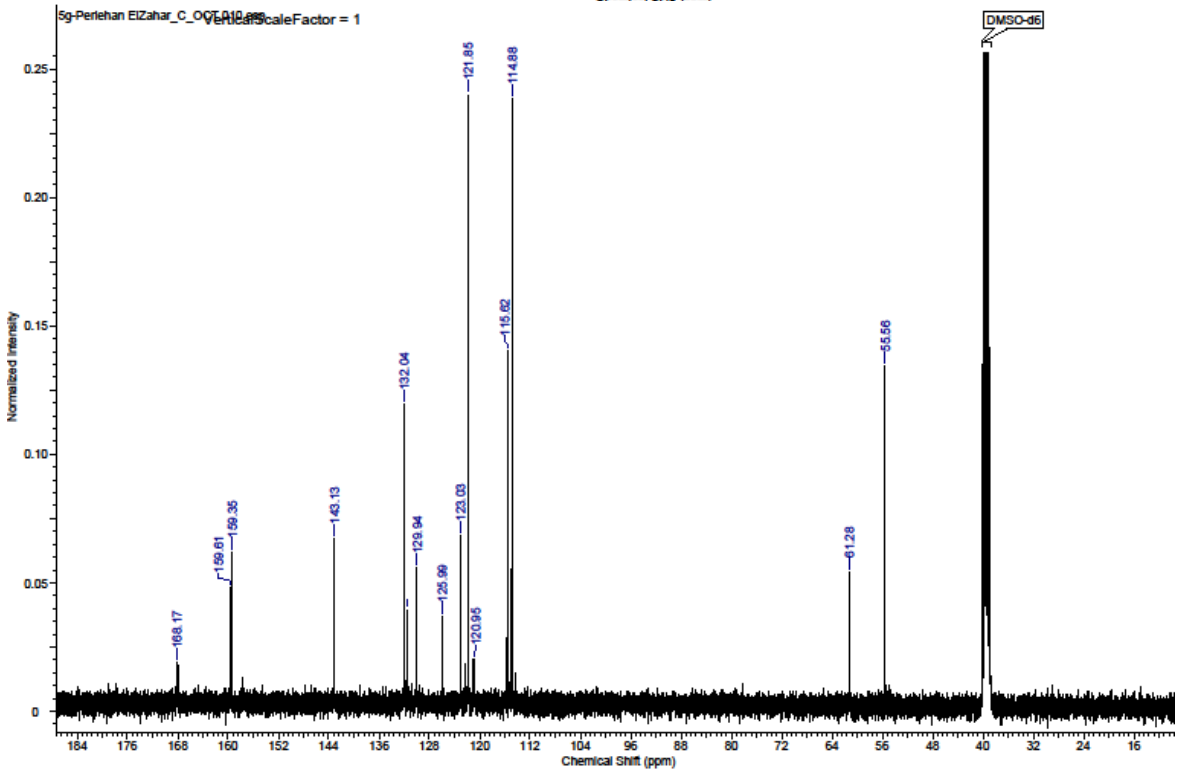

(*Z*)-4-(4-((4-((2,4-dioxothiazolidin-5-ylidene)methyl)phenoxy)methyl)-1*H*-1,2,3-triazol-1-yl)benzoic acid **(5h)**

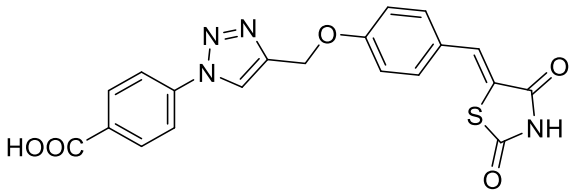

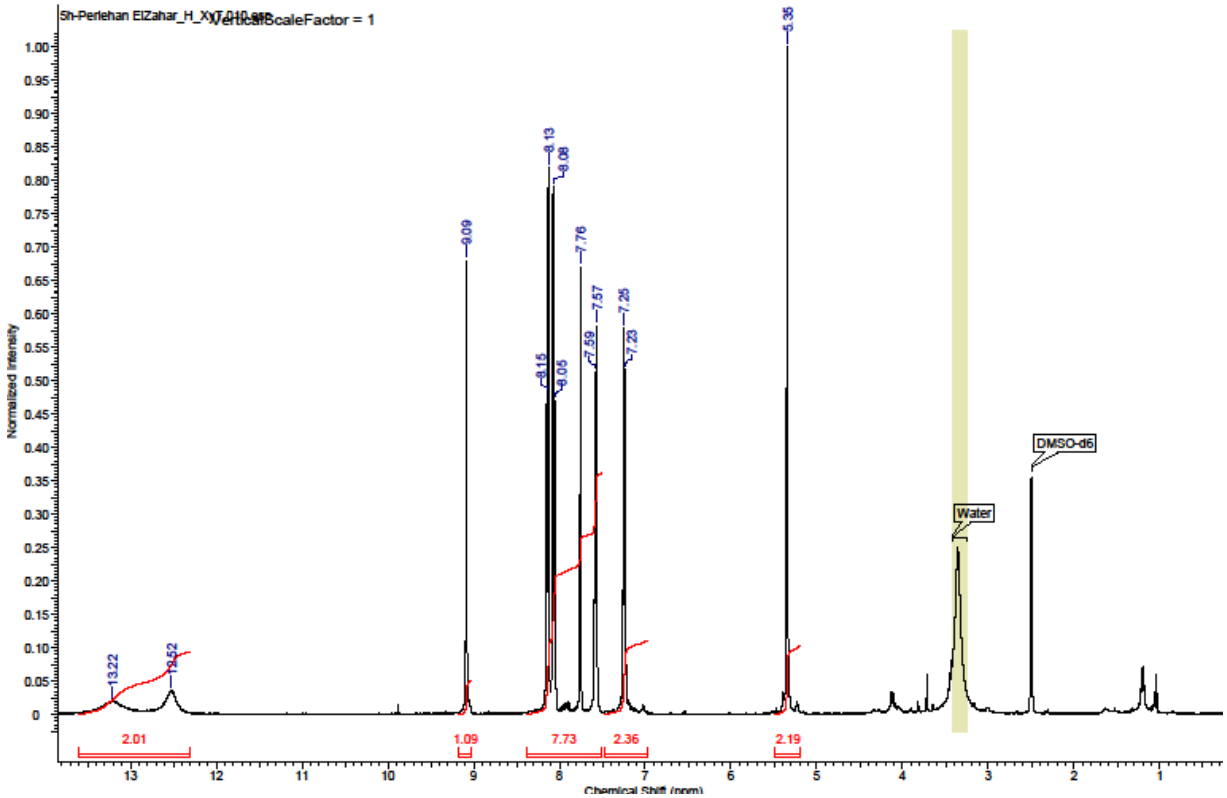

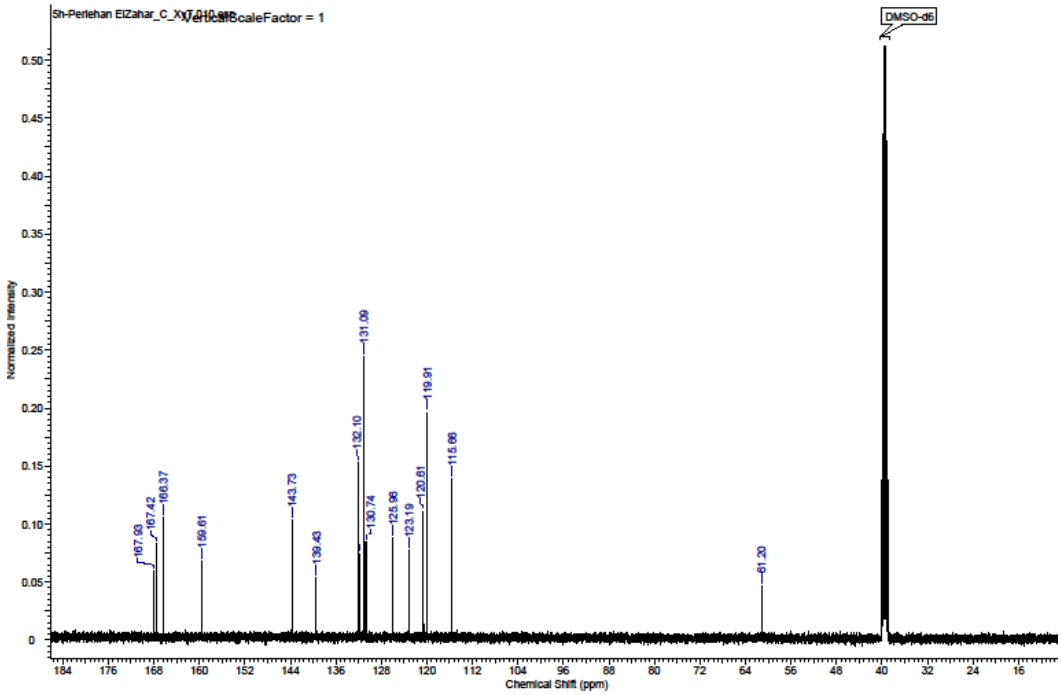

(*Z*)-5-(4-((1-(2-(4-chlorophenyl)-2-oxoethyl)-1*H*-1,2,3-triazol-4-yl)methoxy)benzylidene)thiazolidine-2,4-dione **(5i)**

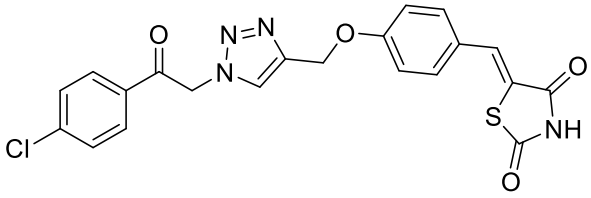

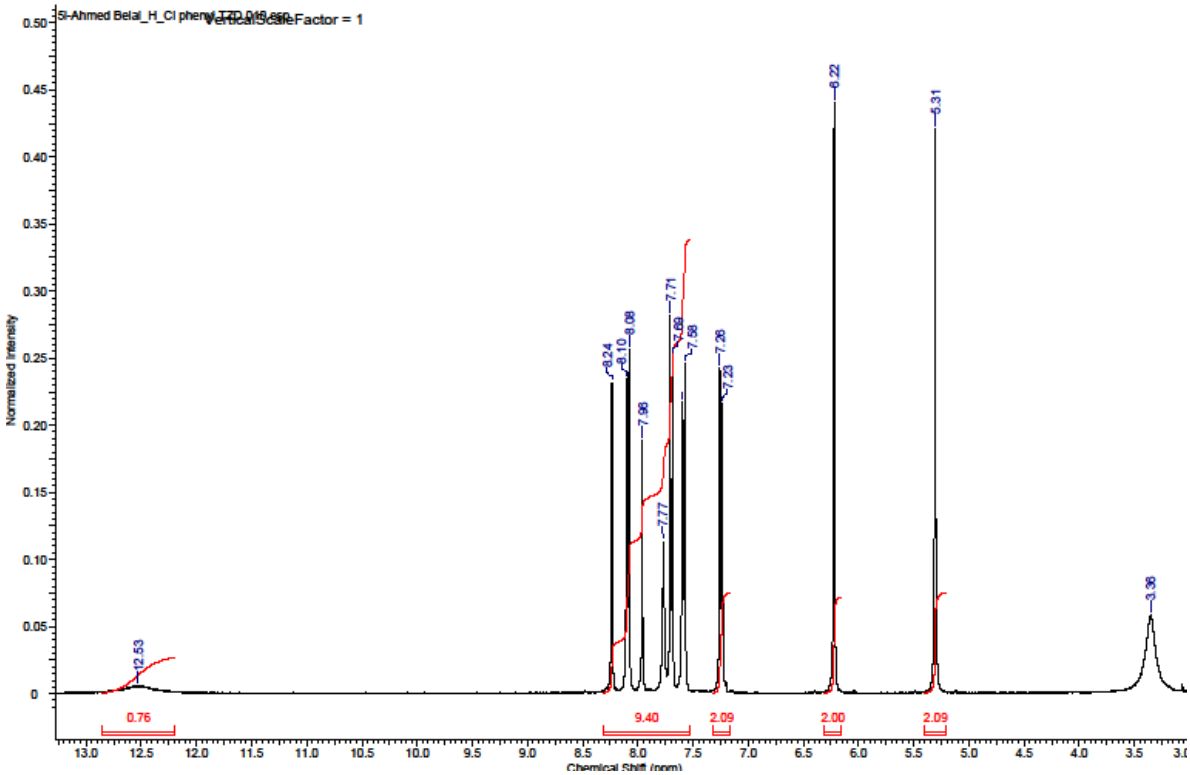

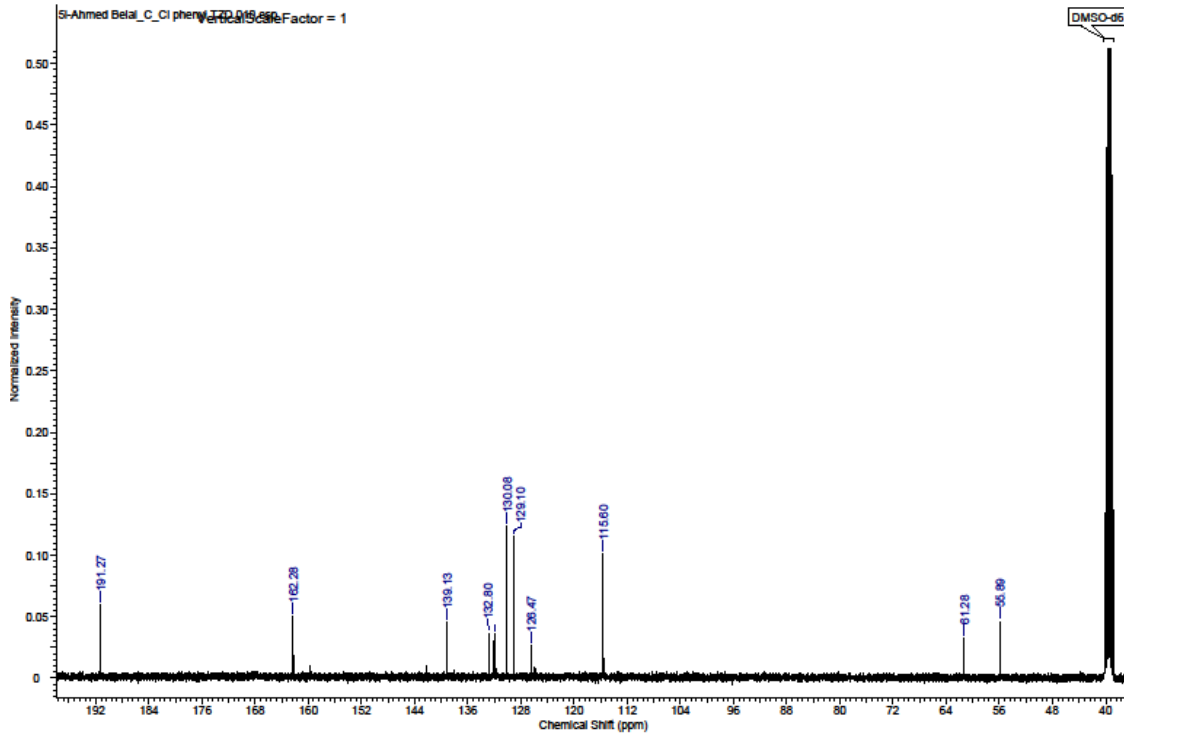

(*Z*)-5-(4-((1-(2-(4-bromophenyl)-2-oxoethyl)-1*H*-1,2,3-triazol-4-yl)methoxy)benzylidene)thiazolidine-2,4-dione **(5j)**

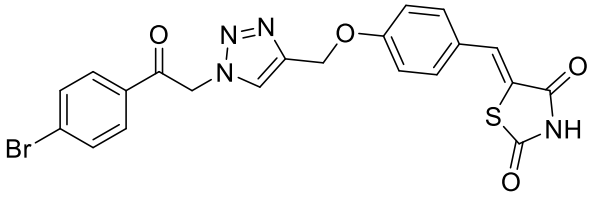

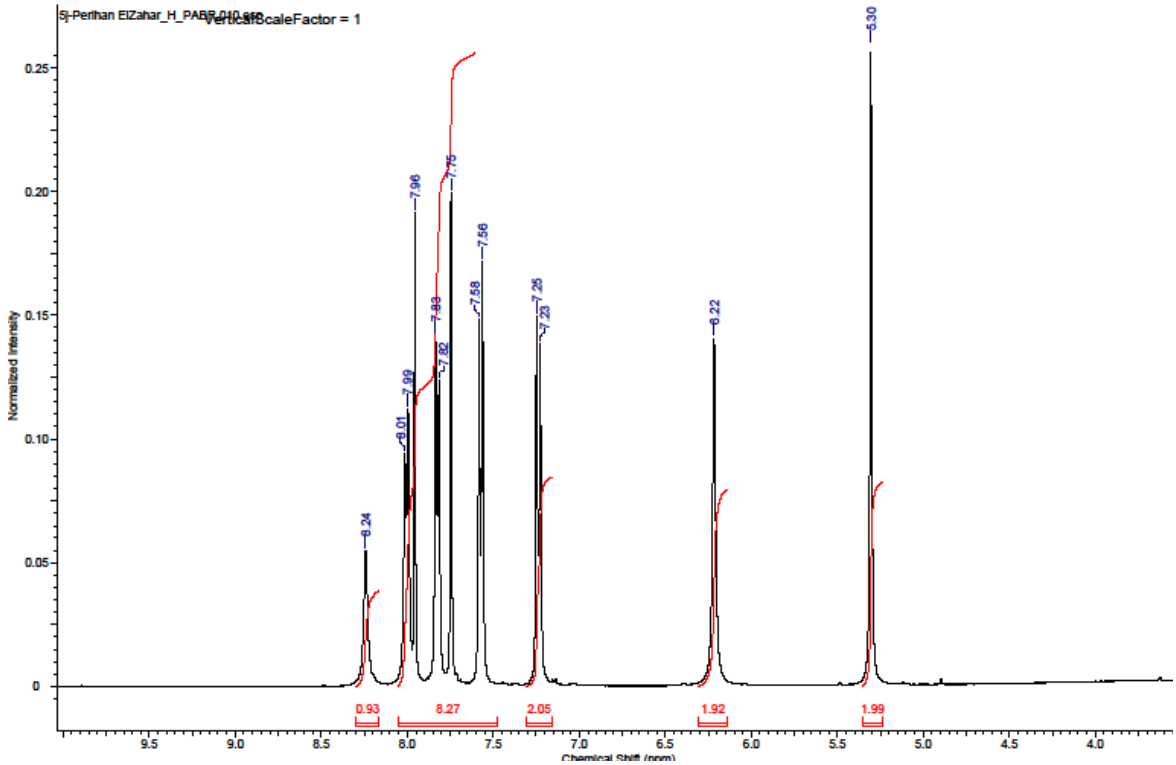

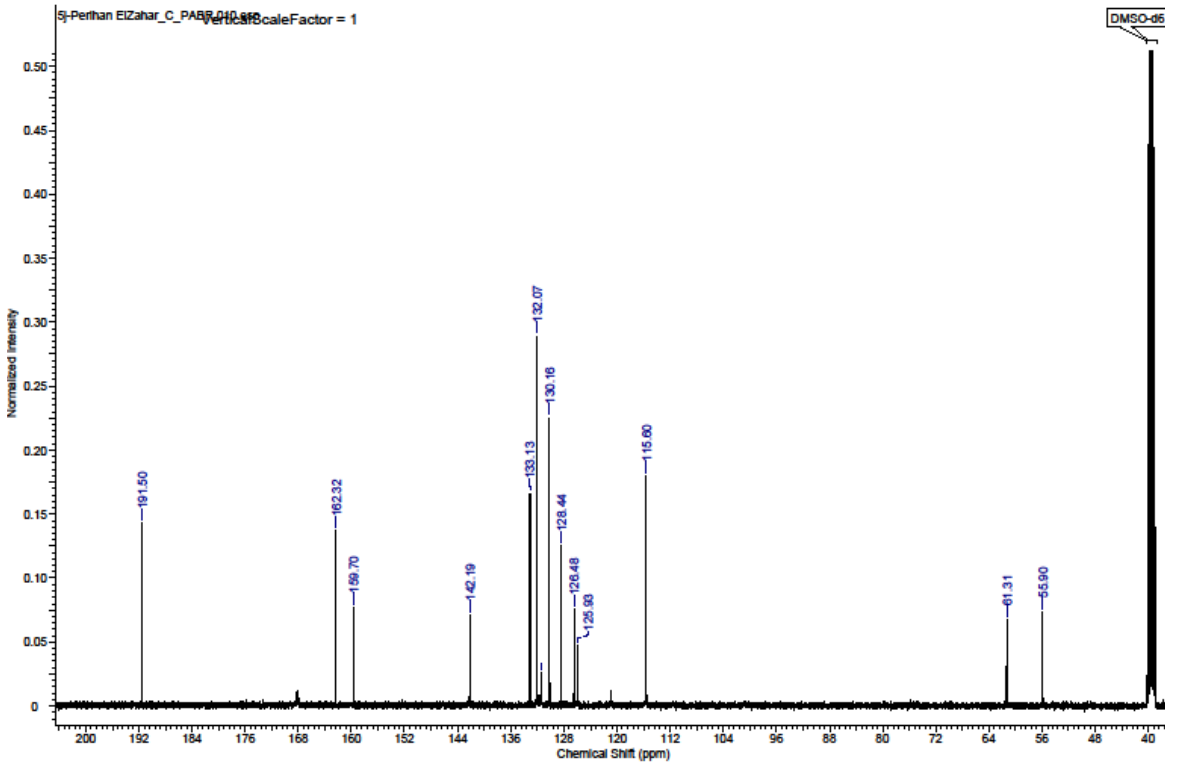

(*Z*)-5-(4-((1-benzyl-1*H*-1,2,3-triazol-4-yl)methoxy)benzylidene)-2-thioxothiazolidin-4-one **(6a)**

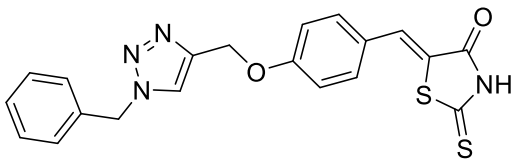

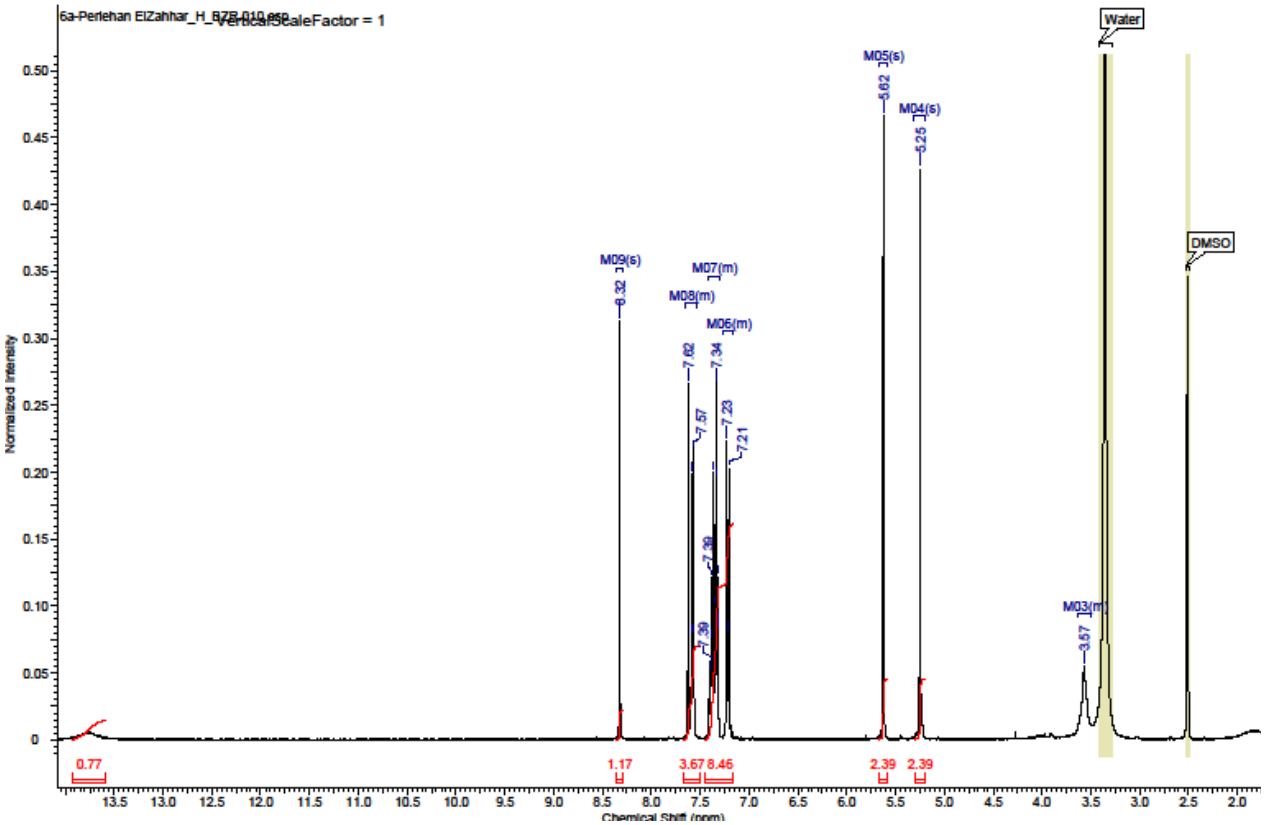

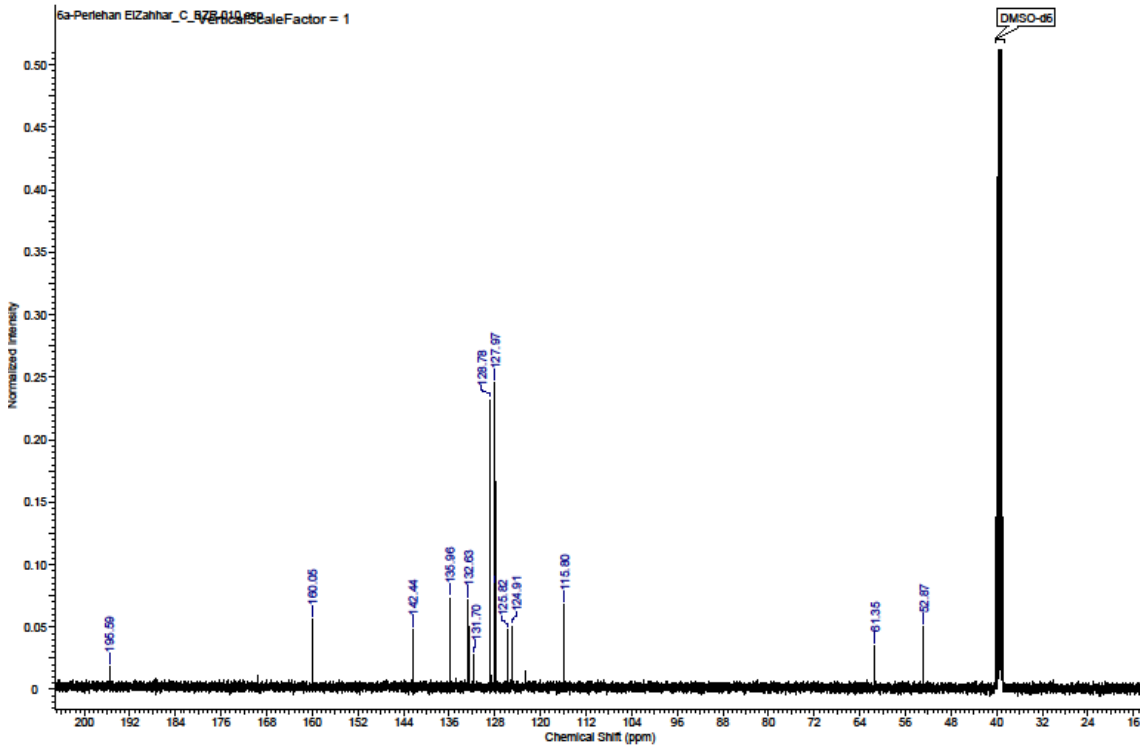

(*Z*)-5-(4-((1-(4-bromobenzyl)-1*H*-1,2,3-triazol-4-yl)methoxy)benzylidene)-2-thioxothiazolidin-4-one **(6b)**

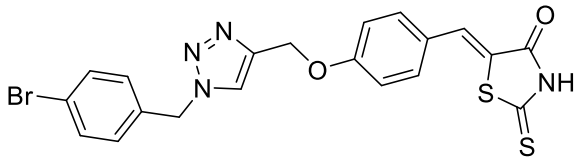

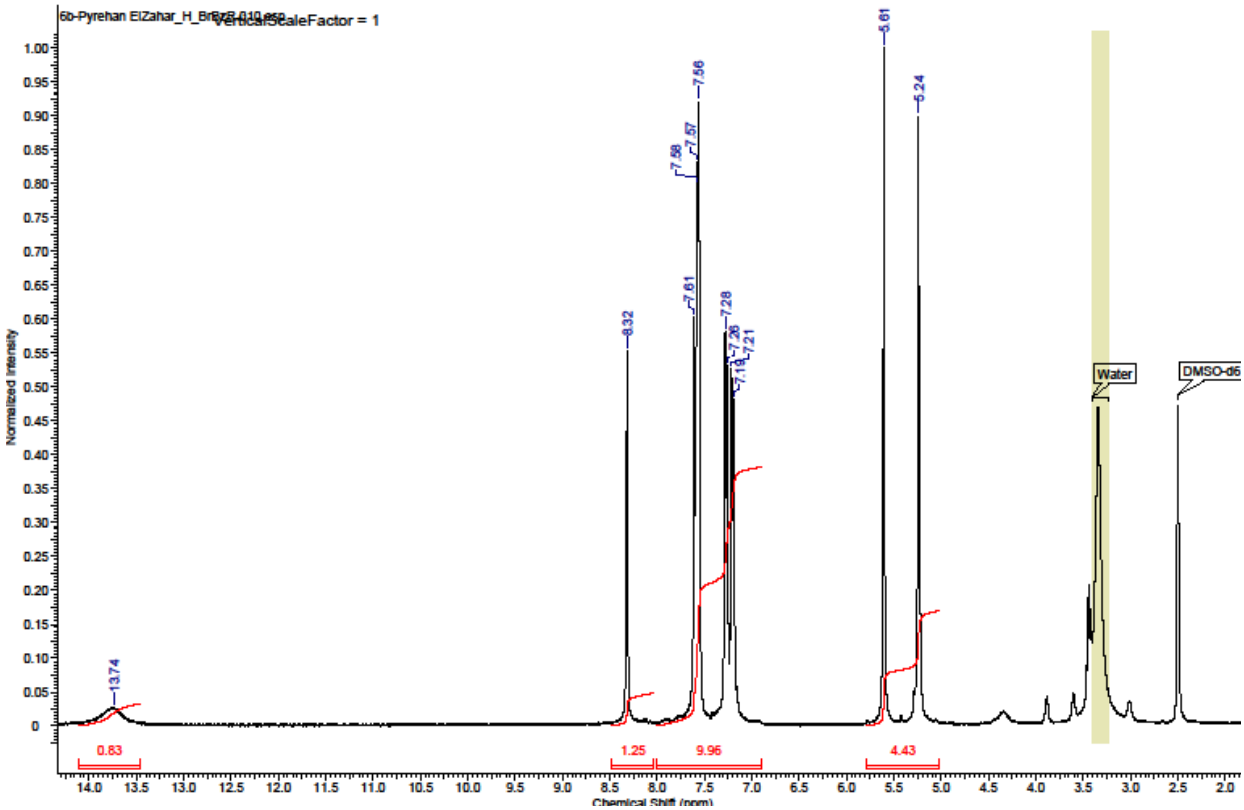

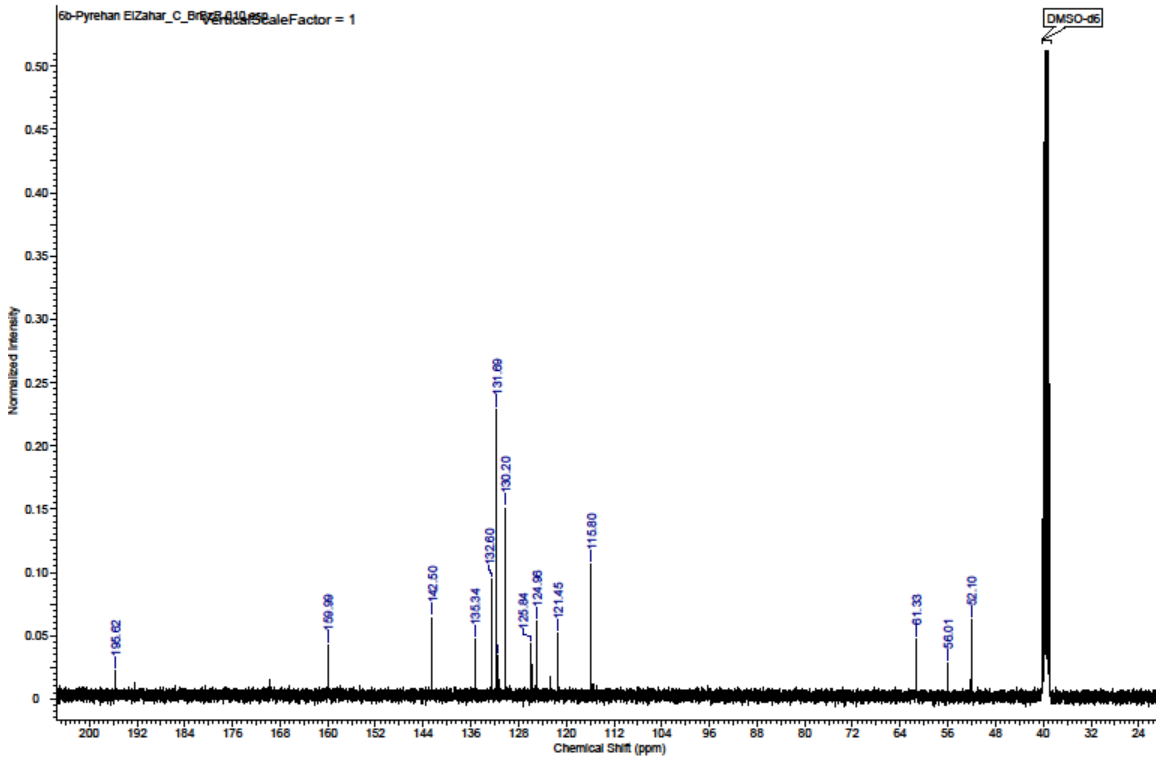

(*Z*)-5-(4-((1-phenyl-1*H*-1,2,3-triazol-4-yl)methoxy)benzylidene)-2-thioxothiazolidin-4-one **(6c)**

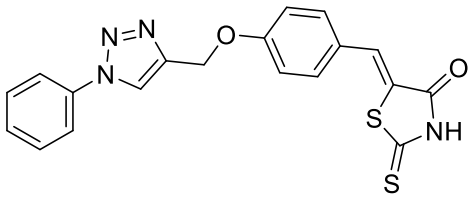

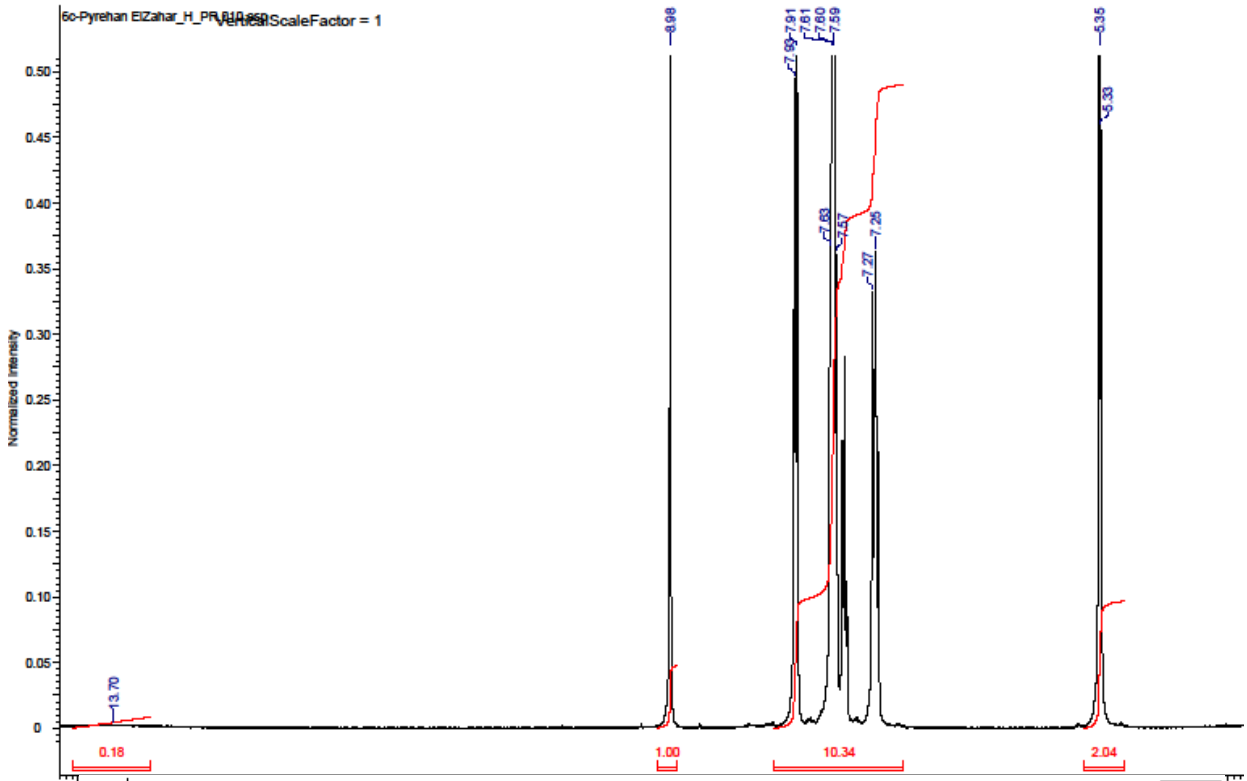

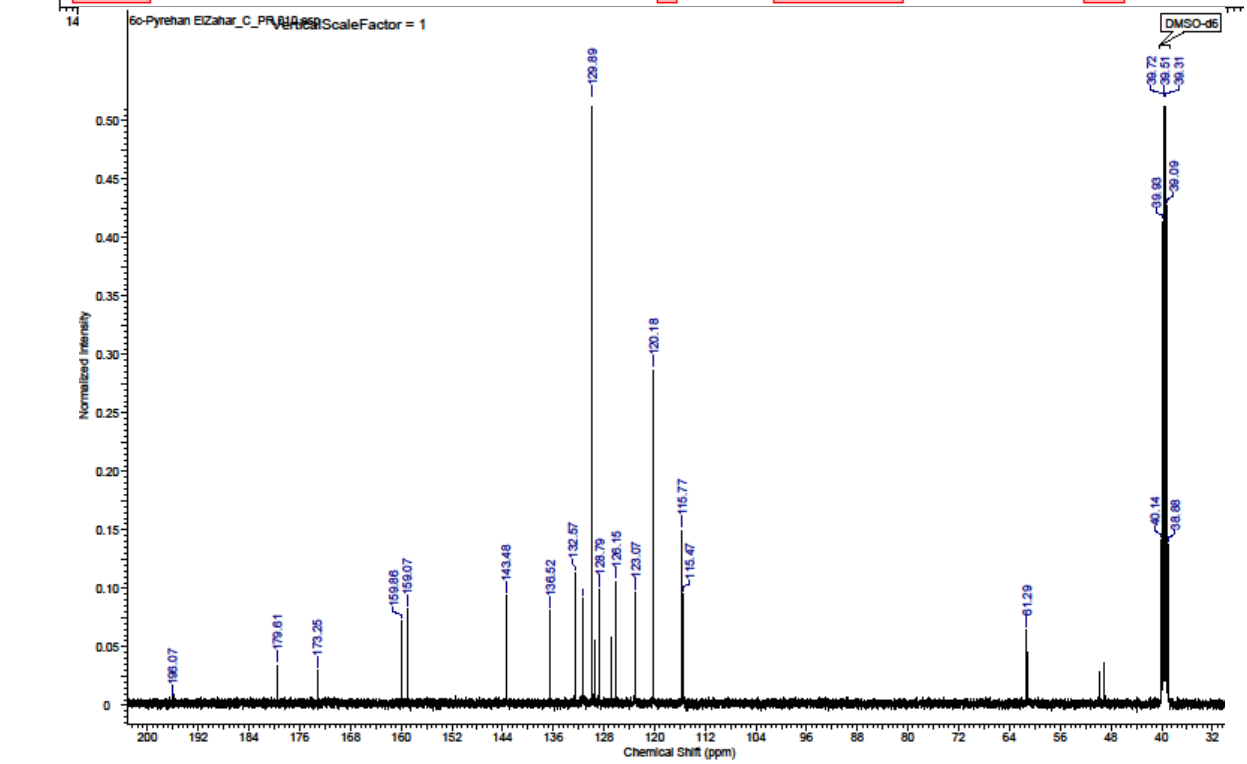

(*Z*)-5-(4-((1-(4-chlorophenyl)-1*H*-1,2,3-triazol-4-yl)methoxy)benzylidene)-2-thioxothiazolidin-4-one **(6d)**

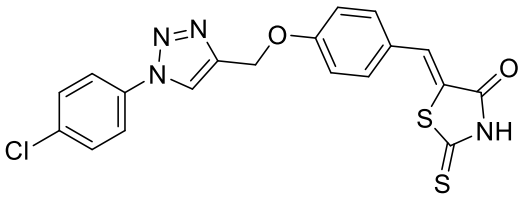

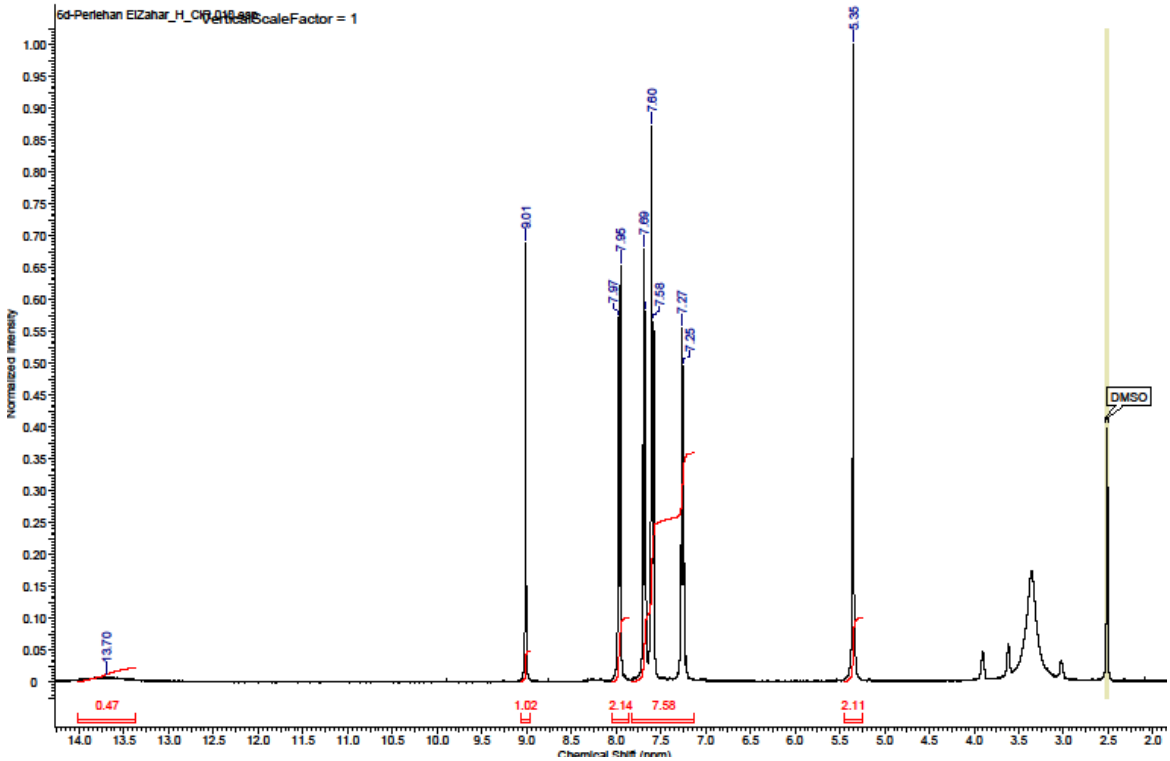

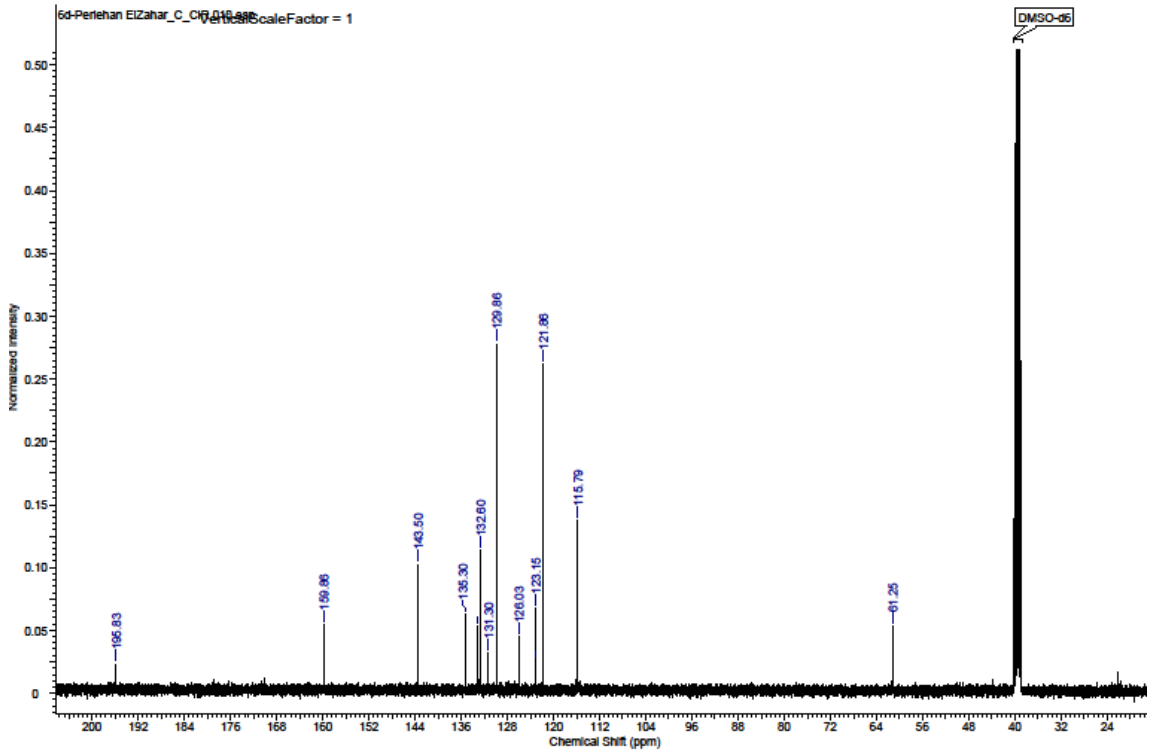

(*Z*)-5-(4-((1-(4-bromophenyl)-1*H*-1,2,3-triazol-4-yl)methoxy)benzylidene)-2-thioxothiazolidin-4-one **(6e)**

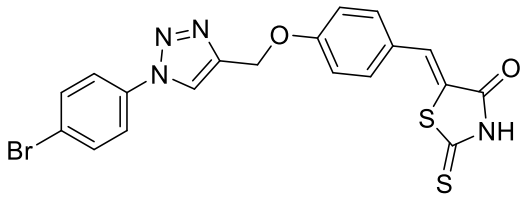

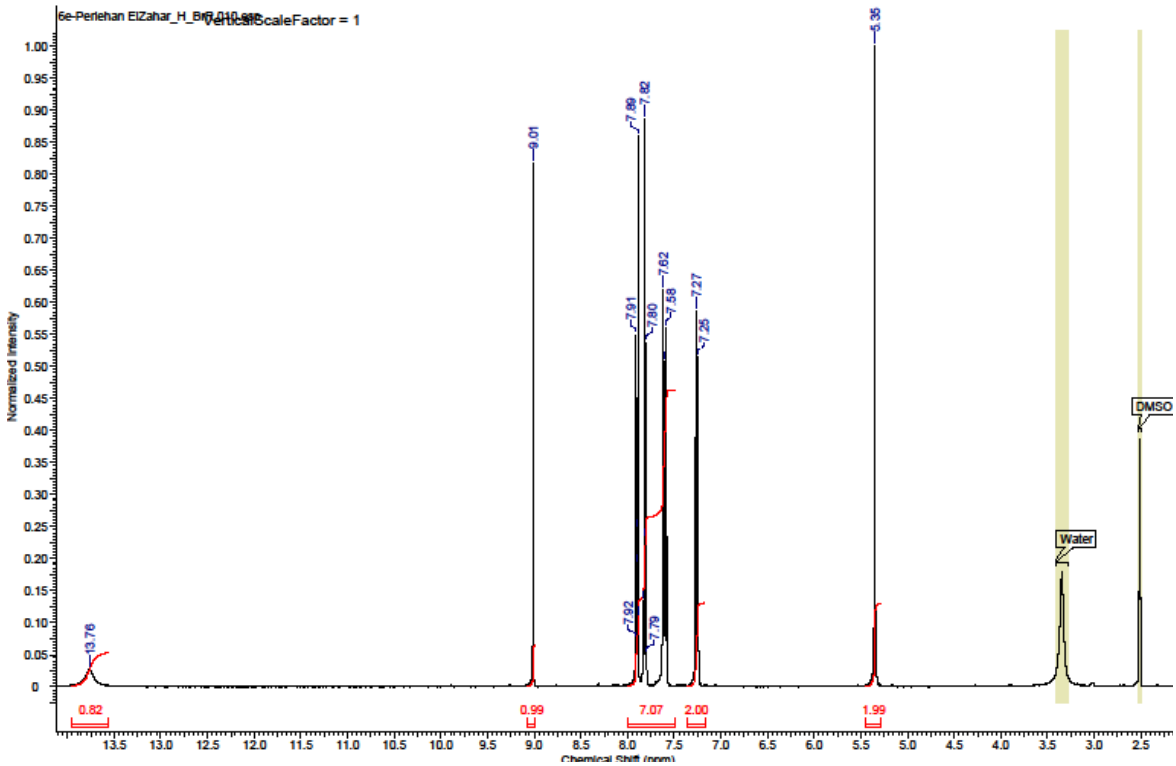

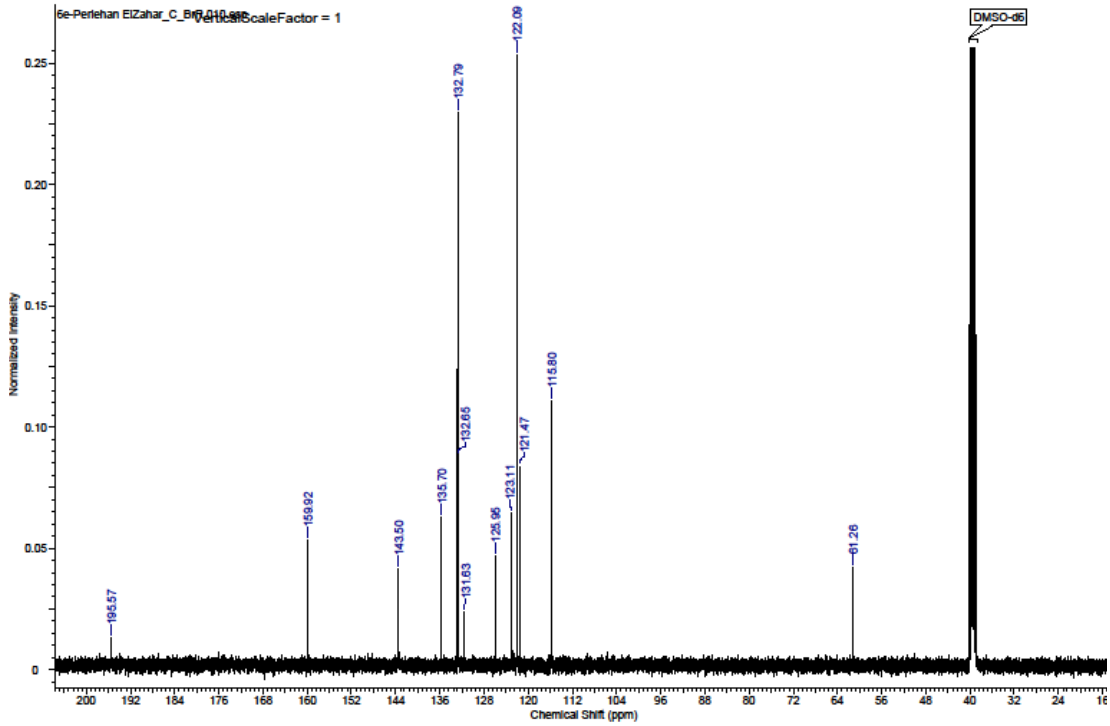

(*Z*)-2-thioxo-5-(4-((1-(p-tolyl)-1*H*-1,2,3-triazol-4-yl)methoxy)benzylidene) thiazolidin-4-one **(6f)**

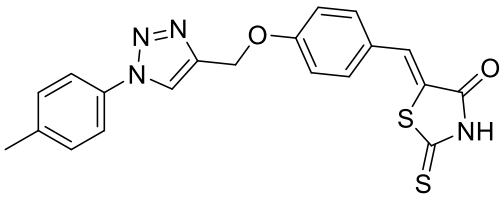

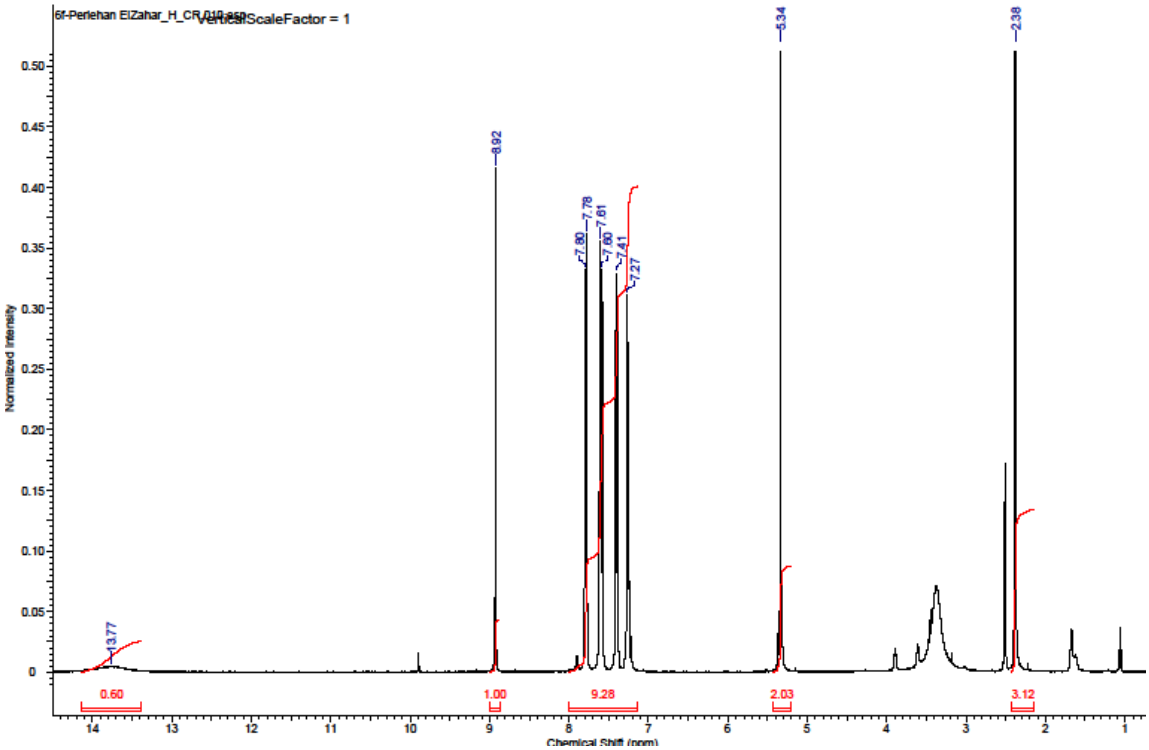

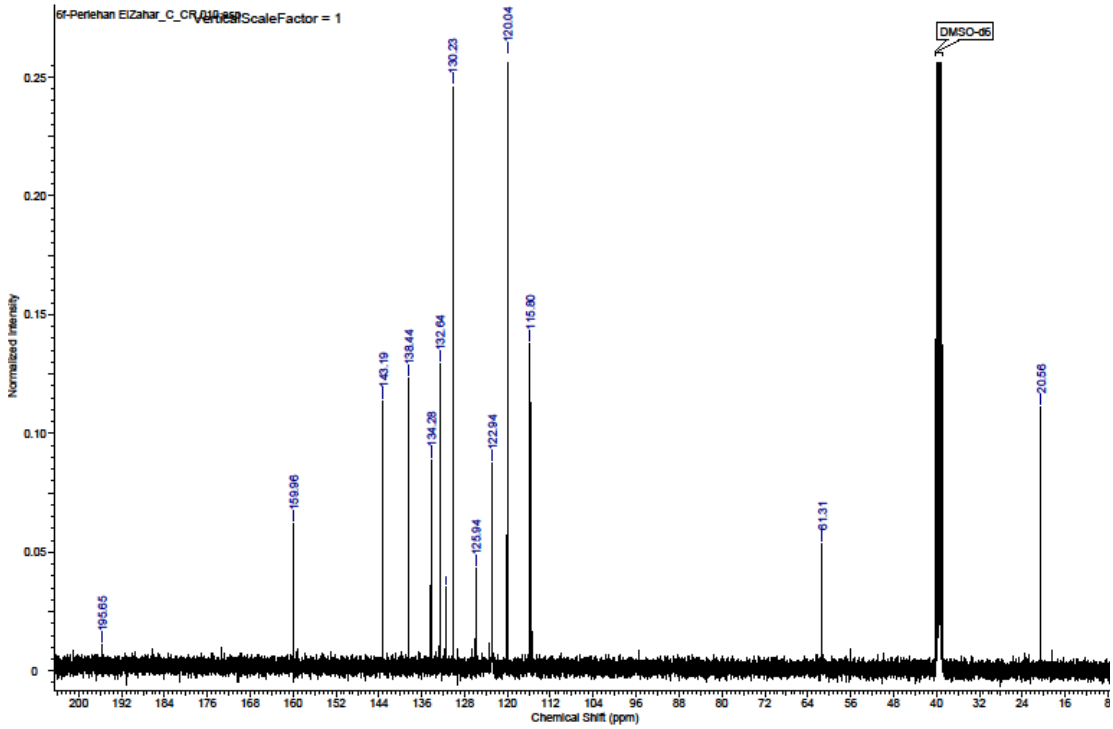

(*Z*)-5-(4-((1-(4-methoxyphenyl)-1*H*-1,2,3-triazol-4-yl)methoxy)benzylidene)-2-thioxothiazolidin-4-one **(6g)**

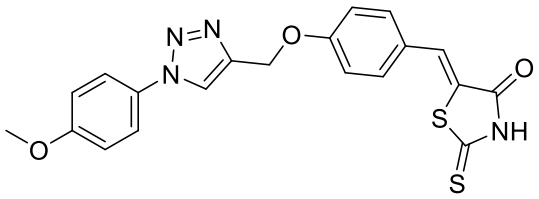

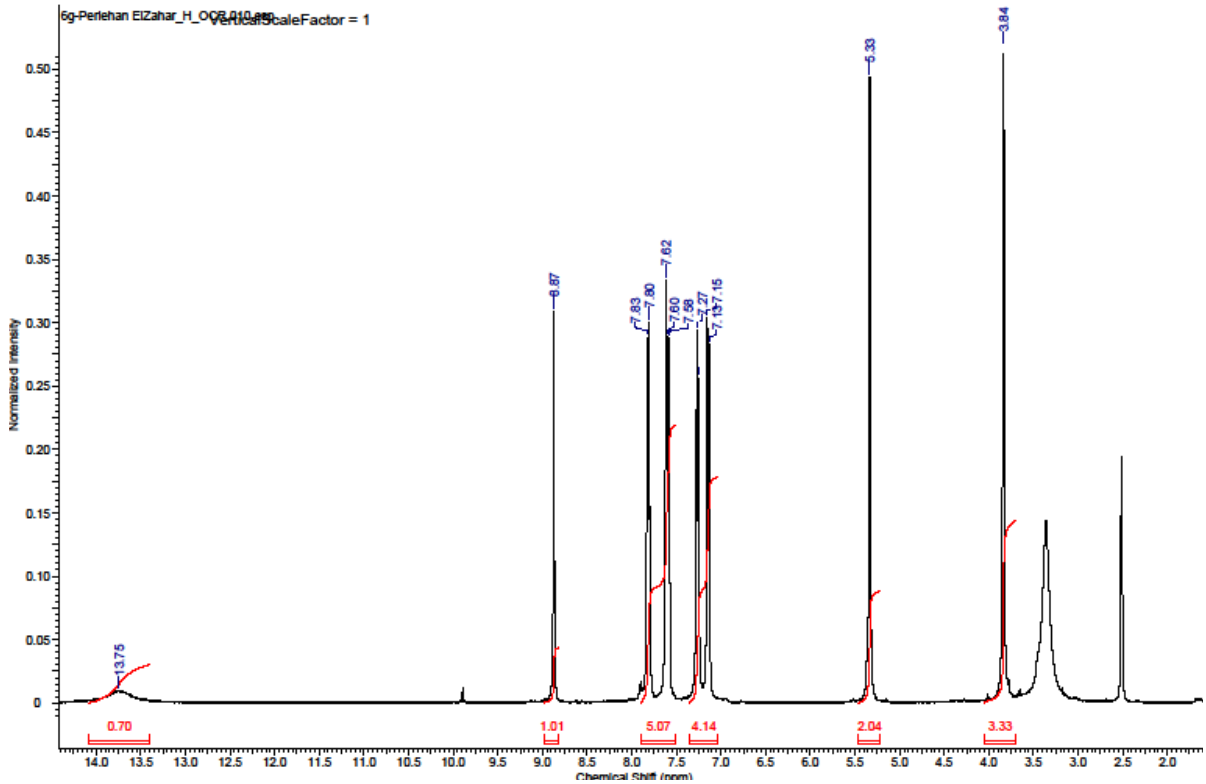

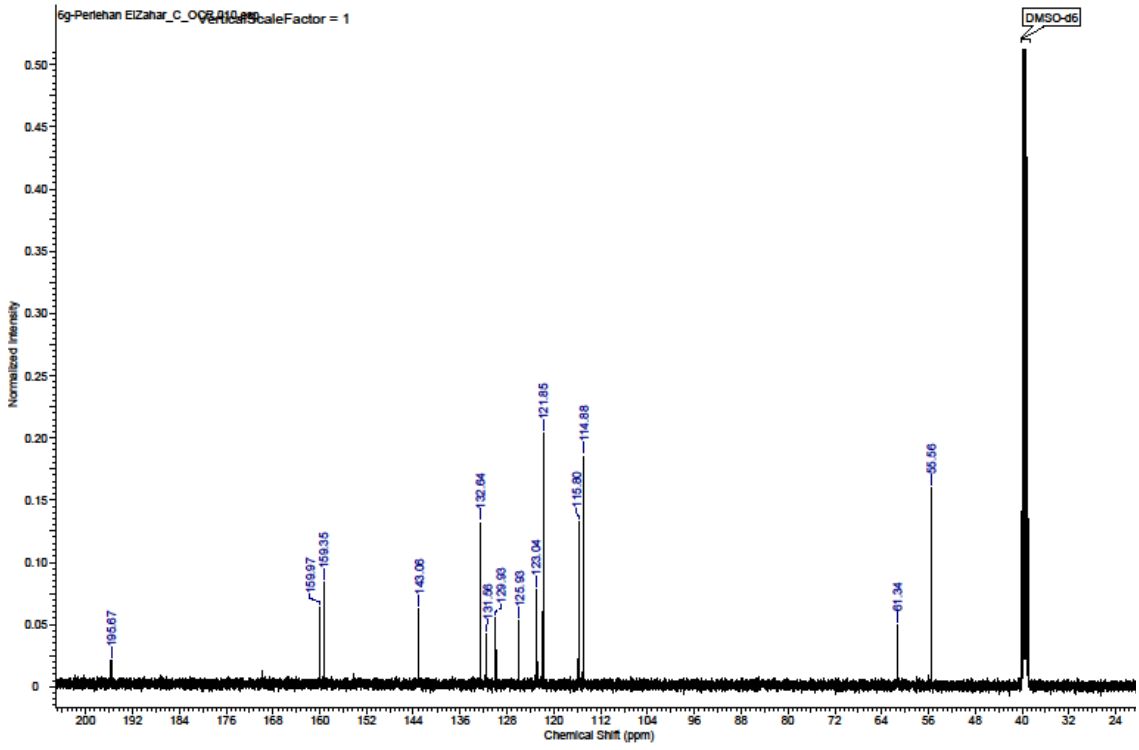

(*Z*)-4-(4-((4-((4-oxo-2-thioxothiazolidin-5-ylidene)methyl)phenoxy)methyl)-1*H*-1,2,3-triazol-1-yl)benzoic acid **(6h)**

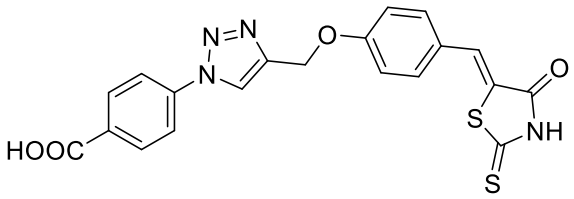

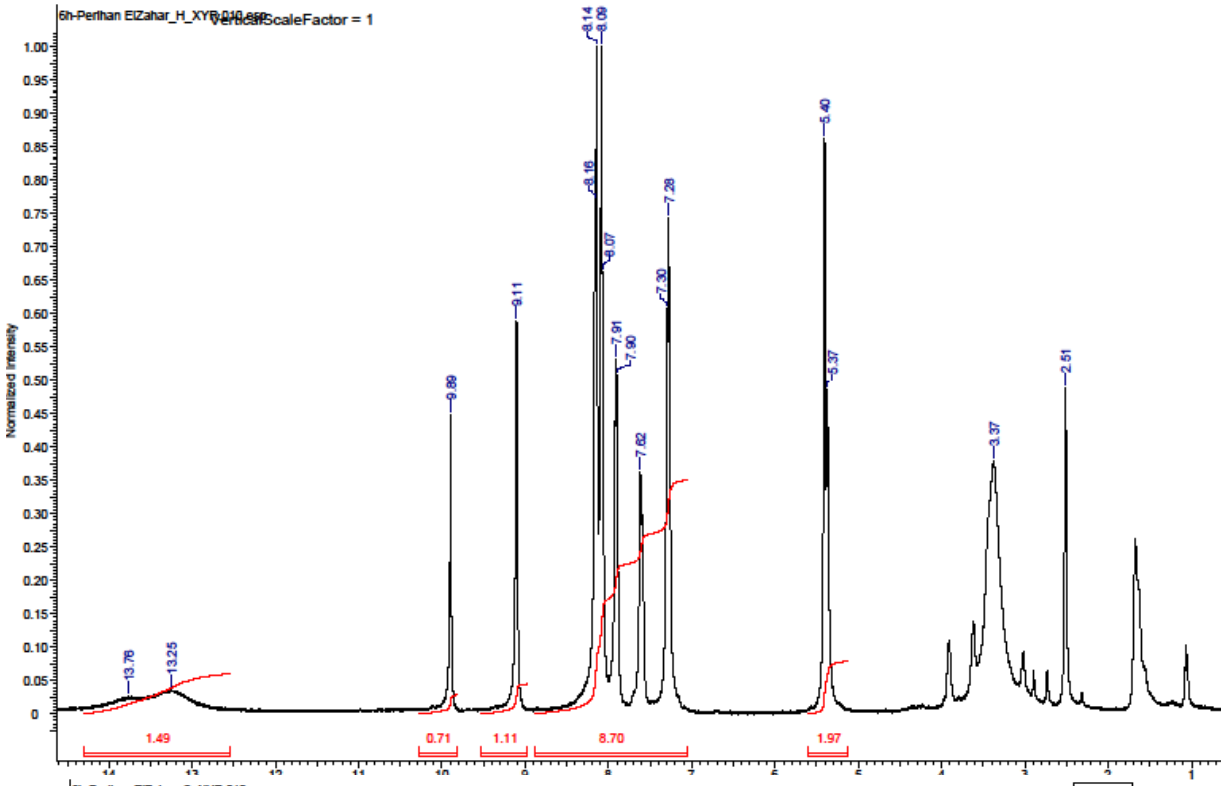

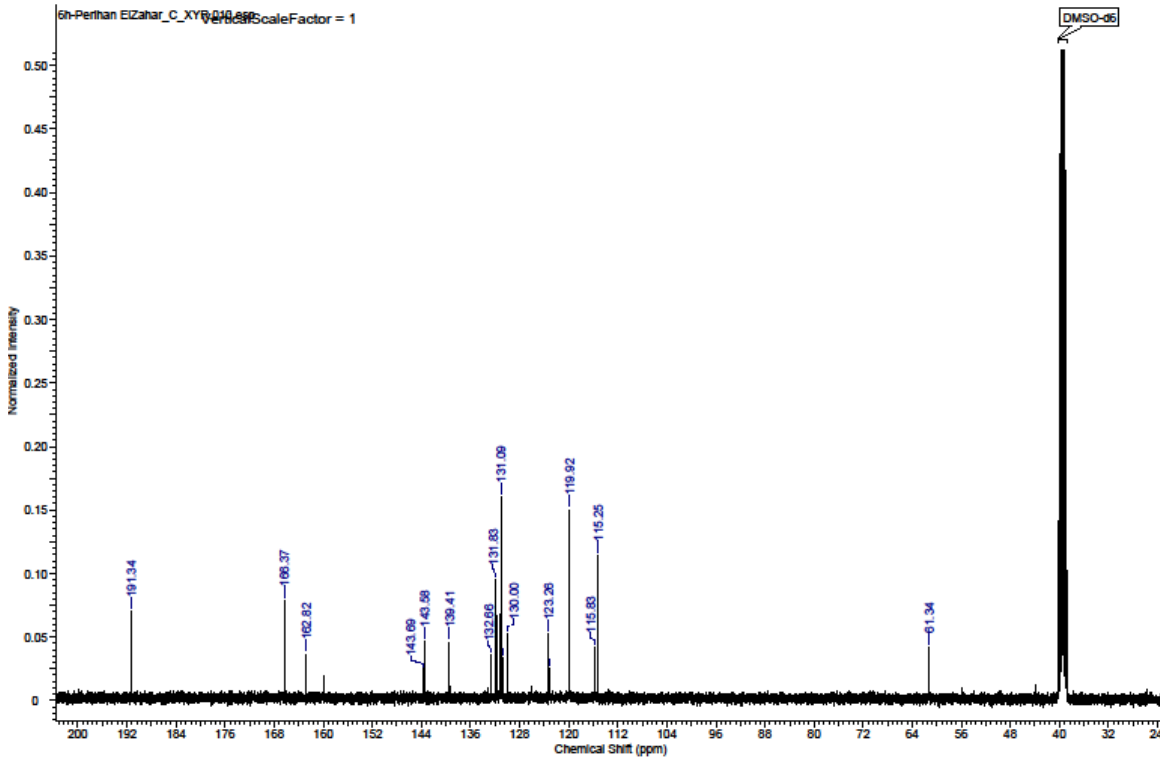

(*Z*)-5-(4-((1-(2-(4-chlorophenyl)-2-oxoethyl)-1*H*-1,2,3-triazol-4-yl)methoxy) benzylidene)-2-thioxothiazolidin-4-one **(6i)**

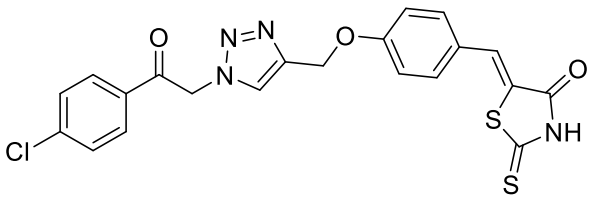

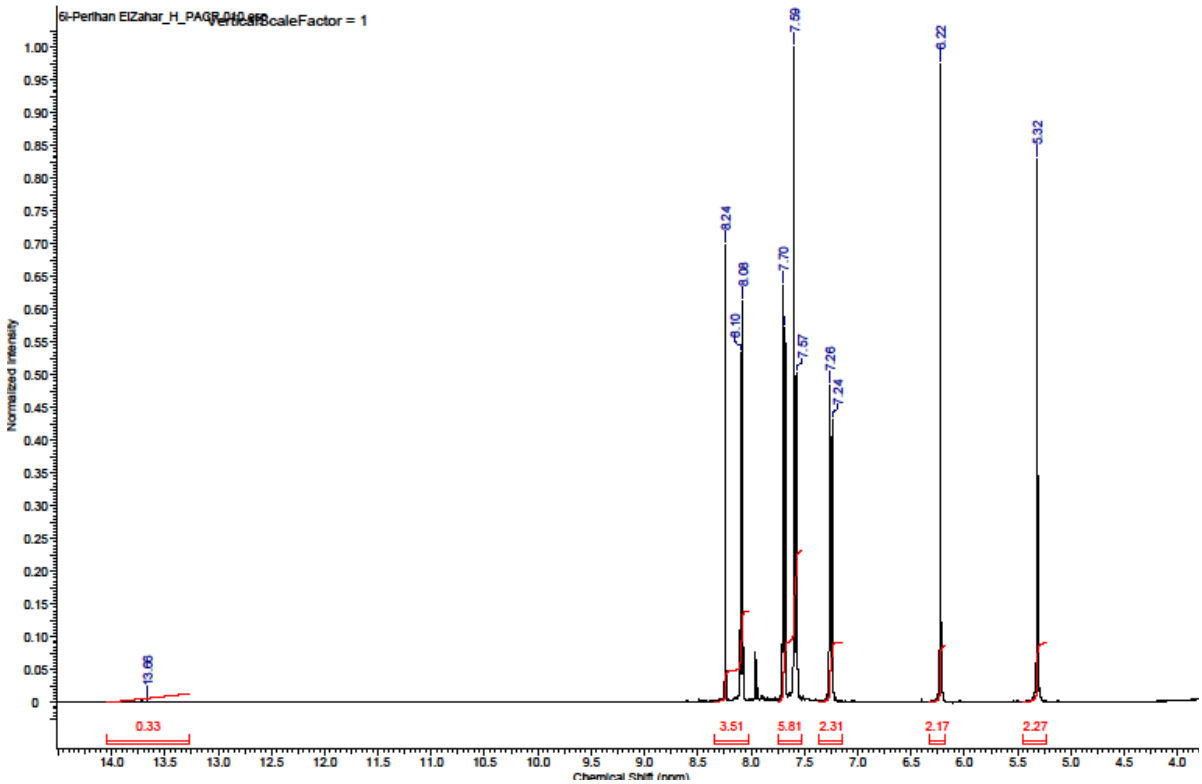

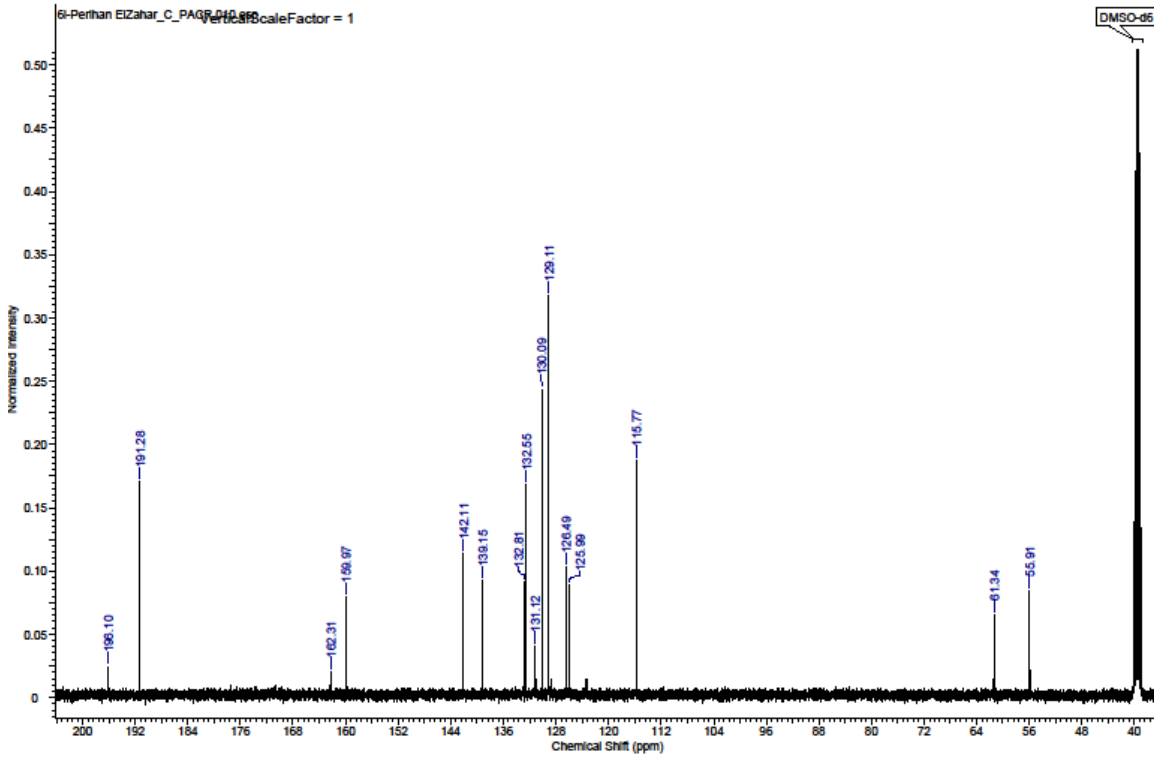

(*Z*)-5-(4-((1-(2-(4-bromophenyl)-2-oxoethyl)-1*H*-1,2,3-triazol-4-yl)methoxy) benzylidene)-2-thioxothiazolidin-4-one **(6j)**

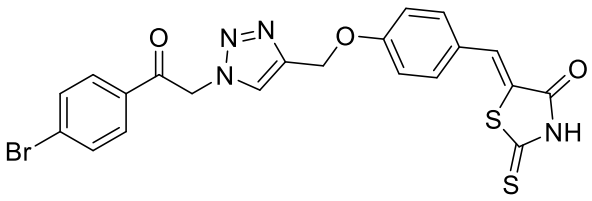

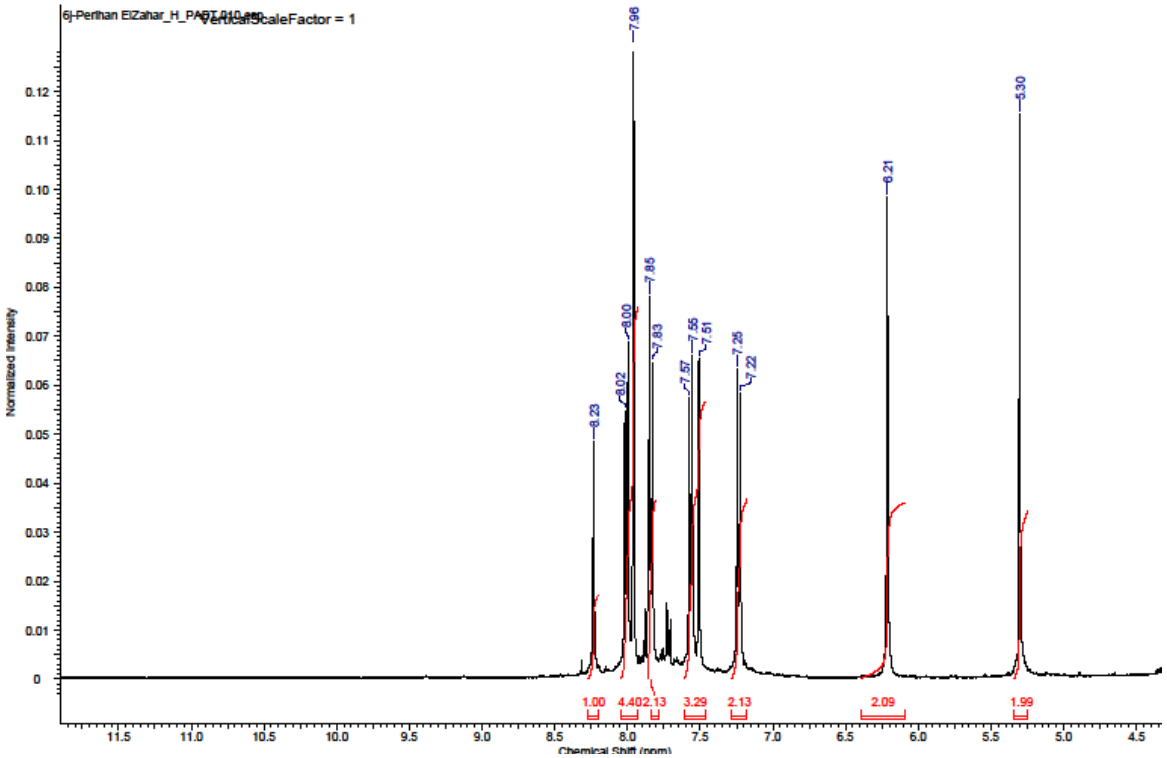

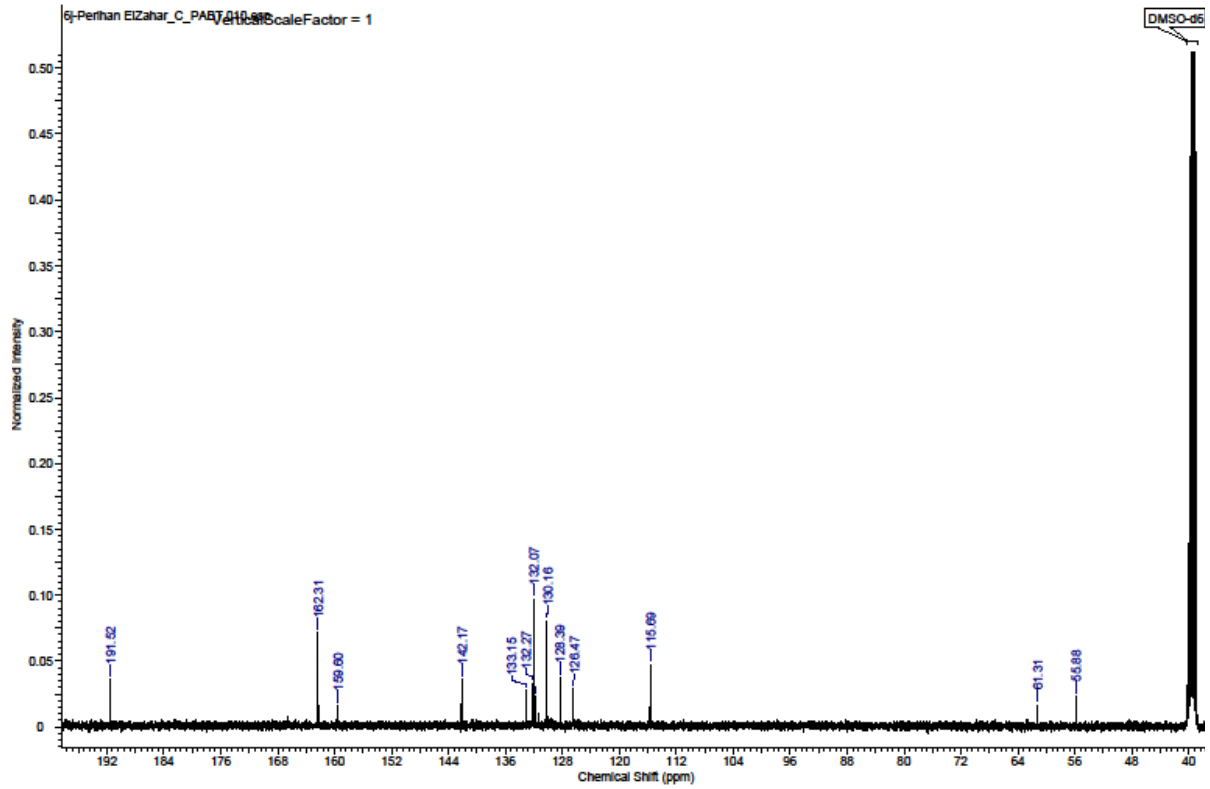

Ascertainment of purity by HPLC:

4a

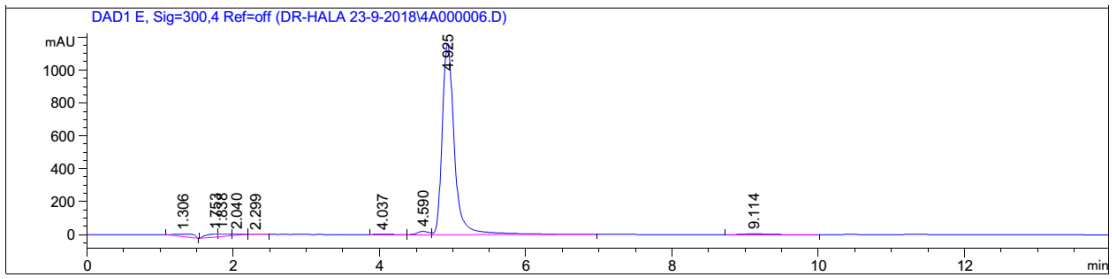

4b

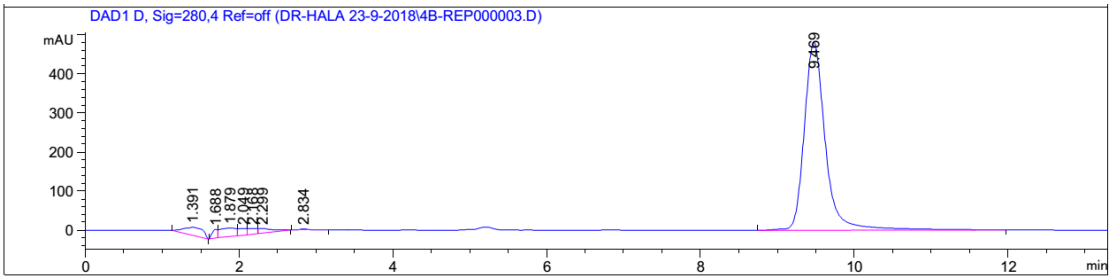

5b

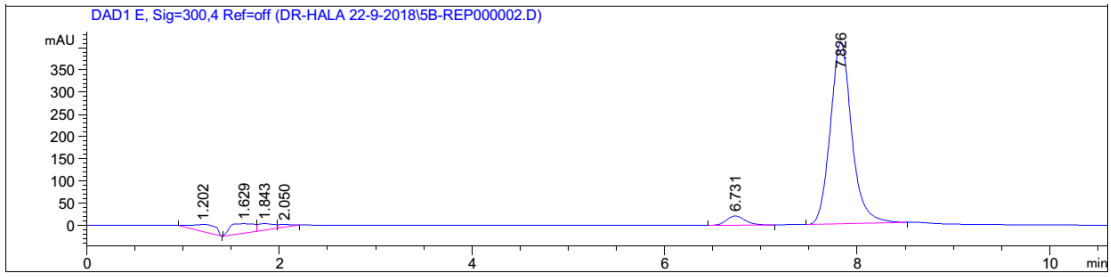

5c

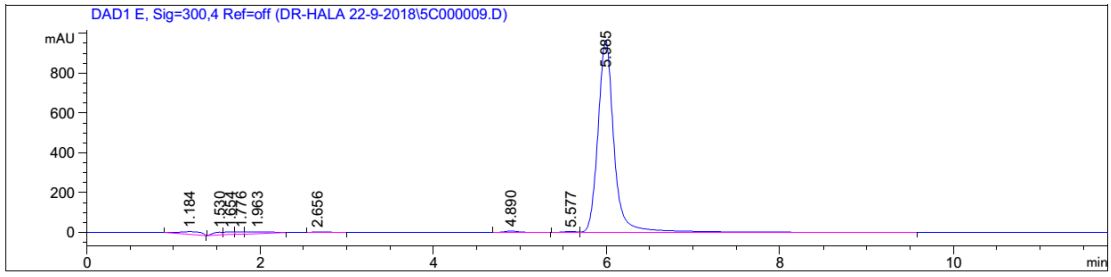

5e

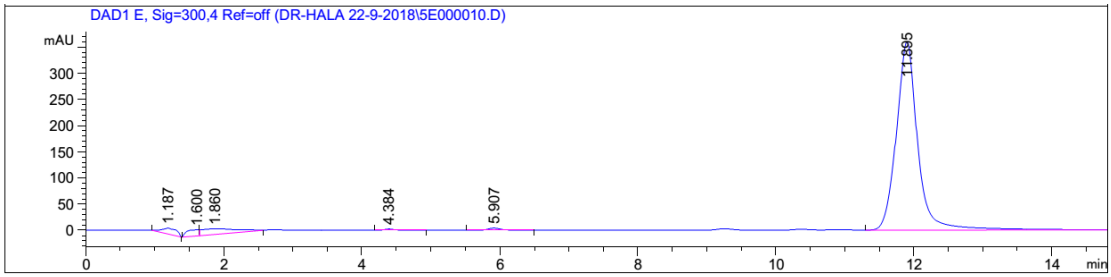

5f

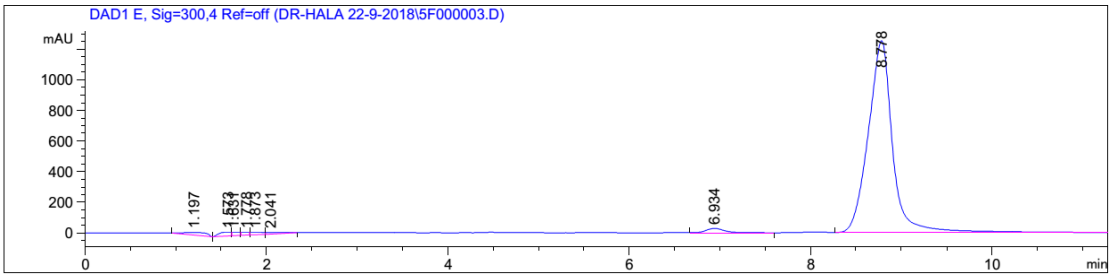
DAD1 E, Sig=300,4 Ref=off (DR-HALA 22-9-2018\5F000003.D)
mAU
1000
800
600
400
200
0
1.197
1.673
2.041
6.934
8.778
0
2
4
6
8
10
min

5h

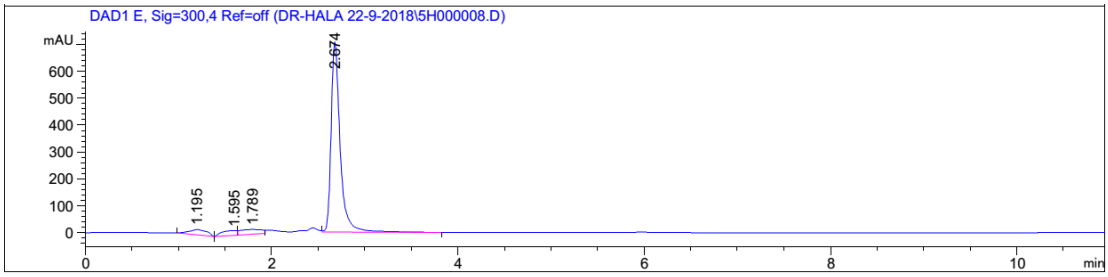
DAD1 E, Sig=300,4 Ref=off (DR-HALA 22-9-2018\5H000008.D)
mAU
600
500
400
300
200
100
0
1.195
1.595
1.789
2.674
0
2
4
6
8
10
min

5j

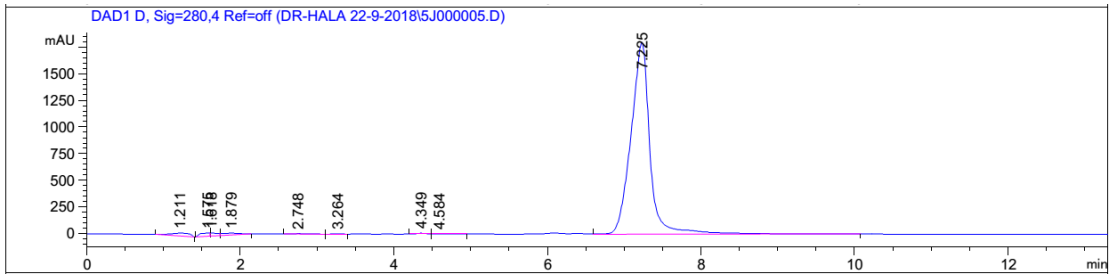
DAD1 D, Sig=280,4 Ref=off (DR-HALA 22-9-2018\5J000005.D)
mAU
1500
1250
1000
750
500
250
0
1.211
1.879
2.748
3.264
4.349
4.584
7.225
0
2
4
6
8
10
12
min

6b

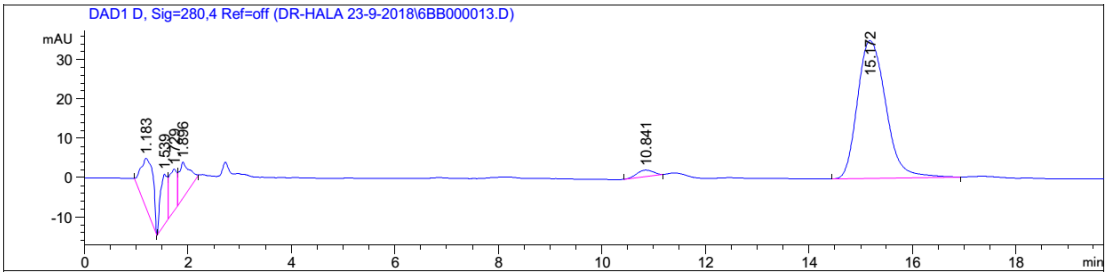
DAD1 D, Sig=280,4 Ref=off (DR-HALA 23-9-2018\6BB000013.D)
mAU
30
20
10
0
-10
1.183
1.896
10.841
15.172
0
2
4
6
8
10
12
14
16
18
min

6e

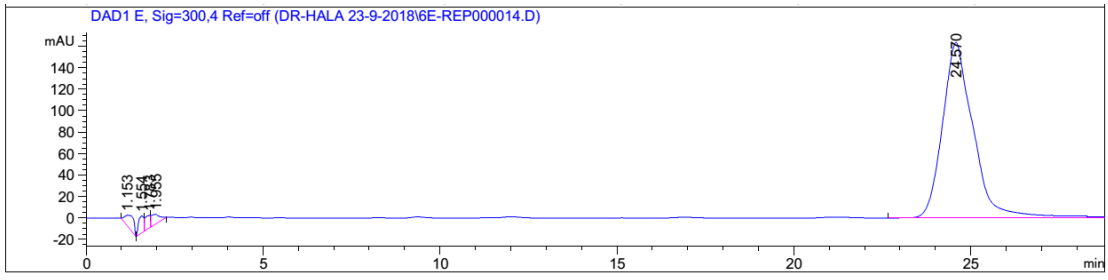
DAD1 E, Sig=300,4 Ref=off (DR-HALA 23-9-2018\6E-REP000014.D)
mAU
140
120
100
80
60
40
20
0
-20
1.153
24.570
0
5
10
15
20
25
min

6g

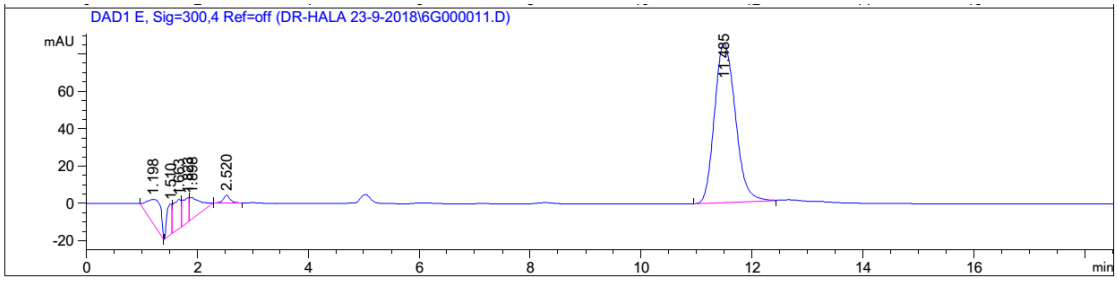
DAD1 E, Sig=300,4 Ref=off (DR-HALA 23-9-2018\6G000011.D)
mAU
60
40
20
0
-20
1.198
2.520
11.485
0
2
4
6
8
10
12
14
16
min

6j

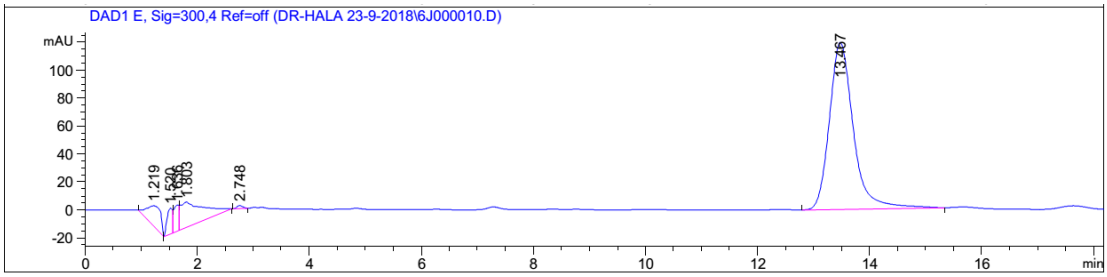
DAD1 E, Sig=300,4 Ref=off (DR-HALA 23-9-2018\6J000010.D)
mAU
100
80
60
40
20
0
-20
1.219
1.803
2.748
13.467
0
2
4
6
8
10
12
14
16
min

Chapter 5

Characterising PPARγ ligands identified by Atomwise, a drug discovery engine based on machine learning.

Benjamin S.K. Chua [a], John B. Bruning [b]

[a] School of Biological Sciences, The University of Adelaide, Adelaide, South Australia, 5005, Australia

[b] Institute for Photonics and Advanced Sensing, The School of Biological Sciences, The University of Adelaide, North Tce, Adelaide, South Australia, 5005, Australia

Statement of Authorship

Title of Paper	Characterizing PPARγ ligands selected by Atomwise, a drug discovery engine based on machine learning.
Publication Status	☐ Published ☐ Accepted for Publication ☐ Submitted for Publication ☑ Unpublished and Unsubmitted w ork w ritten in manuscript style
Publication Details	This paper characterizes a series of AI derived compounds, using in vitro techniques, cell based assays and molecular docking studies.

Principal Author

Name of Principal Author (Candidate)	Benjamin Soon Kai Chua
Contribution to the Paper	Conducted all experiments with compounds provided that were provided by Atomwise, synthesis of information, generation of figures, graphs and tables, and writing.
Overall percentage (%)	90
Certification:	This paper reports on original research I conducted during the period of my Higher Degree by Research candidature and is not subject to any obligations or contractual agreements with a :his thesis. I am the primary author of this paper.
Signature	Date 16/06/2023

Co-Author Contributions

By signing the Statement of Authorship, each author certifies that:

i. the candidate's stated contribution to the publication is accurate (as detailed above);

ii. permission is granted for the candidate in include the publication in the thesis; and

iii. the sum of all co-author contributions is equal to 100% less the candidate's stated contribution.

Name of Co-Author	John B Bruning
Contribution to the Paper	Supervised the research and writing of the paper
Overall percentage (%)	10
Signature	Date 16/06/2023

Please cut and paste additional co-author panels here as required.

1. Introduction

PPARγ is a nuclear receptor, which are a family of transcription factors that regulate a wide variety of processes in the human body (Weikrum et al., 2018). PPARγ is known as the master regulator of adipose biology and is involved in various processes involving metabolism, immunity and even cancer (Lefterova et al., 2014, Gross et al., 2017, Cheng et al., 2021, Christofides et al., 2021). PPARγ ligands have been used for treatment of type 2 diabetes (T2D) due to their effects on adipose tissue, reducing fasting as well as post prandial blood glucose levels. It has benefits over other treatments for T2D, including such as reducing whole body insulin resistance as opposed to increasing insulin availability, as well as longer persistence of positive benefits post treatment (Lebovitz 2019). Thiazolidinediones (TZDs) are one such drug class that is selective for PPARγ, which exerts its functions through binding the PPARγ LBD.

The PPAR ligand binding domain (LBD) is the largest domain of the PPARγ protein, which is made up of 12 helices and 4 β-sheets that folds into a 3-layer α helical sandwich (Figure 1). PPAR ligands typically bind to the PPAR ligand binding pocket (LBP), an approximately 1300Å space in the LBD enclosed by H2', H3, Ω-loop, β-sheet 3 and 4, H6, H7, H11 and H12. This space is delineated by predominantly non-polar amino acid side chains and can be viewed as distinct areas, or 'arms' (Figure 1, 4.6, Chua and Bruning, 2021). Ligands such as TZDs (eg. Rosiglitazone, Pioglitazone) occupy arm 1 and interact with the polar residues here to stabilize H12 and the activation function 2 surface (AF2), recruit coactivators and upregulate PPARγ gene transcription (Choi et al., 2011). Such ligands are known as full agonists (Figure 4.1-4.3). However, studies have suggested that the full activation of PPARγ might be the cause of the undesirable side effects seen with PPARγ agonist therapy, such as weight gain, fluid retention, bone fractures and even heart failure (Lebovitz 2019). Thus, more recent work has been focused on the discovery and optimization of partial agonists, antagonists and even inverse agonists (Bruning et al., 2007, Frkic et al., 2018b). The partial agonists generally occupy Arms 2 and 3 and do not stabilize H12 but instead stabilize the β-sheets to prevent phosphorylation of S243, while antagonists and inverse agonists prevent H12 from occupying the active conformation and recruiting coactivators or promote the inactive conformation and recruitment of corepressors respectively (Choi et al., 2011, Frkic et al., 2018b). Previous attempts to synthesize a safe and efficacious PPARγ selective ligand of any activity profile (full, partial, antagonist or inverse) for therapeutic use have been mostly unsuccessful (Cheng et al., 2019).

Despite the risks of side effects, PPARγ is still a valuable drug target due to its potential for treatment of various diseases (Cheng et al., 2019). In addition, Saroglitazar and Chiglitazar, which are both PPARγ selective, have been recently approved by the Food and Drug Association (FDA) for use with diabetic patients (Krishnappa et al., 2020, Deeks, 2022, Figure 4.1). This supports the hypothesis that side effects might in fact been ligand specific (Dubois et al., 2017). Thus, it might be valuable to continue exploration of ligands from different chemical spaces.

The Atomwise drug discovery program utilizes artificial intelligence in the process of small drug discovery. The program uses the AtomNet® technology to score and identify potential binders of protein targets (Wallach et al., 2015). To do so, AtomNet® incorporates spatial and temporal information from solved, ligand bound protein structures to identify features of favourable ligand-protein interactions or 'fingerprints' that can even be extrapolated to novel protein targets without solved protein structures. In this paper, 87 potential PPARγ activating compounds have been identified through the Atomwise drug discovery program from various chemical libraries. A thermal Shift Assay (TSA) and gene reporter assay was conducted to investigate the activity of these ligands. Pose docking was conducted to further understand the binding mode of several interesting compounds.

2. Methods

2.1. Plasmids

The CM-pBind-hPPARγ-Gal4 plasmid expressing the PPARγ LBD and Gal4 DNA binding domain (DBD) chimeric protein was a gift from the Scripps' Institute, previously used in Bruning et al. (2007). The Renilla luciferase control reporter vector, pRL-TK, was purchased from Promega. The plasmid pG5E1b-Luc was obtained from the Dan Peet laboratory, from the University of Adelaide.

Wildtype PPARγ LBD protein expressing vectors with ampicillin selection genes were purchased from GenScript. The PPARγ LBD (207 - 477aa) was cloned into the pET-11a vector using enzymes NdeI and BamHI.

2.2. Plasmid purification and construction

The plasmids were transformed into DH5α cells, propagated in LB supplemented with Ampicillin and purified using MIDIprep kits from Promega or Macherey-Nagel according to manufacturer's instruction.

The CM-pBind-Gal4-DBD only plasmid was generated using PCR mutagenesis. The primers were designed using the NEBaseChanger webtool (available at https://nebasechanger.neb.com/) and purchased from Sigma Aldrich.

CM-pBind-Gal4-DBD only plasmid

Forward: 5'-TGATAAGGGCGGATGCCACAGGCC-3'

Reverse: 5'-GTTAATTAATCGGATCCCCGGGAATTCCG-3'

PCR was conducted using NEB Phusion polymerase according to manufacturer's protocol. The mutants were verified by sequencing at the Australian Genome Research Facility (AGRF). The sequencing primers are given below:

Gal4 Forward: 5'-AGTGCGACATCATCATCGGAAGAG-3'

T3 Reverse: 5'-AATAACCCTCACTAAAGGGA-3'

2.3. Protein purification

BL21 (DE3) cells were transformed with the pET-11-PPARγ LBD expressing plasmid and propagated in LB broth at 37°C to an Optical density (OD) of 0.4 - 0.6. A portion of this bacterial culture was added to larger volumes of LB for protein expression (1/100) and grown at 37°C to an OD of 0.6. Protein expression in the bacterial cells was induced with IPTG (1mM final concentration) and the culture was incubated overnight at 16°C.

Cells purified by column purification were harvested by centrifugation at 5500RPM for 10 minutes at 4°C. Pelleted cells were resuspended in buffer A (25ml per litre of cell culture; 20 mM Tris pH 8.0, 500 mM NaCl, 10 mM imidazole, 2 mM BME) and then lysed using a cell disruptor. The cell lysate was clarified by centrifugation at 18 000 rpm for 30 minutes at 4°C. The supernatant was filtered (0.2µM), loaded onto a nickel resin IMAC column (immobilized metal affinity chromatography; GE health) and eluted against buffer B (20 mM Tris pH 8.0, 500 mM NaCl, 250 mM imidazole, 2 mM BME). Fractions containing the protein were pooled and dialysed overnight at 4°C against buffer S (20 mM Tris pH 8.0, 150 mM NaCl, 1 mM DTT). The dialysed protein was then loaded onto a HiPrep 26/60 Sephacryl S-500 size

exclusion column and eluted with buffer S. Eluted fractions containing the protein were pooled and concentrated to about 10mg/ml using a 10 000mW concentrator (Amicron). Aliquots of the concentrated, purified protein were flash frozen and stored at -80°C for future use.

2.4. Thermal shift assay

Flash frozen stocks of purified protein (concentrated in Buffer S: 20mM Tris pH 8.0, 150mM NaCl, 1mM DTT) were thawed on ice and used in a thermal shift assay with the SYPRO™ Orange Protein Gel Stain (Invitrogen™). The assay was performed in the 96 well format using the MicroAmp™ Fast Optical 96-Well Reaction plates (Applied Biosystems™). The well solution was initially mixed according to the protocol outlined in Thermofisher's protocol for protein melting experiments (Life Technologies, 2010) and then optimized with suggestions from other publications (Huynh and Partch, 2015). The volumes of the reagents of the TSA were optimized. Final volume in each well was 10 or 50µL, comprised of 0.5X-10X dye concentration, 0.01-0.6mg/ml protein in buffer, with ligand, DMSO control or apo protein. Assay components were pipetted into MicroAmp™ Fast Optical 96-Well Reaction Plate plates on ice and then sealed with adhesive film and centrifuged at 2000 RPM for 1-2 seconds to ensure well solution was mixed. The thermal shift assay was conducted at 4°C-70°C in increments of 0.3°C using the StepOnePlus™ Real-Time PCR System from Applied Biosystems™. Relative Fluorescence units (RFU) results were taken from filter 4 (610nm) unless otherwise specified. Each compound was tested in triplicate for each experiment.

2.5. Human cell culture

HEK293 cells were thawed from stocks of cells in Fetal Calf Serum, (FCS, Sigma Aldrich) and 10% DMSO and frozen at -80°C. Cells passaged at least twice before use in experiments. Cells were grown in DMEM (Gibco) supplemented with Glutamax and 10% FCS (Sigma Aldrich) and passaged when nearing 80% confluency, as calculated using the Bio-Rad TC20 Automated Cell Counter. All incubation steps were conducted at 37°C and 5% CO_2.

2.6. Dual luciferase assay (DLA)

Cells were then seeded onto 96 well plates (30 000 cells/well). 24 hours later, pCMV-PPARγ LBD-Gal4-DBD, G5E1B and RLTK was transfected (1:1:0.1 ratio, 262.5ng total plasmid DNA) using PEI (3 PEI : 1 DNA) as the transfection agent. After 24 hours, cell culture media was

replaced with fresh media supplemented with ligand or an equivalent volume of DMSO not exceeding 1/1000 of the volume of media added per well. Finally, after another 24 hours of incubation, cells were lysed and luciferase activity was determined using Promega's Dual-Luciferase® Reporter Assay System. 50µL of the Luciferase assay reagent II and Stop & Glo® was used. The DLA was performed at least twice in duplicate for initial tests to determine Rosiglitazone concentration test range and twice in triplicate for tests to determine agonist-response curves. Relative transcriptional induction refers to the ratio of Firefly to Renilla luciferase activity. The Akaike's Information Criterion (AIC) method was used to calculate probability of the models. The comparison used on Graphprism was "Do the best-fit values of selected unshared parameters differ between data sets?", comparing between test compounds and Rosiglitazone.

2.7. Structural analysis

2.7.1. Crystallization

Crystallization of ligand bound PPARγ complexes was attempted. 1µl of 10mg/ml of purified PPARγ protein was added to 1µl of well solution comprising of Sodium Citrate (0.7M – 1.3M) and Tris pH 8.0 (0.1 – 0.25M) and grown by vapour diffusion in hanging drop trays (500µL wells) and incubated at 16°C.

2.7.2. Docking with ICM-pro

Ligands were keyed in as SMILES strings and optimized using ELBOW (Phenix). Chain A was extracted from PPARγ structure PDB ID: 2PRG with waters and ligands were removed. Missing sidechains were added, hydrogens and sidechains were optimized in ICM-pro. Binding site was defined as a graphical selection of all residues beneath H4/5 (Figure 1). Thoroughness was set at 10.00, 7 conformations were generated per ligand. All ligand variations were sampled. 2D interaction diagrams were calculated using BIOVIA Discovery Studio Visualizer 2020 client using default settings.

3. Results

3.1. Compound screening for PPARγ

Atomwise kindly provided us with a range of compounds as part of the Artificial Intelligence Molecular Screen (AIMS) Awards program. First a 'trawler' was employed to scan large

chemical databases that contain up to a billion compounds for potential hits. This 'trawler' is a ligand based, target specific tool that uses a surrogate machine learning model (that is improved iteratively while scanning through the database) which predicts a compound's score by AtomNet® rather than its bioactivity. The promising compounds are then scored using the AtomNet® model, which predicts a compounds bioactivity, and the top candidates were selected for further evaluation. This two-step process improves the rate at which the algorithm scans prospective databases (Mysore et al., 2020).

3.2. Thermostability screening of Atomwise compounds with SYPRO™ Orange

To assess the potential of the Atomwise compounds to transactivate PPARγ, a thermal shift assay (TSA) with SYPRO™ Orange was attempted. Starting conditions of 2, 5 or 10X dye was used and protein concentrations of 0.01-0.03mg/ml were used without ligand or DMSO control, for a total well volume of 50µl. PPARγ did not yield acceptable fluorescence curves compared to the DDL protein with DMSO, which used as a positive control for fluorescence curves without a ligand bound (Figure 2.1a, Reinhard et al., 2013). 'Acceptable' TSA curves was defined by Reinhard et al. (2013) as having a sharp increase followed by a decrease in RFU – exemplified by the fluorescent curves achieved with the DDL protein. Optimization was repeated with PPARγ incubated with Rosiglitazone instead, the best fluorescence curves was achieved using PPARγ incubated with 5X dye, 0.03mg/ml protein concentration and 300µM Rosiglitazone (Figure 2.1b).

TSA of Compounds 4-34 was attempted using these conditions (5X dye and 0.03mg/ml protein concentration). Most compounds displayed curves with high starting fluorescence and a decreasing trend resembling the 3 example curves in Figure 2.2a, but some compounds showed curves resembling PPAR protein incubated with Rosiglitazone (Figure 2.2b). The TSA was repeated with increased protein concentration (5X dye, 0.05mg/ml), yielding similar results (Figure 2.2c and d). Like the previous experiment, most compounds displayed poor quality curves, some resembling TSA conducted with apo PPAR protein (Figure 2.1a, 2.2a). Some compounds displayed appreciable curves – with high starting fluorescence followed by sharp increase, peaking at a lower temperature compared to Rosiglitazone (Figure 2.2c). Strangely, the same compounds that yielded acceptable fluorescence curves for the previous test did not yield acceptable curves for this test (Figure 2.2b vs d).

Well conditions were changed and optimized - Protein concentration was increased (0.12-0.48mg/ml) and ligand concentration was decreased (to about 3: 1 ligand: protein ratio, Figure 2.3). In this round of optimization, higher protein and dye concentrations resulted in curves with high starting fluorescence. The condition that yielded the highest peak for the lowest amount of protein was 6X 0.12mg/ml but the condition 2.4X and 0.24mg/ml with a lower dye concentration and lower starting fluorescence was selected instead for use in another TSA with the Atomwise compounds. However, all the compounds that were tested produced poor quality fluorescence curves represented by Figure 2.3b. Finally, well volume was decreased to 10µl and optimized again (0.5-6X dye, 0.1-0.4mg/ml, Figure 2.4a, b). Well volumes (10 vs 50µl) and ligand volumes (3:1 ratio vs 100µM) were also tested at 2X dye concentrations. 6X dye and 0.3mg/ml protein concentration gave the highest fluorescence readings for the lowest amount of protein used. The conditions of higher well volume (50µl) and lower ligand to protein ratio (3:1) gave higher fluorescence readings, but also higher starting fluorescence (Figure 2.4b). Thus, the condition of 6X dye, 0.3mg/ml protein concentration incubated with 100µM ligand for a final well volume of 10µl was used in a final TSA experiment. Some compounds gave satisfactory curves (Figure 2.4c), but most compounds gave fluorescence readings represented by the curves 'Bad 1 and 2' in Figure 2.4d.

To determine if the binding of SYPRO™ Orange was causing irregularities with the TSA, docking of SYPRO™ Orange into 2PRG was attempted, along with Rosiglitazone and Pioglitazone as positive controls. Comparable docking scores were achieved – Edock: -20.14 for SYPRO™ Orange compared to -32.11 and -39.81 for Rosiglitazone and Pioglitazone respectively, for poses matching 3DZY and 2XKW (Figure 2.5). SYPRO™ Orange was predicted to occupy all 3 Arms of the PPARγ LBP. The two hexane chains branching from the core nitrogen stretches into Arms 1 and 3, and the rest of the ligand occupies Arm 2. In this pose, SYPRO™ Orange forms 18 favourable interactions, including Pi-Sulfur interactions with C285, as well as electrostatic and hydrogen bond interactions with polar residues on the Ω loop. Docking results suggest that PPARγ LBP binds SYPRO™ Orange.

3.3. Screening of transactivation activity of Atomwise compounds

Due to the incompatibility of SYPRO™ Orange with PPARγ or the Atomwise compounds, as well as the difficulty of optimizing the thermal shift assay, a screen was conducted with a cell-based luciferase reporter assay instead. At a concentration of 10µM, the Atomwise compounds showed a range of transcriptional activity profiles in HEK293 cells, including full

agonism (3, 19) and suppression of transcriptional activity (40, 79) (Figure 3.1). In order to identify efficacious and potent compounds with different activity profiles, reporter activity ranges likely corresponding to each activity profile were predetermined, relative to activity of negative and positive controls – full agonists were defined as having activity of ≥70%, partial agonists 20 – 69% and inverse agonists ≤-10%. According to this definition, the 87 compounds were split into categories: 3 full agonists, 41 partial agonists, 40 weak/inactive agonists or antagonists, 3 inverse agonists. 7 representative compounds with agonistic and inverse agonistic properties were shortlisted and further tested across a concentration range 0.01µM-50µM (Table 1.1, Figure 3.2).

3.4. Second screen of shortlisted compounds

The shortlisted compounds were subjected to an initial validation test over a smaller concentration range. Of the shortlisted compounds, 3, 19, 28, 42 and 76 seemed to increase gal4 luciferase reporter activity, while 40 and 79 decreased reporter activity below baseline levels (Figure 3.2). Compounds 3, 19 and 76 induced a maximal reporter activity approaching that of Rosiglitazone, which suggests that these compounds may be full agonists. The reporter activity induced by compound 76 seemed to be increasing even at compound concentrations of 50µM, indicating that 76 had a lower potency at activating PPARγ. Of the 3 full agonists, compounds 3 and 19 were selected for further analysis. Compounds 28 and 42 induced reporter activity higher than DMSO control at all concentration points tested but were less efficacious, inducing a lower maximum reporter activity compared to positive control Rosiglitazone, suggesting that these compounds may be partial agonists (Figure 3.2). The reporter activity induced by compound 42 seems to approach maximum and plateaus around 10µM (approximate relative response ratio, RRR: 31.06%, Eggers et al., 2016), suggesting that 42 might be a partial agonist (Figure 3.2). The activity – concentration relationship of compound 28 seemed to increase up till 1µM and then decrease towards 50µM (Figure 3.2). Surprisingly, compounds 40 and 79 seemed to decrease reporter activity below DMSO control levels, possibly indicating inverse agonist activity (Figure 3.2, DMSO grey dashed line). The activity – concentration of compound 79 decreased with increasing compound concentration, while the negative activity – concentration slope of compound 40 reversed past 1µM concentration. Of the partial and inverse agonists, 42 and 79 were selected for further analysis.

To determine the potency of selected compounds 3, 19, 42 and 79, concentration – activity relationship of the compounds in the transactivation assay were further tested at different concentration points (Figure 3.3). The selected compounds were found to have EC_{50} values ranging from 1 to 3 order of magnitudes higher than positive control Rosiglitazone. Of the agonist compounds, 19 seemed to have a highest potency at 0.213μM, but had a lower maximal activity compared to Rosiglitazone (ΔAICc = 3.824, Table 1.2, Figure 3.3). Compound 3 had a lower potency of 2.519μM but displayed similar maximal activity compared to Rosiglitazone (ΔAICc = -5.166). Compound 42 had a much lower maximal activity (15.3% compared to Rosiglitazone) than predicted previously in the initial screen shortlist test (54.41%) and the lowest potency of all the selected compounds (Table 1.1, 1.2, Figure 3.1, 3.2). Inverse agonist compound 79 reduced reporter activity below baseline with an IC_{50} of 4.686μM (Table 1.2, Figure 3.3). Compound 79 also seemed to be able to suppress Rosiglitazone induced reporter activity with an IC_{50} of 9.100μM, in a range similar to the concentration-activity curve in Figure 3.3 (Figure 3.4).

To ensure that the reporter effects seen were solely due to ligand interaction with the PPARγ LBD, HEK293 cells were transiently transfected with a Gal4-DBD only expressing construct, along with the same reporter plasmids and treated with 10 μM of the selected compounds. As expected, 'wildtype' PPARγ-Gal4 chimeric construct exerts baseline activity higher than that of the Gal4-DBD only construct when treated with vehicle control (Figure 3.5). Interestingly, 19 and 79 significantly suppressed Gal4-DBD activity compared to DMSO control. Compound 79 also suppressed reporter activity in a transiently transfected Gal4-DBD only expressing luciferase assay, at a IC_{50} of 2.529 μM (Figure 3.6). This suggests that the inhibition activity of compound 79 might be independent of its interaction with the PPARγ LBD.

Closer examination of the relative transcriptional induction (RTI) ratios (Firefly:Renilla luciferase ratio) of compounds 19 and 79 reveals that the overall changes in RTI can be attributed to changes in Renilla luciferase activity compared to baseline controls (Figure 3.7). Surprisingly, the upward sloping concentration-activity curve of compound 19 was due to small increases in Firefly luciferase activity coupled with concentration dependent decreases in Renilla luciferase activity compared to DMSO controls (Figure 3.3, 3.7a, b, green open circles). The downward sloping concentration-activity curve of compound 79 on the other hand was likely blunted from decreased Renilla luciferase activity at higher concentrations

(50-100 µM, Figure 3.3, 3.7, orange downward triangles). This decrease in Renilla luciferase activity was not seen in PPARγ-Gal4 transfected cells cotreated with compound 79 and Rosiglitazone, but returned with single treatment of 79 in cells transfected with Gal4-DBD expressing plasmids (Figure 3.4, 3.6, 3.7). Crucially, Firefly luciferase activity was suppressed in Gal4-DBD expressing cells (Figure 3.7c), supporting the hypothesis that the inhibition activity of compound 79 might be independent of interaction with the PPARγ LBD.

The positive control full agonist Rosiglitazone showed clear increases in both Firefly and Renilla luciferase activity at higher concentrations (1µM), resulting in a plateauing of the observed slope of relative transcriptional induction (Figure 3.3, 3.7a, b, blue circles). In contrast, Renilla luciferase values remained near DMSO levels with treatment of potential agonist compound 3 while Firefly values plateaued at higher concentrations (5-25µM, Figure 3.7a, b). Interestingly, when treated with DMSO, the Firefly luciferase activity of cells transfected with either the Gal4-DBD only expressing plasmids or the wildtype PPARγ-Gal4 expressing plasmids were similar, but the Renilla luciferase activity was about 10-fold higher in cells transfected with the Gal4-DBD expressing plasmids. The difference in Renilla luciferase activity accounts for the approximately 10-fold difference in RTI of DMSO treated wildtype PPARγ LBD – Gal4 DBD transfected cells and Gal4-DBD transfected cells (Figure 3.5).

3.5. Structural analysis

To better understand the observed changes in RTI, co-crystallization of the compounds with PPARγ LBD protein was attempted. Ligands were incubated with PPARγ protein and added to hanging drops consisting of Sodium Citrate and Tris pH8.0. Protein precipitation was achieved, but no crystallization occurred. In order to overcome difficulties in crystallization, docking of compounds into PPARγ was conducted with ICM-pro to understand the structural properties of the shortlisted Atomwise compounds. The docking model, PDB ID: 2PRG (Nolte et al., 1998) was a cocrystal structure with Rosiglitazone and contained the full structure of the Ω loop. This model was chosen to better simulate possible interactions between Atomwise ligands and the Ω loop, if any. As a control, the model was docked with Rosiglitazone and Pioglitazone. Generally, an Edock score of -32 and below is considered good, or that matching the score of a cocrystal structure redocked with its ligand. 'Higher scoring' refers to a more negative Edock score (Abagyan et al., 2023).

The top and second scoring pose for Rosiglitazone aligned closely with the experimentally determined position of Rosiglitazone in crystal structures PDB ID: 2PRG and 3DZY respectively, differing in the orientation of the N-methyl group extending from the Nitrogen on the 2-piperidinamine (black arrows, Figure 4.2). For Pioglitazone, the second highest scoring pose aligned closely to experimentally determined Pioglitazone positions in crystal structures PDB ID: 2XKW and 5Y2O (Figure 4.3b), whereas the top scoring pose occupies the same area but features a turned TZD group (Black arrows, Figure 4.2).

The docking pose of potential agonist 3 shows a 'tail-down conformation' similar to the full agonist TZDs Rosiglitazone and Pioglitazone (Figure 4.4, 4.5). The head region of 3 reached into Arm 1, to a position comparable to the TZDs, forming hydrogen bond interactions with H449 and Q286 on H3 (Figure 4.4, 4.5c). On the other hand, the tail region of 3 occupied more space anteriorly in Arm 2 compared to the TZDs, wrapping around H3 and forming more interactions with residues on the H3 and the β-sheet (Figure 4.4, 4.5c). The flexibility of the carbon chain linking the head and tail substituents in compound 3 allowed the tail region of 3 to adopt multiple conformations, including the top-down conformation seen in PDB: 2XKW (Figure 4.5 d). In this top-down conformation, compound 3 formed 20 favourable interactions versus 11 for pioglitazone (Figure 4.5a, b).

Compound 19 has a unique fluorene head region, amide linker and a linked oxadiazolidine and phenol tail region (Figure 4.1). The compact ligand did not interact with any of the polar residues in Arm 1 and made interactions mostly in Arm 2, specifically with H3 and the β-sheet in a manner similar to the tail region of compound 3 (Figure 4.6a, b). The ligand adopted a 'T-L-shaped' conformation in most poses, binding mostly to the same region but in different orientations (T from head to core, and L from core to tail, Figure 4.6c, d). Compound 19 also had the lowest docking score of all the shortlisted compounds (Edock: 3.662).

Compound 42 adopted a similar 'L-shaped' conformation. Like 19, 42 also occupies space in Arm 2 / Arm 3 region and formed interactions with residues in Arm 2 (Figure 4.7a, b). The top pose has a score of Edock -0.962, in which the chloride substituent oriented towards H7 and interacted with M364 and Y327 (Figure 4.7a). In this pose, compound 42 made 14 interactions with the PPARγ versus 17 interactions of compound 19 (Figure 4.6b, 4.7b).

Compound 79 shows interactions in the Arm 2/ Arm 3 region, with residues on H3, H5 and the β-sheet, similar to 19 and 42 (Figure 4.8). However, in contrast to 19 and 42, 79 adopts a

Y-shaped conformation which allows for interactions with residues in all 3 Arms at once (Figure 4.8a, b). In the top 3 poses, 79 occupies a similar area in Arm 2 as the TZDs but it does not reach as far towards H12 and occupies more space in Arm 3 in comparison (Figure 4.8c-e). In these poses, 79 showed contacts with S289, Y327 and H449 in Arm 1. In poses 4-5, 79 occupies a space between Arm 2 and the Ω loop, wrapping around the solvent exposed surface of H3 (Figure 4.9). In these positions, 79 makes unfavourable bumps with residues on H3, β-sheet (G284, R280, S342) as well as residues on the Ω loop and H2' (Q271 and I262, Figure 3.9a, b).

4. Discussion

4.1. Thermal shift assay

The TSA was performed previously for PPARγ by Lee et al. (2017) and Ribeiro Filho et al. (2018). However, despite taking extra steps in optimization, our thermal shift assay did not produce acceptable fluorescence curves for most compounds, with the sole exception of compound 13 in the last round of optimization (Green lines Figure 2.4c, Figure 2 from Reinhard et al., 2013). Components in the buffer (Tris, NaCl, Imidazole, DTT) have been used in previous published methodologies and have not been noted to interfere with the assays (Hyunh and Park 2015, Ribeiro Filho 2018). Acceptable fluorescence curves with the positive protein control DDL and PPARγ incubated with Rosiglitazone was achieved with the first set of conditions, suggesting that the assay dye, disposables, pipetting technique and methods used were not directly interfering with the assay (Figure 2). Protein concentration was the focus of latter optimizations, as protocols recommend a wide range of protein concentrations: the ThermoFisher protocol recommended final concentration of 0.02-0.2mg/ml, Reinhard et al. (2013) suggested using 20-100µM, and Huynh and Partch (2015) suggested 1–20 µM of protein. Filho et al. (2018) had success with 4µM protein, but no fluorescence curves were included in the data and other techniques such as nano differential scanning fluorimetry (NanoDSF) and luciferase assay were also used as validation for their TSA results. Wu et al. (2017) had success using 4µM of protein, for a TSA with the related PPARδ protein. Recommended dye concentrations, on the other hand are more similar, usually in the range of 1-10X, which we covered through the course of our experiments (Huynh and Partch 2015).

On initial inspection SYPRO™ Orange seems unable to bind the PPARγ LBP due to the length of the molecule. However, the flexible carbon linkers and the length of the molecule allows

the SYPRO™ Orange molecule to adopt the top-down conformation and form favourable interactions in the LBP (Figure 2.5). The top-down conformation is seen with experimentally crystallized structure of Pioglitazone, and when taken together with the comparable docking score of SYPRO™ Orange to positive controls (Figure 3.5d, Edock -20.14 vs -32.11 and -39.81 for Rosiglitazone and Pioglitazone respectively) suggests that SYPRO™ Orange might be able to bind to PPARγ LBD in its apo, folded state with significant affinity. This might explain why acceptable fluorescence curves were only obtained with the optimization tests using PPARγ protein incubated with Rosiglitazone – In PPARγ protein incubated with control DMSO or low affinity ligands, SYPRO™ Orange molecules likely outcompete and binds to the LBP, resulting in the high starting fluorescence seen with our results. Indeed, in an interactive model created by Wu et al. (2020) adjusting dye binding parameters creates the curve shape seen with our results (high starting peak, sharp decline, slower decrease, Figure 2.2a, 2.4d). Specifically, increasing the 'folded state' and decreasing the 'irreversibly unfolded state' parameters, which refers to the degree of dye binding to and activation of the folded and irreversibly unfolded state of the protein respectively. In a separate study, binding of thermal shift dye (by ThermoFisher) to the Pregnange X Receptor (PXR) was also reported by Sekiguchi et al. (2013) – the fluorescence curve shows the same high starting fluorescence and sharp decrease seen in our results.

Even though some Atomwise compounds yielded satisfactory fluorescence curves, Rosiglitazone, a high affinity, compound that has been structurally optimized was the only available positive control. Atomwise compounds are meant to be further optimized, in other words likely to be low affinity binders – and as such we would expect to see only leftward shifts from Rosiglitazone (Figure 2.2c, 2.4c). It would be hard to distinguish PPARγ binders from non-binders without the TSA fluorescence curves of a true apo-PPARγ (with DMSO) or PPARγ bound to a verified antagonist. Unfortunately, our optimization of TSA of PPARγ incubated with DMSO did not give acceptable fluorescence curves (Figure 2.3b, 2.4c, d). In short, our results suggest that SYPRO™ Orange binds to the PPARγ LBP, interfering with fluorescence readings and may thus, make the TSA unsuitable for investigating the binding of Atomwise compounds to the PPARγ LBD. As an alternative, other in-vitro binding assays such as Hydrogen-Deuterium exchange (HDX), Isothermal Calorimetry (ITC) or Surface Plasmon Resonance (SPR) could also be conducted to validate the binding of these compounds to PPAR.

4.2. Dual Luciferase assay as a screening tool

From our dual luciferase assays, compounds 3 is likely a full agonist and 42 a weak partial agonist, while the agonistic or antagonistic nature of 19 and 79 remains to be confirmed due to changes in Renilla luciferase activity (Figure 3.7). Although Luciferase based assays have been used extensively to determine PPAR ligand activity, various experimental conditions have been shown to affect HSV-TK controlled Renilla luciferase expression. This includes PPARα expression as well as treatment with PPARγ ligand 15d-PGJ2 – likely due to competition for limited cofactors needed for transcription (Everett and Crabb 1999, Zhang et al., 2003, Shifera and Hardin, 2010). Of note, Zhang et al. (2003) also found that Firefly luciferase expression was affected with 15d-PGJ2 treatment. Since the decrease in Firefly luciferase activity in both PPARγ-Gal4 and Gal4-DBD cells treated with 79 occurs past a similar concentration point (≥1μM), it is likely that the antagonistic properties of compound 79 are independent of PPARγ. This highlights the importance of interpreting results in context to appropriate controls. It is interesting to note that even with Rosiglitazone, a well-known PPAR selective ligand, Renilla luciferase activity increases with increasing treatment concentrations, without visual signs of cell toxicity (Figure 3.7). Other experimental treatment groups were also monitored for visual signs of cell toxicity. However, since cell toxicity was not explicitly monitored for across experiments (with a cell viability assay), it remains as a confounding factor that might potentially affect luciferase values, especially in the case of the competitive binding assay of Rosiglitazone versus compound 79 (Figure 3.4). Within our experiments, there was also a large discrepancy between the activity of compound 28 when monitored in a single experiment with a single replicate (about 38% activity compared to Rosiglitazone, Figure 3.1) versus across four concentration points in duplicate (about 51% activity compared to Rosiglitazone, Figure 3.2). This suggests that compound 28 could have been flagged as a false positive.

However, despite the shortfalls, this current assay set-up still achieves our initial purpose to identify compounds with potentially interesting effects on transcription activity for further optimization and testing. Our EC50 values obtained from Rosiglitazone control concentration-activity curves matched previous experiments (Lehmann et al., 1995). Furthermore, it is to be expected that, when screening a wide range of compounds of novel structure and potentially function, assay conditions might not be optimal for every compound tested. Other normalization strategies could be tested, for example the β-galactosidase reporter. In fact, some papers include luciferase assay results without any normalization strategy (Shang et al., 2020). Follow-up experiments could address this decrease in Renilla luciferase signal by

conducting the luciferase reporter assay with Renilla expressing plasmids under the control of different promoters, eg. pCMV-RL or pSV40-RL or in other cell models with different levels of cofactors, altering amounts of cotransfected plasmids, and examining protein expression levels to provide better insight into the action of novel compounds (Ibrahim et al., 2000, Zhang et al., 2003). Experiments should also include tests for cell viability, for example a live-cell protease viability test, to increase the confidence in hits from the compound screen. Although this work focused on characterising a shortlisted group of compounds, the remaining Atomwise compounds that were excluded from further analysis based on the initial screen could have novel properties that are worth investigating in future experiments. To reduce the possibility of false positives, compounds could be investigated with the same dual luciferase screen but conducted with at least two different compound concentrations, with more technical and biological replicates, or with other in vitro techniques as suggested above.

4.3. Structural analysis

Docking poses of compound 3 shows favourable interactions, and the occupation of space in Arms 1 and 2, crucial for increasing affinity and selectivity for PPAR (Chua and Bruning 2021). The 1, 4 substituted phenyl core and the flexible carbon linker between the head and tail substituents allows the ligand to adopt tail-down, tail-up, and even the top-down conformation seen with Pioglitazone (Figure 4.5). The slimmer methyl acetic head region of the ligand occupies less space in Arm 1 and does not form direct hydrogen bond interactions with Y473 on H12 like typical full agonists, which might explain the lowered EC_{50} of compound 3 compared to Rosiglitazone (Figure 4.4, 2.519 vs 0.02µM, Table 1.2). However, the ligand potentially forms interactions with H449 (1/4 polar residues in Arm 1, Chua and Bruning 2021) and residues on H3, including a surprising hydrogen bond with Q286 (Figure 4.4b). Extensive interactions with H3 and the β-sheet leading to its stabilization, is the theorized mechanism by which partial agonists activate PPARγ (Frkic et al., 2018a). Multiple favourable interactions with all Arms across different conformations likely contribute to compound 3's maximal efficacy, which was comparable to Rosiglitazone. In short, the docking results of compound 3 suggest that it might be an atypical full agonist of PPARγ.

Considering the arrangement of chemical motifs in 19, the rigid amide core connecting the head and tail substituents would severely limit the possible conformations of the ligand that would fit the PPARγ LBP. Indeed, the ligand conformation is almost identical in all 7 poses, aside from slight tilting of the tail region, made possible by the carbon atom between the

amide and the oxadiazolidine. The low induction of Firefly luciferase activity seen with 19 likely stems from the lack of interaction with residues in Arm 1 and limited interactions in Arm 2 (Figure 3.7a, 4.6d). The decrease in Renilla values observed might be due to offsite binding of 19 – the overall smaller ligand length might in fact decrease its selectivity for PPARγ.

The low transcriptional induction of compound 42 likely stems from the same rigidity in the ligand as seen in compound 19. The 1,2 substituted core of 42 restricts the possible conformations of the ligand and prevents the head and tail regions from reaching into either Arm 1 or 2 (Figure 4.7d). This positions the ligand in the region between bordered by H7, H5, H3 and β-sheets. The head and tail regions, however, are considerably less bulky and allows for more favourable orientations of the head and tail regions with respect to the 1,2 substituted phenyl ring core. Typically, halogen atoms are added onto the tail end of the ligands which interact with Arm 2 (Chua and Bruning, 2021) but in this case the chloroaniline group interacts with residues M364 and Y327 in the PPARγ LBP (Figure 4.7a). Residue Y327 is unique to the PPARγ subtype and interactions with M364 selects against PPARδ, thus it might be valuable to further optimize the structure compound 42 to improve its efficacy.

Forming interactions with residues on the AF2 surface including hydrogen bonds with polar residues in Arm 1 is crucial for the full agonism of PPARs (Chua and Bruning 2021). Although 79 forms limited interactions with Arm 1 (only S289), most of its interactions occur with residues in Arms 2 and 3. Additionally, in poses 4 and 5, 79 interacts with the omega loop, wrapping around the front of H3, forming unfavourable interactions (Figure 4.9). The position of 79 in these poses is reminiscent of SR10171 (PDB ID: 6C5Q) a PPARγ inverse agonist as well as WY14643 (PDB ID: 4BCR), a PPARα agonist (Frkic et al., 2018b, Bernardes et al., 2013). The unfavourable bumps calculated in poses 4 and 5 could result in the disruption of the H3 and Ω loop – induce tilting of H3 and shifting of H12, moving H12 to occupy antagonist bound conformations (Figure 3.9c, Frkic et al., 2018b, Shang et al., 2020). Despite the probable binding pose, considering the cell transactivation data, the binding of 79 to PPARγ will have to be confirmed using additional binding experiments, such as Förster resonance energy transfer (FRET) assays conducted by Shang et al. (2020).

Taken together with the results from the cell transactivation assay, the in silico structural analysis seems to suggest that the Atomwise program has successfully identified ligands (3 and 42) with novel binding modes to the PPAR LBD. Optimization of compounds, including

other weaker agonists and 'failed' ligands (19 and 79 respectively) with the help of structural information can increase the success rate of the screening program.

4.4. Viability of In-silico methods for drug discovery

While an in-depth discussion of the pros and cons of different AI algorithms and drug discovery methods is out of the scope of this thesis, we can look at this attempt in context of previous methods applied specifically to PPARγ drug discovery. One previous attempt that yielded the Pan-PPAR agonist Indeglitazar (discontinued in Phase 2 trials) relied on the calculation of the 'Molecular Interaction Field' defined by maximal interaction energies with chemical probes, and ranking leads based on crystal structure information (Artis et al., 2009, Hong et al., 2018). Another attempt applied Machine learning on drug discovery for the PPARδ subtype, using the Iterative Stochastic Elimination (ISE) method, which relies on defining 'good' molecular properties of the compounds, generating filters with random combinations of these properties and eliminating the least useful according to the Matthews Correlation Coefficient, and using those filters to sort through databases (Da'adoosh et al., 2019). This ligand-based attempt identified many unique, high affinity binders to PPARδ. The AtomNet distinguishes itself from other methods by being able to predict drug binding affinity or ligand binding from first principles – learning to recognize spatial and temporal cues, generating rules and scoring for bioactivity based on them, instead of using predefined molecular descriptors (Wallach et al., 2015). In theory, given a big enough training set, it would not only allow the model to score ligands for novel protein targets, but even identify molecular features that have not been considered previously. Interestingly, compounds 3 and 19 bear structural resemblance to the recently licensed T2D ligands Saroglitazar and Chiglitazar (Figure 4.1). However, given the nature of the assays used in this study as well as its goal, the true utility of AtomNet in predicting PPARγ binding ligands may have been obscured. Further studies with more comprehensive assays are required to confirm the activity of the rest of the Atomwise compounds, as suggested above. It is also crucial to note that ligands identified from the Atomwise drug discovery program were intended as starting points for further optimization. Ultimately, every method has its advantages and specific use case, but the greatest utility of each method towards drug discovery for PPARγ is its unique perspective, and a chance at identifying new lead compounds that are chemically distinct from those currently available in the market.

In summary, the Atomwise drug discovery program provides a novel, versatile tool that is able to identify readily synthesizable compounds that bind both well-studied and novel protein targets. In this study several compounds were identified that seemed to have diverse activation profiles. TSA might be incompatible with PPAR, but the dual luciferase assay was sufficient for identification of PPAR activating compounds. Examination of the ligand docking poses provided possible explanations for results seen with the dual luciferase assay. However, due to the nature of the assays used, further investigation is required to confirm the properties of the current set of compounds. Future studies should first focus on validating the current results with additional experiments such as cell viability tests to rule out cell toxicity, or other in vitro methods such as HDX, ITC, SPR or FRET to confirm ligand binding to PPAR. Following this, the rest of the Atomwise compounds could be reinvestigated using the dual luciferase assay with more technical and biological replicates at different concentrations to reduce the rate of false positives. Then, chemically distinct hits with interesting activation profiles could be further optimized.

5. Figures

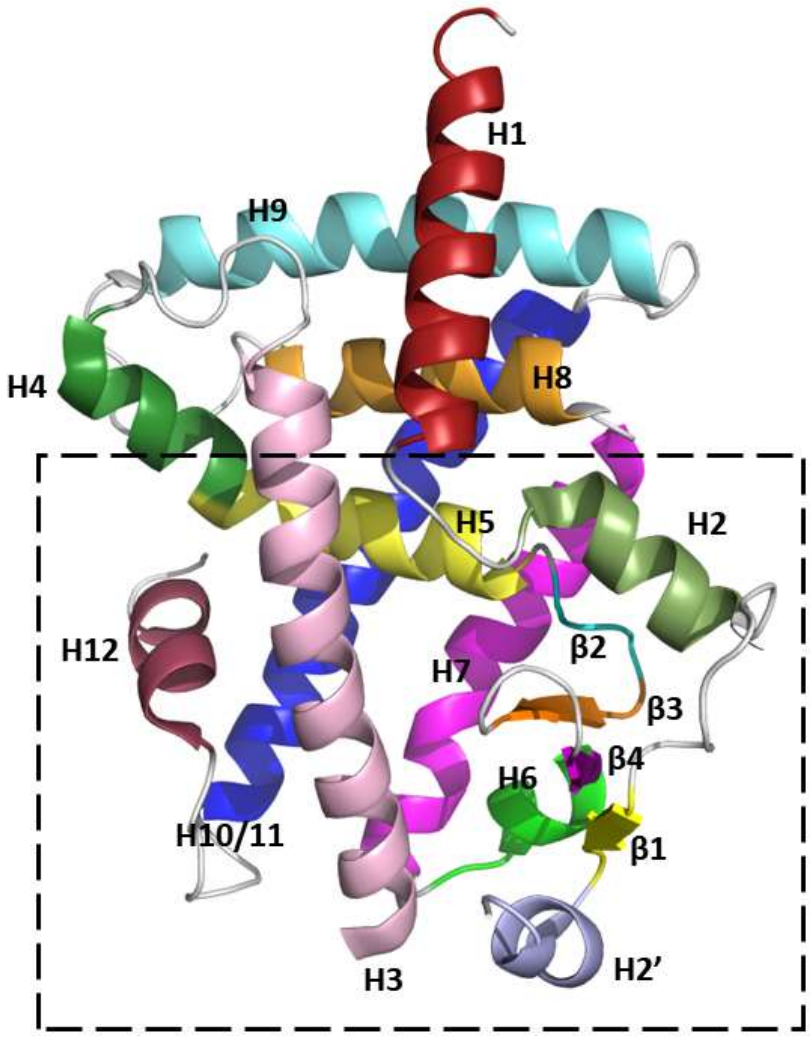

Figure 1. **The PPARγ ligand binding domain.** PPARγ LBD from PDB ID: 3DZY (residues 205-477) with each helices labelled and coloured separately. Dotted box represents the area defined as the 'binding site' for docking with ICM-pro. Helix colour names are taken from Pymol. Helices are coloured are as follows: H1 (Firebrick) H2 (Smudge) H2' (light blue) B1 (yellow) H3 (light pink) H4 (Forest) H5 (Pale Yellow) B2 (Cyan) B3 (Orange) B4 (Magenta) H6 (Green) H7 (Magenta) H8 (Bright orange) H9 (Aquamarine) H10/11 (Blue) H12 (Raspberry). Helices are labelled according to nomenclature established by Uppenberg et al. (1998).

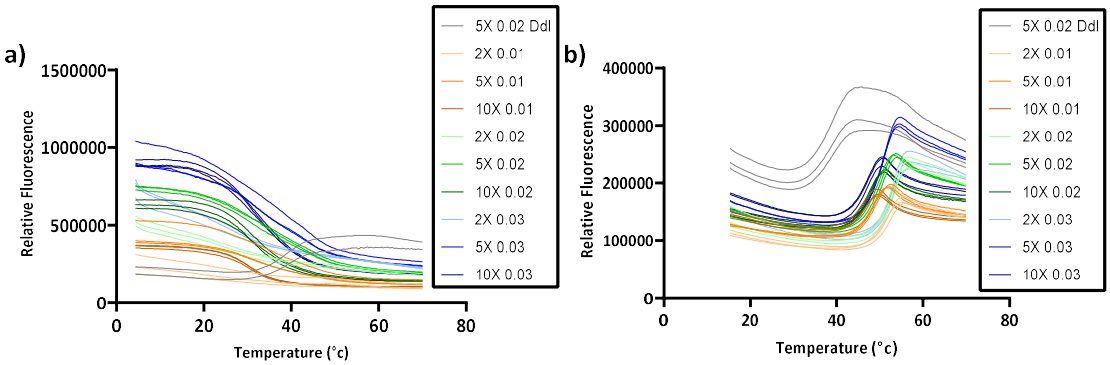

549

550 Figure 2.1 **The Thermal Stability Assay of PPARγ was optimized with and without Rosiglitazone.**
551 Thermostability of purified PPARγ protein was investigated. a) A TSA was conducted with purified
552 PPARγ LBD protein over a range of dye (increasing colour intensities: 2-10X) and protein
553 concentrations, (orange, green, blue; 0.01, 0.02 and 0.03mg/ml respectively) using a total well volume
554 of 50µl. b) The TSA was repeated with purified protein incubated with Rosiglitazone (0.01, 0.02 and
555 0.03mg/ml incubated with 100, 200, 300µM respectively. Purified apo Ddl protein (grey) was included
556 as a positive control. Each condition was tested in triplicate, except for Ddl control in a) which was
557 conducted in duplicate.

558

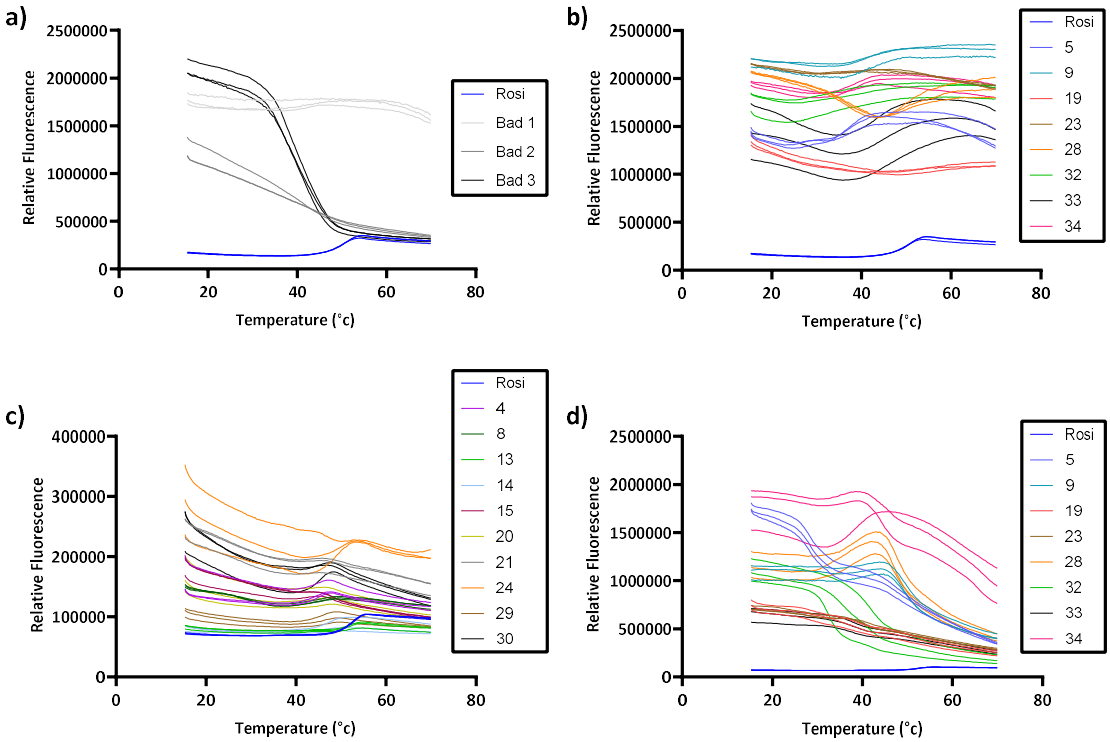

559

560 Figure 2.2 **TSA of PPARγ incubated with compounds 4-34 and Rosiglitazone was unsuccessful with**
561 **optimized conditions.** Thermostability of purified PPARγ protein, incubated with Rosiglitazone or a
562 subset of the Atomwise compounds was investigated. A TSA was conducted with purified PPARγ LBD
563 protein, either using 5X dye and 0.03mg/ml protein concentration incubated with 300µM ligand (a,b)
564 or 5X dye and 0.05mg/ml protein incubated with 500µM ligand (c,d), using a total well volume of 50µl.
565 a) Most compounds displayed poor quality fluorescence curves, resembling flat lines (light grey), high
566 starting fluorescence followed by linear decreasing lines (grey) or high starting fluorescence followed
567 by sharp decrease (black), and are referred to in the figure legend as Bad 1-3 respectively. b, c) Other
568 compounds showed appreciable fluorescence curves. d) The fluorescence curves of the same
569 compounds that displayed acceptable fluorescence curves in b), tested again at the same conditions
570 as in c).

571

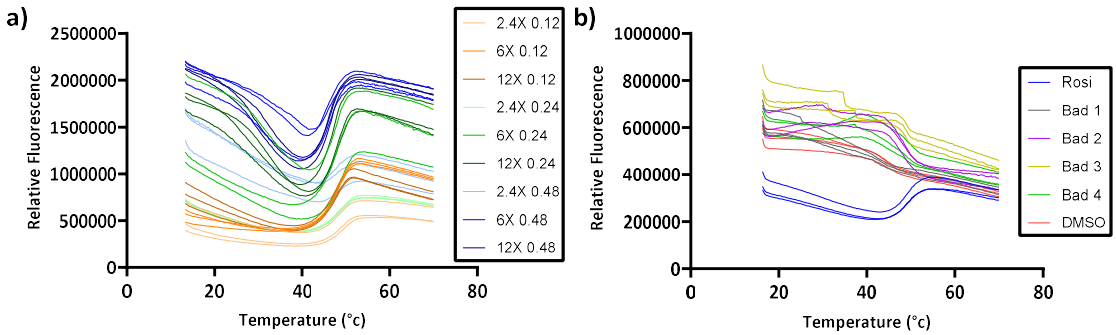

572

573 Figure 2.3 **Protein and ligand concentrations were optimized, but the TSA of PPARγ with compounds**
574 **4-33 was unsuccessful.** Thermostability of purified PPARγ protein, incubated with Rosiglitazone or a
575 subset of the Atomwise compounds was investigated. a) A TSA was conducted with purified PPARγ
576 LBD protein over a range of dye (increasing colour intensities: 2.4-12X) and protein concentrations,
577 incubated with Rosiglitazone (orange: 0.12mg/ml and 9µM, green: 0.24mg/ml and 18µM, blue:
578 0.48mg/ml and 27µM, protein and ligand concentration respectively) using a total well volume of 50µl.
579 b) The optimized conditions from a) (2.4X, 0.24mg/ml, 27µM ligand) were used for another TSA of
580 purified PPARγ LBD protein incubated with compounds 4-33. The compounds yielded poor quality
581 curves represented by fluorescence curves in b) labelled Bad 1-4. DMSO or Rosiglitazone incubated
582 protein was included as controls, however no thermal shifts due to binding of Rosiglitazone could be
583 calculated as DMSO did not display acceptable fluorescence curves.

584

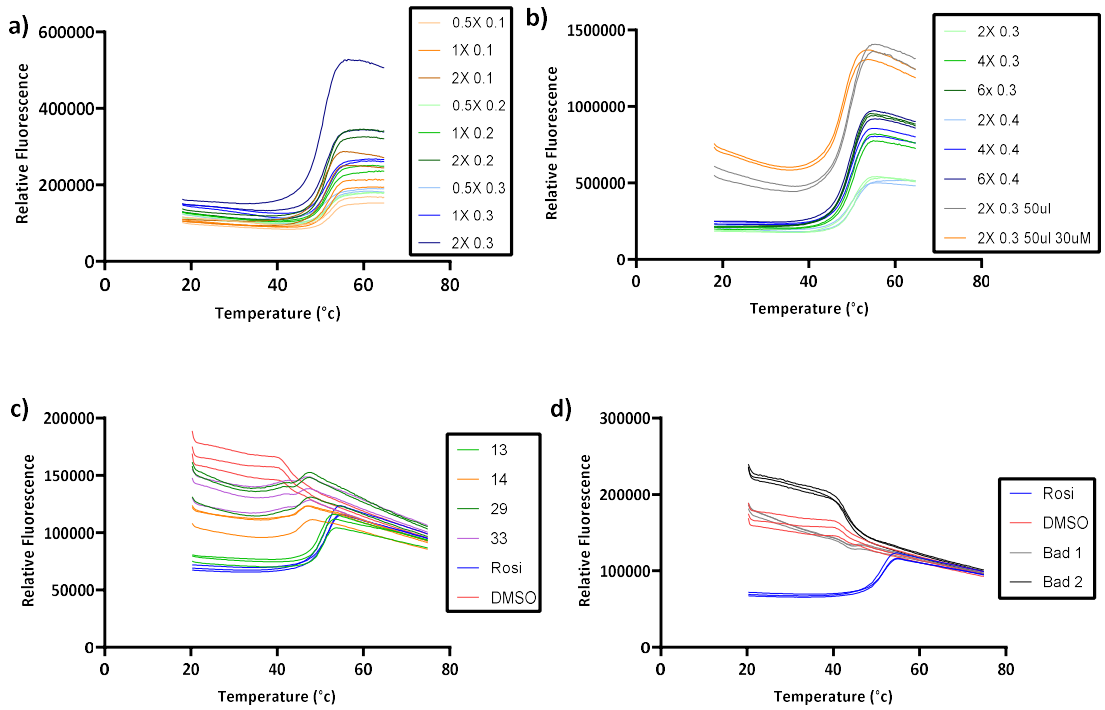

585

586 Figure 2.4 **Well volume, dye and ligand concentration were optimized, but the TSA of PPARγ with**
587 **compounds 4-33 was still unsuccessful.** Thermostability of purified PPARγ protein, incubated with
588 Rosiglitazone or a subset of the Atomwise compounds was investigated. a, b) A TSA with reduced well
589 volume (10µl) was conducted with purified PPARγ LBD protein over a range of dye (increasing colour
590 intensities: 0.5-2X) and protein concentrations (orange: 0.1mg/ml, green: 0.2mg/ml, blue: 0.3mg/ml)
591 incubated with 100µM Rosiglitazone. Two additional conditions were tested, with 2X dye
592 concentration 0.3mg/ml protein and increased well volume of 50µl, and 2X dye concentration
593 0.3mg/ml protein and increased well volume of 50µl incubated with 30µM Rosiglitazone. These were
594 referred to in the figure legend as '2X 0.3 50ul' and '2X 0.3 50ul 30uM' respectively. c, d) The TSA was
595 conducted again with the optimized conditions of 6X dye, 0.3mg/ml purified PPARγ LBD protein
596 concentration incubated with 100µM ligand with final well volume of 10µl. c) Some compounds
597 produced acceptable curves, while most d) produced poor quality curves represented by curves bad
598 1 and 2. DMSO or Rosiglitazone incubated protein was included as controls, however no thermal shifts
599 due to binding of Rosiglitazone could be calculated as DMSO did not display acceptable fluorescence
600 curves.

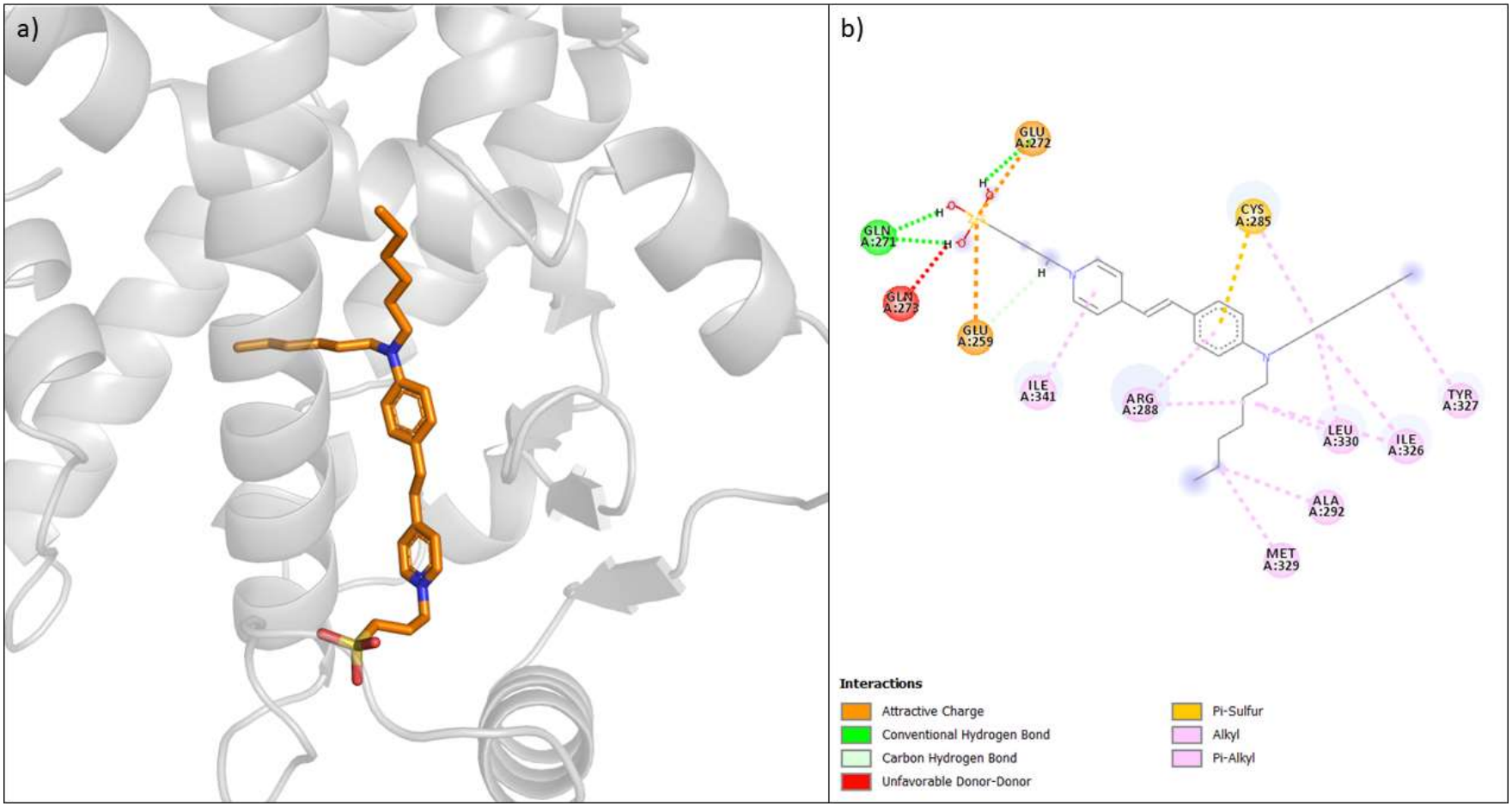
a)
b)
GLU A:272
GLN A:271
GLN A:273
GLU A:259
CYS A:285
ILE A:341
ARG A:288
LEU A:330
ILE A:326
TYR A:327
ALA A:292
MET A:329
Interactions
Attractive Charge
Conventional Hydrogen Bond
Carbon Hydrogen Bond
Unfavorable Donor-Donor
Pi-Sulfur
Alkyl
Pi-Alkyl

601

602 Figure 2.5. **SYPRO™ Orange docks into the PPARγ LBP and forms favourable interactions**. Molecular docking studies were conducted with SYPRO™ Orange. Docking poses
603 for SYPRO™ Orange (in orange) in the PPARγ LBP was determined with ICM-pro using 2PRG as a docking model. a) The top scoring pose for SYPRO™ Orange (Edock -20.14)
604 b) the corresponding 2D interaction diagram of SYPRO™ Orange and the residues in the PPARγ LBP (18 favourable interactions).

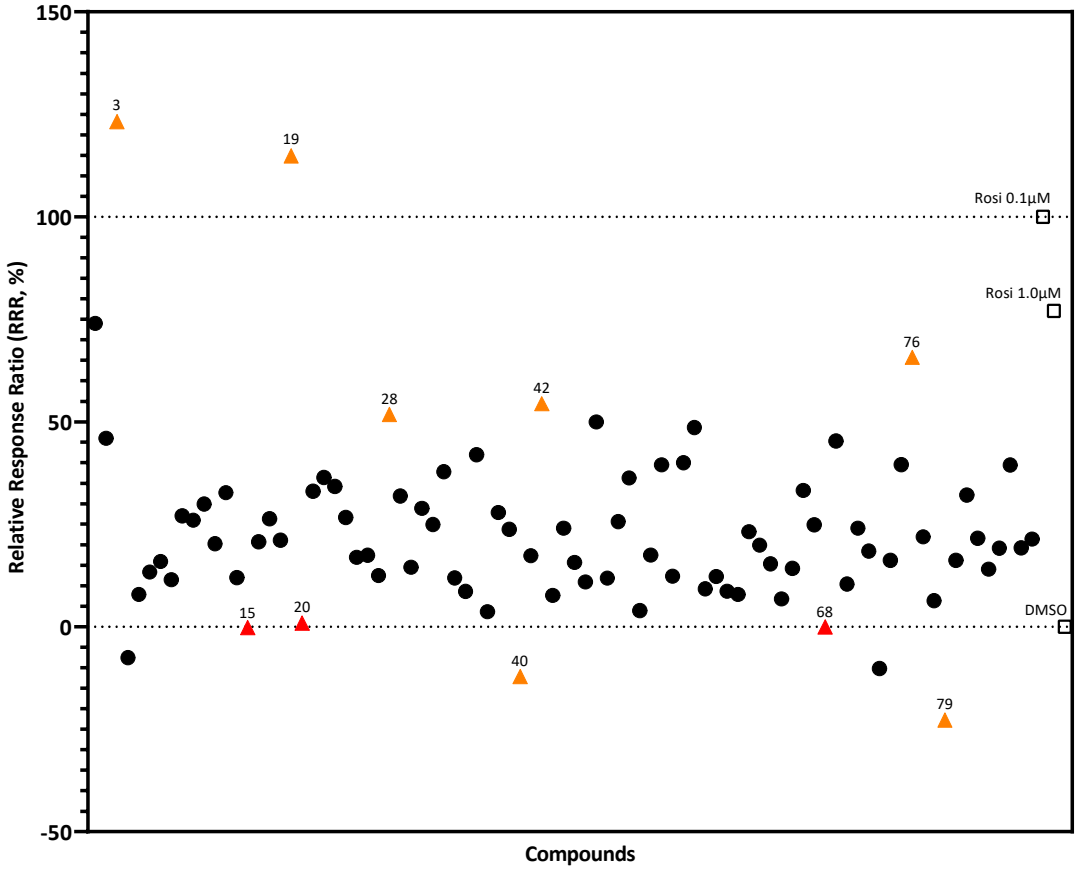

Figure 3.1. **Atomwise compounds activate PPARγ transcription activity in a compound screen.** The reporter gene transactivation induced by the Atomwise compounds was investigated with the dual luciferase assay (DLA). Cells were transiently cotransfected with PPARγ-Gal4 expression plasmids and pG5E1b and pRL-TK reporter plasmids, and treated with 10µM Atomwise compounds or control compounds full agonist Rosiglitazone, at 0.1 µM and 1.0µM, and vehicle DMSO. Squares represent control compounds, triangles represent compounds of interest, and circles represent the rest of the Atomwise compounds. Yellow represents tested compounds, pink represents compounds that were not tested. Relative transcription induction (RTI) represents a ratio of Firefly:Renilla fluorescence. Points represent a single replicate from a single experiment. 0% and 100% RRR are denoted by dotted lines.

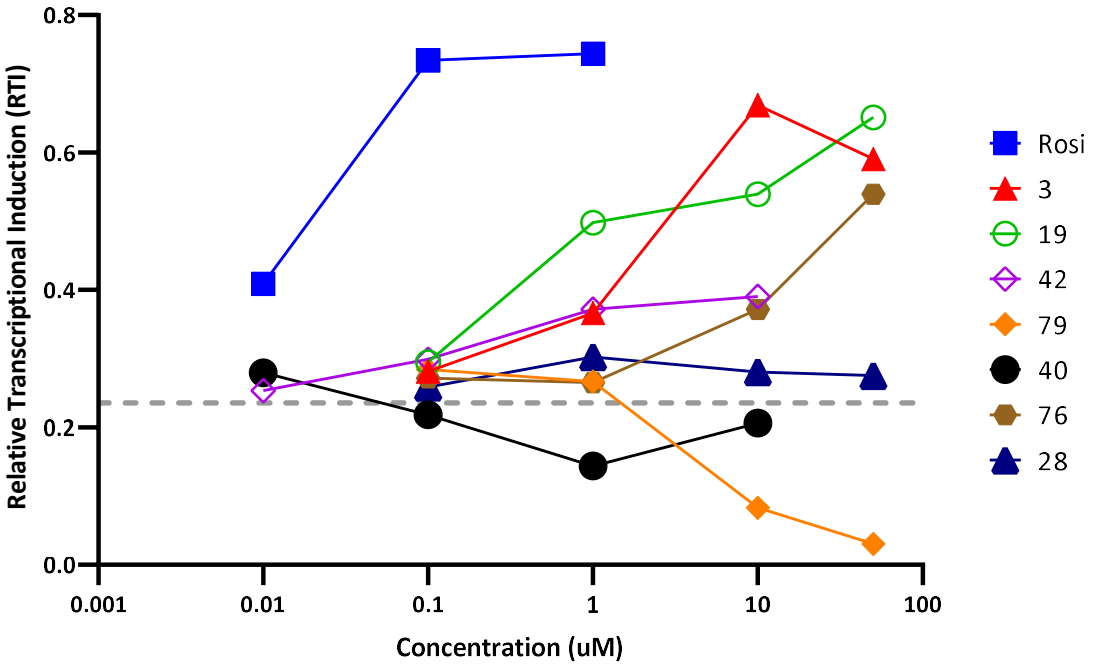

617

618 Figure 3.2. **Shortlisted compounds activate PPARγ over a range of treatment concentrations.** The
619 cell transactivation induced by selected Atomwise compounds was investigated with the dual
620 luciferase assay (DLA). Cells were transiently cotransfected with PPARγ-Gal4 expression plasmids and
621 pG5E1b and pRL-TK reporter plasmids, and treated with shortlisted Atomwise compounds (0.01µM-
622 50µM) as well as control compounds Rosiglitazone (full agonist), at 0.1 µM and 1.0µM, and DMSO.
623 The grey dashed line represents activity of DMSO. Each point represents a duplicate conducted in a
624 single experiment.

625

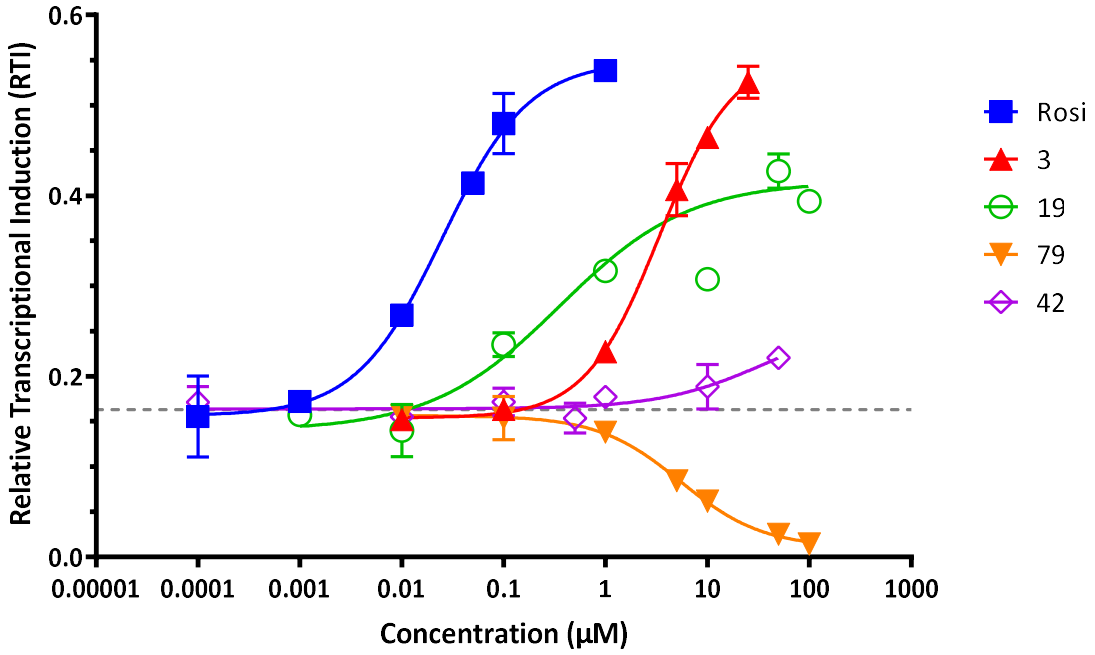

626

627 Figure 3.3. **Transcriptional induction of PPARγ LBD-Gal4-DBD by selected Atomwise compounds.** The
628 cell transactivation induced by Atomwise compounds 3, 19, 42 and 79 was investigated with the dual
629 luciferase assay (DLA). Cells were transiently cotransfected with PPARγ-Gal4 expression plasmids and
630 pG5E1b and pRL-TK reporter plasmids, and treated with Atomwise compounds (6-7 concentration
631 points) as well as control compounds Rosiglitazone (full agonist) and DMSO. The grey dashed line
632 represents activity of DMSO. Each point represents a duplicate, graph is representative of results from
633 two experiments.

634

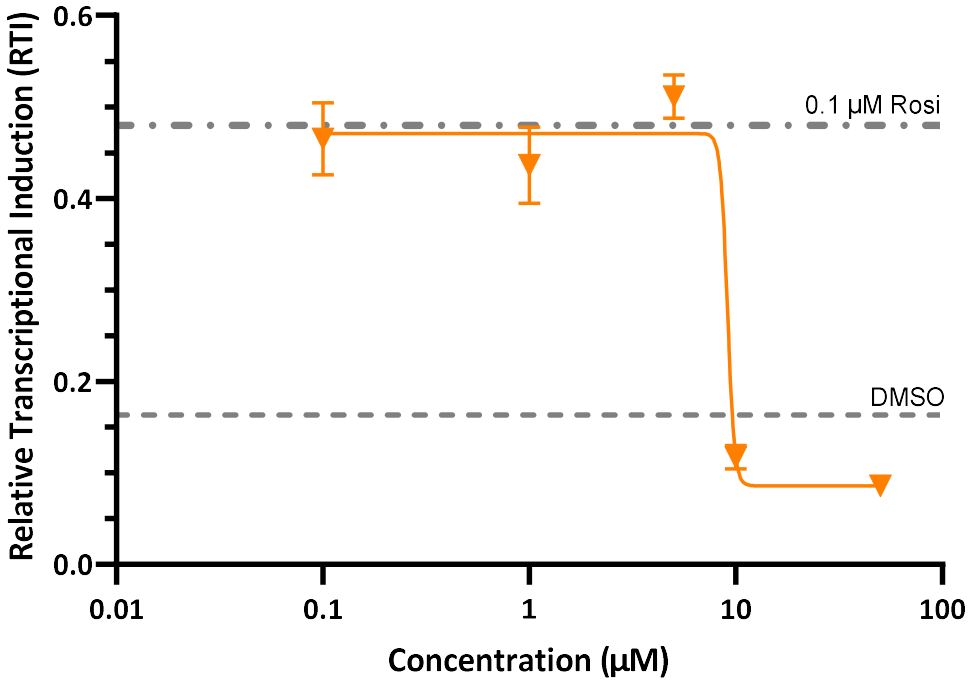

635

636 Figure 3.4. **79 competes with Rosiglitazone to suppress reporter activity.** The inverse agonistic
637 properties of 79 was investigated with the DLA. Cells were transiently cotransfected with PPARγ-Gal4
638 expression plasmids and pG5E1b and pRL-TK reporter plasmids, and treated with 0.1µM Rosiglitazone
639 and increasing amounts of compound 79. The dot/dashed line represents activity of 0.1µM
640 Rosiglitazone only and the grey dashed line represents activity of DMSO. Each point represents a
641 duplicate, graph is representative of results from two experiments.

642

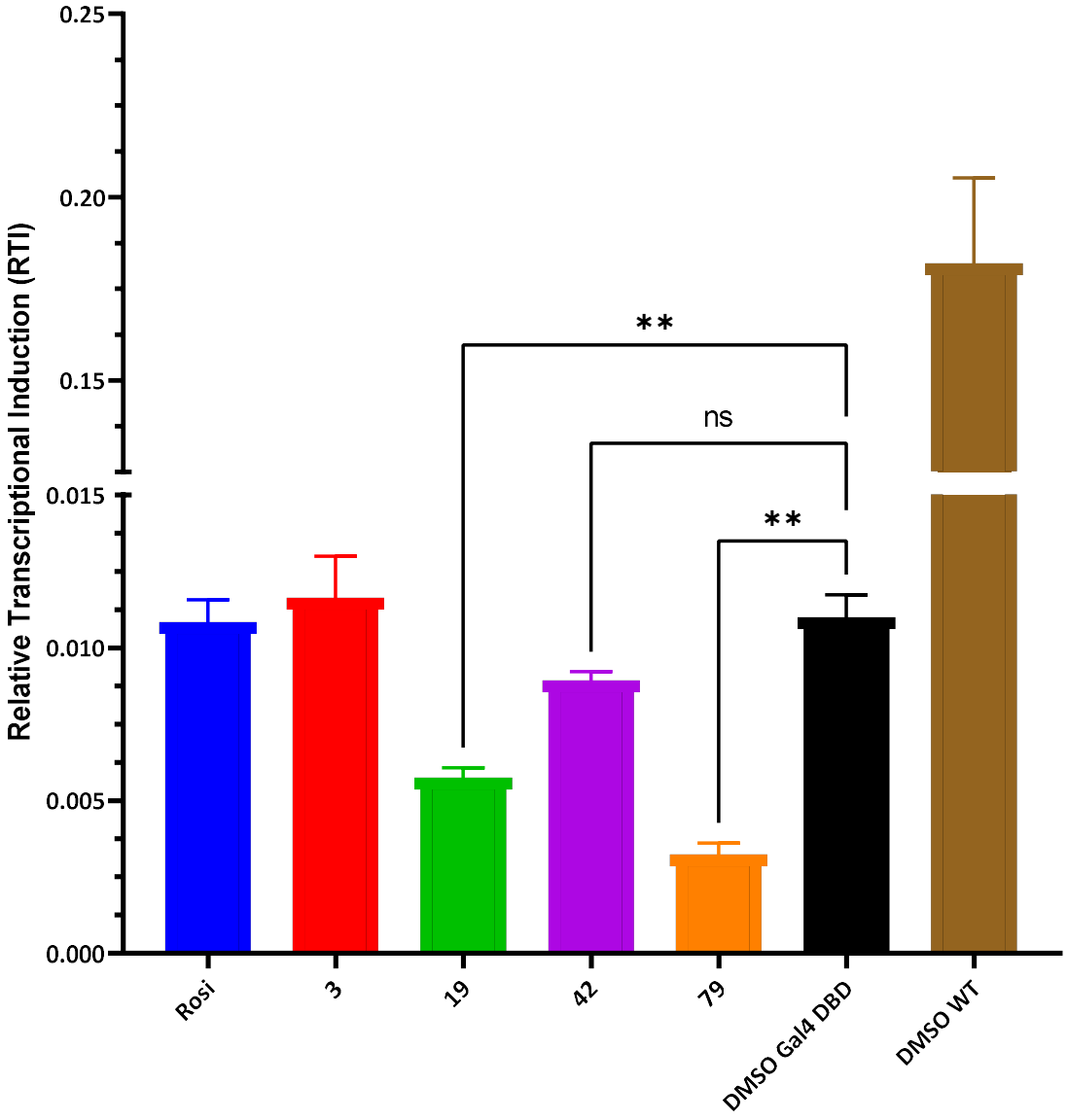

643

644 Figure 3.5. **Atomwise compounds affect transcriptional induction of Gal4-DBD protein.** The effect of
645 ligands on the Gal4-DBD protein was investigated with the DLA. Cells were transiently cotransfected
646 with PPARγ-Gal4 expression plasmids and pG5E1b and pRL-TK reporter plasmids, and treated with
647 10µM of selected Atomwise compounds as well as control compounds full agonist Rosiglitazone
648 (0.1µM) and vehicle DMSO. WT refers to wildtype PPARg-Gal4 protein. Each point represents at least
649 a duplicate, graph is representative of at least two experiments. ** - P≤ 0.01, ns - P > 0.05.

650

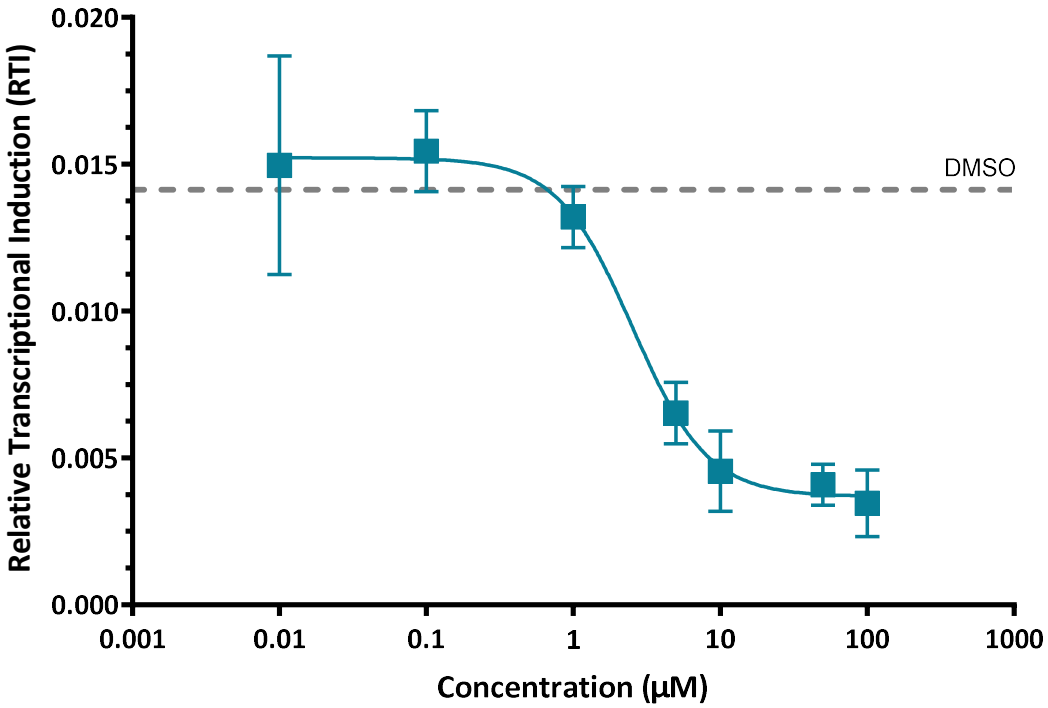

651

652 Figure 3.6. **79 suppresses Gal4-DBD reporter activity.** The effect of 79 on the Gal4-DBD only protein
653 was investigated with the DLA. Cells were transiently cotransfected with Gal4-DBD only expression
654 plasmids and pG5E1b and pRL-TK reporter plasmids, and treated with increasing amounts of
655 compound 79. The grey dashed line represents activity of DMSO treated cells. Each point represents
656 a duplicate.

657

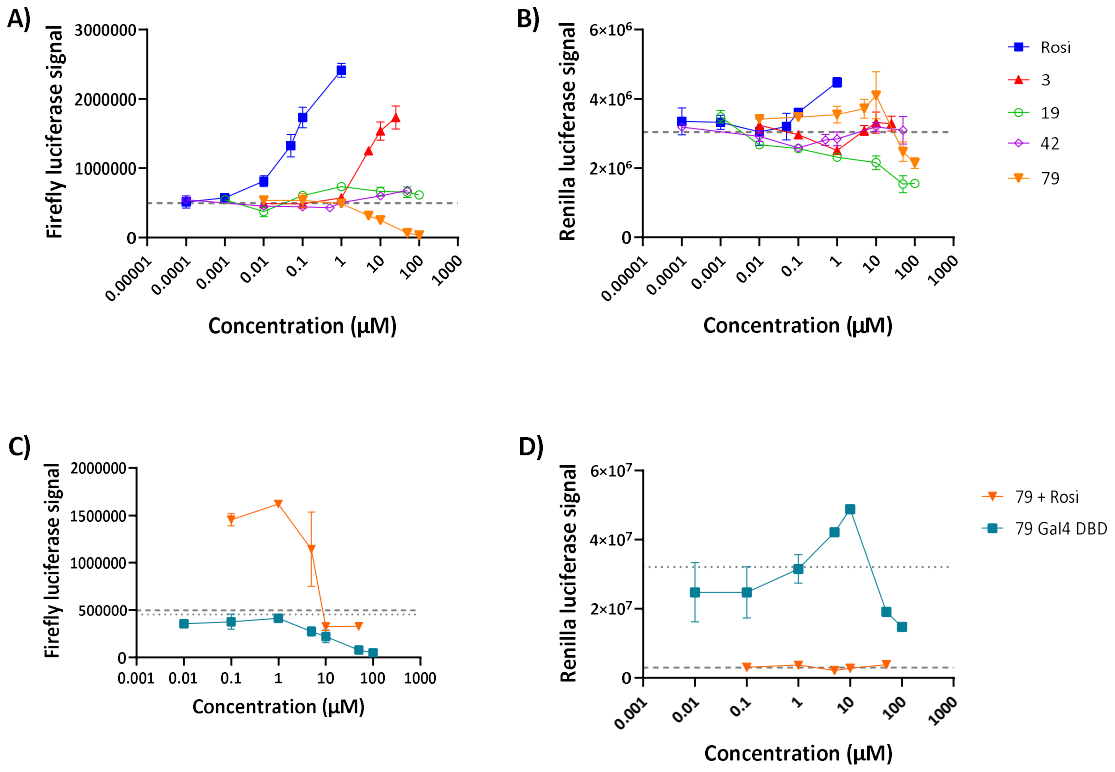

Figure 3.7. **Renilla luciferase activity changes inconsistently with increasing treatment concentration compared to Firefly luciferase activity.** The relative transcription induction values obtained from the dual luciferase assays were further analysed. The Firefly and Renilla values used to calculate relative transcription induction seen in Figures 3.3, 3.4 and 3.6 were visualized in separate graphs. Panels A) and B) represents Firefly and Renilla luciferase activity respectively, corresponding to figure 3.3. Panels C) and D) represents Firefly and Renilla luciferase activity respectively, corresponding to Figure 3.4 (orange) and 3.6 (blue). Cells were transiently cotransfected with PPARγ-Gal4 expression plasmids as well as pG5E1b and pRL-TK reporter plasmids for A) and B). In C) and D), cells were transiently cotransfected with either PPARγ-Gal4 expression plasmids (orange) or Gal4-DBD only expressing plasmids (blue) as well as pG5E1b and pRL-TK reporter plasmids. In A) and B), cells were treated with Atomwise compounds (6-7 concentration points) or control compounds Rosiglitazone (full agonist) and DMSO (vehicle control) as seen in Figure 3.3. In C) and D) cells were treated with Atomwise compound 79 and increasing concentrations of Rosiglitazone (5 concentration points, orange) as seen in Figure 3.4, or only Atomwise compound 79 (7 concentration points, blue) as seen in Figure 3.6, as well as DMSO (vehicle control). The grey dashed line represents activity of cells transfected with PPARγ-Gal4 expressing plasmids, treated with DMSO. Grey dotted line represents activity of cells transfected with Gal4-DBD only expressing plasmids, treated with DMSO. Each point represents a duplicate.

Compound	F:R	RRR
3	0.5861	123.22
19	0.5575	114.82
28	0.3431	51.79
40	0.1256	-12.15
42	0.3520	54.41
76	0.3905	65.74
79	0.0895	-22.75
Rosi 0.1	0.5071	100.00
DMSO	0.1669	0.00

Table 1.1. **Atomwise compounds displays a range of PPARγ activation activate or suppress PPARγ transcription activity to different extents.** Activity of shortlisted compounds relative to full agonist Rosiglitazone and Vehicle control DMSO. F:R refers to Firely:Renilla fluorescence ratio, RRR – Relative Response Ratio.

Compounds	**EC_{50}/IC_{50}*** (μM)	**STD dev** (μM)
Rosi	0.02	0.006
3	2.519	1.218
19	0.213	0.203
42	18.825	24.98
79	4.686*	1.056*

Table 1.2. **Potencies of selected Atomwise compounds vary.** EC_{50} or IC_{50} values of selected compounds from figure 3. EC_{50} values were calculated for individual experiments on Graphprism, values represent the mean of 2 experiments. STD dev – Standard deviation was calculated on Excel. * indicates a value that represents IC_{50}

Full agonist		Partial agonist		Inverse agonist	
3	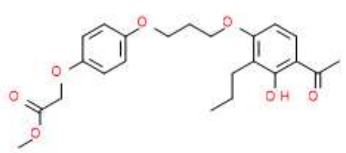	28	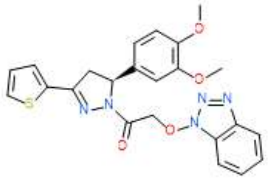	40	
19	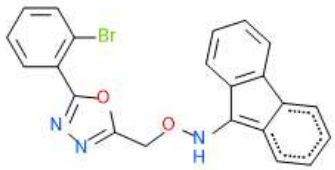	42	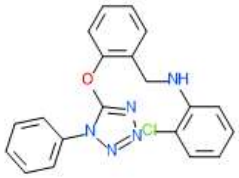	79	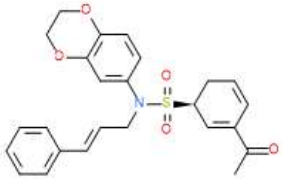
Rosi	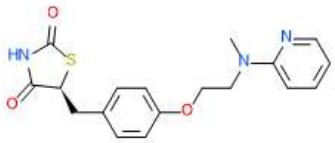	76	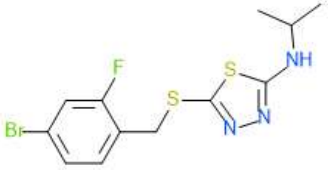	Newly licenced compounds	
Pio	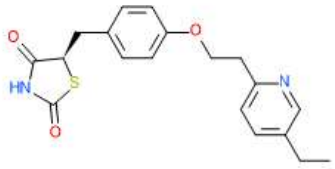			Sar	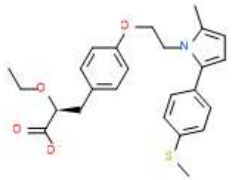
				Chi	

687

688 Figure 4.1. **Structures of compounds examined.** The 2D structures of compounds examined in the study, grouped under ligand activity profile. Numbers
689 refer to Atomwise compound identifiers. Rosi – Rosiglitazone. Pio – Pioglitazone. Sar – Saroglitazar. Chi – Chiglitazar.

690

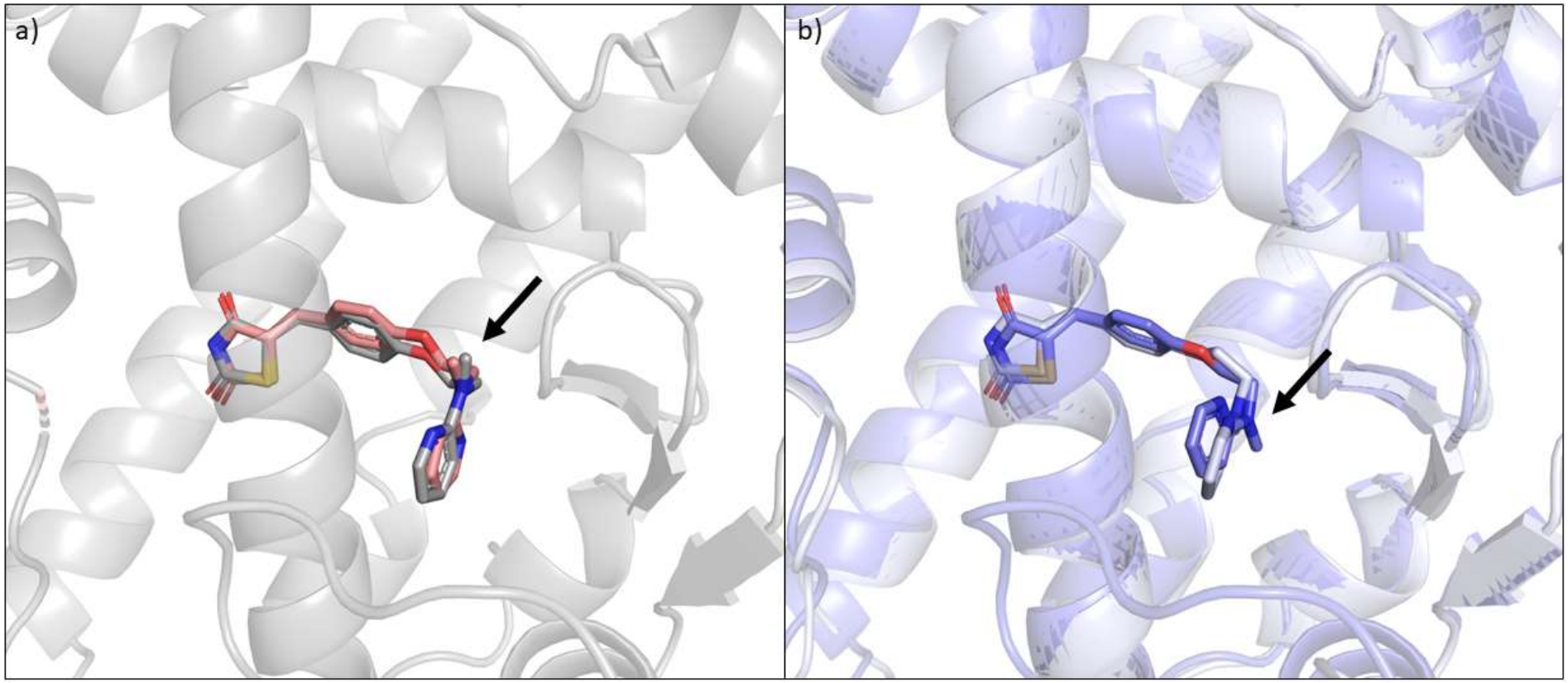

Figure 4.2. **Docking poses for Rosiglitazone matches that of experimental crystal structures.** Interactions between model compound Rosiglitazone and the PPARγ LBP were investigated. Docking poses for Rosiglitazone in the PPARγ LBP was determined with ICM-pro using 2PRG as a docking model. Black arrows indicate the orientation of the methyl group extending from 2-piperidinamine. Docking poses are numbered in decreasing order of binding score. a) Docking pose 1 (Edock -30.47, Salmon) superimposed onto 2PRG (Grey70) b) Docking pose 2 (Edock -30.32, Slate) superimposed onto 3DZY (Blue-white).

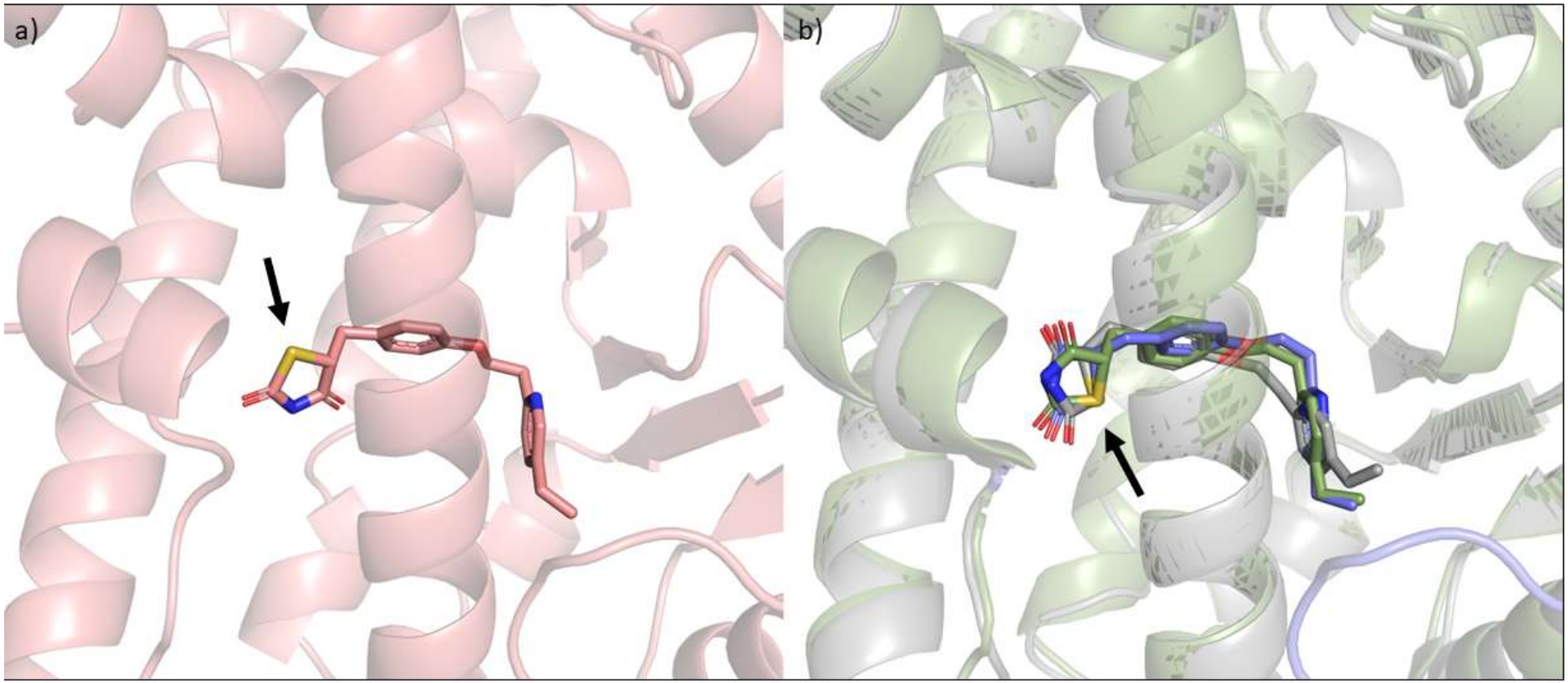

Figure 4.3. **Docking poses for Pioglitazone matches that of experimental crystal structures.** Interactions between model compound Pioglitazone and the PPARγ LBP were investigated. Docking poses for Pioglitazone in the PPARγ LBP was determined with ICM-pro using 2PRG as a docking model. Black arrows indicate the orientation of the thiazolidinedione functional group. Docking poses are numbered in decreasing order of binding score. a) Top scoring docking pose 1 (Edock -39.25, Salmon) and b) Docking pose 2 (Edock -37.09, Slate) superimposed onto 2XKW (Grey 70) and 5Y2O (Sludge).

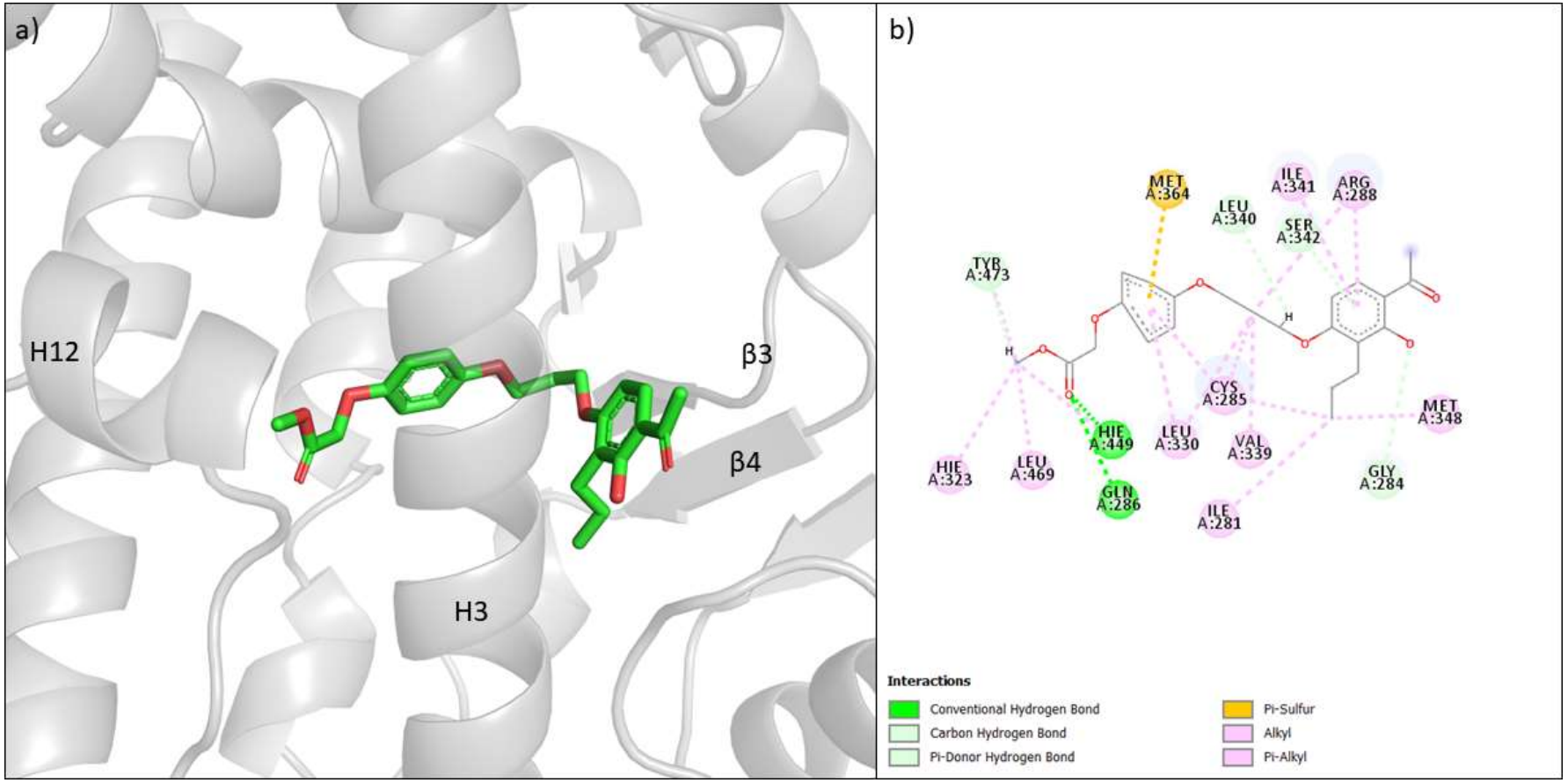

Figure 4.4. **Compound 3 forms extensive interactions with residues in the PPARγ LBP.** Interactions between compound 3 and the PPARγ LBP were investigated. Docking poses for compound 3 (in green) in the PPARγ LBP was determined with ICM-pro using 2PRG as a docking model. a) The top scoring pose for 3 (Edock -16.83) and b) the corresponding 2D interaction diagram of 3 and the residues in the PPARγ LBP (24 favourable interactions).

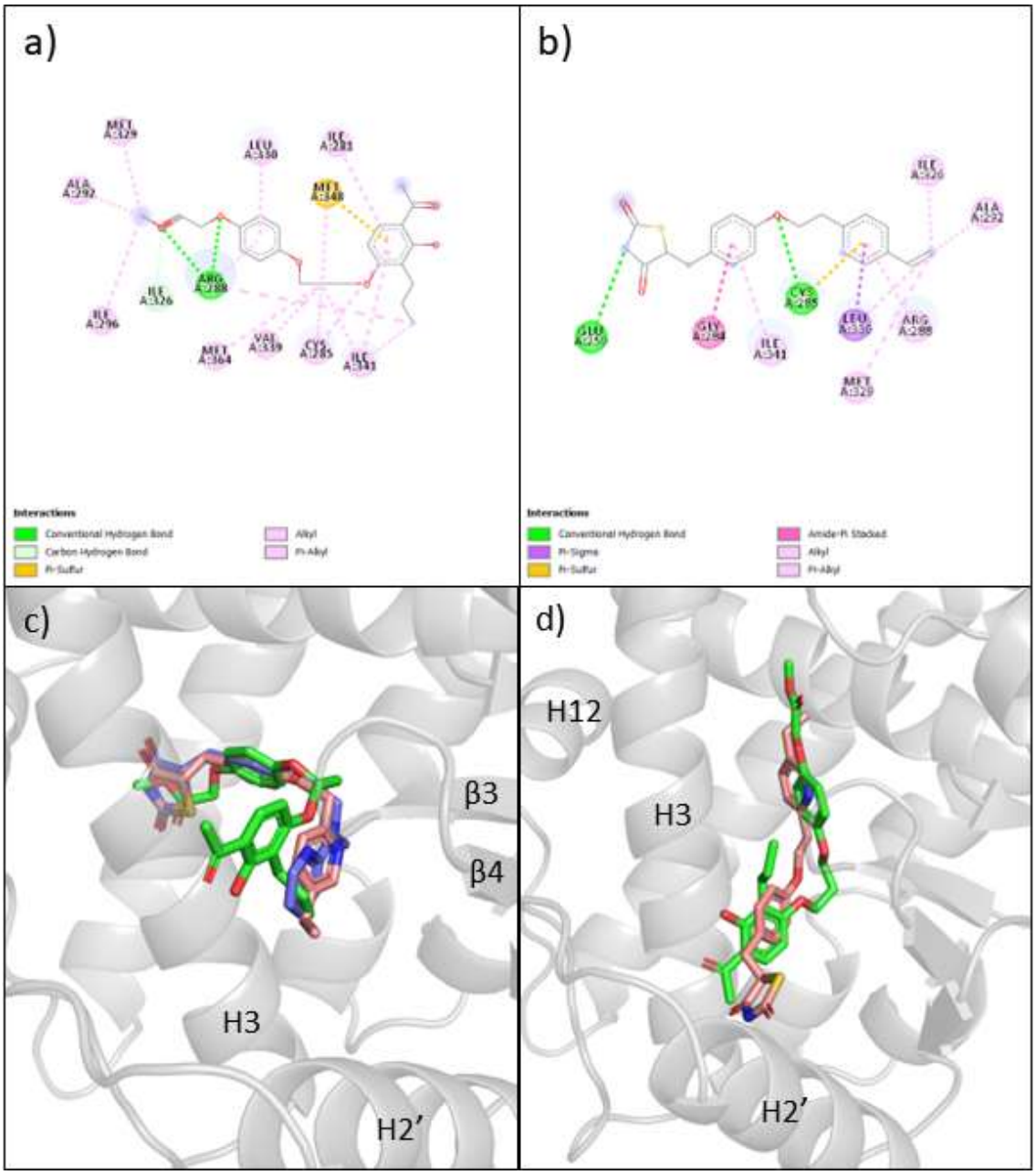

Figure 4.5. **Compound 3 adopts multiple conformations in the PPARγ LBP.** Interactions between compound 3 and the PPARγ LBP were investigated. Docking poses for compound 3 in the PPARγ LBP was determined with ICM-pro using 2PRG as a docking model. a,b) the corresponding 2D interaction diagram of 3 and Rosiglitazone and the residues in the PPARγ LBP in the top-down conformation (20 vs 11 favourable interactions). c) Rosiglitazone and Pioglitazone (PDB ID: 3DZY and 5Y2O respectively) superimposed onto Compound 3. d) Pioglitazone conformation 2 of PDB ID: 2XKW superimposed onto docking pose 4 of compound 3.

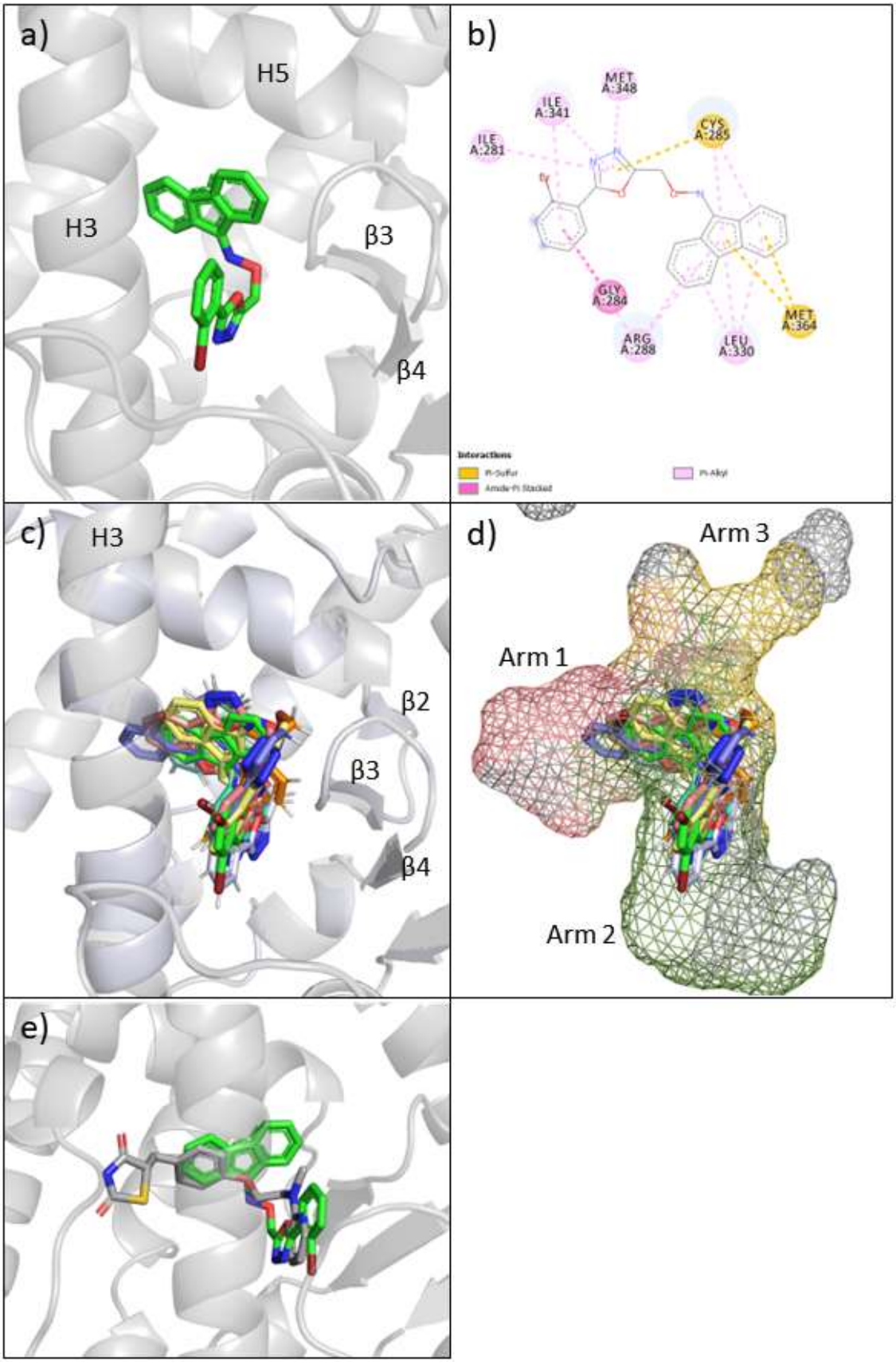

714

715 Figure 4.6. **Compound 19 interacts with Arm 2 of the PPARγ LBP**. Interactions between compound 19

716 and the PPARγ LBP were investigated. Docking poses for compound 19 (in green) in the PPARγ LBP

was determined with ICM-pro using 2PRG as a docking model. a) The top scoring pose for 19 (Edock 3.662) and b) the corresponding 2D interaction diagram of 19 and the residues in the PPARγ LBP (17 favourable interactions). The poses for 19 were overlayed and displayed with the docking model represented as a c) cartoon ribbons (grey) or its cavity d) as a wireframe surface on Pymol (Arm 1 Salmon, Arm 2 Smudge, Arm 3 yellow orange). e) Pose 1 of 19 in comparison to Rosiglitazone in the PPARγ LBP (PDB ID: 2PRG). Ligand poses are represented as follows: Poses 1 green, 2 pale yellow, 3 salmon, 4 slate, 5 orange, 6 cyan, 7 blue-white.

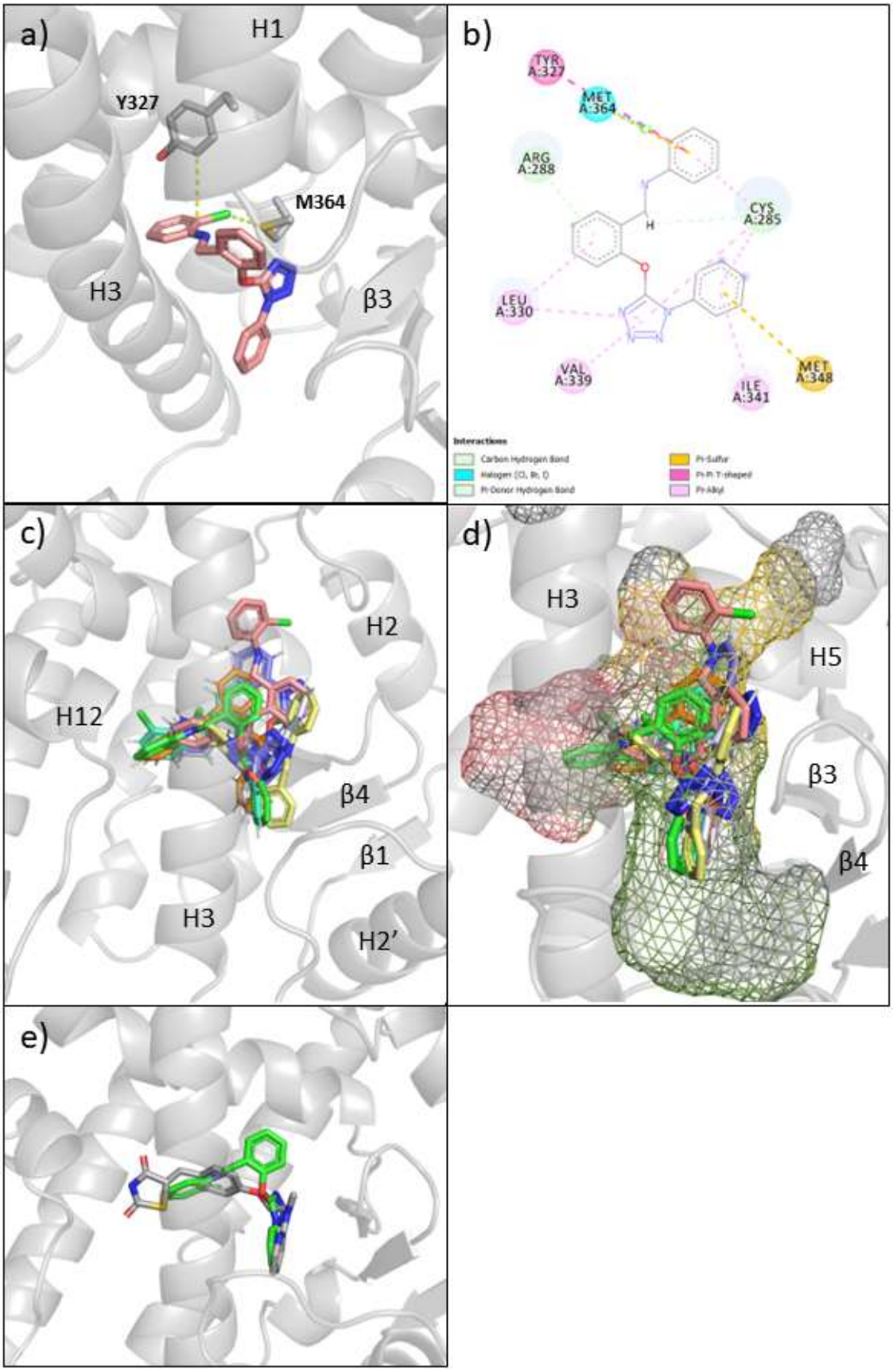

Figure 4.7. **Compound 42 interacts with Arm 2 and 3 of the PPARγ LBP.** Interactions between compound 42 and the PPARγ LBP were investigated. Docking poses for compound 42 (in green) in the

728 PPARγ LBP was determined with ICM-pro using 2PRG as a docking model. a) The top scoring pose for
729 42 (Edock -0.962) and b) the corresponding 2D interaction diagram of 19 and the residues in the PPARγ
730 LBP (14 favourable interactions). The poses for 19 were overlayed and displayed with the docking
731 model represented as a c) cartoon ribbons (grey) or its cavity d) as a wireframe surface on Pymol (Arm
732 1 Salmon, Arm 2 Smudge, Arm 3 yellow orange). e) Pose 1 of 42 in comparison to Rosiglitazone in the
733 PPARγ LBP (PDB ID: 2PRG). Ligand poses are represented as follows: Poses 1 green, 2 pale yellow, 3
734 salmon, 4 slate, 5 orange, 6 cyan, 7 blue-white.

735

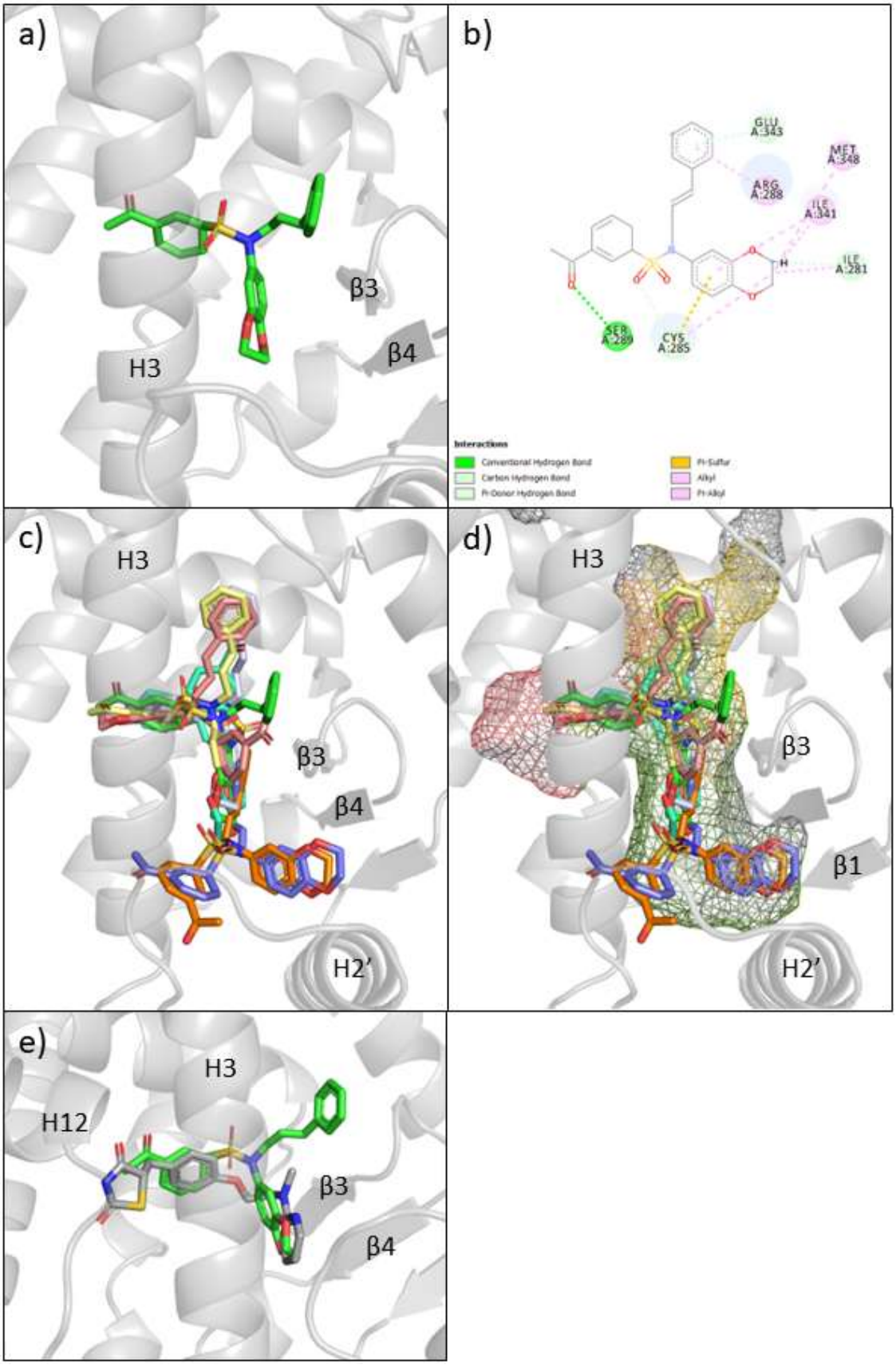

Figure 4.8. **Compound 79 interacts with all regions of the PPARγ LBP.** Interactions between compound 79 and the PPARγ LBP were investigated. Docking poses for compound 79 (in green) in the

PPARγ LBP was determined with ICM-pro using 2PRG as a docking model. a) The top scoring pose for 79 (Edock -5.407) and b) the corresponding 2D interaction diagram of 79 and the residues in the PPARγ LBP (12 favourable interactions). The poses for 79 were overlayed and displayed with the docking model represented as a c) cartoon ribbons (grey) or its cavity d) as a wireframe surface on Pymol (Arm 1 Salmon, Arm 2 Smudge, Arm 3 yellow orange). Ligand poses are represented as follows: Poses 1 green, 2 pale yellow, 3 salmon, 4 slate, 5 orange, 6 cyan, 7 blue-white. e) comparison of 79 versus Rosiglitazone in the PPARγ LBP (PDB ID: 2PRG)

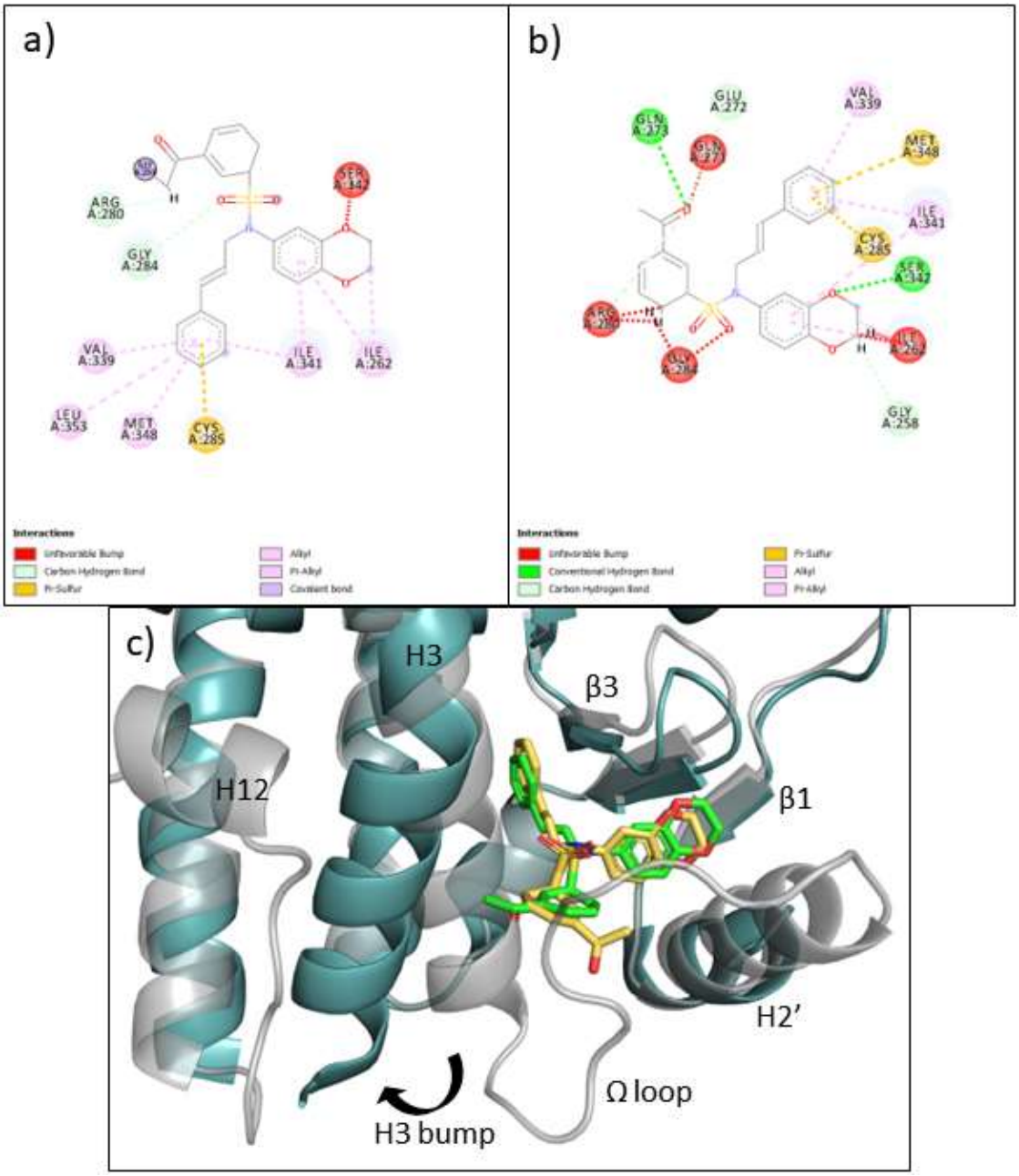

747

748 Figure 4.9. **Compound 79 forms interactions with the Ω loop of the PPARγ LBP.** Interactions between
749 compound 79 and the PPARγ LBP were investigated. The 2D interaction diagram of 79 of poses a) 4
750 (Edock -3.253) and b) 5 (Edock -2.976) and the residues in the PPARγ LBP were determined (10 and 12
751 favourable interactions respectively). c) Poses 4 and 5 (green and yellow orange respectively) for 79
752 were displayed with the docking model represented as a cartoon ribbons (grey) with the structure of
753 PDB ID: 6ONI (light teal) overlayed to show a possible H3 shift.

754

6. Supplementary information

No.	Proteins	Ligands	Concentration (µM)	Dye concentration (X)	Purified protein (mg/ml)	Volume (µl)
1	PPAR, DDL	None	N/A	2 – 10	0.01 – 0.03	50
2	PPAR, DDL	Rosiglitazone, DMSO (for Ddl)	100 – 300	2 – 10	0.01 – 0.03	50
3	PPAR	Rosiglitazone, 4-34	300	5	0.03	50
4	PPAR	Rosiglitazone, 4-34	500	5	0.05	50
5	PPAR	Rosiglitazone	9 – 27	2.4 – 12	0.12 – 0.48	50
6	PPAR	Rosiglitazone, 4-34, DMSO	27	2.4	0.24	50
7	PPAR	Rosiglitazone	100	0.5 – 2	0.10 – 0.30	10
	PPAR	Rosiglitazone	100	2	0.30	50
	PPAR	Rosiglitazone	30	2	0.30	50
8	PPAR	Rosiglitazone, 4-34	100	6	0.30	10

Supplementary table 6.1. **List of optimization experiments for the Thermal Shift Assay (TSA).** Thermostability of purified PPARγ protein, incubated with Rosiglitazone or a subset of the Atomwise compounds was investigated in a thermal shift assay. The thermal shift assay was optimized by changing ligand, dye, protein concentrations as well as well volume.

Compounds	Edock score
Rosiglitazone	-30.47
Pioglitazone	-39.25
SYPRO™ Orange	-20.14
3	-16.83
19	3.662
42	-0.962
79	-5.407

Supplementary table 1.2. **Docking scores of different compounds with the PPARγ LBD.** Docking studies of various compounds were conducted by determining docking poses of each compound with the PPARγ LBP (PDB ID: 2PRG). The Edock score of the highest scoring docking pose of each compound to PPARγ LBP was collated and listed above.

7. References

Abagyan, R., Orry, A., Raush, E. & Totrov, M. (2023) *ICM-Pro User Guide v.3.9.* Available at: https://www.molsoft.com/gui/start-dock.html. [Acesssed 23 June 2023]

Artis, D. R., Lin, J. J., Zhang, C., Wang, W., Mehra, U., Perreault, M., Erbe, D., Krupka, H. I., England, B. P., Arnold, J., Plotnikov, A. N., Marimuthu, A., Nguyen, H., Will, S., Signaevsky, M., Kral, J., Cantwell, J., Settachatgull, C., Yan, D. S., Fong, D., Oh, A., Shi, S., Womack, P., Powell, B., Habets, G., West, B. L., Zhang, K. Y. J., Milburn, M. V., Vlasuk, G. P., Hirth, K. P., Nolop, K., Bollag, G., Ibrahim, P. N. & Tobin, J. F. (2009) Scaffold-based discovery of indeglitazar, a PPAR pan-active anti-diabetic agent. Proceedings of the National Academy of Sciences. 106 (1), 262-267. doi: 10.1073/pnas.0811325106.

Bernardes, A., Souza, P. C. T., Muniz, J. R. C., Ricci, C. G., Ayers, S. D., Parekh, N. M., Godoy, A. S., Trivella, D. B. B., Reinach, P., Webb, P., Skaf, M. S. & Polikarpov, I. (2013) Molecular Mechanism of Peroxisome Proliferator-Activated Receptor α Activation by WY14643: a New Mode of Ligand Recognition and Receptor Stabilization. Journal of Molecular Biology. 425 (16), 2878-2893. doi: 10.1016/j.jmb.2013.05.010.

Bruning, J. B., Chalmers, M. J., Prasad, S., Busby, S. A., Kamenecka, T. M., He, Y., Nettles, K. W. & Griffin, P. R. (2007) Partial Agonists Activate PPARγ Using a Helix 12 Independent Mechanism. Structure. 15 (10), 1258-1271. doi: 10.1016/j.str.2007.07.014.

Cheng, H. S., Tan, W. R., Low, Z. S., Marvalim, C., Lee, J. Y. H. & Tan, N. S. (2019) Exploration and Development of PPAR Modulators in Health and Disease: An Update of Clinical Evidence. *International Journal of Molecular Sciences.* 20 (20), 5055. doi: 10.3390/ijms20205055.

Choi, J. H., Banks, A. S., Kamenecka, T. M., Busby, S. A., Chalmers, M. J., Kumar, N., Kuruvilla, D. S., Shin, Y., He, Y., Bruning, J. B., Marciano, D. P., Cameron, M. D., Laznik, D., Jurczak, M. J., Schürer, S. C., Vidović, D., Shulman, G. I., Spiegelman, B. M. & Griffin, P. R. (2011) Antidiabetic actions of a non-agonist PPARγ ligand blocking Cdk5-mediated phosphorylation. Nature. 477 (7365), 477-481. doi: 10.1038/nature10383.

Christofides, A., Konstantinidou, E., Jani, C. & Boussiotis, V. A. (2021) The role of peroxisome proliferator-activated receptors (PPAR) in immune responses. Metabolism. 114, 154338. doi: 10.1016/j.metabol.2020.154338.

Chua, B. S. K. & Bruning, J. B. (2021) PPARα and δ Ligand Design: Honing the Traditional Empirical Method with a More Holistic Overview. In: Badr, M.Z. (ed.) Nuclear Receptors. Cham, Springer International Publishing, pp. 111-178.

795 Da'adoosh, B., Marcus, D., Rayan, A., King, F., Che, J. & Goldblum, A. (2019) Discovering highly
796 selective and diverse PPAR-delta agonists by ligand based machine learning and structural modeling.
797 Scientific Reports. 9 (1), 1106. doi: 10.1038/s41598-019-38508-8.

798 Deeks, E. D. (2022) Chiglitazar: First Approval. Drugs. 82 (1), 87-92. doi: 10.1007/s40265-021-01648-
799 1.

800 Dubois, V., Eeckhoute, J., Lefebvre, P. & Staels, B. (2017) Distinct but complementary contributions
801 of PPAR isotypes to energy homeostasis. Journal of Clinical Investigation. 127 (4), 1202-1214. doi:
802 10.1172/JCI88894.

803 Eggers, C., Hook, B., Lewis, S., Strayer, C. & Landreman, A. (2016) *Designing a Bioluminescent*
804 *Reporter Assay: Normalization Options.* Available at:
805 https://www.promega.sg/resources/pubhub/bioluminescent-reporter-assay-normalization/
806 [Accessed 02 February 2023]

807 Everett, L. M. & Crabb, D. W. (1999) Sensitivity of virally-driven luciferase reporter plasmids to
808 members of the steroid/thyroid/retinoid family of nuclear receptors. The Journal of Steroid
809 Biochemistry and Molecular Biology. 70 (4-6), 197-201. doi: 10.1016/S0960-0760(99)00109-0.

810 Frkic, R. L., Chua, B. S., Shin, Y., Pascal, B. D., Novick, S. J., Kamenecka, T. M., Griffin, P. R. & Bruning,
811 J. B. (2018) Structural and Dynamic Elucidation of a Non-acid PPARγ Partial Agonist: SR1988. Nuclear
812 Receptor Research. 5. doi: 10.11131/2018/101350.

813 Frkic, R. L., Marshall, A. C., Blayo, A.-L., Pukala, T. L., Kamenecka, T. M., Griffin, P. R. & Bruning, J. B.
814 (2018) PPARγ in Complex with an Antagonist and Inverse Agonist: a Tumble and Trap Mechanism of
815 the Activation Helix. iScience. 5, 69-79. doi: 10.1016/j.isci.2018.06.012.

816 Gross, B., Pawlak, M., Lefebvre, P. & Staels, B. (2017) PPARs in obesity-induced T2DM, dyslipidaemia
817 and NAFLD. Nature Reviews Endocrinology. 13 (1), 36-49. doi: 10.1038/nrendo.2016.135.

818 Hong, F., Xu, P. & Zhai, Y. (2018) The Opportunities and Challenges of Peroxisome Proliferator-
819 Activated Receptors Ligands in Clinical Drug Discovery and Development. International Journal of
820 Molecular Sciences. 19 (8), 2189. doi: 10.3390/ijms19082189.

821 Huynh, K. & Partch, C. L. (2015) Analysis of Protein Stability and Ligand Interactions by Thermal Shift
822 Assay. Current Protocols in Protein Science. 79 (1). doi: 10.1002/0471140864.ps2809s79.

Ibrahim, N. M., Marinovic, A. C., Price, S. R., Young, L. G. & Fröhlich, O. (2000) Pitfall of an Internal Control Plasmid: Response of Renilla Luciferase (pRL-TK) Plasmid to Dihydrotestosterone and Dexamethasone. BioTechniques. 29 (4), 782-784. doi: 10.2144/00294st04.

Krishnappa, M., Patil, K., Parmar, K., Trivedi, P., Mody, N., Shah, C., Faldu, K., Maroo, S., group, f. t. P. X. s., Desai, P., Fatania, K., Murthy, S., Balamurugan, R., Agarwal, M., Singh, K. P., Kalra, G. S., Khandelwal, V., Singwala, A., Thacker, H., Tulle, R., Rao, H., Kumbla, M., Singh, P., Khatri, A., Agrawal, S., Sarkar, R. N., Agarwal, D., Bhatia, G., Agarwal, R. P., Kumar, S., Vamsi Krishna, P. R., Ajmani, A. K., Asalkar, A., Basu, I., Chatterjee, S., Pavithran, V. K., Das, R., Dharmadhikari, A., Vardhan, V., Madusudhan Babu, M., Sengupta, N., Abkari, S., Harikrishna, R., Chovatia, R. & Parmar, D. (2020) Effect of saroglitazar 2 mg and 4 mg on glycemic control, lipid profile and cardiovascular disease risk in patients with type 2 diabetes mellitus: a 56-week, randomized, double blind, phase 3 study (PRESS XII study). Cardiovascular Diabetology. 19 (1), 93. doi: 10.1186/s12933-020-01073-w.

Lebovitz, H. E. (2019) Thiazolidinediones: the Forgotten Diabetes Medications. Current Diabetes Reports. 19 (12), 151. doi: 10.1007/s11892-019-1270-y.

Lee, M. A., Tan, L., Yang, H., Im, Y.-G. & Im, Y. J. (2017) Structures of PPARγ complexed with lobeglitazone and pioglitazone reveal key determinants for the recognition of antidiabetic drugs. Scientific Reports. 7 (1), 16837. doi: 10.1038/s41598-017-17082-x.

Lefterova, M. I., Haakonsson, A. K., Lazar, M. A. & Mandrup, S. (2014) PPARγ and the global map of adipogenesis and beyond. Trends in Endocrinology & Metabolism. 25 (6), 293-302. doi: 10.1016/j.tem.2014.04.001.

Lehmann, J. M., Moore, L. B., Smith-Oliver, T. A., Wilkison, W. O., Willson, T. M. & Kliewer, S. A. (1995) An Antidiabetic Thiazolidinedione Is a High Affinity Ligand for Peroxisome Proliferator-activated Receptor γ (PPARγ). Journal of Biological Chemistry. 270 (22), 12953-12956. doi: 10.1074/jbc.270.22.12953.

Life Technologies (2010) *TmTool Quick Set-Up Guide.* Available at: https://www.thermofisher.com/search/results?query=tmtool&persona=DocSupport&refinementAction=true&filter=document.result_type_s%3AManuals%20%26%20Protocols [Accessed 04 April 2023].

Mysore, V., Gupta, T., Friedland, G. & Wallach, I. (2020) *Billion Trawler Answer: A Scalable and Effective Machine Learning Based Solution for the Virtual High-Throughput Screening of Ultra-Large Libraries.* Available at: https://blog.atomwise.com/scalable-effective-machine-learning-based-solution-for-virtual-high-throughput-screening-of-large-libraries [Accessed 15 June 2023]

Nolte, R. T., Wisely, G. B., Westin, S., Cobb, J. E., Lambert, M. H., Kurokawa, R., Rosenfeld, M. G., Willson, T. M., Glass, C. K. & Milburn, M. V. (1998) Ligand binding and co-activator assembly of the peroxisome proliferator-activated receptor-γ. Nature. 395 (6698), 137-143. doi: 10.1038/25931.

Reinhard, L., Mayerhofer, H., Geerlof, A., Mueller-Dieckmann, J. & Weiss, M. S. (2013) Optimization of protein buffer cocktails using Thermofluor. Acta Crystallographica Section F Structural Biology and Crystallization Communications. 69 (2), 209-214. doi: 10.1107/S1744309112051858.

Ribeiro Filho, H. V., Bernardi Videira, N., Bridi, A. V., Tittanegro, T. H., Helena Batista, F. A., de Carvalho Pereira, J. G., de Oliveira, P. S. L., Bajgelman, M. C., Le Maire, A. & Figueira, A. C. M. (2018) Screening for PPAR Non-Agonist Ligands Followed by Characterization of a Hit, AM-879, with Additional No-Adipogenic and cdk5-Mediated Phosphorylation Inhibition Properties. Frontiers in Endocrinology. 9, 11. doi: 10.3389/fendo.2018.00011.

Sekiguchi, M., Kobashigawa, Y., Moriguchi, H., Kawasaki, M., Yuda, M., Teramura, T. & Inagaki, F. (2013) High-Throughput Evaluation Method for Drug Association with Pregnane X Receptor (PXR) Using Differential Scanning Fluorometry. SLAS Discovery. 18 (9), 1084-1091. doi: 10.1177/1087057113491826.

Shang, J., Mosure, S. A., Zheng, J., Brust, R., Bass, J., Nichols, A., Solt, L. A., Griffin, P. R. & Kojetin, D. J. (2020) A molecular switch regulating transcriptional repression and activation of PPARγ. Nature Communications. 11 (1), 956. doi: 10.1038/s41467-020-14750-x.

Shifera, A. S. & Hardin, J. A. (2010) Factors modulating expression of Renilla luciferase from control plasmids used in luciferase reporter gene assays. Analytical Biochemistry. 396 (2), 167-172. doi: 10.1016/j.ab.2009.09.043.

Uppenberg, J., Svensson, C., Jaki, M., Bertilsson, G., Jendeberg, L. & Berkenstam, A. (1998) Crystal Structure of the Ligand Binding Domain of the Human Nuclear Receptor PPARγ. Journal of Biological Chemistry. 273 (47), 31108-31112. doi: 10.1074/jbc.273.47.31108.

Wallach, I., Dzamba, M. & Heifets, A. (2015) AtomNet: A Deep Convolutional Neural Network for Bioactivity Prediction in Structure-based Drug Discovery.

Weikum, E. R., Liu, X. & Ortlund, E. A. (2018) The nuclear receptor superfamily: A structural perspective: The Nuclear Receptor Superfamily. Protein Science. 27 (11), 1876-1892. doi: 10.1002/pro.3496.

Wu, C.-C., Baiga, T. J., Downes, M., La Clair, J. J., Atkins, A. R., Richard, S. B., Fan, W., Stockley-Noel, T. A., Bowman, M. E., Noel, J. P. & Evans, R. M. (2017) Structural basis for specific ligation of the

886 peroxisome proliferator-activated receptor δ. Proceedings of the National Academy of Sciences. 114
887 (13). doi: 10.1073/pnas.1621513114.

888 Wu, T., Yu, J., Gale-Day, Z., Woo, A., Suresh, A., Hornsby, M. & Gestwicki, J. E. (2020) *Three Essential*
889 *Resources to Improve Differential Scanning Fluorimetry (DSF) Experiments.* Available at:
890 https://gestwickilab.shinyapps.io/dsfworld/ [Accessed 01 May 2023]

891 Zhang, X., Chen, H.-Z. & Rovin, B. H. (2003) Unexpected sensitivity of synthetic Renilla luciferase
892 control vectors to treatment with a cyclopentenone prostaglandin. BioTechniques. 35 (6), 1144-
893 1148. doi: 10.2144/03356bm04.

Chapter 6

Mutations in the PPARγ LBD affect responses to known ligands

Benjamin S.K. Chua [a], Yong Mei Guan [a], John B. Bruning [b]

[a] School of Biological Sciences, The University of Adelaide, Adelaide, South Australia, 5005, Australia

[b] Institute for Photonics and Advanced Sensing, The School of Biological Sciences, The University of Adelaide, North Tce, Adelaide, South Australia, 5005, Australia

Statement of Authorship

Title of Paper	Mutations in the PPARγ LBD affect responses to known ligands
Publication Status	☐ Published ☐ Accepted for Publication ☐ Submitted for Publication ☑ Unpublished and Unsubmitted work written in manuscript style
Publication Details	This paper characterizes the effect of mutations on the activity of PPAR

Principal Author

Name of Principal Author (Candidate)	Benjamin Soon Kai Chua
Contribution to the Paper	Conducted thermostability assays, cell-based assays, western blots, crystal structure collection and refinement, synthesis of information, generation of figures, graphs and tables, and writing.
Overall percentage (%)	75
Certification:	This paper reports on original research I conducted during the period of my Higher Degree by Research candidature and is not subject to any obligations or contractual agreements with a third part at would constrain its inclusion in this thesis. I am the primary author of this paper.
Signature	Date: 16/06/2023

Co-Author Contributions

By signing the Statement of Authorship, each author certifies that:

i. the candidate's stated contribution to the publication is accurate (as detailed above);

ii. permission is granted for the candidate in include the publication in the thesis; and

iii. the sum of all co-author contributions is equal to 100% less the candidate's stated contribution.

Name of Co-Author	Yong Mei Guan
Contribution to the Paper	Conducted the purification of mutant protein, crystallization of protein and crystal structure collection
Overall percentage (%)	15
Signature	plus of Yong Mei → author not available to Date: 4/7/2023

Name of Co-Author	John B Bruning
Contribution to the Paper	Supervised the research and writing of the paper
Overall percentage (%)	10
Signature	Date: 16/6/2023

1. Introduction

Peroxisomal proliferator activated receptor γ (PPARγ) is a transcription factor that is part of the nuclear receptor family (NR1C3), which are proteins that bind to DNA to regulate gene expression (Weikrum et al., 2018). PPARγ follows the canonical NR protein architecture, consisting of 5 domains A-E. Domains A/B is an unstructured domain that contains the activation function 1 (AF1) region that is involved in ligand independent transcription activation (Mosure et al., 2022). Domain C is the DNA binding domain (DBD) consisting of 2 zinc-finger motifs that bind to PPAR response elements (PPRE), which are a stretch of two hexameric direct repeats of the DNA sequence 5'-ACCTCA-3' separated by 1 nucleotide spacer (Penvose et al., 2022). Domain D contains a hinge region, linking domains C and E. Domain E is the ligand binding domain (LBD), which contains the activation function 2 (AF2) motif, part of the AF2 surface (solvent exposed surface formed by H3, 4 and 12) that is involved in ligand dependent transcription activation (Nolte et al., 1998, Choi et al., 2011). The LBD is made of 12 helices (H) and 4 β-sheets, arranged in a 3-layer alpha helical sandwich, which forms a ligand binding pocket demarcated by H4 and 5 at the top, H6, H7 and H10/11 at the back, H3 and the Ω loop at the front, H12 on the left, and β sheet 3, 4 and H2' on the right (Figure 1.1). Upon ligand binding, the interactions between the ligand and the amino acids in the ligand binding pocket results in stabilization of the overall LBD, allowing for the recruitment of coactivators to the PPARγ-RXR complex (Bruning et al., 2007).

PPARγ is known as the master regulator of adipose biology and plays an important part in human physiology (Lefterova et al., 2014, Dubois et al., 2017). The proper function of PPARγ is potentially essential to the prevention of several diseases affecting a wide proportion of people globally (Gross et al., 2017). Currently in the clinic, PPARγ – selective ligands have been used to treat insulin resistance and hyperglycemia seen with type 2 diabetes (T2D, Cheng et al., 2019). However, previously, treatment with PPARγ – selective ligands that induce 'full activation' of the PPARγ receptor (such as Rosiglitazone, a Thiazolidinedione) come with side effects that include cardiovascular dysfunction, weight gain, fluid retention and increased risk of bone fractures (Lebovitz 2019). This full activation by Thiazolidinediones (TZDs), also viewed as supraphysiological activation of the PPARγ when compared to endogenous ligands, has been proposed as one of the potential reasons for side effects with PPARγ – selective ligand treatment (Dubois et al., 2017). Whether or not this supraphysiological activation can be due to individual differences in PPARγ has not been explored.

It is estimated that mutations resulting in amino acid changes in the PPARγ protein are fairly common, occurring at a rate of about 1 in 500 people (Majithia et al.,2016). Mutations of the PPARγ protein have been previously documented, typically resulting in the condition Familial partial lipodystrophy 3 (FLPD 3), which presents with fat loss and varying degrees of metabolic abnormalities (Barroso et al., 1999, Agarwal and Garg, 2002, Hegele et al., 2002, Ludtke et al., 2007, Broekema et al., 2019). However, studies comparing the gene transcription activity between mutants and the structural basis for these mutations have been limited. With regards to supraphysiological activation, it was proposed that ligand interactions with the side chains of amino acid residues in H12 resulted in full activation and thus side effects (Bruning et al., 2007, Choi et al., 2011). Thus, several ligand design philosophies have been explored through the years, culminating in ligands with different activation profiles (full, partial, antagonist, inverse agonist) that bind to different parts of the LBD – For example, partial agonists stabilize H3 and the β-sheet region without interaction with H12 (Bruning et al., 2007, Frkic et al., 2018). However, it is still unclear how much each amino acid residue in the ligand binding pocket contributes to the activation of the PPARγ.

In this paper, a set of clinically observed mutations to the PPARγ LBD were selected (Figure 1.2) and their effects on gene transactivation activity was characterised, and X-ray crystallographic structural information was used to explain these changes. In addition, a number of residues in the PPARγ ligand binding pocket were mutated to alanine (alanine scan, Figure 1.3) to attempt to quantify the contribution of an amino acid residue to the binding of a ligand.

2. Materials and methods

2.1 Plasmids

The CM-pBind-hPPARγ-Gal4 plasmid with zeocin selection genes expressing the PPARγ LBD and Gal4 DBD chimeric protein was a gift from the Scripps' Institute, previously used in Bruning et al. (2007). The *Renilla* luciferase control reporter vector, pRL-TK, was purchased from Promega. The plasmid pG5E1b-Luc was obtained from the Dan Peet laboratory from the University of Adelaide. Several CM-pBind-hPPARγ-Gal4 mutant plasmid constructs (Y327A, F360A and H449A) were prepared by Dr. Rebecca Frkic from the Bruning laboratory.

Primers for generating CM-pBind-PPARγ-Gal4 mutant constructs prepared by Dr. Rebecca Frkic:

F360A-Gal4 plasmid

Forward: 5'- CTGCTGGTGACTTTATGGAGCCCAAGTTTGAGTTTGCTGTG -3'

Reverse: 5'- CACAGCAAACTCAAACTTGGGCTCCATAAAGTCACCAGCAG -3'

Y327A-Gal4plasmid

Forward: 5'- ACAATGCTGGCCTCCTTGATGAATAAAGATGGGGTTCTCATATCC -3'

Reverse: 5'- GGATATGAGAACCCCATCTTTATTCATCAAGGAGGCCAGCATTGT -3'

H449A-Gal4 plasmid

Forward: 5'- GTGCAGCTACTGCAGGTGATCAAGAAGAACGGAGACAGAC -3'

Reverse: 5'- GTCTGTCTCCGTTCTTCTTGATCACCTGCAGTAGCTGCAC -3'

Wildtype PPARγ LBD protein expressing vectors with ampicillin selection genes were purchased from GenScript. The PPARγ LBD (207 - 477aa) was cloned into the pET-11a vector using enzymes NdeI and BamHI. Several constructs with mutations within the LBD sequence were also purchased. The purchased PPARγ LBD mutants were: I281A, F282A, H323A, I341A, F363A, H449A, V290M, F387L, R397C, K422Q, P467L.

2.1.1 Plasmid construction

Other mutant constructs were generated using PCR mutagenesis. Primers for mutagenesis of I281A, F282A, R288A, H323A and I341A were designed by Dr. Rebecca Frkic. Primers for mutagenesis of F387L, K422Q and P467L were designed according to the protocol outlined by Liu and Naismith (2008). Other primers were designed using the NEBaseChanger webtool (available at: https://nebasechanger.neb.com/) and purchased from Sigma Aldrich. PCR was conducted using NEB's Phusion polymerase according to manufacturer's protocol. The mutants were verified by sequencing at the Australian Genome Research Facility (AGRF). The Gal4 mutants were verified using the Gal4 forward and T3 reverse primers, while the pET-11a vectors were verified using the T7 promotor forward and T7 terminator reverse primers.

Primers for generating the CM-pBind-PPARγ-Gal4 mutant constructs:

I281A-Gal4 plasmid

Forward: 5’- CTTTCAGGGCTGCCAGTTTCGCTCCGTGGAGG -3’

Reverse: 5’- CCTCCACGGAGCGAAACTGGCAGCCCTGAAAG -3’

F282A-Gal4 plasmid

Forward: 5’- CAGGGCTGCCAGTTTCGCTCCGTGGAGGCTG -3’

Reverse: 5’- CAGCCTCCACGGAGCGAAACTGGCAGCCCTG -3’

R288A-Gal4 plasmid

Forward: 5’- CCTCCGTGGAGGCTGTGCAGGAGATCACAG -3’

Reverse: 5’- CTGTGATCTCCTGCACAGCCTCCACGGAGG -3’

H323A-Gal4 plasmid

Forward: 5’- CGAGATCATTTACACAATGCTGGCCTCCTTGATGAATAAAGATG -3’

Reverse: 5’- CATCTTTATTCATCAAGGAGGCCAGCATTGTGTAAATGATCTCG -3’

I341A-Gal4 plasmid

Forward: 5’- GAGGGCCAAGGCTTCATGACAAGGGAGTTTCTAAAGAGCC -3’

Reverse: 5’- GGCTCTTTAGAAACTCCCTTGTCATGAAGCCTTGGCCCTC -3’

C285A-Gal4 plasmid

Forward: 5’- CTTTCAGGGCGCGCAGTTTCGCTCCGTGG -3’

Reverse: 5’- ATGCGGATGGCCACCTCT -3’

F363A-Gal4 plasmid

Forward: 5’- TTTTGGTGACGCGATGGAGCCCAAGTTTG -3’

Reverse: 5’- GGCTTTCGCAGGCTCTTT -3’

K367A-Gal4 plasmid

Forward: 5’- TATGGAGCCCGCGTTTGAGTTTG -3’

Reverse: 5’- AAGTCACCAAAAGGCTTTC -3’

Y473A-Gal4 plasmid

Forward: 5’- GCAGGAGATCGCGAAGGACTTGTACGGCGC -3’

Reverse: 5’- AGGAGCGGGTGAAGACTC -3’

F387L-Gal4 plasmid

Forward: 5’- CTTGGCAATACTGATTGCTGTCATTATTCTCAGTGGAGACCGCCC -3’

Reverse: 5’- TGACAGCAATCAGTATTGCCAAGTCGCTGTCATCTAATTCCAGTGC -3’

K422Q-Gal4 plasmid

Forward: 5’- CCAGCTGCAGCTGAACCACCCTGAGTCCTCACAGCTGTTTG -3’

Reverse: 5’- GTGGTTCAGCTGCAGCTGGAGCTCCAGGGCTTGTAGCAG -3’

P467L-Gal4 plasmid

Forward: 5’- GTCTTCACCTGCTCCTGCAGGAGATCTACAAGGACTTGTACGGCG -3’

Reverse: 5’- CTGCAGGAGCAGGTGAAGACTCATGTCTGTCTCCGTCTTCTTGATC -3’

V290M-Gal4 plasmid

Forward: 5’- GTTTCGCTCCATGGAGGCTGTGC -3’

Reverse: 5’- TGGCAGCCCTGAAAGATGC -3’

R397C-Gal4 plasmid

Forward: 5’- CAGTGGAGACTGCCCAGGTTTGC -3’

Reverse: 5’- AGAATAATGACAGCAATAAATATTGCCAAGTC -3’

Q286P-Gal4 plasmid

Forward: 5’- TCAGGGCTGCCCGTTTCGCTCCG -3’

Reverse: 5’- AAGATGCGGATGGCCACC -3’

R288H-Gal4 plasmid

Forward: 5’- CTGCCAGTTTCACTCCGTGGAGG -3’

Reverse: 5’- CCCTGAAAGATGCGGATG -3’

F360L-Gal4 plasmid

Forward: 5’- GCGAAAGCCTTTAGGTGACTTTA -3’

Reverse: 5’- AGGCTCTTTAGAAACTCC -3’

D396N-Gal4 plasmid

Forward: 5’- TCTCAGTGGAAACCGCCCAGGTT -3’

Reverse: 5’- ATAATGACAGCAATAAATATTGCCAAGTCGC -3’

L423P-Gal4 plasmid

Forward: 5’- CCAGCTGAAGCCGAACCACCCTG -3’

Reverse: 5’- AGCTCCAGGGCTTGTAG -3’

Gal4 DBD only plasmid

Forward: 5’- TGAGGGCGGATGCCACAGGCC -3’

Reverse: 5’- GTTAATTAATCGGATCCCTGGCGATCCC -3’

Primers for generating the pET-11a PPAR protein expression plasmids:

pET-11a-Q286P plasmid

Forward: 5’- CCAGGGCTGCCCGTTTCGTAGCG -3’

Reverse: 5’- AAAATACGGATCGCAACTTC -3’

pET-11a-R288H plasmid

Forward: 5’- CTGCCAATTTCATAGCGTGGAAG -3’

Reverse: 5’- CCCTGGAAAATACGGATC -3’

pET-11a-R288H plasmid

Forward: 5’- CTGCCAATTTCATAGCGTGGAAG -3’

Reverse: 5’- CCCTGGAAAATACGGATC -3’

pET-11a-F360L plasmid

Forward: 5’- GCGTAAGCCGCTGGGCGATTTTA -3’

Reverse: 5’- AGGCTTTTCAGAAATTCACGG -3’

pET-11a-D396N plasmid

Forward: 5’- TCTGAGCGGTAACCGTCCGGGCC -3’

Reverse: 5’- ATGATCACCGCAATAAAGATCGCCAG -3’

pET-11a-L423P plasmid

Forward: 5’- GCAACTGAAGCCGAACCACCCGG -3’

Reverse: 5’- AGCTCCAGCGCTTGCAGC -3’

pET-11a-Y327A plasmid

Forward: 5’- CGAAATCATTGCGACCATGCTGGC -3’

Reverse: 5’- TGAACGCCGTATTTCAGC -3’

Primers used for sequencing:

CM-pBind-PPARγ-Gal4 plasmid

Gal4 Forward: 5'-AGTGCGACATCATCATCGGAAGAG-3'

T3 Reverse: 5'-AATAACCCTCACTAAAGGGA-3'

pET-11a PPAR protein expression plasmids

T7 promoter Forward: 5'- TAATACGACTCACTATAGGG -3'

T7 terminator Reverse: 5'- GCTAGTTATTGCTCAGCGG -3'

2.1.2 Plasmid purification

The plasmids were transformed into DH5α cells, using heat shock treatment at 42°C for 10 seconds followed by a 1-hour outgrowth step in SOC broth, plated onto ampicillin (50 µg/ml, for protein expressing pET-11a vectors, pG5E1b-Luc, pRL-TK) or Zeocin (20 µg/ml, for CM-pBind-hPPARγ-Gal4 wildtype and mutant plasmids) LB plates and incubated at 37°C overnight. Single colonies were picked and propagated in ampicillin (100 µg/ml) or zeocin (50 µg/ml) supplemented LB broth for 12-16 hours overnight at 37°C.

For minipreps, 5ml of the antibiotic supplemented bacterial culture was then miniprepped using the Monarch® Plasmid Miniprep Kit according to the manufacturer's instruction. Glycerol stocks (40% glycerol, 100 µg/ml ampicillin) were also made from the bacterial culture. For Midipreps, 5ml of the antibiotic supplemented bacterial culture was Midiprepped using MIDIprep kits from Promega or Macherey-Nagel according to manufacturer's instruction.

2.2 Protein expression and purification

The miniprepped PPARγ LBD expressing vector was transformed into BL21 (DE3) cells using the same heat shock and outgrowth treatment described above, plated onto ampicillin (50 µg/ml) LB plates and incubated at 37°C overnight. Single colonies were picked and grown in ampicillin (100 µg/ml) LB broth at 37°C to an OD of 0.4-0.6. Glycerol stocks (40% glycerol, 100 µg/ml ampicillin) were made from the bacterial culture. A portion of this bacterial culture was added to larger volumes of LB for protein expression (1/100) and grown at 37°C to an OD of 0.6. Protein expression in the bacterial cells was induced with IPTG (1mM final concentration) and the culture was incubated overnight at 16°C.

For protein purified by immobilized metal affinity chromatography (IMAC) and Size exclusion chromatography (SEC): Cells were harvested by centrifugation at 5500RPM for 10 minutes at

4°C. Pelleted cells were resuspended in buffer A (25ml per litre of cell culture; 20 mM Tris pH 8.0, 500 mM NaCl, 10 mM imidazole, 2 mM BME) and then lysed using a cell disruptor. The cell lysate was clarified by centrifugation at 18 000 rpm for 30 minutes at 4°C. The supernatant was filtered (0.2µM), loaded onto a nickel resin IMAC column (immobilized metal affinity chromatography; ZE health) and eluted against buffer B (20 mM Tris pH 8.0, 500 mM NaCl, 250 mM imidazole, 2 mM BME). Fractions containing the protein were pooled and dialysed overnight at 4°C against buffer S (20 mM Tris pH 8.0, 150 mM NaCl, 1 mM DTT). The dialysed protein was then loaded onto a HiPrep 26/60 Sephacryl S-500 size exclusion column and eluted with buffer S. Eluted fractions containing the protein were pooled and concentrated to about 10mg/ml using a 10 000mW concentrator (Amicron). Aliquots of the concentrated, purified protein were flash frozen and stored at -80°C for future use.

For protein purified by batch purification: Cells were harvested, lysed, clarified and then filtered in the same way as described above. 2ml of prepared Nickel resin was then added to filtered supernatant from 2L of bacterial culture. This mixture was incubated at 4°C for 30 minutes with mild shaking. The slurry was centrifuged at 500g for 5 minutes and the supernatant was removed. The protein bound resin was washed 5 times with 2 X resin volume of Wash buffer (20 mM Tris pH 8.0, 500 mM NaCl, 25 mM imidazole, 2 mM BME). Each was step was followed by centrifugation at 500g for 5 minutes. The protein was eluted from the slurry 10 times with 1X resin volume of buffer B (20 mM Tris pH 8.0, 500 mM NaCl, 250 mM imidazole, 2 mM BME). Each elution step was followed by centrifugation at 500g for 5 minutes and the supernatant was collected. The collected supernatant was concentrated to about 10mg/ml using a 10 000mW concentrator (Amicron). Aliquots of the concentrated, purified protein were flash frozen and stored at -80°C for future use.

2.3 Thermal shift assay

Flash frozen stocks of purified protein (concentrated buffer B: 20 mM Tris pH 8.0, 500 mM NaCl, 250 mM imidazole, 2 mM BME) were thawed on ice and used in a thermal shift assay with the SYPRO™ Orange Protein Gel Stain (Invitrogen™). The assay was performed in the 96 well format using the MicroAmp™ Fast Optical 96-Well Reaction plates (Applied Biosystems™). The well solution was initially mixed according to the protocol outlined in Thermofisher's protocol for protein melting experiments (Life Technologies, 2010) and then optimized with suggestions from other publications (Huynh and Partch, 2015). The individual reagents of the TSA were optimized. Final volume in each well was 20 µL, comprised of 0.5X-10X dye

concentration, 0.01-0.6mg/ml protein in buffer, with ligand, DMSO control or apo protein. Assay components were pipetted into MicroAmp™ Fast Optical 96-Well Reaction Plate plates on ice and then sealed with adhesive film and centrifuged at 2000 RPM for 1-2 seconds to ensure well solution was mixed. The thermal shift assay was conducted at 4°C-70°C in increments of 0.3°C using the StepOnePlus™ Real-Time PCR System from Applied Biosystems™. Relative fluorescence units (RFU) were taken from filter 1 (520nm) unless otherwise specified. The negative of the first derivative (-dRFU/dT) of the fluorescence curves were calculated on Graphprism, data was truncated to include data from 20.2°C. The minimum point of this curve was extracted from excel. The corresponding temperature of this point was taken to represent the melting temperature (Tm, °C). Each construct was tested in triplicate over 3 experiments. The experiment would be excluded from calculation of average melting temperature if at least one replicate showed abnormal results.

2.4 Cell-based transactivation assay

2.4.1 Human cell culture

HEK293 cells were thawed from stocks of cells in Fetal Calf Serum, (FCS, Sigma Aldrich) and 10% DMSO and frozen at -80°C. Cells passaged at least twice before use in experiments. Cells were grown in DMEM (Gibco) supplemented with Glutamax and 10% FCS (Sigma Aldrich) and passaged when nearing 80% confluency, as calculated using the Bio-Rad TC20 Automated Cell Counter. All incubation steps were conducted at 37°C and 5% CO_2.

2.4.2 Dual luciferase assay (DLA)

HEK293 Cells were then seeded onto 96 well plates (30 000 cells per well). 24 hours later, pCMV-PPARγ LBD-Gal4 DBD, G5E1B and RLTK was transfected (1:1:0.1 ratio, 262.5ng total plasmid DNA) using PEI (3 PEI : 1 DNA) as the transfection agent. After 24 hours, cell culture media was aspirated and replaced with fresh media supplemented with ligand or equivalent volume of DMSO not exceeding 1/1000 of the volume of media added per well. Finally, after another 24 hours of incubation, cells were lysed and luciferase activity was determined using Promega's Dual-Luciferase® Reporter Assay System. 50µL of the Luciferase assay reagent II and Stop & Glo® was used. The DLA was performed at least twice in duplicate for initial tests to determine Rosiglitazone concentration test range and twice in triplicate for tests to determine agonist-response curves. Relative transcriptional induction refers to the ratio of Firefly to Renilla luciferase activity. EC_{50} values, maximum relative transcriptional induction

(RTI), confidence intervals, Ratio of probability (RP) and ΔAICc values were calculated by Graphprism using the four parameter model. The Akaike's Information Criterion (AIC) method was used to calculate probability of the models. The comparison used on Graphprism was "Do the best-fit values of selected unshared parameters differ between data sets?", comparing between individual mutant constructs and matched wildtype control. An average of EC_{50} values and maximum RTI experiments and standard deviation was calculated on Excel. For the EC_{50} of R288H, the comparison "For each data set, does the best-fit value of a parameter differ from a hypothetical value" was used instead, hypothetical value used was the EC_{50} of the matched wildtype control.

For the DLA comparing ligands Rosiglitazone, INT131 and SR10221, the procedure was conducted in the same way except for the following differences: 10 000 cells per well was seeded into 96 well plates; the ratio of pCMV-PPARγ LBD-Gal4 DBD, G5E1B and RLTK transfected was 1:1:1 amounting to 375ng of plasmid DNA. A two-way ANOVA (corrected for multiple corrections using the Tukey test) was used to compare the effects between each ligand on a single mutation as well as between mutations. 95% confidence interval was used.

The DLA used to investigate the PPARγ mutations was set up according to figure 3.1a: The wildtype PPARγ LBD was cloned into a modified pBIND expression plasmid downstream of the Gal4 DBD under the control of a T7 promoter. The resulting protein contains the PPARγ LBD and hinge region downstream of the Gal4 DBD. Mutations were then generated in the PPARγ LBD region of this chimeric protein by conducting mutagenesis. These PPARγ-Gal4 expressing plasmids, along with the pG5E1B Firefly and the pRL-TK Renilla luciferase reporter plasmids were cotransfected into HEK293 cells and treated with Rosiglitazone. Upon activation by a PPAR ligand, PPARγ-Gal4 chimeric protein binds to Gal4 response elements on pG5E1B, increasing transcription of Firefly Luciferase, thus increasing Firefly Luciferase activity and the bioluminescent signal output upon addition of DLA reagents. pRL-TK contains a constitutively active promoter expressing constant levels of Renilla Luciferase, allowing for normalization for transfection efficiency (Shifera and Hardin, 2010).

2.5 Western blot

HEK293 cells were transiently transfected using the same method detailed above and lysed before ligand treatment. Whole cell extract buffer (20mM HEPES 0.42 NaCl, 0.5% IGEPAL, 25%

Glycerol, 0.2mM EDTA, 1.5mM $MgCl_2$ and 1mM DTT, 1mM PMSF 1X Protease inhibitor cocktail was added immediately before use) was added to individual wells and transferred to Eppendorf tubes. Cell sample protein concentrations were matched using a Bradford assay with BSA as a control. Appropriate amounts of protein were added to sample buffer (final concentration 9% Glycerol, 0.01% Bromophenol Blue, 1% SDS, 25mM Tris pH 7.0, 1.25% BME) and loaded onto 10% Mini-PROTEAN® TGX™ pre-cast polyacrylamide gels from Bio-Rad. The gels were transferred onto Nitrocellulose membrane (Bio-Rad Trans-Blot Turbo Transfer System) and blocked with 10% Skim milk in 1X PBS and 0.1% Tween 20. The membrane was then incubated with rabbit Anti-GAL4 DBD primary antibody (diluted 1 in 1000, Sigma-Aldrich, Cat #G3042, Lot #D0506), goat anti-Rabbit HRP secondary antibody (diluted 1 in 10 000, Pierce) and then imaged. Membranes were then stripped and incubated with the rat anti-α tubulin primary antibody (1 in 3000, YL1/2 clone, Invitrogen, Lot # VI3078261), goat anti-Rat IgG (H+L) HRP secondary antibody (1 in 10 000, Invitrogen, Cat #31470, Lot #20200324) and imaged again. Each membrane is then imaged using the Chemidoc XRS+ (Bio-Rad) and images were then analysed on ImageJ.

2.6 Structural analysis

2.6.1 Crystallization and data collection

For apo crystals, 1ul of 10mg/ml of purified PPARγ protein was added to 1ul of well solution of 0.7M – 1.2M sodium citrate tribasic dihydrate (Hampton Research) and 0.1M – 0.25M Tris (pH 8.0). Crystals were then grown by vapour diffusion in 2µl hanging drop trays (500µL wells) at 16°C. For Rosiglitazone-PPARγ cocrystals, Rosiglitaone was added to 10mg/ml PPARγ protein in a 2 ligand :1 protein ratio and incubated on ice for 1 hour. The mixture was centrifuged for 15 minutes at 18 000 rpm 4°C. 1ul of the supernatant was added to 1ul of well solution of 0.7M to 1.3M sodium citrate and 0.1 to 0.25 Tris (pH 8.0). All crystals were transferred into 15% ethylene glycol cryoprotectant before being flash frozen and sent to the Synchrotron and diffracted using either MX1 or MX2 beams.

2.6.2 Structure determination and refinement

Data collected from the Australian Synchrotron was processed using XDS. Data was then processed using XDS, symmetry determination was conducted with POINTLESS and scaling was conducted with AIMLESS (CCP4I). Structures were solved by molecular replacement using Phaser-MR (PHENIX) and PDB ID: 5U5L as the search model. Structure refinement was carried

out in using Phoenix and model rebuilding was done in Coot. The refinement and rebuilding process was carried out several times to better fit the Fo-Fc difference maps. 2D ligand-protein interaction diagrams were generated using the BIOVIA Discovery Studio Visualizer 2020 client using default settings. For figure 7.3, residue F360 was mutated to L360 using Pymol's mutagenesis function. 3 rotamers were generated, the one with the least strain was picked (strain=14.55).

3. Results

3.1 Thermal shift assay of PPARγ mutants

3.1.1 Mutations alter thermostability of PPARγ LBD protein

To determine if the amino acid mutations of the PPARγ LBD change the stability of the protein, a thermal shift assay (TSA) with SYPRO™ Orange was conducted. PPARγ LBD protein purified using the Batch method (concentrated in buffer B) was used in the assay. Starting conditions of 0.5-1.5mg/ml of protein and 2-10X dye concentrations were used with a total well volume of 20µL, without ligand or DMSO (Figure 2a). The assay produced acceptable TSA curves when read on Filter 1 (520nm, Reinhard 2013). The best TSA curve was achieved with 5X dye and 1.5mg/ml of purified protein, but 1.0mg/ml was used instead as that condition produced a comparable change in RFU with less protein.

The TSA of the PPARγ constructs was conducted over a wider melting range (4-70°C for test vs 25-58°C for optimization). Most constructs displayed acceptable TSA curves – higher starting RFU was observed but curves contained a sharp increase followed by a decrease in RFU as temperature increased (Figure 2b., Reinhard 2013). Certain constructs showed high starting fluorescence and with a single but small peak, represented by F282A, F360A and F363A in Figure 2c (12596, 2906 and 24103 RFU respectively, vs 138556 RFU for wildtype). Other constructs like R397C and showed high starting fluorescence with no peak in RFU, or multiple peaks (Figure 2c). The calculated Tm of any construct from any experiment that showed curves similar to these two situations were highlighted in yellow and red respectively (Table 1.1). In general, constructs containing the K367A, C285A, K422Q, V290M, P467L mutations seemed to have increased thermostability, while constructs with mutations Y473A, H323A, F387L, F282A, F363A, H449A, I281A and F360A seemed to have decreased thermostability compared to wildtype PPARγ LBD (arranged in decreasing order of stability,

Table 1.2). PPARγ construct C285A showed the highest consistency in Tm across experiments (Average 44.400 ± 0.346°C, Table 1.1), K367A construct resulted in the biggest rightward thermal shift and I281A produced the most consistent leftward thermal shift on average compared to wildtype, while R397C did not produce any acceptable TSA curves across all 3 experiments. F360A construct produced the biggest leftward thermal shift but displayed undesirable, small RFU peaks across 2 experiments (Figure 2c, Table 1.1).

3.2 Dual luciferase assay of PPARγ-Gal4 transfected cells

3.2.1 Assay Setup

To determine the effect of the individual mutations on the transcription activation of the PPARγ receptor, we utilized a luciferase-based reporter assay (Figure 3.1a). The relative transcriptional induction (RTI) was measured for each PPARγ-Gal4 construct in response to Rosiglitazone, which was the measured bioluminescence of Firefly luciferase activity normalized to that of Renilla (ratio of Firefly:Renilla Luciferase activity). RTI was measured across different concentrations of Rosiglitazone to obtain a dose-response curve. From these curves, EC_{50} values and max RTI values were calculated for each PPARγ-Gal4 construct as indicators of potency and efficacy respectively. All experiments for the dual luciferase assay were conducted with cells transfected with wildtype PPARγ-Gal4 plasmid as a positive control (Table 2.1-2.4). Figures 3.2-3.4 show curves that are representative of the trends of each construct with respect to the wildtype construct.

The Akaike's Information Criterion (AIC) method was chosen to answer the question if the best-fit values of unshared parameters differ across datasets, specifically, between every mutant and the matched wildtype control. For K422Q, R288H and V290M, the shared model for EC_{50} used for this comparison was not able to be calculated, so the AIC method was used instead to answer the question if the parameter differed from a hypothetical value – which was defined as the EC_{50} value of wildtype control from the same experiment. The AIC method measures the probability of a model accounting for the observation. A ratio of probabilities (RP) is given for every comparison, the ratio of probability of the chosen model to the rejected model. The two models refer to a single curve that share the same parameter, or curves that have different parameters. An RP value close to 1 indicates that both models are equally likely. ΔAICc refers to difference in AICc, a negative ΔAICc means that probability of calculated

parameter being the same is higher. All RP and ΔAICc values are calculated in comparison to the wildtype control of the same experiment (Table 2.4).

In this and the next section, all constructs treated with Rosiglitazone will be referred to by their construct name for simplicity, for example, 'Cells transfected with plasmids expressing wildtype PPARγ-Gal4' will be referred to as wildtype, 'cells transfected with plasmids expressing the PPARγ-Gal4 plasmid containing the C285A mutation' will be referred to as C285A, unless otherwise stated.

3.2.2 Clinical mutations alter transcriptional response to Rosiglitazone

The average EC_{50} and RTI of the clinical mutants are listed in Table 2.1. In all experiments, the concentration-activity curve of wildtype in response to Rosiglitazone follows that seen in previous studies, characterised by a sigmoidal relationship (Lehmann et al., 1995, Figure 3.3, blue circles). The EC_{50} of wildtype ranges from 0.0082-0.0304μM, and activity peaks at around 0.05-0.10μM Rosiglitazone concentration, at 0.4895-0.7761 RTI. From our experiments, all clinical mutations affected concentration-activity curves in response to Rosiglitazone compared to wildtype (Figure 3.2, Table 2.1).

The potency of Rosiglitazone against the clinical mutant constructs could be split into 3 groups, around 0.001-0.01, 0.1 and 1-10μM. The first group, R288H, D396N and K422Q displayed EC_{50} values similar to or lower than wildtype. From figure 3.2b, it seems that the R288H and D396N mutations lowered the EC_{50} of the response to Rosiglitazone (Average EC_{50} D396N: 0.0084 ± 0.0081 μM, R288H: 0.0014 ± 0.0003μM, Table 2.1). The EC_{50} of R288H differed from the EC_{50} of wildtype with high probability (ΔAICc *18.19, *17.63, R1 and 2 respectively, Table 2.4) but D396N had low ΔAICc values across experiment replicates, suggesting that it may not have had any effect on transcriptional activity compared to wildtype (ΔAICc: -2.937, -0.7558, R1 and 2 respectively, Table 2.4). Across the experiments, R288H displayed lowered or similar maximal RTI (R1 R288H: 0.5535 vs wildtype: 0.7506, ΔAICc 16.92; R2 R288H: 0.5128 vs wildtype: 0.5547, ΔAICc 0.03061 respectively, Table 2.4), while the D396N mutation seemed to have increased maximal activity over wildtype (Average max RTI 0.6698 ± 0.0221, ΔAICc 16.48, 15.27, R1 and 2 respectively, Table 2.4). The EC_{50} of K422Q was slightly increased (Average EC_{50} 0.0316 ± 0.0295, ΔAICc 13.2, *5.434, R1 and 2 respectively Table 2.1, 2.4), while max RTI was increased by about 120% over wildtype (Average max RTI 0.6049 ± 0.0475, ΔAICc 5.368, 12.09, R1 and 2 respectively Table 2.1, 2.4).

The second group of mutants, F387L, V290M and F360L showed increased EC_{50} values of almost 1 order of magnitude in response to Rosiglitazone, in the 0.1-1µM range (Average EC_{50} F387L: 0.2251 ± 0.1066µM, V290M: 0.4480 ± 0.4354µM, F360L: 0.3172 ± 0.0146µM, Table 2.1, Figure 3.2c). Maximal activity of F387L seemed to exceed that of wildtype by about 0.09 RTI on average, similar to K422Q (F387L ΔAICc: 3.609, 7.428 R1 and 2 respectively, Table2.4). Maximal activity of F360L was lower than matched wildtype control across both replicates by about 0.1 RTI (Average max RTI F360L: 0.5259 ± 0.1140 vs wildtype: 0.6302 ± 0.1067, ΔAICc 10.22 and 25.87, R1 and 2 respectively, Table 2.4). V290M showed about a reduction of 0.15 RTI compared to wildtype across both replicates but had low ΔAICc scores in R1, which suggested that max RTI may have been lower compared to wildtype (Average max RTI 0.3517 ± 0.0280, ΔAICc: 0.005727, 18.2, R1 and 2 respectively Table 2.1, 2.4).

The third group of mutants, P467L, L423P and R397C resulted in increased EC_{50} values of Rosiglitazone by 2 or 3 orders of magnitude, ranging around 1-10µM (Average EC_{50} P467L: 2.1820 ± 0.9320µM, L423P: 3.2260 ± 1.9120µM, R397C: 9.5290 ± 0.5629 µM, Table 2.1). Maximal activity of P467L was higher than wildtype in both experimental replicates but had low ΔAICc scores in R1 (R1 P467L: 0.7355, wildtype: 0.7297 ΔAICc -3.232; R2 P467L: 0.6111, wildtype: 0.5267 ΔAICc 3.876, Table 2.4). L423P had slightly higher RTI values than wildtype in both replicates, but also had low ΔAICc scores across R1 and 2 (ΔAICc -3.261, 0.632, R1 and 2 respectively, Table 2.4). This suggested that only P467L may have had increased max RTI compared to wildtype. R397C displayed the lowest max RTI, decreasing by about 0.17 RTI on average, or about 35% decreased activity compared to wildtype (ΔAICc: 9.063, 12.6, R1 and 2 respectively, Table 2.4).

In short, R288H decreased, D396N had no effect and K422Q may have slightly increased EC_{50} compared to wildtype. F387L, V290M and F360L increased EC_{50} by one magnitude compared to wildtype. P467L, L423P, R397C increased EC_{50} by two to almost 3 magnitudes compared to wildtype. F387L, K422Q, D396N (in increasing order) resulted in increased max RTI compared to wildtype. P467L may have increased max RTI while L423P likely had no effect on max RTI, compared to wildtype. F360L lowered max RTI across both replicates compared to wildtype. R288H, V290M may have slightly lowered max RTI compared to wildtype.

3.2.3 Ligand binding pocket residues contribute differently to Rosiglitazone induced transcription

The average EC_{50} and RTI of the alanine scanning mutants are also listed in Table 2.1. Generally, in these experiments, the alanine scanning mutations decreased both the potency and efficacy of Rosiglitazone treatment. The potency of the mutant constructs formed less distinct groups than that seen with clinical mutants, with most mutants displaying an average EC_{50} value in the range of 1-10 µM. The closest to wildtype, C285A, increased the EC_{50} by almost one order of magnitude, C285A: 0.0991 ± 0.0011 vs wildtype: 0.0145 ± 0.0004 µM (ΔAICc: 15.79, 29.13, R1 and 2 respectively, Table 2.4). Max RTI of C285A was lower than wildtype in R1 but higher in R2, suggesting that there may not have been a difference compared to wildtype (R1 C285A: 0.5648 vs wildtype: 0.5821, ΔAICc: -2.948; R2 C285A: 0.6997 vs wildtype: 0.6286, ΔAICc 2.158, Table 2.4).

The increase in EC_{50} of the rest of the constructs were considerably larger (Table 2.1). Values ranged from 0.7461 to 36.3µM, and on average increased in order: F363A (0.7720 ± 0.0366µM), F282A (1.0848 ± 0.4175µM), H449A (2.2190 ± 0.0410µM), Y327A (2.9450 ± 0.2404µM), H323A (3.9025 ± 1.2777µM), I281A (4.9465 ± 0.0177µM) and F360A (30.55 ± 8.1317µM). EC_{50} of constructs I341A and Y473 varied widely across two replicates (I341A vs wildtype: 8.889 vs 0.01481µM, 1.523 vs 0.01426µM; Y473 vs wildtype: 12.83 vs 0.01117µM, 2.457 vs 0.009546µM R1 and 2 respectively, Table 2.4).

The max RTI formed more distinct groups. F363A had higher RTI than wildtype in two replicates (Average max RTI F363A: 0.7447 ± 0.0639 vs wildtype: 0.6054 ± 0.0329, ΔAICc: 3.881, 16.89, R1 and 2 respectively, Table 2.1, 2.4). Similar to C285A, max RTI of H449A was only higher than wildtype in R1 but not R2, suggesting that max RTI may not have been different compared to wildtype (R1 H449A: 0.6723 vs wildtype: 0.6067, ΔAICc: 4.705; R2 H449A: 0.6444 vs wildtype: 0.6764, ΔAICc -2.195 Table 2.4). The constructs Y327A, F282A, I341A, I281A displayed lowered max RTI compared to wildtype (in decreasing order of RTI: 76.8, 75.5, 62.1, 57.8% of RTI of wildtype on average, respectively, Table 2.1). F282A showed reduced max RTI compared to wildtype in both replicates but had low ΔAICc scores in R1 (R1 ΔAICc: -1.859), suggesting that max RTI may have been lowered compared to wildtype (Table 2.4). Y473A and H323A had the greatest decrease in max RTI (38.7, 38.3% RTI of wildtype on average, respectively, Table 2.1). The concentration activity curve of F360A was still increasing at max Rosiglitazone dose but max RTI was calculated at 0.3655 ± 0.0503, 57.4% of wildtype RTI on average (Table 2.1).

In short, all alanine mutants resulted in increased EC_{50} compared to wildtype. In decreasing order of potency: C285A, F363A, F282A, H449A, Y327A, H323A, I281A, I341A, Y473A, F360A. The max RTI was increased in the case of F363A and similar to wildtype for C285A and H449A. The rest of the mutants displayed decreased max RTI. In decreasing order of max RTI: Y327A, F282A, I341A, I281A, F360A, Y473A, H323A.

3.2.4 Constitutively active or inactive mutations

Surprisingly, mutation K367A seemed to be constitutively active (Average EC_{50} 1.3764 ± 0.6641µM, Table 2.1, Figure 3.4). Measured firefly luciferase RLU was about 5.5X compared to wildtype without ligand (with DMSO) and increased by an average of 145% with treatment of Rosiglitazone compared to DMSO across two experiments (Table 2.2). Renilla luciferase RLU value trends for K367A closely followed that of wildtype but was notably higher (Table 2.2). Calculated RTI values suggest that K367A constitutive expression stays around, on average, 64% of the max RTI of wildtype activated by Rosiglitazone. Interestingly, Q286P mutation seemed to have abolished transcriptional response to Rosiglitazone entirely (Table 2.3). Luciferase RFU stayed close to levels measured for a truncated construct expressing only the Gal4-DBD, with DMSO control or Rosiglitazone treatment (Table 2.3). Renilla values also closely followed that of wildtype and Gal4-DBD.

3.3 Western blot of PPARγ-Gal4 transfected cells

3.3.1 Differences in expression of PPARγ-gal4 protein between plasmids

To further characterise the in vivo properties of the mutant PPARγ-Gal4 constructs, a western blot was conducted to see if the above mutations of the PPARγ LBD residues affected the expression of the PPARγ-Gal4 protein (Figure 4). Protein expression of each construct was represented as a ratio of intensity of the band of PPARγ to the intensity of the band α-tubulin, calculated on ImageJ (Table 3). For the clinical mutations, the R288H, P467L, V290M, and Q286P displayed slightly increased expression of the PPARγ-Gal4 protein (in increasing order of PPARγ:α-tubulin ratio compared to wildtype), while F387L, K422Q, L423P, F360L, D396N, R397C on the other hand displayed decreased expression of the PPARγ LBD protein (in decreasing order of PPARγ:α-tubulin ratio compared to wildtype). For the alanine scanning mutations, the F363A, I281A, F282A, and K367A mutations increased PPARγ protein expression (in increasing order of PPARγ:α-tubulin ratio), while the C285A, Y473A, H323A, F360A, Y327A, H449A, I341A mutations decreased protein expression relative to wildtype (in

decreasing order of PPARγ:α-tubulin ratio, compared to wildtype). The construct expressing the truncated PPARγ-Gal4 plasmid to express Gal4 DBD only also seemed to increased expression of protein compared to wildtype (Figure 4, Table 3).

3.3.2 Differences in expression and implications on gene transactivation activity

Max RTI or efficacy could be affected by increased expression of proteins. For example, an increased amount of PPARγ-Gal4 protein (due to increased expression) would directly result in greater activity of firefly luciferase activity and hence increasing RTI. If the protein amounts were matched between a mutant construct and wildtype, the 'actual RTI' might be lower than the 'observed RTI' from the cell-based gene transactivation assay. Generally, the results from the western blot contextualized the results from the gene transactivation assays in 3 ways.

In the first group of mutants, the mutation had an effect on maximal RTI, but the protein expression might have reduced these effects. K422Q, D396N, F387L displayed higher RTI (On average, 117.7% - 131.9%, Table 2.1) but protein expression was reduced compared to wildtype (Ratio 0.637, 0.394 and 0.703 vs wildtype 0.975 respectively, Table 3), indicating that actual increase in RTI over wildtype was higher than observed. I281A had lower RTI (On average, 57.8% Table 2.1) but increased expression (Ratio 0.257 vs wildtype 0.165, Table 3), indicating that actual RTI was much lower than observed.

In the second group, the mutations may have affected maximal RTI, and the differences in protein expression supports this hypothesis. H449A and C285A had higher RTI that wildtype on average (On average 103.0% and 104.2% respectively, Table 2.1), but were shown to have lower RTI than wildtype in one experimental replicate. However, these replicates had low probability of being different compared to wildtype (ΔAICc H449A: -2.195, C285A: -2.948, Table 2.4). The reduced protein expression of these constructs (C285A 0.234 vs wildtype 0.271, H449A 0.064 vs wildtype 0.165, Table 3) indicates that if protein amounts were matched, the constructs might show a larger or more consistent increase of RTI over wildtype. Conversely, V290M, R288H and F282A had lower RTI across all experiments (On average, 69.2%, 85.4%, 75.5%, Table 2.1) but had a low probability of being different to wildtype in one experiment (Table 2.4). These constructs showed increased protein expression (V290M 1.182 vs wildtype 0.975, R288H 0.552 vs wildtype 0.500 and F282A 0.510 vs wildtype 0.271, Table 3), which supports the observation that it might have a lower max RTI compared to wildtype if protein amounts were matched. Cell activation assays suggested that the max RTI

for L423P was not different from wildtype (On average, 105.9%, ΔAICc R1: -3.261 and R2: 0.632, Table 2.1, 2.4). However, looking at the protein expression of L423P (Ratio L423P 0.544 vs wildtype 0.975, Table 3), the decreased protein expression might have contributed to this lack of difference, suggesting that it might have had a higher RTI than wildtype.

In the last group the mutations resulted in changes to maximal RTI, but these differences may be accounted for by changes in protein expression. P467L and F363A had increased RTI (On average *108% and 122.9% respectively, Table 2.1) but also increased protein expression (Ratio P467L 1.123 vs wildtype 0.975, F363A 0.704 vs wildtype 0.5, Table 3), indicating that the actual max RTI would have been much closer to wildtype. On the other hand, R397C (65.6%), F360L (83.1%), I341A (62.1%), Y327A (76.8%), H323A (38.3%), Y473 (38.7%), F360A (57.4%), had decreased RTI but also decreased protein expression (Ratio: R397C 0.300 and F360L 0.703 vs wildtype 0.975; I341A 0.179, H323A 0.314 and Y473A 0.341 vs wildtype 0.500; Y327A 0.083 and F360A 0.096 vs wildtype 0.165), also indicating that the actual RTI may have been closer to wildtype (Table 2.1, 3).

For the constitutively active/ inactive mutants, Q286P has almost 3X the protein expression compared to wildtype (1.580 vs wildtype 0.500, Table 3), suggesting that firefly luciferase activity might be even lower than thought when protein amounts are matched, supporting the hypothesis that Q286P might be inactive. Expression of K367A was also increased (1.587 vs wildtype 0.500), indicating that the actual activity of K367A might be much lower. This suggests that K367A might have an activity profile closer to Q286P.

To summarize, protein expression may have affected the differences in max RTI between PPARγ mutant constructs in gene transactivation assays with Rosiglitazone. K422Q, D396N, F387L and L423P most likely resulted increased max RTI over wildtype, while I281A resulted in lowered max RTI compared to wildtype. For H449A, C285A, V290M, R288H, F282A and L423P, protein expression provided extra evidence to support conclusions drawn from inconsistent results between experimental replicates. For P467L, F363A, R397C, F360L, I341A, Y327A, H323A, Y473, F360A, the changes in max RTI seemed to be due to increased or decreased protein expression. Ideally, samples from the same biological replicate should be used when comparing protein expression and transactivation assay results. However, for this application, the experimental design for the western blot was sufficient for the purposes of giving further context to the results from the dual luciferase assay.

3.4 Dual luciferase assay of PPARγ-Gal4 transfected cells with different ligands

3.4.1 Different mutants have different responses to ligands

To determine the effect of the individual mutations on the responses to different ligands, the luciferase-based reporter assay described above was used to characterise a subset of the PPARγ-Gal4 mutants in response to a full agonist Rosiglitazone, partial agonist INT131 and inverse agonist SR10221 at 1μM or 10μM concentration of ligand (Figure 5). RTI measured for wildtype matched the activation profiles of the ligands (full activity, partial or decreased activity, Figure 5). Generally, the dose response of each mutant follows that previously demonstrated with Rosiglitazone. Most mutations displayed increased activity with increased Rosiglitazone concentrations, except for wildtype and K422Q which follows the results previously seen with the dose response curves (Figure 3.2a, decrease in RTI at higher concentrations). Strikingly, mutations changed the response profile of mutations R397C, P467L and Y473A to the partial agonist INT131 (Figure 5). R397C induced higher activity than Rosiglitazone at 1μM (P value = 0.0023) but was not significantly different at 10μM (P value = 0.9059, Figure 5). For P467L, RTI by Rosiglitazone was much higher at 10μM than 1μM, but activity of INT131 remained relatively similar and not significantly different from DMSO control (Figure 5). Based on the graphs it seemed like for Y473A, INT131 induced higher activity than Rosiglitazone at both the 1μM and 10μM concentrations, however this difference was not significant (For 1μM P value = 0.2838, for 10μM P value = 0.5889, Figure 5). For K367A, INT131 induced higher activity than Rosiglitazone at 10μM (P value = 0.0013), whereas Rosiglitazone did not induce a significant difference compared to vehicle control (P value = 0.2904, Figure 5).

3.5 Structural analysis

3.5.1 Crystallization of PPARγ mutants

To better understand the changes in EC_{50} and RTI seen in PPARγ LBD mutants when treated with Rosiglitazone, crystallization of purified PPARγ mutant protein with or without Rosiglitazone was attempted. Crystals were obtained with protein purified using the batch-spin purification method and Sodium Citrate and Tris pH 8.0 as the crystallization solution, described in the methods. Structures of 6 alanine scanning mutants and 1 clinical mutant were successfully solved (Supplementary figures 1.1-1.5). PDB ID: 5U5L was used as the search model for phasing, model structures used for comparison are PDB ID: 5YCP, 7AWC and

2PRG for structures of PPARγ with Rosiglitazone bound, PDB ID: 6MD4 for PPARγ structure with Rosiglitazone and fatty acid bound in the same ligand binding pocket , and PDB ID: 1PRG for apo PPARγ structure. For most of the structures, electron density (as indicated by the omit map) branching out from C285 in the PPARγ ligand binding pocket of A or B chain was observed that could not be fitted with water, ions from the crystallization conditions or ligands (except for the ligand bound structures and K367A_A1, Y473A_A1 and 4). This could have been oxidized cysteine, however, as it is difficult to identify the oxidation state of cysteine, it was left unmodelled (Garrido Ruiz et al., 2022). Density from the omit map that could not be accounted for by waters or other small molecules present in the crystallization buffer was also left unmodelled. The discussion moving forward will involve the 'active chain' of the protein – the unit cell of most of our PPARγ crystal structures typically contain 2 LBD protein units that dimerize with each other, one with H12 in the active position and the other with H12 missing residues or misaligned. The results below mainly describe the LBD unit that aligns with PDB ID: 5YCP, which referred to chain A for most proteins except H323A_A1.

Apo PPARγ structures (PDB ID: 1PRG), PPARγ structures bound with Rosiglitazone (PDB ID: 5YCP, 7AWC, 2PRG) and Rosiglitazone with fatty acid (PDB ID: 6MD4) were used as 'model' structures. Overall, the obtained crystal structures of PPAR were relatively similar to the model structures (PDB ID: 5YCP, 7AWC, 2PRG and 6MD4) in terms of overall fold and positions of all helices (RMSD to 5YCP: 0.345-0.449, Table 4.1).

Aside from the overall fold, there were slight differences noted in the mutant LBD structure. These include: Alternative H2-H2' loop position in some PPAR mutants; Full (F363A_L, H449A_A2) or partial (C285A_A, C285A_R, F363A_A, H323A_A1-3, H449A_A1, K422Q_A1-2, Y473A_A1-4) Ω loops in PPAR mutants; Some structures contained density that was modelled with sodium ions (C285A_A, F363A_A, F363A_L, H323A_A1, H323A_A3, K422Q_A1, H449A_A1, Y473A_A3, Y473A_A4); Some PPAR mutant structures contained density that matches Rosiglitazone (C285A_R, K367A_R, Y473A_A4), another (F363A_L) contained density that could not be fit to Rosiglitazone and might instead fit a fatty acid.

The structure of the PPAR mutants closely resemble 5U5L, since it was used as the search model during phasing. At least one structure of every mutant contained alternate H2-H2' loop (residues 238-245, Figure 6.9c, 6.11a, 6.12, 6.13a, 6.14a, b, 6.15a).

The Ω loop in the PPARγ mutant structures adopted a 'latched' position compared to other model structures (PDB ID: 1PRG and 2PRG) with visible Ω loops (Figure 6.1a, b, d). As seen in C285A_R, H266 points in the Y-direction (upwards) with the histidine side chain sitting parallel to H3, displacing F282 from its usual position (in yellow) to a new position (in green, Figure 6.1a). In this position, H266 forms hydrogen bonds with E291, 'closing up' the ligand binding pocket from the solvent exposed surface (Figure 6.1a). In Y473A_A2, polar interactions were formed between K265, H266 on the Ω loop and E291 on H3, and E343 on β2- β3 loop (Figure 6.1b). This 'double latch' was also observed in H323A_A1. A similar Ω loop configuration is seen in H323A_A2 and H323A_3, but in these structures residue K265 did not have full density. Other latching mechanisms could be seen in the model structures: In the Saroglitazar bound PPARγ LBD structure, a different latching mechanism is seen between K265 and E291, instead of H266 and E291 (PDB ID: 7E0A, Figure 6.1c); In 2PRG, a unique latching mechanism is seen, between residues L270 and F287, but not for 1PRG (Figure 6.1d).

In many of the mutant structures, the H2' shifts more in the X-direction than seen in the model structures, with the exception of PDB ID: 1PRG and 6MD4 (Figure 6.2). This was measured as the distance between residue L255 of structures versus L255 of 5YCP. In some structures, residues near the end of H2' displayed a slightly bigger shift than residues at the start of H2' (Figure 6.2, Table 4.2). This shift was characterised by measuring the distance between I281 and E259 and comparing to 5YCP. These two measurements captured both shifts in H2' as well as tilts – exemplified by 6MD4 and K367A (Figure 6.2, Table 4.2). This observed shift in H2' could be a result of accommodating the Ω loop structure described above, which was not seen in model structures PDB ID: 5YCP, 2PRG and 7AWC. On visual inspection, the latter half of H10 in the mutant structures seem to move closer towards H3. Using I456 and F282 as reference points, our measurements confirmed this observation in most PPARγ mutant structures, except for H449_A1 and K422Q_A1 (10.7Å and 10.8Å respectively, Table 4.2). Most structures had H10-H3 distances similar to or smaller than 10.4Å, a distance observed in model structures 1PRG and 2PRG (Table 4.2). However, these shifts in the helices does not occur in the middle of H10/11 where ligand binding typically occurs, marked by reference points H449 and C285. In general, the H10/11 and H2' shifts do not result in large changes in the left-to-right length of the PPARγ LBD, measured using reference points I456 and L255 (Figure 6.3, Table 4.2).

For the alanine scanning mutants, crystal structures of C285A, H323A, F363A, H449A and Y473A were successfully solved, K367A will be discussed separately below. From the gene transactivation assay experiments we can see that these 5 mutations displayed increased EC_{50} (decreased potency) compared to wildtype, arranged in increasing order: C285, F363A, H449A, H323A, Y473A (Table 2.1). As mentioned above, the mutant structures did not show any major differences in the overall fold of the protein.

For C285A, both the apo and Rosiglitazone bound structures were solved. The A chain of the apo structure resembled that of C285A Rosiglitazone bound structure closely (RMSD = 0.168, 1748 to 1748 atoms Table 4.1), but there were a few noted differences (Figure 6.7). The 'single latch mechanism' described above was seen for the Rosiglitazone bound structure but not for the apo structure, as H266 in the Ω loop could not be modelled (Figure 6.7). Alternate conformations for residues F363 and F282 in the apo structure and deviations in position of Q286 between the apo and ligand bound structures were also observed. These differences were likely due to the presence or absence of Rosiglitazone, which could have affected the stabilization (and thus modelling) of the Ω loop residues. Similar ligand interactions with ligand binding pocket residues were seen when comparing C285A_R to the model structures, as determined by Discovery Studio Visualizer (Figure 6.4-6.6). Visual inspection revealed that Rosiglitazone in C285A_R adopts a slightly different position as compared to 5YCP, 2PRG and 7AWC (Figure 6.8). The central phenoxy group of Rosiglitazone shifted slightly more towards H5, by 0.4Å compared to 5YCP. This is likely the result of the C285A mutation – the alanine substitution at position 285 could possibly result in a weaker hydrophobic bond with the Rosiglitazone molecule compared to cysteine at position 285.

F363A apo and ligand bound structures were very similar (RMSD = 0.117, 1892 to 1892 atoms, Table 4.1) as such we will focus on discussing the ligand bound structure (Figure 6.9). F363A seemed to contain density that could possibly fit the ligand 3-oxopalmitic acid. The hydrophobic end of this fatty acid was bound to an area near F363 in the ligand binding pocket in the distal part of arm 1, and the polar end stretches over to arm 3 (Figure 6.10b). This area was not accessible in 2PRG for ligand binding but was accessible in fatty acid bound structures (PDB ID: 3U9Q, 4EM9) and a Farglitazar bound structure (PDB ID: 7AHJ), through the slight displacement of L452 and L456 (Figure 6.10 c, d). In F363A, the alanine substitution allows access to an area near H7 formed by residues A278, I281, F282, L356 and F360 without rearrangement of these residues (Figure 6.10c, d, 7.3c). This fatty acid forms an ionic

interaction with R288 and other hydrophobic interactions in arm1, as well as atypical interactions with residues I281, F282 and L356 (Figure 6.5). Due to the position of the Ω loop, the size of arm 2 differs between F363_L and 2PRG (in white, Figure 6.10d)

For H323A, H449A and Y473A mutations, only apo structures were solved as protein incubated with Rosiglitazone did not yield cocrystals. H323A structures were also very similar to one another (RMSD = 0.141, 1727 to 1727 atoms, RMSD = 0.154, 1749 to 1749 atoms, H323A_A2 and H323A_A3 aligned with H323A_A1 respectively, Table 4.1). H323A_A3 was the only H323A structure to have an alternate H2-H2' loop modelled (Figure 6.11a). On comparison with model structures, H323A displays an obvious shift in H12 in the X direction (in the X direction, Figure 1.1, 6.11) which could be quantified by the decreased distance between Y473 and V339 (Figure 6.3, Table 4.2). H323A_A1, 2 and 3 displayed decreased distances of 22.7, 22.8 and 22.4Å respectively compared to 24.1Å for 5YCP (Figure 6.11, Table 4.2). This shift is likely due to the alanine substitution at position 323 – Y473 occupies the space that was previously taken up by H323 (Figure 6.11). H449A structures were very similar to each other (RMSD = 0.227, 1675 to 1675 atoms, Table 4.1) differing slightly in the Ω loop and H2-H2' regions (Figure 6.12). The Ω loop structure was similar to that seen in F363A_L (Figure 6.9, 6.12). Although H449A structures did not contain features that were unique compared to other mutant or model structures, there was a slight decrease in distance between H10 and H3, as measured using H449 and C285 as reference points (Figure 6.3, Table 4.2). Likewise, the Y473A structures were very similar but differed in the Ω loop and H2-H2' regions, similar to H449A (RMSD = 0.157, 1695 to 1695 atoms, RMSD = 0.093, 1856 to 1856 atoms, RMSD = 0.121, 1803 to 1803 atoms, Y473A_A2, A3 and A4 compared to Y473A_A1, Table 4.1, Figure 6.13). In the Y473A structures, a slight shift (of about 1.3Å to the right, measured between Cα of residue 473 in both Y473A_4 and 5YCP) in H12 was observed, likely as a result of the tyrosine to alanine mutation (Figure 6.13). This shift corresponded to a smaller distance of about 0.5Å between Y473 and V339 compared to model structures (Table 4.2). A Rosiglitazone molecule was also found in structure Y473A_A4 in the B chain bound near the β-sheet and H2-H2' loop regions, likely an artefact from crystal packing (Figure 6.13c).

K422Q was the only clinical mutant that was successfully crystallized, and only apo structures were obtained (Figure 6.14). The transactivation and western blot results suggested that this mutation slightly decreased potency (increased EC_{50}) in response to Rosiglitazone but also increased of efficacy (increased max RTI) over wildtype. Both obtained K422Q structures were

relatively similar (RMSD = 0.329, 1604 to 1604 atoms, Table 4.1). Examination of both structures did not reveal major differences in the overall fold of the apo K422Q structures. One important point to note was that the K422Q residue could only be modelled in one structure (K422Q_A1), suggesting that this side chain is very mobile since the mutation was confirmed via sequencing (Figure 6.14a, b). Comparisons against the model structures did not reveal any major differences that could explain the decrease in potency or increase in efficacy. In the full-length DNA bound PPARγ-RXR structure (PDB ID: 3DZY), K422Q does not directly participate in ligand interaction, dimerization with RXR or interaction with the DBDs of PPARγ or RXR. Since K422Q is also outside the PPARγ ligand binding pocket , it is likely that these changes might be mediated by changes in coregulator interaction (Figure 6.14c).

Crystal structures of both the apo and Rosiglitazone-bound K367A PPARγ mutant structures were successfully obtained. Previously, the transactivation and western blot results suggested that K367A might be inactive, or constitutively active at a level of transcriptional activity lower than 64% of wildtype (Table 2.1). Examination of the apo and Rosiglitazone-bound K367A structures did not reveal any major differences between the overall fold of K367A to any of the other model structures to explain its gene transactivation activity profile (Figure 6.15). Based on the ligand interactions determined by Discovery Studio Visualizer, none of the model structures nor the Rosiglitazone bound K367A structure forms interactions with residue K367 (Figure 6.6). The K367A mutation also did not change Rosiglitazone's interactions with the ligand binding pocket. On closer inspection, K367 can interact with H449 within the same LBD via a hydrogen bond and the K367A mutation disrupts this interaction (Figure 6.15b). This interaction was seen in most mutant structures and in some but not all Rosiglitazone bound model structures (Seen in PDB ID: 5YCP, 7AWC, 6MD4; Not seen in PDB ID: 2PRG, 3DZY), and was also not in the apo model structure (PDB ID: 1PRG). Of note, K367A_R was also the only ligand bound structure with alternate conformations for C285 (Figure 6.15c). Looking at the dimensions of the ligand binding pocket, H2' in K367A did not deviate much from 5YCP as much as the other structures of PPARγ mutants (Table 4.2).

In summary, for the mutations with successfully solved crystal structures, there were not any major structural changes observed that might indicate deficiencies in protein folding or in ligand binding.

4. Discussion

4.1 Using TSA to optimize crystallization conditions

The thermostability of PPAR mutants as suggested by the TSA did not have consistent effects on EC_{50}, max RTI or protein expression. This could easily be attributed to the relevance of the experimental context of the TSA (in vitro) versus the cell-based gene transactivation assays. More often, the TSA has instead been used to optimize crystallization conditions (Reinhard et al., 2018). However, in our experiments, TSA results did not reliably predict success attempts at crystallization. The PPAR mutants Y473A, H449A, K422Q, K367A, F363A, H323A and C285A yielded suitable X-ray diffraction data. PPAR mutants K422Q, K367A and C285A showed the greatest increases in thermostability and yielded crystal structures accordingly. However, V290M and P467L both showed increases in thermostability but did not yield crystal structures. Conversely, the PPAR mutants H449A, F363A and H323A showed decreases in thermostability but still yielded crystal structures. Interestingly, both P467L and I281A, each with increased and decreased thermostability respectively, displayed phase separation (oil droplets) but no formation of protein crystals. This inconsistency might have been due to the potential binding of SyproOrange to the PPARγ ligand binding pocket, as suggested in Chapter 5.

Attempts were made to crystallize the other PPAR mutants – PPAR mutants that did not produce protein crystals and were previously purified with batch purification (stored in buffer B) were repurified using IMAC and SEC and stored in buffer S (20 mM Tris pH 8.0, 150 mM NaCl, 1 mM DTT). The standard PPARγ crystallization condition Tris pH 8.0 and Sodium citrate, crystallization screens as well as other buffers and additives were used, but none of these efforts yielded protein crystals suitable for X-ray diffraction.

4.2 The clinical mutations affect transcription induction in different ways

The effect of clinical mutations on transcription activity was explored using reporter assays to find out if different mutations could increase or decrease, potency (EC_{50}) and/or efficacy (max RTI). From our results, the mutations had very varied effects on EC_{50}, maximum transcription activity and protein expression (Table 5 and Figure 8.1, 8.2). Changes in EC_{50} could be typically attributed to ligand binding and changes in maximum activity to the recruitment and stabilization of the coactivator complex. However, these simple attributions do not hold in reality as the residues might play multiple roles such as in stabilizing the protein, forming intra-protein interactions or forming inter-protein interactions for post translational

modifications as well as coregulator interactions. In our experiments we attempted to link the observed gene transactivation activity of mutations with structural data.

For mutations targeting residues that do not interact with the ligand directly or take part in intra-protein interactions, changes in max RTI might affect interactions with coregulators. In our experiments, K422Q increased max RTI compared to wildtype but did not display any obvious changes to the overall fold of the protein (Figure 6.15). Residue K422 sits on H9 in a region before the dimerization interface H10/11. This area, as seen in the full-length structure (PDB ID: 3DZY), sits at a solvent exposed area away from the DNA or DBD, potentially making interactions with coregulators, as suggested by the arrangement of the coactivator-ER structure (Yi et al., 2015). This hypothesis is supported by a previous study which reported that even though K422Q PPARγ receptor did not change luciferase activity compared to wildtype, it was unable to express and repress certain genes to the same extent as wildtype (Gupta et al., 2003).

Other mutations target residues that do not interact with the ligand directly but may take part in intra-protein interactions. The changes in activity might be explained by the instability introduced by the mutations. Most clinical mutations fall into this category – including D396N, R397C, P467L, V290M, L423P, F360L and R288. In our experiments D396N showed no change in EC_{50} but an increase in maximum activity, in contrast to results that were previously reported (Ludtke et al., 2007). Our results also showed that R397C resulted in increased EC50 and likely no change in max activity. This differs slightly from the result of previous studies, which could be explained by the use of different cell models (Jeninga et al., 2007). Looking at the full length PPARγ structure, D396 was located on H8-H9 loop (PDB ID: 3DZY). This position is outside the ligand binding pocket, near the dimerization interface and this residue forms an intra protein ionic interaction with R443 on H10/11 (Figure 7.1). This position suggests that this residue could affect maximum activity through its effect on dimerization or recruitment of coactivators similar to K422Q, while having minimal effect on EC_{50} (Yi et al., 2015). Residue R397 possibly forms ionic interactions with E324 on H4 (Figure 7.1). E324 could also possibly form interactions with Y477A on H12 and R443 on H10/11. This intra-protein interaction network spanning H4, H10/11 and H12 could be lost with the cysteine mutation, causing the protein to be unstable as well as unable to form the AF2 surface, which is important for coactivator recruitment (Choi et al., 2011). E324 is also in close proximity to residues H323 and Y327 on H4 which are involved in forming hydrogen bonds in Arm 1 (Figure 6.10a, Figure

7.1) This interaction network might explain the mutation's effects on ligand binding, RXR dimerization and coactivator recruitment (Jeninga et al., 2007).

In our experiments, V290M and P467L also displayed increased EC_{50} (V290M less affected than P467L), and V290M decreased max RTI compared to wildtype, while P467L likely did not affect max RTI in response to Rosiglitazone. This was in agreement with the results in a previous study (Barroso et al., 1999). These two resides are relatively close in 3D space and both mutations potentially affect H12 in different ways (Figure 7.2a). In a structure of V290M (Previously mentioned Farglitazar bound structure, PDB ID: 7AHJ) uploaded to the PDB, the methionine mutation at position 290 seemed to cause steric interference with residue H466, shifting the position of H466 by about 1.3 angstroms compared to H466 in the model structure 3DZY (Figure 7.2b). Possibly as a result of this, the position of H12 is also shifted in the Z direction or into the page by 1.3 angstroms (into the page, Figure 1.1, 7.2b). This movement in H12 could affect binding of coregulators to the AF2 surface as it affects the distance between K301 and E471 (residues that interact with coactivator peptides) and would affect max RTI as suggested by our results (Nolte et al., 1998, Choi et al., 2011, Figure 7.2c). Despite the movement, Y473 is still able to interact with ligands in Arm 1, resulting in a smaller effect on EC_{50} compared to P467L (Figure 7.2b). Leucine substitution at position 467 likely introduces more flexibility into H12, decreasing the likelihood of H12 assuming the 'active position' (Nolte et al., 1998). This would decrease EC_{50} since it disrupts Y473 interaction with Rosiglitazone but would not affect coregulator interaction when H12 is in position, as suggested by our results. The mutation L423P also had increased EC_{50} (similar to P467L) but likely had higher max RTI compared to wildtype. Residue 423 is in H9 and is solvent facing similar to residue K422 (Figure 1.2). However, the leucine to proline mutation would introduce changes in the helix, affecting a nearby intra-protein interaction between N424 and D380. Protein instability would affect EC_{50}, but the proline mutation might introduce structural rigidity that positively affects coregulator recruitment.

Our results for F360L closely matched that of a previous study describing the mutation, despite the use of different cell models (Hegele et al., 2002). The F360L mutation resulted in impaired EC_{50} but did not affect max RTI in the presence of Rosiglitazone compared to wildtype. F360 does not typically interact with synthetic ligands like Rosiglitazone but do form interactions with certain synthetic ligands that have motifs that interact with residues between H3 and H7 such as Farglitazar (PDB ID: 7AHJ). This area of interaction was also seen

in other fatty acid bound PPARγ structures (PDB ID: 3U9Q and 4EM9) and in our F363A_L structure (Figure 7.3d). F360 may form hydrophobic interactions with nearby residues L456, P359, L356, F282, I279 and A278 (Figure 7.3c). Substitution with the smaller leucine side chain might disrupt these interactions, possibly leaving solvent accessible pockets that disrupts ligand binding, but not overall coactivator recruitment (Figure 7.3a, b).

The R288H mutation showed decreased EC_{50} in response to Rosiglitazone but decreased maximum activity (along with increased protein expression) over wildtype. In the wildtype protein, residue R288 typically forms intra-protein interactions with E295 (Egawa et al., 2021). In a previous study, R288H was noted to have decreased activity only in response to endogenous ligands but not synthetic ligands (Sarraf et al., 1999). Our experiments closely match the activity induced by synthetic ligands in that report (Figure 3.2, Table 2.1, Sarraf et al., 1999). The difference between the response to endogenous and synthetic ligands was attributed to a 'clamping effect' caused by the rearrangement of ligand binding pocket residues (Egawa et al., 2021). This clamping translates to a smaller distance of 11.7Å between residues H449 and C285 with the next smallest distance of all structures analysed at 12.4Å (Table 4.2) Since the protein is narrowed compared to wildtype, the clamping effect of R288H might also affect dimerization or destabilize coregulator interactions and affect max RTI, as shown in our results. This, however, does not fully explain the slightly decreased EC_{50} (increased potency) by Rosiglitazone due to the mutation. A possible explanation could be that histidine at position 288 sits close enough to interact with Rosiglitazone when bound to the ligand binding pocket (Figure 7.4a).

The Q286P mutation was found to be inactive in a previous (Sarraf et al., 1999). In our cell-based gene transactivation assays, we confirmed the inactivity of Q286P, which matches the activity of the Gal4-DBD only truncated construct (Figure 7.4b). Examination of the full-length structure (PDB ID: 3DZY) does not reveal any obvious interactions that Q286 participates in. However, a proline substitution at this position in the middle of H3, near to Arm 1 might disrupt the overall structure of the helix (Figure 6.10a).

4.3 Alanine scanning mutations can also affect transcription induction in different ways

The effect of alanine mutations of ligand binding pocket residues on transcription activity was investigated to attempt to quantify the importance of an amino acid residue to PPARγ activation. In our experiments, the alanine scanning mutations were thought to affect

interactions with ligands, but not take part in intra-protein interaction, allowing us to assess the importance of the residue in binding a certain ligand. All of the alanine scanning mutations affected EC50 to varying degrees. However, there were differences in max RTI compared to wildtype even when protein expression was taken into account, suggesting that the mutations affected other aspects related to transcription – for example through coregulator interactions. Some mutations with observed changes in RTI could have been explained by changes in protein expression, these mutations are: F363A, F360A, I341A and Y327A. Mutations H323A and Y473A also showed reduced max activity that were accompanied by changes in protein expression. However, our solved structures suggested that these mutations caused shifts in H12, which would have affected coregulator recruitment (Figure 6.11, 6.13).

C285A and H449A mutations resulted in reduced EC_{50} as expected, since both residues form interactions with Rosiglitazone (Figure 6.4-6.6). Surprisingly, both constructs also resulted in increased max RTI. Protein expression for both constructs were reduced compared to wildtype, indicating that maximum activity was likely higher than observed. As mentioned in the results, for C285A, no obvious changes could be identified except a slight shift in position of Rosiglitazone in the ligand bound structure (Figure 6.8). For H449A, only a slight decrease in ligand binding pocket size was noted (Table 4.2, Figure 6.12). Two other mutations, F282A and I281A also resulted in a 2-log increase in EC_{50}. But both mutations also resulted in decreased max RTI accompanied by increased protein expression – suggesting that RTI might be lower than observed. F282 and I281 could possibly interact with ligands based on their positions in the ligand binding pocket, explaining the mutations effect on EC_{50}. However, further experiments are required to explain the changes in max RTI seen with these 4 mutations.

The mutations F360A and F360L was particularly interesting as it provided an opportunity to study the differences between the substitution of two amino acids. Both mutations likely did not affect max RTI after taking protein expression into account, but there was a 2-log difference between the gene transcription activities of F360L (EC_{50} = 0.3172 µM) and F360A (EC_{50} = 30.5500 µM, table 4). This difference is in line with our above explanation for the changes in gene transcription activity of F360L, the smaller alanine residue results in a bigger solvent accessible pocket than leucine, resulting in a bigger disruption to ligand binding (Figure 7.3a).

The cell-based gene transactivation assays and protein expression experiments seem to suggest that K367A, initially thought to be constitutively active, might instead have very low activity similar to Q286P. However, the Rosiglitazone bound structure suggests that K367A is still able to bind (at least to synthetic) ligands. As mentioned above, K367 participates in a polar interaction with H449, which itself forms polar interactions with ligands in Arm 1 (Chua and Bruning 2021). The alanine substitution disrupts this interaction between the residues, causing slight changes in interaction between ligand binding pocket residues and the ligand, possibly explaining the effect on EC_{50} (Figure 6.15). However, this does not explain the dose-response curve and protein expression seen with K367A mutation. A literature search found studies demonstrating that SUMOylation of PPARγ reduces transcriptional activity of PPARγ and Rosiglitazone treatment enhances SUMOylation of K367. This SUMOylation results in recruitment to corepressor bound REs (such as INOS) and prevents corepressor complex removal by ubiquitin (Ohshima et al., 2004, Pascual et al., 2005, Brunmeir and Xu, 2018). The alanine mutation at K367 prevents SUMOylation and thus prevents the recruitment of PPAR to corepressor complexes, which could explain the upregulated activity seen in our assays. However, K367's role in SUMOylation has been disputed in a more recent study and was instead shown to play an indirect role influencing SUMOylation of residues in the PPARγ DBD, a region that was not included in our PPARγ-Gal4 DBD constructs (Diezko and Suske, 2013).

4.4 Ligands with different activity profiles

The difference in response of mutations to ligands with different activity profiles for mutations R397C and P467L was also surprising. Since INT131 binds to Arm 2, the R397C mutation which affects arm 1 (discussed above) would not have affected the affinity of the PPARγ ligand binding pocket for INT131 as much as Rosiglitazone, which binds to Arm 1, potentially explaining the increased activity of INT131 compared to Rosiglitazone at lower concentrations (Figure 6.10a, 7.4c). But this explanation seemingly contradicts the observation that, for P467L, INT131 induced activity was not different from DMSO (P value = 0.8287). This mutation lies on H12 which might also affect ligand interactions in arm 1. If the lack of response to INT131 was due to the P467L mutation affecting coactivator recruitment ability, the same decrease should be seen with Rosiglitazone. In addition, INT131 also seemed to induce a higher gene transactivation activity for K367A mutants than Rosiglitazone or DMSO (P value = 0.0013 and <0.0001 respectively) even though K367A sits in close proximity to the area of interaction of INT131 (Figure 6.15, 7.4).

4.5 Conclusion

Our experiments demonstrated that each mutation had varying impact on PPARγ function (Table 5, Figure 8.1, 8.2). These findings demonstrate that at least some mutations could increase the gene transcription activity of PPARγ mutations compared to wildtype, in essence giving a 'supernormal' response to the same ligand – in this case, Rosiglitazone (Dubois et al., 2017). This phenomenon, as seen with R288H, could only occur with synthetic ligands but not endogenous ligands (Egawa et al., 2021). This mutation could, under physiological conditions (with endogenous ligands) could lead to lowered PPARγ activation and thus metabolic disruption, but with Rosiglitazone treatment, lead to supraphysiological activation. The results of the alanine scan of the ligand binding pocket residues suggest that some alanine mutations to residues in the ligand binding pocket affected efficacy along with potency. Quantifying the contribution of each residue to ligand binding requires additional experiments to uncover the basis of these changes in efficacy. Future experiments involving alanine mutations must take into consideration these unexpected changes in max RTI.

Our results leave some pressing questions – additional experiments are needed to confirm our observations regarding mutations changing the stability of helices (eg. Q286P, F360L, L423P), mutations affecting coregulator recruitment (eg. K422Q, P467L) or dimerization (D396N, R397C), or to clarify the cause of changes to potency and efficacy observed (alanine scanning mutants, K367A). Immediate future steps could be to use HDX to quantify any instability caused by the mutations. Mutations' effect on coregulator recruitment could also be tested using the methods that explore coactivator interactions but also take into account RXR heterodimerization, as outlined in Kilu et al. (2021). Crystallization of PPARγ could be improved by purifying and storing proteins in other PPARγ buffers, as well as explore other conditions that recently led to uploaded structures on the PDB. Finally, the DLA conducted with different ligands (with different activity profiles) could be expanded to cover all the clinical mutations examined in this study, followed by the mutations that were left out from this study.

5. Figures

Construct	Rep 1		Rep 2		Rep 3		Avg Tm (°C)	Std dev (°C)
	Tm (°C)	ΔTm (°C)	Tm (°C)	ΔTm (°C)	Tm (°C)	ΔTm (°C)		
Wildtype	43.45		41.8		42.2		42.483	0.861
I281A	39.6	-3.85	38.7	-3.1	38.4	-3.8	38.900	0.624
F282A	41.5	-1.95	21.7	-20.1	39.9	-2.3	40.700	1.131
C285A	44.2	0.75	44.8	3	44.2	2	44.400	0.346
H323A	43	-0.45	40.4	-1.4	41.7	-0.5	41.050	0.919
F360A	34.4	-9.05	36.6	-5.2	34.4	-7.8	35.500	1.556
F363A	41.3	-2.15	38.4	-3.4	40	-2.2	39.900	1.453
K367A	50.5	7.05	45.9	4.1	48.7	6.5	48.367	2.318
H449A	41	-2.45	37.8	-4	40.1	-2.1	39.633	1.650
Y473A	43.2	-0.25	40.3	-1.5	41.7	-0.5	41.733	1.450
V290M	43.8	0.35	43.2	1.4	42.5	0.3	43.167	0.651
F387L	41.5	-1.95	35.6	-6.2	40.6	-1.6	41.050	0.636
R397C	33	-10.45	29.8	-12	31.1	-11.1	-	-
K422Q	44.6	1.15	32.6	-9.2	43.5	1.3	44.050	0.778
P467L	44.2	0.75	42.5	0.7	42.4	0.2	43.033	1.012

Table 1.1. **The PPARγ constructs showed altered thermostability compared to wildtype.** A TSA was conducted with PPARγ mutant LBD protein purified in buffer B to investigate the effects of mutations on thermostability. Melting temperature (Tm) of PPARγ constructs was calculated for each experimental replicate (Rep) and then averaged. ΔTm refers to the change in melting temperature relative to the melting temperature of wildtype PPARγ of the same experiment. Yellow highlights indicate curves that show a small, distinct peak (approximately 20 000 RFU, experiment 3). Red highlights indicate curves that show high starting fluorescence followed by a small increase that peaks lower than the initial fluorescence. Values highlighted in red were excluded from Tm average and standard deviation calculations.

	Rep 1	Rep 2	Rep 3	By Average	Average Tm (°C)	Std dev
Stabilize	K367A		K367A	K367A	48.367	2.318
	K422Q	K367A	C285A	C285A	44.400	0.346
	C285A	C285A	K422Q	K422Q	44.050	0.778
	P467L	V290M	V290M	V290M	43.167	0.651
	V290M	P467L	P467L	P467L	43.033	1.012
Wildtype	WT	WT	WT	WT	42.483	0.861
Destabilize	Y473A	H323A	H323A	Y473A	41.733	1.450
	H323A	Y473A	Y473	H323A	41.050	0.919
	F387L	I281A	F387L	F387L	41.050	0.636
	F282A	F363A	H449A	F282A	40.700	1.131
	F363A	H449A	F363A	F363A	39.900	1.453
	H449A	F360A	F282A	H449A	39.633	1.650
	I281A		I281A	I281A	38.900	0.624
				F360A	35.500	1.556
				R397C	31.300	1.609

Table 1.2. **PPARγ mutant constructs showed trends in thermostability.** The PPARγ constructs were ranked in decreasing order of melting temperature (Tm) for each experimental replicate (Rep), and for the average Tm calculated from the 3 replicates. Constructs were arranged relative to wildtype (WT).

	Construct	Average EC_{50} (µM)	Std dev	Top (RTI)	Std dev	Average max RTI (%)
Exp 1	WT	0.0104	0.0011	0.5081	0.0263	
	P467L	2.1820	0.9320	0.6733	0.0880	*108.4095 74728415
	L423P	3.2260	1.9120	0.5394	0.0697	105.9
	K422Q	0.0316	0.0295	0.6049	0.0475	119.0
	R397C	9.5290	0.5629	0.3346	0.0598	65.6
	D396N	0.0084	0.0081	0.6698	0.0221	131.9
	F387L	0.2251	0.1066	0.5983	0.0460	117.7
	V290M	0.4480	0.4354	0.3517	0.0280	69.2
	Y473A	7.6435	7.3348	0.1973	0.0335	38.7
Exp 2	WT	0.0145	0.0004	0.6054	0.0329	
	K367A	1.3764	0.6641	0.3921	0.0380	*64.78655 92138618
	F363A	0.7720	0.0366	0.7447	0.0639	122.9
	I341A	5.2060	5.2085	0.3771	0.0708	62.1
	H323A	3.9025	1.2777	0.2312	0.0071	38.3
	C285A	0.0991	0.0011	0.6323	0.0954	104.2
	F282A	1.0848	0.4175	0.4561	0.0061	75.5
Exp 3	WT	0.0110	0.0038	0.6302	0.1067	
	F360L	0.3172	0.0146	0.5259	0.1140	83.1

	R288H	0.0014	0.0003	0.5332	0.0288	85.4
Exp 5	WT	0.0288	0.0023	0.6416	0.0493	
	H449A	2.2190	0.0410	0.6584	0.0197	103.0
	F360A	30.5500	8.1317	0.3655	0.0503	57.4
	Y327A	2.9450	0.2404	0.4894	0.0542	76.8
Exp 6	WT	0.0174	0.0019	0.7529	0.0328	
	I281A	4.9465	0.0177	0.4357	0.0342	57.8

992 Table 2.1. **Average EC50 and max RTI values for the mutant constructs.** %max RTI is calculated by
993 expressing max RTI as a percentage of the matched wildtype (WT) control. * refers to the values of
994 constructs that were calculated from two different experiment sets.

995

	Treatment	Rep 1		Rep 2	
		WT	**K367**	**WT**	**K367**
Firefly (RLU)	DMSO	457500	2464333	553266.7	3101000
	Increasing Rosiglitazone	502033.3	2563000	590100	3352333
		563266.7	2657667	675433.3	3316333
		1063367	2909667	1205667	3579333
		1915667	3433667	2213667	4101333
		2086333	3853333	2627000	4682000
		2809667	3446667	3395667	4917333
Renilla (RLU)	DMSO	2983333	7066000	3145667	9856333
	Increasing Rosiglitazone	3150000	7408667	3400667	11730000
		3213666	7739667	3269333	11790000
		3339667	7356667	3506000	11510000
		3299000	7791667	4189333	11646667
		3390667	8820000	4401667	12716667
		4521000	9108667	6043333	13576667

Table 2.2. **Construct K367A displays constitutive activity compared to wildtype.** The Firefly and Renilla values (RLU) measured for wildtype (WT) positive control and K367A from both experimental replicates (rep) are listed (experiment 3 rep2 and experimental 4 rep 1. The constructs were tested over a concentration range of WT: 0.0001 to 1 µM, K367A: 0.01 to 50µM.

	Treatment	R1			R2		
		WT	Q286P	Gal4 DBD	WT	Q286P	Gal4 DBD
Firefly	DMSO	466433.3	465133.3	494866.7	205333.3	302600	308700
	Increasing Rosiglitazone	539066.7	468866.7	513500	264200	288733.3	353566.7
		670066.7	507700	513000	352533.3	322166.7	341733.3
		1386000	516700	372900	642933.3	306200	244100
		2362333	480633.3		1299333	362733.3	
		2671333	479000		1698667	302366.7	
		3718333	369700		2260333	248233.3	
Renilla	DMSO	2658000	3506667	42526667	1450667	2652333	22993333
	Increasing Rosiglitazone	2664333	3995667	43873333	2055333	2627333	26590000
		3004000	3935000	41730000	2180667	3211667	31416667
		2782333	3965667	51880000	2347000	3095000	36776667
		3428333	4454000		2431000	3237000	
		3586000	3996000		2977667	3156667	
		5623000	4405667		4217000	3824333	

Table 2.3. **Construct Q286P is inactive compared to wildtype and Gal4 DBD control.** The Firefly and Renilla values (RLU) measured for wildtype (WT) positive control, Q286P and Gal4 DBD only negative control from both experimental replicates are listed. The constructs were tested over a concentration range of WT: 0.0001 to 1 µM, Q286P: 0.001 to 100µM, Gal4 DBD: 1 to 100µM.

Exp 1	Rep 1								Rep 2							
	EC50 (µM)	95% CI	RP	ΔAICc	**Top (RTI)**	95% CI	RP	ΔAICc	**EC50 (µM)**	95% CI	RP	ΔAICc	**Top (RTI)**	95% CI	RP	ΔAICc
WT	0.01117	??? to 0.02455			0.4895	0.4380 to 0.5411			0.009546	???			0.5267	0.4733 to 0.5800		
P467L									1.523	1.213 to 1.929	>99.99 %	21.48	0.6111	0.5654 to 0.6598	6.944	3.876
L423P	4.578	2.677 to 7.389	947.6	13.71	0.4901	0.3839 to 0.6428	5.107	-3.261	1.874	??? to 2.531	>99.99 %	25.79	0.5887	0.5492 to 0.6332	1.372	0.632
K422Q	0.05242	0.04190 to 0.06653	733.6	13.2	0.5713	0.5508 to 0.5925	14.64	5.368	0.01075	???	*15.13	*5.434	0.6385	0.6084 to 0.6685	421	12.09
R397C	9.927	???	>99.99 %	34.11	0.2923	0.2631 to 0.3261	92.88	9.063	9.131	2.411 to ???	>99.99 %	23.09	0.3769	0.3376 to 0.4162	544.1	12.6
D396N	0.01412	0.009474 to 0.02150	4.343	-2.937	0.6541	0.5976 to 0.7234	3798	16.48	0.002614	???	1.459	-0.7558	0.6854	0.6403 to 0.7393	2068	15.27

F387L	0.3004	0.2066 to ???	>99.99 %	27.85	0.5657	0.5283 to 0.6045	6.077	3.609	0.1497	0.1226 to 0.1860	>99.99 %	25.74	0.6308	0.5975 to 0.6670	41.02	7.428
V290M	0.7558	0.5116 to 1.299	>99.99 %	33.13	0.3319	0.2949 to 0.4079	1.029	0.05727	0.1401	???	* >99.99%	*28.39	0.3715	0.3351 to 0.4132	8935	18.2
Y473A	12.83	6.773 to ???	>99.99 %	34.77	0.1736	0.1354 to ???	2.807	-2.064	2.457	???	>99.99 %	24.88	0.221	0.1936 to 0.2537	54.19	7.985

1005

Exp 2	Rep 1								Rep 2							
	EC50 (µM)	95% CI	RP	ΔAICc	**Top (RTI)**	95% CI	RP	ΔAICc	**EC50 (µM)**	95% CI	RP	ΔAICc	**Top (RTI)**	95% CI	RP	ΔAICc
WT	0.01481	0.008970 to 0.02467			0.5821	0.5267 to 0.6477			0.01426	??? to 0.02118			0.6286	0.5831 to 0.6833		
K367A									0.9068	??? to 2.283	4.034	2.79	0.4189	0.3947 to 0.4433	4.739	3.112

F363A	0.7978	0.5755 to 1.334	>99.99 %	33.45	0.6995	0.6361 to 0.8341	6.961	3.881	0.7461	0.5850 to 0.9219	>99.99 %	45.2	0.7899	0.7359 to 0.8530	4663	16.89
I341A	8.889	???	>99.99 %	35.33	0.327	0.2941 to 0.3600	209.1	10.69	1.523	???	>99.99 %	28.69	0.4271	0.3803 to 0.4738	>99.99 %	21.27
H323A	2.999	1.909 to ???	>99.99 %	40.93	0.2362	0.2118 to 0.2735	2.568	1.886	4.806	3.261 to ???	>99.99 %	58.88	0.2261	0.2153 to 0.2375	42.77	7.512
C285A	0.0983 1	???	2685	15.79	0.5648	0.5235 to 0.6061	4.366	-2.948	0.0998 1	???	>99.99 %	29.13	0.6997	0.6611 to 0.7384	2.942	2.158
F282A	1.38	0.9323 to 4.623	>99.99 %	34.68	0.4604	0.3982 to 0.7114	2.534	-1.859	0.7895	??? to 0.9531	>99.99 %	53.13	0.4518	0.4328 to 0.4731	5811	17.33

1006

Exp 3	Rep 1								Rep 2							
	EC50 (µM)	95% CI	RP	ΔAICc	**Top (RTI)**	95% CI	RP	ΔAICc	**EC50 (µM)**	95% CI	RP	ΔAICc	**Top (RTI)**	95% CI	RP	ΔAICc
WT	0.008254	0.004743 to			0.7056	0.6645 to 0.7546			0.01367	??? to 0.01792			0.5547	0.5297 to 0.5837		

		0.01096														
F360L	0.3275	0.2753 to 0.3874	>99.99 %	57.68	0.6065	0.5794 to 0.6346	165.6	10.22	0.3068	0.2586 to 0.3602	>99.99 %	79.32	0.4453	0.4234 to 0.4681	>99.99 %	25.87
R288H	0.00124	0.0008133 to 0.002079	*8918	*18.19	0.5535	0.5128 to 0.6031	4717	16.92	0.001619	??? to 0.002922	*6735	*17.63	0.5128	0.4704 to 0.5626	1.015	0.03061

1007

Exp 4	Rep 2							
	EC50 (µM)	95% CI	RP	ΔAICc	**Top (RTI)**	95% CI	RP	ΔAICc
WT	0.0125	0.008050 to 0.01952			0.5803	0.5373 to 0.6324		
K367A	1.846	0.6871 to 5.985	78.91	8.737	0.3652	0.3466 to 0.3980	1.511	0.8256

1008

Exp 5	Rep 1								Rep 2							
	EC50 (µM)	95% CI	RP	ΔAICc	**Top (RTI)**	95% CI	RP	ΔAICc	**EC50 (µM)**	95% CI	RP	ΔAICc	**Top (RTI)**	95% CI	RP	ΔAICc
WT	0.03042	0.02351 to 0.03901			0.6067	0.5745 to 0.6431			0.0272	0.01945 to 0.03709			0.6764	0.6371 to 0.7222		
H449A	2.19	1.759 to 2.701	>99.99 %	37.42	0.6723	0.6424 to 0.7039	10.51	4.705	2.248	???	>99.99 %	21.6	0.6444	0.5942 to 0.6990	2.996	-2.195
F360A	36.3	31.90 to 44.13	>99.99 %	71.72	0.401	0.3713 to 0.4482	1.328	0.5676	24.8	24.07 to 25.58	>99.99 %	62.84	0.3299	0.3242 to 0.3358	>99.99 %	18.91
Y327A	3.115	2.584 to 3.847	>99.99 %	51.96	0.5277	0.5049 to 0.5586	80.28	8.771	2.775	2.149 to 4.424	>99.99 %	25.03	0.4511	0.4169 to 0.4969	2046	15.25

1009

Exp 6	Rep 1								Rep 2							
	EC50 (µM)	95% CI	RP	ΔAICc	**Top (RTI)**	95% CI	RP	ΔAICc	**EC50 (µM)**	95% CI	RP	ΔAICc	**Top (RTI)**	95% CI	RP	ΔAICc

WT	0.0161	0.01059 to 0.02409			0.7297	0.6782 to 0.7913			0.01876	0.01363 to 0.02597			0.7761	0.7297 to 0.8276		
P467L	2.841	2.365 to 3.397	>99.99 %	28.73	0.7355	0.6816 to 0.7973	5.033	-3.232								
I281A	4.934	4.492 to ???	>99.99 %	43.51	0.4115	0.3879 to 0.4351	>99.99 %	46.92	4.959	??? to 5.132	>99.99 %	50.79	0.4599	0.4318 to 0.4880	>99.99 %	65.06

Table 2.4. **EC_{50} and maximum relative transcriptional induction (RTI) values of PPARγ constructs.** The EC_{50} and maximum RTI was calculated for each construct and reported above, along with the 95% confidence interval and Akaike information criterion scores (AIC). Each table represents a separate set of experiments, Exp stands for experiment and Rep 1 2 stands for experimental replicate 1 and 2 respectively. Top refers to the maximum RTI value of the best fit curve. RP refers to the ratio of probabilities of the chosen model versus the rejected model. The two models are: one of having a unique value for the mutant construct and wildtype (WT) versus one sharing the same parameter. Parameter here refer to either EC_{50} or Top value of any mutant compared to the same set and repeat of experiments. A low ratio indicates that both models are as likely to be true. ΔAICc stands for difference in AICc – the score calculated for each model. A positive difference means that EC_{50} or Top values likely differ from wildtype, negative difference means that the construct likely shares the same value as wildtype. Red highlights indicate 1) values that have nearing equal probability of having a unique value or sharing the same value as wildtype or 2) values that have a high probability of sharing the same value as wildtype. Grey highlights means that the construct was not calculated in that experimental set or repeat. P467L (experiment 1 r1) had unusually high max RTI values compared to all other

1019 experimental repeats as well as constructs and was repeated in experiment 5 r2. *values represent calculation of ΔAICc scores for EC_{50} to answer a different question, as
1020 mentioned in the methods.

	WT	P467L	L423P	K422Q	R397C	D396N	F387L	V290M	F360L
Ratio	0.975	1.123	0.544	0.637	0.300	0.394	0.703	1.182	0.511
	WT	**R288H**	**Q286P**	**Gal4**	**Y473A**	**K367A**	**F363A**	**I341A**	**H323A**
Ratio	0.500	0.552	1.580	4.067	0.341	1.587	0.704	0.179	0.314
	WT	**I281A**	**F360A**	**Y327A**	**Gal4**	**H449A**			
Ratio	0.165	0.257	0.096	0.083	0.251	0.064			
	WT	**C285A**	**F282A**						
Ratio	0.271	0.234	0.510						

Table 3. **Expression of PPARγ constructs.** Ratio of intensities of anti-Gal4 DBD to anti-αtubulin bands from the western blot in Figure 4. Intensities were calculated on ImageJ. Every experimental set was conducted with wildtype (WT) PPARγ expressing cells as a positive control, each row represents a different experiment set.

	RMSD				
Structure	5YCP	1PRG	5U5L	2PRG	7AWC
C285A_R	0.385 (1614 to 1 614 atoms)	0.301 (1527 to 1 527 atoms)	0.315 (1642 to 1 642 atoms)	0.426 (1551 to 1 551 atoms)	0.549 (1635 to 1 635 atoms)
C285A_A	0.345 (1583 to 1 583 atoms)	0.279 (1524 to 1 524 atoms)	0.277 (1626 to 1 626 atoms)	0.416 (1564 to 1 564 atoms)	0.510 (1597 to 1 597 atoms)
F363A_A	0.347 (1561 to 1 561 atoms)	0.315 (1534 to 1 534 atoms)	0.310 (1637 to 1 637 atoms)	0.416 (1519 to 1 519 atoms)	0.533 (1578 to 1 578 atoms)
F363A_L	0.358 (1571 to 1 571 atoms)	0.331 (1546 to 1 546 atoms)	0.320 (1635 to 1 635 atoms)	0.420 (1536 to 1 536 atoms)	0.555 (1604 to 1 604 atoms)
H323A_A1	0.423 (1588 to 1 588 atoms)	0.306 (1487 to 1 487 atoms)	0.347 (1623 to 1 623 atoms)	0.500 (1572 to 1 572 atoms)	0.606 (1594 to 1 594 atoms)
H323A_A2	0.449 (1580 to 1 580 atoms)	0.336 (1512 to 1 512 atoms)	0.375 (1640 to 1 640 atoms)	0.529 (1571 to 1 571 atoms)	0.641 (1594 to 1 594 atoms)
H323A_A3	0.419 (1575 to 1 575 atoms)	0.310 (1486 to 1 486 atoms)	0.356 (1594 to 1 594 atoms)	0.482 (1550 to 1 550 atoms)	0.609 (1586 to 1 586 atoms)
H449A_A1	0.423 (1674 to 1 674 atoms)	0.297 (1509 to 1 509 atoms)	0.285 (1575 to 1 575 atoms)	0.513 (1593 to 1 593 atoms)	0.568 (1639 to 1 639 atoms)
H449A_A2	0.378 (1568 to 1 568 atoms)	0.302 (1530 to 1 530 atoms)	0.288 (1556 to 1 556 atoms)	0.452 (1552 to 1 552 atoms)	0.540 (1587 to 1 587 atoms)
K367A_A1	0.344 (1571 to 1 571 atoms)	0.287 (1536 to 1 536 atoms)	0.229 (1613 to 1 613 atoms)	0.437 (1550 to 1 550 atoms)	0.517 (1553 to 1 553 atoms)
K367A_R	0.362 (1623 to 1 623 atoms)	0.292 (1493 to 1 493 atoms)	0.228 (1564 to 1 564 atoms)	0.453 (1538 to 1 538 atoms)	0.520 (1571 to 1 571 atoms)
K422Q_A1	0.399 (1656 to 1 656 atoms)	0.303 (1490 to 1 490 atoms)	0.277 (1572 to 1 572 atoms)	0.488 (1577 to 1 577 atoms)	0.546 (1632 to 1 632 atoms)
K422Q_A2	0.446 (1561 to 1 561 atoms)	0.355 (1512 to 1 512 atoms)	0.387 (1585 to 1 585 atoms)	0.507 (1544 to 1 544 atoms)	0.552 (1520 to 1 520 atoms)
Y473A_A1	0.354 (1532 to 1 532 atoms)	0.314 (1489 to 1489 atoms)	0.317 (1554 to 1 554 atoms)	0.425 (1564 to 1 564 atoms)	0.551 (1576 to 1 576 atoms)
Y473A_A2	0.370 (1542 to 1 542 atoms)	0.294 (1482 to 1 482 atoms)	0.284 (1531 to 1 531 atoms)	0.437 (1556 to 1 556 atoms)	0.538 (1566 to 1 566 atoms)
Y473A_A3	0.377 (1562 to 1 562 atoms)	0.324 (1500 to 1 500 atoms)	0.329 (1556 to 1 556 atoms)	0.438 (1554 to 1 554 atoms)	0.553 (1562 to 1 562 atoms)
Y473A_A4	0.363 (1552 to 1 552 atoms)	0.297 (1497 to 1 497 atoms)	0.299 (1551 to 1 551 atoms)	0.430 (1560 to 1 560 atoms)	0.553 (1587 to 1 587 atoms)

Range	0.344 – 0.449	0.279 – 0.355	0.228 – 0.387	0.416 – 0.529	
1PRG	0.404 (1533 to 1 533 atoms)		0.340 (1552 to 1 552 atoms)	0.458 (1553 to 1 553 atoms)	0.619 (1550 to 1 550 atoms)
5YCP		0.404 (1533 to 1 533 atoms)	0.320 (1575 to 1 575 atoms)	0.348 (1576 to 1 576 atoms)	0.460 (1616 to 1 616 atoms)
5U5L	0.320 (1575 to 1 575 atoms)	0.340 (1552 to 1 552 atoms)		0.412 (1559 to 1 559 atoms)	0.534 (1600 to 1 600 atoms)
2PRG	0.348 (1576 to 1576 atoms)	0.458 (1553 to 1 553 atoms)	0.412 (1559 to 1 559 atoms)		0.636 (1648 to 1 648 atoms)
7AWC	0.460 (1616 ato ms)	0.619 (1550 to 1 550 atoms)	0.534 (1600 to 1 600 atoms)	0.636 (1648 to 1 648 atoms)	
7E0A	0.461 (1554 to 1 554 atoms)	0.543 (1470 to 1 470 atoms)	0.483 (1515 to 1 515 atoms)	0.610 (1560 to 1 560 atoms)	0.311 (1752 to 1 752 atoms)
6MD4	0.345 (1591 ato ms)	0.268 (1595 to 1 595 atoms)	0.254 (1598 to 1 598 atoms)	0.440 (1602 to 1 602 atoms)	0.541 (1565 to 1 565 atoms)

Table 4.1. **Alignment of PPARγ mutant structures to model structures.** Every mutant and other model structures were aligned to every model structure. The target structure for alignment was listed in the 2nd row from the top and represented as grey boxes in the corresponding cell in the same column. The mobile structures to be aligned to the target structure were listed in the first column from the left.

	Measured points	H10 – H2’	H10 – H3	H10 – H3	H3 – H2’	H2’ – H2’	B3 – H12
Mutations		I456 L255	I456 F282	H449 C285	I281 E259	Structure 5YCP L255	Y473-V339
K422Q	K422Q_A1	22.8	10.8	12.7	11.8	0.7	24.2
	K422Q_A2	22.4	9.9	12.4	12.9	1.2	24.1
C285	C285A_R	22.5	10.1	12.8	12.2	1.1	24.2
	C285A_A	22.6	10.2	12.9	11.9	1.0	24.1
H323A	H323A_A1	22.9	10.4	12.9	12.2	1.2	22.7
	H323A_A2	22.7	10.3	12.8	12.0	1.1	22.8
	H323A_A3	22.6	10.3	12.9	12.1	1.1	22.4
F363A	F363A_A	22.9	10.4	13.0	12.4	1.2	24
	F363A_L	22.7	10.3	13.1	12.0	1.2	23.9
K367A	K367A_A	22.7	10.4	12.6	11.8	0.6	24.1
	K367A_R	22.5	10.4	12.7	12.0	0.4	24.3
H449A	H449A_A1	22.9	10.7	12.4	12.5	0.7	24.2
	H449A_A2	22.7	10.3	12.4	12	1.1	24
Y473A	Y473A_A1	22.4	10.1	12.9	na	1.4	23.4
	Y473A_A2	22.5	10.1	12.9	12.2	1.3	23.5
	Y473A_A3	22.4	10.1	12.9	na	1.5	23.5
	Y473A_A4	22.4	10.2	12.8	12.3	1.2	23.5

	Range	22.4 - 22.9	9.9 - 10.8	12.4 - 13.1	11.8 - 12.9	0.4 - 1.5	22.4 – 24.3
Apo	1PRG	22.5	10.4	12.6	13.2	0.8	24.5
Phasing	5U5L	23.1	11	12.8	11	0.6	23.7
Rosiglitazone	5YCP	23.3	11.3	12.7	11.1		24.1
	2PRG	22.3	10.4	12.7	11.1	0.9*	24.2
	7AWC	22.3	11	12.7	10.8	0.5	24
Other ligands	7E0A	22.1	10.7	na	10.5	0.3	24.3
	6MD4	22.8	10.7	12.6	12.5	0.7	24.2
V290M	7AHJ	22.3	10.0	12.6	11.6	0.7	24.2
R288H	7E2O	22.2	10.5	11.7	11.2	0.3	24.1

Table 4.2. **Dimensions of the PPARγ LBD structures.** Measurements of the ligand binding pocket was taken, as shown in Figure 6.3. All measurements are taken between the Cα carbon of the stated residues, given in angstroms and calculated in Pymol. Mutant structures are grouped by mutations. Structure names of mutations are given in the second column. Range refers to range of measurements taken from the mutant PPARγ structures. Model structures are grouped according to ligand binding status. PDB IDs of model structures are given in the second column. na – indicates that the measurement was impossible due to missing structures. The last column compares positions of L255 in all structures versus 5YCP.

Constructs	EC_{50}	Max RTI	Expression	TSA	Structure
WT					
P467L					
L423P					
K422Q					/
R397C					
D396N					
F387L					
V290M					
R288H					
Q286P	Nil.	Nil.			
F360L					
Y473A					/
H449A					/
K367A					/
F363A					/
F360A					
I341A					
Y327A					
H323A					/
C285A					/
F282A					
I281A					

Table 5. **Overall summary of in vitro and in vivo tests.** The results from the various experiments were collated in this table. Dark green box indicates a positive effect, i.e. increased potency (decreased ec50), max RTI, protein expression or protein stability. Red boxes refer to a negative effect. Light green boxes and yellow refer to may have increased/decreased respectively – defined by having one acceptable ΔAICc score for increase or decrease and one low or negative ΔAICc score (Table 2.4, cell highlighted in red). White boxes refer to having no effect (two low or negative ΔAICc scores). Grey boxes refer to samples that were not tested. Increases and decreases are relative to wildtype (WT), represented by shaded boxes. / represents mutations with successfully solved structures. Nil refers to values that couldn't be calculated by GraphPrism, Q286P had no dose response curve fitted.

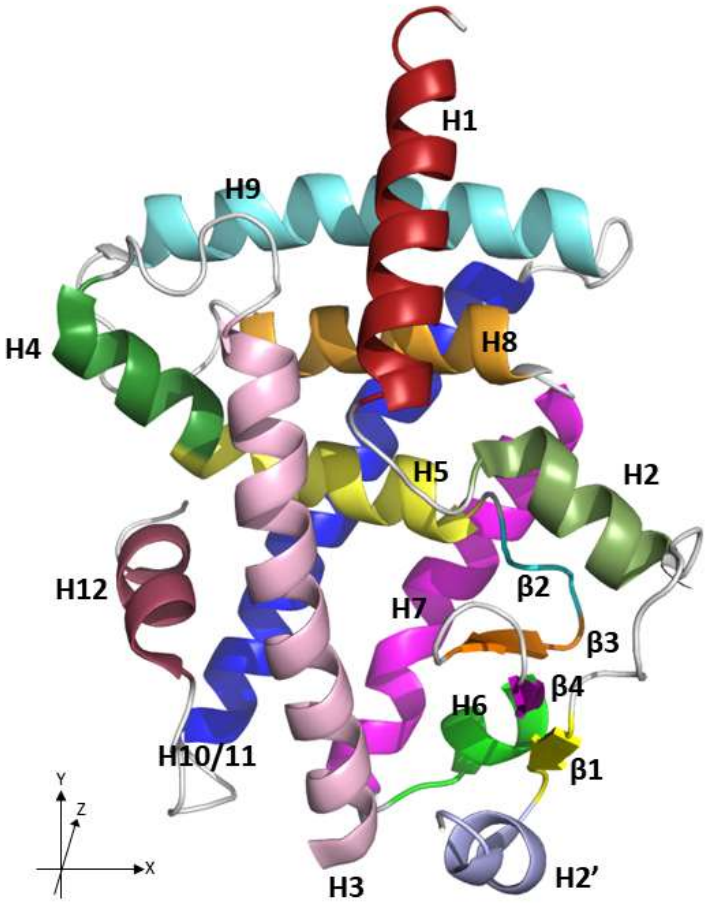

1049

1050 Figure 1.1. **PPARγ LBD.** PPARγ LBD from PDB ID: 3DZY (residues 205-477) with each helices labelled
1051 and coloured separately. Helix colour names are taken from Pymol. Helices are coloured are as follows:
1052 H1 (Firebrick) H2 (Smudge) H2' (light blue) B1 (yellow) H3 (light pink) H4 (Forest) H5 (Pale Yellow) B2
1053 (Cyan) B3 (Orange) B4 (Magenta) H6 (Green) H7 (Magenta) H8 (Bright orange) H9 (Aquamarine)
1054 H10/11 (Blue) H12 (Raspberry). Helices are labelled according to nomenclature established by
1055 Uppenberg et al. (1998).

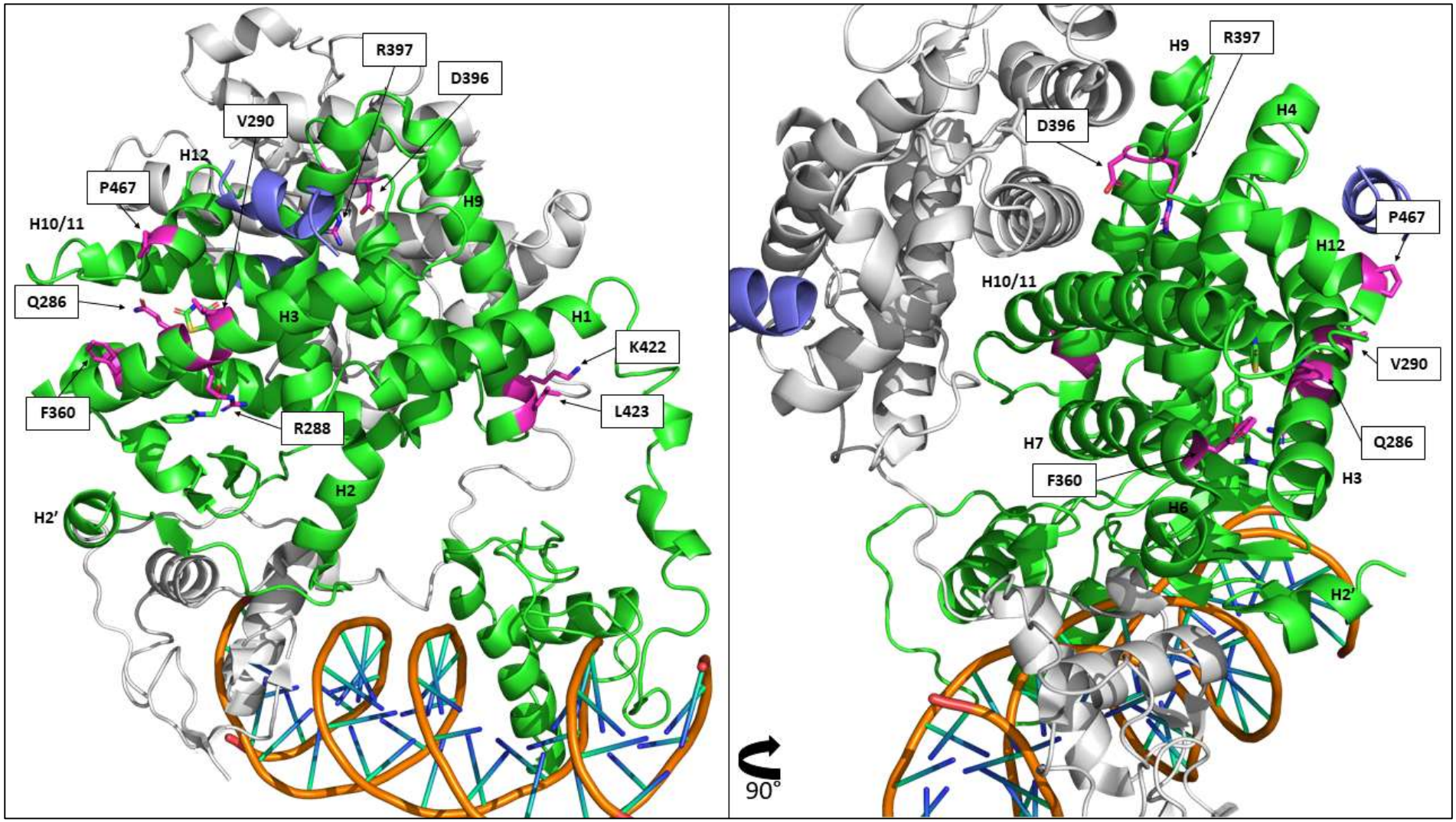
R397
D396
V290
H12
P467
H9
H10/11
Q286
H3
H1
K422
F360
R288
L423
H2
H2'
H9
R397
H4
D396
P467
H12
H10/11
V290
Q286
H7
F360
H3
H6
H2'
90°

1056

Figure 1.2. **Positions of the clinical mutations in the full-length PPARγ-RXR structure.** The full-length structure of 3DZY, including the PPARγ subunit (in green), the RXRα subunit (in grey 90), the nuclear receptor coactivator 2 (NCoA2) peptides (in slate), ligands Rosiglitazone and 9-retinoic acid and DNA (in orange) was presented. Side chains of residues that were observed to be mutated in patients were shown (in magenta). a) and b) represent the same structure from two different views. Colour names are taken from Pymol. PPARγ helix numbers are labelled as in Fig 1.

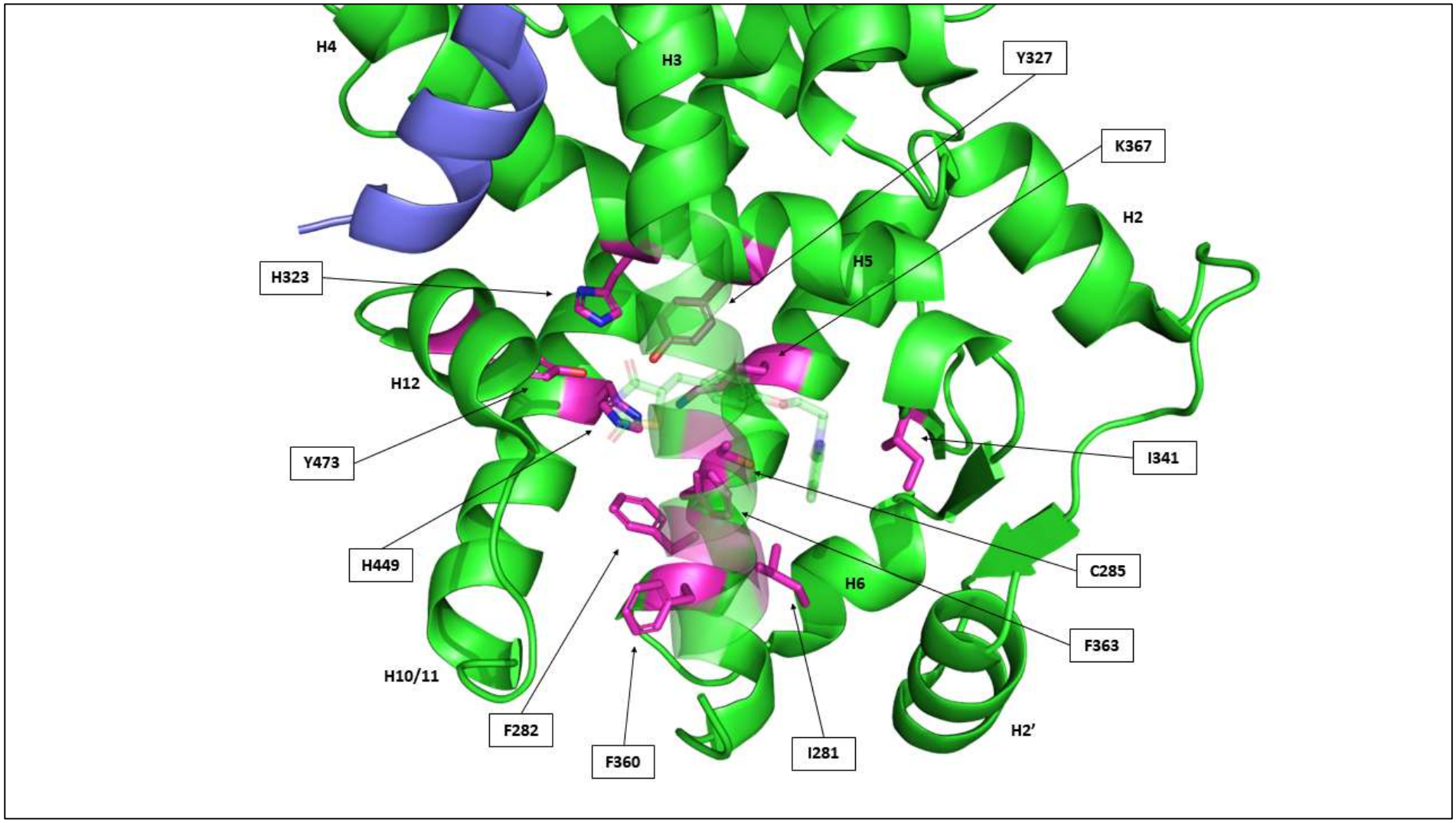
H4
H3
Y327
K367
H2
H5
H323
H12
Y473
I341
H449
C285
H6
F363
H10/11
F282
F360
I281
H2'

1061

Figure 1.3. **Positions of the alanine scan mutations in 5YCP.** The structure of 5YCP (in green) and nuclear coactivator peptide 1 (NCoA1, in slate) with H3 facing the viewer. Side chains of residues targeted for alanine scan shown (in magenta) and labelled. Residues 279-292 and Rosiglitazone of 5YCP was made translucent for ease of visualization. Exact colour names used in Pymol is given in parenthesis.

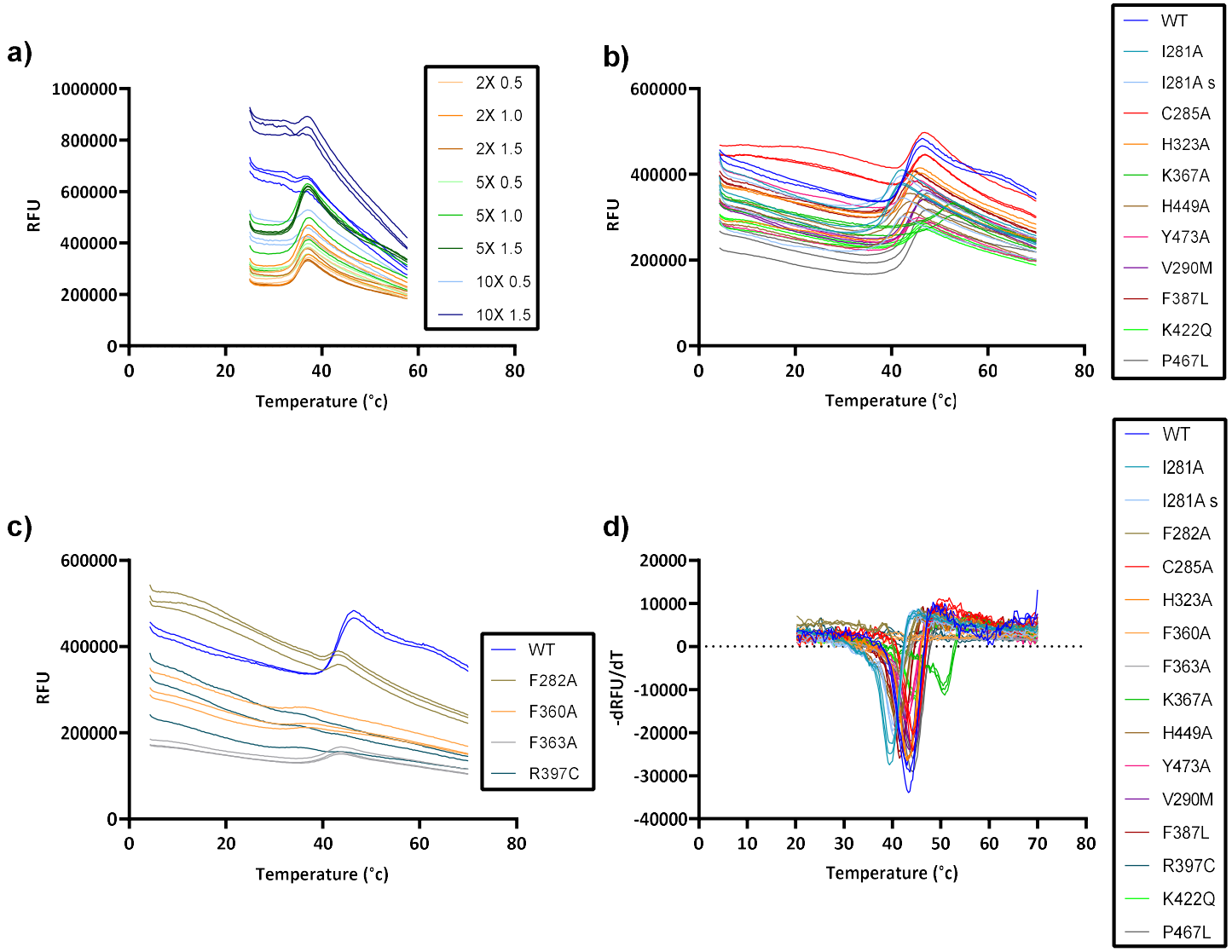
a)
RFU
1000000
800000
600000
400000
200000
0
0
20
40
60
80
Temperature (°c)
2X 0.5
2X 1.0
2X 1.5
5X 0.5
5X 1.0
5X 1.5
10X 0.5
10X 1.5
b)
RFU
600000
400000
200000
0
0
20
40
60
80
Temperature (°c)
WT
I281A
I281A s
C285A
H323A
K367A
H449A
Y473A
V290M
F387L
K422Q
P467L
c)
RFU
600000
400000
200000
0
0
20
40
60
80
Temperature (°c)
WT
F282A
F360A
F363A
R397C
d)
-dRFU/dT
20000
10000
0
-10000
-20000
-30000
-40000
0
10
20
30
40
50
60
70
80
Temperature (°c)
WT
I281A
I281A s
F282A
C285A
H323A
F360A
F363A
K367A
H449A
Y473A
V290M
F387L
R397C
K422Q
P467L

1066

Figure 2. **Thermostability assay of PPARγ LBD proteins.** A TSA was conducted with PPARγ mutant LBD protein purified in buffer B to investigate the effects of mutations on thermostability. a) Optimization of dye (2X-10X) and protein (0.5-1.5mg/ml) concentrations was conducted with wildtype PPARγ LBD protein. Optimization consisted of a single experiment conducted in triplicate. b) Condition 5X 1.0mg/ml was used in a TSA of the different PPARγ constructs. c) PPARγ constructs displaying small or no peak in RFU signal. d) The first derivative of the fluorescence curves from b) and c) were used to determine melting temperature (Tm). RFU stands for Relative Fluorescence Units. Curves showed for b-d are represents data from a single experiment.

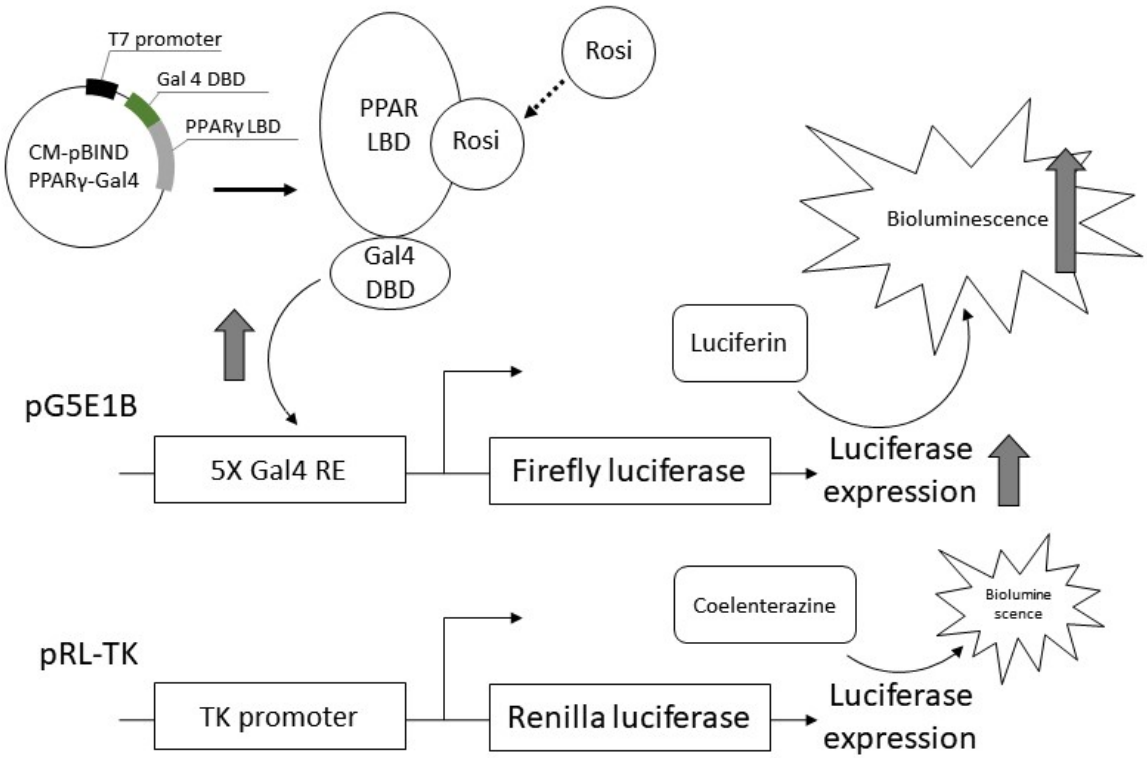
T7 promoter
Gal 4 DBD
PPARγ LBD
CM-pBIND
PPARγ-Gal4
PPAR
LBD
Rosi
Rosi
Gal4
DBD
Bioluminescence
Luciferin
pG5E1B
5X Gal4 RE
Firefly luciferase
Luciferase
expression
Coelenterazine
Biolumine
scence
pRL-TK
TK promoter
Renilla luciferase
Luciferase
expression

1073

Figure 3.1. **The Dual Luciferase Assay (DLA) setup.** The plasmid CM-pBIND-PPARγ-Gal4 expresses the PPAR LBD-Gal4 DBD chimera protein. On binding to Rosiglitazone, this protein binds to the Gal4 response elements (RE) on plasmid pG5E1B, which expresses the firefly luciferase enzyme. On addition of luciferin, the substrate of firefly luciferase, bioluminescence is produced and the output is read. pRL-TK expresses the renilla luciferase enzyme is under the control of the constitutively active promoter TK. On addition of coelenterazine, the substrate of renilla luciferase bioluminescence is produced and the output is read. Both outputs are then represented as a ratio, firefly:renilla luciferase activity.

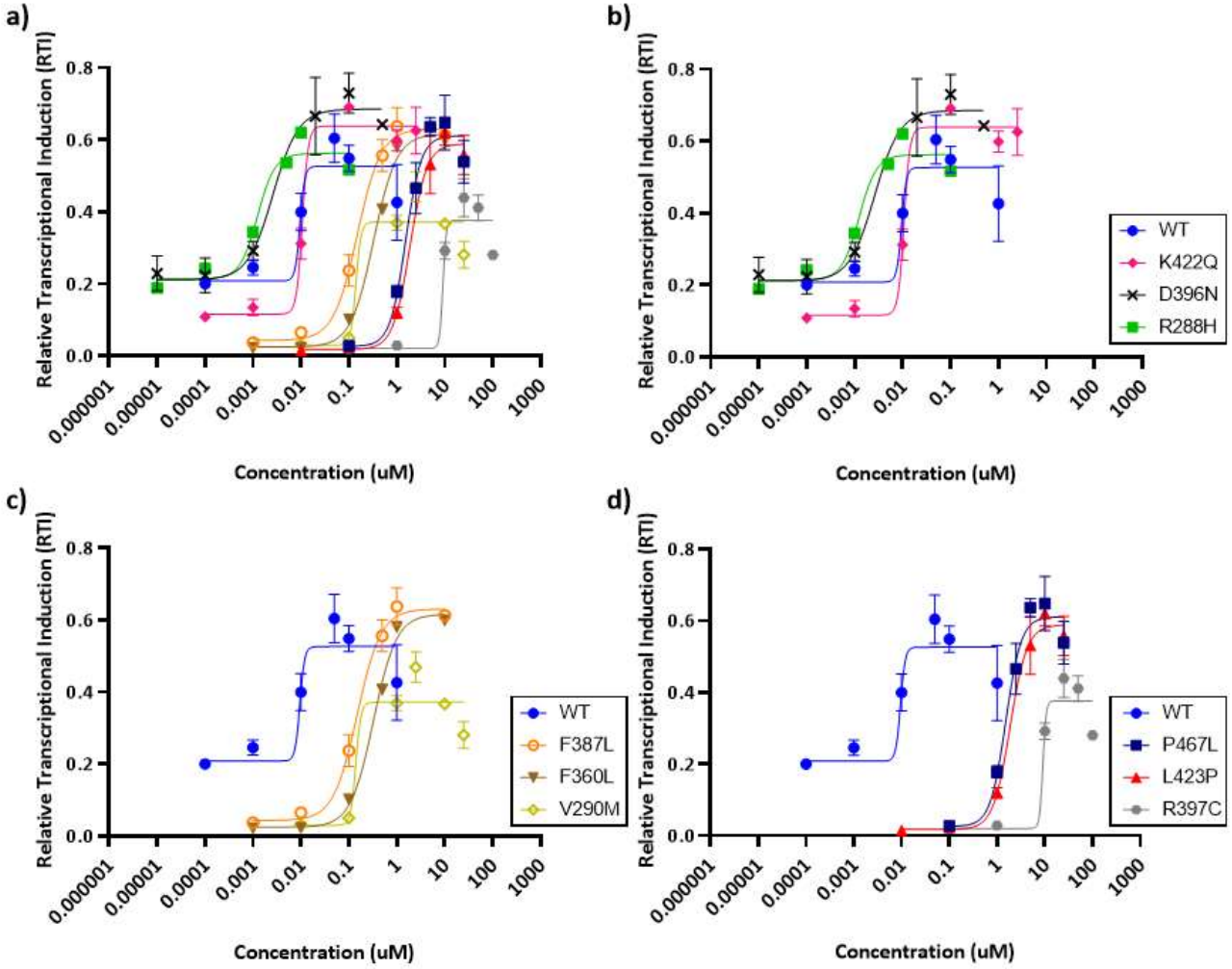
a)
b)
c)
d)
Relative Transcriptional Induction (RTI)
0.0
0.2
0.4
0.6
0.8
0.000001
0.00001
0.0001
0.001
0.01
0.1
1
10
100
1000
Concentration (uM)
WT
K422Q
D396N
R288H
F387L
F360L
V290M
P467L
L423P
R397C

1080

Figure 3.2. **Clinically observed mutations affect response of PPARγ to Rosiglitazone.** To investigate the effects of clinically observed mutations on the Rosiglitazone induced gene transactivation ability of PPARγ, a DLA was conducted. Dose response curves for each mutation were calculated in Graphprism, from at least 6 concentration points in triplicate. Relative transcriptional induction (RTI) refers to the ratio of firefly to renilla luciferase activity. The curves, taken from experimental 1 replicate 2 in the figure are representative of all the experiments. Figures b) to d) represents the same curves from a) but split into 3 different groups. Boxes detail which mutation each curve represented. R288H and F360L curves were calculated in a separate experiment (experiment 3 replicate 1) and transformed by normalizing to wildtype DMSO control of the above experiment for visualization purposes only.

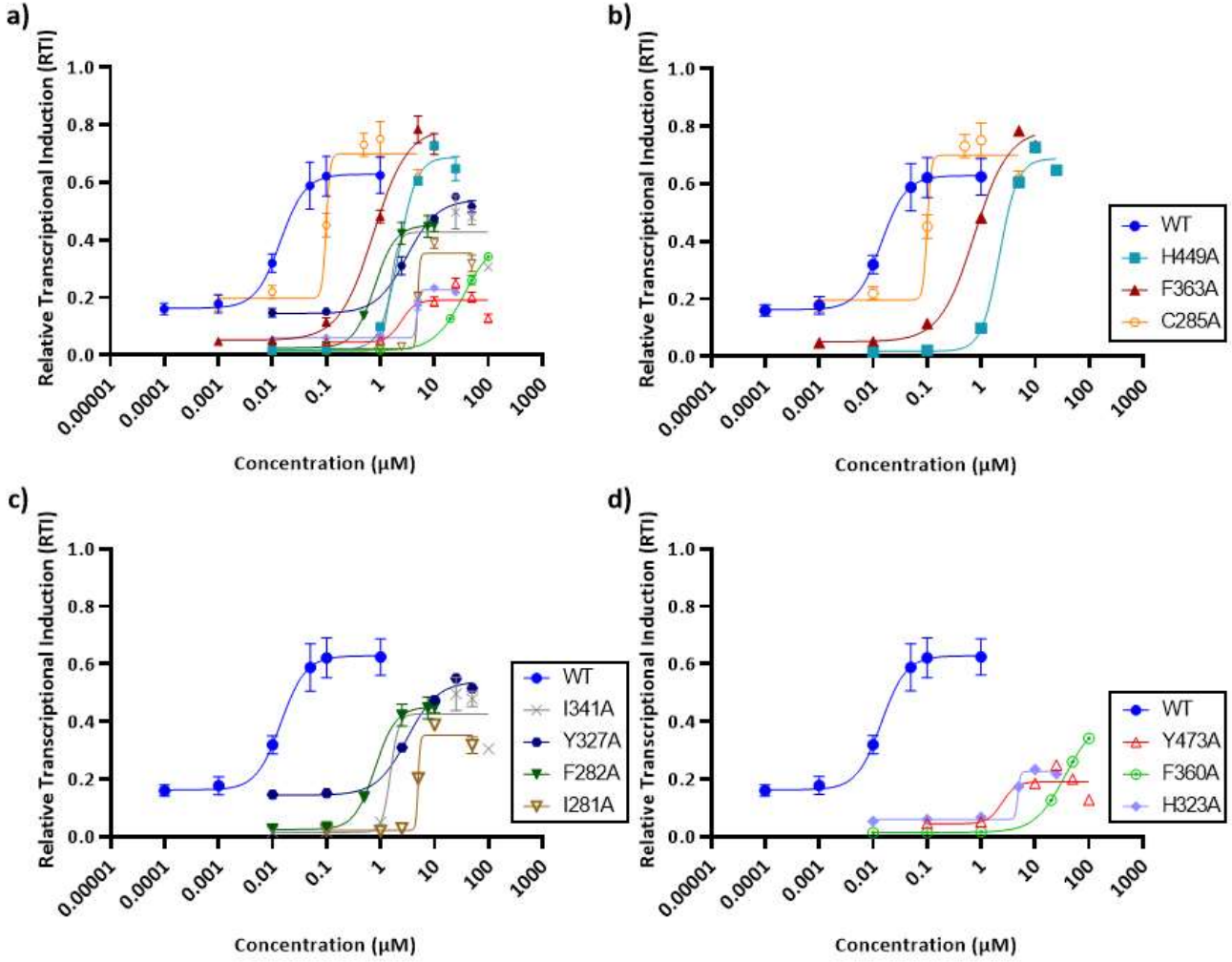
a)
b)
c)
d)
Relative Transcriptional Induction (RTI)
Concentration (µM)
0.00001
0.0001
0.001
0.01
0.1
1
10
100
1000
0.0
0.2
0.4
0.6
0.8
1.0
WT
H449A
F363A
C285A
I341A
Y327A
F282A
I281A
Y473A
F360A
H323A

1087

Figure 3.3. **PPARγ LBD residues contribute differently to transcription induction by Rosiglitazone.** To investigate the contribution of each ligand binding pocket residue to the Rosiglitazone induced gene transactivation ability of PPARγ, a DLA was conducted. Dose response curves for each mutation were calculated in Graphprism, from at least 6 concentration points in triplicate. Relative transcriptional induction (RTI) refers to the ratio of firefly to renilla luciferase activity. The curves, taken from experimental 2 replicate 2 in the figure are representative of all the experiments. Figures b) to d) represents the same curves from a) but split into 3 different groups. Boxes detail which mutation each curve represented. The curves for Y473A (experiment 1 replicate 2), H449A, F360A, Y327A (experiment 5 replicate 1) and I281A (experiment 6 replicate 2) were calculated in a separate experiment and transformed by normalizing to wildtype DMSO control of the above experiment for visualization purposes only.

.

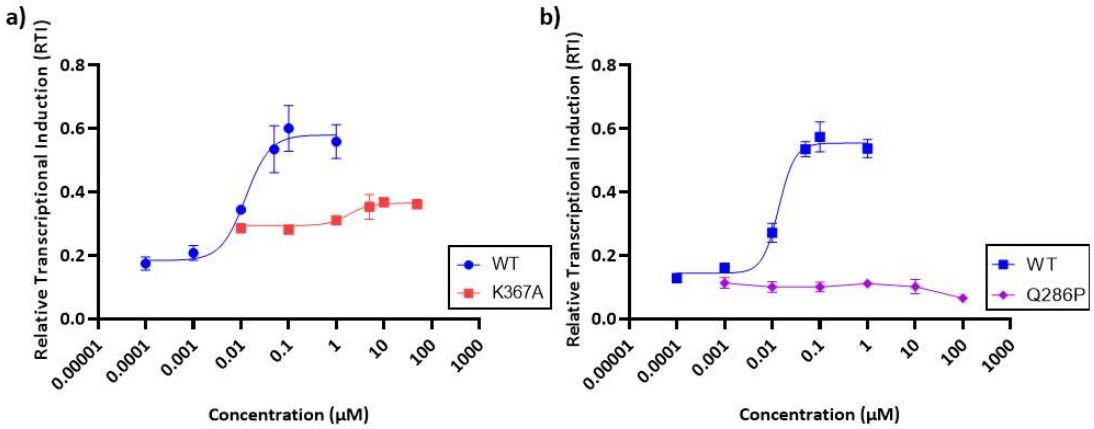

Figure 3.4. **PPARγ mutations K367A and Q286P alter dose response curves in unexpected ways.** To investigate the effects of mutations on the Rosiglitazone induced gene transactivation ability of PPARγ, a DLA was conducted. a) Dose response curves for K367A (experiment 4 replicate 2) was calculated in Graphprism, from at least 6 concentration points in triplicate. b) Graph of Q286P (experiment 3 replicate 2) represents a line joining the data points as dose response curves could not be calculated. Relative transcriptional induction (RTI) refers to the ratio of firefly to renilla luciferase activity. Boxes detail which mutation each curve represented. The curves are representative of all the experiments.

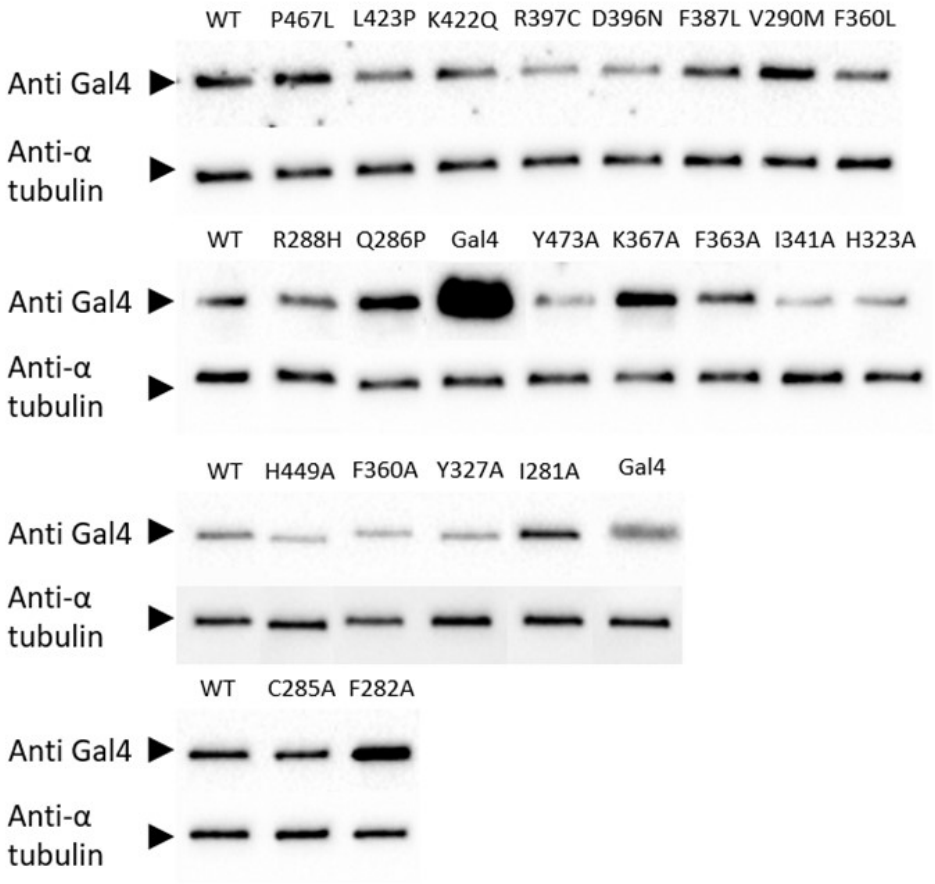

1105

1106 Figure 4. **Protein expression of each PPARγ mutants differs from wildtype.** HEK293 cells were
1107 transfected with PPARγ plasmids as detailed in the methods. α-tubulin was used as a loading control,
1108 and wildtype (WT) PPARγ expressing cells were used as a positive control. Bio-Rad 's precision plus
1109 protein dual colour standards were used. The calculated size of the PPARγ LBD-Gal4 DBD protein and
1110 Gal 4 DBD protein was about 50kDa and 17kDa respectively. The size of loading control α-tubulin was
1111 about 50kDa. Bands for PPARγ LBD-Gal4 DBD protein (wildtype and mutant) were observed
1112 corresponding to the 50kDa band on the protein standard ladder, while bands for the Gal4 DBD
1113 protein were observed between the 15kDa and 20kDa bands on the protein standard ladder. Bands
1114 for α-tubulin was observed at the 50kDa band on the protein standard ladder.

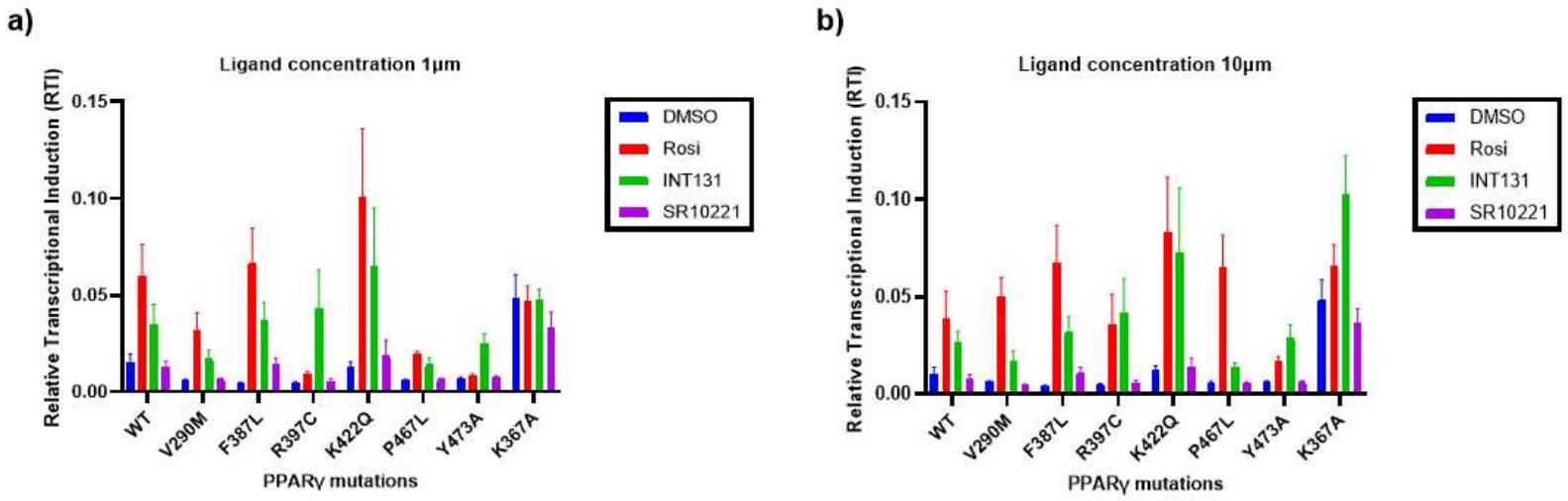

Figure 5. **PPARγ mutations differentially alter the transcription induction activity of ligands with different activity profiles.** Relative transcriptional induction by ligands Rosiglitazone (full agonist), INT131 (partial agonist) and SR10221 (Inverse agonist) was measured. Graphs represent an average of 3 experiments, each conducted in triplicate. Figures a) and b) represents the experiment conducted with 1µM and 10 µM of ligands respectively. For this experiment, 10 000 cells per well were seeded and a 1:1:1 pCMV-PPARγ LBD-Gal4 DBD, pG5E1B and pRLTK ratio was transfected for these experiments.

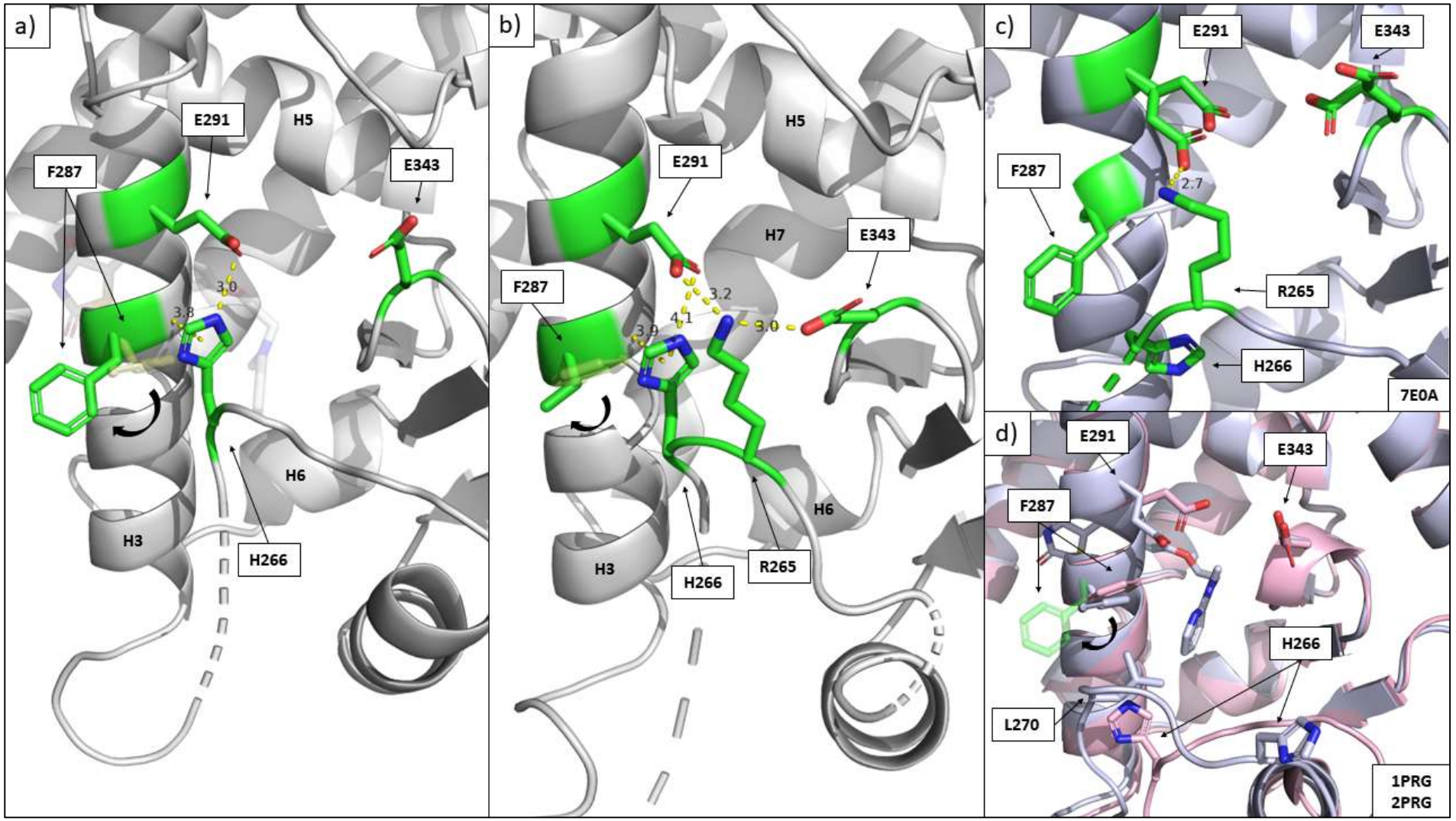

Figure 6.1. **PPARγ mutants contain a unique Ω loop conformation.** a-c) The Ω loops of the PPARγ LBD, from structures C285A_R, Y473A_A2 and model structures 1PRG,

2PRG and 7E0A. Panels show residues involved in the: a) single latch between H266 and E291, C285A_R is the structure represented in white (in grey 90) with residues involved in the Ω loop conformation highlighted in green. Position of F287 from model structure 2PRG is overlayed in yellow (pale yellow); b) double latch between H266-E291-R265-E343, Y473A_A2 is the structure represented in white (in grey 90) with residues involved in the Ω loop conformation highlighted in green. Position of F287 from model structure 1PRG is overlayed in yellow (pale yellow). Other latching mechanisms are seen in other structures: c) In 7E0A (represented in grey 90), a latching mechanism is seen between R265-E291. Residues involved in the Ω loop conformation are highlighted in green; d) In 2PRG (in blue-white), an interaction between L270 and F287. In 1PRG (in light pink), no latch was seen. The position of F287 from 7E0A (in green) was shown in comparison. All structures were aligned to 5YCP. Exact colour names used in Pymol is given in parenthesis.

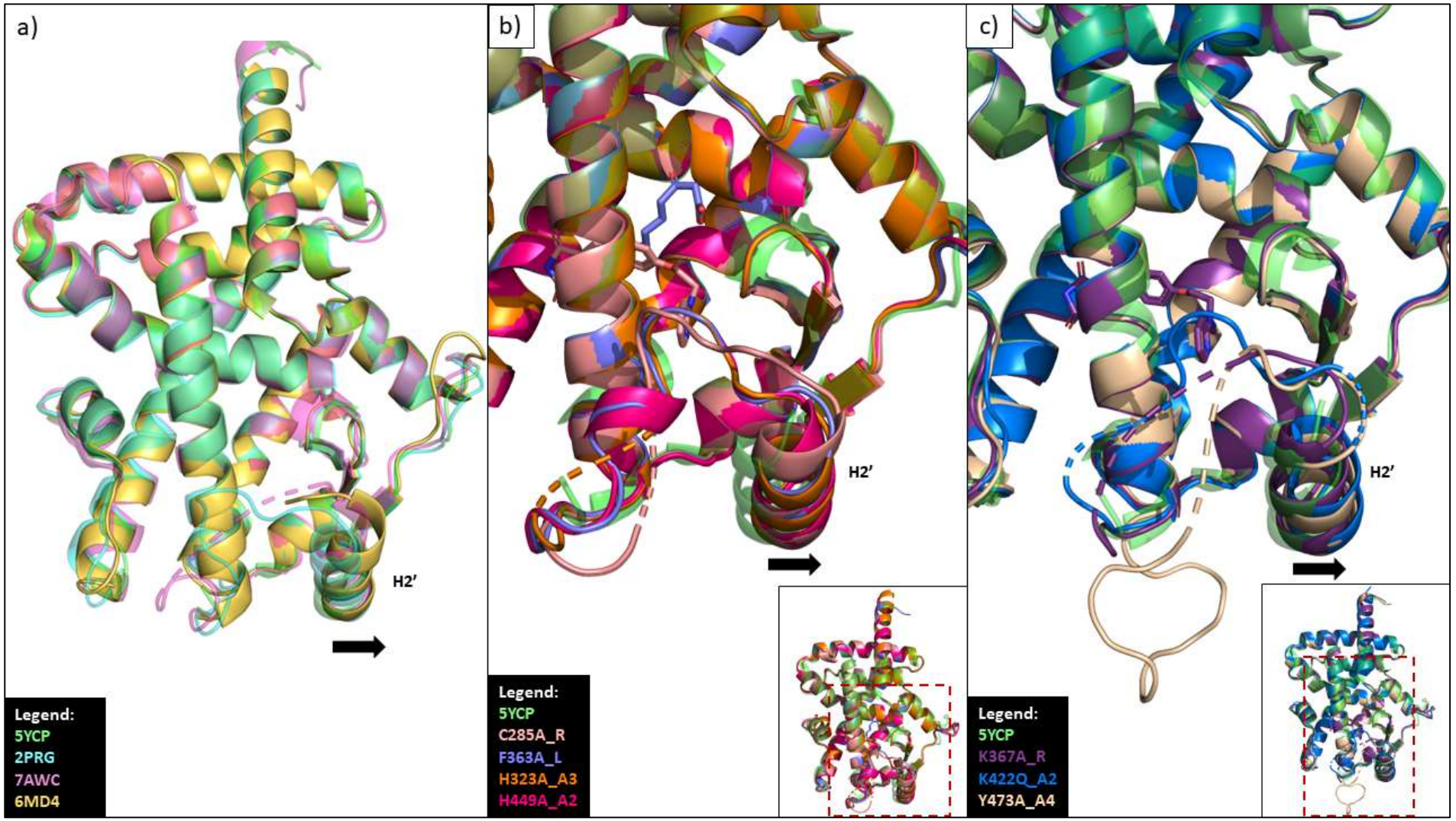

Figure 6.2. **H2' of mutant structures differ compared to model structures.** a-c) The PPARγ LBD of all mutants and model structures. The H2' shifts to the right in some

structures compared to 5YCP, 2PRG and 7AWC (in green, cyan and light magenta, transparent). The mutant structures presented were representative of the structure of every mutation. All structures were aligned to 5YCP. The 5YCP and 2PRG structures contained residues representing the coactivator motif that was hidden for visual clarity. For all panels a figure legend is given with the PDB ID or name of the model or mutant structure coloured in the same colour as the visualized structure. For b) and c) the incut boxes in each panel shows a zoomed-out view of the scene. Exact colour names used in Pymol is given in parenthesis.

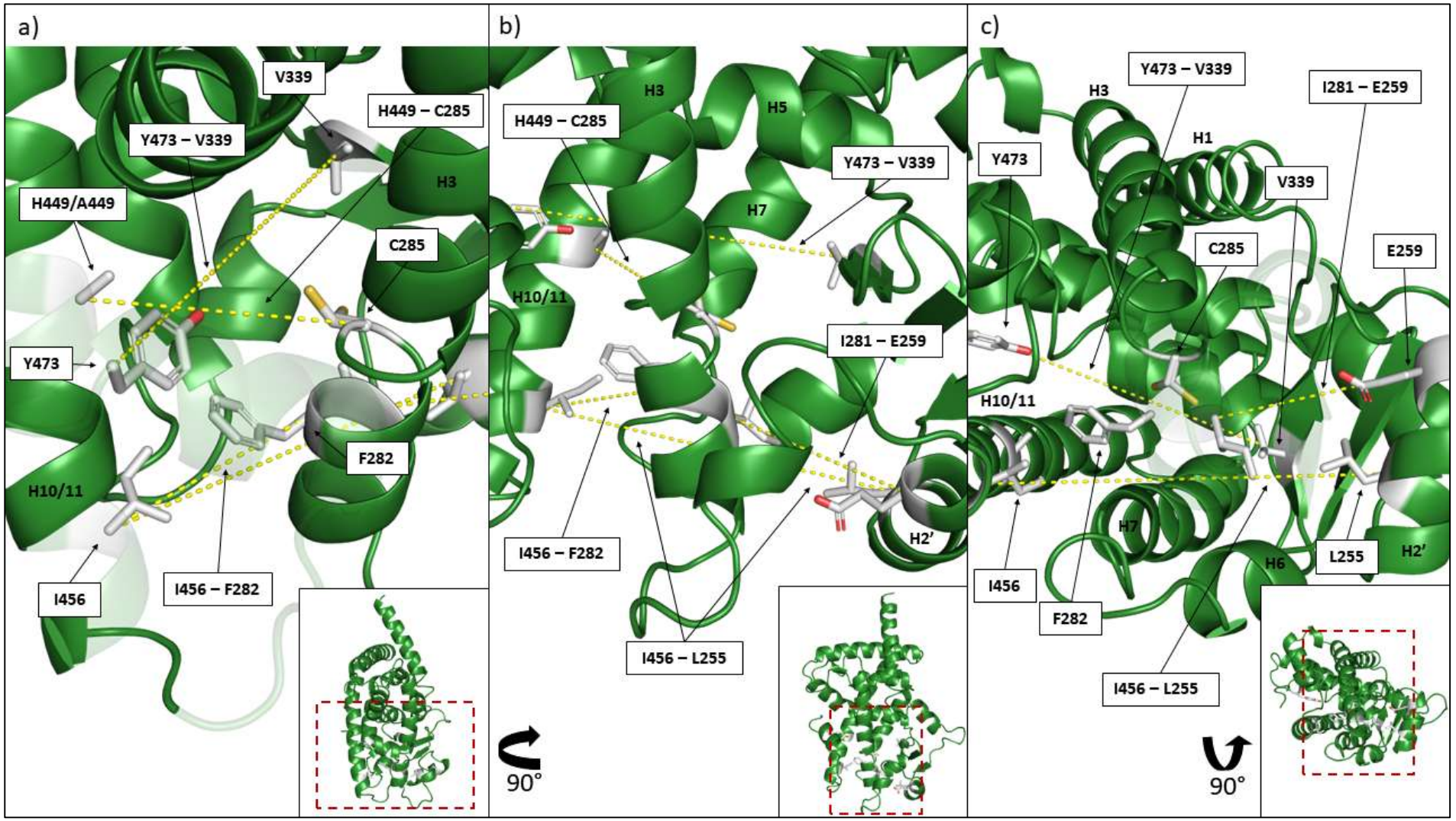

Figure 6.3. **Points of measurements for PPARγ ligand binding pocket.** The differences in the PPARγ ligand binding pocket of the mutants were quantified by distances

between certain residues, compiled in Table 4.2. a-c) The PPARγ ligand binding pocket of mutant H449A (in forest) with residues used for measurements in white (in grey 90). 5 of 6 measurements were shown in the figure, in a) Y473-V339, I456-F282, H449-C285. In b) Y473-V339, I456-F282, H449-C285, I456-L255, I281-E259. In c) Y473-V339, I456-F282, I281-E259. a) to c) represents the same ligand binding pocket viewed from different angles and the incut boxes in each panel shows a zoomed-out view of the scene. Some residues were made translucent for ease of visualization: a) 449-450, 456-457, 462-477; c) 266-283. The last measurement not pictured here is L255 to L255 measurement between structures. Exact colour names used in Pymol is given in parenthesis.

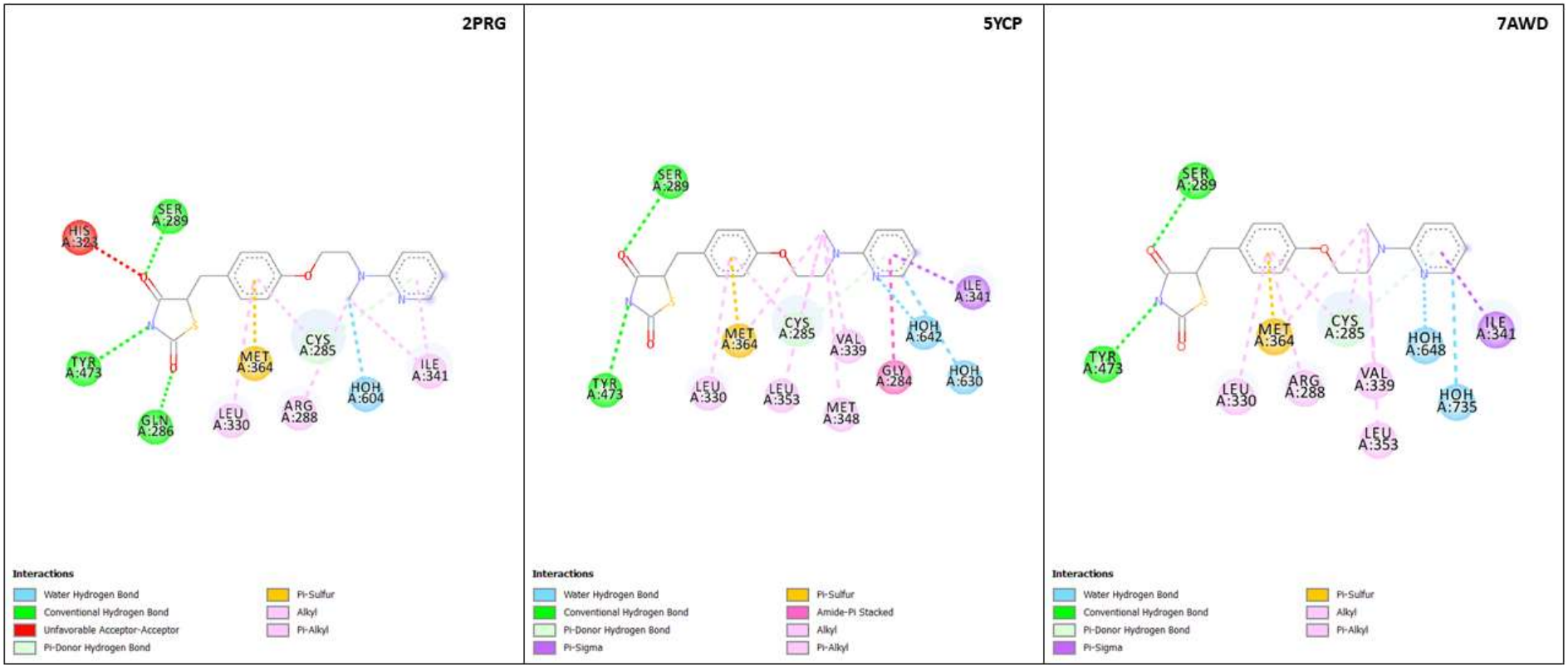

Figures 6.4. **Interaction diagram of PPARγ ligand binding pocket residues and ligands for 2PRG, 5YCP and 7AWD.** Interaction diagram was calculated using the BIOVIA Discovery Studio Visualizer 2020 client for the ligand bound mutants. Each colour corresponds to different types of interactions as given in the legend in each panel. All ligand interactions represent the 'A chain' of the PPARγ protein structure.

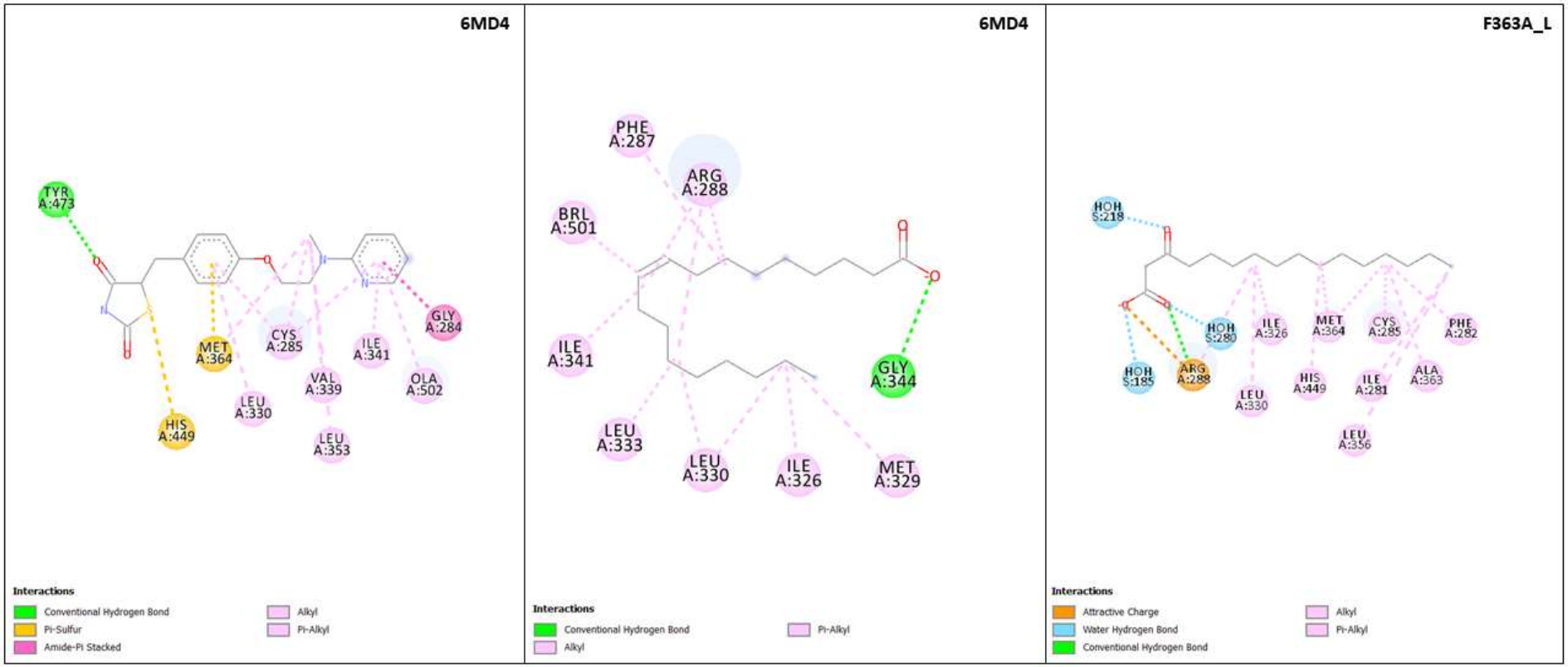

Figure 6.5. **Interaction diagram of PPARγ ligand binding pocket residues and ligands for 6MD4 and F363A_L.** Interaction diagram was calculated using the BIOVIA Discovery Studio Visualizer 2020 client for the ligand bound mutants. Each colour corresponds to different types of interactions as given in the legend in each panel. All ligand interactions represent the 'A chain' of the PPARγ protein structure. 6MD4 has both Rosiglitazone and Oleic acid bound in the ligand binding pocket of A chain.

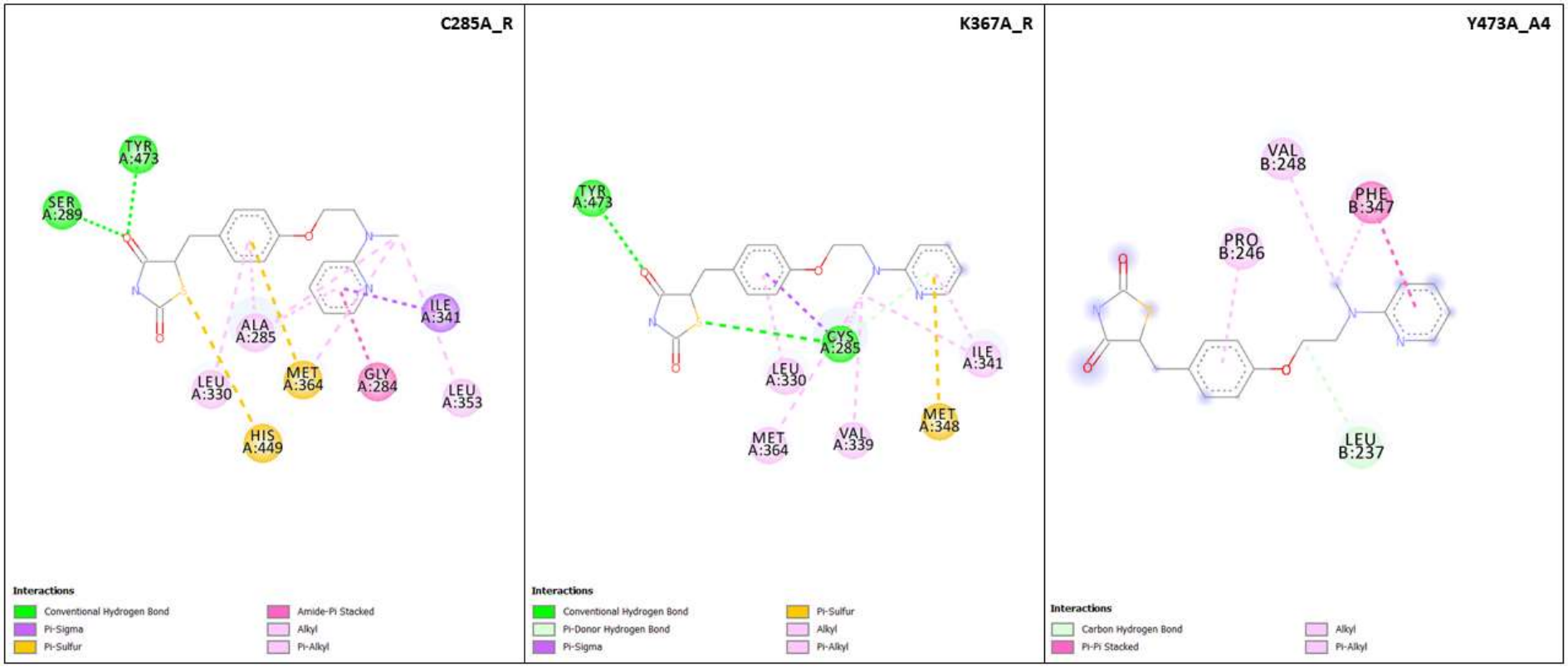

Figure 6.6. **Interaction diagram of PPARγ ligand binding pocket residues and ligands for mutant PPARγ structures C285A_R, K367A_R and Y473A_A4.** Interaction diagram was calculated using the BIOVIA Discovery Studio Visualizer 2020 client for the ligand bound mutants. Each colour corresponds to different types of interactions as given in the legend in each panel. All ligand interactions represent the 'A chain' of the PPARγ protein structure, except for Rosiglitazone in Y473A_A4, which was bound to the H2-H2' loop region in the 'B chain".

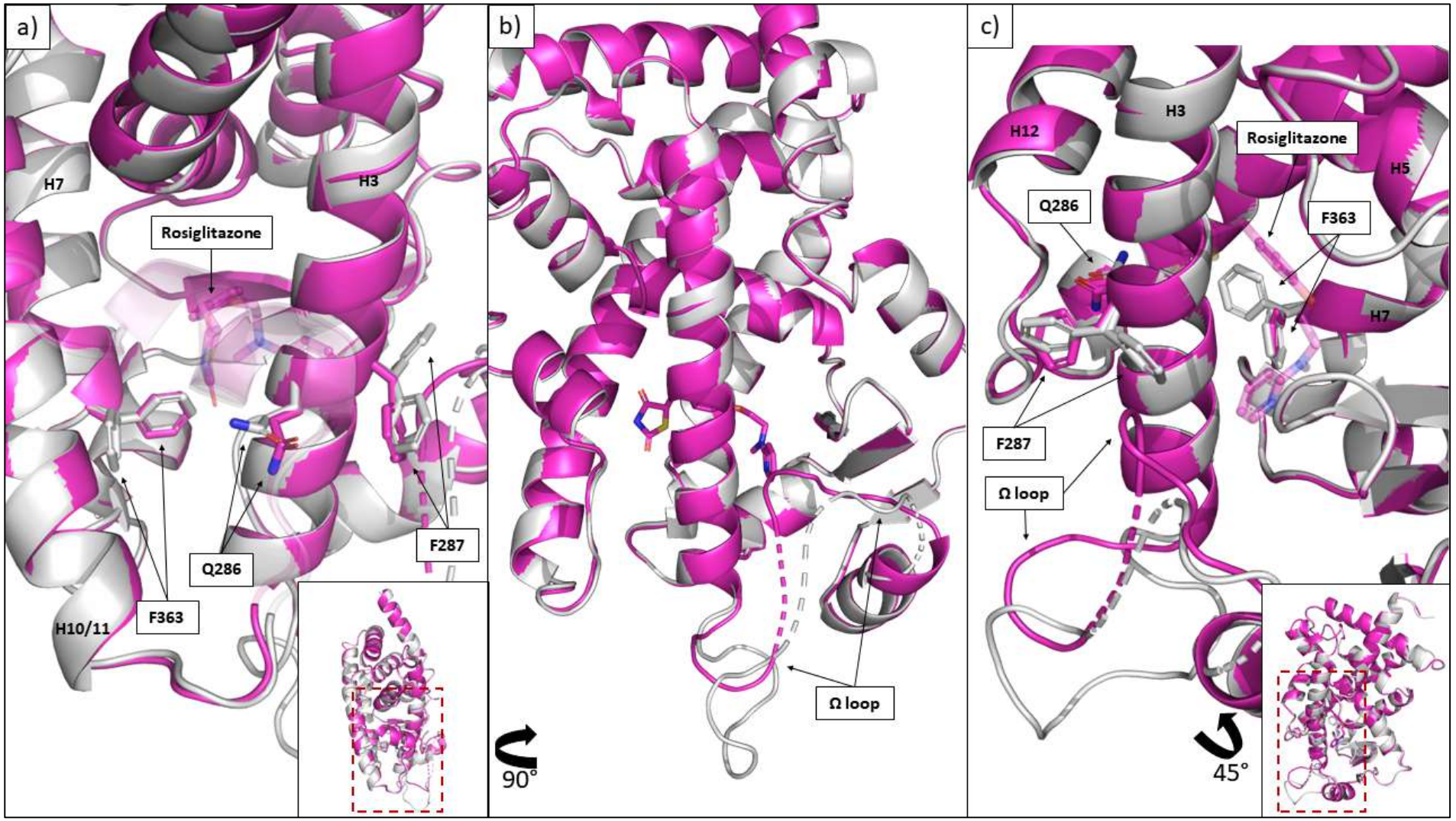

Figure 6.7. **Comparison between structures C285A_A and C285A_R.** a-c) The PPARγ ligand binding pocket of C285A_A and C285A_R with Rosiglitazone and side chains of

residues shown. C285A_A (in grey 90) and C285A_R (in light magenta) was aligned to each other and overlayed. A few points of differences were noted, including alternate conformations of F363, differing positions of Q286 and differences in the Ω loop. a) to c) represents the same ligand binding pocket structures viewed from different angles and the incut boxes in panels a) and c) shows a zoomed-out view of the scene. Some residues were made translucent for ease of visualization: a) 464-477, Rosiglitazone. Residues in c) were hidden for visual clarity: 341-345, Rosiglitazone. DMSO in C285A_A was hidden. Exact colour names used in Pymol is given in parenthesis.

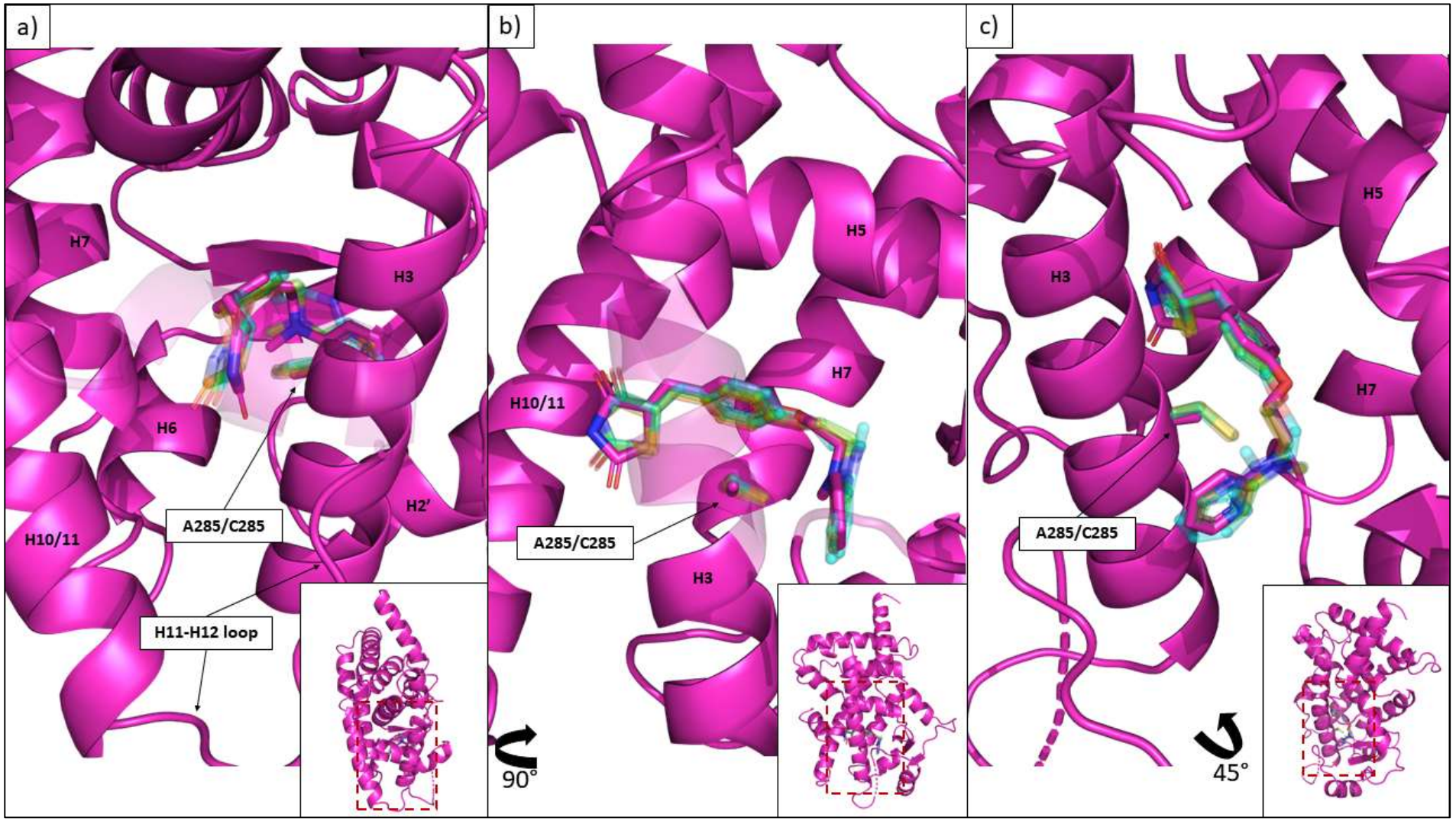
a)
H7
H3
H6
H2'
A285/C285
H10/11
H11-H12 loop
b)
H5
H7
H10/11
A285/C285
H3
90°
c)
H5
H3
H7
A285/C285
45°

1161

Figure 6.8. **Position of Rosiglitazone in C285A_R differs slightly compared to model structures.** The position of Rosiglitazone in the ligand binding pocket changes slightly due to C285A mutation. a-c) The PPARγ ligand binding pocket of C285A_R with Rosiglitazone and side chain of A285 shown. Rosiglitazone molecule and side chain of C285 of model structures were overlayed onto C285A_R (in light magenta). Model structures used were 5YCP (in green), 2PRG (in cyan) and 7AWC (in orange). All structures were aligned to 5YCP. a) to c) represents the same ligand binding pocket structure viewed from different angles and the incut boxes in panels a) to c) shows a zoomed-out view of the scene. Some residues were made translucent for ease of visualization: a) 464-477, Rosiglitazone of 5YCP, 2PRG and 7AWC; b) 285-290; c) 227-228, 341-345, Rosiglitazone of 5YCP, 2PRG and 7AWC. Exact colour names used in Pymol is given in parenthesis.

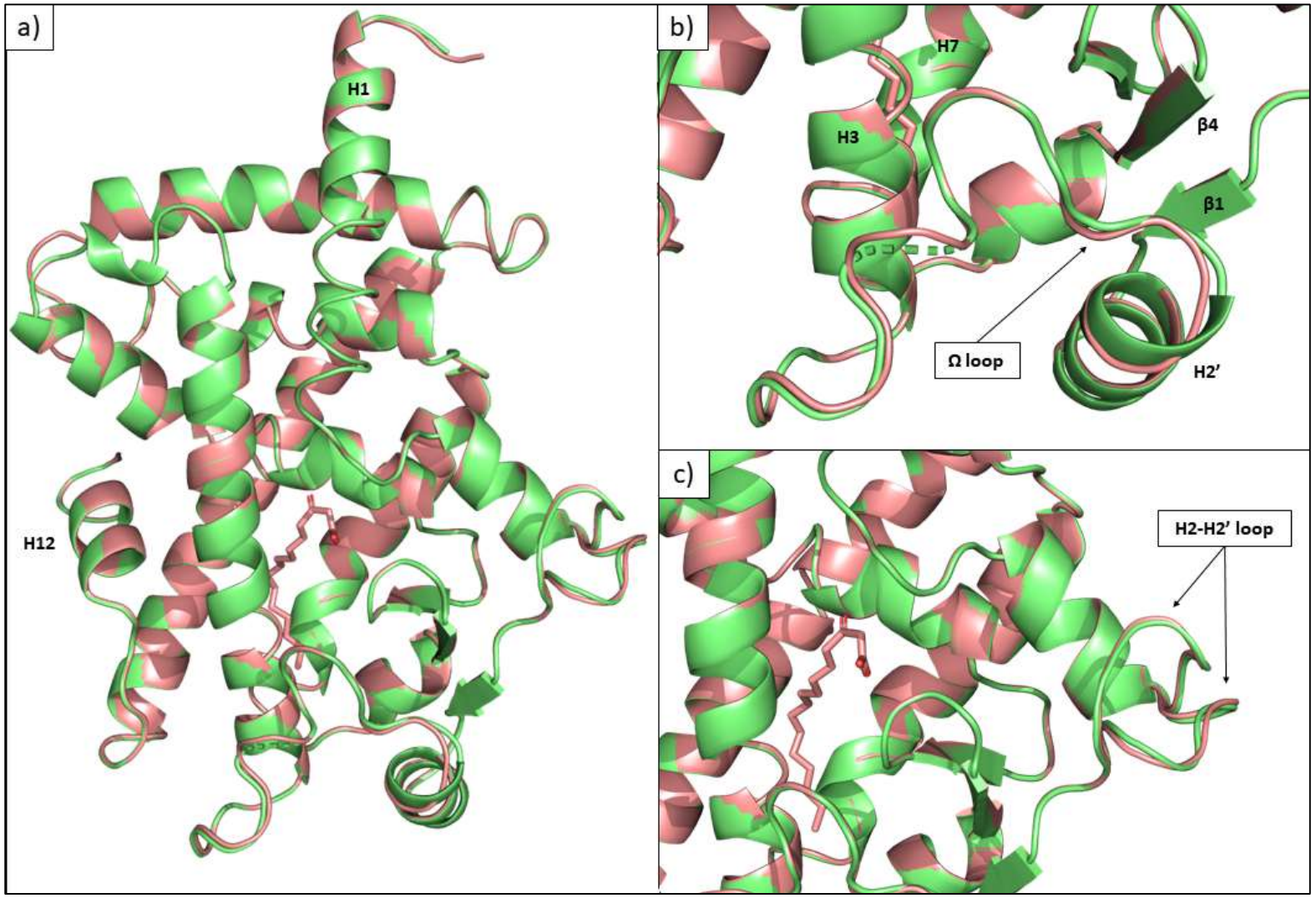

1169

Figure 6.9. **Comparison between structures F363A_A and F363A_L.** F363A_A (in lime) and F363_L (in salmon) aligned to each other closely, with a RMSD of 0.117Å. a) Full view of the structure of F363A LBD with H3 facing the viewer (Figure 1.1). b) Close up of the Ω loop region. c) Close up of H2-H2' loop region, with alternate loops pictured (residue 239-244). Both structures were aligned to each other. Exact colour names used in Pymol is given in parenthesis.

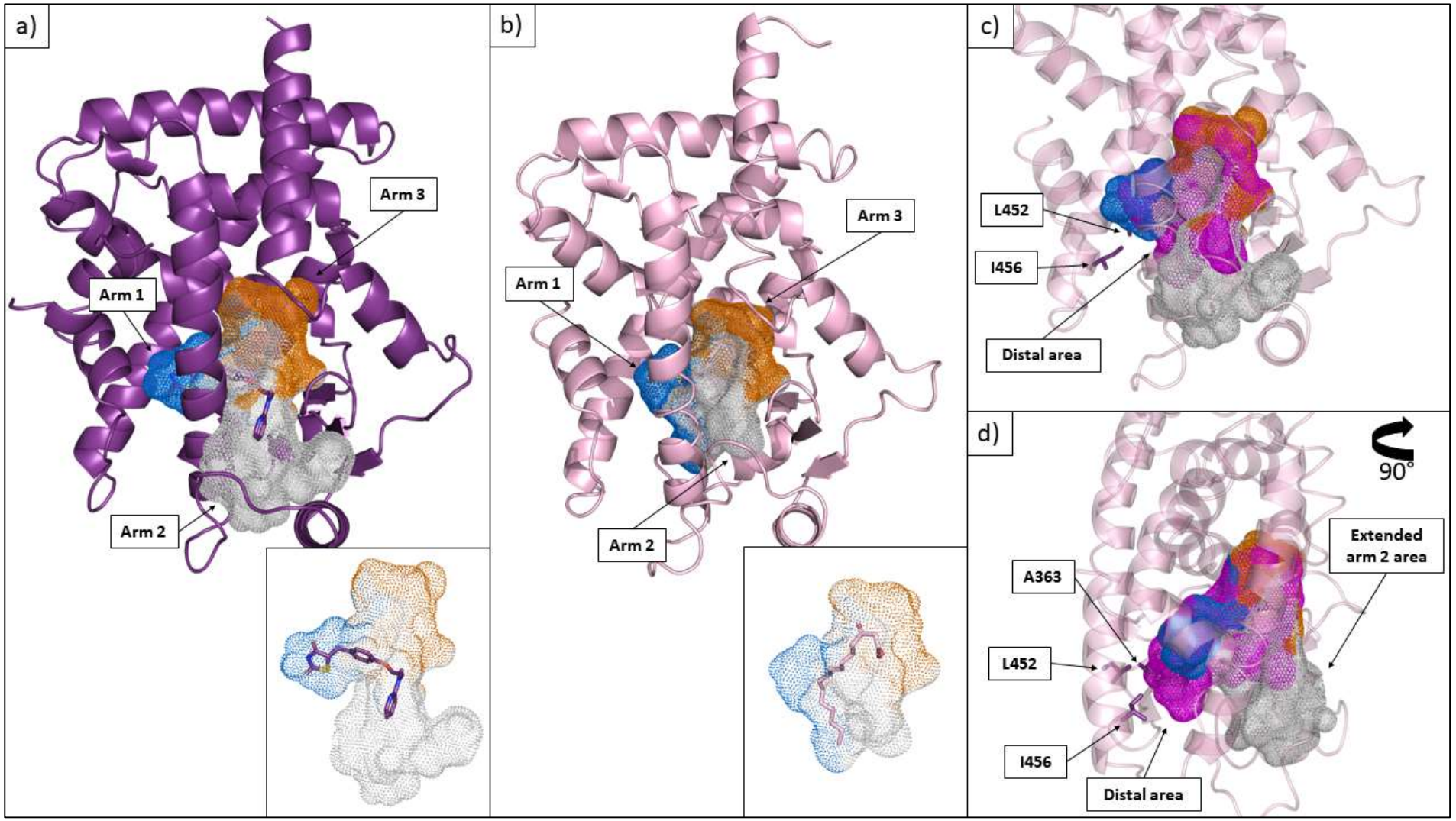

Figure 6.10. **Ligand binding pocket of F363A differs from model structure.** The inner cavity of F363A_L was shaped differently compared to the model structure 2PRG

due to rearrangement of amino acid residues. a) 2PRG (in violet-purple with SRC peptide visible) with the ligand binding pocket displayed, split into areas named Arm1, 2 and 3 (Marine, white and orange respectively). Incut shows the ligand binding pocket cavity of 2PRG. b) F363A_L (in light pink) with the ligand binding pocket displayed, split into areas named Arm1, 2 and 3 (Marine, white and orange respectively). Incut shows the ligand binding pocket cavity of F363A_L. c) Comparison of the cavity of 2PRG (Arms 1-3 in marine, white and orange) vs F363A_L (in magenta) overlayed onto the structure of F363A_L with cavity (in light pink). The side chain of residues L452 and I456 were shown in sticks (violet-purple). d) Side on view of c), facing H12. The F363A_L cavity contains an extended portion labelled 'distal area' near to L452, while the 2PRG cavity shows an extended arm 2 area. The side chain of residues A363, L452 and I456 were shown in sticks (violet-purple). All structures were aligned to 5YCP. Exact colour names used in Pymol is given in parenthesis.

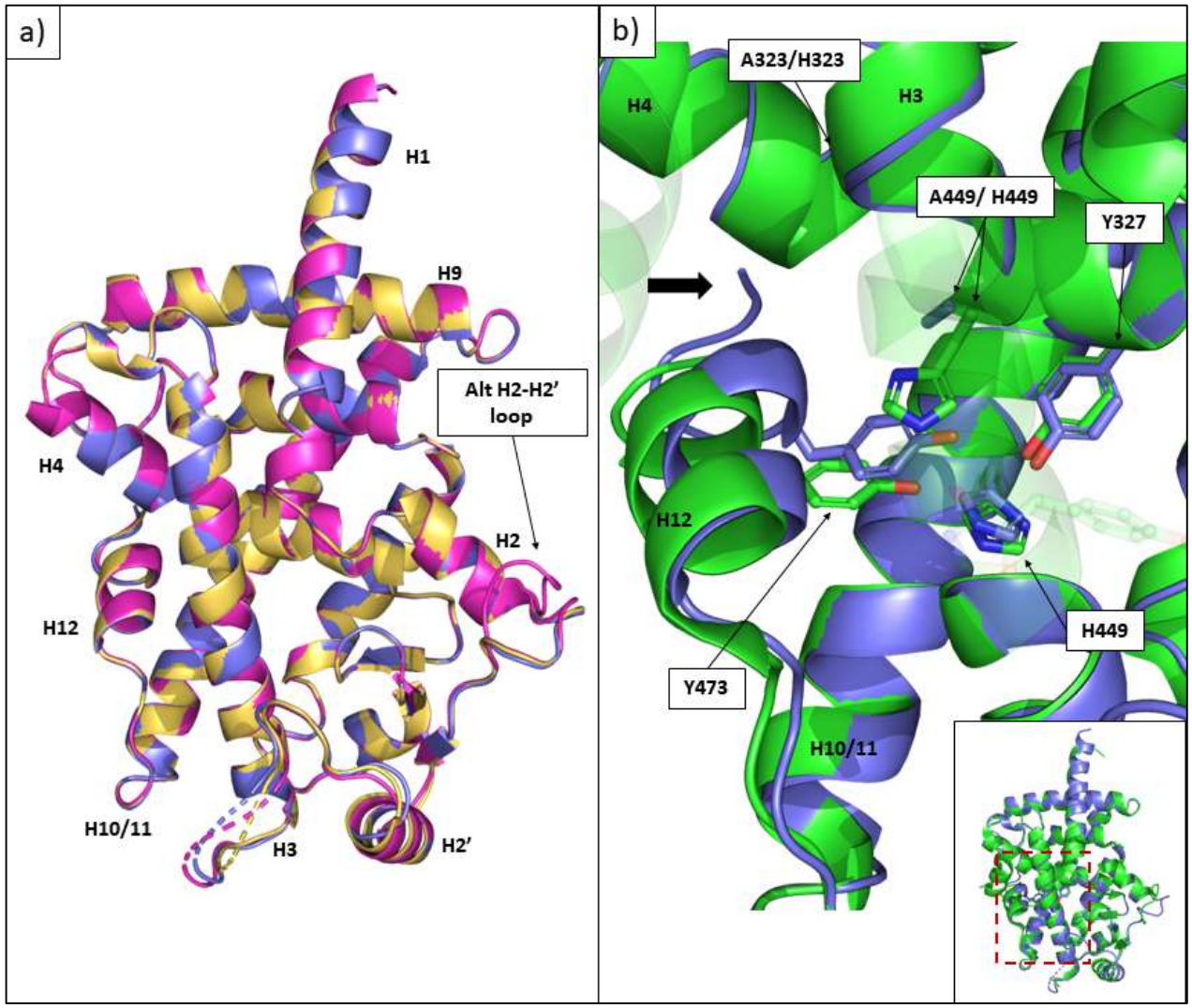

Figure 6.11. **H323A structures displayed a shift in H12 compared to model structures.** The H323A structures were very similar, and consistently resulted in a rightward shift of H12 due to the H323A mutation. a) H323A structures were overlayed and aligned to H323A_A1. Alternate H2-H2' loop of H323A_A3 was labelled. b) 5YCP (in green) and H323A (in marine) overlayed and aligned to 5YCP. The side chain of residues involved in arm 1 interactions (Y473, H449, Y327 and H323A) were shown. Absence of Histidine at position 449 allows Y473 to move into further into arm 1, indicated by black arrow. Incut box in panel shows a zoomed-out view of the scene. Some residues were made translucent for ease of visualization: in b) Residues 288-294 and 322, Rosiglitazone and SRC1 peptide. Only the translucent structure of 5YCP was shown for visual clarity. Exact colour names used in Pymol is given in parenthesis.

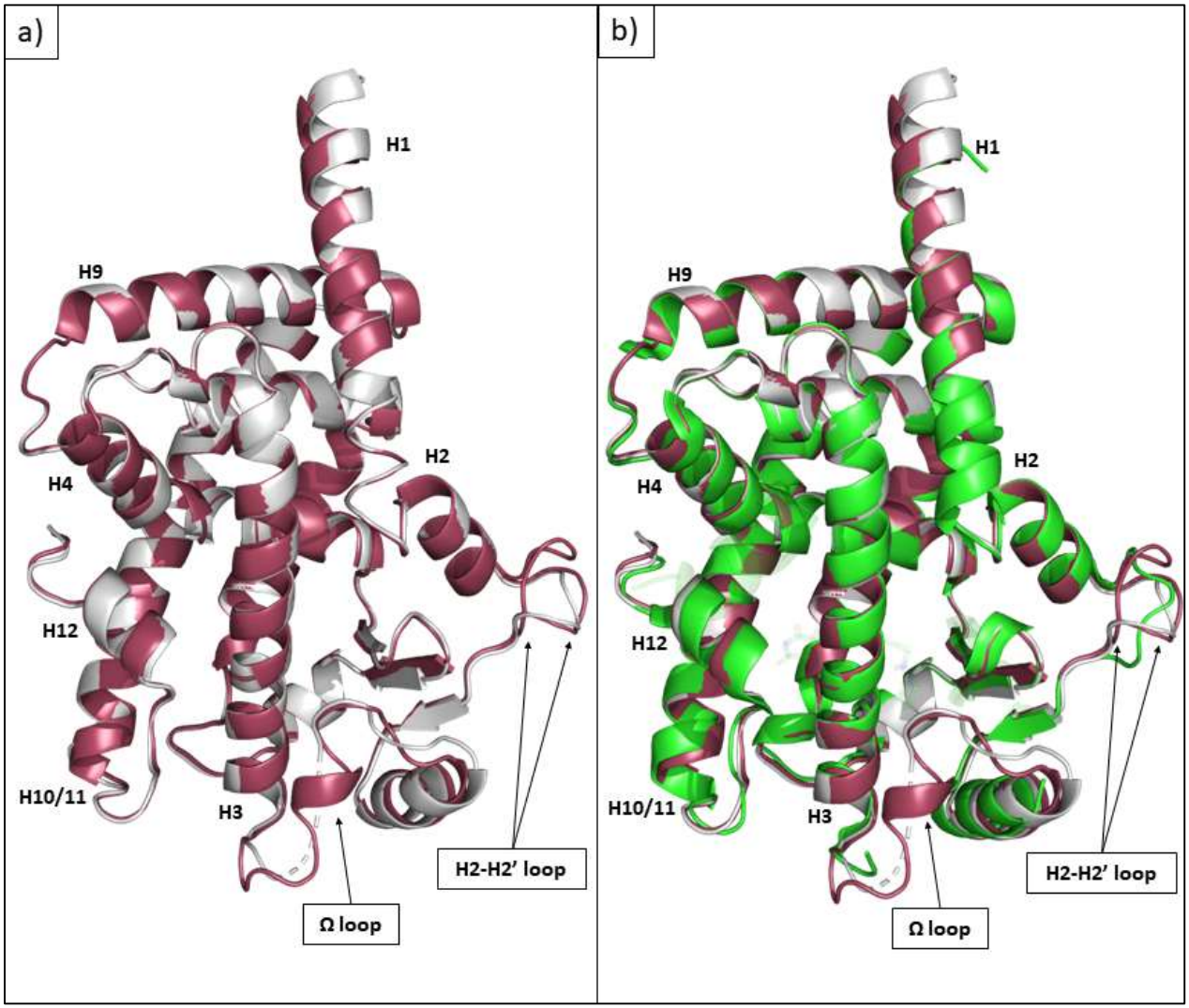

Figure 6.12. **Comparison between H449A structures and model structure 5YCP.** H449A_A1 and H449A_A2 aligned to each other closely with a RMSD of 0.227Å and contained slight differences when compared to model structures a) Full view of the PPARγ LBD structure of H449A_A1 (in grey 90) and H449A_A2 (in raspberry) with H3 facing the viewer and aligned to H449A_A1. H449A_A2 contains an alternate H2-H2' loop, as well as a full Ω loop. b) H449A_A1 and H449A_A2 aligned to and overlayed with 5YCP (in green). Exact colour names used in Pymol is given in parenthesis.

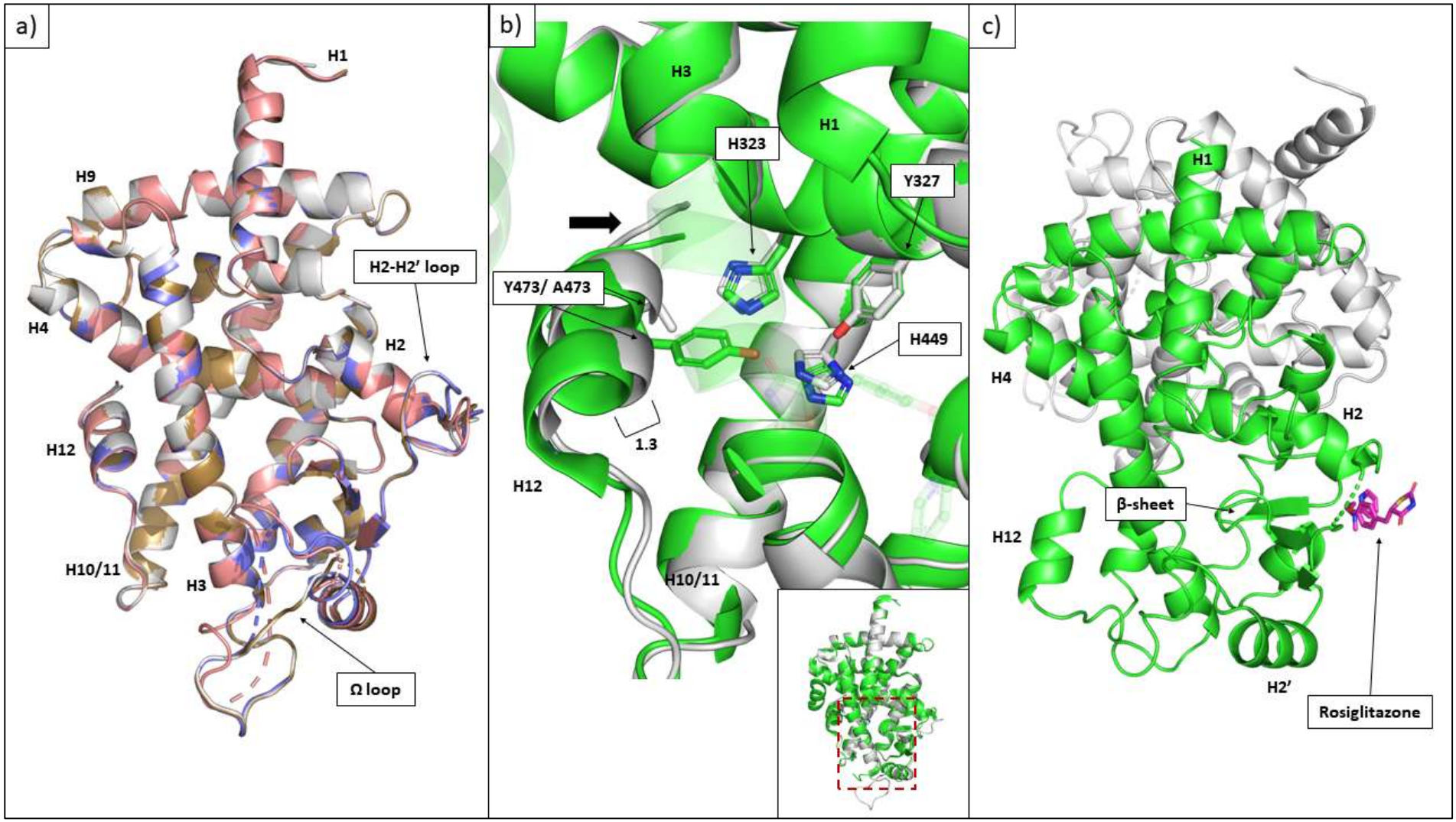
a)
H1
H9
H2-H2' loop
H4
H2
H12
H10/11
H3
Ω loop
b)
H3
H1
H323
Y327
Y473/ A473
H449
1.3
H12
H10/11
c)
H1
H4
H2
β-sheet
H12
H2'
Rosiglitazone

1213

Figure 6.13. **Y473A structures also displayed a shift in H12 compared to model structure 5YCP.** a) Full view of the PPARγ LBD structure of Y473A_A1 (in grey 90), Y473A_A2 (in salmon), Y473A_A3 (in sand) and Y473A_A4 (in slate) with H3 facing the viewer and aligned to Y473A_A1. b) Y473A_A1 aligned to and overlayed with 5YCP (in green). The side chain of residues involved in arm 1 interactions (Y473, H449, Y327 and H323A) were shown. 1.3Å difference in H12 position between Cα of Y473 in both structures was noted. c) Structure of Y473A_A4, with the Rosiglitazone bound B chain (in magenta and green respectively) facing the viewer and A chain (in grey 90) in the back. Some residues were made translucent for ease of visualization: in b) Residues 287-294, Rosiglitazone and SRC1 peptide. Only the translucent helix structure of 5YCP was shown for visual clarity. Exact colour names used in Pymol is given in parenthesis.

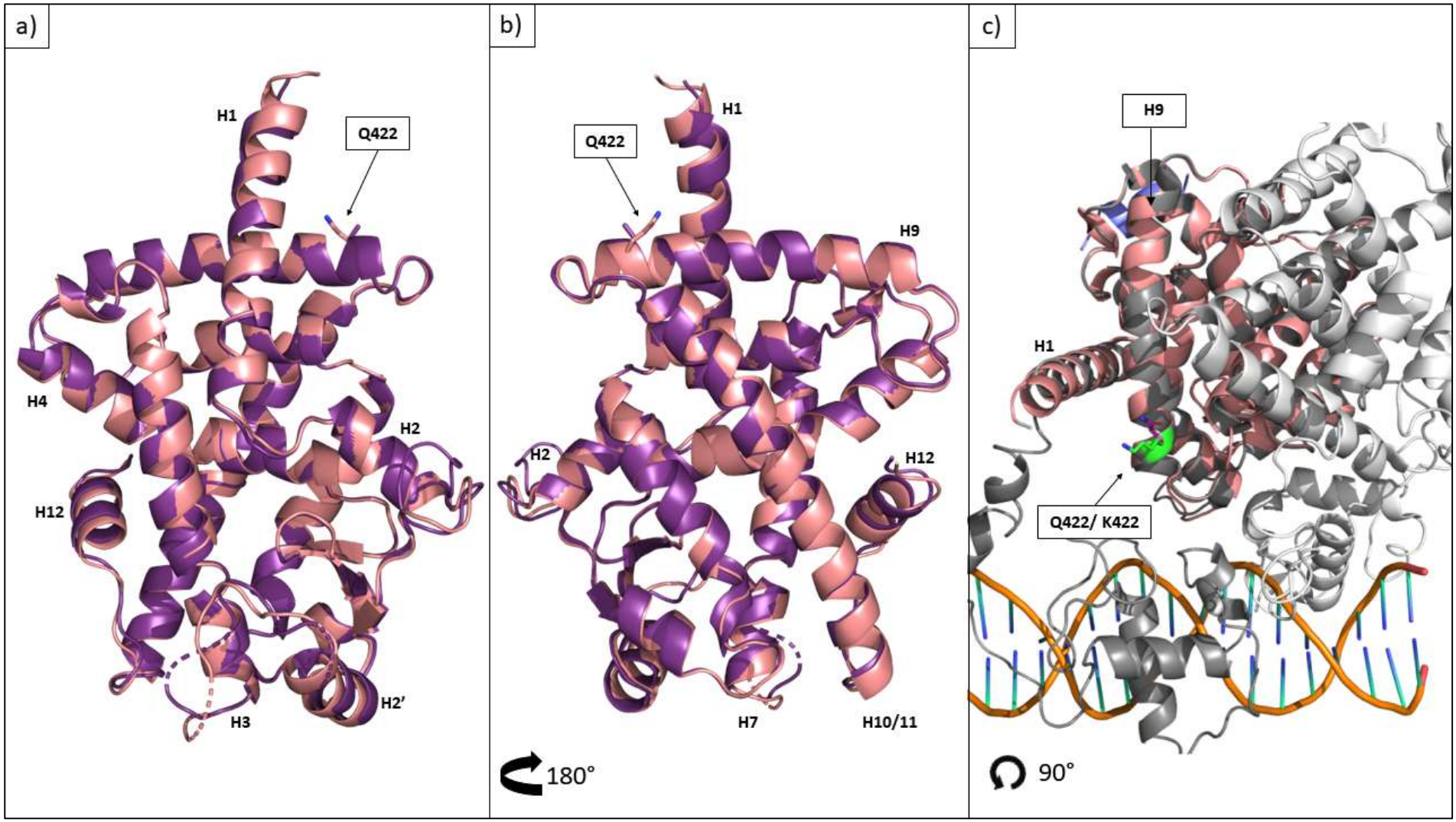
a)
H1
Q422
H4
H2
H12
H3
H2'
b)
H1
Q422
H9
H2
H12
H7
H10/11
180°
c)
H9
H1
Q422/ K422
90°

1220

Figure 6.14. **Comparison between K422Q structures and full-length structure 3DZY.** a, b) Full view of the PPARγ LBD structure of K422Q_A1 (in salmon) and K422Q_A2 (in violet-purple) with side chain of residue Q422 shown and aligned to K422Q_A1. a) and b) represents the same ligand binding pocket viewed from opposite angles. c) K422Q_A1 was overlayed onto the PPARγ LBD portion of structure 3DZY (in grey 50). The RXR subunit of 3DZY was coloured in white (in grey 90) and DNA helix was coloured in orange. The side chain of residue 422 was shown for K422Q_A1 (in magenta) and 3DZY (in green). Exact colour names used in Pymol is given in parenthesis.

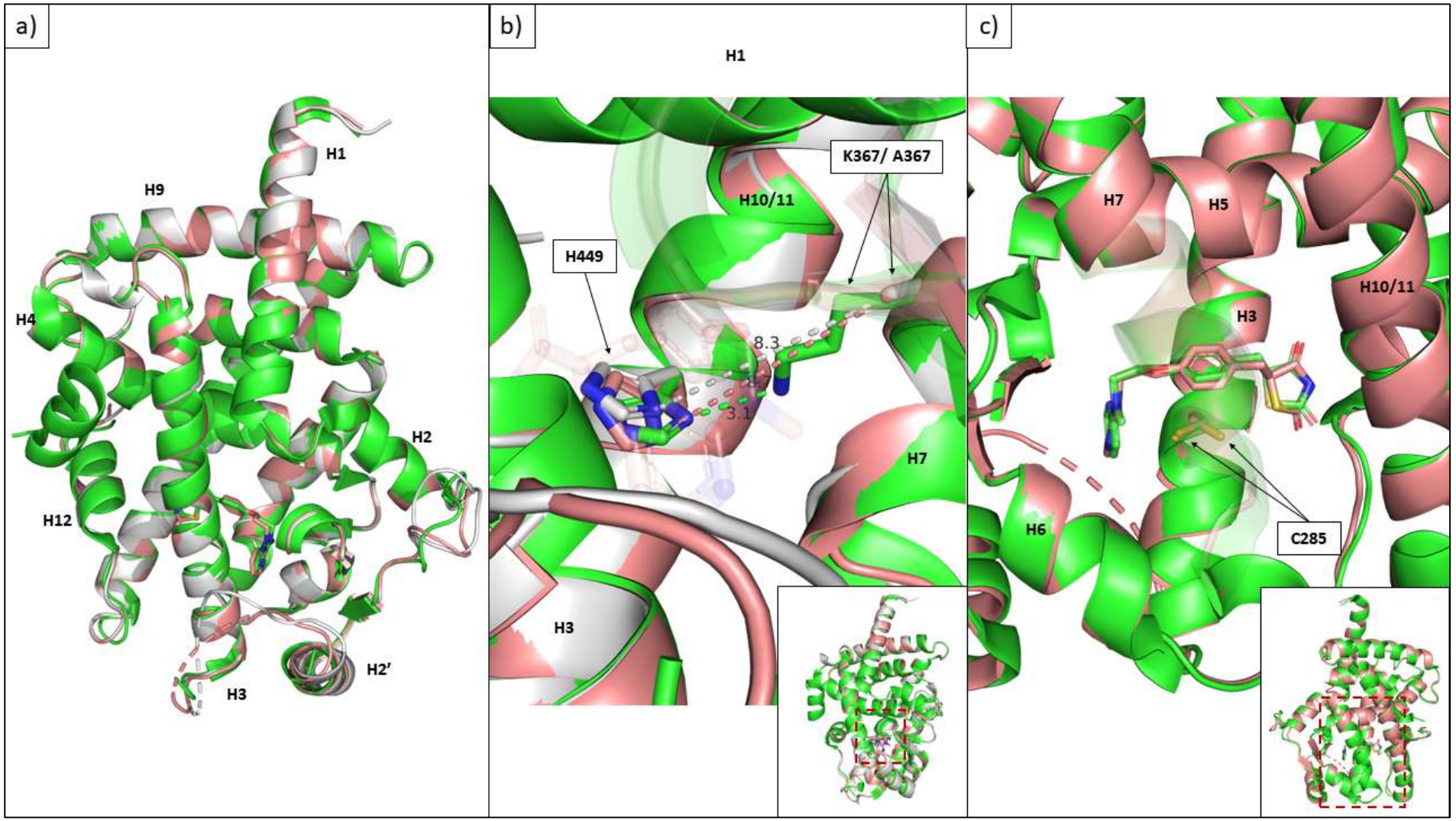
a)
H1
H9
H4
H2
H12
H2'
H3
b)
H1
K367/ A367
H10/11
H449
8.3
3.1
H7
H3
c)
H7
H5
H10/11
H3
H6
C285

1225

Figure 6.15. **Comparison between K367A structures and model structure 5YCP.** a-c) Full view of the PPARγ LBD structure of K367A_A (in white) and K367A_R (in salmon), overlayed with 5YCP (in green). b) PPARγ ligand binding pocket of K367A_A, K367A_R and 5YCP. Shortest distance measured between side chains of resides H449 and K/A367 of the structures. c) PPARγ ligand binding pocket of K367A_R (in salmon) and 5YCP (in green) with H7 ahd H10/11 facing the viewer. Side chain of residue C285 was shown. All structures shown were aligned to 5YCP. Incut boxes in panels b) and c) shows a zoomed-out view of the scene. Some residues were made translucent for ease of visualization: in b) Residues 341-345, Rosiglitazone of K367A_R; c) Residues 362-371. In b), Rosiglitazone of 5YCP was hidden for visual clarity. Exact colour names used in Pymol is given in parenthesis.

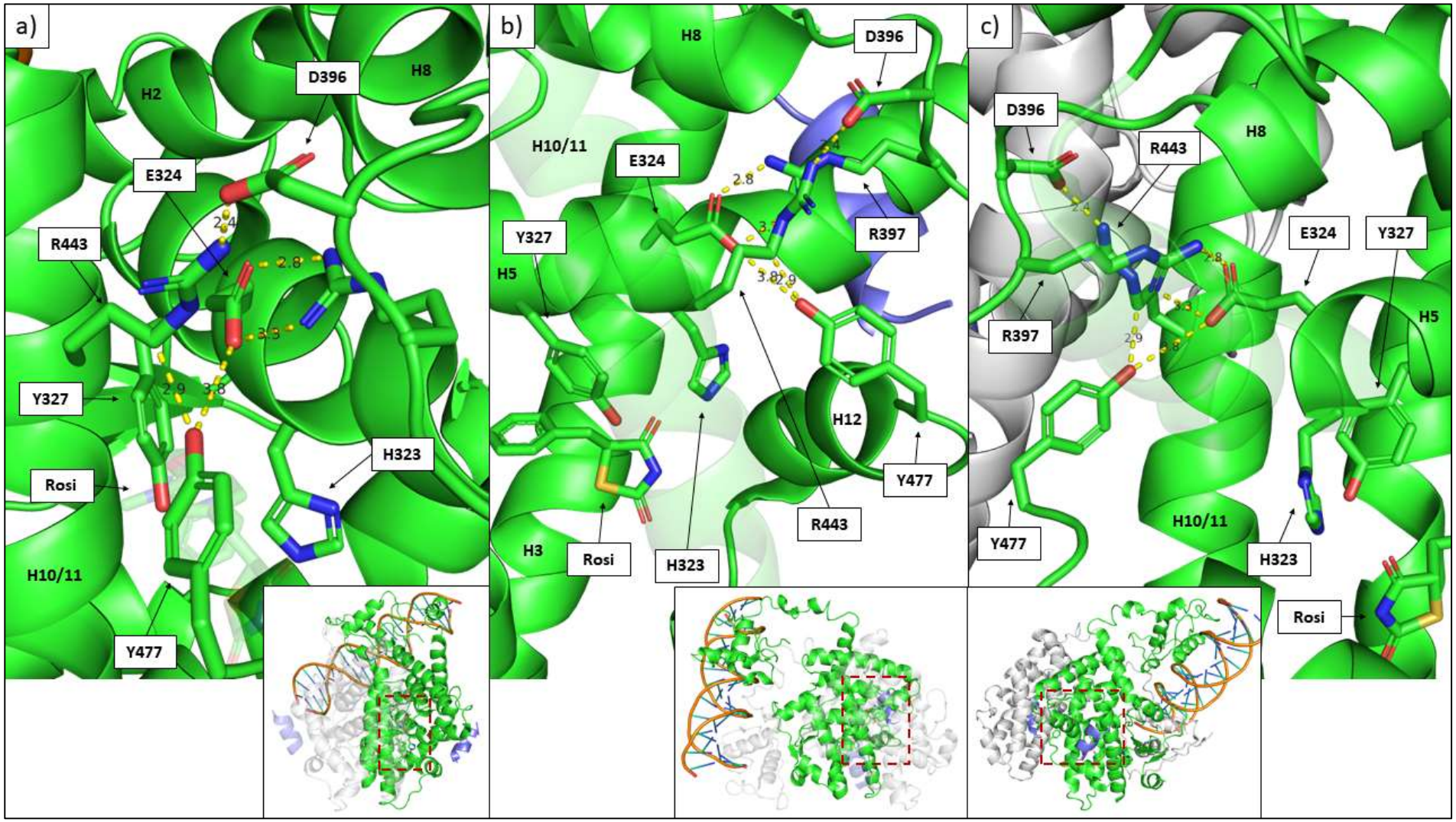
a)
H2
D396
H8
E324
R443
Y327
Rosi
H323
H10/11
Y477
b)
H8
D396
H10/11
E324
Y327
H5
R397
H12
Y477
R443
H3
Rosi
H323
c)
D396
R443
H8
E324
Y327
R397
H5
H10/11
Y477
H323
Rosi

Figure 7.1. **Interaction network involving residues D396 and R397.** a-c) The full-length structure of 3DZY, including the PPARγ subunit (in green), the RXRα subunit (in grey 90), the nuclear receptor coactivator 2 (NCoA2) peptides (in slate), ligands Rosiglitazone and 9-retinoic acid and DNA (in orange) was presented. Side chains of residues which were involved in the interaction network, D396-R443-Y477 and Y477-E324-R397, as well as other residues involved in arm 1 interactions Y473, Y327, H323 was shown. Distances between resides involved in the interaction network was shown. All panels show the same ligand binding pocket from different angles. Incut boxes in panels a) - c) shows a zoomed-out view of the scene. Some residues were made translucent for ease of visualization: in b) Residues 437-451; c) Residues 310-322. In c), NCoA2 peptide bound to the PPARγ LBD was hidden for visual clarity. Exact colour names used in Pymol is given in parenthesis.

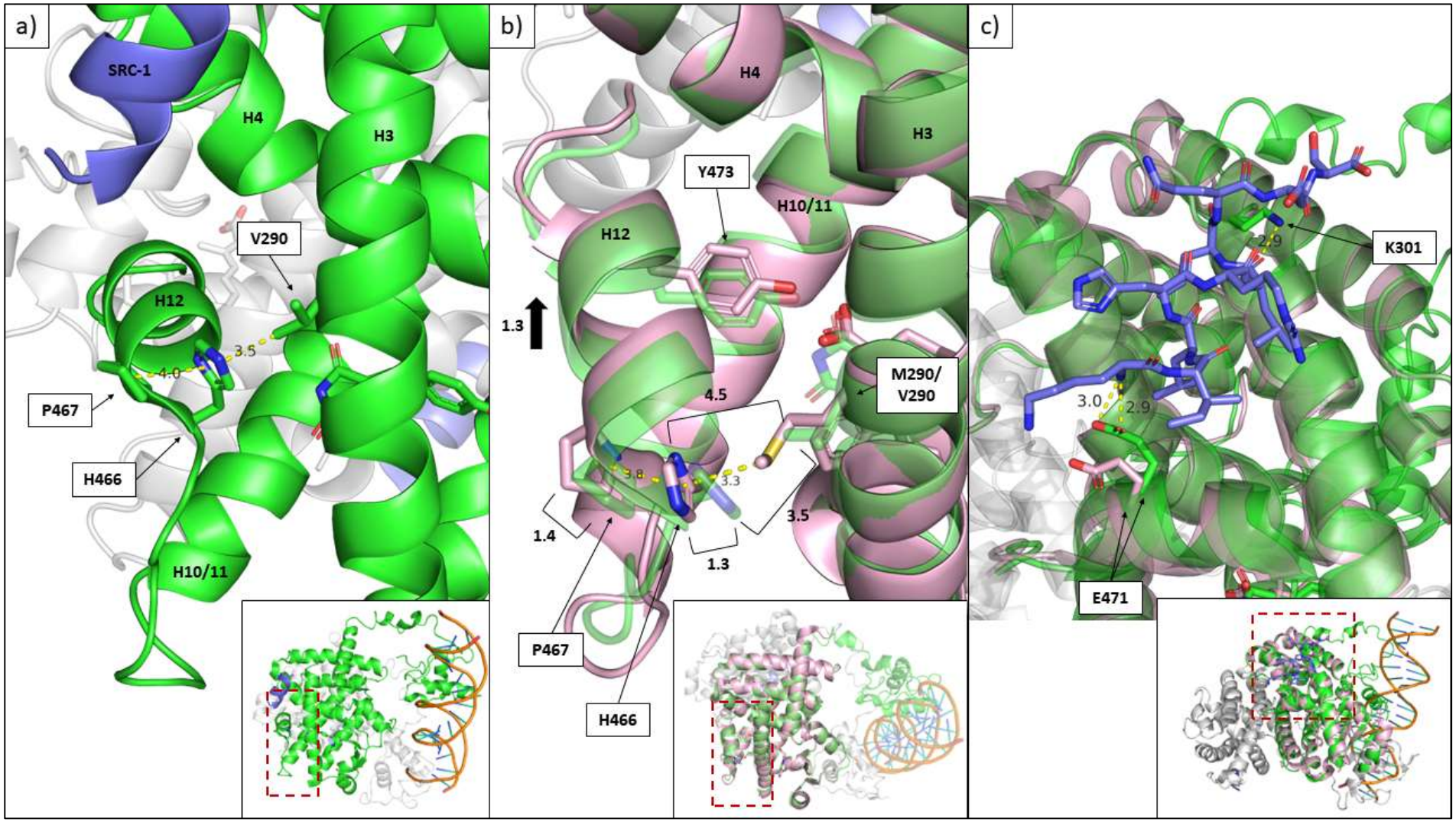
a)
SRC-1
H4
H3
V290
H12
3.5
4.0
P467
H466
H10/11
b)
H4
H3
Y473
H10/11
H12
1.3
M290/
V290
4.5
3.8
3.3
3.5
1.4
1.3
P467
H466
c)
2.9
K301
3.0
2.9
E471

Figure 7.2. **Interaction network involving residues V290 and P467.** a-c) The full-length structure of 3DZY, including the PPARγ subunit (in green), the RXRα subunit (in grey 90), the nuclear receptor coactivator 2 (NCoA2) peptides (in slate), ligands Rosiglitazone and 9-retinoic acid and DNA (in orange) was presented. a) Side chains of residues V290, H466 and P467 and distances between the residues were shown. b) The structure of PPARγ LBD with the V290M mutation (PDB ID: 7AHJ) overlayed onto the PPARγ LBD portion of structure 3DZY (in green, translucent). Distances between residues V290, H466 and P467 were shown in yellow dotted lines. Several measurements were shown in brackets: between V290 of 3DZY and H466 of both 3DZY and 7AHJ, between H466 of 3DZY and 7AHJ, and between P467 of 3DZY and 7AHJ. An additional measurement was taken between the Cα of Residue 472 of both 3DZY and 7AHJ, represented by the black arrow. c) NCoA2 peptide bound to the PPARγ LBD was shown in stick representation and residues E471 and K301 of 3DZY and 7AHJ, involved in coactivator interactions, were shown. Distances between these residues and the coactivator peptide was shown for 3DZY. All structures were aligned to 5YCP. Some residues were made translucent for ease of visualization: in b) PPARγ subunit including side chains; c) 3DZY and 7AHJ. In b) NCoA2 peptide bound to the PPARγ LBD was hidden for visual clarity. Exact colour names used in Pymol is given in parenthesis.

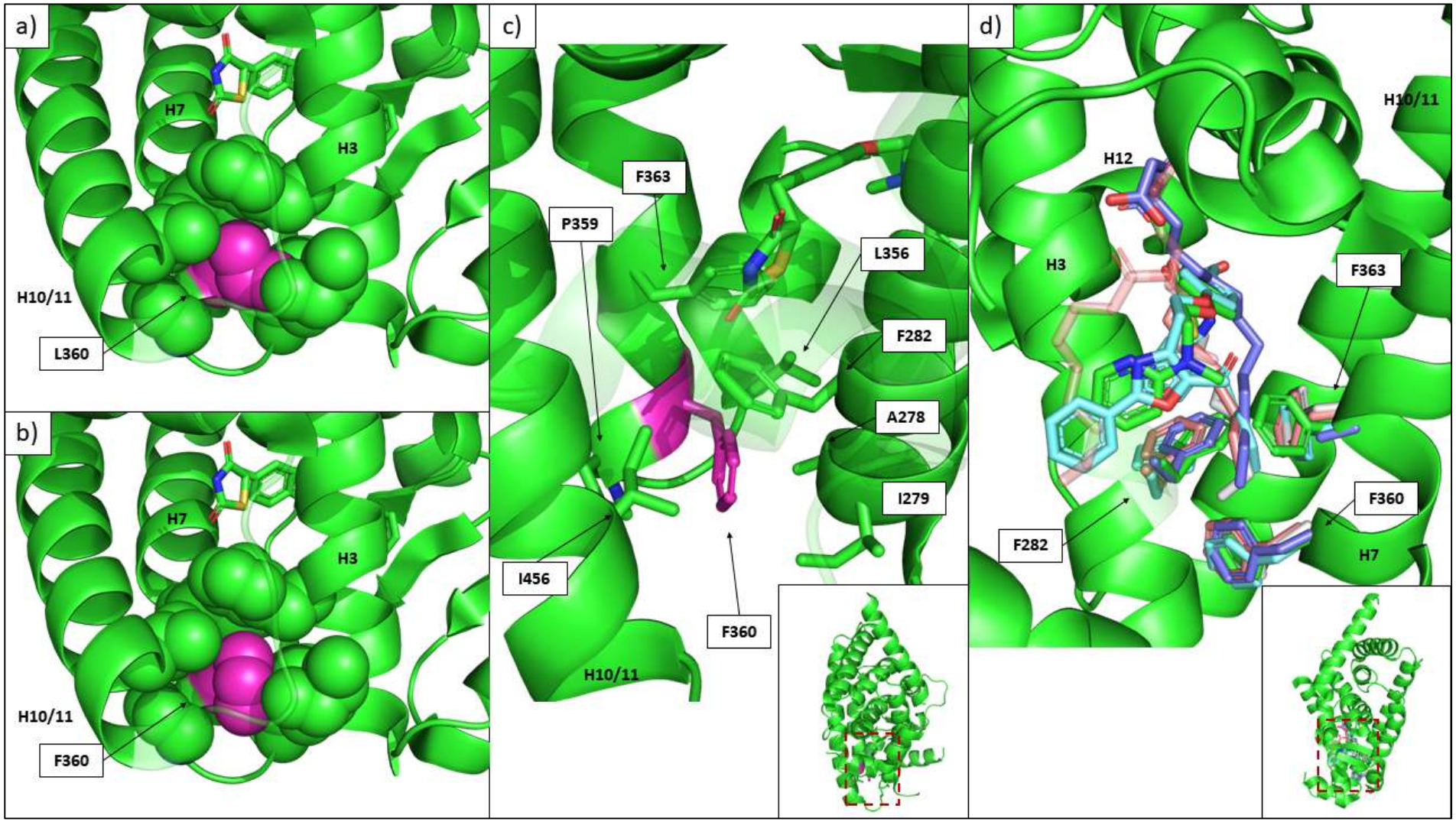
a)
H7
H3
H10/11
L360
b)
H7
H3
H10/11
F360
c)
F363
P359
L356
F282
A278
I279
I456
F360
H10/11
d)
H10/11
H12
H3
F363
F282
F360
H7

Figure 7.3. **Residue F360 and interactions with surrounding amino acid side chains.** a-d) The PPARγ LBD of 5YCP was shown in green. a) The view of the 5YCP ligand binding pocket with H12 facing the viewer. Residue 360 was mutated to leucine using mutagenesis in Pymol (in magenta). Residues L456, P359, L356, F282, I279 and A278 were represented with spheres. b) The same parameters as a), but without the mutation at residue F360 (in magenta). c) The same parameters as b), but with residue sidechains represented as sticks. d) The PPARγ LBD of 5YCP was shown in green, with residue sidechains of F282, F360 and F363 shown. 5YCP was overlayed with the ligands of structures 7AHJ (Farglitazar, in aquamarine), 4EM9 (nonanoic acid, in Salmon), 3U9Q (decanoic acid, in grey 90) and F363A_L (3-oxopalmitic acid in violet-purple) as well as the side chains of residues F282, F360 and F363 or A363. All structures were aligned to 5YCP. Incut boxes in panels c) and d) shows a zoomed-out view of the scene. Some residues were made translucent for ease of visualization: in a) and b) Residues 460-465; c) Residues 464-477; d) Residue F282 and the arm2 and arm 3 binding ligand molecules of 4EM9 (in Salmon). In d), residues 246-249 and 336-353 of 5YCP was hidden for visual clarity. Exact colour names used in Pymol is given in parenthesis.

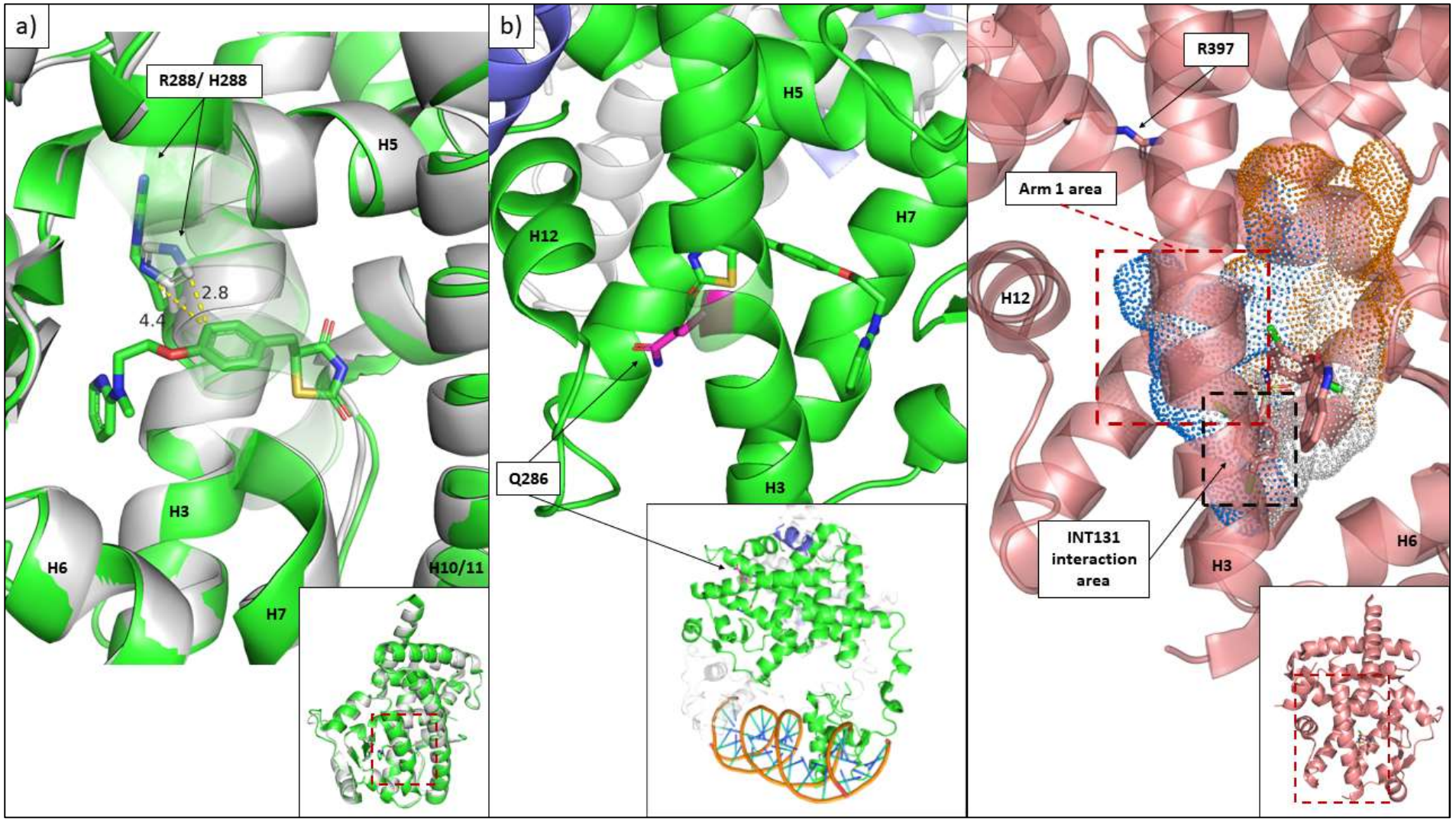

Figure 7.4. **Interactions involving mutations R288H, Q286P and INT131.** a) The PPARγ LBD of 7E2O (in grey 90) containing the R288H mutation overlaid onto 5YCP (in

green) with H7 facing the viewer. Residue 288 was shown in sticks. Distances between residue 288 of 7E2O and 5YCP and Rosiglitazone of 5YCP was measured. b) The PPARγ LBD subunit (in green) of structure 3DZY (RXRα in grey90 and DNA in orange) with H3 facing the viewer. Side chain of residue Q286 was shown (in magenta). c) The PPARγ LBD of 3FUR with H3 facing the viewer. The ligand binding pocket cavity was highlighted, with arms 1-3 coloured (in marine, white and orange respectively). Sidechain of residue Q286 was shown. Red dotted box denotes the arm 1 area of the ligand binding pocket, black dotted box denotes the area of arm 1 where INT131 interacts. Incut boxes in panels shows a zoomed-out view of the scene. All structures were aligned to 5YCP. Some residues were made translucent for ease of visualization: In a) Residues 330-331 and 365-373; b) Residue 287; c) 3FUR. Exact colour names used in Pymol is given in parenthesis.

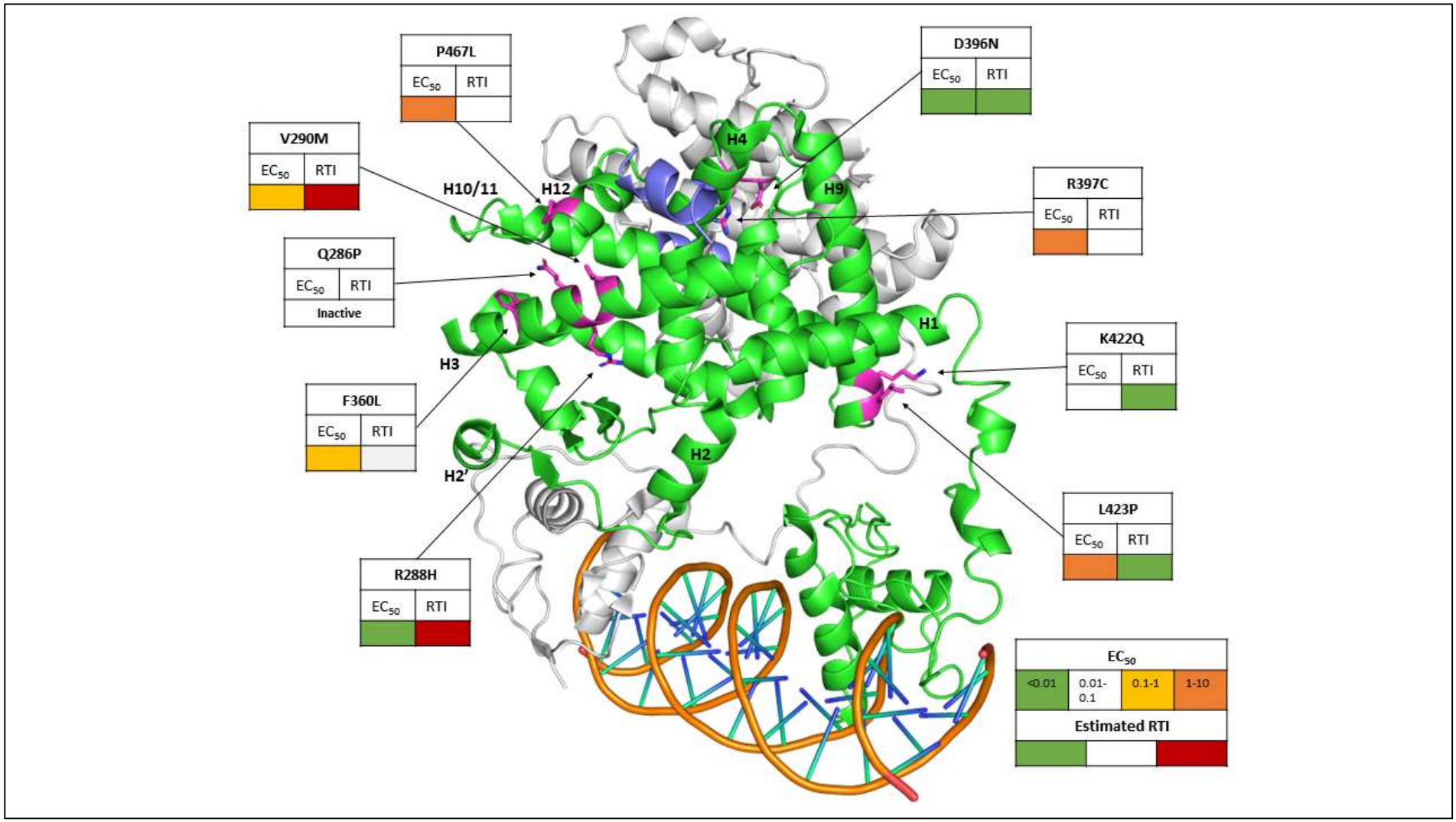
P467L
EC50
RTI
D396N
EC50
RTI
V290M
EC50
RTI
H4
H10/11
H12
H9
R397C
EC50
RTI
Q286P
EC50
RTI
Inactive
H1
K422Q
EC50
RTI
H3
F360L
EC50
RTI
H2
H2'
L423P
EC50
RTI
R288H
EC50
RTI
EC50
<0.01
0.01-0.1
0.1-1
1-10
Estimated RTI

1268

Figure 8.1. **Summary of clinical scanning mutations.** The full-length structure of 3DZY, including the PPARγ subunit (in green), the RXRα subunit (in grey 90), the nuclear receptor coactivator 2 (NCoA2) peptides (in slate), ligands Rosiglitazone and 9-retinoic acid and DNA (in orange) was presented with H3 of PPARγ facing the viewer. Side chains of residues with clinical significance investigated in this study was shown (in magenta). Each residue is labelled with a box containing information on the residue and mutation, changes in EC_{50} and relative transcriptional induction (RTI). Colours correspond to figure legend given in the bottom right corner. Estimated RTI refers to the combination of: RTI as calculated from the experiments and information on protein expression changes from the western blots. Green – increased, white – no change, red – decreased.

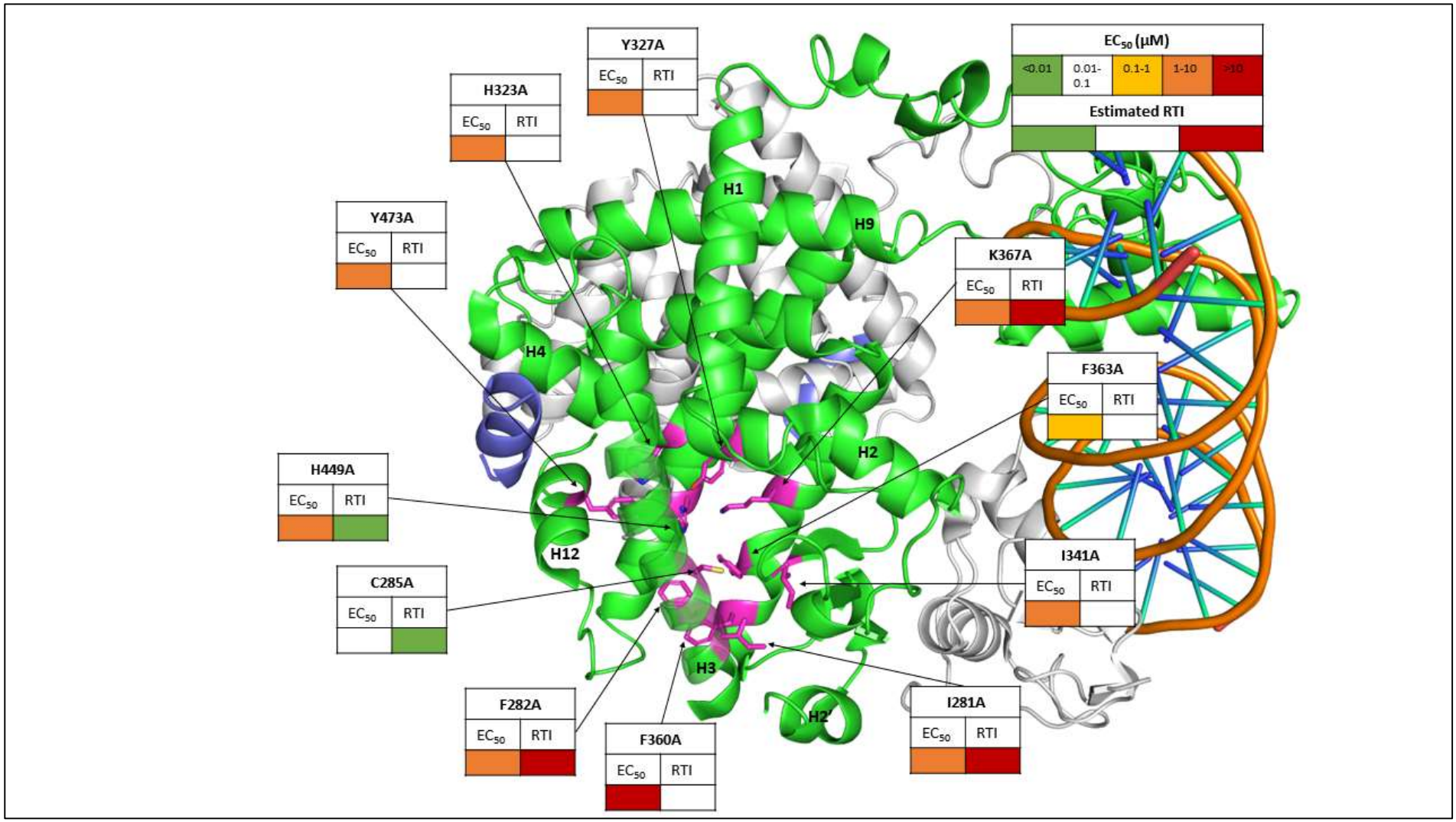
EC50 (μM)
<0.01
0.01-0.1
0.1-1
1-10
>10
Estimated RTI
Y327A
EC50 RTI
H323A
EC50 RTI
Y473A
EC50 RTI
K367A
EC50 RTI
F363A
EC50 RTI
H449A
EC50 RTI
C285A
EC50 RTI
I341A
EC50 RTI
F282A
EC50 RTI
F360A
EC50 RTI
I281A
EC50 RTI
H1
H9
H4
H2
H12
H3
H2'

1276

Figure 8.2. **Summary of alanine scanning mutations.** The full-length structure of 3DZY, including the PPARγ subunit (in green), the RXRα subunit (in grey 90), the nuclear receptor coactivator 2 (NCoA2) peptides (in slate), ligands Rosiglitazone and 9-retinoic acid and DNA (in orange) was presented with H3 of PPARγ facing the viewer. Side chains of residues investigated by alanine scanning was shown (in magenta). Each residue is labelled with a box containing information on the residue and mutation, changes in EC_{50} and relative transcriptional induction (RTI). Colours correspond to figure legend given in the top right corner. Estimated RTI refers to the combination of: RTI as calculated from the experiments and information on protein expression changes from the western blots. Green – increased, white – no change, red – decreased.

6. References

Agarwal, A. K. & Garg, A. (2002) A Novel Heterozygous Mutation in Peroxisome Proliferator-Activated Receptor-γ Gene in a Patient with Familial Partial Lipodystrophy. *The Journal of Clinical Endocrinology & Metabolism.* 87 (1), 408-408. doi: 10.1210/jcem.87.1.8290.

Barroso, I., Gurnell, M., Crowley, V. E. F., Agostini, M., Schwabe, J. W., Soos, M. A., Maslen, G. L., Williams, T. D. M., Lewis, H., Schafer, A. J., Chatterjee, V. K. K. & O'Rahilly, S. (1999) Dominant negative mutations in human PPARγ associated with severe insulin resistance, diabetes mellitus and hypertension. *Nature.* 402 (6764), 880-883. doi: 10.1038/47254.

Broekema, M. F., Savage, D. B., Monajemi, H. & Kalkhoven, E. (2019) Gene-gene and gene-environment interactions in lipodystrophy: Lessons learned from natural PPARγ mutants. *Biochimica et Biophysica Acta (BBA) - Molecular and Cell Biology of Lipids.* 1864 (5), 715-732. doi: 10.1016/j.bbalip.2019.02.002.

Bruning, J. B., Chalmers, M. J., Prasad, S., Busby, S. A., Kamenecka, T. M., He, Y., Nettles, K. W. & Griffin, P. R. (2007) Partial Agonists Activate PPARγ Using a Helix 12 Independent Mechanism. *Structure.* 15 (10), 1258-1271. doi: 10.1016/j.str.2007.07.014.

Brunmeir, R. & Xu, F. (2018) Functional Regulation of PPARs through Post-Translational Modifications. *International Journal of Molecular Sciences.* 19 (6), 1738. doi: 10.3390/ijms19061738.

Cheng, H. S., Tan, W. R., Low, Z. S., Marvalim, C., Lee, J. Y. H. & Tan, N. S. (2019) Exploration and Development of PPAR Modulators in Health and Disease: An Update of Clinical Evidence. *International Journal of Molecular Sciences.* 20 (20), 5055. doi: 10.3390/ijms20205055.

Choi, J. H., Banks, A. S., Kamenecka, T. M., Busby, S. A., Chalmers, M. J., Kumar, N., Kuruvilla, D. S., Shin, Y., He, Y., Bruning, J. B., Marciano, D. P., Cameron, M. D., Laznik, D., Jurczak, M. J., Schürer, S. C., Vidović, D., Shulman, G. I., Spiegelman, B. M. & Griffin, P. R. (2011) Antidiabetic actions of a non-agonist PPARγ ligand blocking Cdk5-mediated phosphorylation. *Nature.* 477 (7365), 477-481. doi: 10.1038/nature10383.

Chua, B. S. K. & Bruning, J. B. (2021) PPARα and δ Ligand Design: Honing the Traditional Empirical Method with a More Holistic Overview. In: Badr, M.Z. (ed.) *Nuclear Receptors.* Cham, Springer International Publishing, pp. 111-178.

Diezko, R. & Suske, G. (2013) Ligand Binding Reduces SUMOylation of the Peroxisome Proliferator-activated Receptor γ (PPARγ) Activation Function 1 (AF1) Domain. *PLoS ONE.* 8 (6), e66947. doi: 10.1371/journal.pone.0066947.

Dubois, V., Eeckhoute, J., Lefebvre, P. & Staels, B. (2017) Distinct but complementary contributions of PPAR isotypes to energy homeostasis. *Journal of Clinical Investigation.* 127 (4), 1202-1214. doi: 10.1172/JCI88894.

Egawa, D., Ogiso, T., Nishikata, K., Yamamoto, K. & Itoh, T. (2021) Structural Insights into the Loss-of-Function R288H Mutant of Human PPARγ. *Biological and Pharmaceutical Bulletin.* 44 (9), 1196-1201. doi: 10.1248/bpb.b21-00253.

Frkic, R. L., Chua, B. S., Shin, Y., Pascal, B. D., Novick, S. J., Kamenecka, T. M., Griffin, P. R. & Bruning, J. B. (2018) Structural and Dynamic Elucidation of a Non-acid PPARγ Partial Agonist: SR1988. *Nuclear Receptor Research.* 5. doi: 10.11131/2018/101350.

Garrido Ruiz, D., Sandoval-Perez, A., Rangarajan, A. V., Gunderson, E. L. & Jacobson, M. P. (2022) Cysteine Oxidation in Proteins: Structure, Biophysics, and Simulation. *Biochemistry.* 61 (20), 2165-2176. doi: 10.1021/acs.biochem.2c00349.

Gross, B., Pawlak, M., Lefebvre, P. & Staels, B. (2017) PPARs in obesity-induced T2DM, dyslipidaemia and NAFLD. *Nature Reviews Endocrinology.* 13 (1), 36-49. doi: 10.1038/nrendo.2016.135.

Gupta, R. A., Sarraf, P., Mueller, E., Brockman, J. A., Prusakiewicz, J. J., Eng, C., Willson, T. M. & DuBois, R. N. (2003) Peroxisome Proliferator-activated Receptor γ-mediated Differentiation. *Journal of Biological Chemistry.* 278 (25), 22669-22677. doi: 10.1074/jbc.M300637200.

Hegele, R. A., Cao, H., Frankowski, C., Mathews, S. T. & Leff, T. (2002) *PPARG* F388L, a Transactivation-Deficient Mutant, in Familial Partial Lipodystrophy. *Diabetes.* 51 (12), 3586-3590. doi: 10.2337/diabetes.51.12.3586.

Jeninga, E. H., Van Beekum, O., Van Dijk, A. D. J., Hamers, N., Hendriks-Stegeman, B. I., Bonvin, A. M. J. J., Berger, R. & Kalkhoven, E. (2007) Impaired Peroxisome Proliferator-Activated Receptor γ Function through Mutation of a Conserved Salt Bridge (R425C) in Familial Partial Lipodystrophy. *Molecular Endocrinology.* 21 (5), 1049-1065. doi: 10.1210/me.2006-0485.

Kilu, W., Merk, D., Steinhilber, D., Proschak, E. & Heering, J. (2021) Heterodimer formation with retinoic acid receptor RXRα modulates coactivator recruitment by peroxisome proliferator-activated receptor PPARγ. *Journal of Biological Chemistry.* 297 (1), 100814. doi: 10.1016/j.jbc.2021.100814.

Lebovitz, H. E. (2019) Thiazolidinediones: the Forgotten Diabetes Medications. *Current Diabetes Reports.* 19 (12), 151. doi: 10.1007/s11892-019-1270-y.

Lefterova, M. I., Haakonsson, A. K., Lazar, M. A. & Mandrup, S. (2014) PPARγ and the global map of adipogenesis and beyond. *Trends in Endocrinology & Metabolism.* 25 (6), 293-302. doi: 10.1016/j.tem.2014.04.001.

Lehmann, J. M., Moore, L. B., Smith-Oliver, T. A., Wilkison, W. O., Willson, T. M. & Kliewer, S. A. (1995) An Antidiabetic Thiazolidinedione Is a High Affinity Ligand for Peroxisome Proliferator-activated Receptor γ (PPARγ). *Journal of Biological Chemistry.* 270 (22), 12953-12956. doi: 10.1074/jbc.270.22.12953.

Life Technologies (2010) *TmTool Quick Set-Up Guide.* Available at: https://www.thermofisher.com/search/results?query=tmtool&persona=DocSupport&refinementAction=true&filter=document.result_type_s%3AManuals%20%26%20Protocols [Accessed 04 April 2023].

Liu, H. & Naismith, J. H. (2008) An efficient one-step site-directed deletion, insertion, single and multiple-site plasmid mutagenesis protocol. BMC Biotechnol. 8, 91. doi: 10.1186/1472-6750-8-91.

Ludtke, A., Buettner, J., Schmidt, H. H.-J. & Worman, H. J. (2007) New PPARG mutation leads to lipodystrophy and loss of protein function that is partially restored by a synthetic ligand. *Journal of Medical Genetics.* 44 (9), e88-e88. doi: 10.1136/jmg.2007.050567.

Majithia, A. R., Tsuda, B., Agostini, M., Gnanapradeepan, K., Rice, R., Peloso, G., Patel, K. A., Zhang, X., Broekema, M. F., Patterson, N., Duby, M., Sharpe, T., Kalkhoven, E., Rosen, E. D., Barroso, I., Ellard, S., Kathiresan, S., O'Rahilly, S., Chatterjee, K., Florez, J. C., Mikkelsen, T., Savage, D. B. & Altshuler, D. (2016) Prospective functional classification of all possible missense variants in PPARG. *Nature Genetics.* 48 (12), 1570-1575. doi: 10.1038/ng.3700.

Mosure, S. A., Munoz-Tello, P., Kuo, K.-T., MacTavish, B., Yu, X., Scholl, D., Williams, C. C., Strutzenberg, T. S., Bass, J., Brust, R., Deniz, A. A., Griffin, P. R. & Kojetin, D. J. (2022) *Structural basis of interdomain communication in PPARγ*. Biochemistry. [Accessed 2023-06-22 13:28:41]

Nolte, R. T., Wisely, G. B., Westin, S., Cobb, J. E., Lambert, M. H., Kurokawa, R., Rosenfeld, M. G., Willson, T. M., Glass, C. K. & Milburn, M. V. (1998) Ligand binding and co-activator assembly of the peroxisome proliferator-activated receptor-γ. *Nature.* 395 (6698), 137-143. doi: 10.1038/25931.

Ohshima, T., Koga, H. & Shimotohno, K. (2004) Transcriptional Activity of Peroxisome Proliferator-activated Receptor γ Is Modulated by SUMO-1 Modification. *Journal of Biological Chemistry.* 279 (28), 29551-29557. doi: 10.1074/jbc.M403866200.

Pascual, G., Fong, A. L., Ogawa, S., Gamliel, A., Li, A. C., Perissi, V., Rose, D. W., Willson, T. M., Rosenfeld, M. G. & Glass, C. K. (2005) A SUMOylation-dependent pathway mediates transrepression of inflammatory response genes by PPAR-γ. *Nature.* 437 (7059), 759-763. doi: 10.1038/nature03988.

Penvose, A., Keenan, J. L., Bray, D., Ramlall, V. & Siggers, T. (2019) Comprehensive study of nuclear receptor DNA binding provides a revised framework for understanding receptor specificity. *Nature Communications.* 10 (1), 2514. doi: 10.1038/s41467-019-10264-3.

Reinhard, L., Mayerhofer, H., Geerlof, A., Mueller-Dieckmann, J. & Weiss, M. S. (2013) Optimization of protein buffer cocktails using Thermofluor. *Acta Crystallographica Section F Structural Biology and Crystallization Communications.* 69 (2), 209-214. doi: 10.1107/S1744309112051858.

Sarraf, P., Mueller, E., Smith, W. M., Wright, H. M., Kum, J. B., Aaltonen, L. A., De La Chapelle, A., Spiegelman, B. M. & Eng, C. (1999) Loss-of-Function Mutations in PPARγ Associated with Human Colon Cancer. *Molecular Cell.* 3 (6), 799-804. doi: 10.1016/S1097-2765(01)80012-5.

Shifera, A. S. & Hardin, J. A. (2010) Factors modulating expression of Renilla luciferase from control plasmids used in luciferase reporter gene assays. *Analytical Biochemistry.* 396 (2), 167-172. doi: 10.1016/j.ab.2009.09.043.

Uppenberg, J., Svensson, C., Jaki, M., Bertilsson, G., Jendeberg, L. & Berkenstam, A. (1998) Crystal Structure of the Ligand Binding Domain of the Human Nuclear Receptor PPARγ. *Journal of Biological Chemistry.* 273 (47), 31108-31112. doi: 10.1074/jbc.273.47.31108.

Weikum, E. R., Liu, X. & Ortlund, E. A. (2018) The nuclear receptor superfamily: A structural perspective: The Nuclear Receptor Superfamily. *Protein Science.* 27 (11), 1876-1892. doi: 10.1002/pro.3496.

Yi, P., Wang, Z., Feng, Q., Chou, C.-K., Pintilie, G. D., Shen, H., Foulds, C. E., Fan, G., Serysheva, I., Ludtke, S. J., Schmid, M. F., Hung, M.-C., Chiu, W. & O'Malley, B. W. (2017) Structural and Functional Impacts of ER Coactivator Sequential Recruitment. *Molecular Cell.* 67 (5), 733-743.e4. doi: 10.1016/j.molcel.2017.07.026.

1401 # 7. Supplementary figures

	C285A_A	C285A_R	F363A_A	F363A_L
Wavelength	0.9537Å	0.9537Å	0.9537Å	0.9537Å
Resolution range	35.86 - 1.86 (1.926 - 1.86)	43.76 - 2.0 (2.071 - 2.0)	38.48 - 1.87 (1.937 - 1.87)	45.82 - 1.95 (2.02 - 1.95)
Space group	C 1 2 1	C 1 2 1	C 1 2 1	C 1 2 1
Unit cell	93.1 61.1 118.3 90 103.1 90	92.7 60.3 117.9 90 104.0 90	93.3 60.7 118.6 90 103.4 90	92.8 60.4 118.2 90 103.5 90
Total reflections	377926 (38642)	290155 (30362)	361965 (34239)	325239 (33355)
Unique reflections	54510 (5392)	42128 (4153)	53458 (5296)	45761 (4459)
Multiplicity	6.9 (7.2)	6.9 (7.3)	6.8 (6.5)	7.1 (7.5)
Completeness (%)	99.90 (99.85)	98.18 (97.40)	99.80 (99.34)	98.17 (96.93)
Mean I/sigma(I)	25.62 (3.35)	12.55 (2.43)	13.94 (0.82)	10.55 (0.91)
Wilson B-factor	33.25	30.97	36.25	33.97
R-merge	0.03931 (0.5302)	0.106 (0.9139)	0.07746 (1.808)	0.1258 (2.082)
R-meas	0.04255 (0.5716)	0.1148 (0.9835)	0.08405 (1.969)	0.1357 (2.237)
R-pim	0.01614 (0.2123)	0.04343 (0.3616)	0.03228 (0.7651)	0.05052 (0.8128)
CC1/2	1 (0.928)	0.998 (0.818)	0.999 (0.443)	0.998 (0.422)
CC*	1 (0.981)	0.999 (0.948)	1 (0.783)	1 (0.77)
Reflections used in refinement	54485 (5384)	42118 (4152)	53411 (5267)	45748 (4453)
Reflections used for R-free	2794 (266)	2142 (204)	2692 (265)	2296 (218)
R-work	0.1681 (0.2222)	0.1894 (0.2619)	0.1955 (0.3404)	0.1957 (0.3237)
R-free	0.2058 (0.2488)	0.2287 (0.3236)	0.2273 (0.3731)	0.2136 (0.3518)
CC (work)	0.972 (0.924)	0.965 (0.861)	0.967 (0.729)	0.964 (0.658)
CC (free)	0.960 (0.872)	0.964 (0.724)	0.972 (0.593)	0.970 (0.630)
Number of non-hydrogen atoms	4821	4615	4550	4717

macromolecules	4449	4327	4296	4475
ligands	30	30	16	8
solvent	342	258	238	234
Protein residues	541	534	532	536
RMS (bonds)	0.018	0.004	0.005	0.005
RMS (angles)	1.38	0.59	0.69	0.8
Ramachandran favored (%)	97.18	98.46	98.46	96.56
Ramachandran allowed (%)	2.45	1.15	1.35	2.48
Ramachandran outliers (%)	0.38	0.38	0.19	0.95
Rotamer outliers (%)	2.12	2	2.42	2.9
Clashscore	8.36	3.81	3.81	5.02
Average B-factor	45.45	40.23	46.21	42.35
macromolecules	45.3	40.03	46.15	42.38
ligands	60.35	62.41	54.51	53.09
solvent	46.05	41	46.7	41.53
Number of TLS groups	13	1	1	1

1402 Supplementary table 1.1. Model statistics for the crystal structures of PPARγ mutants C285A_A,
1403 C285A_R, F363A_A and F363A_L.

1404

	H323A_A1	H323A_A2	H323A_A3	H449A_A1
Wavelength	0.9537Å	0.9537Å	0.9537Å	0.9537Å
Resolution range	40.88 - 2.15 (2.227 - 2.15)	45.83 - 2.35 (2.434 - 2.35)	45.77 - 1.8 (1.864 - 1.8)	44.62 - 2.21 (2.289 - 2.21)
Space group	C 1 2 1	C 1 2 1	C 1 2 1	C 1 2 1
Unit cell	93.5 61.5 119.1 90 102.6 90	93.0 61.2 119.0 90 102.8 90	92.9 60.9 118.5 90 103.0 90	93.6 60.9 118.6 90 102.1 90
Total reflections	249390 (24859)	187332 (18233)	417849 (42717)	209734 (21834)
Unique reflections	35607 (3497)	27416 (2722)	59873 (5941)	32794 (3272)
Multiplicity	7.0 (7.1)	6.8 (6.7)	7.0 (7.2)	6.4 (6.7)
Completeness (%)	98.55 (97.76)	99.83 (99.85)	99.89 (99.80)	99.09 (99.60)
Mean I/sigma(I)	10.20 (1.16)	7.21 (1.06)	15.98 (0.86)	13.06 (2.69)
Wilson B-factor	41.54	44.33	32.49	42.94
R-merge	0.1249 (1.355)	0.1713 (1.642)	0.07819 (2.23)	0.08123 (0.7547)
R-meas	0.1349 (1.461)	0.1854 (1.78)	0.08452 (2.402)	0.08853 (0.82)
R-pim	0.05051 (0.5439)	0.07036 (0.6814)	0.03181 (0.8867)	0.03472 (0.3169)
CC1/2	0.998 (0.575)	0.996 (0.424)	0.999 (0.419)	0.998 (0.869)
CC*	1 (0.854)	0.999 (0.772)	1 (0.769)	0.999 (0.964)
Reflections used in refinement	35589 (3494)	27407 (2719)	59828 (5929)	32709 (3265)
Reflections used for R-free	1708 (178)	1369 (137)	3010 (289)	1663 (181)
R-work	0.2056 (0.3199)	0.2048 (0.2999)	0.1795 (0.3308)	0.2052 (0.2657)
R-free	0.2393 (0.3572)	0.2575 (0.3480)	0.2167 (0.3509)	0.2433 (0.3134)
CC (work)	0.970 (0.757)	0.964 (0.670)	0.974 (0.694)	0.966 (0.866)
CC (free)	0.954 (0.594)	0.960 (0.527)	0.967 (0.654)	0.963 (0.831)
Number of non-hydrogen atoms	4493	4355	4749	4334
macromolecules	4343	4278	4383	4191
ligands	1	0	2	2

solvent	149	77	364	141
Protein residues	542	534	542	533
RMS (bonds)	0.003	0.002	0.007	0.002
RMS (angles)	0.56	0.45	0.79	0.41
Ramachandran favored (%)	97.56	95.8	97.55	97.51
Ramachandran allowed (%)	1.88	3.82	2.26	2.1
Ramachandran outliers (%)	0.56	0.38	0.19	0.38
Rotamer outliers (%)	1.71	2.14	1.07	0.46
Clashscore	2.88	3.71	4.56	3.6
Average B-factor	52.81	51.69	43.55	61.48
macromolecules	53.04	51.83	43.43	61.79
ligands	43.72	44.03	35.19	60.84
solvent	46.36	1	45.01	52.07
Number of TLS groups	1		16	13

Supplementary table 1.2. Model statistics for the crystal structures of PPARγ mutants H323A_A1, H323A_A2, H323A_A3 and H449A_A1.

	H449A_A2	K367A_A	K367A_R	K422Q_A1
Wavelength	0.9537Å	0.9537Å	0.9537Å	0.9537Å
Resolution range	45.8 - 2.1 (2.175 - 2.1)	36.08 - 2.08 (2.154 - 2.08)	45.52 - 2.3 (2.382 - 2.3)	46.14 - 2.28 (2.361 - 2.28)
Space group	C 1 2 1	C 1 2 1	C 1 2 1	C 1 2 1
Unit cell	92.8 60.0 118.3 90 103.4 90	93.1 61.4 118.5 90 102.5 90	93.2 61.8 119.2 90 102.3 90	93.8 61.6 120.0 90 102.2 90
Total reflections	257947 (25522)	266207 (24720)	203319 (18577)	197095 (18246)
Unique reflections	37230 (3695)	38979 (3849)	29680 (2952)	30705 (3045)
Multiplicity	6.9 (6.9)	6.8 (6.4)	6.9 (6.3)	6.4 (6.0)
Completeness (%)	99.93 (99.95)	98.78 (98.14)	99.81 (99.36)	98.90 (97.84)
Mean I/sigma(I)	13.18 (1.73)	13.37 (1.25)	11.25 (0.99)	6.75 (1.20)
Wilson B-factor	32.63	38.37	53.5	40.19
R-merge	0.1136 (1.052)	0.1107 (1.816)	0.09384 (2.028)	0.1589 (1.526)
R-meas	0.1229 (1.137)	0.12 (1.977)	0.1017 (2.206)	0.1731 (1.673)
R-pim	0.04651 (0.4298)	0.04584 (0.7731)	0.03872 (0.8601)	0.06757 (0.6735)
CC1/2	0.998 (0.68)	0.998 (0.525)	0.998 (0.432)	0.988 (0.496)
CC*	1 (0.9)	1 (0.83)	0.999 (0.777)	0.997 (0.814)
Reflections used in refinement	37220 (3693)	38954 (3843)	29652 (2938)	30437 (2995)
Reflections used for R-free	1855 (170)	1970 (195)	1496 (153)	1607 (159)
R-work	0.1912 (0.2871)	0.1889 (0.2947)	0.2050 (0.3482)	0.2143 (0.3136)
R-free	0.2328 (0.3468)	0.2333 (0.3278)	0.2407 (0.3588)	0.2535 (0.3334)
CC (work)	0.964 (0.804)	0.970 (0.748)	0.974 (0.648)	0.955 (0.689)
CC (free)	0.931 (0.717)	0.960 (0.821)	0.976 (0.536)	0.947 (0.561)
Number of non-hydrogen atoms	4615	4473	4250	4400
macromolecules	4340	4265	4136	4218
ligands	0	0	50	1

solvent	275	208	64	181
Protein residues	541	533	531	535
RMS (bonds)	0.002	0.002	0.002	0.003
RMS (angles)	0.5	0.5	0.48	0.49
Ramachandran favored (%)	97.19	96.37	95.39	96.95
Ramachandran allowed (%)	2.44	2.68	3.84	2.1
Ramachandran outliers (%)	0.38	0.96	0.77	0.95
Rotamer outliers (%)	1.08	1.56	2.59	1.81
Clashscore	3.23	3.64	5.19	3.34
Average B-factor	41.98	52.41	69.07	54.19
macromolecules	41.95	52.6	69.19	54.48
ligands	42.48	48.47	74.85	53.99
solvent	1	9	57.27	47.39
Number of TLS groups			13	12

Supplementary table 1.3. Model statistics for the crystal structures of PPARγ mutants H449A_A2, K367A_A, K367A_R and K422Q_A1.

	K422Q_A2	Y473A_A1	Y473A_A2	Y473A_A3
Wavelength	0.9537Å	0.9537Å	0.9537Å	0.9537Å
Resolution range	40.38 - 1.99 (2.061 - 1.99)	33.3 - 1.77 (1.833 - 1.77)	41.09 - 1.96 (2.03 - 1.96)	35.93 - 1.59 (1.647 - 1.59)
Space group	C 1 2 1	C 1 2 1	C 1 2 1	C 1 2 1
Unit cell	92.5 59.6 118.3 90 103.9 90	92.8 61.0 118.9 90 103.0 90	93.0 62.1 119.9 90 102.1 90	92.5 61.3 119.1 90 103.2 90
Total reflections	295221 (30955)	420715 (34877)	332745 (31032)	594207 (59940)
Unique reflections	43103 (4312)	63110 (6263)	48200 (4764)	87208 (8648)
Multiplicity	6.8 (7.2)	6.7 (5.6)	6.9 (6.5)	6.8 (6.9)
Completeness (%)	99.80 (99.88)	99.71 (99.08)	99.85 (100.00)	99.90 (99.95)
Mean I/sigma(I)	12.72 (0.97)	12.04 (0.85)	13.03 (2.30)	16.90 (1.75)
Wilson B-factor	37.73	28.39	33.21	22.89
R-merge	0.1001 (1.773)	0.08891 (1.429)	0.09102 (0.7998)	0.06218 (1.091)
R-meas	0.1085 (1.912)	0.09648 (1.58)	0.0986 (0.8701)	0.06736 (1.18)
R-pim	0.04147 (0.7092)	0.03704 (0.6627)	0.03751 (0.3389)	0.02566 (0.4445)
CC1/2	0.999 (0.462)	0.999 (0.608)	0.997 (0.766)	0.999 (0.642)
CC*	1 (0.795)	1 (0.87)	0.999 (0.931)	1 (0.884)
Reflections used in refinement	43091 (4310)	63072 (6252)	48178 (4764)	87197 (8648)
Reflections used for R-free	2154 (187)	3124 (305)	2378 (255)	4365 (418)
R-work	0.2059 (0.2867)	0.1895 (0.3323)	0.1826 (0.2517)	0.1824 (0.2514)
R-free	0.2275 (0.3090)	0.2282 (0.3697)	0.2212 (0.3168)	0.2130 (0.2782)
CC (work)	0.962 (0.730)	0.968 (0.760)	0.971 (0.850)	0.968 (0.824)
CC (free)	0.949 (0.644)	0.951 (0.686)	0.949 (0.775)	0.958 (0.776)
Number of non-hydrogen atoms	4356	4829	4767	4999
macromolecules	4230	4483	4460	4556
ligands	0	0	0	15

solvent	126	346	307	434
Protein residues	535	539	539	539
RMS (bonds)	0.003	0.01	0.007	0.007
RMS (angles)	0.6	1.03	0.82	0.88
Ramachandran favored (%)	96.75	97.36	97.16	98.31
Ramachandran allowed (%)	2.29	1.88	2.27	1.69
Ramachandran outliers (%)	0.96	0.75	0.57	0
Rotamer outliers (%)	1.84	2.03	2.07	1.01
Clashscore	4.89	3.54	4.13	6.96
Average B-factor	48.19	36.62	40.73	29.24
macromolecules	48.2	36.34	40.65	28.51
ligands	47.77	40.36	42.02	40.57
solvent	1	14	1	36.67
Number of TLS groups				1

Supplementary table 1.4. Model statistics for the crystal structures of PPARγ mutants K422Q_A2, Y473A_A1, Y473A_A2 and Y473A_A3.

	Y473A_A4
Wavelength	0.9537Å
Resolution range	40.26 - 1.64 (1.699 - 1.64)
Space group	C 1 2 1
Unit cell	92.7 61.6 119.6 90 102.6 90
Total reflections	545653 (52157)
Unique reflections	80586 (7986)
Multiplicity	6.8 (6.5)
Completeness (%)	99.89 (99.87)
Mean I/sigma(I)	22.14 (2.40)
Wilson B-factor	27.13
R-merge	0.04136 (0.6352)
R-meas	0.04485 (0.6909)
R-pim	0.01717 (0.2687)
CC1/2	1 (0.875)
CC*	1 (0.966)
Reflections used in refinement	80557 (7977)
Reflections used for R-free	4049 (386)
R-work	0.1807 (0.2456)
R-free	0.2097 (0.2753)
CC (work)	0.967 (0.891)
CC (free)	0.956 (0.795)
Number of non-hydrogen atoms	5076
macromolecules	4558
ligands	28

solvent	490
Protein residues	544
RMS (bonds)	0.008
RMS (angles)	0.81
Ramachandran favored (%)	98.13
Ramachandran allowed (%)	1.49
Ramachandran outliers (%)	0.37
Rotamer outliers (%)	1.24
Clashscore	3.37
Average B-factor	35.21
macromolecules	34.3
ligands	45.49
solvent	43.06
Number of TLS groups	1

1414 Supplementary table 1.5. Model statistics for the crystal structures of PPARγ mutants Y473A_A4.

1415

Chapter 7

Summary and future directions

7.1 Summary

In this thesis, we explored PPARγ ligands and the various principles of ligand design, to synthesize new ligands that can activate PPARγ safely.

7.1.1 Chapter 2

Since cross selectivity was hypothesized to cause side effects with PPAR activation, we started by studying PPAR selectivity. In this book chapter, ligand bound PPARα and δ structures from the Protein Data Bank (PDB) were compiled and analysed to determine the structural basis for its selectivity and potency. The Y-shaped ligand binding pocket was divided into three areas and designated Arms 1-3. Based on the structures and the unique configuration of amino acid residues of each PPAR subtype, we suggested design principles that could increase selectivity for a single subtype. This paper also highlighted ways in which in-silico techniques were used to scan and shortlist compounds or inform compound design. Techniques that evaluated the pharmacokinetic and pharmacodynamic properties of prospective compounds were also mentioned, such as cell permeability tests, metabolite analysis and cross reactivity tests. These tests are important as it increases the odds of success in preclinical and clinical trials. Finally, other confounding factors are also mentioned, such as the individual mutations in PPAR, post-translational modifications, binding of coregulator and transport proteins.

7.1.2 Chapter 3

Due to safety issues with PPARγ selective full agonists, there has been a pivot towards developing partial agonists that do not strongly activate transcriptional activity. In this paper, the partial agonist SR1988 was designed and its properties were characterised. This ligand was designed specifically to reduce transcriptional activation of PPARγ by introducing a non-acidic head moiety. This non-acidic head moiety also prevents ligand degradation by the liver, which increases the bioavailability of SR1988. This ligand displayed a four-fold decrease in EC_{50} as well as 45% transactivation activity relative to Rosiglitazone (defined as 100%), indicating that ligands could bind to PPARγ with high affinity, without high transactivation induction. SR1664, previously shown to have anti-diabetic effects in mice, was used as a negative control (Choi et al., 2011). X-ray crystallographic studies show that SR1988 made contacts with arms 2 and 3, forming hydrogen bonds to T327 and S289 on H5 and 3 respectively. Like a previously examined ligand SR2067, the non-acidic head moiety formed hydrophobic interactions with residues on H11 and H12 instead of hydrophilic interactions. This was supported by data from Hydrogen/Deuterium Exchange (HDX) experiments, which showed that SR1988 increased stabilization of H2, 3, 6 and 7 compared to H12. SR1988 did increase stabilization of the H10/11 and 12 regions like full agonist Rosiglitazone, but not to the same extent. Future studies should focus on investigating the differences between partial agonists and antagonists in humans to determine which ligand activity profile is more beneficial for treatment of metabolic conditions.

7.1.3 Chapter 4

Both the PPAR and COX2/LOX pathways share similar endogenous ligands and are involved in similar physiological responses. In this collaboration, a series of triazolyl-thiazolidinedione/rhodanine hybrid compounds were designed to target PPARγ as well as inhibit COX-2/LOX receptors which will be referred to as Multi Target Directed Ligands (MTDLs). First, an In silico molecular docking study was conducted to evaluate the MTDL compounds. Then, in vitro assays were used to determine the inhibition of COX1, COX2 and 15-LOX by the MTDL compounds. All MTDL compounds were sufficiently potent compared to reference inhibitors and more selective for inhibiting COX2 than COX1. In addition, the compounds were also comparatively potent compared to reference compounds in 15-LOX assays. Then, the MTDL compounds were shortlisted based on COX and LOX activities and was assessed for induction of glucose uptake with the rat hemi-diaphragm method. Of these compounds, 4b, 5e, 5b and 5g were further shortlisted, and were found to induce nuclear localization of PPARγ to a similar degree compared to Pioglitazone. In cell-based transactivation assays, the four compounds activated PPARγ to 25-40% of Pioglitazone. These two experiments indicated that the compounds were partial agonists but had the same insulin sensitizing activity as Pioglitazone. Further tests were conducted, such as induction of macrophage differentiation, expression of inflammatory cytokines as well as an in vivo anti-inflammatory assay in rats. The 4b bound structure of PPARγ was determined, showing predominant binding to Arm 2 of the PPARγ ligand binding pocket, supporting its observed activity profile as a partial agonist. Additional docking studies of the four compounds to the COX and LOX active site, as well as in silico pharmacokinetic studies were conducted showing favourable results. In summary, the compounds were shown to be promising candidates for further development. Future efforts should focus on validating the observed differential ligand effects of 4b and 5e in different animal and human cell models, to ensure that the effects are not model-specific and relevant to human physiology. Additionally, cross selectivity of the compounds (especially the sterically compact 4b) to other targets should be ruled out with other in vitro experiments.

7.1.4 Chapter 5

PPARγ agonism comes with side effects that might be ligand specific. In an effort to find new ligands with different activity profiles and chemical spaces, Atomwise uses machine learning algorithms to scan chemical libraries for potential binders to protein targets. In this paper, Atomwise's two-step, machine learning-based strategy was used to select ligands with predicted activity at the PPARγ from a wide range of chemicals. This set of compounds were first screened using a thermal shift assay (TSA) to identify strong stabilizers of PPARγ. Despite optimization, this approach did not work. In silico molecular docking study suggested that SYPRO™ Orange could bind to PPARγ and interfere with the TSA. Next, the compounds were instead screened with the dual luciferase assay (DLA). The compounds displayed a range of activities at 10μM, and the compounds with the highest potencies of

each ligand activity profile were shortlisted for additional tests. Based on activity at four different concentration points, compounds 3, 19, 42, 79 were selected for investigation. A full dose response curve suggested that compounds 3 and 19 were full agonists, 42 was a partial agonist and 79 was an inverse agonist. Further investigation with a ligand unresponsive negative control reporter plasmid revealed that inverse agonism of 79 was independent of the PPARγ LBD. Closer examination revealed that dose response curves of 19 and 79 were affected by changes in Renilla reporter values. Molecular docking studies were conducted revealing multiple configurations for compounds 3, 19, 42 and 79 in the PPARγ ligand binding pocket. In summary, compound 3 represents a promising lead as an atypical PPARγ agonist, although the other compounds not investigated in this study are still worth evaluating. Future studies should confirm the validity of current hits with other in vitro techniques such as surface plasmon resonance (SPR) before reevaluating the other Atomwise compounds, followed by optimization of the chemical structure of compound hits.

7.1.5 Chapter 6

In the previous chapters, we looked at the structural determinants of PPAR binding and activation by studying interactions of different ligands to PPAR. In this chapter, we investigated the structural determinants of PPAR binding and activation by examining mutations in the PPAR LBD and its effects on binding to the same ligand. Since mutations in PPAR were hypothesized to be fairly common, we studied the effects of several clinical mutations on transcription activation in response to ligands. Residues were also mutated using alanine scanning to estimate the contribution of an amino acid residue to the binding of a ligand. Mutagenesis of WT plasmid constructs was first conducted to obtain plasmids with mutations to PPARγ LBD for protein expression and for the cell-based assays. Next, a Thermostability assay (TSA) was used to estimate the effects of mutations on overall protein stability. The assay revealed that mutations change the thermostability of PPARγ LBD. The TSA yielded acceptable results for this application but did not work as intended in Chapter 5. This might be due to a difference in buffer conditions – in Chapter 5, PPARγ LBD protein was purified in buffer S (20 mM Tris pH 8.0, 150 mM NaCl, 1 mM DTT), while in Chapter 6, PPARγ LBD protein was purified in buffer B (20 mM Tris pH 8.0, 500 mM NaCl, 250 mM imidazole, 2 mM BME). BME could possibly form adducts with residue C285 in the binding pocket of PPARγ LBD, preventing the binding of SYPRO orange to non-denatured PPARγ LBD protein. Then, dose response curves of each PPARγ mutation in response to Rosiglitazone was obtained. The mutations affected the potency as well as the efficacy of Rosiglitazone to varying degrees, compared to wildtype (WT) PPARγ protein. Notably, some mutations might have increased the potency and/or efficacy of Rosiglitazone (R288H, D396N, K422Q). In addition, K367A seemed to be constitutively active, while Q286P was inactive. A western blot was conducted to ensure that increase in efficacy was not due to an increase in protein expression. Our results revealed that protein expression varied across the different mutant constructs. In some cases,

protein expression supported the increase/decrease of efficacy seen in some mutant PPARγ proteins, in others, protein expression disputed observed changes in efficacy. Importantly, the western blot results were not from the same biological replicate as the gene transcription assays, it is unknown if protein expression varies across biological replicates. After this, a subset of PPARγ mutants were induced with ligands of different activity profiles. Notably for R397C, INT131 had higher activity than Rosiglitazone at lower concentrations, suggesting that R397C had less of an effect on the potency of INT131 than Rosiglitazone. P467L on the other hand affected potency of INT131 more than Rosiglitazone. Protein crystals of K422Q, Y473A, H449A, K367A, F363A, H323A and C285A were obtained. Minor differences were noted between the PPARγ mutants and published structures, including differences in the Ω loop, shifts in H2', H12 in certain structures. Some ligand bound structures were obtained - Rosiglitazone bound C285A and K367A and a fatty acid bound structure of F363A. Analysis did not reveal major differences compared to published structures, suggesting that changes in transcription activity were likely not due changes in ligand binding pose in the ligand binding pocket. By analysing previously published structures, some structural mechanisms affecting the whole PPAR LBD were suggested to exaplain the changes in potency and efficacy of PPARγ mutants. Changes in potency and efficacy due to alanine scanning mutations might also affect the structure of PPARγ, so its use in ligand binding assays must be carefully considered. In summary, our analysis revealed differences in potency and efficacy between PPARγ mutants and PPARγ wildtype, but further experiments are required to determine the molecular basis for this difference. Future experiments could examine stability of mutations using HDX or investigate the ability of PPARγ mutants to recruit coregulators.

7.2 Future directions

Trends in the types of PPAR ligands being investigated in publications are largely dictated by successes or failures in clinical trials. Initially, after Rosiglitazone was first described, studies focused on characterising increasingly potent PPARγ ligands (Damkaci et al., 2022). Then after long term studies revealed safety issues with Rosiglitazone and the subsequent action by the FDA, studies shifted away from full activation of PPARγ and towards ligands with different activity profiles (Frkic et al., 2018, Hong et al., 2018). The pivot towards partial agonism was in part due to the findings by Choi et al. (2010) which correlated the insulin sensitization effects of PPARγ activation with the phosphorylation of S245 (PPARγ1) and not the full transcriptional activation of PPARγ (Choi et al., 2011). The dual agonism of PPARγ/α aimed to alleviate the safety issues of full PPARγ activation by simultaneously activating the fat catabolic activity of PPARα, was also met with a range of safety issues and many compounds dropped out of clinical trials (Kalliora and Drosatos 2020). The lack of success with partial agonism and dual agonism then led to the development of antagonists or

inverse agonists (Frkic et al., 2018). Other ligand types, such as multitarget ligands was devised to deal with multifactorial diseases (Tassopoulou et al., 2022).

Thus in this context, it was very surprising that Saroglitazar, a dual PPARγ/α agonist with full activity at both receptors, was successfully licensed for T2D treatment (Krishnappa et al., 2020). Saroglitazar did not exhibit the same side effects observed with traditional PPARγ full agonists even though it is a full agonist for the PPARγ subtype, and had a good safety profile despite being a PPAR γ/α dual agonist (Lebovitz 2019, Krishnappa et al., 2020). Whether or not Saroglitazar will prove to be as safe and efficacious for non-asian populations (specifically for T2D) or reveal unanticipated side effects after long-term use remains to be seen. One way forward would be to delineate the biochemical pathways under the control of the PPARs across different cell types, to fully appreciate the mechanisms behind the side effects seen with PPAR activation. Clarifying the genes under the control of the different PPAR subtypes in the context of interaction with different cofactors is also paramount. This could possibly allow us to differentiate between on and off-target side effects that are PPAR subtype specific or ligand specific, which would be invaluable in the decision of PPAR subtype(s) to target as well as the chosen activation profile of the prospective PPAR ligand.

Regardless, this is encouraging news since it demonstrates that the PPARs could still be exploited safely as a drug target for conditions outside of dyslipidemia, that side effects are indeed ligand specific, and that PPAR ligands with different activation profiles and subtype selectivity may still be viable (Dubois et al., 2017, Cheng et al., 2019). As such, over the course of this work, we explored how to design ligands to target the PPAR subtypes selectively and investigated PPARγ selective ligands with different activation profiles. However, to understand why side effects come with PPAR activation, we explored how mutations in PPAR changes its induction by ligands. One area that is currently not well understood is the structural arrangement of the full DNA bound, ligand-PPARγ-RXR-coregulator complex. Knowing how coregulators interact with PPARγ in 3D space could provide explanations for changes in the ligand induced activity of some PPARγ mutants that could not be explained by the crystal structures or direct effects on ligand binding. Importantly, this knowledge can inform ligand design, to bind to and stabilize certain areas of the PPARγ ligand binding pocket, so that ligand design can progress more rationally. In this area, some work has been done uncovering facets of this question, including how PPAR-RXR assembles in solution, how ligands affect dimerization and coregulator interaction, how ligands affect recruitment of different coactivator peptides and how the AF1 acts in the full length PPAR structure (Bernardes et al., 2012, Kilu et al., 2021, Mosure et al., 2022). Additionally, as interest in the application of AI in drug discovery increases, it is important to understand that not only is well designed in vitro experimental validation still required, it should take into consideration the nature of the target, in this case, the large hydrophobic binding pocket of the PPARs.

In conclusion, the work detailed in this thesis has provided novel ways of targeting PPAR, however more work must be done to understand PPAR biology and safely exploit the receptor in different diseases.

7.3 References

Bernardes, A., Batista, F. A. H., de Oliveira Neto, M., Figueira, A. C. M., Webb, P., Saidemberg, D., Palma, M. S. & Polikarpov, I. (2012) Low-Resolution Molecular Models Reveal the Oligomeric State of the PPAR and the Conformational Organization of Its Domains in Solution. *PLoS ONE.* 7 (2), e31852. doi: 10.1371/journal.pone.0031852.

Cheng, H. S., Tan, W. R., Low, Z. S., Marvalim, C., Lee, J. Y. H. & Tan, N. S. (2019) Exploration and Development of PPAR Modulators in Health and Disease: An Update of Clinical Evidence. *International Journal of Molecular Sciences.* 20 (20), 5055. doi: 10.3390/ijms20205055.

Choi, J. H., Banks, A. S., Estall, J. L., Kajimura, S., Boström, P., Laznik, D., Ruas, J. L., Chalmers, M. J., Kamenecka, T. M., Blüher, M., Griffin, P. R. & Spiegelman, B. M. (2010) Anti-diabetic drugs inhibit obesity-linked phosphorylation of PPARγ by Cdk5. *Nature.* 466 (7305), 451-456. doi: 10.1038/nature09291.

Choi, J. H., Banks, A. S., Kamenecka, T. M., Busby, S. A., Chalmers, M. J., Kumar, N., Kuruvilla, D. S., Shin, Y., He, Y., Bruning, J. B., Marciano, D. P., Cameron, M. D., Laznik, D., Jurczak, M. J., Schürer, S. C., Vidović, D., Shulman, G. I., Spiegelman, B. M. & Griffin, P. R. (2011) Antidiabetic actions of a non-agonist PPARγ ligand blocking Cdk5-mediated phosphorylation. *Nature.* 477 (7365), 477-481. doi: 10.1038/nature10383.

Damkaci, F., Szymaniak, A. A., Biasini, J. P. & Cotroneo, R. (2022) Synthesis of Thiazolidinedione Compound Library. *Compounds.* 2 (3), 182-190. doi: 10.3390/compounds2030013.

Dubois, V., Eeckhoute, J., Lefebvre, P. & Staels, B. (2017) Distinct but complementary contributions of PPAR isotypes to energy homeostasis. *Journal of Clinical Investigation.* 127 (4), 1202-1214. doi: 10.1172/JCI88894.

Frkic, R. L., Marshall, A. C., Blayo, A.-L., Pukala, T. L., Kamenecka, T. M., Griffin, P. R. & Bruning, J. B. (2018) PPARγ in Complex with an Antagonist and Inverse Agonist: a Tumble and Trap Mechanism of the Activation Helix. *iScience.* 5, 69-79. doi: 10.1016/j.isci.2018.06.012.

Hong, F., Xu, P. & Zhai, Y. (2018) The Opportunities and Challenges of Peroxisome Proliferator-Activated Receptors Ligands in Clinical Drug Discovery and Development. *International Journal of Molecular Sciences.* 19 (8), 2189. doi: 10.3390/ijms19082189.

Kalliora, C. & Drosatos, K. (2020) The Glitazars Paradox: Cardiotoxicity of the Metabolically Beneficial Dual PPARα and PPARγ Activation. *Journal of Cardiovascular Pharmacology.* 76 (5), 514-526. doi: 10.1097/FJC.0000000000000891.

Kilu, W., Merk, D., Steinhilber, D., Proschak, E. & Heering, J. (2021) Heterodimer formation with retinoic acid receptor RXRα modulates coactivator recruitment by peroxisome proliferator-activated receptor PPARγ. *Journal of Biological Chemistry.* 297 (1), 100814. doi: 10.1016/j.jbc.2021.100814.

Krishnappa, M., Patil, K., Parmar, K., Trivedi, P., Mody, N., Shah, C., Faldu, K., Maroo, S., group, f. t. P. X. s., Desai, P., Fatania, K., Murthy, S., Balamurugan, R., Agarwal, M., Singh, K. P., Kalra, G. S., Khandelwal, V., Singwala, A., Thacker, H., Tulle, R., Rao, H., Kumbla, M., Singh, P., Khatri, A., Agrawal, S., Sarkar, R. N., Agarwal, D., Bhatia, G., Agarwal, R. P., Kumar, S., Vamsi Krishna, P. R., Ajmani, A. K., Asalkar, A., Basu, I., Chatterjee, S., Pavithran, V. K., Das, R., Dharmadhikari, A., Vardhan, V., Madusudhan Babu, M., Sengupta, N., Abkari, S., Harikrishna, R., Chovatia, R. & Parmar, D. (2020) Effect of saroglitazar 2 mg and 4 mg on glycemic control, lipid profile and cardiovascular disease risk in patients with type 2 diabetes mellitus: a 56-week, randomized, double blind, phase 3 study (PRESS XII study). *Cardiovascular Diabetology.* 19 (1), 93. doi: 10.1186/s12933-020-01073-w.

Mosure, S. A., Munoz-Tello, P., Kuo, K.-T., MacTavish, B., Yu, X., Scholl, D., Williams, C. C., Strutzenberg, T. S., Bass, J., Brust, R., Deniz, A. A., Griffin, P. R. & Kojetin, D. J. (2022) *Structural basis of interdomain communication in PPARγ*. Biochemistry. [Accessed 2023-06-17 13:58:56]

Tassopoulou, V. P., Tzara, A. & Kourounakis, A. P. (2022) Design of Improved Antidiabetic Drugs: A Journey from Single to Multitarget Agents. *ChemMedChem.* 17 (23). doi: 10.1002/cmdc.202200320.

Chapter 8

Abbreviations

ABC Adenosine triphosphate – Binding Cassette

ACSL Long Chain Acetyl-Coa Synthetases

AD Alzheimer's Disease

AF1 Activation Function 1

AF2 Activation Function 2

ANGPTL Angiopoietin like Protein

AP-1 Activator Protein 1

APO Apolipoproteins

BCL B Cell Lymphoma

C3 Complement Component 3

CACT Carnitine-Acylcarnitine Translocase

CDK Cyclin-Dependent Kinases

CNS Central Nervous System

CPT Carnitine Palmitoyltransferases

CVD Cardiovascular Disease

DALY Disability-Adjusted Life Year

DBD DNA Binding Domain

DR Direct Repeat

EGFR Epidermal Growth Factor Receptor

ER Estrogen Receptor

ERK Extracellular Signal-Regulated Kinases

FAAR Fatty Acid Activated Receptor

FABP Fatty Acid Binding Protein

FAO Fatty Acid Oxidation

FATP Fatty Acid Transport Protein

FBP1 Fructose Biphosphatase 1

FGF Fibroblast Growth Factor

FRET Förster Resonance Energy Transfer

GYK Glycerol Kinase

H Helix

HAT Histone Acetyl Transferase

HDAC Histone Deacetylases

HDL High Density Lipoprotein

HDX Hydrogen Deuterium Exchange

HMG-CoA 3-Hydroxy-3-Methylglutaryl Coenzyme A

ICAM Intercellular Cell Adhesion Molecule

IκBα Nuclear Factor of Kappa Light Polypeptide Gene Enhancer in B-cells Inhibitor, Alpha

IL Interleukin

IL1-ra Interleukin-1 Receptor Antagonist

IRS Insulin Receptor Substrate

JKN p38/ c-Jun N-terminal Kinases

LBD Ligand Binding Domain

LC3 Microtubule-Associated Proteins 1A/1B Light Chain 3B

LPL Lipoprotein Lipase

LXR Liver X Receptors

MAPK Mitogen-Activated Protein Kinases

MBL Mannose Binding Lectin

MCT Monocarboxylate Transporter

MetS Metabolic Syndrome

MNS Mental and Neurological and Substance abuse

MuRF Muscle specific RING finger

MS Multiple Sclerosis

NAFLD Non-Alcoholic Fatty Liver Disease

NCoR Nuclear CoRepressor

NES Nuclear Export Signal

NF-κB Nuclear Factor Kappa-Light-Chain-Enhancer of Activated B Cells

NLRP3 NLR family pyrin domain containing 3

NLS Nuclear Localization Signal

Ni-NTA Nickel- Nitrilotriacetic Acid

NPC1L1 Niemann-Pick C1-like 1

NR Nuclear Receptor

NR1C1 Nuclear Receptor Subfamily 1 Group C

PBC Primary Biliary Cholangitis

Pck1 Phosphoenol Pyruvate Carboxykinase 1

PDC Pyruvate Dehydrogenase Complex

PDK Pyruvate Dehydrogenase Kinase

PGC1α PPARγ coactivator 1α

(m/h) PPAR (mouse/human) Peroxisome Proliferator Activated Receptor

PPRE PPAR Response Element

PR Progesterone Receptor

PRE Progesterone Receptor Element

PTM Post-Translational Modification

RE Response Element

ROS Reactive Oxygen Species

RXR Retinoid X Receptor

SCD Stearoyl-CoA 9-Desaturase

SENP2 SUMO-specific protease 2

SMRT Silencing Mediator for Retinoid and Thyroid hormone receptor

SRC Steroid Receptor Complex

SREBP Sterol Regulatory Element-Binding Protein

STAT Signal Transducer and Activator of Transcription

SUMO Small Ubiquitin-like Modifier

T2D Type 2 Diabetes

TME Tumour Microenvironment

TR-FRET Time Resolved Förster Resonance Energy Transfer

TRIM Tripartite motif containing

TSA Thermal Shift Assay

TZD Thiazolidoine

UCP Uncoupling Protein

US United States

VCAM Vascular Cell Adhesion Molecule

VDR Vitamin D Receptor